Computational and Mathematical Methods in Medicine

Machine Learning for Human-Machine Interaction

Lead Guest Editor: Kelvin Wong
Guest Editors: Simon Fong and Dhanjoo N. Ghista

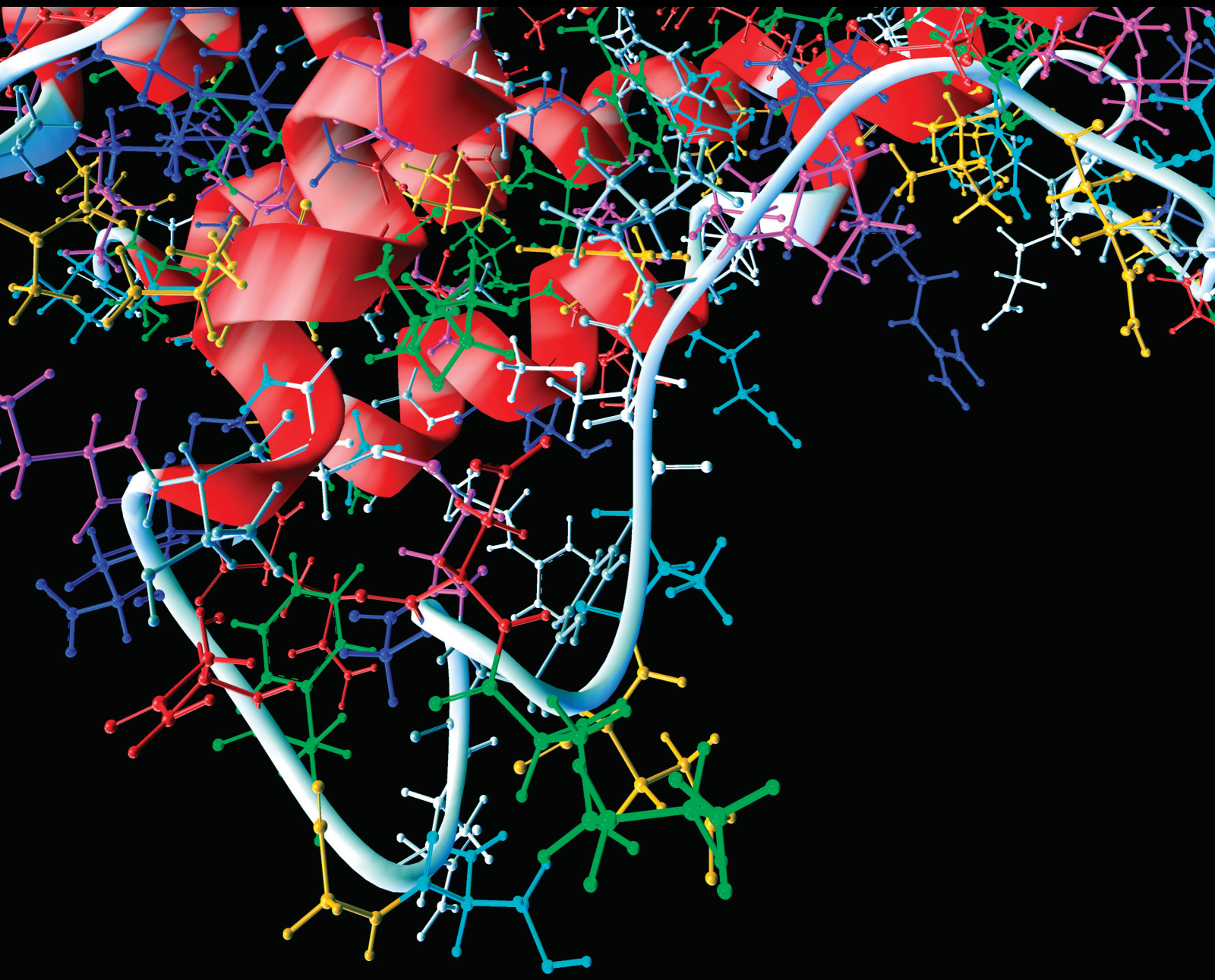

Machine Learning for Human-Machine Interaction

Computational and Mathematical Methods in Medicine

Machine Learning for Human-Machine Interaction

Lead Guest Editor: Kelvin Wong
Guest Editors: Simon Fong and Dhanjoo N. Ghista

Contents

Contents

Contents

Hindawi
Computational and Mathematical Methods in Medicine
Volume 2022, Article ID 4316507, 10 pages
https://doi.org/10.1155/2022/4316507

Research Article

Diagnosing Diabetic Retinopathy in OCTA Images Based on Multilevel Information Fusion Using a Deep Learning Framework

Qiaoyu Li,[1] Xiao-rong Zhu,[2,3] Guangmin Sun,[1] Lin Zhang,[2,3] Meilong Zhu,[1] Tian Tian,[1] Chenyu Guo,[1] Sarah Mazhar,[1] Jin-Kui Yang,[2,3] and Yu Li[1]

[1]*Faculty of Information Technology, Beijing University of Technology, Beijing 100124, China*
[2]*Department of Endocrinology, Beijing Tongren Hospital, Capital Medical University, Beijing 100730, China*
[3]*Beijing Diabetes Institute, Beijing 100730, China*

Correspondence should be addressed to Guangmin Sun; gmsun@bjut.edu.cn and Yu Li; yuli@bjut.edu.cn

Received 20 November 2021; Accepted 18 July 2022; Published 4 August 2022

Academic Editor: A. S. Albahri

Objective. As an extension of optical coherence tomography (OCT), optical coherence tomographic angiography (OCTA) provides information on the blood flow status at the microlevel and is sensitive to changes in the fundus vessels. However, due to the distinct imaging mechanism of OCTA, existing models, which are primarily used for analyzing fundus images, do not work well on OCTA images. Effectively extracting and analyzing the information in OCTA images remains challenging. To this end, a deep learning framework that fuses multilevel information in OCTA images is proposed in this study. The effectiveness of the proposed model was demonstrated in the task of diabetic retinopathy (DR) classification. *Method*. First, a U-Net-based segmentation model was proposed to label the boundaries of large retinal vessels and the foveal avascular zone (FAZ) in OCTA images. Then, we designed an isolated concatenated block (ICB) structure to extract and fuse information from the original OCTA images and segmentation results at different fusion levels. *Results*. The experiments were conducted on 301 OCTA images. Of these images, 244 were labeled by ophthalmologists as normal images, and 57 were labeled as DR images. An accuracy of 93.1% and a mean intersection over union (mIOU) of 77.1% were achieved using the proposed large vessel and FAZ segmentation model. In the ablation experiment with 6-fold validation, the proposed deep learning framework that combines the proposed isolated and concatenated convolution process significantly improved the DR diagnosis accuracy. Moreover, inputting the merged images of the original OCTA images and segmentation results further improved the model performance. Finally, a DR diagnosis accuracy of 88.1% (95%CI ± 3.6%) and an area under the curve (AUC) of 0.92 were achieved using our proposed classification model, which significantly outperforms the state-of-the-art classification models. As a comparison, an accuracy of 83.7 (95%CI ± 1.5%) and AUC of 0.76 were obtained using EfficientNet. *Significance*. The visualization results show that the FAZ and the vascular region close to the FAZ provide more information for the model than the farther surrounding area. Furthermore, this study demonstrates that a clinically sophisticated designed deep learning model is not only able to effectively assist in the diagnosis but also help to locate new indicators for certain illnesses.

1. Introduction

Diabetic retinopathy (DR) is a microvascular impairment of the fundus caused by diabetes and is one of the leading causes of blindness and visual impairment [1]. DR has various and complex pathogenesis that are still unclear. For the diagnosis of DR, the most common methods are fluorescence fundus angiography (FFA) and indocyanine green angiography (ICGA) [2]. Both of these methods, however, are invasive medical imaging examinations. Moreover, the leakage of contrast media and retinal hemorrhage may disturb the media transparency, blurring the image of retinal vessels. As a result, the lesion area is difficult to precisely identify and assess.

Optical coherence tomography (OCT) is a new noninvasive imaging technique that can be used to effectively observe subtle changes in the superficial and deep capillary plexus of the human retinal microvasculature and has

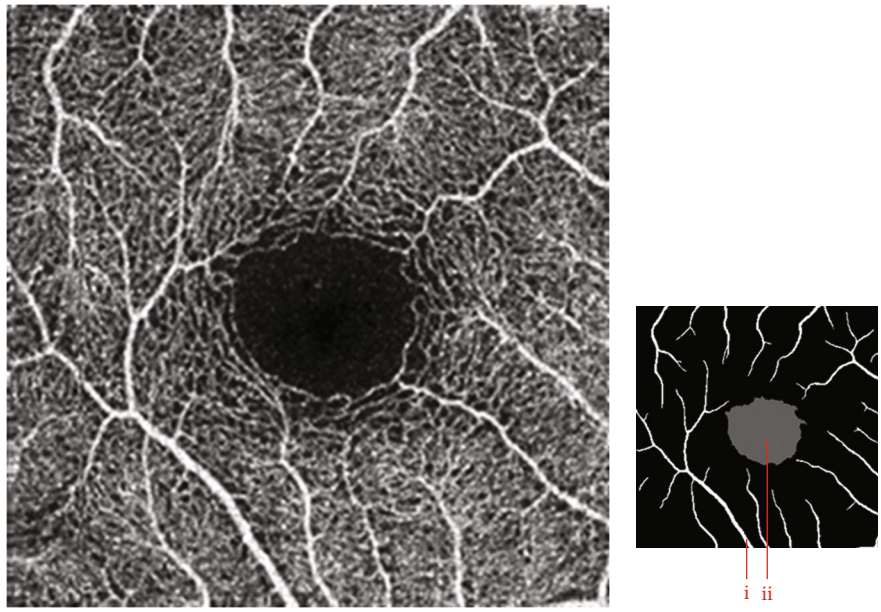

Figure 1: Examples of the OCTA image and the mask image. (a) OCTA image. (b) Mask image of (i) the main vessels (surrounding area) and (ii) the FAZ (center).

become popular in recent years [3]. As an extension of OCT, optical coherence tomographic angiography (OCTA) is used to capture and analyze the movement of blood cells in the field of vision by repeatedly capturing images of the same retinal position to obtain an image of the capillary network [4]. Studies have shown that several fundus diseases, such as age-related macular degeneration (AMD) [5], choroidal neovascularization (CNV) [6, 7], and retinal arterial macroaneurysms (RAM) [8], can be detected using OCTA images. OCTA is sensitive to the deterioration of vascular networks, hence providing a novel way of monitoring and evaluating the progression of DR [9, 10]. Liu et al. compared several machine learning models for DR discrimination based on 3 $\times$ 3 mm OCTA scans of different segmentation layers, including the superficial vascular plexus (SVP), deep vascular plexus (DVP), and retinal vascular network (RVN). The best DR diagnosis performance, with an overall accuracy of 0.82 and AUC of 0.83, was obtained by logistic regression regularized with the elastic net penalty (LR-EN) [11]. Abdelsalam and Zahran used a support vector machine (SVM) to diagnose early nonproliferative diabetic retinopathy (NPDR) based on multifractal geometry and obtained promising results [12]. However, due to the special imaging mechanism of OCTA, conventional image analysis technology does not always work well on OCTA images, and very different features are extracted. Moreover, the image quality of OCTA images is largely affected by factors such as a turbid refractive medium, image noise, and artifacts of vascular projection. Consequently, studies are urgently needed on feature extraction and analysis techniques for OCTA images.

Compared with traditional machine learning algorithms, deep learning shows higher performance in analyzing medical images [13–15]. The deep convolutional neural network (CNN) is one of the most common methods used to implement image segmentation and classification due to its powerful feature extraction and function fitting abilities [16–20]. Ma et al. published a dedicated Retinal OCTA SEgmentation (ROSE) dataset and proposed split-based coarse segmentation modules for vessel segmentation [21]. CNNs have also been considered for DR classification by jointly using en-face OCT and OCTA [22]. Currently, the number of OCTA data samples with high-quality labels is much smaller than that of fundus images; therefore, better utilization of multilevel information and a combination of domain knowledge is the key to improving deep learning-based OCTA analysis techniques.

In this paper, we proposed a deep learning framework that extracts and analyzes the multilevel information in OCTA images and demonstrated its advantage in DR diagnosis. We presented a segmentation model based on U-Net to segment the boundaries of vessels and the foveal avascular zone (FAZ) in OCTA images. Then, a new deep learning framework was proposed to predict the class of OCTA images based on fusing the original OCTA image and the segmentation results. A visualization method was used to indicate the regions of interest (ROIs) in the CNN model to locate the key lesion areas that are focused on by the prediction model to provide guidance for researchers on the key features for DR diagnosis.

2. Materials and Methods

2.1. Dataset. The OCTA-500 dataset compiled by Li et al. [23] was the dataset that was used in this study. Three different OCTA data projections were provided in this dataset. In this study, we used the maximum projection between ILM and OPL (B5), which is generated by the maximum projection of the inner retina and can clearly show the vascular

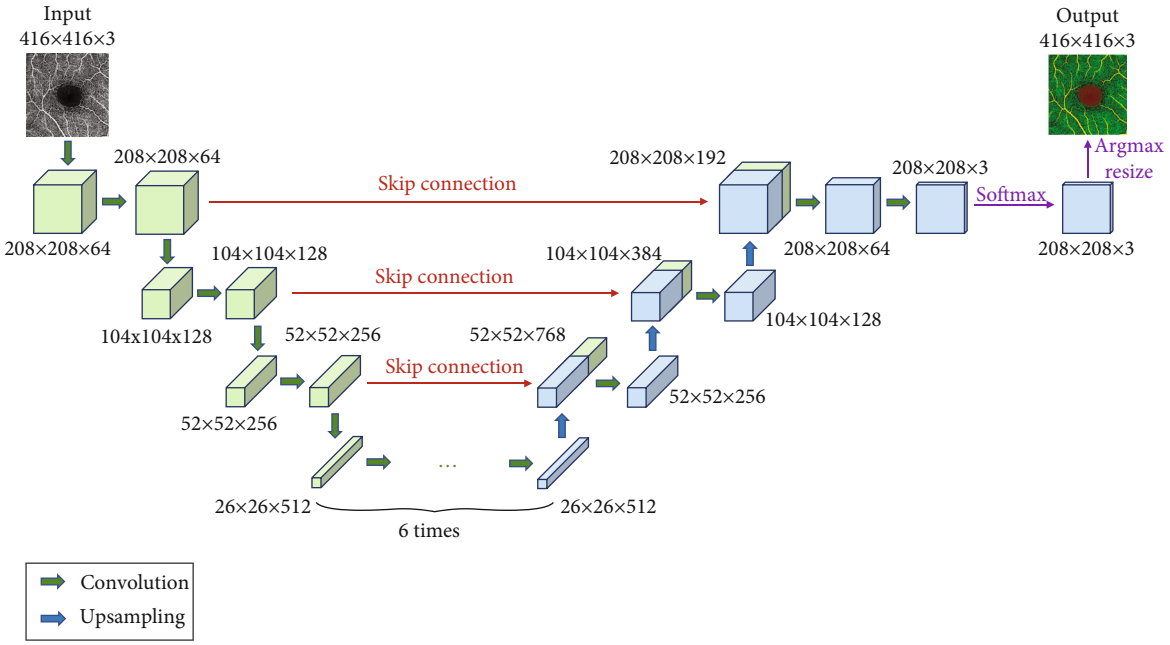

Figure 2: The segmentation model in this study based on the U-Net architecture.

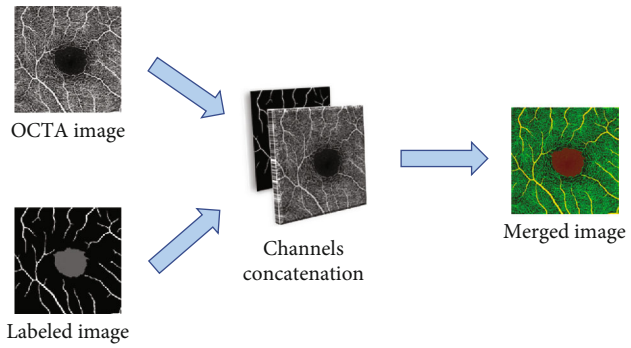

Figure 3: The process of obtaining a merged image with an OCTA image and a labeled image by channel concatenation.

morphology of the inner retina and the shape of the FAZ. Therefore, it is the most frequently used OCTA projection map for retinal vessel and FAZ segmentation [23].

The dataset contains two subsets with different fields of view (FOVs). As shown in Figure 1(a), the white parts in the image are vessels, while the black zone in the center that is surrounded by vessels is the FAZ, which is a concave zone in the postretinal area that is approximately 2 mm in diameter and does not contain any vessels. One data subset had a 6 mm × 6 mm FOV, while the other subset had a 3 mm × 3 mm FOV. Fifty-seven DR samples and 244 normal samples were labeled in the dataset. The DR diagnosis was provided by ophthalmologists. Moreover, the masking labels of vessels and FAZ were provided. Figure 1(b) shows one of the mask images: the white parts denote vessels, the gray part denotes the FAZ, and the black part is the background.

2.2. Segmentation of the Vessels and FAZ. To acquire the labeled image that indicates the vessels and FAZ, we proposed a segmentation method based on the U-Net [24] architecture, as shown in Figure 2. The OCTA image and its corresponding mask image are used as the input and ground truth, respectively. The network architecture can be divided into contracting and expansive paths. More specifically, the contracting path consists of a series of convolutional layers that reduce the size of the feature map. The expansive path is composed of upsampling operations and convolutional layers. The upsampling operations expand the size of the feature map, and the convolutional layers reduce the number of feature channels. The feature maps with the same size from contracting and expansive paths are concatenated by a skip connection. Eventually, the final segmentation result is given by the softmax and ArgMax operations.

The loss function is designed as follows:

$$L = -\frac{1}{H \times W}\left[\sum_{m \in H}\sum_{n \in W} y_{m,n} \log f_{m,n}(x) + \left(1 - y_{m,n}\right) \log\left(1 - f_{m,n}(x)\right)\right], \tag{1}$$

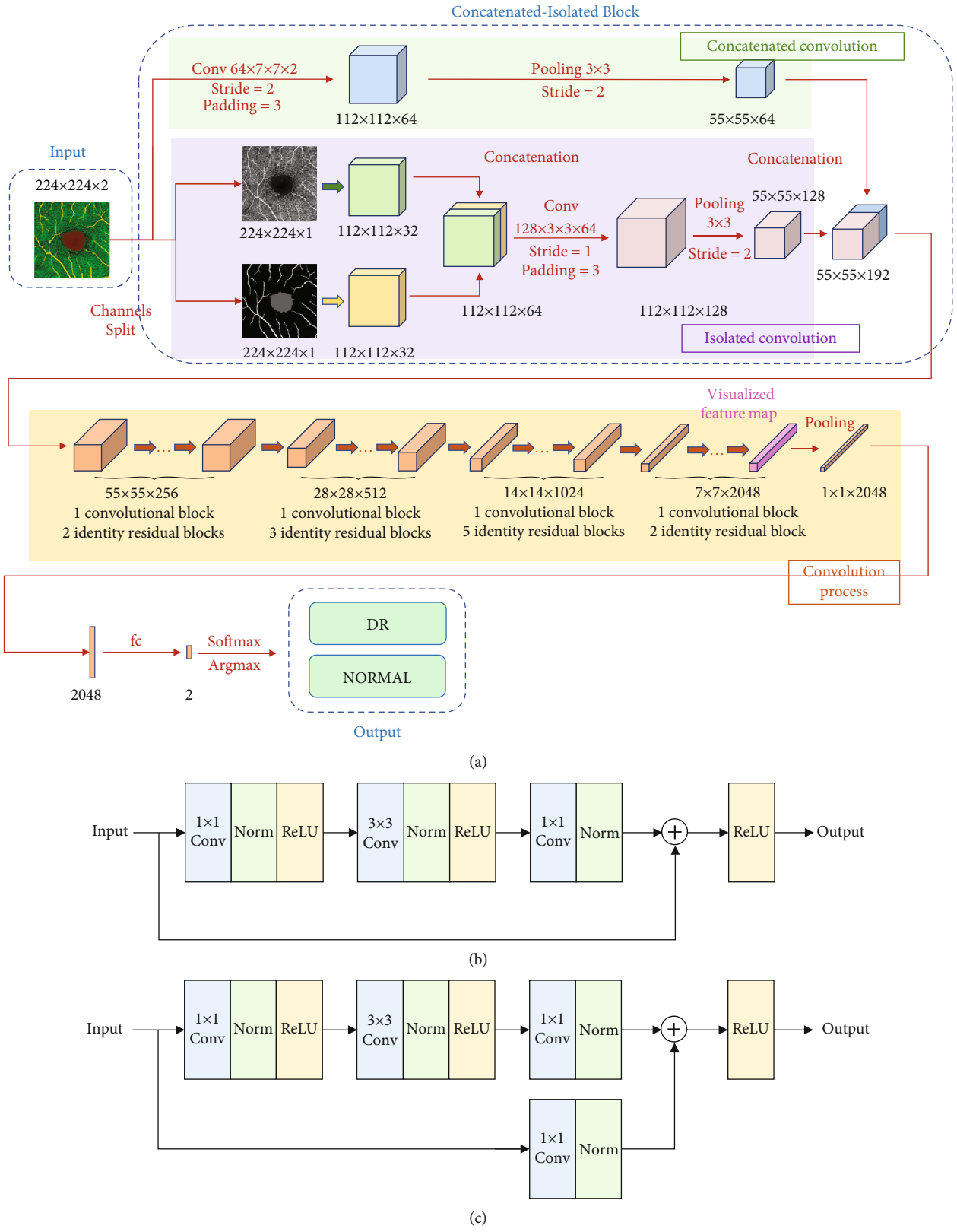

Figure 4: The CNN model used in this paper. (a) The total architecture, which consists of convolutional blocks and identity residual blocks in the convolution process. (b) The identity residual block. (c) The convolutional block.

where H denotes the height of the input image, W denotes the width, $y_{m,n}$ denotes the true label of the sample, and $f_{m,n}(x)$ denotes the output of the segmentation model.

2.3. Image Channel Concatenation. The labeled images that indicate the vessels and FAZ can be used as expert opinions (i.e., domain knowledge), which provide more effective information to the deep learning model. Therefore, the labeled images are input with the OCTA images as additional domain knowledge. These two types of images are single-channel images. Therefore, they can be concatenated by the channel dimension to obtain double-channel images. In other words, the labeled image and OCTA image are two independent channels of the merged image. The concatenation process is shown in Figure 3.

2.4. Deep Learning Framework Based on Multilevel Information Fusion. The proposed deep learning framework for DR diagnosis in this study is designed based on the ResNet50 [25] architecture, and its structure is shown in Figure 4(a). To sufficiently extract information from the merged image, we designed a deep learning framework with an isolated concatenated block (ICB) architecture based on ResNet50. More specifically, in the isolated convolutional process, the input is a double-channel image composed of the original OCTA image and labeled image. They are separately processed by convolutional layers to extract the primary features. The two feature maps are concatenated to form a composite feature map. The new feature map is input into a convolutional layer and a pooling layer for information integration and parameter reduction. In the concatenated convolutional process, the input double-channel image is directly processed by a convolutional layer with a pooling layer to resize the feature map and make it consistent with the output of the isolated convolutional process. Eventually, the output feature maps of the isolated and concatenated convolutional processes are concatenated.

Then, the feature maps are processed by the following convolution process. More specifically, the convolution process is composed of four-stage residual convolutional blocks according to ResNet50. These blocks are made up of a convolutional block and several identity residual blocks. These block types are shown in Figures 4(b) and 4(c). Eventually, the classification results are given by a full connection layer followed by a softmax operation.

The loss function is designed as follows:

$$L = -\sum_{c \in D} t_c \log f_c(x), \tag{2}$$

where c denotes the current class, D denotes all classes of the whole dataset, t_c denotes the true label of the sample, and $f_c(x)$ denotes the output of the classification model.

2.5. Model Visualization. In this study, we used gradient-weighted class activation mapping (Grad-CAM) [26] to visually analyze our model. Studies have shown that convolutional layers can retain spatial information [27, 28], while deeper layers contain more advanced feature information [29, 30]. Therefore, we focused on the last convolutional layer, which indicates the location of the region that is important for determining classification.

The class activation map P_C is calculated by the following algorithm:

$$P_C = \sigma\left(\sum_l \left(\frac{1}{N}\sum_i \sum_j \frac{\partial f_C}{\partial M_{ij}^l}\right) M^l\right), \tag{3}$$

where M^l denotes the lth channel of the output feature map, f_C denotes the output of the sigmoid function of the current class, N denotes the number of feature points in the feature map, σ denotes the activation function, and a rectified linear unit (ReLU) is used in this study.

Table 1: The segmentation accuracy and IOU for every class using our model.

Class	Accuracy	IOU
Background	93.2%	92.6%
Vessels	93.8%	54.1%
FAZ	92.3%	84.6%
Average	93.1%	77.1%

3. Results and Discussion

A total of 301 images were used for the training and testing process in the cross-validation. Among these images, the ophthalmologists labeled 57 images as DR and 244 as normal (the ground truth).

An accuracy of 93.1% and a mean intersection over union (mIOU) of 77.1% were achieved using our segmentation model. These values were calculated as the average of three classes. As shown in Table 1, the segmentation task includes three classes, namely, the background, vessels, and FAZ classes. The classification accuracy is 93.2% for the background, 93.8% for vessels, and 92.3% for the FAZ. Several typical segmentation results are shown in Table 2.

An ablation experiment was conducted to verify the performance of the proposed classification model. Three models were compared in the ablation test, namely, a model with only an isolated convolution process, with only a concatenated convolution process, and with both isolated and concatenated convolution processes. Obviously, the model using only the concatenated convolution process is equivalent to ResNet50, and the model using both isolated and concatenated convolution processes is the proposed model. Moreover, images with only segmentation results, only OCTA images, and merged images were taken as the input of the above three classification models. As shown in Table 3, the best accuracy of 88.1% with 95%CI ± 3.6% is achieved using the model using both isolated and concatenated convolution processes with merged images as the input. We also found that, given the same input, the model using both isolated and concatenated convolution processes achieved the best performance. While using the

Table 2: Examples of segmentation results.

Case	OCTA image	Label	Segmentation result
Case 1	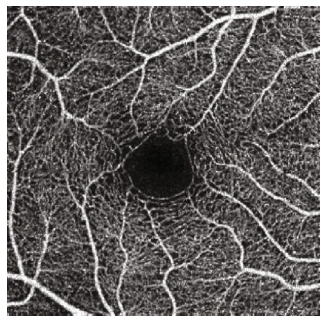	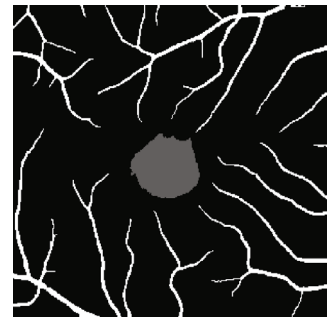	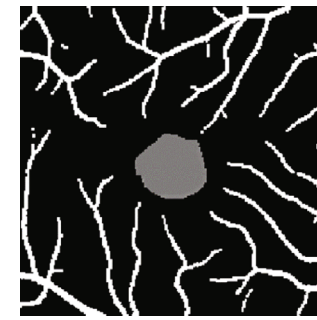
Case 2	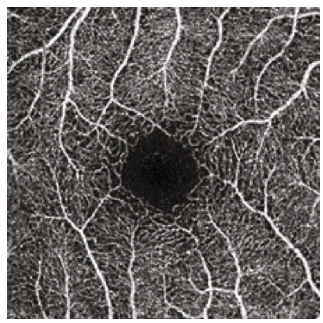	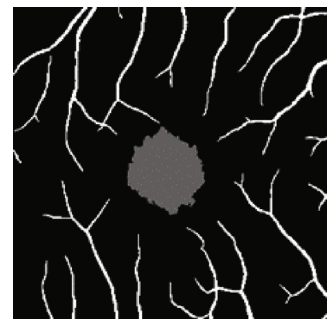	
Case 3	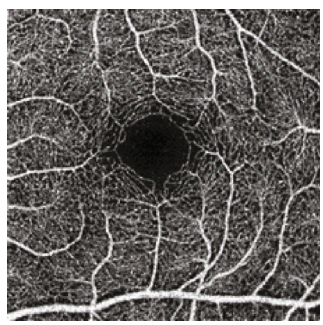		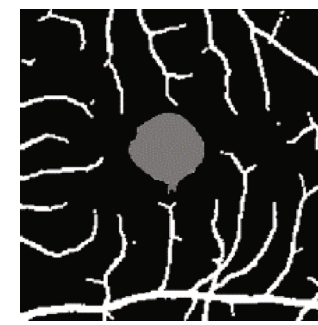

Table 3: The ablation experiment results of our classification model.

Input	Model	Accuracy
Segmentation results	Concatenated convolution (ResNet50)	75.2% (95%CI ± 7.5%)
	Isolated convolution	78.9% (95%CI ± 4.6%)
	Isolated and concatenated convolution	80.6% (95%CI ± 2%)
OCTA images	Concatenated convolution (ResNet50)	77.6% (95%CI ± 6.2%)
	Isolated convolution	84.4% (95%CI ± 2.7%)
	Isolated and concatenated convolution	87.8% (95%CI ± 3.1%)
Merged images	Concatenated convolution (ResNet50)	79.6% (95%CI ± 3.6%)
	Isolated convolution	84.7% (95%CI ± 2.0%)
	Isolated and concatenated convolution	88.1% (95%CI ± 3.6%)

same model, the highest accuracy for each model was obtained using the merged images. Sixfold cross-validation was applied for the above analysis.

We compared our model with other existing models on the DR classification task for the same dataset with 6-fold cross-validation. In this comparison, the inputs for every model were merged images. As shown in Table 4, the highest accuracy of 88.1% with 95%CI ± 3.6% was achieved using our classification model. The sensitivity of our proposed model (51.8%) is also significantly larger than other methods, with a comparable specificity. Due to the unbalanced number of positive and negative training samples,

Table 4: The classification results of several CNN models.

Model	Accuracy	Sensitivity	Specificity
EfficientNet	83.7% (95%CI ± 1.5%)	13.0% (95%CI ± 13.1%)	99.6% (95%CI ± 0.8%)
MobileNet v2	81.6% (95%CI ± 1.0%)	3.7% (95%CI ± 4.6%)	99.2% (95%CI ± 13.1%)
ResNet50	79.6% (95%CI ± 3.6%)	20.4% (95%CI ± 19.8%)	93.7% (95%CI ± 8.0%)
ShuffleNet v2	82.0% (95%CI ± 1.2%)	24.1% (95%CI ± 19.0%)	95.0% (95%CI ± 4.6%)
SqueezeNet	82.7% (95%CI ± 1.4%)	13.0% (95%CI ± 11.8%)	98.3% (95%CI ± 1.6%)
Ours	88.1% (95%CI ± 3.6%)	51.8% (95%CI ± 13.4%)	96.3% (95%CI ± 2.8%)

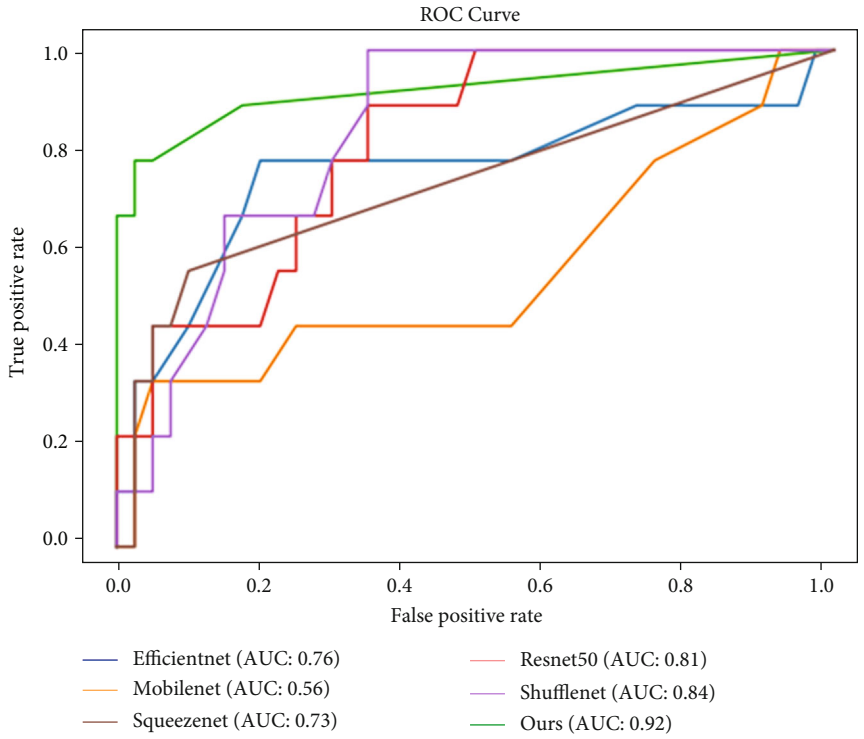

Figure 5: The ROC curves and AUCs of several CNN models.

the proposed model tends to underestimate the number of positive samples, which limits its sensitivity. However, this effect can be easily alleviated by setting another judging threshold to meet the need for a high sensitivity requirement of clinical diagnosis.

The receiver operating characteristic (ROC) curves, which more comprehensively represent the performance of the classification model, of the above models are shown in Figure 5. The largest area under the curve (AUC) of 0.92 was obtained using our model.

The class activation maps of the last feature map were generated by Grad-CAM. The weight heatmaps were added to the merged images to indicate the ROIs for the classification model, as shown in Figure 6. Features in the region of the higher heatmap (in red) have a larger impact on the classification judgment. It can be observed that most red-colored regions are close to the central part of the images, which indicates that the FAZ and the vascular area around it are the most important regions considered by the model for DR classification. In other words, we found that pathological changes in DR may appear around the FAZ region based on the visualization results. In addition, compared to the narrow FOV images, the red color in the activation map has a smaller proportion of the whole image in the wide FOV image. We will explore more specific pathological changes through more experiments and by consulting medical experts in our future work.

We performed an experiment on another OCTA dataset, and the results are shown in Table 5. It was found that the highest accuracy was also achieved by using our model.

4. Conclusion

Deep learning can be used to analyze OCTA images by combining multilevel information and domain knowledge. The key discoveries in this study can be summarized as follows:

(i) The proposed deep learning framework with isolated and concatenated convolution processes

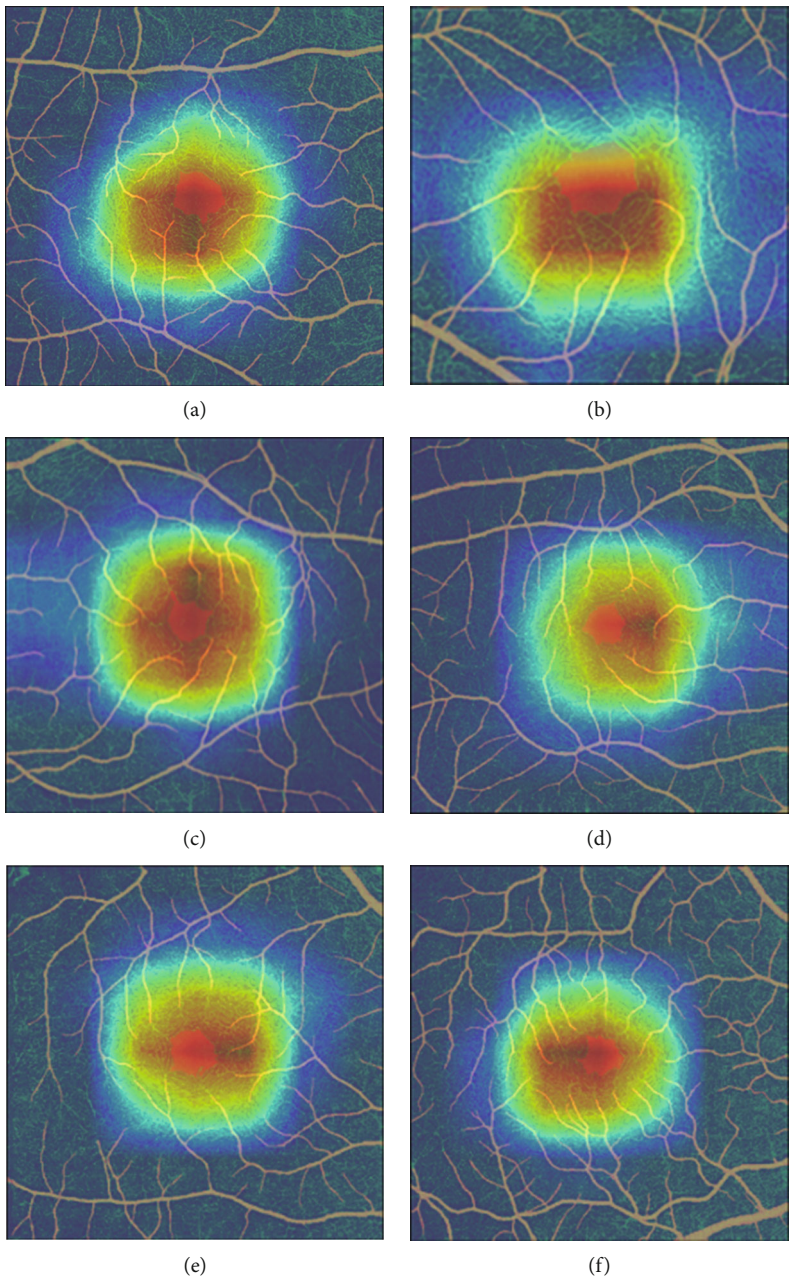

Figure 6: Examples of the visualization results.

Table 5: The classification results on another OCTA dataset.

Model	Accuracy	Sensitivity	Specificity
EfficientNet	68.2% (95%CI ± 5.3%)	56.7% (95%CI ± 21.0%)	64.8% (95%CI ± 12.7%)
MobileNet v2	66.2% (95%CI ± 5.2%)	68.9% (95%CI ± 24.0%)	53.7% (95%CI ± 22.0%)
ResNet50	75.8% (95%CI ± 2.7%)	62.2% (95%CI ± 16.1%)	69.4% (95%CI ± 25.3%)
ShuffleNet v2	73.8% (95%CI ± 3.3%)	62.2% (95%CI ± 30.1%)	71.3% (95%CI ± 16.0%)
SqueezeNet	57.0% (95%CI ± 5.0%)	0.9% (95%CI ± 17.4%)	98.2% (95%CI ± 3.6%)
Ours	76.0% (95%CI ± 5.8%)	76.2% (95%CI ± 11.8%)	75.9% (95%CI ± 14.3%)

significantly improved the accuracy of DR classification

(ii) Fusing the information from the original OCTA image and labeled images that indicate the FAZ and vessel parts, which work as domain knowledge, provided more features and helped to lessen the DR classification errors

(iii) Visualization analysis confirmed that the FAZ and the vascular region around it contain more useful information, such as the shape of the FAZ and the density of vessels around it, than the surrounding areas to distinguish DR samples from normal samples

The proposed analysis not only demonstrated the effectiveness of the deep learning algorithm and multilevel information fusion on DR diagnosis but also highlighted a potential indicator for DR in OCTA images. Hence, it was found that images with a larger FAZ area or a smaller density of vessels around the FAZ may be highly associated with the risk of DR in fundus screening. In the future, a study will be conducted on larger multicenter datasets, and the potential of the proposed deep learning framework in other related biomedical image analysis applications will also be explored.

Data Availability

The OCTA-500 dataset is publicly available at http://ieee-dataport.org/open-access/octa-500. The U-Net framework can be accessed through https://github.com/bubbliiiing/Semantic-Segmentation/tree/master/Unet_Mobile. The full code of the proposed method is available at https://github.com/liyuatbjut/OCTA-Analysis.

Conflicts of Interest

The authors declare that there is no conflict of interest regarding the publication of this paper.

Authors' Contributions

Qiaoyu Li and Xiao-rong Zhu contributed equally.

Acknowledgments

This work was supported by grants from the National Key R&D Program of China (2017YFC0909600), the National Natural Science Foundation of China (8151101058, 11527801), and the Strategic Priority Research Program of the Chinese Academy of Sciences (XDB41020104).

References

[1] J. H. Kempen, B. J. O'colmain, C. Leske, S. M. Haffner, and D. S. Friedman, "The prevalence of diabetic retinopathy among adults in the United States," *Archives of Ophthalmology*, vol. 122, no. 4, pp. 552–563, 2004.

[2] S. Wang, Y. Zuo, N. Wang, and B. Tong, "Fundus fluorescence angiography in diagnosing diabetic retinopathy," *Pakistan Journal of Medical Sciences*, vol. 33, no. 6, pp. 1328–1332, 2017.

[3] H. Akil, S. Karst, M. Heisler, M. Etminan, E. Navajas, and D. Maberley, "Application of optical coherence tomography angiography in diabetic retinopathy: a comprehensive review," *Canadian Journal of Ophthalmology*, vol. 54, no. 5, pp. 519–528, 2019.

[4] K. Sambhav, S. Grover, and K. V. Chalam, "The application of optical coherence tomography angiography in retinal diseases," *Survey of Ophthalmology*, vol. 62, no. 6, pp. 838–866, 2017.

[5] N. Phasukkijwatana, A. S. Tan, X. Chen, K. B. Freund, and D. Sarraf, "Optical coherence tomography angiography of type 3 neovascularisation in age-related macular degeneration after antiangiogenic therapy," *British Journal of Ophthalmology*, vol. 101, no. 5, pp. 597–602, 2017.

[6] Y. Jia, S. T. Bailey, D. J. Wilson et al., "Quantitative optical coherence tomography angiography of choroidal neovascularization in age-related macular degeneration," *Ophthalmology*, vol. 121, no. 7, pp. 1435–1444, 2014.

[7] A. Miere, H. Oubraham, F. Amoroso et al., "Optical coherence tomography angiography to distinguish changes of choroidal neovascularization after anti-VEGF therapy: monthly loading dose versus pro re nata regimen," *Journal of Ophthalmology*, vol. 2018, Article ID 3751702, 7 pages, 2018.

[8] L. H. Limia and L. P. Cunha, "Angiographie par tomographie a coherence optique dans un cas de macroanevrismes arteriels retiniens multiples," *Journal Françaisd'Ophtalmologie*, vol. 43, no. 5, pp. 442-443, 2020.

[9] Y. Wang and Y. Luo, "The applications of optical coherence tomography angiography in diabetic retinopathy," *Annals of Eye Science*, vol. 2, no. 7, p. 52, 2018.

[10] G. Liu, D. Xu, and F. Wang, "New insights into diabetic retinopathy by OCT angiography," *Diabetes Research and Clinical Practice*, vol. 142, pp. 243–253, 2018.

[11] Z. Liu, C. Wang, X. Cai, H. Jiang, and J. Wang, "Discrimination of diabetic retinopathy from optical coherence tomography angiography images using machine learning methods," *IEEE Access*, vol. 9, pp. 51689–51694, 2021.

[12] M. M. Abdelsalam and M. A. Zahran, "A novel approach of diabetic retinopathy early detection based on multifractal geometry analysis for OCTA macular images using support vector machine," *IEEE Access*, vol. 9, pp. 22844–22858, 2021.

[13] Y. LeCun, Y. Bengio, and G. Hinton, "Deep learning," *Nature*, vol. 521, no. 7553, pp. 436–444, 2015.

[14] J. Ker, L. Wang, J. Rao, and T. Lim, "Deep learning applications in medical image analysis," *IEEE Access*, vol. 6, pp. 9375–9389, 2017.

[15] N. Chakrabarty, "A deep learning method for the detection of diabetic retinopathy," in *2018 5th IEEE Uttar Pradesh Section International Conference on Electrical, Electronics and Computer Engineering (UPCON)*, pp. 1–5, Gorakhpur, India, 2018.

[16] N. Ma, X. Zhang, H. Zheng, and J. Sun, "ShuffleNet v2: practical guidelines for efficient CNN architecture design," in *Computer Vision – ECCV 2018*, pp. 122–138, Springer, Cham, Munich, Germany, 2018.

[17] M. Sandler, A. Howard, M. Zhu, A. Zhmoginov, and L. C. Chen, "MobileNetV2: inverted residuals and linear bottlenecks," in *2018 IEEE/CVF Conference on Computer Vision*

and Pattern Recognition, pp. 4510–4520, Salt Lake City, United States, 2018.

[18] F. N. Iandola, S. Han, M. W. Moskewicz, K. Ashraf, W. J. Dally, and K. Keutzer, "SqueezeNet: AlexNet-level accuracy with 50x fewer parameters and <0.5MB model size," 2016, https://arxiv.org/abs/1602.07360.

[19] M. Tan and Q. Le, "EfficientNet: rethinking model scaling for convolutional neural networks," 2019, https://arxiv.org/abs/1602.07360.

[20] W. Rawat and Z. Wang, "Deep convolutional neural networks for image classification: a comprehensive review," *Neural Computation*, vol. 29, no. 9, pp. 2352–2449, 2017.

[21] Y. Ma, H. Hao, J. Xie et al., "ROSE: a retinal OCT-angiography vessel segmentation dataset and new model," *IEEE Transactions on Medical Imaging*, vol. 40, no. 3, pp. 928–939, 2021.

[22] P. Zang, L. Gao, T. T. Hormel et al., "DcardNet: diabetic retinopathy classification at multiple levels based on structural and angiographic optical coherence tomography," *IEEE Transactions on Biomedical Engineering*, vol. 68, no. 6, pp. 1859–1870, 2021.

[23] M. Li, Y. Chen, Z. Ji, K. Xie, and S. Li, "Image projection network: 3D to 2D image segmentation in OCTA images," *IEEE Transactions on Medical Imaging*, vol. 39, no. 11, pp. 3343–3354, 2020.

[24] O. Ronneberger, P. Fischer, and T. Brox, "U-Net: convolutional networks for biomedical image segmentation," in *International Conference on Medical image computing and computer-assisted intervention*, pp. 234–241, Munich, Germany, 2015.

[25] K. He, X. Zhang, S. Ren, and J. Sun, "Deep residual learning for image recognition," in *Proceedings of the IEEE Conference on Computer Vision and Pattern Recognition*, pp. 770–778, 2016.

[26] R. R. Selvaraju, M. Cogswell, A. das, R. Vedantam, D. Parikh, and D. Batra, "Grad-CAM: visual explanations from deep networks via gradient-based localization," *International Journal of Computer Vision*, vol. 128, no. 2, pp. 336–359, 2020.

[27] B. Zhou, A. Khosla, A. Lapedriza, A. Oliva, and A. Torralba, "Learning deep features for discriminative localization," in *Proceedings of the IEEE conference on Computer Vision and Pattern Recognition*, pp. 2921–2929, Las Vegas, United States, 2016.

[28] W. Xiong, B. Du, L. Zhang, R. Hu, and D. Tao, "Regularizing deep convolutional neural networks with a structured decorrelation constraint," in *2016 IEEE 16th International Conference on Data Mining (ICDM)*, pp. 519–528, Barcelona, Spain, 2016.

[29] A. Khan, A. Sohail, U. Zahoora, and A. S. Qureshi, "A survey of the recent architectures of deep convolutional neural networks," *Artificial Intelligence Review*, vol. 53, no. 8, pp. 5455–5516, 2020.

[30] M. Zeiler and R. Fergus, "Visualizing and understanding convolutional networks," in *European conference on computer vision*, vol. 8689, pp. 818–833, Zurich, Switzerland, 2014.

Hindawi
Computational and Mathematical Methods in Medicine
Volume 2022, Article ID 3796202, 13 pages
https://doi.org/10.1155/2022/3796202

Research Article

Computerized-Assisted Scoliosis Diagnosis Based on Faster R-CNN and ResNet for the Classification of Spine X-Ray Images

Peiji Chen,[1] **Zhangnan Zhou**,[1] **Haixia Yu**,[2] **Kun Chen**,[1] **and Yun Yang**[2]

[1]*Department of Orthopedics, Huaqiao University Affiliated Strait Hospital, Quanzhou, Fujian 362000, China*
[2]*Department of Medical Examination Center, Huaqiao University Affiliated Strait Hospital, Quanzhou, Fujian 362000, China*

Correspondence should be addressed to Kun Chen; ck180@sina.com and Yun Yang; 2359894336@qq.com

Received 12 January 2022; Revised 22 February 2022; Accepted 6 April 2022; Published 6 June 2022

Academic Editor: Kelvin Wong

In order to reduce the subjectivity of preoperative diagnosis and achieve accurate and rapid classification of idiopathic scoliosis and thereby improving the standardization and automation of spinal surgery diagnosis, we implement the Faster R-CNN and ResNet to classify patient spine images. In this paper, the images are based on spine X-ray imaging obtained by our radiology department. We compared the results with the orthopedic surgeon's measurement results for verification and analysis and finally presented the grading results for performance evaluation. The final experimental results can meet the clinical needs, and a fast and robust deep learning-based scoliosis diagnosis algorithm for scoliosis can be achieved without manual intervention using the X-ray scans. This can give rise to a computerized-assisted scoliosis diagnosis based on X-ray imaging, which has strong potential in clinical utility applied to the field of orthopedics.

1. Introduction

Adolescent idiopathic scoliosis (AIS) is the most common three-dimensional spinal deformity, accounting for about 80% of the total number of idiopathic scoliosis. In my country, the prevalence of scoliosis is still increasing year by year [1]. The incidence rate among 6-year-old adolescents is 1%-3%, which not only seriously affects the physical appearance of adolescents but also impairs their respiratory function, motor function, mental state, and overall quality of life. In addition, spinal surgery is time-consuming and risky, and the instruments used for surgical correction are complicated, difficult, traumatic, and complicated (major orthopedic surgery). Moreover, the preoperative diagnosis is subjective, which can lead to different diagnoses. Therefore, how to standardize and automate the diagnosis of spine surgery is the significance of this paper.

Generally, orthopedic surgeons manually measure and calculate the Cobb (which relates to the surgeon by the name of John Robert Cobb) angle according to the shape of the spine presented by the X-ray film taken by the patient to determine whether the patient has scoliosis and its severity. Judging from the current research status of the Cobb angle measurement method of scoliosis images, the Cobb angle measurement method has been researched and applied to a certain extent, but more are based on manual and semiautomatic measurement methods proposed for the Cobb angle measurement of scoliosis images. Now, the manual measurement of Cobb angle for scoliosis images still has certain shortcomings and challenges. Notably, manual diagnosis method will increase the workload of the doctor at the same time and waste a large amount of medical resources. With the continuous development of computer hardware and artificial intelligence technology, computer-aided diagnosis

based on deep learning has become an important means to assist doctors [2], and certain results have been achieved, which provides a new direction for the medical status of scoliosis diseases. In this paper, we choose X-ray imaging and study the screening method for scoliosis diseases based on the convolutional neural network [3].

2. Methods

2.1. Target Localization Method Based on Convolutional Neural Network

2.1.1. Faster R-CNN Model (Target Localization Model in the Spine Area) Construction. The Faster R-CNN model [4] consists of two parts: region proposal networks (RPN) and fast region-based convolutional network method (Fast R-CNN). The Faster R-CNN used in this paper obtains the feature map through the basic network structure composed of multiple layers of conv and ReLU (small 5-layer deep ZF network model with low video memory requirements or large 16-layer deep VGG-16 network model with high video memory requirements), and the feature map is shared in the following two parts of the network. The first part is to input the feature map into the RPN to get the region proposal on the feature map. The second part uses Fast R-CNN to classify and accurately locate the region proposal. Finally, the location information and category information of the target can be obtained. Figure 1 shows the detailed network structure of the spine X-ray image positioning based on Faster R-CNN.

The experimental data used in this paper is the X-ray image of the patient's spine, and the size of the image is $224 \times 224 \times 3$ (3 is the number of channels of the image). A 5-layer deep ZF network is used to extract features, including 5 conv layers, 2 ReLU layers, 2 LRN layers, and 2 maxpool layers. As shown in Figure 1, each conv layer is connected to the ReLU layer, using the ReLU activation function [5].

The basic structure of the first depth of the Faster R-CNN has four layers. The first layer is the conv layer, consisting of 96 $7 \times 7 \times 3$ convolution kernels, using stride as 2, padding as 3, and get a result of size $112 \times 112 \times 96$; the second layer is the ReLU layer, and the size of the output result is still $112 \times 112 \times 96$; the third layer is the LRN layer, drawing on the concept of lateral inhibition in biology to achieve local inhibition in the neural network. LRN is used in conjunction with ReLU to enhance pixels with large response, suppress pixels with small response, achieve local normalization, improve the generalization ability of the network, and improve the recognition rate; the fourth layer is the maxpool layer, using a 3×3 pooling window, stride is 2, padding is 1, and the size of the output result is $56 \times 56 \times 96$. The structure of the second layer depth of the network is the same as the first depth. The first layer conv layer uses 256 $5 \times 5 \times 3$ convolution kernels, stride is 2, padding is 2, and the size of the result is $28 \times 28 \times 256$; the second layer is the ReLU layer; the third layer is the LRN layer; the fourth layer is the maxpool layer, using a 3×3 pooling window, stride is 2, padding is 1, and the size of the output result is $28 \times 28 \times 256$. The third layer depth, fourth layer depth, and fifth layer depth of the network have the same structure. They all use the basic conv layer combined with the ReLU layer. The conv layer uses 384, 384, and 256 3×3 convolution kernels, respectively, stride is 1, padding is 1, and the depths of the third and fourth layers of the network are both $14 \times 14 \times 384$. The fifth layer depth of the network gets a result with a size of $14 \times 14 \times 256$. Therefore, through the calculation of a simple neural network, a $14 \times 14 \times 256$ feature map is finally obtained.

The RPN is composed of a simple convolutional neural network. First, convolution is performed through 256 3×3 convolution kernels to produce a result of $14 \times 14 \times 256$. Then pass two 1×1 convolution kernels to form two branches. The first branch is composed of 18 convolution kernels and produces a result of $14 \times 14 \times 18$ ($14 \times 14 \times (9 \times 2)$: 9 anchors, each with two parameters, representing the foreground and background, a total of 18 dimensions). The second branch is composed of 36 convolution kernels and produces a result of $14 \times 14 \times 36$ ($14 \times 14 \times (9 \times 4)$: 9 anchor boxes, each with four parameters, representing the coordinate center, width, and height of the anchor boxes, a total of 36 dimensions). Before entering the ROI Definition network, reshape the result obtained from the first branch (while changing the dimension of the input data without changing the data content) to obtain the required vector.

The RPN is composed of a three-layer network of softmax, reshape, and proposal to generate ROI Definition. Input the 18-dimensional feature vector into softmax to get the probability that each anchor box is foreground and not foreground. After the calculation of this layer is completed, the calculation result is reshaped again to obtain a vector of $14 \times 14 \times 18$. The input of the Definition layer includes the original image ($224 \times 224 \times 3$), the vector obtained from the previous layer, and the result obtained by the second branch of the eighth layer depth, as shown in Figure 2. According to the overlap ratio of the real boxes and the predicted boxes, a candidate set of the boxes is generated, and the boxes that exceed the edge and the boxes that do not meet the overlap criterion are discarded.

The R-CNN is composed of ROI pooling, softmax, and four fully connected layers. The feature map and the anchor boxes calculated by the RPN are input to the ROI pooling layer, the feature of the anchor boxes is calculated, and the fully connected layer and the softmax layer are connected. The pooling parameters of this layer are 6×6, stride is 6, and the spatial scale is selected to be 1/16 of the original image. The maximum pooling is still selected. Finally, a 6×6-dimensional feature vector is obtained. Each anchor area has four parameters, which represent the position information relative to the original image $[x_1, y_1, x_2, y_2]$. To input the result into the final classification network, only four fully connected layers and one softmax layer are needed. The fully connected layers fc6 and fc7; both use the dropout method to reduce the parameters in the connected layer with a certain probability and reduce the calculation amount of the model [6]. Then connect the fully connected layers boxes_

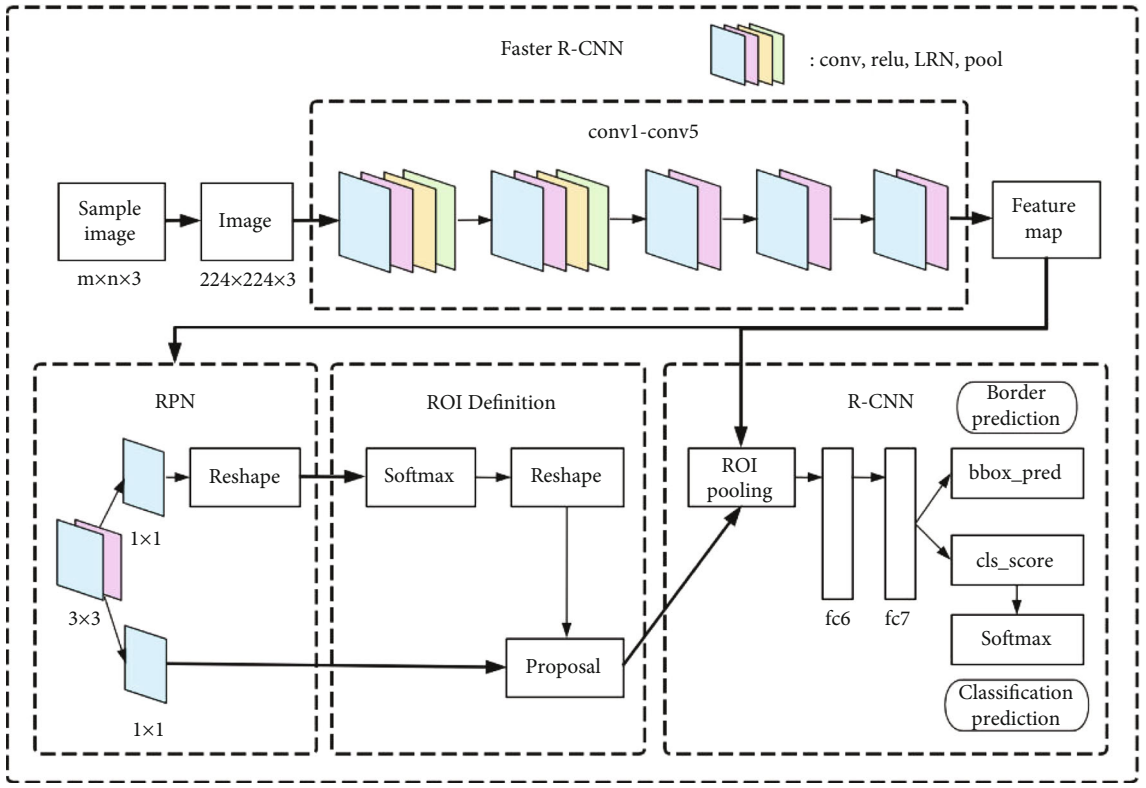

Figure 1: Network structure diagram of spine image positioning based on Faster R-CNN.

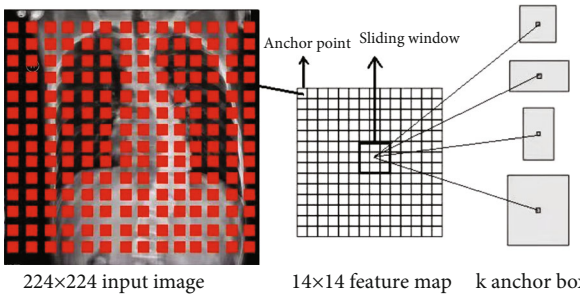

Figure 2: The relationship between the input image and the feature map.

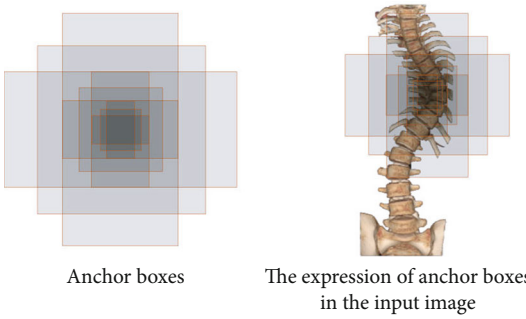

Figure 3: The expression of anchor boxes in the CT image.

pred and cls_score, respectively. boxes_pred outputs the position information of the precise target box, and cls_score connects the softmax layer to output the probability of the category corresponding to each target, as shown in Figure 3.

The RPN obtains preliminary anchor boxes after passing the IoU restrictions. These anchor boxes cannot correctly detect the position of the target. If you fine-tune the anchor boxes, you can get anchor boxes that are more similar to the ground truth bound so that the frame position information will be more accurate. This paper uses bounding-box regression to fine-tune the anchor boxes. In the current algorithm, input N sets of data $\{(P^i, G^i)\}$ where $i = 1, 2, \cdots, N$, of which $P^i = (P^i_x, P^i_y, P^i_w, P^i_h)$, $G^i = (G^i_x, G^i_y, G^i_w, G^i_h)$. As shown in Figure 4, G represents the ground truth bound, and P represents the anchor boxes filtered out.

The idea of bounding-box regression is to input the four values of $G = (G_x, G_y, G_w, G_h)$ of the ground truth bound and the four values of $P = (P_x, P_y, P_w, P_h)$ of the anchor boxes to represent the center coordinates, width, and height of the input box and continue to learn to find the appropriate function f so that $(G_x, G_y, G_w, G_h) = f(P_x, P_y, P_w, P_h)$ and make the prediction window $\widehat{G}$ as close to the real window G as possible. Four transformation methods $d_x(P), d_y(P), d_w(P), d_h(P)$ are used, where $d_x(P), d_y(P)$ refer to the translation of the center position without changing the scale, and $d_w(P), d_h(P)$ are the translation of the width and height of the specified anchor boxes. Mainly by learning Equation (1), the network translates and zooms the screened anchor

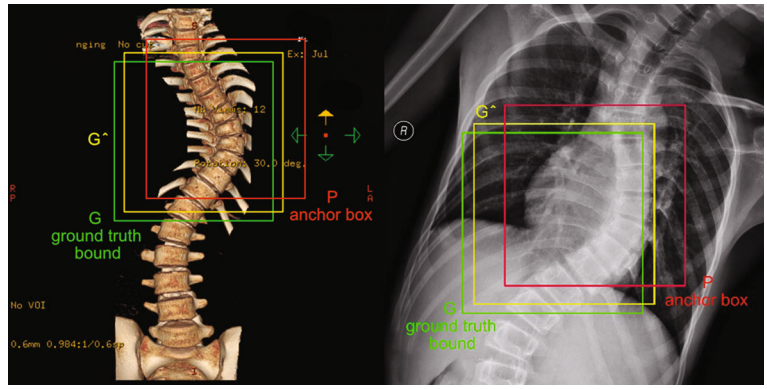

Figure 4: Schematic diagram of border regression.

boxes to obtain the position information of the prediction window $\hat{G}$.

$$\begin{cases} \hat{G}_x = P_w d_x(P) + P_x, \\ \hat{G}_y = P_h d_y(P) + P_y, \\ \hat{G}_w = P_w \exp\left(d_w(P)\right), \\ \hat{G}_h = P_h \exp\left(d_h(P)\right). \end{cases} \tag{1}$$

In Equation (1), $d_*(P) = w_*^T \varphi(P)$ where $*$ represents x, y, w, h. When the anchor boxes are close to the ground truth bound, they can become a linear function to achieve regression. The objective function of the regression is defined according to the training data (P, G). As in Equation (2), the translation scale and scaling scale (t_x, t_y, t_w, t_h) of the optimized model can be obtained.

$$\begin{cases} t_x = \dfrac{(G_x - P_x)}{P_w}, \\ t_y = \dfrac{(G_y - P_y)}{P_h}, \\ t_x = \log\left(\dfrac{G_w}{P_w}\right), \\ t_h = \log\left(\dfrac{G_h}{P_h}\right). \end{cases} \tag{2}$$

Linear regression is $Y = WX$, input vector X, and continuously learn parameter W so that output Y' is constantly close to the true value Y. In $d_*(P) = w_*^T \varphi(P)$ ($*$ represents x , y, w, h) in this paper, $\varphi(P)$ is the linear feature vector obtained by convolution operation, and w_* is a vector used to represent the parameters that can be learned in the model. The calculation formula of w_* is Equation (3), which is learned by the least square method of optimization regularization.

$$w_* = \arg\min_{\hat{w}_*} \sum_i^N \left(t_*^i - \hat{w}_*^T \phi\left(P^i\right)\right)^2 + \lambda \|\hat{w}_*\|^2. \tag{3}$$

For the Faster R-CNN training method, this paper uses a 5-layer ZF network and adopts the 4-step alternating training method to train the spine images of patients with scoliosis. Such a method can optimize training parameters and improve network efficiency. The training process of the entire Faster R-CNN can be divided into four stages, as shown in Figure 5.

(1) Use the first 5 layers of basic network (conv+ReLU) in the ZF network model to extract the required feature map to train the RPN 1 network model of stage 1

(2) Still use the first 5 layers of the basic network (conv +ReLU) in the ZF network model, but use the output of the RPN 1 network model (region proposal) as the input of the training network, and train the Fast R-CNN 1 network model of stage 1. At this stage, RPN and Fast R-CNN do not share convolutional layers

(3) Use the Fast R-CNN 1 network parameters of stage 1 to reinitialize the RPN model, fine-tune the unique network layer in RPN, and generate the RPN 2 network model of stage 2. In this way, the two networks of RPN and Fast R-CNN can share the convolutional layer and reduce the number of parameters

(4) Fix the shared convolutional layer, and merge the PRN 2 network model generated by stage 2 with the unique layer in the Fast R-CNN model to form a unified network. Continuous iteration, fine-tuning the unique parameters of the Fast R-CNN model, and finally generating the required target positioning model

2.1.2. ResNet Model (Grading Screening Model for Scoliosis Disease) Construction. The ResNet (residual network) convolutional neural network consists of 5 groups of convolutions. Since the number and parameters of each group of convolutions are different, a ResNet convolutional neural network with different layers is formed. There are five forms: ResNet18, ResNet34, ResNet50, ResNet101, and ResNet152. As shown in Figure 6, all ResNet convolutional neural

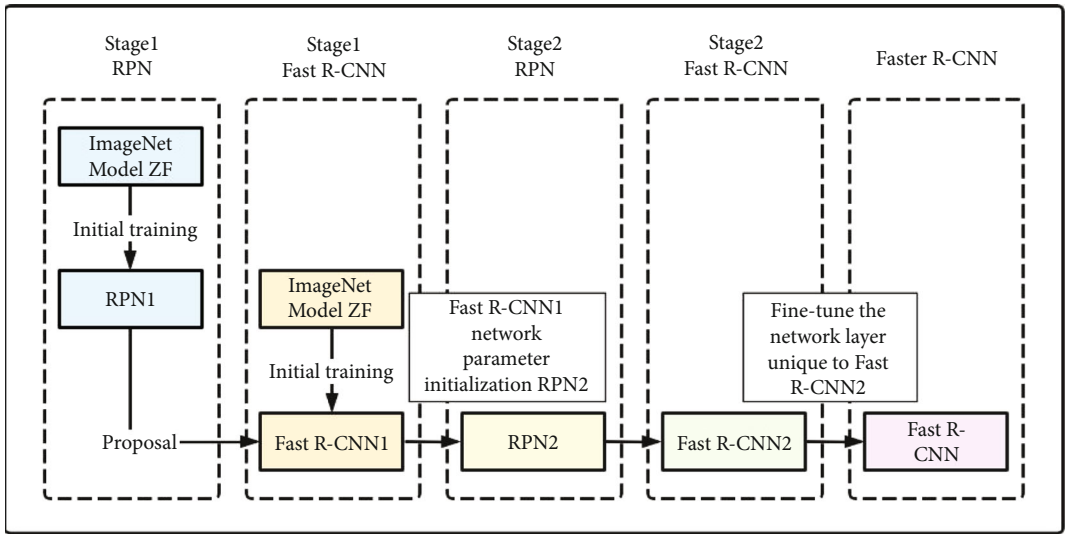

Figure 5: Faster R-CNN training process diagram.

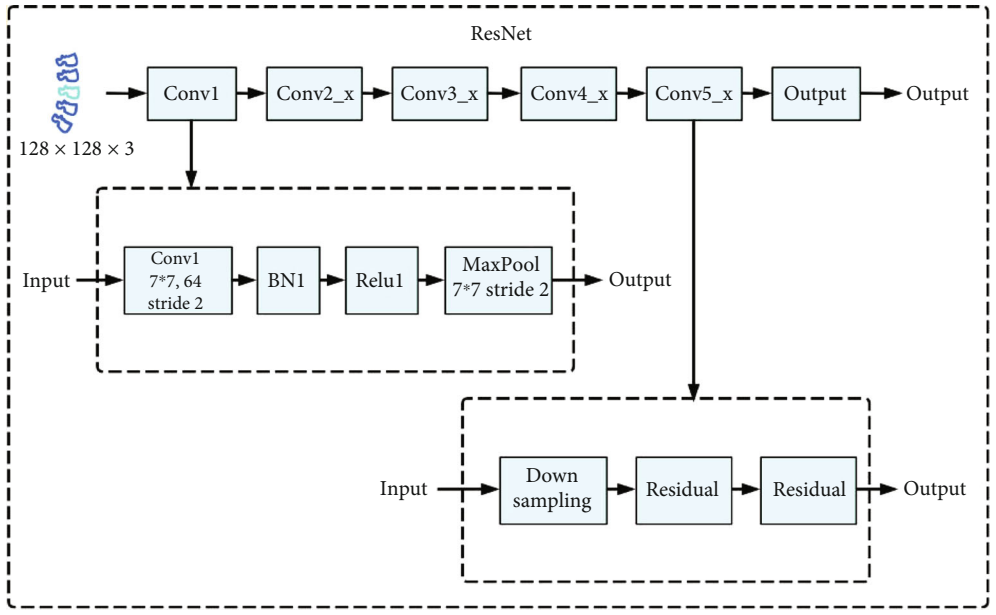

Figure 6: Scoliosis hierarchical network structure diagram based on ResNet.

networks include three main parts: the input part, the convolution part of each stage in the middle (the blue box in the figure contains four stages from Conv2_x to Conv5_x), and the output part. Although there are different variants of ResNet convolutional neural networks, they basically follow the structural characteristics shown in the figure. The number of network layers is different, mainly because of the differences in the number of convolutional parameters and building block parameters in the middle groups.

As shown in Figure 6, the input part of the ResNet convolutional neural network is composed of conv layer, batch normalization (batch norm, BN) layer, ReLU layer, and maxpool layer. The experimental data used in this paper is the medical image of the patient's spine area generated by the Faster R-CNN. The size of the image is $128 \times 128 \times 3$ (3 is the number of image channels). The first layer of the input part is the conv layer, which is composed of 64 $7 \times 7 \times 3$ convolution kernels, using stride as 2, padding as 3, and getting a result of size $65 \times 65 \times 64$; the second layer is the BN layer, called the batch normalization layer, which can accelerate the convergence speed of the network, improve the gradient dispersion in the network, and prevent the network from overfitting. It is generally used after the convolutional layer; the third layer is the ReLU layer, and the output result is still $65 \times 65 \times 64$; the fourth layer is the maxpool layer, using a 3×3 pooling window, stride is 2, no padding, and the output result is $32 \times 32 \times 64$.

The second to fifth depths of the network are composed of different numbers of building blocks. Different numbers of building blocks can form convolution operations of

Layer name	ResNet 18		ResNet 34		ResNet 50		ResNet 101		ResNet 152		Output
Conv1	7 × 7, 64, stride 2 3 × 3, max pooling, stride 2										32 × 32 × 64
Conv2_x	3 × 3, 64 3 × 3, 64	× 2	3 × 3, 64 3 × 3, 64	× 3	1 × 1, 64 3 × 3, 64 1 × 1, 256	× 3	1 × 1, 64 3 × 3, 64 1 × 1, 256	× 3	1 × 1, 64 3 × 3, 64 1 × 1, 256	× 3	16 × 16
Conv3_x	3 × 3, 128 3 × 3, 128	× 2	3 × 3, 128 3 × 3, 128	× 4	1 × 1, 128 3 × 3, 128 1 × 1, 512	× 4	1 × 1, 128 3 × 3, 128 1 × 1, 512	× 4	1 × 1, 128 3 × 3, 128 1 × 1, 512	× 8	8 × 8
Conv4_x	3 × 3, 256 3 × 3, 256	× 2	3 × 3, 256 3 × 3, 256	× 6	1 × 1, 256 3 × 3, 256 1 × 1, 1024	× 6	1 × 1, 256 3 × 3, 256 1 × 1, 1024	× 23	1 × 1, 256 3 × 3, 256 1 × 1, 1024	× 36	4 × 4
Conv5_x	3 × 3, 512 3 × 3, 512	× 2	3 × 3, 512 3 × 3, 512	× 3	1 × 1, 512 3 × 3, 512 1 × 1, 2048	× 3	1 × 1, 512 3 × 3, 512 1 × 1, 2048	× 3	1 × 1, 512 3 × 3, 512 1 × 1, 2048	× 3	2 × 2
Output	Average pooling, softmax										1 × 1

Figure 7: ResNet structure details.

different depths (as shown in Figure 7, the four stages of convolution operations in the blue box). The data in the red box in Figure 7 $\{2, 2, 2, 2\}$, $\{3, 4, 6, 3\}$, $\{3, 4, 6, 3\}$, $\{3, 4, 23, 3\}$, and $\{3, 8, 36, 3\}$ are the repeated stacking times of building blocks in ResNet18, ResNet34, ResNet50, ResNet101, and ResNet152, respectively. For example, ResNet50 is composed of an input layer, each module from Conv2_x to Conv5_x corresponding to {3, 4, 6, 3} repeated stacking, and the final output layer (calculation process: $1 + 3 \times 3 + 3 \times 4 + 3 \times 6 + 3 \times 3 + 1 = 50$). As you can see in Figure 7, there are two different forms of building blocks (purple boxes in the figure). They are the two-layer computing building block in ResNet18 and ResNet34 and the three-layer computing building block in ResNet50, ResNet101, and ResNet152.

Figure 8 shows the detailed structure diagram of different building blocks. Figure 8 (left) shows the original building block structure. The input feature map is divided into two data streams. One data stream undergoes two 3×3 convolution operations. After the first layer of convolution operation, there is a ReLU operation. The number of convolution kernels is 64. The stride is 1, the padding is 1, and the output result is $32 \times 32 \times 64$. The other data stream is the input data, $32 \times 32 \times 64$; both have the same dimension and can be added directly across two levels so that the ReLU calculation can be output to the next building block structure. Figure 8 (right) shows that the building block structure introduces 1×1 convolution. Through the 1×1 convolution operation, the feature map can be arbitrarily increased or reduced in dimension while keeping the size of the feature map unchanged, which reduces the complexity of the convolution operation. The input feature map is still divided into two data streams. One data stream is subjected to three-layer convolution operations. The first layer is 64 1×1 convolution kernels, using stride as 1, no padding, and the output result is $32 \times 32 \times 64$. Then, perform a ReLU operation; the second layer is 64 3×3 convolution kernels, using stride as 1, padding as 1, and the output result is $32 \times 32 \times 64$, performing a ReLU operation; the third layer is 256 1×1 convolution kernels, using stride as 1, no padding, and the output result is $32 \times 32 \times 256$. The other data stream is the input data. After 256 1×1 convolution cores, the original $32 \times 32 \times 64$ is upgraded so that the data dimensions in the two data streams are the same, and they are directly added across three levels to perform ReLU calculations. Then, these are output to the structure of the next building block.

2.1.3. Stochastic Gradient Descent Method in ResNet Model. In the ResNet convolutional neural network, the method of batch stochastic gradient descent [7] is generally selected for training. In this way, it is possible to avoid gradient oscillations or falling into local optimal conditions to a certain extent. In ResNet convolutional neural network, the objective function is generally concave function. The gradient descent algorithm is to find the smallest point in the concave function through continuous calculation. Derivatives are very useful for maximum or minimum problems in functions. For the function $y = f(x)$, the derivative is denoted as $f'(x)$. Use a sufficiently small ε to make $f(x - \varepsilon \operatorname{sign}(f'(x)))$ smaller than $f(x)$, so move a small step in the opposite direction of the derivative to reduce $f(x)$. This technique is gradient descent. The gradient descent method used in this paper is the stochastic gradient descent algorithm. Its core idea is to randomly select a small sample of $B = \{x^{(1)}, \cdots,$

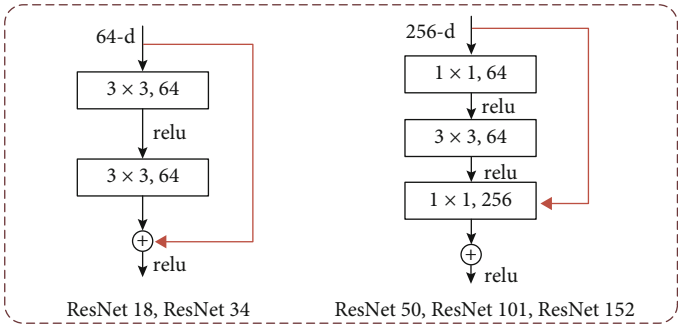

Figure 8: Detailed structure diagrams of different building blocks.

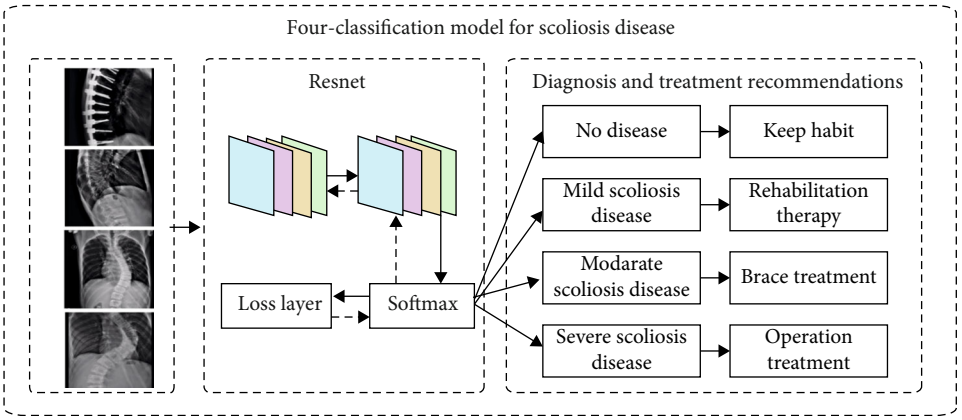

Figure 9: Four-classification model for scoliosis disease.

Table 1: Statistical table of samples of X-ray images of the patient's spine.

Cobb angle	Category	Number of samples	Label
0°~10°	No disease	991	1
11°~25°	Mild scoliosis disease	890	2
26°~45°	Moderate scoliosis disease	820	3
>45°	Severe scoliosis disease	899	4

$x^{(m')}\}$ from the training set, and the value of m' is generally small. When the entire training set m grows, m' is fixed. In this way, only m' samples are needed for each update, which greatly reduces the computational cost of a large training set. The calculation process of the gradient is Equation (4). The calculation process of stochastic gradient descent is Equation (5), where ε is the learning rate.

$$g = \frac{1}{m'}\nabla_\theta \sum_{i=1}^{m'} L\left(x^{(i)}, y^{(i)}, \theta\right), \tag{4}$$

$$\theta \longleftarrow \theta - \varepsilon g. \tag{5}$$

2.2. Patient's Spine Image Data and Screening. The X-ray images of the patient's spine used in this paper were collected over a period of nearly 3 years from 2019 to 2021. There are two different labels for scoliosis screening data. One is used as a four-classification model for scoliosis disease, as shown in Figure 9, including no disease (Cobb angle is 0°-10°), mild scoliosis (Cobb angle is 11°-25°), moderate scoliosis (Cobb angle is 26°-45°), and severe scoliosis (Cobb angle > 45°) [8], as shown in Table 1. The other is based on the actual needs of patients with scoliosis, with three levels of two categories. Among them, the binary classification model of scoliosis disease is to check whether the patient is sick; the binary classification model of mild scoliosis disease is to check whether the patient has mild scoliosis disease; the binary classification model of severe scoliosis disease is to judge whether the patient has severe scoliosis disease, as shown in Figures 10–12. In this paper, in order to effectively judge the degree of scoliosis in patients, a large number of comparative experiments have been carried out, and different experimental data have been used. A total of 6834 X-ray images of the patient's spine were used in this paper. After preprocessing the data, excluding duplicate data and poor quality data, there are a total of 3600 experimental data.

In order to have all the data used as the training set and test set, increase the reliability of the model, improve the generalization ability of the model, and avoid problems such as overfitting of the model; the experiments in this paper adopt the fourfold cross-validation method for training

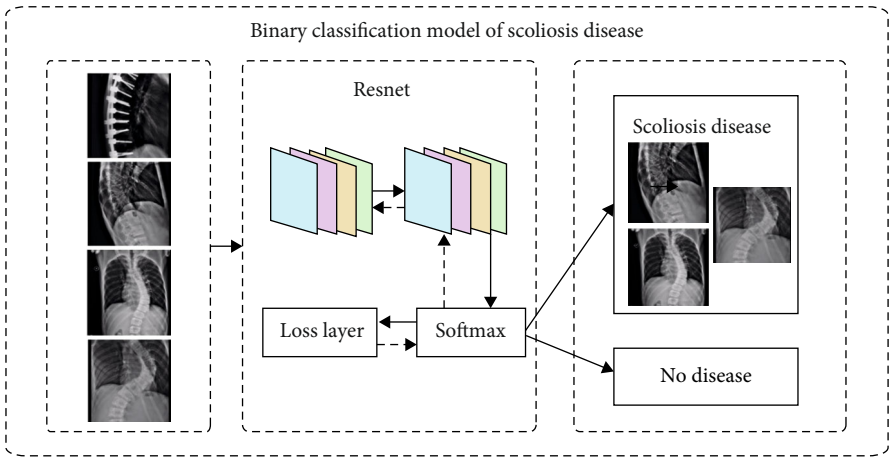

Figure 10: Binary classification model of scoliosis disease.

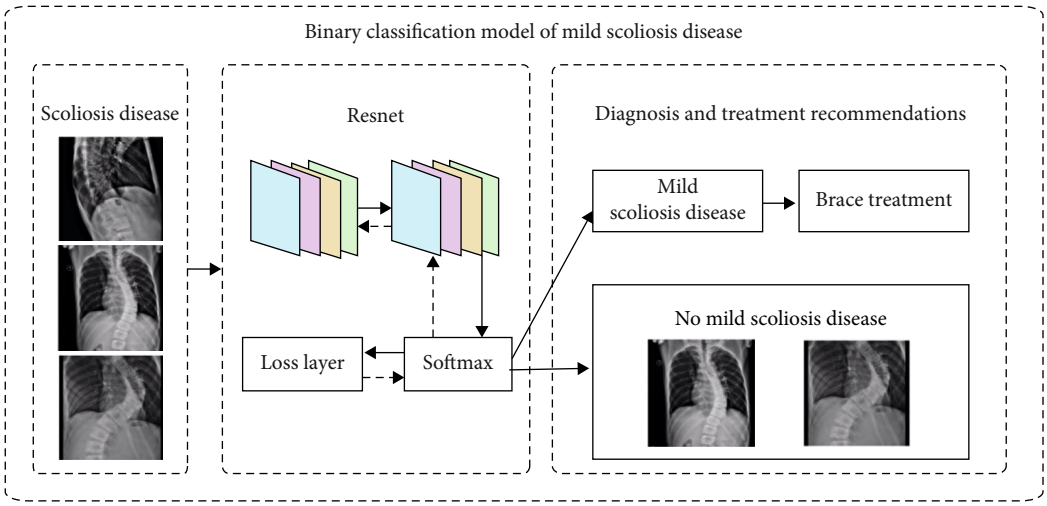

Figure 11: Binary classification model of mild scoliosis disease.

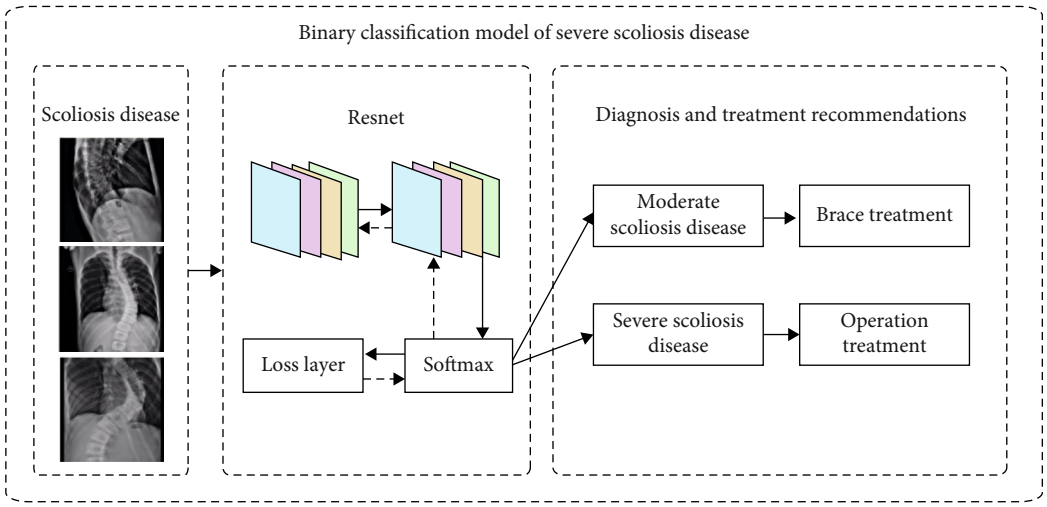

Figure 12: Binary classification model of severe scoliosis disease.

Table 2: Faster R-CNN fourfold cross-validation data allocation table.

Faster R-CNN model	Model 1	Model 2	Model 3	Model 4
Target	Spine	Spine	Spine	Spine
Number of samples in the training set (sample label)	2700 (2, 3, 4)	2700 (1, 3, 4)	2700 (1, 2, 4)	2700 (1, 2, 3)
Number of samples in the test set (sample label)	900 (1)	900 (2)	900 (3)	900 (4)

Table 3: Fourfold cross-validation data allocation table for scoliosis disease binary classification.

Scoliosis disease binary classification ResNet50 model	Model 1 (1982)	Model 2 (1982)	Model 3 (1982)	Model 4 (1982)
Number of samples in the training set (1/2 sample size) (3/4 sample size)	1534 (768/322) (322/322)	1537 (768/323) (323/323)	1537 (768/323) (323/323)	1538 (769/323) (323/323)
Number of samples in the test set (1/2/3/4 sample size)	448 (223/75/75/75)	445 (223/74/74/74)	445 (223/74/74/74)	444 (222/74/74/74)

Table 4: Fourfold cross-validation data allocation table for mild scoliosis disease binary classification.

Mild scoliosis disease binary classification ResNet50 model	Model 1 (1780)	Model 2 (1780)	Model 3 (1780)	Model 4 (1780)
Number of samples in the training set (2/3/4 sample size)	1384 (692/346/346)	1384 (692/346/346)	1385 (693/346/346)	1387 (693/347/347)
Number of samples in the test set (2/3/4 sample size)	396 (198/99/99)	396 (198/99/99)	395 (197/99/99)	393 (197/98/98)

Table 5: Fourfold cross-validation data allocation table for severe scoliosis disease binary classification.

Severe scoliosis disease binary classification ResNet50 model	Model 1 (1719)	Model 2 (1719)	Model 3 (1719)	Model 4 (1719)
Number of samples in the training set (3/4 sample size)	1339 (640/699)	1339 (640/699)	1339 (640/699)	1340 (640/700)
Number of samples in the test set (3/4 sample size)	380 (180/200)	380 (180/200)	380 (180/200)	379 (180/199)

Table 6: Actual testing situation table.

True positive (TP)	Predicted scoliosis disease and actual scoliosis disease
False positive (FP)	Predicted scoliosis disease and actually no scoliosis disease
True negative (TN)	Predict no scoliosis disease and actually no scoliosis disease
False negative (FN)	Predict no scoliosis disease and actually have scoliosis disease

and testing. Fourfold cross-validation [9–14] refers to the use of the nonrepetitive sampling method in simple random sampling to divide the entire data into four parts; each of which three parts is selected for training the model, and the other one is used for testing the model. In this way, four model training can be performed, four models can be obtained, and four sets of test results can be obtained.

Verification of the target positioning of the spine area is shown in Table 2. In the table, no disease, mild scoliosis disease, moderate scoliosis disease, and severe scoliosis disease [15–19] are represented by 1, 2, 3, and 4, respectively. Model 1, Model 2, Model 3, and Model 4 are four models generated by the fourfold cross-validation.

In order to verify the scoliosis classification screening experiment, the training data and test data distribution of the scoliosis disease binary classification model, mild scoliosis disease binary classification model, and severe scoliosis disease binary classification model is shown in Tables 3–5. In the table, no disease, mild scoliosis disease, moderate scoliosis disease, and severe scoliosis disease are represented by

Table 7: Main evaluation indicators.

Sensitivity TPR	$\frac{TP}{TP + FN}$
Specificity TNR	$\frac{TN}{FP + TN}$
FNR	$\frac{FN}{TP + FN}$
FPR	$\frac{FP}{FP + TN}$
Precision	$\frac{TP}{TP + FP}$

1, 2, 3, and 4, respectively. Model 1, Model 2, Model 3, and Model 4 are four models generated by the fourfold cross-validation.

2.3. Classic Feature Extraction Method and SVM Classifier. In order to make the experiment more convincing, this paper uses traditional machine learning methods and Support Vector Machine (SVM) classifiers as comparative experiments to verify the effect of using Faster R-CNN and ResNet convolutional neural network in the grading experiment of scoliosis disease. This experiment uses the feature extraction of the texture feature and Local Binary Pattern (LBP) to detect the region of interest and uses the SVM classifier to classify scoliosis disease in detail.

Texture feature is used to describe the relationship between different pixels in an image. This paper uses the calculation of a single point pixel and its surrounding point pixels to extract the texture features of the image.

Local Binary Pattern (LBP) can describe the local texture features of the image and extract the local features of the image through different LBP operators. This paper uses the traditional LBP calculation method, defines a 3×3 window, sets the gray value of the center of the window as a threshold, and compares the gray values of the 8 pixels around the center with it. If the pixel value is greater than the center, it is marked as 0; otherwise, it is marked as 1. In this way, an 8-bit binary number can be obtained, that is, the LBP code of the center pixel (usually the 8-bit binary code is converted to a decimal code). This paper uses the decimal code of the center pixel to reflect texture information and complete feature extraction.

Support Vector Machine (SVM) is a binary classification classifier commonly used in machine learning. Using this method, this paper fits three binary classification problems of scoliosis disease. In a specific data set, manually label positive and negative samples, find a hyperplane, separate two different types of samples as much as possible, and find the optimal decision surface for data classification. For the binary classification problem of medical images, this paper uses Receiver Operating Characteristic (ROC) curve and Area Under the Curve (AUC) to evaluate the pros and cons of the binary classification classifier. The data can be divided into positive samples and negative samples. In the binary classification model of scoliosis disease, there is scoliosis disease, which is called positive, and there is no scoliosis disease, which is called negative. In the actual data detection process, four situations will occur, as shown in Table 6.

Sensitivity can also be called recall rate or true positive rate (TPR). The specificity is the proportion of all samples without scoliosis that are predicted to be free of scoliosis. The abscissa of the ROC curve is FPR, which is the proportion of all samples without scoliosis that are predicted to have scoliosis. The ordinate of the ROC curve is TPR, which is the proportion of all samples with scoliosis that are predicted to have scoliosis and actually have scoliosis. Ideally, it is expected that FPR is 0 and TPR is 1. If the value of AUC is 1, it is an ideal classifier, and the classification effect is perfect. Therefore, the closer the AUC value is to 1, the better the classification effect. The calculation process of the main evaluation indicators is shown in Table 7.

3. Results

Figure 13 shows the four-level labels of the scoliosis screening data, which are operated spine, mild scoliosis, moderate scoliosis, and severe scoliosis.

For the binary classification model of scoliosis disease, from the overall point of view of image classification, the combination of Faster R-CNN and ResNet convolutional neural network has the best classification effect. The AUC value is 0.9087, which fully illustrates that the combination of Faster R-CNN and ResNet convolutional neural network has a better classification effect on scoliosis diseases than traditional machine learning methods. The texture features of the image are TX, combined with the SVM classifier, and a good classification result is also obtained, with an AUC value of 0.8553. The combination of LBP and SVM classifier has the worst effect, with an AUC value of 0.8142.

In Figure 14, for the binary classification model of mild scoliosis disease, the combination of Faster R-CNN and ResNet convolutional neural network has the best classification effect, with an AUC value of 0.8659. The TX of the image combined with the SVM classifier also got a good classification result, with an AUC value of 0.8884. The combination of LBP and SVM classifier has an AUC value of 0.8432.

For the binary classification model of severe scoliosis disease, the combination of Faster R-CNN and ResNet convolutional neural network has the best classification effect, and the AUC value is 0.8603. The combination of LBP and SVM classifier also got a good classification result, with an AUC value of 0.8316. The TX of the image, combined with the SVM classifier, has the worst effect, with an AUC value of 0.8219.

It can be seen from Tables 8–10 that the binary classification model of scoliosis disease, the binary classification model of mild scoliosis, and the binary classification model of severe scoliosis using Faster R-CNN combined with ResNet convolutional neural network are better than using traditional feature extraction combined with SVM classifier in terms of accuracy, sensitivity, and specificity.

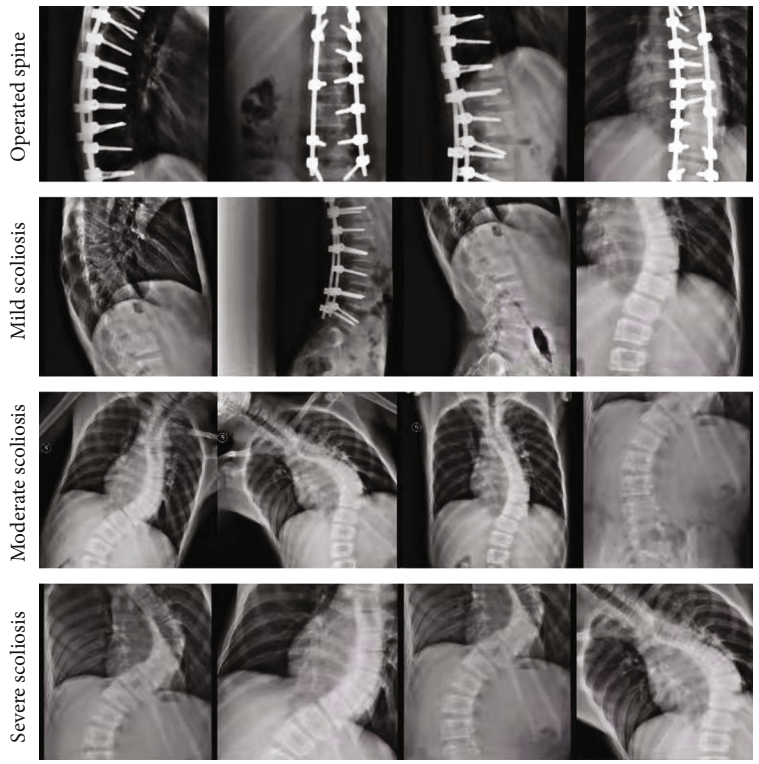

Figure 13: Classification of scoliosis by Faster R-CNN and ResNet.

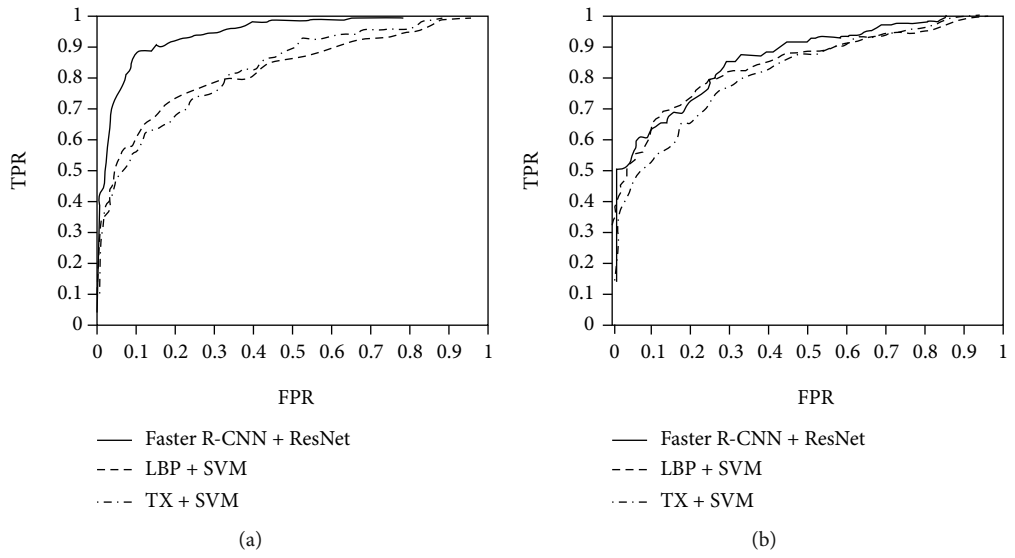

Figure 14: ROC curve of (a) nonsevere and (b) severe scoliosis disease binary classification model comparison experiment.

4. Discussion

In this paper, we use the method of combining traditional feature extraction and SVM classifier to conduct comparative experiments. Analysis of the experimental results shows that the combination of Faster R-CNN and ResNet50 convolutional neural network has a better screening effect for scoliosis diseases. The final experimental results can meet clinical needs.

At present, the preoperative diagnosis of Lenke [20–24] type surgery for idiopathic scoliosis in major domestic hospitals is performed by doctors observing the patient's spine X-rays, using markers and rulers to manually measure the Cobb angle for diagnosis. Different doctors may have deviations in the observation results, and the angle of measurement will also change, so there will be errors between observers. However, the same doctor may have different measurement results every time the same patient is

Table 8: Quantitative index results of scoliosis disease binary classification model.

	Faster R-CNN+ResNet	TX+SVM	LBP+SVM
Precision	0.9132	0.7554	0.7123
Sensitivity	0.8722	0.7426	0.6721
Specificity	0.9140	0.7856	0.8576

Table 9: Quantitative index results of mild scoliosis disease binary classification model.

	Faster R-CNN+ResNet	TX+SVM	LBP+SVM
Precision	0.8693	0.7780	0.7397
Sensitivity	0.8415	0.7540	0.6902
Specificity	0.9336	0.7461	0.7373

Table 10: Quantitative index results of severe scoliosis disease binary classification model.

	Faster R-CNN+ResNet	TX+SVM	LBP+SVM
Precision	0.8243	0.7545	0.7784
Sensitivity	0.8604	0.7212	0.7203
Specificity	0.9352	0.7853	0.8839

measured, so there are errors within the observer. The error between the observer and the observer affects the accuracy of the operation. The main reason is that the angle is manually measured. In order to replace the doctor in the Cobb angle measurement and classification, to achieve accurate and rapid classification of idiopathic scoliosis, this paper uses a popular deep learning framework and validates and analyzes the results measured by doctors under the test set and shows the classification results. The final experimental results can meet clinical needs. A new algorithm for scoliosis diagnosis based on deep learning that is fast and robust without manual definition is obtained. Note that predictive control algorithms [25, 26] can be used to improve medical image diagnostics and facilitate treatment procedures.

5. Conclusion

This paper includes two parts: the location of the region of interest in the X-ray image of the patient's spine and the detailed classification of scoliosis disease using X-ray imaging. In the study of locating the region of interest in the upright image of the patient's spine, this paper chooses the Faster R-CNN convolutional neural network to locate the patient's spine region. In the grading study of scoliosis diseases, this paper first combines the clinical experience of orthopedics experts and divides the patients into four grades according to the size of the Cobb angle of the spine. At the same time, the ResNet convolutional neural network is used to classify scoliosis diseases in detail, and then, the network is optimized. Finally, this paper compares the convolutional neural network method and the classic feature extraction method in machine learning (texture composite features, local binary mode) with the combination of Support Vector Machine (SVM) method, which increases the reliability of the model and improves the generalization ability of the model. From the research results, the combination of Faster R-CNN and three ResNet binary classification models studied in this paper can be used as a reference for orthopedic surgeons to diagnose scoliosis diseases.

Data Availability

Data are available on request from the authors due to privacy/ethical restrictions.

Consent

All human subjects in this study have given their written consent for the participation of our research.

Conflicts of Interest

The authors declare no conflict of interests in this paper.

Authors' Contributions

Peiji Chen and Zhangnan Zhou contributed equally to this work.

References

[1] Z. Cai, R. Wu, S. Zheng, Z. Qiu, and K. Wu, "Morphology and epidemiological study of idiopathic scoliosis among primary school students in Chaozhou, China," *Environmental Health and Preventive Medicine*, vol. 26, no. 1, pp. 54-55, 2021.

[2] L. Deng and D. Yu, "Deep learning: methods and applications," *Foundations & Trends in Signal Processing*, vol. 7, no. 3, pp. 197–387, 2013.

[3] Y. Lecun, B. Boser, J. S. Denker et al., "Backpropagation applied to handwritten zip code recognition," *Neural Computation*, vol. 1, no. 4, pp. 541–551, 1989.

[4] S. Ren, K. He, R. Girshick, and J. Sun, "Faster R-CNN: towards real-time object detection with region proposal networks," vol. 26, no. 1, pp. 28–30, 2015.

[5] B. Digvijay, S. S. Dey, and L. Guanghui, "Complexity of training ReLU neural network," *Discrete Optimization*, vol. 60, no. 6, article 100620, 2020.

[6] H. Wu and X. Gu, "Towards dropout training for convolutional neural networks," *Neural Information Processing*, vol. 71, pp. 1–10, 2015.

[7] T. Ferguson, "An inconsistent maximum likelihood estimate," *Publications of the American Statistical Association*, vol. 77, no. 380, pp. 831–834, 1982.

[8] P. Dayan and L. F. Abbott, "Theoretical neuroscience," *Computational & Mathematical Modeling of Neural Systems*, vol. 6, no. 1, pp. 54-55, 2001.

[9] M. Subhabrata and S. C. Basak, "Beware of Naïve q2, use true q2: some comments on QSAR model building and cross validation," *Current Computer-Aided Drug Design*, vol. 14, no. 1, pp. 64–75, 2018.

[10] L. Valentin, B. Hagen, S. Tingulstad, and S. Eik-Nes, "Comparison of 'pattern recognition' and logistic regression models for discrimination between benign and malignant pelvic masses: a prospective cross validation," *Ultrasound in obstetrics &*

gynecology : the official journal of the International Society of Ultrasound in Obstetrics and Gynecology, vol. 18, no. 4, pp. 168–174, 2001.

[11] M. N. Ivanov, "Prototype sample selection based on minimization of the complete cross validation functional," *Pattern recognition and image analysis: advances in mathematical theory and applications in the USSR*, vol. 20, no. 4, pp. 427–437, 2010.

[12] M. Kearns, "A bound on the error of cross validation using the approximation and estimation rates, with consequences for the training-test split," *Neural Computation*, vol. 9, no. 5, pp. 1143–1161, 1997.

[13] D. Ruan, W. Shao, J. DeMarco et al., "Plan quality inference and cross validation for standardization and consistency evaluation," *International Journal of Radiation Oncology • Biology • Physics*, vol. 84, no. 3, pp. S129–S359, 2012.

[14] P. G. Rusconi, D. A. Ludwig, S. Sandhu et al., "Cross validation of NT-proBNP as a predictor of cardiac transplant in children with dilated cardiomyopathy," *Journal of the American College of Cardiology*, vol. 57, no. 14, p. E425, 2011.

[15] E. A. Terhune, C. I. Wethey, M. T. Cuevas et al., "Whole exome sequencing of 23 multigeneration idiopathic scoliosis families reveals enrichments in cytoskeletal variants, suggests highly polygenic disease," *Genes*, vol. 12, no. 6, p. 4, 2021.

[16] J. Piotr, C. Małgorzata, A. Mirosław, K. Małgorzata, and K. Tomasz, "Methylation of estrogen receptor 1 gene in the paraspinal muscles of girls with idiopathic scoliosis and its association with disease severity," *Genes*, vol. 12, no. 6, p. 10, 2021.

[17] L. L. Cohen, R. Przybylski, A. C. Marshall, J. B. Emans, and D. J. Hedequist, "Surgical correction of scoliosis in children with severe congenital heart disease and palliated single ventricle physiology," *Spine*, vol. 46, no. 14, pp. E791–E796, 2020.

[18] C. Toombs, B. Lonner, A. Fazal et al., "The adolescent idiopathic scoliosis international disease severity study: do operative curve magnitude and complications vary by country?," *Spine Deformity*, vol. 7, no. 6, pp. 883–889, 2019.

[19] C. Fortin, J. P. Pialasse, I. S. Knoth, S. Lippé, C. Duclos, and M. Simoneau, "Musculoskeletal diseases and conditions - scoliosis; findings from University of Montreal update knowledge of scoliosis (cortical dynamics of sensorimotor information processing associated with balance control in adolescents with and without idiopathic scoliosis)," *Information Technology Newsweekly*, pp. 96–105, 2019.

[20] S. Yossi, T. Eran, M. Yigal, R. Oded, L. Dror, and A. Yoram, "Height gain prediction in adolescent idiopathic scoliosis based on preoperative parameters," *Journal of Pediatric Orthopaedics*, vol. 41, no. 8, pp. 502–506, 2021.

[21] P. Janusz, Ł. Stepniak, and T. Kotwicki, "Cervical spine sagittal alignment following surgical correction of Lenke type 1 idiopathic scoliosis - early results," *Studies in Health Technology and informatics*, vol. 280, pp. 10–15, 2021.

[22] B. Garg, N. Mehta, A. Gupta et al., "Cervical sagittal alignment in Lenke 1 adolescent idiopathic scoliosis and assessment of its alteration with surgery: a retrospective, multi-centric study," *Spine Deformity*, vol. 9, no. 6, pp. 1559–1568, 2021.

[23] W. H. Chung, Y. Mihara, C. K. Chiu, M. S. Hasan, C. Y. W. Chan, and M. K. Kwan, "Factors affecting operation duration in posterior spinal fusion (PSF) using dual attending surgeon strategy among Lenke 1 and 2 adolescent idiopathic scoliosis (AIS) patients," *Clinical Spine Surgery*, vol. 35, no. 1, pp. 18–23, 2022.

[24] M. Tanaka, Y. Fujiwara, K. Uotani, T. Yamauchi, and H. Misawa, "C-arm-free anterior correction for adolescent idiopathic scoliosis (Lenke type 5C): analysis of early outcomes and complications," *World Neurosurgery*, vol. 150, pp. e561–e569, 2021.

[25] Z. H. Tang and Z. J. Zhang, "The multi-objective optimization of combustion system operations based on deep data-driven models," *Energy*, vol. 182, pp. 37–47, 2019.

[26] H. Lin and S. Jegelka, "ResNet with one-neuron hidden layers is a universal approximator," *Advances in Neural Information Processing Systems*, vol. 31, 2018.

Hindawi
Computational and Mathematical Methods in Medicine
Volume 2022, Article ID 6991218, 7 pages
https://doi.org/10.1155/2022/6991218

Research Article

Construction of Prediction Model of Renal Damage in Children with Henoch-Schönlein Purpura Based on Machine Learning

Tingting Cao,[1] **Ying Zhu**,[2] **and Youyu Zhu**[3]

[1]*Department of Dermatology, Anhui Provincial Children's Hospital, Hefei 230051, China*
[2]*Department of Nephrology, Anhui Provincial Children's Hospital, Hefei 230051, China*
[3]*School of Basic Medical Sciences, Anhui Medical University, Hefei 230032, China*

Correspondence should be addressed to Youyu Zhu; zhuyy0103@126.com

Received 15 January 2022; Revised 8 May 2022; Accepted 10 May 2022; Published 23 May 2022

Academic Editor: Kelvin Wong

Objective. The children with Henoch-Schönlein purpura (HSP) may suffer from renal insufficiency, which seriously affects the life and health of the children. This study aims to construct a prediction model of Henoch-Schönlein purpura nephritis (HSPN). *Methods*. A total of 240 children with HSP treated in dermatology and pediatrics in our hospital were selected. The general information, patients' clinical symptoms, and laboratory examination indicators were collected for feature selection, and the XGBoost algorithm prediction model was built. *Results*. According to the input feature indexes, the top ten crucial feature indicators output by the XGBoost model were urine N-acetyl-β-D-aminoglucosidase, urinary retinol-binding protein, IgA, age, recurrence of purpura, purpura area, abdominal pain, 24-h urinary protein quantification, percentage of neutrophils, and serum albumin. The areas under the curves of the training set (0.895, 95% CI: 0.827-0.963) and test set (0.870, 95% CI: 0.799-0.941) models were similar. *Conclusion*. The prediction model based on XGBoost is used to predict HSP renal damage based on clinical data of children, which can reduce the harm caused by invasive examination for patients.

1. Introduction

Henoch-Schönlein purpura (HSP) is one of the most common systemic vasculitides in childhood, a common vascular allergic disease. It mainly affects the skin, kidneys, intestines, joints, and other body parts [1]. In recent years, the number of children with HSP has increased significantly, and some studies show that the annual incidence of HSP is 160-191 cases per million children [2]. HSP points to the body receiving the stimulation of all kinds of sensitizing material, bringing about capillary brittleness and permeability enhancement inside the body, and causing inflammation or bleeding in the place such as skin, joints, and bowel [1, 3]. Clinical features of Henoch-Schönlein purpura nephritis (HSPN) were the fibrosis in patients with renal fibrosis [4]. HSPN is the most common secondary glomerular disease in children [5, 6].

Epidemiology suggests that HSP patients develop HSPN at a rate as high as 30% to 50% [7]. Although most HSPN patients have a good prognosis, 1%-3% of the children still suffer from renal insufficiency to end-stage renal failure, which seriously affects the life and health of the children [8]. Therefore, an early and accurate diagnosis of HSPN is crucial for prognosis and individualized treatment. Kidney biopsy is the gold standard for the diagnosis of HSPN. Still, this method is invasive and difficult for parents and children to accept, leading to some patients with severe kidney disease at the time of diagnosis [9].

Machine learning can use clinical data to build a prediction model and verify its predictive efficiency [10–12]. In recent years, the application in the medical field has been increasing gradually [13–16]. To our knowledge, there are few studies on machine learning to predict HSPN. Therefore, this paper mainly constructed a prediction model based

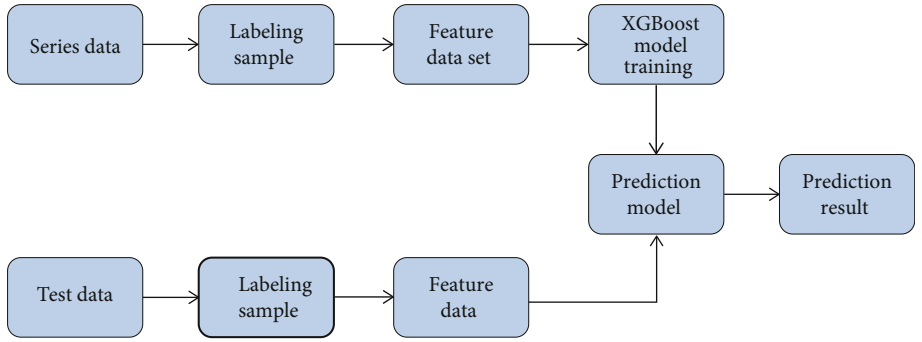

Figure 1: Flowchart of XGBoost detection.

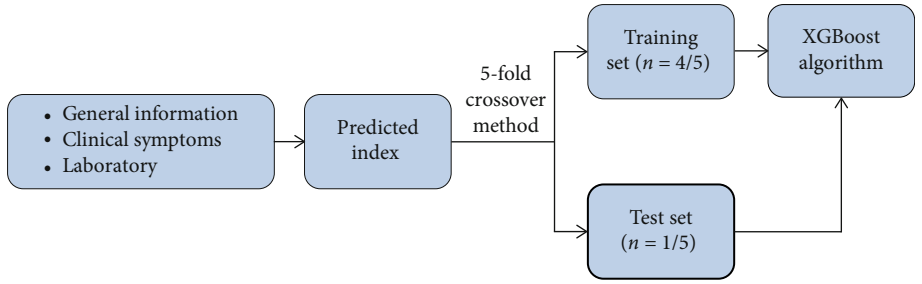

Figure 2: Modeling flowchart of XGBoost algorithm.

on machine learning to predict the occurrence of renal damage in HSP through clinical data, providing a new method for the efficient diagnosis of HSPN in children diagnosed with HSP for the first time in dermatology.

2. Methods

2.1. General Information. A total of 240 children with HSP treated in dermatology and pediatrics in our hospital from October 2019 to December 2021 were selected, of which 153 were complicated with HSPN. According to the European Union Against Rheumatism [17], HSP is diagnosed as a palpable rash (essential) with at least one of four clinical symptoms: Abdominal pain, arthritis or arthralgia, renal involvement, and histopathological findings suggest IgA deposition. Renal impairment was predominantly clinical: abnormalities in hematuria, proteinuria, and renal function, such as increased serum creatinine (SCr) and decreased estimated glomerular filtration rate (eGFR), within 6 months of the course of HSP. The calculation formula of eGFR is as follows: ≤16 years old using Schwartz formula [18]; CKD-EPI formula was used when >16 years old [19]. When the eGFR <90 ml/(min·1.73 m^2), it is considered as renal insufficiency.

2.2. Predicted Index. The indicators tested in this study mainly include general information, clinical symptoms, and laboratory indicators. General information includes sex, age, and season of onset. Clinical signs and symptoms include joint swelling, abdominal pain and gastrointestinal bleeding, purpura of the upper body skin, and recurrence of purpura. Laboratory indicators include blood routine tests, urine routine tests, and biochemical tests.

2.3. Machine Learning. The machine learning used in this study is the integrated machine learning XGBoost algorithm based on a classification and regression tree [20]. XGBoost algorithm has high scalability and high computing speed. Under the same environment and conditions, the XGBoost algorithm is more than 10 times faster than similar algorithms [21]. The specific detection process is shown in Figure 1.

XGBoost is an ensemble learning algorithm based on gradient boosting. Its principle is to achieve an accurate classification effect through the iterative calculation of a weak classifier [22]. It is an additive expression consisting of K base models:

$$\widehat{y}_i = \sum_{t=1}^{k} f_t(x_i), \tag{1}$$

where f_t is k basis models and $\widehat{y}_i$ is the predicted value of the ith sample.

The model's deviation and variance jointly determine the model's prediction accuracy, and the variation of the model is embodied as the loss function. Therefore, the objective function is composed of the model's loss function and the regular term Ω that inhibits the complexity of the model. Thus, the objective function can be expressed as

$$\text{obj} = \sum_{i=1}^{n} l\left(y_i, \widehat{y}_i^{\,t}\right) + \sum_{t=1}^{k} \Omega(f_t). \tag{2}$$

According to the calculation method of the Taylor

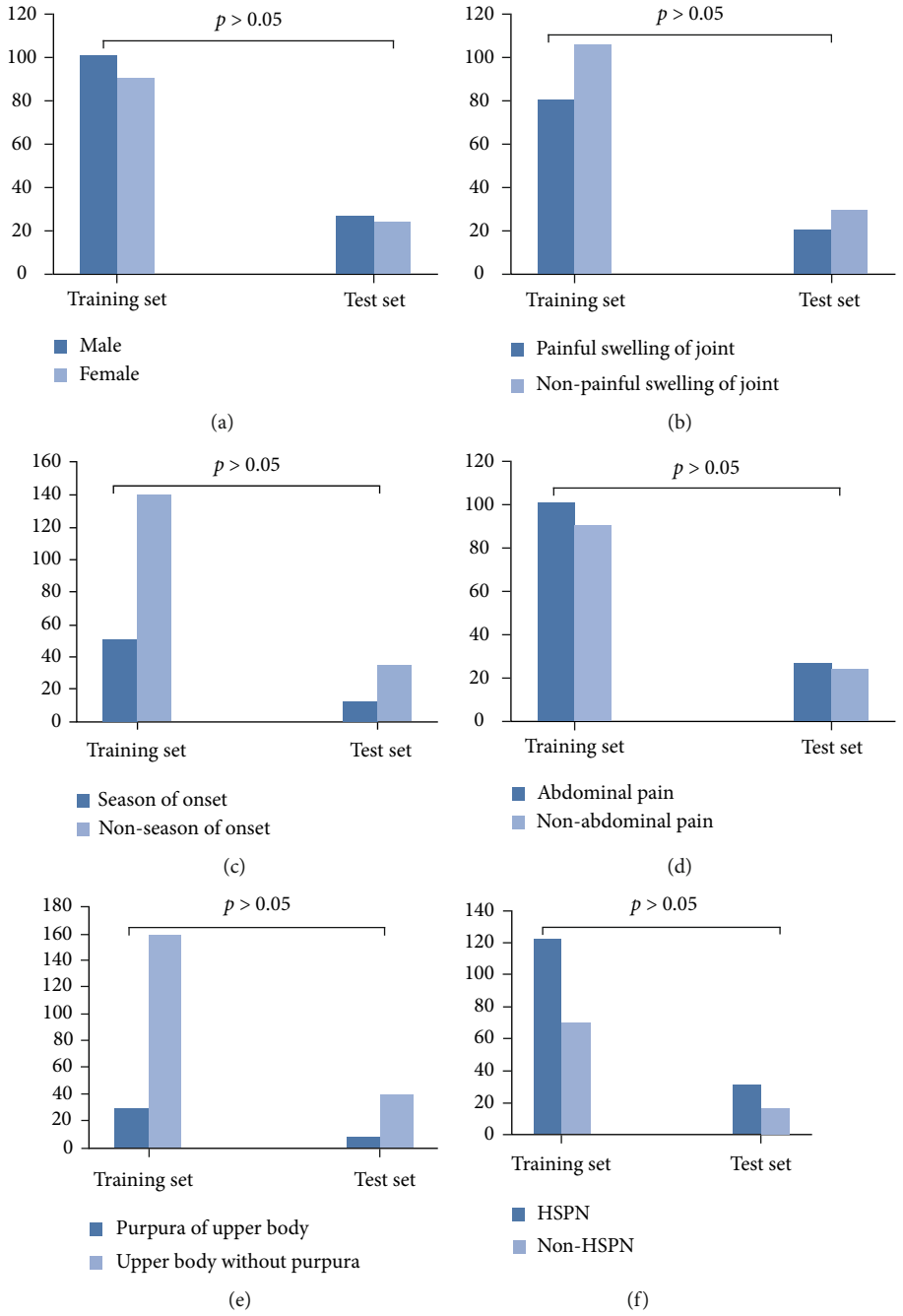

Figure 3: Comparison of clinical data between the training set and test set. There were no significant differences between training set and test set in gender (a), painful swelling of joint (b), season of onset (c), abdominal pain (d), purpura of upper body (e), and HSPN (f).

formula, the above objective function can be written as

$$\text{obj}^{(t)} = \sum_{i=1}^{n} l\left(y_i, \hat{y}_i^{\,t}\right) + \sum_{t=1}^{k} \Omega(f_t) = \sum_{i=1}^{n} l\left(y_i, \hat{y}_i^{t-1} + f_t(x_i)\right) + \sum_{i=1}^{t} \Omega(f_i). \tag{3}$$

The CRT is defined as $f_t = w_q(x)$, x is a certain text, $q(x)$ represents the leaf node where the sample is located, and w_q represents the value of the leaf node w. Therefore, $w_q(x)$ represents the value of w of each sample (i.e., the predicted value). The regular term of the objective function can be defined as

$$\Omega(f_t) = \lambda T + \frac{1}{2}\lambda \sum_{j=1}^{T} w_j^2. \tag{4}$$

Gradient enhancement generates a series of CRTs in the training process. The corresponding value of the leaf node of the CRT is an actual score, and the cumulative score of each

Table 1: Test results of general information and clinical symptom indexes.

Indexes	χ^2	P
General information		
Gender	0.038	0.758
Age	385.874	<0.001
Season of onset	8.983	0.009
Clinical symptom		
Abdominal pain	4.213	0.023
Painful swelling of joint	7.896	0.014
Purpura area	238.705	<0.001
Recurrence of purpura	7.942	0.012

Table 2: Test results of biochemical laboratory indexes.

Indexes	t	P
White cell count	-4.763	0.019
Percentage of neutrophils	1.684	0.041
Percentage of eosinophil	3.980	0.027
Platelet count	-1.415	0.185
C-reactive protein	0.970	0.384
Serum albumin	-4.542	0.021
Serum creatinine	-3.425	0.032
Total cholesterol	-0.468	0.571
D-dimer	-1.538	0.214
IgG	-3.978	0.030
IgA	-2.342	0.034
IgM	0.795	0.436
IgE	3.012	0.028
Hospitalization time	2.031	0.037
Urinary retinol-binding protein	-5.784	0.014
Urine N-acetyl-β-D-aminoglucosidase	3.869	0.028
24 h urinary protein quantification	4.825	0.024

CRT is the final predicted value. We test the accuracy of the algorithm using the 5-fold crossover method. The data set was divided into five parts, 4 of which were taken as the training set and the other as the test set. The accuracy of each experiment was obtained, and the average accuracy of the 5 results was taken as the estimation of the algorithm's accuracy. The specific modeling process is shown in Figure 2.

2.4. Statistical Analysis. Counting data were counted by χ^2 test. Measurement data were expressed by mean ± standard deviation and t test was adopted. $P < 0.05$ means the difference is statistically significant.

3. Results

3.1. General Information. Among the 240 children with HSP, there were 126 males and 114 females. The onset age was 2-16 years old, with an average age of 9.03 ± 2.68 years old. Among them, 62 cases (25.8%) occurred in winter, 102 cases (42.5%) had joint swelling and pain, 128 cases (53.3%) had abdominal pain and gastrointestinal bleeding, and 38 cases (15.8%) had upper body skin purpura. There were 153 cases of HSPN children and 87 cases without renal damage. There was no significant difference between the training group and the test group in gender, onset season, joint swelling and pain, abdominal pain, purpura of the upper body, and HSPN (Figure 3, $P > 0.05$).

3.2. Selection of Predictive Features. According to the statistical analysis results, gender is an insignificant factor in predicting the occurrence of HSPN in general information. The indicators of clinical symptoms are all statistically significant ($P < 0.05$) (Table 1).

The correlation of HSPN occurrence was predicted according to laboratory indexes such as biochemical tests, among which there was no significant difference in HSPN in platelet count, C-reactive protein, total cholesterol, IgM, and D-dimer ($P > 0.05$) (Table 2). However, the other indexes including white cell count, percentage of neutrophils, percentage of eosinophil, serum albumin, serum creatinine, IgG, IgA, IgE, hospitalization time, rinary retinol-binding protein (RBP), urine N-acetyl-β-D-aminoglucosidase (NAG), and 24-h urinary protein quantification were significantly correlated with HSPN ($P < 0.05$).

3.3. Prediction Results of XGBoost Algorithm Model. The XGBoost model automatically calculates features. According to the input feature indexes, the top ten important feature indicators output by the XGBoost model are as follows (Figure 4): NAG, RBP, IgA, age, recurrence of purpura, purpura area, abdominal pain, 24-h urinary protein quantification, percentage of neutrophils, and serum albumin.

3.4. Performance Evaluation of Model Prediction. In the training set, the area under the curve of the XGBoost model was 0.895 (95% CI: 0.827-0.963). In the test set, the area under the curve of the model was 0.870 (95% CI: 0.799-0.941). The XGBoost prediction model has good sensitivity and specificity. The receiver operation characteristic curves of XGBoost algorithm model is shown in Figure 5.

4. Discussion

HSP is a kind of systemic vasculitis, which mainly involves the skin, joints, gastrointestinal tract, capillaries, and small blood vessels of the kidney, accompanied by significant deposition of IgA [23]. Clinically, it is more common in children. It has been reported that more than 90% of HSPN occurs in children and adolescents, accounting for the first place in children with secondary nephropathy. Kidney biopsy is invasive and difficult for parents and children to accept [9]. Therefore, we predicted the incidence of HSPN from clinical data, clinical symptoms, and laboratory test indicators based on the XGBoost prediction model.

The XGBoost model can automatically obtain the importance score of each attribute, thus effectively filtering features. Our study screened children for general information, clinical symptoms, and laboratory test indicators. The

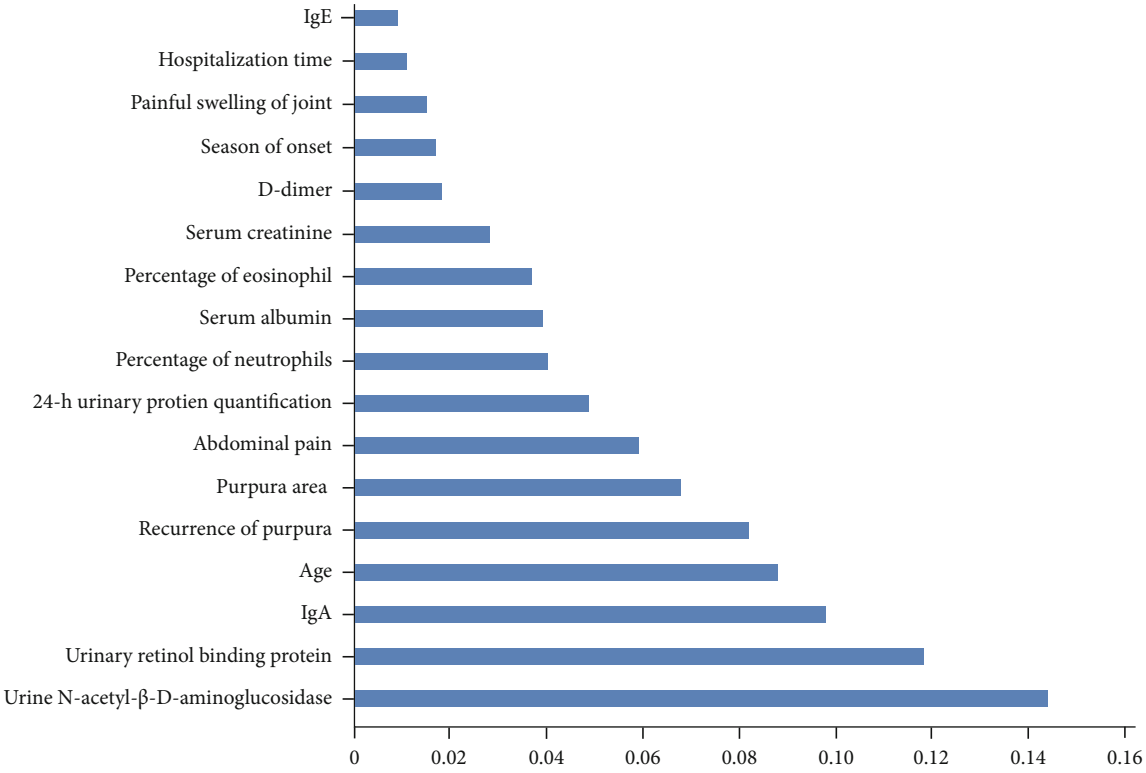

Figure 4: Ranking of important features of XGBoost model output.

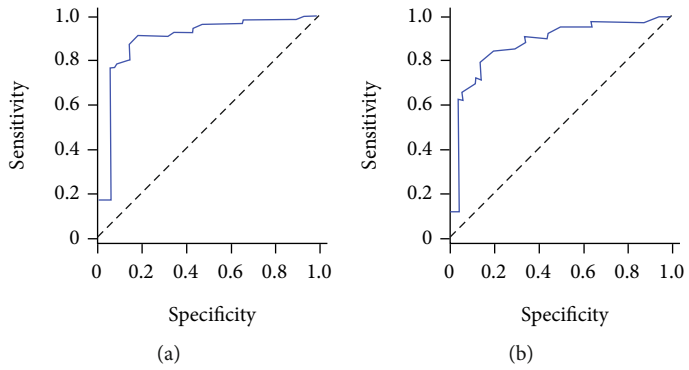

Figure 5: The receiver operation characteristic curves of XGBoost algorithm model. (a) Training set. (b) Test set.

top 3 indicators based on the XGBoost model are NAG, RBP, and IGA. Our results are consistent with Karadag et al. [24], who believe that vascular endothelial injury was an essential link in the pathogenesis of HSP. The possible reasons are as follows: (1) The permeability of the tube wall increased due to allergic reaction, and extravasation increased the concentration and slowed the blood flow. In a high viscosity state, immune complexes were more likely to deposit, further damaging the vascular endothelium and increasing the chances of platelet counting adhesion and self-aggregation. (2) Inflammatory reaction damages vascular endothelium. The damaged vascular endothelium enhances the coagulation promoting effect, stimulates the release of platelet count activating factor, and further promotes the activation and adhesion of platelet count.

Serum IgA is the main component of the body's mucosal defense system. It is widely distributed in milk, saliva, and mucosal secretions of the gastrointestinal tract, respiratory tract, and urogenital tract. Therefore, it plays a vital role in the first line of defense against infection, especially in the respiratory tract and intestinal tract. This is also an essential indicator in the prediction model of this paper. NAG is a lysosomal enzyme that occurs in the urinary system and is usually found in very low levels of urine. When the tubular cells are damaged, many NAG is released from the tubular epithelial cells into the urine, where NAG levels are elevated. RBP is the third important feature in the prediction model in our study. Liu et al. believed that the RBP has an important predictive value for delayed renal involvement in children with HSP [25].

In this study, the prediction model constructed based on the XGBoost algorithm can effectively reduce the overfitting problem and automatically specify the default branch direction for missing values, thus improving the algorithm's efficiency [26, 27]. Therefore, this provides more possibilities for the extensive application of the model. In addition, the areas under the curves of the training set (0.895, 95% CI: 0.827-0.963) and test set (0.870, 95% CI: 0.799-0.941) models are similar and have good sensitivity and specificity. Thus, the prediction model based on XGBoost can provide a new method for diagnosing HSPN in children diagnosed with HSP for the first time in dermatology.

There are several limitations to our study. It was a single-center retrospective study with a small sample size and no external validation. Secondly, due to the limitation of data sources, although this study included many predictive variables for screening, it was still not comprehensive. There may be potential predictive variables that were not included. In addition, this will further limit the advantage of the XGBoost algorithm. The next study will increase the sample size and expand the prediction index.

5. Conclusion

Based on the XGBoost prediction model, we can preliminarily predict HSP renal damage according to clinical test data in dermatological outpatient work. This can reduce the harm caused by invasive examination of children. It provides a new idea for the prognosis of children with Henoch-Schönlein purpura in the first diagnosis of dermatology. In future work, we will improve the shortcomings, starting from clinical needs, to better serve the clinical application.

Data Availability

The data used to support the findings of this study are available from the corresponding author upon request.

Conflicts of Interest

The authors declare no conflict of interest.

References

[1] L. E. Hetland, K. S. Susrud, K. H. Lindahl, and A. Bygum, "Henoch-Schönlein purpura: a literature review," *Acta Dermato-Venereologica*, vol. 97, no. 10, pp. 1160–1166, 2017.

[2] M. Mossberg, M. Segelmark, R. Kahn, M. Englund, and A. J. Mohammad, "Epidemiology of primary systemic vasculitis in children: a population-based study from southern Sweden," *Scandinavian Journal of Rheumatology*, vol. 47, no. 4, pp. 295–302, 2018.

[3] A. Audemard-Verger, E. Pillebout, L. Guillevin, E. Thervet, and B. Terrier, "IgA vasculitis (Henoch-Shonlein purpura) in adults: diagnostic and therapeutic aspects," *Autoimmunity Reviews*, vol. 14, no. 7, pp. 579–585, 2015.

[4] A. K. C. Leung, B. Barankin, and K. F. Leong, "Henoch-Schönlein purpura in children: an updated review," *Current Pediatric Reviews*, vol. 16, no. 4, pp. 265–276, 2020.

[5] S. Nie, W. He, T. Huang et al., "The spectrum of biopsy-proven glomerular diseases among children in China," *Clinical Journal of the American Society of Nephrology*, vol. 13, no. 7, pp. 1047–1054, 2018.

[6] R. López-Mejías, S. Castañeda, F. Genre et al., "Genetics of immunoglobulin-A vasculitis (Henoch-Schonlein purpura): an updated review," *Autoimmunity Reviews*, vol. 17, no. 3, pp. 301–315, 2018.

[7] A. Audemard-Verger, B. Terrier, A. Dechartres et al., "Characteristics and management of IgA vasculitis (Henoch-Schönlein) in adults: data from 260 patients included in a French multicenter retrospective survey," *Arthritis & Rhematology*, vol. 69, no. 9, pp. 1862–1870, 2017.

[8] D. Shi, H. Chan, X. Yang et al., "Risk factors associated with IgA vasculitis with nephritis (Henoch-Schönlein purpura nephritis) progressing to unfavorable outcomes: a meta-analysis," *PLoS One*, vol. 14, no. 10, article e0223218, 2019.

[9] Y. H. Yang, H. H. Yu, and B. L. Chiang, "The diagnosis and classification of Henoch-Schonlein purpura: an updated review," *Autoimmunity Reviews*, vol. 13, no. 4-5, pp. 355–358, 2014.

[10] G. Currie, K. E. Hawk, E. Rohren, A. Vial, and R. Klein, "Machine learning and deep learning in medical imaging: intelligent imaging," *Journal of Medical Imaging and Radiation Sciences*, vol. 50, no. 4, pp. 477–487, 2019.

[11] K. Lan, S. Fong, L.-S. Liu et al., "A clustering based variable sub-window approach using particle swarm optimisation for biomedical sensor data monitoring," *Enterprise Information Systems*, vol. 15, no. 1, pp. 15–35, 2021.

[12] S. Deb, Z. Tian, S. Fong, R. Wong, R. Millham, and K. Wong, "Elephant search algorithm applied to data clustering," *Soft Computing*, vol. 22, no. 8, pp. 6035–6046, 2018.

[13] N. Peiffer-Smadja, T. M. Rawson, R. Ahmad et al., "Machine learning for clinical decision support in infectious diseases: a narrative review of current applications," *Clinical Microbiology and Infection*, vol. 26, no. 5, pp. 584–595, 2020.

[14] S. E. Awan, F. Sohel, F. M. Sanfilippo, M. Bennamoun, and G. Dwivedi, "Machine learning in heart failure," *Current Opinion in Cardiology*, vol. 33, no. 2, pp. 190–195, 2018.

[15] J. Li, S. Fong, R. K. Wong, R. Millham, and K. Wong, "Elitist binary wolf search algorithm for heuristic feature selection in high-dimensional bioinformatics datasets," *Scientific Reports*, vol. 7, no. 1, pp. 1–14, 2017.

[16] J. Shi, Y. Ye, D. Zhu, L. Su, Y. Huang, and J. Huang, "Automatic segmentation of cardiac magnetic resonance images based on multi-input fusion network," *Computer Methods and Programs in Biomedicine*, vol. 209, article 106323, 2021.

[17] S. Ozen, A. Pistorio, S. M. Iusan et al., "EULAR/PRINTO/PRES criteria for Henoch-Schonlein purpura, childhood polyarteritis nodosa, childhood wegener granulomatosis and childhood takayasu arteritis: Ankara 2008. Part ii: final classification criteria," *Annals of the Rheumatic Diseases*, vol. 69, no. 5, pp. 798–806, 2010.

[18] A. N. Mian and G. J. Schwartz, "Measurement and estimation of glomerular filtration rate in children," *Advances in Chronic Kidney Disease*, vol. 24, no. 6, pp. 348–356, 2017.

[19] X. H. Chi, G. P. Li, Q. S. Wang et al., "CKD-EPI creatinine-cystatin c glomerular filtration rate estimation equation seems more suitable for chinese patients with chronic kidney disease than other equations," *BMC Nephrology*, vol. 18, no. 1, pp. 1–7, 2017.

[20] K. Davagdorj, V. H. Pham, N. Theera-Umpon, and K. H. Ryu, "Xgboost-based framework for smoking-induced noncommunicable disease prediction," *International Journal of Environmental Research and Public Health*, vol. 17, no. 18, article 6513, 2020.

[21] B. Yu, W. Qiu, C. Chen et al., "Submito-XGBoost: predicting protein submitochondrial localization by fusing multiple feature information and extreme gradient boosting," *Bioinformatics*, vol. 36, no. 4, pp. 1074–1081, 2020.

[22] Y. Li, M. Li, C. Li, and Z. Liu, "Forest aboveground biomass estimation using Landsat 8 and Sentinel-1A data with machine learning algorithms," *Scientific Reports*, vol. 10, no. 1, pp. 1–12, 2020.

[23] B. V. Reamy, J. T. Servey, and P. M. Williams, "Henoch-Schönlein purpura (IgA vasculitis): rapid evidence review," *American Family Physician*, vol. 102, no. 4, pp. 229–233, 2020.

[24] Ş. G. Karadağ, F. Çakmak, B. Çil et al., "The relevance of practical laboratory markers in predicting gastrointestinal and renal involvement in children with henoch-schönlein purpura," *Postgraduate Medicine*, vol. 133, no. 3, pp. 272–277, 2021.

[25] H. Liu, W. Cui, H. Liu, and C. Zhang, "Predicative value of urinary protein biomarkers on delayed renal involvement in children with henoch-schönlein purpura," *Science China. Life Sciences*, vol. 62, no. 12, pp. 1594–1596, 2019.

[26] N. Q. K. Le, D. T. Do, F. Y. Chiu, E. K. Y. Yapp, H. Y. Yeh, and C. Y. Chen, "Xgboost improves classification of mgmt promoter methylation status in idh1 wildtype glioblastoma," *Journal of Personalized Medicine*, vol. 10, no. 3, article 128, 2020.

[27] P. Liu, B. Fu, S. X. Yang, L. Deng, X. Zhong, and H. Zheng, "Optimizing survival analysis of xgboost for ties to predict disease progression of breast cancer," *IEEE Transactions on Biomedical Engineering*, vol. 68, no. 1, pp. 148–160, 2021.

Hindawi
Computational and Mathematical Methods in Medicine
Volume 2022, Article ID 2492667, 7 pages
https://doi.org/10.1155/2022/2492667

Research Article

Ultrasound Radiomics-Guided Iliac Fascia Block on Postoperative Cognitive Dysfunction in Elderly Patients Undergoing Hip Surgery

Jun Zha,[1] **Jinping Ni**,[2] **Shuo Chen**,[1] **Haijun Feng**,[1] **Tuanjie Che**,[3,4] **and Shigang Qiao**[1]

[1]*Faculty of Anesthesiology, Affiliated Suzhou Science & Technology Town Hospital of Nanjing Medical University, Suzhou, Jiangsu 215153, China*
[2]*Department of Anesthesiology, Suzhou Kowloon Hospital, Shanghai Jiaotong University School of Medicine, Suzhou, Jiangsu 215028, China*
[3]*Laboratory of Precision Medicine and Translational Medicine, Affiliated Suzhou Science and Technology Town Hospital of Nanjing Medical University, Suzhou 215153, China*
[4]*Gansu Key Laboratory of Functional Genomics and Molecular Diagnosis, Lanzhou 730000, China*

Correspondence should be addressed to Tuanjie Che; chetj@126.com and Shigang Qiao; qiaos@njmu.edu.cn

Received 20 January 2022; Revised 25 March 2022; Accepted 26 April 2022; Published 17 May 2022

Academic Editor: Kelvin Wong

Objective. Elderly patients with hip surgery are prone to postoperative cognitive dysfunction (POCD), leading to health management difficulties. This study is aimed at investigating the effect of ultrasound radiomics-guided iliac fascia block on POCD. *Methods*. A total of 67 cases of patients who had undergone hip joint surgery were divided into a training set ($n = 47$) and a validation set (radiomics-guided group, $n = 20$). The patients were intervened with ultrasound radiomics-guided iliac fascia block, and the maximum relevance minimum redundancy sifts out the image omics features obtained from 2D ultrasound images of patients. Another 20 patients undergone general anesthesia served as control. The incidence of POCD, the total amount of fentanyl, the visual analogue score (VAS) at different time points, and the levels of CRP and NSE in plasma were compared between the two groups. *Results*. The AUC on the training and validation sets were higher than 0.940. The incidence of POCD in the radiomics-guided and general anesthesia group was 5% and 30%, respectively ($P = 0.037$). Compared with the general anesthesia group, the dosage of fentanyl in the radiomics-guided was lower, the VAS score at 6 h, 1 d, and 2 d after operation was smaller, and the levels of CRP and NSE were lower (all $P < 0.05$). *Conclusions*. For elderly patients with hip surgery, the ultrasound radiomics-guided iliac fascia block can reduce the incidence of POCD and improve the effect of nerve block.

1. Introduction

The postoperative cognitive dysfunction (POCD) often occurs in elderly patients; it refers to a series of neurological complication after surgery [1–3]. Early intervention can reduce the incidence of POCD and minimize the degree of brain injury [4, 5]. Therefore, intervention in the influencing factors of POCD is an effective measure to reduce the occurrence of POCD.

In addition to old age, pain is also considered a high risk factor for POCD [6–9]. The mechanism of central inflammatory response also plays an essential role [10]. Patients with hip disease not only have severe pain before the operation but also suffer from pain interference after the operation

[11–14], resulting in abnormal difficulty in health management. Therefore, appropriate preoperative and postoperative analgesia may be helpful for the control of POCD.

In the surgical treatment of hip joint lesions, some studies have shown that iliac fascia block can play a better analgesic effect and reduce postoperative complications [15–19]. However, it is not clear whether POCD can be affected. The radiomics features are of great value in diagnosing clinical diseases and evaluating treatment response [20–22]. In recent years, the clinical application has gradually increased. In this study, based on iliac fascia block ultrasound radiomics-guided, we tried to reduce the impact of surgery on COPD in addition to reducing pain.

2. Materials and Methods

2.1. General Information. All the participants were patients in Suzhou Science and Technology Town Hospital and Suzhou Kowloon Hospital for elective surgery in patients with hip disease. The research design was approved by the ethics committee of our hospital, and the operation plan was informed consent of patients and their families.

Inclusive criteria are as follows: hip joint surgery patients, normal nerve function can cooperate with treatment, and age ≥ 60 years. Exclusion criteria are as follows: patients with a history of mental or neurological diseases, patients with abnormal visual or auditory function, patients with severe organ abnormalities, and patients with missing clinical and follow-up data or voluntarily applying to withdraw from the study.

Finally, 87 patients were enrolled in the study, including 55 males and 32 females. Among then, 67 cases were divided into a training set ($n = 47$) and a validation set (radiomics-guided group, $n = 20$) according to the 10-fold crossover method. Another 20 patients undergone general anesthesia served as the control group.

2.2. Anesthesia Method. The general anesthesia group was given sufentanil 0.5 μg/kg, propofol medium/long chain fat emulsion 2.5 mg/kg, rocuronium 0.8 mg/kg intravenous anesthesia induction, after the human pump propofol 6 mg/kg/h, and 0.8 MAC sevoflurane to maintain anesthesia.

The radiomics-guided group was blocked in the iliac fascia space: supine, the affected side of the limb slightly extended outward, conventional disinfection spread sterile towel, the Sonosite S-nerve color Doppler was used. After the probe was placed vertically at the position of anterior superior iliac spine, it was rotated about 20° clockwise and then moved slowly to the middle and outer 1/3 of the anterior superior iliac spine and pubic symphysis. The probe was adjusted to determine the structure of the iliac fascia space. When the needle tip penetrates below the iliac fascia, inject 30 mL of 0.25% ropivacaine hydrochloride after no blood is drawn back, pay attention to the diffusion of local anesthetic to the head, and keep the needle route within the visual range to prevent the needle from entering the abdominal cavity too deep.

2.3. Postoperative Analgesia. Patients in both sets were given patient-controlled intravenous analgesia. Fentanyl (20 μg/kg) was dissolved in 100 mL 0.9% sodium chloride solution. The injection speed was controlled at 2 mL/h and locked for 15 min. The single self-control volume was 0.5 mL.

2.4. Image Preprocessing and Region of Interest Segmentation. Image preprocessing can be divided into two steps: image gray balance and image noise reduction. Histogram equalization reduces feature differences caused by image gain differences between patients. To reduce the influence of image noise on image omics feature extraction, median filtering is applied to image denoising.

Image segmentation was performed manually by an ultrasound physician. Region of interest (ROI) was plotted on the maximum cross-section of the injected ultrasound image of each patient. The complete structural range of iliac fascia was plotted by adjusting the spatial structure position. The segmented images were finally validated by an ultrasound physician with 5 years of experience. The specific flow chart for image preprocessing and region of interest segmentation is shown in Figure 1.

2.5. Radiomics Analysis. The deep learning model in this research is generated by the Deep Red AI Toolbox. Firstly, the image omics features of the region of interest are extracted from the preprocessed images. Then, the extracted features are normalized to make the data normalized and conform to the standard normal distribution. The transformation function is as follows:

$$x^* = \frac{(\chi - \bar{x})}{\sigma}. \tag{1}$$

In addition, the maximum relevance minimum redundancy (mRMR) and the least absolute shrinkage and selection operation (LASSO) algorithm sift out the image omics features obtained from 2D ultrasound images of patients and establish the image omics score.

The mRMR algorithm is a feature selection method that maximizes the correlation between feature variables and targets and minimizes the correlation between features. More mutual information is used to measure the feature redundancy and the correlation between categories, and information entropy and information difference are used to select the optimal feature subset.

$$\mathrm{I}(x, y) = \iint P(x, y) \log \frac{P(x, y)}{P(x)P(y)} dxdy. \tag{2}$$

In the formula, x and y are given two random variables, $P(x, y)$ is the joint probability distribution function of x and y, and $P(x)$ and $P(y)$ are probability distributions of x and y, respectively.

To find the feature subset S containing m features, the following formula can be used to calculate its correlation:

$$\max D(S, c)\,; D = \frac{1}{|S|} \sum_{x_i \in S} I(x_i\,; c). \tag{3}$$

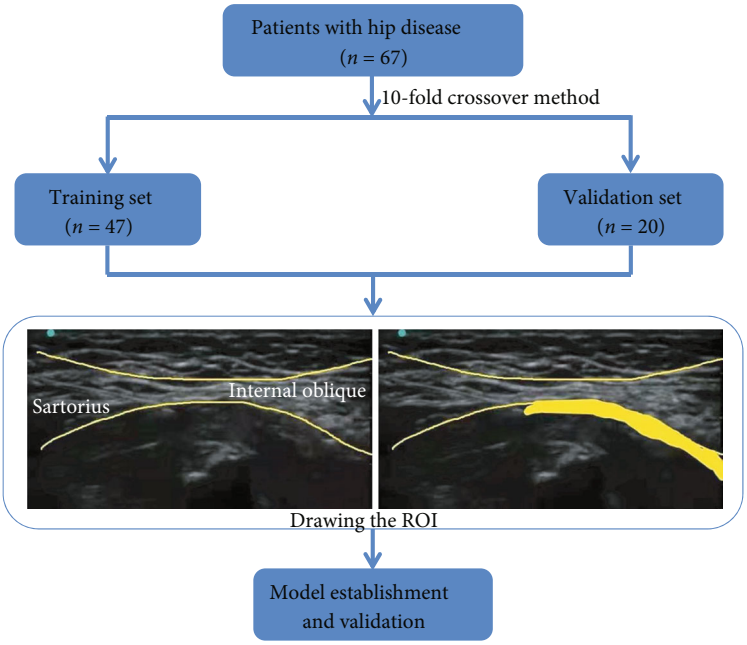

Figure 1: Flow chart of image preprocessing and region of interest segmentation.

A subset with m features may not be the best subset of features, and when two features are highly interdependent and one of them is removed, the class discrimination of the two will not change much.

The selection of variables is mainly based on the LASSO algorithm proposed by Tibshirani et al. in 1996 [23]. The loss function is as follows:

$$\min_{\beta} \sum_{n=1}^{N} \left(y^n - \sum_{P=1}^{m} \beta_p x_p^n \right)^2 + \lambda \sum_{P=1}^{m} \left| \beta_p \right|, \tag{4}$$

where y^n is the category label of the Nth sample and N is the number of samples. λ is the regularization parameter, which controls the sparsity of the model.

2.6. Evaluation Index. The incidence of POCD, the operation time, and the total amount of fentanyl were recorded.

The visual analogue score (VAS) was used to evaluate patients' pain before the operation, 20 minutes after the puncture, 6 hours after the operation, and 1, 2, and 3 days after the operation.

The right jugular vein blood was collected before operation and at 6 h, 1 d, 2 d, and 3 d after operation. The levels of CRP (C-reactive protein) and neuron specific enolase (NSE) in plasma were detected by enzyme-linked immunosorbent assay (ELISA). Taking into account the influence of intraoperative bleeding and transfusion, the postoperative results were recorded, and corrected values were used, and the calculation was as follows:

$$\text{Corrected value} = \text{measured value} \times \frac{\text{HCT before anesthesia}}{\text{actual HCT}}. \tag{5}$$

2.7. Statistical Methods. The SPSS 21.0 software was used for statistical analysis. The area under the receiver operating characteristic (ROC) curve was used to evaluate the effectiveness of the model. The count data were described by frequency and constituent ratio, and the comparison between the radiomics-guided and general anesthesia groups was performed by chi-square test. Quantitative data are expressed as the mean ± standard deviation. Shapiro–Wilk tests were performed to determine the normality of the data distributions. If the measurement data conform to the normal distribution, use t-test to compare between above two groups.

3. Results

3.1. Diagnostic Efficacy of Radiomics Models. The selected models were evaluated, and the AUC of the model on the training set was 0.942 (95% CI 0.890-0.994), and the AUC of the model on the validation set was 0.941 (95% CI 0.885-0.996). The ROC curve is shown in Figure 2.

3.2. Comparison of General Information and Surgical Features. The basic information of patients is shown in Table 1. There was no significant difference in gender, age, and BMI between the radiomics-guided and general anesthesia groups ($P > 0.05$). All patients successfully completed hip surgery; postoperative showed promising results (Figures 3 and 4). The operation time of the radiomics-guided group was 96.4 ± 26.3 min, while that of general anesthesia group was 97.7 ± 31.2 min. There was no significant difference between the two groups ($P > 0.05$). The incidence of POCD in the radiomics-guided group was significantly lower than that in the general anesthesia group (5% vs. 30%, $\chi^2 = 4.329$, $P = 0.037$). The dosage of fentanyl in the radiomics-guided group was 411.5 ± 47.2 μg, and that

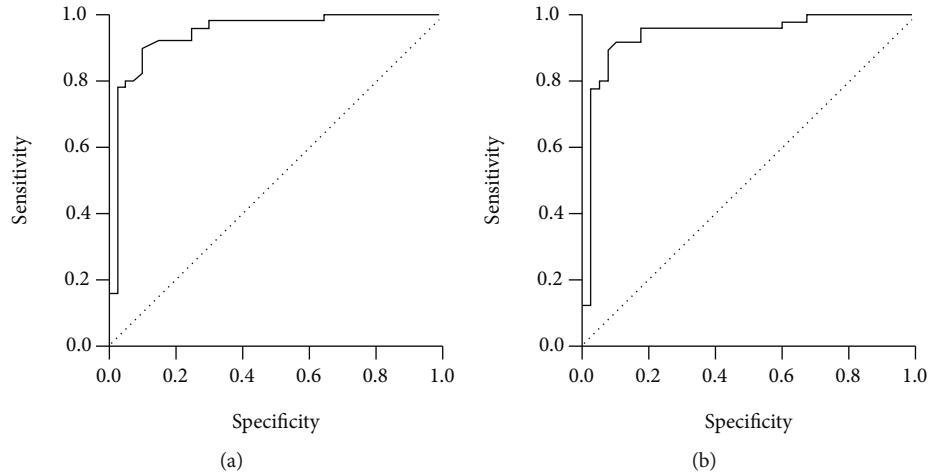

Figure 2: The ROC curve of ultrasound radiomics models: (a) training set; (b) validation set.

Table 1: General information between the radiomics-guided and general anesthesia groups.

Groups	n	Gender		Age (years)	BMI (kg/m^2)
		Male	Female		
Radiomics-guided		14	6	69.6 ± 7.1	22.4 ± 2.7
Control		12	8	67.2 ± 5.8	21.9 ± 2.3
x^2/t value		0.440		1.170	0.630
P value		0.507		0.249	0.532

in the general anesthesia group was 738.7 ± 82.4 μg, and the dosage of fentanyl in the radiomics-guided group was significantly less than that in the general anesthesia group ($P < 0.05$).

3.3. VAS Scores at Each Time Point. The VAS scores in the radiomics-guided and general anesthesia groups are shown in Figure 5. Compared with the general anesthesia group, the radiomics-guided group decreased significantly 20 minutes after puncture and 6 hours, 1 day, and 2 days after operation.

3.4. Serological Indexes at Each Time Point. The detailed comparison of CRP and NSE between the radiomics-guided and general anesthesia groups before and after the operation is shown in Table 2. Compared with that before operation, CRP and NSE increased significantly at each time point after operation, especially in the general anesthesia group.

4. Discussion

4.1. Analysis of POCD in Elderly Patients with Hip Surgery. The cognitive dysfunction is a common complication after hip arthroplasty. The incidence rate of POCD increases with age. The clinical incidence rate of elderly patients is 40% to 50% [24–26]. Anxiety, cognitive impairment, memory impairment, attention deficit, language, and social skill decline are common clinical manifestations, which seriously affect the quality of life of patients after. However, some scholars pointed out that surgical stress, operation time, physiological characteristics, anesthetic methods, extracorporeal circulation, anesthesia mode, residual anesthetic, and postoperative pain may be closely related to this complication [6–9]. Elderly patients still need general anesthesia because of their long-term special body position intolerance, difficulty in puncture in spinal canal, and use of anticoagulants and other factors, which may lead to postoperative cognitive dysfunction.

4.2. Advantages of Combined General Anesthesia and Iliac Fascia Block. Peripheral nerve block is often used as an important supplement and auxiliary means of general anesthesia [15–17]. The anesthetic effect is clear, which can shorten the recovery time, reduce the dosage of general anesthetic, and effectively reduce the incidence rate of related complications. Among various regional block techniques, iliac fascia space block is a simple and easy to master technique. Its mechanism is to inject local anesthetics into the space between the iliac fascia and the iliac muscle. Then, the femoral nerve and lateral femoral cutaneous nerve between them were blocked assisted by ultrasound-guided operation. This technology is used to treat the pain of patients with hip diseases, with rapid onset and exact effect. Some studies scored the pain of patients admitted to the emergency department [15, 27, 28]. It was found that the preoperative score was high, and the pain was not well controlled. However, immediate iliac fascia space block could effectively control the preoperative pain.

4.3. Comparison of Diagnostic Efficacy of Radiomics Models. The results showed that the AUC of ultrasonic image radiomics in the training set (AUC: 0.942, 95% CI 0.890-0.994) and the validation set (AUC: 0.941, 95% CI 0.885-0.996) is similar. It is proved that the ultrasonic image radiomics has great efficiency for the successful puncture.

4.4. Comparison of POCD Characteristics. The dosage of fentanyl in the radiomics-guided group was significantly lower than that in the general anesthesia group. The VAS score

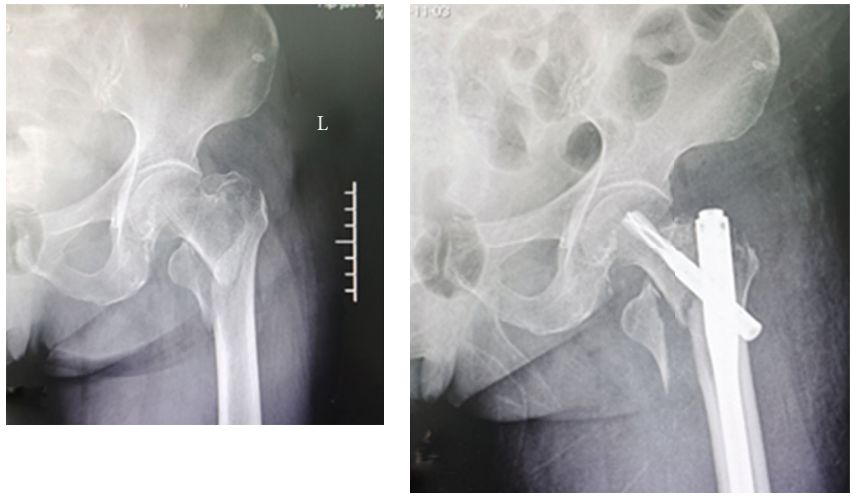

(a) (b)

Figure 3: Typical case of internal fixation from a patient with hip fracture: (a) before operation; (b) after operation.

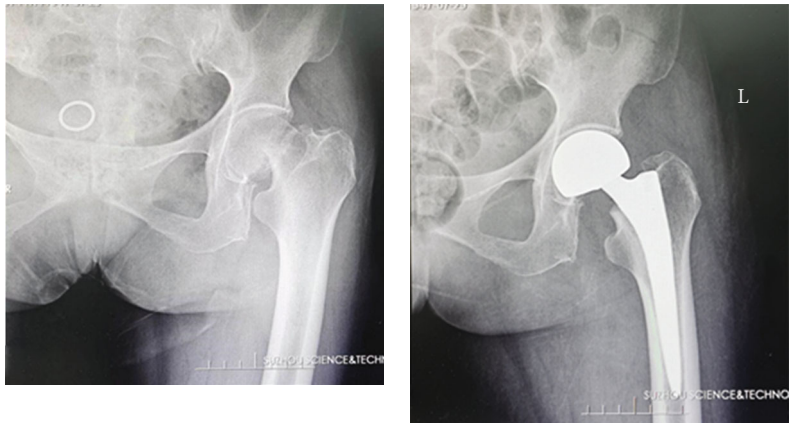

(a) (b)

Figure 4: Typical case of hip replacement: (a) before operation; (b) after operation.

in the radiomics-guided group was significantly lower than that in the general anesthesia group at 6 h, 1 d, and 2 d after operation. In addition, the incidence of POCD in the radiomics-guided group (5%) was significantly lower than that in the general anesthesia group (30%). All these results indicated that the ultrasound radiomics-guided iliac fascia block can reduce the incidence of POCD after hip operation in elderly patients.

4.5. Comparison of CRP and NSE Levels. Some studies have shown that the central nervous system damage in patients with serum CRP and other inflammatory factors [29]. The CRP is an important cytokine with extensive biological activity in human body, which plays an important role in the central neuropathy progression. NSE is an enzyme widely existing in neurons, and its level changes are closely related to the degree of brain injury and prognosis of patients. Some studies have pointed out that inflammatory reaction and chronic oxidative stress reaction may lead to the synthesis and secretion of NSE [30, 31]. When it accumulates in the brain, it may lead to memory loss and progressive cognitive impairment. In this study, the CRP and NSE levels in both groups increased in a short period of time, indicating that proinflammatory factors are related to cognitive function. Compared with the general anesthesia group, the dosage of fentanyl in the radiomics-guided was lower, and the levels of CRP and NSE after operation were also lower. The results indicate that the ultrasound radiomics-guided iliac fascia block can reduce the use of general anesthesia drugs, reduce the release of inflammatory factors after and during operation, and improve postoperative cognitive function.

5. Conclusion

In conclusion, for elderly patients with hip surgery, the ultrasound radiomics-guided iliac fascia block can reduce the incidence of POCD and improve the effect of nerve block. However, the number of samples in this study is small, which needs to be further studied. The patients

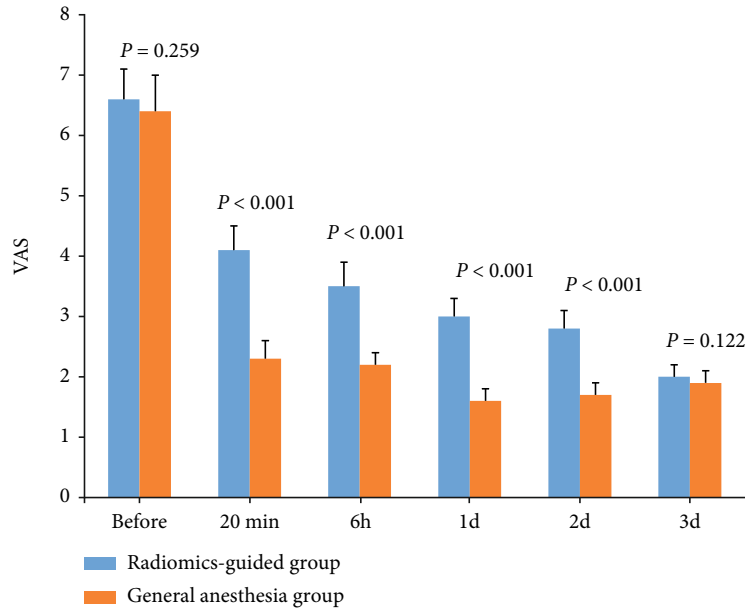

Figure 5: The VAS scores at each time point.

Table 2: Serological indexes at each time point.

Index	Radiomics-guided group	General anesthesia group	t value	P vlaue
CRP (mg/L)				
Before operation	3.2 ± 0.4	3.3 ± 0.4	0.791	0.434
1 d after operation	7.8 ± 0.8	8.2 ± 1.1	2.302	0.027
2 d after operation	6.4 ± 0.7	6.9 ± 0.6	2.425	0.020
3 d after operation	3.6 ± 0.3	4.7 ± 0.5	8.437	< 0.001
NSE (μg/L)				
Before operation	5.8 ± 1.2	5.9 ± 0.8	0.310	0.758
1 d after operation	12.3 ± 3.1	14.6 ± 3.4	2.236	0.031
2 d after operation	11.8 ± 2.8	13.7 ± 2.5	2.264	0.029
3 d after operation	6.2 ± 1.6	7.4 ± 1.5	2.447	0.019

included in this study were insufficient and came from the same center. In addition, sufficient specimen is essential in ensuring the machine learning model's efficiency.

Data Availability

The data used to support the findings of this study are available from the corresponding authors upon request.

Conflicts of Interest

All authors declare no conflicts of interest in this paper.

Authors' Contributions

Jun Zha and Jinping Ni contributed equally to this work.

Acknowledgments

This work was supported by grants QNRC2016219 (to Dr. Qiao) from the Jiangsu Key Talent Youth Awards in Medicine, GSWS2019092 (to Dr. Qiao) from the Gusu Health Youth Talent Awards, 2020BYGT009 from the Open Project of Key Laboratory of Functional Genomics and Molecular Diagnosis of Gansu Province (to Dr. Zha), and 2019Y03 (to Dr. Zha) from the Young Talent Scientific Research Foundation of Suzhou Science & Technology Town Hospital.

References

[1] R. Ehsani, S. Djalali Motlagh, B. Zaman, S. Sehat Kashani, and M. R. Ghodraty, "Effect of general versus spinal anesthesia on postoperative delirium and early cognitive dysfunction in elderly patients," *Anesthesiology and Pain Medicine*, vol. 10, no. 4, article e101815, 2020.

[2] Y. X. Shen, Y. P. Chen, H. C. Zang, and G. Shao, "Evaluation of the efficiency of propofol versus isoflurane anesthesia interventions in treating elderly patients with postoperative cognitive dysfunction," *Medicine (Baltimore)*, vol. 99, no. 49, article e23511, 2020.

[3] W. Zhao, Y. Hu, H. Chen et al., "The effect and optimal dosage of dexmedetomidine plus sufentanil for postoperative analgesia in elderly patients with postoperative delirium and early postoperative cognitive dysfunction: a single-center, prospective, randomized, double-blind, controlled trial," *Frontiers in Neuroscience*, vol. 14, article 549516, 2020.

[4] Y. Gao, L. Liu, B. Zhao, Y. Wang, S. Yu, and H. Wang, "Effect of general and non-general anesthesia on postoperative

cognitive dysfunction," *Journal of the College of Physicians and Surgeons–Pakistan*, vol. 30, no. 4, pp. 407–411, 2020.

[5] U. Nilsson, K. Liander, O. Rooyackers, and L. I. Eriksson, "Patients' experiences of early postoperative cognition and its relation to cognitive decline and inflammatory responses: a protocol for a mixed-methods study," *BMJ Open*, vol. 9, no. 12, article e032650, 2019.

[6] B. Gao, B. Zhu, and C. Wu, "Preoperative serum 25-hydroxyvitamin D level, a risk factor for postoperative cognitive dysfunction in elderly subjects undergoing total joint arthroplasty," *The American Journal of the Medical Sciences*, vol. 357, no. 1, pp. 37–42, 2019.

[7] S. Otomo, K. Maekawa, T. Baba, T. Goto, and T. Yamamoto, "Evaluation of the risk factors for neurological and neurocognitive impairment after selective cerebral perfusion in thoracic aortic surgery," *Journal of Anesthesia*, vol. 34, no. 4, pp. 527–536, 2020.

[8] R. Yong and Y. Meng, "Preoperative neutrophil–lymphocyte ratio, an independent risk factor for postoperative cognitive dysfunction in elderly patients with gastric cancer," *Geriatrics & Gerontology International*, vol. 20, no. 10, pp. 927–931, 2020.

[9] Y. Zhang, H. G. Bao, Y. L. Lv et al., "Risk factors for early postoperative cognitive dysfunction after colorectal surgery," *BMC Anesthesiology*, vol. 19, no. 1, p. 6, 2019.

[10] C. Knaak, G. Vorderwülbecke, C. Spies et al., "C-reactive protein for risk prediction of post-operative delirium and postoperative neurocognitive disorder," *Acta Anaesthesiologica Scandinavica*, vol. 63, no. 10, pp. 1282–1289, 2019.

[11] A. Dizdarevic, F. Farah, J. Ding et al., "A comprehensive review of analgesia and pain modalities in hip fracture pathogenesis," *Current Pain and Headache Reports*, vol. 23, no. 10, p. 72, 2019.

[12] S. N. Hofstede, M. G. J. Gademan, T. Stijnen, R. Nelissen, and P. J. Marang-van de Mheen, "The influence of preoperative determinants on quality of life, functioning and pain after total knee and hip replacement: a pooled analysis of dutch cohorts," *BMC Musculoskeletal Disorders*, vol. 19, no. 1, p. 68, 2018.

[13] T. A. Lentz, S. Z. George, O. Manickas-Hill et al., "What general and pain-associated psychological distress phenotypes exist among patients with hip and knee osteoarthritis?," *Clinical Orthopaedics and Related Research*, vol. 478, no. 12, pp. 2768–2783, 2020.

[14] R. Shah, Y. F. Kuo, J. Westra, Y. L. Lin, and M. A. Raji, "Opioid use and pain control after total hip and knee arthroplasty in the us, 2014 to 2017," *JAMA Network Open*, vol. 3, no. 7, article e2011972, 2020.

[15] C. Falyar and D. Tola, "Ultrasound-guided fascia iliaca blocks in the emergency department," *Geriatric Nursing*, vol. 40, no. 4, pp. 441–444, 2019.

[16] J. L. Glomset, E. Kim, J. M. Tokish et al., "Reduction of postoperative hip arthroscopy pain with an ultrasound-guided fascia iliaca block: a prospective randomized controlled trial," *The American Journal of Sports Medicine*, vol. 48, no. 3, pp. 682–688, 2020.

[17] H. Wang, Q. Li, and Y. Ni, "Ultrasound-guided "hourglass-pattern" fascia iliac block combined with sacral plexus and gluteal epithelial nerve block for an elderly hip fracture patient with organ failure," *Medicine (Baltimore)*, vol. 99, no. 25, article e19732, 2020.

[18] Z. Han, K. Liu, Z. Li, and P. Luo, "A pre-check operator for reducing algorithmic optimisation time in image processing applications," *Enterprise Information Systems*, vol. 13, pp. 1–13, 2021.

[19] D. Hua, Y. Wang, S. Ji, J. Zha, and Y. Xia, "The multi-objective optimization of combustion system operations based on deep data-driven models," *Journal of Medical Imaging and Health Informatics*, vol. 9, no. 5, pp. 951–955, 2019.

[20] H. Cui, D. Zhang, F. Peng et al., "Identifying ultrasound features of positive expression of Ki67 and P53 in breast cancer using radiomics," *Asia-Pacific Journal of Clinical Oncology*, vol. 17, no. 5, pp. e176–e184, 2021.

[21] Y. Guo, Y. Hu, M. Qiao et al., "Radiomics analysis on ultrasound for prediction of biologic behavior in breast invasive ductal carcinoma," *Clinical Breast Cancer*, vol. 18, no. 3, pp. e335–e344, 2018.

[22] Y. Liu, Q. Fang, A. Jiang, Q. Meng, G. Pang, and X. Deng, "Texture analysis based on u-net neural network for intracranial hemorrhage identification predicts early enlargement," *Computer Methods and Programs in Biomedicine*, vol. 206, 2021.

[23] Y. Antonacci, J. Toppi, D. Mattia, A. Pietrabissa, and L. Astolfi, "Single-trial connectivity estimation through the least absolute shrinkage and selection operator," in *2019 41st Annual International Conference of the IEEE Engineering in Medicine and Biology Society (EMBC)*, vol. 2019, pp. 6422–6425, Berlin, Germany, 2019.

[24] S. Tang, W. Huang, K. Zhang, W. Chen, and T. Xie, "Comparison of effects of propofol versus sevoflurane for patients undergoing cardiopulmonary bypass cardiac surgery," *Pakistan Journal of Medical Sciences*, vol. 35, no. 4, pp. 1072–1075, 2019.

[25] Q. X. Xiao, Q. Liu, R. Deng, Z. W. Gao, and Y. Zhang, "Postoperative cognitive dysfunction in elderly patients undergoing hip arthroplasty," *Psychogeriatrics*, vol. 20, no. 4, pp. 501–509, 2020.

[26] W. Yan, H. Mao, and P. Qiu, "Effects of different analgesia regimens on early post-operative cognitive dysfunction in elderly patients undergoing radical resection of cervical carcinoma," *Experimental and Therapeutic Medicine*, vol. 18, no. 2, pp. 1465–1469, 2019.

[27] E. Dochez, G. J. van Geffen, J. Bruhn, N. Hoogerwerf, H. van de Pas, and G. Scheffer, "Prehospital administered fascia iliaca compartment block by emergency medical service nurses, a feasibility study," *Scandinavian journal of trauma, resuscitation and emergency medicine*, vol. 22, no. 1, p. 38, 2014.

[28] L. Haines, E. Dickman, S. Ayvazyan et al., "Ultrasound-guided fascia iliaca compartment block for hip fractures in the emergency department," *The Journal of Emergency Medicine*, vol. 43, no. 4, pp. 692–697, 2012.

[29] X. Liu, Y. Yu, and S. Zhu, "Inflammatory markers in postoperative delirium (POD) and cognitive dysfunction (POCD): a meta-analysis of observational studies," *PLoS One*, vol. 13, no. 4, article e0195659, 2018.

[30] T. Luescher, J. Mueller, C. Isenschmid et al., "Neuron-specific enolase (NSE) improves clinical risk scores for prediction of neurological outcome and death in cardiac arrest patients: results from a prospective trial," *Resuscitation*, vol. 142, pp. 50–60, 2019.

[31] D. W. Park, S. H. Park, and S. K. Hwang, "Serial measurement of S100B and NSE in pediatric traumatic brain injury," *Child's Nervous System*, vol. 35, no. 2, pp. 343–348, 2019.

Hindawi
Computational and Mathematical Methods in Medicine
Volume 2022, Article ID 4311434, 6 pages
https://doi.org/10.1155/2022/4311434

Research Article

Construction and Evaluation of Prognosis Prediction Model for Patients with Brain Contusion and Laceration Based on Machine Learning

Shaoquan Li, Limei Bai, and Zhixia Zheng

Department of Neurosurgery, Cangzhou Central Hospital, Hebei 061000, China

Correspondence should be addressed to Shaoquan Li; lsq402181850@163.com

Received 18 January 2022; Revised 28 April 2022; Accepted 2 May 2022; Published 12 May 2022

Academic Editor: Kelvin Wong

Objective. Finding valuable risk factors for the prognosis of brain contusion and laceration can help patients understand the condition and improve the prognosis. This study is aimed at analyzing the risk factors of poor prognosis in patients with brain contusion after the operation. *Methods*. A total of 136 patients with cerebral contusion and laceration combined with cerebral hernia treated by neurosurgical craniotomy in our hospital were retrospectively selected and divided into a training set ($n = 95$) and a test set ($n = 41$) by the 10-fold crossover method. Logistic regression and back-propagation neural network prediction models were established to predict poor prognosis factors. The receiver operating characteristic curve (ROC) and the calibration curve were used to verify the differentiation and consistency of the prediction model. *Results*. Based on logistic regression and back-propagation neural network prediction models, GCS score ≤ 8 on admission, blood loss ≥ 30 ml, mannitol ≥ 2 weeks, anticoagulants before admission, and surgical treatment are the risk factors that affect the poor prognosis of patients with a cerebral contusion after the operation. The area under the ROC was 0.816 (95% *CI* 0.705~0.926) and 0.819 (95% *CI* 0.708~0.931), respectively. *Conclusion*. The prediction model based on the risk factors that affect the poor prognosis of patients with brain contusion and laceration has good discrimination and accuracy.

1. Introduction

In recent years, brain contusion and laceration have been increasing with the continuous renewal of transportation [1]. In traffic accidents, the head and neck are some of the most seriously injured parts. Severe traumatic brain injury (TBI) can lead to brain contusion and laceration, mainly manifested by the cooccurrence of contusion and laceration tissues and intracranial edema, with high mortality and disability rates [2]. Brain contusion and laceration refer to two diseases: brain contusion and brain laceration. If the patient only suffers from brain parenchyma injury and the pia mater is not damaged, it is brain contusion. In addition to brain parenchyma damage, it is brain laceration if the patient's pia mater is torn. Brain contusion and laceration refer to the phenomenon that both brain contusion and brain laceration coexist in the patient [3].

Cerebral contusion and laceration mean that patients are prone to increase intracranial pressure and have a greater chance of forming cerebral hernias [4]. Existing research generally advocates that surgical treatment should be recommended on the premise that patients have surgical indications. A craniotomy is an effective treatment, but it is difficult to handle and has a high mortality rate [5]. Brain contusion and laceration in primary TBI are one of the most common diseases. The influencing factors of prognosis of patients with severe traumatic brain injury are issues that scholars pay extensive attention [6]. Progressive brain contusion and laceration are related to many factors. Through early analysis of the relevant factors, we can obtain the valuable risk factors for the prognosis, which is of great significance to

helping patients with brain contusion and laceration to study the condition and improve the prognosis [7, 8]. Therefore, it is helpful to improve the prognosis of patients with brain contusion by identifying the risk factors that affect the poor prognosis after the operation and giving appropriate treatment at an early stage.

Machine learning algorithm has unique advantages in dealing with high-dimensional variables, complex interactions, and nonlinear relationships among variables [9–12]. The prediction analysis of machine learning has been widely used in the biomedical field [13–15]. Based on logistic regression and neural network, this paper constructs a prediction model to study the high-risk factors of poor prognosis in brain contusion and laceration patients. The results can provide suggestions for the surgical plan and postoperative prognosis.

2. Methods

2.1. General Data. A total of 136 patients with brain contusion and laceration admitted to our hospital from 2016 to 2021 were selected as the research object. There were 102 males and 34 females, aged from 18 to 65 (57.54 ± 11.43) years. All patients meet the clinical diagnostic criteria of brain contusion and laceration, and all patients have signed the research consent before participating in this study. Inclusion criteria are as follows: (1) there is a clear history of traumatic brain injury, and a head CT examination is performed to confirm the diagnosis. (2) There are indications for craniotomy. Exclusion criteria are as follows: (1) severe dysfunction of other organs, (2) suffering from blood system diseases, (3) patients complicated with a malignant tumor, and (4) suffering from mental illness.

2.2. Collection of Predictive Variables. The gender, age, Glasgow coma scale (GCS) score, blood loss, the application time of mannitol, whether anticoagulants were used before admission, and operation methods were collected.

2.3. Construction of Machine Learning Model. Logistic regression is the most commonly used statistical model for predicting the outcome variable as a binary variable, which is often used in data mining, automatic diagnosis of diseases, and other fields. One result of the dichotomous response variable Y is denoted as "success," denoted by 1. The other result is denoted as "failure," denoted by 0 [16]. Its general form is as follows:

$$\text{Logit}(P) = \log\left(\frac{P}{1-P}\right) = a + b_1x_1 + b_2x_2 + \cdots + b_mx_m. \quad (1)$$

$x_1, x_2, \ldots, x_m$ are predictors, and $b_1, b, \ldots, b_m$ are regression coefficients of m predictors.

The probability p of the predicted event can be obtained by simple transformation of formula (1).

$$P = \frac{\exp\ (a + b_1x_1 + b_2x_2 + \cdots + b_mx_m)}{1 + \exp\ (a + b_1x_1 + b_2x_2 + \cdots + b_mx_m)}. \quad (2)$$

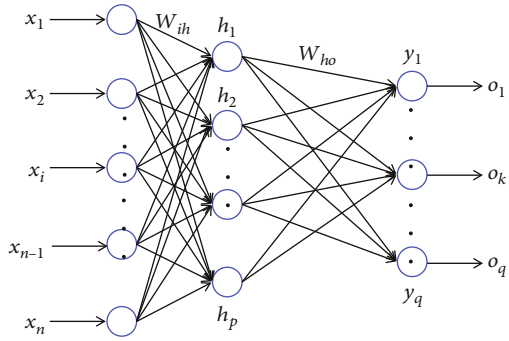

Figure 1: Classical BPNN structure diagram.

2.4. Artificial Neural Network. The neural network model used in this paper is the back-propagation neural network (BPNN). It has a good ability to solve nonlinear problems, and it is the most popular and classic neural network model so far [17]. As a supervised learning process, BPNN algorithm repeatedly replaces the weights and thresholds of network connection with known input and output sample data so that the network's output is closer to the expected output [18]. As far as the whole neural network is concerned, a learning process is completed by two subprocesses of forwarding propagation of input data and backward propagation of error [19]. The classical BPNN structure is shown in Figure 1.

There are n neurons in the input layer, p neurons in the hidden layer, and q neurons in the output layer. Define the input vector as follows:

$$X = (x_1, x_2, \cdots, x_n). \quad (3)$$

Selecting randomly the k-th input sample and its corresponding expected output:

$$x(K) = (x_1(k), x_2(k), \cdots, x_n(k)). \quad (4)$$

Calculating the input and output of neurons in the hidden layer:

$$hi_h(k) = \sum_{i=1}^{n} w_{ih}x_j(k) - b_h h = 1, 2, \cdots, p. \quad (5)$$

Finally, calculating the global error:

$$E = \frac{1}{2m}\sum_{k=1}^{m}\sum_{o=1}^{q}(d_o(k) - y_o(k))^2. \quad (6)$$

All patients were divided into a training set ($n = 95$) and a test set ($n = 41$) by stratified random sampling. The ratio of the training set to the test set is about 7 : 3. The 10-fold crossover method is used to validate the data. The advantage of

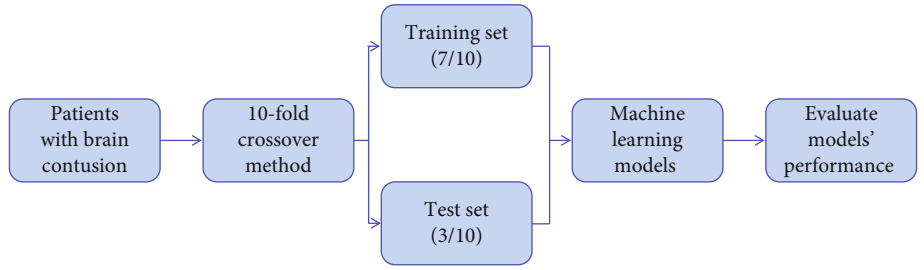

Figure 2: Modeling flow chart of machine learning.

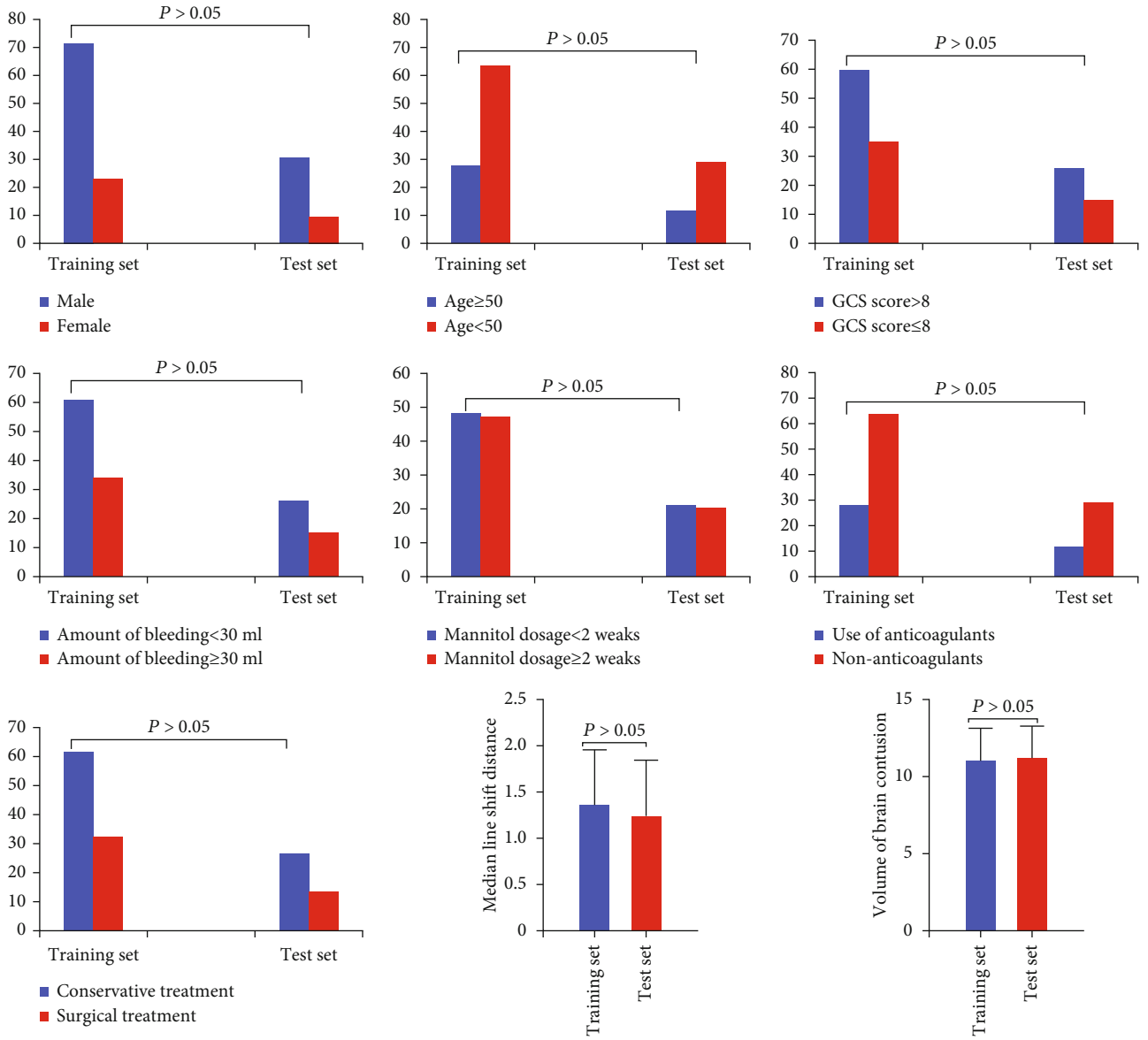

Figure 3: Comparison of clinical data of patients with brain contusion and laceration in the training and test sets. There was no statistically significant difference between the two sets ($P > 0.05$).

this method is that all data are used in the training set and the test set, and each data set is divided into independent verification. The specific process is shown in Figure 2.

2.5. Statistical Analysis. The measurement data is expressed by $\overline{x \pm s}$, the data accords with normal distribution, the comparison between groups adopts an independent sample t

Table 1: Logistic regression analysis of prognostic factors in patients with brain contusion and laceration.

Factors	SE	*P*	OR	95% CI
Volume of brain contusion	0.631	0.025	2.902	1.182-7.123
GCS scores ≤ 8	2.015	0.023	2.757	1.152-6.600
Amount of bleeding ≥ 30 mL	0.591	<0.001	5.935	2.246-15.683
Mannitol application time ≥ 2 weeks	0.408	0.003	4.164	1.648-10.517
Use of anticoagulants	0.614	0.003	4.017	1.592-10.139
Surgical treatment	0.315	0.002	4.943	1.821-13.417

-test, and the counting data is expressed by percentage. The *Chi*-square test was used to analyze the differences between different groups, and $P < 0.05$ means the difference is statistically significant.

3. Results

3.1. Comparison of Predictive Variables Influencing the Prognosis between Two Sets. There was no significant difference between the training set and test in gender, age, admission GCS score, blood loss, the application time of mannitol, use of anticoagulants within 1 week before admission, treatment methods, midline shift distance and brain contusion, and laceration volume ($P > 0.05$), as shown in Figure 3.

3.2. Logistic Regression Analysis of Predictive Variables of Postoperative Prognosis. Logistic regression analysis showed that GCS score ≤ 8, blood loss ≥ 30 mL, mannitol application time ≥ 2 weeks, the use of anticoagulants within 1 week before admission, and surgical treatment were the influencing factors of prognosis of brain contusion and laceration. The details are shown in Table 1.

3.3. BPNN Model Analysis of Predictive Variables of Postoperative Prognosis. Based on the BPNN model, the prediction model of poor prognosis of patients with brain contusion and laceration after operation shows that the GCS score < 8 is 65.0 points at admission, the bleeding volume ≥ 30 ml at admission is 80.0 points, the mannitol application ≥ 2 weeks is 87.0 points, the anticoagulants before admission is 100.0 points, and the surgical treatment after admission 24 hours is 71.3 points, as shown in Figure 4.

3.4. Comparison of Prediction Model Performance. The receiver operator characteristic (ROC) curve showed that the area under the curve (AUC) of the logistic regression model for predicting the poor prognosis of patients with brain contusion and laceration after the operation was 0.816 (95% *CI* 0.705~0.926). The AUC of the BPNN model is 0.819 (95% *CI* 0.708~0.931). The ROC is shown in Figure 5.

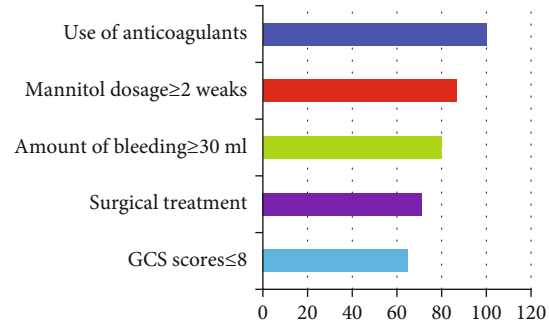

Figure 4: Characteristic factors of poor prognosis in patients with brain contusion and laceration after operation.

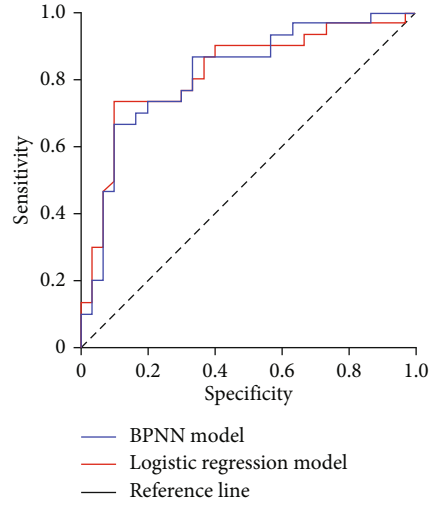

Figure 5: ROC curve of poor postoperative prognosis in patients with brain contusion and laceration.

4. Discussion

With the development of social modernization and the improvement of economic level, the number of patients with TBI caused by traffic accidents is increasing. The head and neck are some of the most seriously injured organs in traffic accidents [20]. Patients with mild traumatic brain injury can show signs and symptoms of unconsciousness or unconsciousness, forgetfulness, vomiting, or diffuse headache. The disease may develop rapidly in severe cases, leading to irreversible severe disability or death [21]. Brain contusion and laceration are the terms of brain contusion and laceration. Severe contusion and laceration of the brain often complicated with a cerebral hernia are a typical critical illnesses, and patients are often accompanied by obvious neurological impairment. Operation is an important treatment strategy.

According to the relevant survey data, the prognosis of patients is generally unsatisfactory, with a high disability rate and mortality rate [22]. The key step to improving the prognosis of patients with brain contusion and laceration is to accurately determine the risk factors that affect the poor prognosis of patients after craniotomy.

Brain contusion and laceration are a common primary TBI. Clinically, the diagnosis of brain contusion and laceration is mainly based on the history of TBI, the findings of clinical physical examination, the results of the imaging-assisted examination, and comprehensive analysis combined with the experience of clinicians [23, 24]. CT, MRI, and other imaging examinations provide objective imaging data for clinical diagnosis of cardiovascular and cerebrovascular diseases [25]. However, these imaging findings are also very different at different stages of the disease [26, 27]. To judge the prognosis more accurately, it is necessary to consider the related factors as much as possible.

In this study, the patients with brain contusion and laceration admitted to our hospital in recent years were selected as the research object. The prediction model was built based on logistic regression and BPNN. The clinical data of the two groups of patients were retrospectively analyzed. The details of age, gender, the volume of brain contusion and laceration, blood loss, GCS score of patients admitted to hospital, and treatment methods were sorted out and analyzed, to predict the prognosis of patients after operation. In this study, we concluded that GCS score < 8 on admission, blood loss ≥ 30 ml on admission, mannitol application ≥ 2 weeks, anticoagulants before admission, and surgical treatment were five high-risk factors for poor prognosis after brain contusion and laceration. This study showed that the weight of the model score was 87.0 when mannitol was used for ≥2 weeks. Mannitol is a commonly used drug in clinical practice. Relevant literature reports that using the appropriate amount of mannitol at the right time is helpful to quickly improve cerebral vascular circulation, significantly reduce the degree of brain edema damage, and protect neurological function [28, 29]. Santing et al. [30] demonstrated that TBI is an independent factor of venous vascular embolism. It is a vital link for clinical treatment of TBI to prevent venous vascular embolism by formulating scientific preventive strategies effectively. It is also pointed out that although anticoagulants can prevent venous thrombosis, they may increase the risk of bleeding. In addition, Shehadeh et al. [31] believed that reducing the lesion volume and improving the survival rate of neurons play an essential role in improving the prognosis of brain contusion and laceration. Our research results are consistent with these previous studies.

This study verified the prediction model of poor prognosis of patients with brain contusion and laceration. The logistic regression model and the BPNN prediction models predict the poor prognosis of patients with brain contusion and laceration. The areas under the curve are 0.816 (95% *CI* 0.705-0.926) and 0.819 (95% *CI* 0.708-0.931), respectively. This result shows that the established prediction model has good discrimination, but the BPNN model has better predictive efficiency than the logistic regression model.

5. Conclusion

This study builds a prediction model based on the risk factors that affect the poor prognosis of patients with brain contusion and laceration, with good discrimination and accuracy. The number of cases included in this study is small, and the promotion of this prediction model still needs to be verified by large-scale and multicenter prospective studies. In future research work, it is also suggested to further screen the independent risk factors of poor prognosis in patients with brain contusion and laceration and continuously optimize the prediction model to better serve the clinical decision-making.

Data Availability

All data analyzed during this study are available from the corresponding author on reasonable request.

Conflicts of Interest

The author declares that there is no conflict of interest regarding the publication of this article.

Acknowledgments

This study was funded by the Hebei Medical Science Research Project Plan (No.: 20191252).

References

[1] X. P. Wang, J. Zhong, T. Lei et al., "Epidemiology of traumatic brain injury-associated epilepsy in western China: an analysis of multicenter data," *Epilepsy Research*, vol. 164, no. 1, article 106354, 2020.

[2] X. DeGrauw, D. Thurman, L. Xu, V. Kancherla, and T. DeGrauw, "Epidemiology of traumatic brain injury-associated epilepsy and early use of anti-epilepsy drugs: an analysis of insurance claims data, 2004-2014," *Epilepsy Research*, vol. 146, no. 1, pp. 41–49, 2018.

[3] H. Wu, J. Zheng, S. Xu et al., "Mer regulates microglial/macrophage m1/m2 polarization and alleviates neuroinflammation following traumatic brain injury," *Journal of Neuroinflammation*, vol. 18, no. 1, p. 2, 2021.

[4] D. Y. C. Chan, A. C. O. Tsang, L. F. Li et al., "Improving survival with tranexamic acid in cerebral contusions or traumatic subarachnoid hemorrhage: univariate and multivariate analysis of independent factors associated with lower mortality," *World Neurosurgery*, vol. 125, no. 1, pp. e665–e670, 2019.

[5] S. Yousefzadeh-Chabok, M. Safaei, E. Kazemnejad, D. Mahmoudi, and S. Andalib, "Lobectomy in traumatic brain injury patients with intracerebral hemorrhage and delayed contusion," *Journal of Injury and Violence Research*, vol. 12, no. 2, p. 111, 2020.

[6] K. Adatia, V. F. J. Newcombe, and D. K. Menon, "Contusion progression following traumatic brain injury: a review of clinical and radiological predictors, and influence on outcome," *Neurocritical Care*, vol. 34, no. 1, pp. 312–324, 2021.

[7] M. L. Fournier, T. Clément, J. Aussudre, N. Plesnila, A. Obenaus, and J. Badaut, "Contusion rodent model of

traumatic brain injury: controlled cortical impact," *Methods in Molecular Biology*, vol. 2193, no. 1, pp. 49–65, 2021.

[8] M. L. Pearn, I. R. Niesman, J. Egawa et al., "Pathophysiology associated with traumatic brain injury: current treatments and potential novel therapeutics," *Cellular and Molecular Neurobiology*, vol. 37, no. 4, pp. 571–585, 2017.

[9] C. W. Connor, "Artificial intelligence and machine learning in anesthesiology," *Anesthesiology*, vol. 131, no. 6, pp. 1346–1359, 2019.

[10] Y. Ye, J. Shi, D. Zhu, L. Su, J. Huang, and Y. Huang, "Management of medical and health big data based on integrated learning-based health care system: A review and comparative analysis," *Computer Methods and Programs in Biomedicine*, vol. 209, article 106293, 2021.

[11] Z. Han, Z. Li, K. Liu, and L. Yan, "Named data networking with neural networks for intelligent image processing information systems," *Enterprise Information Systems*, vol. 12, no. 1, pp. 1–16, 2020.

[12] Z. Han, K. Liu, Z. Li, and P. Luo, "A pre-check operator for reducing algorithmic optimisation time in image processing applications," *Enterprise Information Systems*, vol. 13, no. 1, pp. 1–13, 2021.

[13] G. S. Handelman, H. K. Kok, R. V. Chandra, A. H. Razavi, M. J. Lee, and H. Asadi, "eDoctor: machine learning and the future of medicine," *Journal of Internal Medicine*, vol. 284, no. 6, pp. 603–619, 2018.

[14] H. Gao, C. Wu, D. Huang, D. Zha, C. Zhou, and The Third People's Hospital of HeFei, Heifei 230000, China, "Prediction of fetal weight based on back propagation neural network optimized by genetic algorithm," *Mathematical Biosciences and Engineering*, vol. 18, no. 4, pp. 4402–4410, 2021.

[15] Y. Liu, Q. Fang, A. Jiang, Q. Meng, G. Pang, and X. Deng, "Texture analysis based on u-net neural network for intracranial hemorrhage identification predicts early enlargement," *Computer Methods and Programs in Biomedicine*, vol. 206, no. 1, article 106140, 2021.

[16] T. Xiang, P. Z. Wu, and S. Yuan, "Application analysis of combining bp neural network and logistic regression in human resource management system," *Computational Intelligence and Neuroscience*, vol. 2022, no. 1, Article ID 7425815, 2022.

[17] J. Feng, Q. Sun, Z. Li, Z. Sun, and K. Jia, "Back-propagation neural network-based reconstruction algorithm for diffuse optical tomography," *Journal of Biomedical Optics*, vol. 24, no. 5, pp. 1–12, 2019.

[18] V. Geetha, K. S. Aprameya, and D. M. Hinduja, "Dental caries diagnosis in digital radiographs using back-propagation neural network," *Health Information Science and Systems*, vol. 8, no. 1, p. 8, 2020.

[19] Z. Cao, N. Guo, M. Li, K. Yu, and K. Gao, "Back propagation neutral network based signal acquisition for brillouin distributed optical fiber sensors," *Optics Express*, vol. 27, no. 4, pp. 4549–4561, 2019.

[20] A. Capizzi, J. Woo, and M. Verduzco-Gutierrez, "Traumatic brain injury: an overview of epidemiology, pathophysiology, and medical management," *The Medical Clinics of North America*, vol. 104, no. 2, pp. 213–238, 2020.

[21] B. Dang, W. Chen, W. He, and G. Chen, "Rehabilitation treatment and progress of traumatic brain injury dysfunction," *Neural Plasticity*, vol. 2017, no. 1, 2017.

[22] M. Galgano, G. Toshkezi, X. Qiu, T. Russell, L. Chin, and L. R. Zhao, "Traumatic brain injury: current treatment strategies and future endeavors," *Cell Transplantation*, vol. 26, no. 7, pp. 1118–1130, 2017.

[23] T. Araki, H. Yokota, and A. Morita, "Pediatric traumatic brain injury: characteristic features, diagnosis, and management," *Neurologia Medico-Chirurgica (Tokyo)*, vol. 57, no. 2, pp. 82–93, 2017.

[24] A. Khellaf, D. Z. Khan, and A. Helmy, "Recent advances in traumatic brain injury," *Journal of Neurology*, vol. 266, no. 11, pp. 2878–2889, 2019.

[25] M. Zhao, Y. Wei, and K. K. L. Wong, "A generative adversarial network technique for high-quality super-resolution reconstruction of cardiac magnetic resonance images," *Magnetic Resonance Imaging*, vol. 85, no. 1, pp. 153–160, 2022.

[26] K. K. Wang, Z. Yang, T. Zhu et al., "An update on diagnostic and prognostic biomarkers for traumatic brain injury," *Expert Review of Molecular Diagnostics*, vol. 18, no. 2, pp. 165–180, 2018.

[27] H. Chen, W. Li, and Y. Zhu, "Improved window adaptive gray level co-occurrence matrix for extraction and analysis of texture characteristics of pulmonary nodules," *Computer Methods and Programs in Biomedicine*, vol. 208, no. 1, p. 106263, 2021.

[28] H. S. Mangat, X. Wu, L. M. Gerber et al., "Hypertonic saline is superior to mannitol for the combined effect on intracranial pressure and cerebral perfusion pressure burdens in patients with severe traumatic brain injury," *Neurosurgery*, vol. 86, no. 2, pp. 221–230, 2020.

[29] J. Gu, H. Huang, Y. Huang, H. Sun, and H. Xu, "Hypertonic saline or mannitol for treating elevated intracranial pressure in traumatic brain injury: a meta-analysis of randomized controlled trials," *Neurosurgical Review*, vol. 42, no. 2, pp. 499–509, 2019.

[30] J. A. L. Santing, C. L. Van den Brand, and K. Jellema, "Traumatic brain injury in patients receiving direct oral anticoagulants," *The Journal of Emergency Medicine*, vol. 60, no. 3, pp. 285–291, 2021.

[31] M. Shehadeh, E. Palzur, L. Apel, and J. F. Soustiel, "Reduction of traumatic brain damage by tspo ligand etifoxine," *International Journal of Molecular Sciences*, vol. 20, no. 11, p. 2639, 2019.

Hindawi
Computational and Mathematical Methods in Medicine
Volume 2022, Article ID 4799248, 7 pages
https://doi.org/10.1155/2022/4799248

Research Article

Logistic Model and Gradient Boosting Machine Model for Physical Therapy of Lumbar Disc Herniation

Ping Zhao,[1] **Jin Xue**,[2] **Xiaomei Xu**,[2] **Lifei Wang**,[2] **and Dan Chen**[3]

[1]*Nursing Department, The Third People's Hospital of Hefei, Hefei Third Clinical College of Anhui Medical University, Hefei 230022, China*
[2]*Department of Orthopaedics, The Third People's Hospital of Hefei, Hefei Third Clinical College of Anhui Medical University, Hefei 230022, China*
[3]*Department of Neurosurgery, The Third People's Hospital of Hefei, Hefei Third Clinical College of Anhui Medical University, Hefei 230022, China*

Correspondence should be addressed to Lifei Wang; wlf680802@sina.com and Dan Chen; cd810424@126.com

Received 21 January 2022; Revised 26 March 2022; Accepted 19 April 2022; Published 11 May 2022

Academic Editor: Kelvin Wong

Objective. Physical therapy is a common clinical treatment for patients with lumbar disc herniation. The study is aimed at exploring the feasibility of mathematical expression and curative effect prediction of physical therapy in patients with lumbar disc herniation using a logistic model and gradient boosting machine (GBM). *Methods*. A total of 142 patients with lumbar disc herniation were treated with physical therapy. The pain was evaluated by the visual analogue scale (VAS) before each treatment. The logistic model was used to conduct a global regression analysis on patients with lumbar disc herniation. The final results of the whole course of treatment were predicted by the measured values of 2-9 times of treatment. The GBM model was used to predict and analyze the curative effect of physical therapy. *Results*. The mathematical expression ability of the logistic regression model for patients with lumbar disc herniation undergoing physical therapy was sufficient, and the global determination coefficient was 0.721. The results would be better for more than five measurements. The AUC of GBM mode logistic regression analysis was 0.936 and 0.883, and the prediction effect is statistically significant. *Conclusion*. Both the logistic and GBM model can fully express the changes in patients with lumbar disc herniation during physical therapy.

1. Introduction

Lumbar disc herniation, the most common degenerative spine disease, can cause low back pain and sciatica, causing great distress to patients' daily life [1]. Timely physical treatment can achieve traction disc, joint loosening, and other effects to relieve the patient's lumbar pain and sciatica. Physical therapy has many advantages, such as easy and reliable efficacy. Thus, it is widely used in the clinic and plays an important therapeutic role [2]. In clinical rehabilitation practice, how to optimize the prescription and further improve the efficacy is one of the important topics of concern for clinical rehabilitation workers. There are numerous reports on analyzing rehabilitation efficacy in lumbar disc herniation. However, due to interindividual variability and the diversity of physical therapy, physical therapy prescriptions often have distinct individualized characteristics, which also poses some difficulties for efficacy prediction [3]. In clinical practice, predicting efficacy by an investigational treatment is widely adopted. In this process, three aspects have become the key to optimizing the configuration of medical resources and improving the efficiency of rehabilitation treatment: how to determine the appropriate length of treatment time, accurately estimate the efficacy of the entire course of therapy; timely termination of the treatment regimens that may be less effective [4–9].

Machine learning is a multidomain interdisciplinary emerging over the last 20 years, involving several disciplines such as probability theory, statistics, approximation, convex analysis, and algorithmic complexity theory [10–14]. It is an essential branch of computer science mainly used to model complex relationships between predictor and response

variables and has the potential to transform modern methods of epidemiological research. With "big data" attracting much attention, machine learning can provide epidemiologists with new tools and ideas for solving problems that traditional methods cannot solve [15]. The gradient boosting machine (GBM), a machine learning algorithm for regression and classification, can train many models in order. Then, each new model updates the prediction using the gradient descent method [16–20]. GBM has shown great success in a wide range of practical applications and can be highly customized to the application's specific needs, gradually minimizing the loss of function. The logistic regression model is a classical linear regression model that can mine the linear relationship before variables and establish an effective model to predict future variable results.

The logistic curve model was used for the mathematical expression on the treatment process of cervical radicular pain. The prediction of the effect of physical therapy on cervical radicular pain was achieved by further mathematical feature analysis and predictive ability analysis [21–23]. During physical therapy, patients with cervical spondylosis show a closer course of remission than patients with lumbar disc herniation. Based on the above background, this study attempted to apply the GBM model and logistic model to describe the process of physical therapy and the prediction of efficacy in patients with lumbar disc herniation.

2. Material and Method

2.1. General Data. A total of 142 patients with lumbar disc herniation, aged 17 to 87 years (53.1 ± 15.2) years, who were treated at the Department of physical medicine and rehabilitation of our hospital from December 2018 to June 2021, were selected, including 89 males and 53 females. Inclusion criteria were as follows: (1) they met the diagnostic criteria of lumbar disc herniation according to the diagnosis and treatment code of China Rehabilitation Medicine based on the symptom presentation, physical examination, and auxiliary examinations, accompanied by radicular radiation pain; (2) they can understand and apply visual analog scale for pain rating; (3) they can adhere to completion of more than ten physical therapy sessions; (4) the patient's condition was stable.

The patient after admission determined the corresponding physical therapy prescription according to his actual condition. The treatment contents included traction, joint loosening, and physical factor therapy. These treatments were used once daily for five consecutive days each week, ten times for one course. The visual analogue scale (VAS) pain assessment was performed simultaneously before each treatment. The specific method is to draw a 10 cm long line segment in front of the patient and inform the patient that the left end of the line segment represents no pain, and the right end of the line segment represents intolerable severe pain and asked patients to label the average degree of pain in the past 24 h on the line segment. The researcher then used a ruler to measure the distance from the left endpoint of the line segment to the marked point and recorded each patient to the end of the course to obtain ten pain VAS score values. Throughout treatment, every effort was made to guarantee that each patient's treatment time point was relatively fixed.

2.2. Mathematical Expression and Predictive Power Analysis. Using the logistic model as a regression analysis model, y represents the degree of pain during treatment, and x represents the time point to complete treatment. The corresponding x values at the 10 measurement time points in this study are 1, 2,…, 9, 10. The a, b is the parameter, and the H is the distance between the upper and lower asymptotes representing the maximum possible relief during treatment as determined by the pain level at the initial visit. According to the vas minimal clinically significant difference (MCSD) theory proposed by Kelly [24], the position of the upper asymptote is defined as the level 1.2 above the 1st pain score value, i.e., K value = 1st VAS + 1.2. Since the maximum value of the VAS score is 10, the K value was taken as 10 when the VAS ≥ 8.8 at the first assessment.

To explore the predictive ability of different treatment duration, the predictive models were constructed with the measurement results of 1st to 2nd, 1st to 3rd, 1st to 4th, 1st to 5th, 1st to 6th, 1st to 7th, 1st to 8th, and 1st to 9th. The logistic model curve fitting analysis were completed. The predicted value of each model for the degree of pain at the 10th rating time point was then evaluated, and the difference between this expected value and the actual measurement was calculated.

Based on the actual measured values and MCSD theory, cases with a decrease of more than 1.2 VAS score on the whole course were defined as clinically effective cases, and the cases with less than 1.2 points were defined as invalid cases. The magnitude of decline predicted by each model was calculated simultaneously, and cases with a decrease of more than 1.2 points were defined as predicted valid cases. Cases with a decrease of less than 1.2 points were defined as predicted null cases. When the expected outcome was consistent with the actual measured outcome, it was defined as the predicted successful case and vice versa as the expected unsuccessful case. The predictive ability of different predictive models was compared between groups.

Remission magnitude was defined as predicting a successful case and vice versa an unsuccessful case when the difference between the predicted value and the actual measured last score value was within 1.2 points. The success rate predicted by the remission magnitude was calculated for each length of treatment, and the difference between the models in predicting remission magnitude was compared.

2.3. GBM Model Construction. Data acquisition, data preprocessing, training, model evaluation, and prediction for GBM models were implemented using Python 3.8 (https://www.python.org/downloads/Guido van Rossum). The data were randomly divided into training and test sets in a 7 : 3 ratio, and the optimal parameters were trained in the GBM model using the data from the training set, and the simple algorithm for GBM proceeds as follows:

Step 1. Construct a training dataset $\{y_i, x_i\}_i^N$ trained on N samples, where y is the outcome variable and x is the

independent variable. The outcome variable y was defined as efficacy (classified as poor efficacy and good efficacy), and the independent variable x included 14 indicators including age, gender, prominence, and type of prominence.

Step 2. Set initial prediction model

$$F_0(x) = 0, \tag{1}$$

and residual

$$r_i = y_i. \tag{2}$$

Step 3. For iteration

$$m = 1, 2, 3, \cdots, M. \tag{3}$$

Step 4. The fitting regression tree $\widehat{f}_m$ has L endpoints, and the interaction depth is

$$d = L - 1. \tag{4}$$

Step 5.

$$F_m(x) = F_{m-1}(x) + \mu\widehat{f}_m(x). \tag{5}$$

Step 6.

$$r_i \longleftarrow r_i - \mu\widehat{f}_m(x). \tag{6}$$

Step 7.

$$F_M(x) = \sum_{m=1}^{M} \mu\widehat{f}_m(x). \tag{7}$$

The test set finally validated the predictive model. At the same time, the effects of independent variables on outcome variables were analyzed to find the most critical factors affecting the outcome variables.

2.4. Statistical Analysis. The SPSS 23.0 software was used for statistical data analysis. The comparison of success rates of each model was performed using the chi-square test. When the difference was found to be statistically significant by the chi square test, to avoid excessive multiple comparisons to improve the power of the test, the differences among the groups were further analyzed by the pooled cell method. The t-test was used to analyze the differences between groups at different times of treatment time. The receiver-operator characteristics curve (ROC) was used to evaluate the sensitivity and specificity of the model.

3. Result

3.1. Efficacy Analysis. Before treatment, the pain VAS score of 142 patients with lumbar disc herniation in this study was 6.8 (3.0-10.0) points, and the posttreatment pain VAS score was 4.3 (0.1-7.8) points. After physical therapy, the patient's pain was significantly relieved. The symptoms of lumbar disc herniation were also considerably improved by comparing the MRI of the lumbar disc before and after treatment (Figure 1).

3.2. Mathematical Expressivity Analysis. The regression curves of each case showed some differences, and the regression curves of some patients showed "S" type characteristics (Figure 2(a)). Some additional patients showed regression lines that resembled straight lines (Figure 2(b)). The coefficient of determination of the 142 patients in this study was 0.731 (0.001-0.979). The global coefficient of determination was 0.721, suggesting that this model can better express the course of physical therapy for patients with lumbar disc herniation.

3.3. Effective Case Prediction Power Analysis. The predictive ability of the length of treatment for effective vs. ineffective cases gradually improved with the number of treatment sessions, and specific data are detailed in Table 1. The difference between them was statistically significant by the chi-square test for the data in the table. Their success rates were all predicted to be above 80% based on validity completed with more than five measurements, and they were relatively close to each other. However, the predictions obtained based on 2-4 measurements are relatively close to each other and have low predictive power. After merging the cells, the predicted outcomes of measurements more than 5 times were compared with those of measurements within 4 times, and the difference between them was found to be statistically significant.

3.4. Remission Magnitude Predictive Power Analysis. The predictive ability of the remission range of the whole course of treatment varied in different treatment duration. With the increase in treatment times, the difference between the predicted and measured values gradually decreases. The prediction success rate of remission amplitude obtained by each prediction model increases with treatment times (Table 2). The predictive power of 2-4 measurements was low, and all of them had less than 50% correct. The accurate rates of prediction results of 5-7 measurements were all at 60% sufficient, and the accurate rates of 8-9 measurements were relatively high. All of them reached more than 80%.

According to the characteristics of prediction ability, the treatment duration was combined into 2~4 times, 5~7 times, and 8-9 times. It was found that the difference between the groups of 2-4 times and 5-7 times was statistically significant ($P < 0.01$). The difference between the groups of 8-9 times and the group of 5-7 times was also statistically significant ($P < 0.01$).

3.5. Prediction Model of Short-Term Prognosis Based on GBM. The optimal parameters of GBM model were obtained through grid search and manual debugging. The final parameters are adjusted to (learning_rate = 0.1, n_estimators = 1000, max_depth = 4, min_samples_split = 2, min_samples_leaf = 1, subsample = 1, max_features = 'sqrt', random_state = 10). The test set data verify the prediction model constructed by the training set. The influencing factors in the GBM model were ranked by importance, and

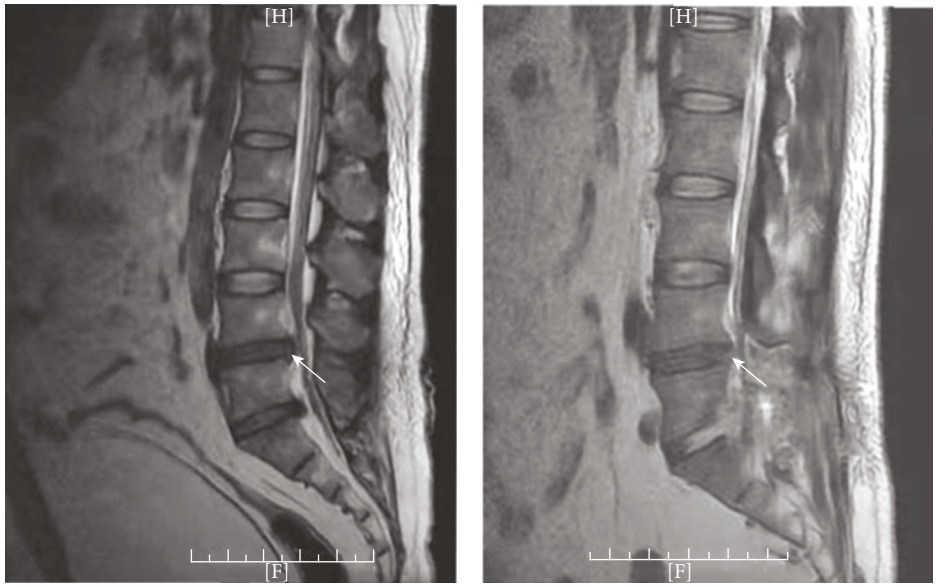

(a) (b)

Figure 1: Comparison of magnetic resonance images before and after physical therapy. Compared with the image before treatment (a), disc herniation (arrow) after treatment (b) decreased significantly.

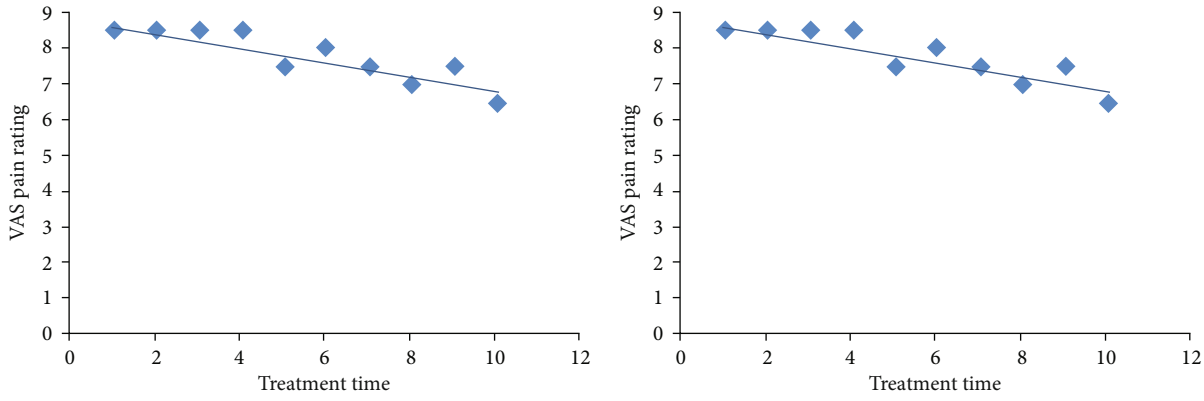

(a) (b)

Figure 2: Comparison of regression curves of typical patients. (a) "S" type characteristics. (b) Linear characteristics.

Table 1: Analysis of ability to predict curative effect for different treatment duration (cases, %).

Length of treatment	Successful prediction	Unsuccessful prediction
1^{st}-2^{nd}	87/61.3	55/38.7
1^{st}-3^{rd}	105/73.9	37/26.1
1^{st}-4^{th}	110/77.5	32/22.5
1^{st}-5^{th}	120/84.5	22/15.5
1^{st}-6^{th}	121/85.2	21/14.8
1^{st}-7^{th}	114/80.3	28/19.8
1^{st}-8^{th}	119/83.8	23/16.2
1^{st}-9^{th}	128/90.1	14/9.9

the top five are the sagittal diameter of protrusion, the degeneration level of the surgical segment, age, the time from initial symptom to operation, and the degeneration level of the adjacent segment.

The area under the ROC curve (AUC) of the GBM prediction model was 0.936 [95% CI (0.782, 0.973)]. The sensitivity, specificity, and Youden index were 93.3%, 87.5%, and 0.808, respectively. The AUC of logistic regression analysis was 0.883 [95% CI (0.756, 0.914)]. The sensitivity, specificity, and Youden index were 88.6%, 67.8%, and 0.624, respectively. The prediction effects of the two prediction models were statistically significant ($P < 0.001$) (Figure 3).

4. Discussion

Rehabilitation therapy plays an essential role in many treatment fields, including bone and joint system diseases, nervous system diseases, and circulatory and respiratory

Table 2: Analysis of ability to predict remission amplitude for different treatment time lengths (cases, %).

Length of treatment	Successful prediction	Unsuccessful prediction
1st-2nd	46/32.4	96/67.6
1st-3rd	59/41.6	83/58.5
1st-4th	64/15.1	78/64.9
1st-5th	93/65.5	49/34.5
1st-6th	82/57.7	60/42.3
1st-7th	92/64.8	50/.35.2
1st-8th	114/80.3	28/19.7
1st-9th	124/87.3	18/12.7

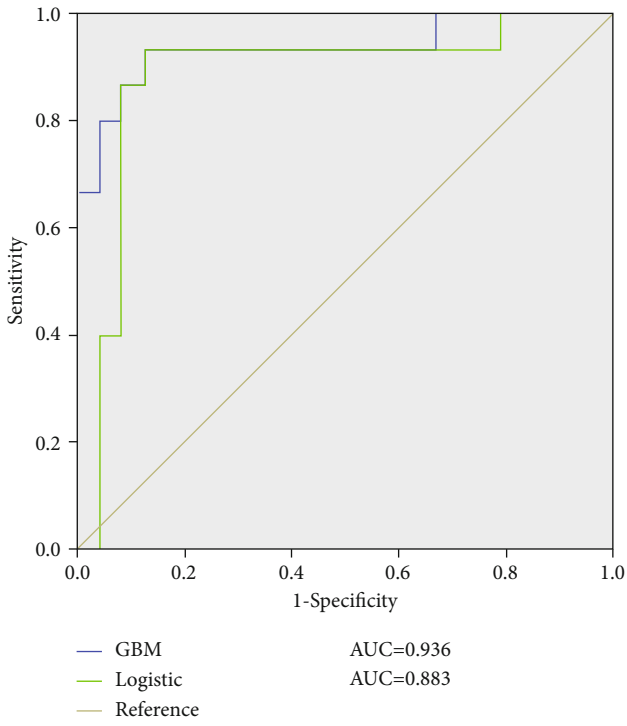

Figure 3: ROC curve of GBM model and logistic regression analysis model.

system diseases [25–27]. From the analysis of treatment purpose, rehabilitation treatment pays more attention to function acquisition. From the comparison of characteristic entropy, rehabilitation treatment means are diverse and targeted, making rehabilitation treatment prescriptions richer and more complex than drug treatment, showing more apparent individualized treatment characteristics [28]. However, it also brings difficulties to efficacy evaluation and prediction. For example, there are a large number of reports on efficacy prediction. Many researchers try to predict the treatment outcome by looking for the relationship between clinical characteristics and functional outcomes. Still, the prediction ability is significantly reduced due to the complexity of patient characteristics and the richness of treatment methods.

In the actual rehabilitation treatment, it is found that the true efficacy of rehabilitation prescription can be understood to a certain extent by observing the patient's treatment feedback information, which can predict the treatment effect [29, 30]. However, how to choose a reasonable length of treatment time so that we can save medical resources to the greatest extent terminates the treatment scheme with poor curative effect in time, accurately predicts the curative effect, and prevents unnecessary prescription adjustment. Thus, we need to have a sufficient understanding of the characteristics of the treatment process. Through the long-term observation of the treatment process, this study proposed to use the logistic curve model and GBM model to predict and analyze the curative effect of physical therapy and nursing of lumbar disc herniation.

In clinical treatment, the remission process of different patients is different. The main difference is the remission speed and onset time [31, 32]. A mathematical model that can fully reflect the above characteristics must be constructed [33–35]. The logistic model is an "S" curve with upper and lower asymptotes. In the model construction, we pay special attention to the parameter design: for example, the characteristics of onset time and descent rate are fully expressed by parameters a and b. Relevant research shows that GBM has a strong classification ability in many machine learning. GBM is an improved forward learning machine learning enhancement algorithm for regression and classification problems. Its fundamental theory is to produce a prediction model composed of weak learners or essential learners and gradually obtain approximately accurate prediction results from vulnerable learners to solid learners.

From the analysis of mathematical expression ability, the logistic regression model is satisfied with the expression ability of the physical treatment process of lumbar disc herniation. The global determination coefficient is 0.721. In the analysis of the predictive ability of different treatment practice lengths on the efficacy of the whole course of treatment, with the extension of treatment time, both effectiveness prediction and remission amplitude prediction show a good change prediction trend. In the effectiveness prediction analysis, when the forecast is made according to the measured values more than five times (because the pain evaluation is completed before each treatment, that is, more than four experimental treatments), the prediction ability is close. The accuracy rate is stable at more than 80% in the prediction analysis of lumbar disc herniation. When 8-9 measurements are used for prediction in the mitigation amplitude analysis, the accuracy is more than 80%. GBM usually takes the weak prediction model as the benchmark model to generate a complex prediction model. It constructs the model in a phased manner and optimizes it by selecting any differentiable function as the loss function, which can better fit the data. However, there are still some limitations to this study. The sample size of this study was not large enough, which may cause the overfitting of the model. Moreover, the model's prediction accuracy requires the physical therapy process of patients many times, the experimental data are more strictly adopted, and subsequent studies can simplify the model and take a more convenient approach.

5. Conclusions

In conclusion, it is feasible and accurate to use the logistic curve model and GBM model to predict rehabilitation treatment's mathematical expression and curative effect for patients with lumbar disc herniation. The treatment effectiveness and remission range can be effectively expected by analyzing more than five measured values obtained from more than four experimental treatments.

Data Availability

The data used to support the findings of this study are available from the corresponding author upon request.

Conflicts of Interest

All authors declare no conflicts of interest in this paper.

References

[1] T. Sınmaz and N. Akansel, "Experience of pain and satisfaction with pain management in patients after a lumbar disc herniation surgery," *Journal of Perianesthesia Nursing*, vol. 36, no. 6, pp. 647–655, 2021.

[2] S. Heisinger, D. Huber, M. P. Matzner et al., "Online videos as a source of physiotherapy exercise tutorials for patients with lumbar disc herniation-a quality assessment," *International Journal of Environmental Research and Public Health*, vol. 18, no. 11, 2021.

[3] F. Hao, "Analysis of the effect of traction combined with paraffinotherapy on lumbar function in patients with lumbar disc herniation," *American Journal of Translational Research*, vol. 13, no. 6, pp. 6759–6765, 2021.

[4] P. Azimi and E. C. Benzel, "Cut-off value for pain sensitivity questionnaire in predicting surgical success in patients with lumbar disc herniation," *PLoS One*, vol. 11, no. 8, article e0160541, 2016.

[5] S. H. Moon, J. I. Lee, H. S. Cho, J. W. Shin, and W. U. Koh, "Factors for predicting favorable outcome of percutaneous epidural adhesiolysis for lumbar disc herniation," *Pain Research & Management*, vol. 2017, article 1494538, no. 1, p. 10, 2017.

[6] K. Ostafiński, W. Świątnicki, J. Szymański et al., "Predicting conservative treatment failure in patients with lumbar disc herniation. Single center, case-control study," *Clinical Neurology and Neurosurgery*, vol. 193, no. 1, article 105867, 2020.

[7] C. F. Pedersen, M. Andersen, L. Y. Carreon, and S. Eiskjær, "Applied machine learning for spine surgeons: predicting outcome for patients undergoing treatment for lumbar disc herniation using pro data," *Global Spine Journal*, vol. 10, 2020.

[8] H. Wang, D. Zhang, L. Ma, Y. Shen, and W. Ding, "Factors predicting patient dissatisfaction 2 years after discectomy for lumbar disc herniation in a Chinese older cohort," *Medicine*, vol. 94, no. 40, article e1584, 2015.

[9] B. R. Yoo, S. Son, S. G. Lee, W. K. Kim, and J. M. Jung, "Factors predicting the clinical outcome after trans-sacral epiduroscopic laser decompression for lumbar disc herniation," *Neurospine*, vol. 18, no. 2, pp. 336–343, 2021.

[10] M. Han, L. Liu, M. Hu, G. Liu, and P. Li, "Medical expert and machine learning analysis of lumbar disc herniation based on magnetic resonance imaging," *Computer Methods and Programs in Biomedicine*, vol. 213, no. 1, article 106498, 2022.

[11] Z. Han, Z. Li, K. Liu, and L. Yan, "Named data networking with neural networks for intelligent image processing information systems," *Enterprise Information Systems*, vol. 12, no. 1, pp. 1–16, 2020.

[12] Z. Han, K. Liu, Z. Li, and P. Luo, "A pre-check operator for reducing algorithmic optimisation time in image processing applications," *Enterprise Information Systems*, vol. 13, no. 1, pp. 1–13, 2021.

[13] J. Shi, Y. Ye, D. Zhu, L. Su, Y. Huang, and J. Huang, "Automatic segmentation of cardiac magnetic resonance images based on multi-input fusion network," *Computer Methods and Programs in Biomedicine*, vol. 209, no. 1, Article ID 106323, 2021.

[14] Y. Liu, Q. Fang, A. Jiang, Q. Meng, G. Pang, and X. Deng, "Texture analysis based on U-Net neural network for intracranial hemorrhage identification predicts early enlargement," *Computer Methods and Programs in Biomedicine*, vol. 206, no. 1, article 106140, 2021.

[15] Y. Yang, J. Zheng, Z. Du, Y. Li, and Y. Cai, "Accurate prediction of stroke for hypertensive patients based on medical big data and machine learning algorithms: retrospective study," *JMIR Medical Informatics*, vol. 9, no. 11, article e30277, 2021.

[16] B. Hu, C. Wang, K. Jiang et al., "Development and validation of a novel diagnostic model for initially clinical diagnosed gastrointestinal stromal tumors using an extreme gradient-boosting machine," *BMC Gastroenterology*, vol. 21, no. 1, 2021.

[17] S. Kumar and K. K. Singh, "Rain garden infiltration rate modeling using gradient boosting machine and deep learning techniques," *Water Science and Technology*, vol. 84, no. 9, pp. 2366–2379, 2021.

[18] Z. Luo, F. Huang, and H. Liu, "$PM_{2.5}$ concentration estimation using convolutional neural network and gradient boosting machine," *Journal of Environmental Sciences (China)*, vol. 98, no. 1, pp. 85–93, 2020.

[19] S. Mahapatra and S. S. Sahu, "ANOVA-particle swarm optimization-based feature selection and gradient boosting machine classifier for improved protein-protein interaction prediction," *Proteins*, vol. 90, no. 2, pp. 443–454, 2022.

[20] D. D. Rufo, T. G. Debelee, A. Ibenthal, and W. G. Negera, "Diagnosis of diabetes mellitus using gradient boosting machine (lightgbm)," *Diagnostics*, vol. 11, no. 9, p. 1714, 2021.

[21] F. Pilato, R. Calandrelli, M. Distefano, and F. C. Tamburrelli, "Multidimensional assessment of cervical spondylotic myelopathy patients. Usefulness of a comprehensive score system," *Neurological Sciences*, vol. 42, no. 4, pp. 1507–1514, 2021.

[22] L. Gong, H. N. Ma, P. Yi, and M. S. Tan, "Flexion dysfunction of atlanto-occipital joint associated with cervical spondylosis," *Orthopaedic Surgery*, vol. 13, no. 1, pp. 267–275, 2021.

[23] T. Therriault, A. Rospert, M. Selhorst, and A. Fischer, "Development of a preliminary multivariable diagnostic prediction model for identifying active spondylolysis in young athletes with low back pain," *Physical Therapy in Sport*, vol. 45, no. 1, pp. 1–6, 2020.

[24] A. M. Kelly, "The minimum clinically significant difference in visual analogue scale pain score does not differ with severity of pain," *Emergency Medicine Journal*, vol. 18, no. 3, pp. 205–207, 2001.

[25] M. Arai, "Evaluating the usefulness of *Ninjin'yoeito Kampo* medicine in combination with rehabilitation therapy in

patients with frailty complicated by intractable dizziness," *Neuropeptides*, vol. 90, no. 1, article 102189, 2021.

[26] H. Lou, Z. Li, T. Pang et al., "Electrocupuncture combined rehabilitation therapy for upper limb spasticity after stroke," *Medicine*, vol. 100, no. 47, article e27963, 2021.

[27] M. Tsukagoshi, N. Harimoto, K. Araki et al., "Impact of preoperative nutritional support and rehabilitation therapy in patients undergoing pancreaticoduodenectomy," *International Journal of Clinical Oncology*, vol. 26, no. 9, pp. 1698–1706, 2021.

[28] P. Langhorne, J. Bernhardt, and G. Kwakkel, "Stroke rehabilitation," *The Lancet*, vol. 377, no. 9778, pp. 1693–1702, 2011.

[29] J. H. Van Stan, J. Whyte, J. R. Duffy et al., "Rehabilitation treatment specification system: methodology to identify and describe unique targets and ingredients," *Archives of Physical Medicine and Rehabilitation*, vol. 102, no. 3, pp. 521–531, 2021.

[30] J. Whyte, M. P. Dijkers, T. Hart et al., "The importance of voluntary behavior in rehabilitation treatment and outcomes," *Archives of Physical Medicine and Rehabilitation*, vol. 100, no. 1, pp. 156–163, 2019.

[31] R. Gassert and V. Dietz, "Rehabilitation robots for the treatment of sensorimotor deficits: a neurophysiological perspective," *Journal of Neuroengineering and Rehabilitation*, vol. 15, no. 1, p. 46, 2018.

[32] L. M. Tijsen, E. W. Derksen, W. P. Achterberg, and B. I. Buijck, "Challenging rehabilitation environment for older patients," *Clinical Interventions in Aging*, vol. 14, no. 1, pp. 1451–1460, 2019.

[33] D. Formanowicz, J. B. Krawczyk, B. Perek, D. Lipski, and A. Tykarski, "Management of high-risk atherosclerotic patients by statins may be supported by logistic model of intima-media thickening," *Journal of Clinical Medicine*, vol. 10, no. 13, 2021.

[34] Z. Guo, L. Meng, S. Tian et al., "A five-parameter logistic model to predict the possibility of misdiagnosis for improving the specificity of lugol chromoendoscopy in the diagnosis of esophageal neoplastic lesions," *Frontiers in Oncology*, vol. 11, no. 1, article 763375, 2021.

[35] S. Jeong, G. Luo, Q. Gao et al., "A combined cox and logistic model provides accurate predictive performance in estimation of time-dependent probabilities for recurrence of intrahepatic cholangiocarcinoma after resection," *Hepatobiliary Surgery and Nutrition*, vol. 10, no. 4, pp. 464–475, 2021.

Hindawi
Computational and Mathematical Methods in Medicine
Volume 2022, Article ID 5317509, 7 pages
https://doi.org/10.1155/2022/5317509

Research Article

Value of CT Radiomics Combined with Clinical Features in the Diagnosis of Allergic Bronchopulmonary Aspergillosis

Xiaojun Qian[1], **Hengmo Rong**[2], **Xue Wei**[1], **Guangsheng Rong**[1] and **Mengxing Yao**[3]

[1]*Department of Allergy, The Third People's Hospital of Hefei, The Third Clinical College of Hefei of Anhui Medical University, Hefei, China*
[2]*Department of Respiratory and Critical Care Medicine, Beijing Chaoyang Hospital, Capital Medical University, Beijing, China*
[3]*Department of Respiratory and Critical Care Medicine, The Second Hospital of Anhui Medical University, Anhui, China*

Correspondence should be addressed to Guangsheng Rong; rhm2007.ok@163.com
and Mengxing Yao; yaomengxing8101@163.com

Received 13 January 2022; Revised 2 March 2022; Accepted 13 April 2022; Published 5 May 2022

Academic Editor: Kelvin Wong

Objective. Early diagnosis of allergic bronchopulmonary aspergillosis (ABPA) and targeted treatment can block the process of the disease. This study explores the diagnostic value of CT radiomics combined with clinical features in allergic ABPA. *Methods*. A total of 40 patients with ABPA were studied retrospectively, divided into training set ($n = 28$) and test set ($n = 12$). Based on CT imaging, the radiomics features are extracted and combined with clinical features to build a diagnostic model. The diagnosis model was based on support vector machine algorithm. The receiver operating characteristic curve (ROC) and area under the curve (AUC) were used to evaluate the diagnostic efficiency of the model. *Results*. There was no significant difference in general information and clinical data between the training and test sets ($P > 0.05$). The AUC of the training set and the test set is 0.896 (95% CI: 0.836-0.963) and 0.886 (95% CI: 0.821-0.952), respectively. *Conclusion*. Based on the CT radiomics model combined with clinical data, it has high efficiency in the diagnosis of ABPA.

1. Introduction

Allergic bronchopulmonary aspergillosis (ABPA) is an allergic and noninfectious lung disease caused by Aspergillus fumigatus, which is an allergic disease caused by Aspergillus fumigatus [1]. The pathogenesis of ABPA is still unclear, which may be related to genetic factors. After inhaling Aspergillus fumigatus spores, the bronchi of genetically susceptible individuals showed an immune response to Aspergillus fumigatus fungal antigen, which damaged cilia elimination function and acted as a barrier, and caused lung infiltration and proximal bronchiectasis [2]. Due to repeated exposure to Aspergillus antigen caused by persistent fungal colonization in the airway, ABPA is characterized by an early allergic reaction and late lung injury [3–5].

Clinical manifestations of ABPA can be acute or chronic disease courses. The most common symptom is recurrent asthma, and systemic symptoms such as fever, headache, and fatigue may occur during an acute attack [6]. ABPA is not common clinically, and its incidence is low, so it is often misdiagnosed as chronic pneumonia, bronchiectasis with infection, tuberculosis, and lung tumor [7]. Clinically, patients cannot get the correct treatment due to misdiagnosis, and the disease often recurs, eventually leading to pulmonary fibrosis and respiratory failure [8]. Therefore, early diagnosis is of great significance to the prognosis and prognosis of patients.

Radiomics method can transform images into high-dimensional features by machine, and make images digital [9–12]. In recent years, the application of CT imaging omics in medical diagnosis systems has gradually matured [13]. Therefore, this paper aims to explore the diagnostic value of CT radiomics combined with clinical feature diagnosis in ABPA.

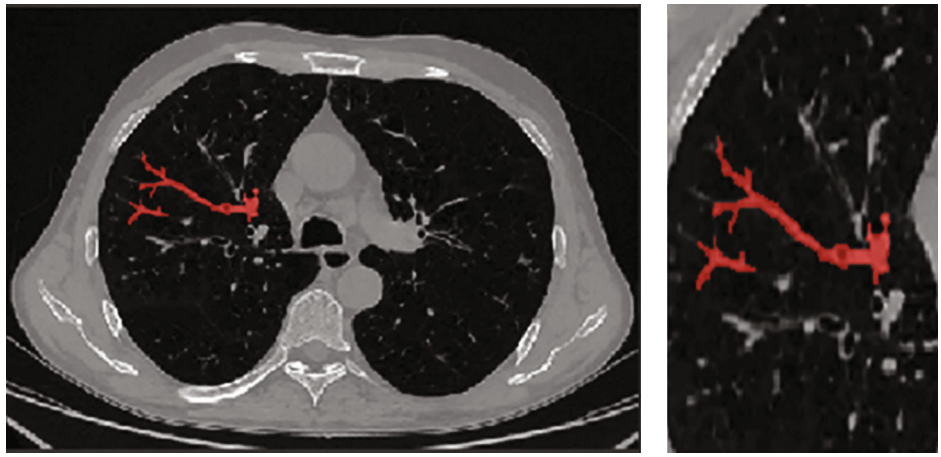

(a) (b)

Figure 1: Delineation of lesion region of interest. (a) Bronchial showed "tree-in-bud sign". (b) Magnification of region of interest.

2. Methods

2.1. Clinical Data. A total of 40 patients with ABPA who were clinically diagnosed in the Department of Allergy of The Third People's Hospital of Hefei, Department of Respiratory and Critical Care Medicine of The Second Hospital of Anhui Medical University, and Beijing Chaoyang Hospital of Capital Medical University from 2017 to 2021. There were 16 males and 24 females, aged 21-84 years (50.58 ± 13.77 years). The clinical manifestations are mainly wheezing, cough, expectoration, chest tightness, and history of bronchial asthma.

All the cases were clinically diagnosed, and all of them met the primary and secondary diagnostic criteria of ABPA established by The International Society for Human and Animal Mycology (ISHAM) [14]. Inclusion criteria: (1) bronchial asthma; (2) elevated IgE levels against Aspergillus fumigatus; (3) elevated total IgE levels (>1000 IU/mL); (4) total eosinophil count >500 cells/μL in steroid naïve patients (may be historical); (5) the chest radiographic features consistent with ABPA may be transient (i.e., consolidation, nodules, tram-track opacities, toothpaste/finger-in-glove opacities, and fleeting opacities) or permanent (i.e., parallel line and ring shadows, bronchiectasis, and pleuropulmonary fibrosis). If the patient has symptoms and signs of type I and III allergy and infection of bronchus and lungs by Aspergillus, and Aspergillus hyphae are found on the smear of deep bronchial secretion or Aspergillus grows for many times, it can be diagnosed as ABPA [15]. Exclusion criteria: (1) the patient already has severe pulmonary dysfunction and (2) possible lung malignancies. In this study, 40 patients met the above diagnostic criteria.

2.2. Instruments and Methods. GE64-row light speed spiral CT was used to scan, and all graphic raw data were transmitted to the ADW4.4 workstation for postprocessing. Scanning parameters: tube voltage 140 kV, tube current 300 mA, rotating speed 0.6 r/s, screw pitch 0.984: 1, collimator width 0.625 mm × 64 layers, and scanning layer thickness 0.625 mm. The lung window was reconstructed by the bone algorithm, and the thickness of the reconstructed layer was 1.25 mm. The mediastinal window was reconstructed by the soft tissue algorithm, with a reconstruction layer thickness of 5 mm, a reconstruction interval of 0 mm, and a matrix of 512 × 512. All patients were in a supine position with their hands on their heads, and the scanning range was 3 cm from the thoracic entrance to the diaphragm. Enhanced chest scan: use nonionic iodine contrast agent with a concentration of 320 mgI/ml, dosage of 1.3 ml/kg, and the scanning parameters are the same as those of plain scan.

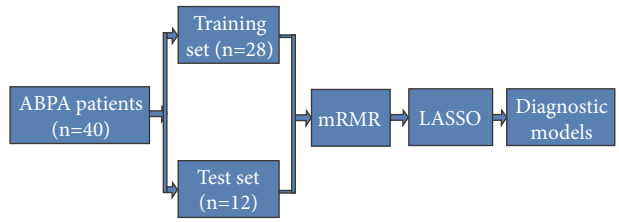

Figure 2: The process of model establishment and verification.

2.3. Image Segmentation. At the level of the most significant section of the image lesion, the image window width and window position is unified (set the window width of 400 Hu and the window position of 40 Hu). Then, using ITK-SNAP 3.8 software, the regions of interest (ROI) are delineated along the lesion contour. An attending physician with 10 years of working experience in radiation diagnosis specialty used the blind method to check the outlined ROI (Figure 1). Import the maximum slice image of the focus-enhanced CT horizontal axis, and the corresponding ROI image was drawn into A.K. software for feature extraction. There are 396 features extracted from the axial images of the largest slice of each lesion, including morphological features, first-order histogram features, second-order histogram features, and higher-order features.

2.4. Feature Extraction. Patients were randomly divided into training group ($n = 28$) and verification group ($n = 12$)

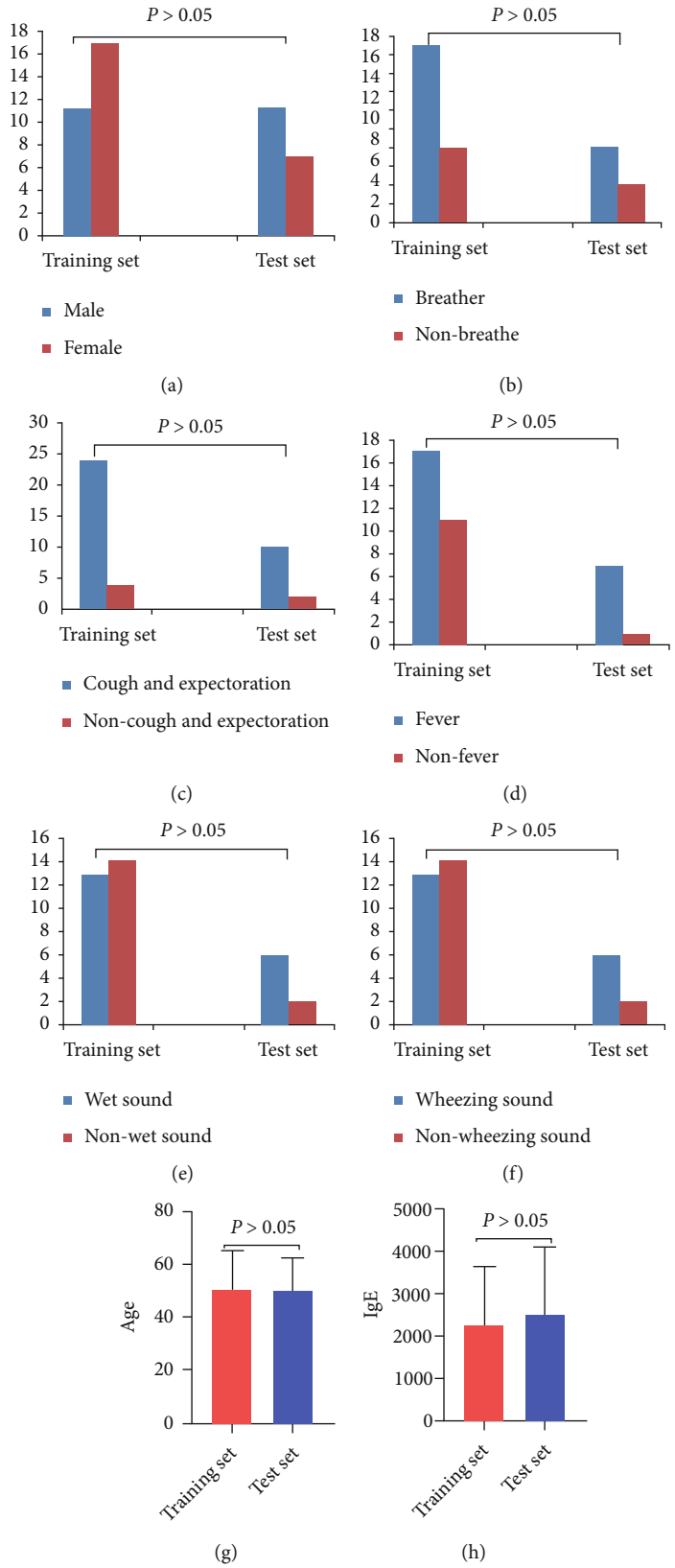

Figure 3: Continued.

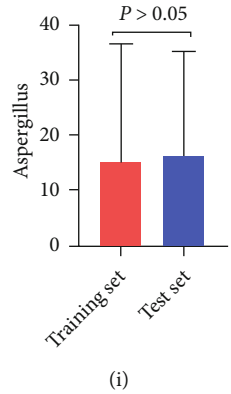

Figure 3: Comparison of patient information and clinical data between training set and test set.

according to 7: 3. First, standardize the data indicators to eliminate the influence of the difference between dimensions and value range. The minimum redundancy maximum correlation (mRMR) algorithm is used to preliminarily screen the features in the training set, eliminating redundant and irrelevant features and retaining the features with the greatest prediction efficiency.

$$\text{mRMR} = \underset{f_i \in X}{\text{argmax}} \left[I(c; f_i) - \frac{1}{|S|} \sum_{f_j \in S} I\left(f_i; f_j\right) \right]. \quad (1)$$

In this study, the "minimum-maximum normalization" is used to linearly transform the original data and map the data to [0, 1], to facilitate comprehensive analysis and make the results more accurate.

$$\text{NMIFS} = \underset{f_i \in X}{\text{argmax}} \left[I(f_i; c) - \frac{1}{|S|} \sum_{f_j \in S} \frac{I\left(f_i; f_j\right)}{\min\left(H(f_i), H\left(f_j\right)\right)} \right]. \quad (2)$$

Finally, the least absolute shrinkage and selection operator (LASSO) algorithm is applied to further screen the remaining omics features. The objective function of the prediction model based on LASSO regression is expressed as follows:

$$\sum_{i=1}^{n} \left(y_i - \sum_{j=1}^{p} x_{ij} \beta_j \right)^2 + \lambda \sum_{j=1}^{p} \left| \beta_j \right| = \text{RSS} + \lambda \sum_{j=1}^{p} \left| \beta_j \right|. \quad (3)$$

2.5. Establishment and Verification of the Model. A support vector machine (SVM) classifier is used to build a diagnosis model by combining clinical factors and imaging characteristics. The linear inseparable data of SVM is projected into the high-dimensional space by mapping function, so that the features become linearly separable in this space, and then the features are divided by a hyperplane with the maximum boundary interval. The effectiveness of training set and test set models is verified. The specific process is shown in Figure 2.

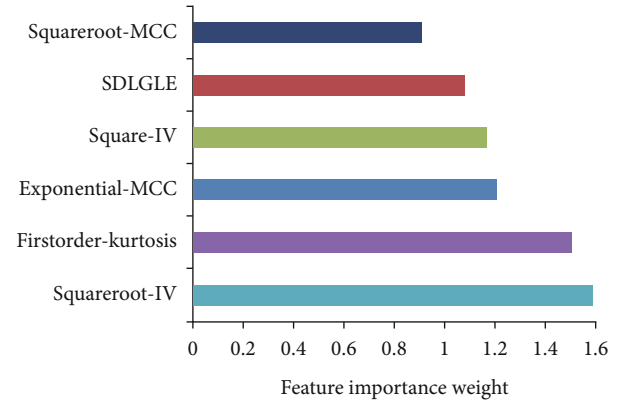

Figure 4: Optimal tuning parameter screening, feature dimensionality reduction, and optimal feature importance ranking chart.

3. Result

3.1. General Information and Clinical Data. General information and clinical data of patients in the training set and the test set were analyzed. There was no significant difference in gender, age, wheezing, cough and expectoration, fever, wet sound, wheezing sound, total IgE, and aspergillus between the training set and the test set ($P > 0.05$) (Figure 3).

3.2. Selection of Image Features. A total of 936 radiomics features were extracted, and 6 optimal radiomics features were obtained after processing, namely, the squareroot-glcm-inverse variance (Squareroot-IV), the square-glcm-inverse variance (Square-IV), the exponential-MCC (E-MCC), the squareroot-MCC (S-MCC), the firstorder-kurtosis (FK), and the small dependence low gray-level emphasis (SDLGLE). Figure 4 shows the six imaging features arranged according to the weight coefficient from low to high.

3.3. Composition and Prediction Efficiency of the Model. The diagnosis model consists of the clinical data of central bronchiectasis; mucoid impaction of dilated bronchial, a cylindrical capsule like toothpaste; patchy infiltration; and centrilobular nodules with a tree-in-bud pattern, and extracted six radiomics characteristics. In the training set, the area under the curve (AUC) of the model was 0.896

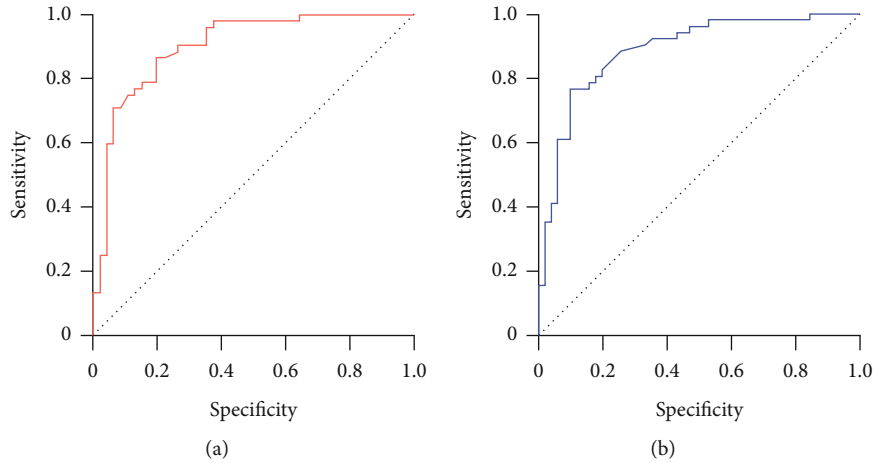

Figure 5: ROC of training set and test set models. (a) Training set; (b) test set.

(95% CI: 0.836-0.963). In the test set, the AUC of the model was 0.886 (95% CI: 0.821-0.952). The diagnosis model has high prediction efficiency (Figure 5).

4. Discussion

ABPA is mainly caused by Aspergillus infection, and Aspergillus fumigatus is the most common clinically. Healthy people rarely cause ABPA because of the function of the bronchial mucosa-epithelial barrier, mucociliary clearance, and phagocytosis of alveolar macrophages. ABPA is common in patients with asthma or cystic fibrosis, and it is also related to the gene-phenotype of the host [16]. When Aspergillus is inhaled by genetically susceptible individuals, it releases antigens, proteolytic enzymes, and other toxic substances activate T lymphocytes, releases interleukin- (IL-) 4, IL-5, and IL-13, and secretes IgE and IgG antibodies, which act on mast cells, alveolar macrophages, and eosinophils, causing an inflammatory reaction in the airway wall and surrounding lung tissues, leading to increased secretion of mucus glands accompanied by bronchospasm [17, 18]. With the development of the disease, bronchial mucus impaction and eosinophil pneumonia can be seen, followed by bronchiolitis obliterans and pulmonary interstitial fibrosis [19].

ABPA can occur at any age, but most are middle-aged and older adults, and there is no obvious gender difference [20]. Clinical manifestations can be acute or chronic disease course, the most common symptom is recurrent asthma, and systemic symptoms such as fever, headache, and fatigue may occur during acute attack [6]. HRCT examination showed central bronchial and pulmonary parenchyma changes, and blood examination showed eosinophils in peripheral blood increased. Immunological examination showed serum total IgE, Aspergillus fumigatus IgE, and IgG antibody increased [21]. Our study shows that IgE and eosinophils in ABPA patients are significantly increased. Muthu et al. [22] systematically evaluated and meta-analyzed previous studies. Their results showed that recombinant Aspergillus fumigatus antigen-specific IgE might play an essential role in the early diagnosis of ABPA.

Pathological features of ABPA mainly include central bronchiectasis and noncaseous granuloma formation [23]. The main change is central granuloma in bronchi and bronchioles, which is characterized by edema of the bronchial wall and infiltration of inflammatory cells such as eosinophils. Central bronchiectasis is dilated affected segment, subsegmental bronchi, and normal distal bronchi. Soft tissue density mucus plugs can be seen in the lumen of dilated bronchi. The main components of mucus plugs are mucus and Aspergillus filaments [24]. If the disease worsens repeatedly, the airway structure will be destroyed permanently, eventually leading to pulmonary interstitial fibrosis [25]. Central bronchiectasis; mucoid impaction of dilated bronchial, a cylindrical capsule like toothpaste; patchy infiltration; and centrilobular nodules with a tree-in-bud pattern may appear on chest CT in patients with ABPA, but pleural effusion is rare on imaging [26]. Patients with ABPA with central bronchiectasis and high attenuation mucus embolism are the most serious and prone to repeated attacks. Therefore, an early and effective diagnosis is crucial for the individualized treatment and prognosis of ABPA.

The clinical diagnosis of ABPA is mainly based on the following clinical indicators: whether there are asthma symptoms, the rapid positive reaction of Aspergillus antigen skin test, a noticeable increase of serum IgE and IgG antibody titers, and the diagnosis is made in combination with imaging data [27]. In this study, the diagnostic efficacy of ABPA was evaluated by constructing CT radiomics combined with clinical data. In this study, 6 imaging omics features were included in the prediction, and the AUC in the training group, and the verification group reached 0.896 and 0.886, respectively, showing good diagnostic ability. This result is similar to previous studies [28]. Radiomics is to transform cross-sectional image arrays (such as CT, MRI, and PET-CT) into quantitative image features. Essentially, it is to digitize images for accurate quantitative analysis [29–31]. A large number of image data can realize the integration of medical data that cannot be achieved by conventional imaging. Compared with the traditional morphological diagnosis mode, it is more detailed, objective, and accurate, which may be the reason for the higher diagnostic efficiency of radiomics model [32].

5. Conclusion

There is a correlation between the CT radiomics model and some imaging characteristics of ABPA. Based on clinical data, the radiomics characteristics are expected to become a new means of diagnosing ABPA. There are several limitations to this study. First, the sample size is small. Second, the ROI of lesions is manually segmented by radiologists, which is influenced by the subjective consciousness of observers to some extent. In addition, this study is retrospective, and there is some bias.

Data Availability

The data used to support the findings of this study are available from the corresponding author upon request.

Conflicts of Interest

The authors declared that there was no conflict of interest.

Acknowledgments

The study was supported by the Key Project of Applied Medicine of Hefei Health Commission (no: Hwk2020zd0015) and Scientific Research Project of Anhui Provincial Health Commission (no: AHWJ2021b071).

References

[1] J. Barry, A. Gadre, and P. Akuthota, "Hypersensitivity pneumonitis, allergic bronchopulmonary aspergillosis and other eosinophilic lung diseases," *Current Opinion in Immunology*, vol. 66, no. 1, pp. 129–135, 2020.

[2] D. W. Denning, J. Cadranel, C. Beigelman-Aubry et al., "Chronic pulmonary aspergillosis: rationale and clinical guidelines for diagnosis and management," *The European Respiratory Journal*, vol. 47, no. 1, pp. 45–68, 2016.

[3] S. Ueki, A. Hebisawa, M. Kitani, K. Asano, and J. S. Neves, "Allergic bronchopulmonary aspergillosis-a luminal hypereosinophilic disease with extracellular trap cell death," *Frontiers in Immunology*, vol. 9, no. 1, 2018.

[4] A. Kanj, N. Abdallah, and A. O. Soubani, "The spectrum of pulmonary aspergillosis," *Respiratory Medicine*, vol. 141, no. 1, pp. 121–131, 2018.

[5] R. Agarwal, A. Chakrabarti, A. Shah et al., "Allergic bronchopulmonary aspergillosis: review of literature and proposal of new diagnostic and classification criteria," *Clinical and Experimental Allergy*, vol. 43, no. 8, pp. 850–873, 2013.

[6] G. Patel and P. A. Greenberger, "Allergic bronchopulmonary aspergillosis," *Allergy and Asthma Proceedings*, vol. 40, no. 6, pp. 421–424, 2019.

[7] A. Alastruey-Izquierdo, J. Cadranel, H. Flick et al., "Treatment of chronic pulmonary aspergillosis: current standards and future perspectives," *Respiration*, vol. 96, no. 2, pp. 159–170, 2018.

[8] Y. Gao and A. Soubani, "Advances in the diagnosis and management of pulmonary aspergillosis," *Advances in Respiratory Medicine*, vol. 87, no. 6, pp. 231–243, 2019.

[9] A. Bhandari, M. Ibrahim, C. Sharma, R. Liong, S. Gustafson, and M. Prior, "CT-based radiomics for differentiating renal tumours: a systematic review," *Abdominal Radiology*, vol. 46, no. 5, pp. 2052–2063, 2021.

[10] Z. Han, K. Liu, Z. Li, and P. Luo, "A pre-check operator for reducing algorithmic optimisation time in image processing applications," *Enterprise Information Systems*, vol. 13, no. 1, pp. 1–13, 2021.

[11] Z. Tang and Z. Zhang, "The multi-objective optimization of combustion system operations based on deep data-driven models," *Energy*, vol. 182, no. 1, pp. 37–47, 2019.

[12] Z. Han, Z. Li, K. Liu, and L. Yan, "Named data networking with neural networks for intelligent image processing information systems," *Enterprise Information Systems*, vol. 12, no. 1, pp. 1–16, 2020.

[13] M. Bogowicz, D. Vuong, M. W. Huellner et al., "CT radiomics and pet radiomics: ready for clinical implementation?," *The Quarterly Journal of Nuclear Medicine and Molecular Imaging*, vol. 63, no. 4, pp. 355–370, 2019.

[14] T. J. Walsh, E. J. Anaissie, D. W. Denning et al., "Treatment of aspergillosis: clinical practice guidelines of the infectious diseases society of america," *Clinical Infectious Diseases*, vol. 46, no. 3, pp. 327–360, 2008.

[15] A. León-Buitimea, J. A. Garza-Cervantes, D. Y. Gallegos-Alvarado, M. Osorio-Concepción, and J. R. Morones-Ramírez, "Nanomaterial-based antifungal therapies to combat fungal diseases aspergillosis, coccidioidomycosis, mucormycosis, and candidiasis," *Pathogens*, vol. 10, no. 10, 2021.

[16] R. Agarwal, I. S. Sehgal, S. Dhooria et al., "Allergic bronchopulmonary aspergillosis," *The Indian Journal of Medical Research*, vol. 151, no. 6, pp. 529–549, 2020.

[17] V. S. Muniz, J. C. Silva, Y. A. V. Braga et al., "Eosinophils release extracellular DNA traps in response to *Aspergillus fumigatus*," *Journal of Allergy and Clinical Immunology*, vol. 141, no. 2, pp. 571–585.e7, 2018.

[18] M. V. Barroso, I. Gropillo, M. A. A. Detoni et al., "Structural and signaling events driving aspergillus fumigatus-induced human eosinophil extracellular trap release," *Frontiers in Microbiology*, vol. 12, no. 1, article 633696, 2021.

[19] Y. Yamauchi, S. Ueki, Y. Konno et al., "The effect of hepatocyte growth factor on secretory functions in human eosinophils," *Cytokine*, vol. 88, no. 1, pp. 45–50, 2016.

[20] V. Muthu, I. S. Sehgal, K. T. Prasad et al., "Epidemiology and outcomes of allergic bronchopulmonary aspergillosis in the elderly," *Mycoses*, vol. 65, no. 1, pp. 71–78, 2022.

[21] S. Phuyal, M. K. Garg, R. Agarwal et al., "High-attenuation mucus impaction in patients with allergic bronchopulmonary aspergillosis: objective criteria on high-resolution computed tomography and correlation with serologic parameters," *Current Problems in Diagnostic Radiology*, vol. 45, no. 3, pp. 168–173, 2016.

[22] V. Muthu, I. S. Sehgal, S. Dhooria, A. N. Aggarwal, and R. Agarwal, "Utility of recombinantAspergillus fumigatusantigens in the diagnosis of allergic bronchopulmonary aspergillosis: a systematic review and diagnostic test accuracy meta-analysis," *Clinical and Experimental Allergy*, vol. 48, no. 9, pp. 1107–1136, 2018.

[23] J. T. Jones, K. W. Liu, X. Wang et al., "Aspergillus fumigatus strain-specific conidia lung persistence causes an allergic broncho-pulmonary aspergillosis-like disease phenotype," *mSphere*, vol. 6, no. 1, 2021.

[24] A. Dietschmann, S. Schruefer, S. Krappmann, and D. Voehringer, "Th2 cells promote eosinophil-independent

pathology in a murine model of allergic bronchopulmonary aspergillosis," *European Journal of Immunology*, vol. 50, no. 7, pp. 1044–1056, 2020.

[25] F. El-Baba, Y. Gao, and A. O. Soubani, "Pulmonary aspergillosis: what the generalist needs to know," *The American Journal of Medicine*, vol. 133, no. 6, pp. 668–674, 2020.

[26] M. P. Ledoux, B. Guffroy, Y. Nivoix, C. Simand, and R. Herbrecht, "Invasive pulmonary aspergillosis," *Seminars in Respiratory and Critical Care Medicine*, vol. 41, no. 1, pp. 080–098, 2020.

[27] K. Asano, A. Hebisawa, T. Ishiguro et al., "New clinical diagnostic criteria for allergic bronchopulmonary aspergillosis/mycosis and its validation," *Journal of Allergy and Clinical Immunology*, vol. 147, no. 4, pp. 1261–1268.e5, 2021.

[28] A. Russo, G. Tiseo, M. Falcone, and F. Menichetti, "Pulmonary aspergillosis: an evolving challenge for diagnosis and treatment," *Infectious Disease and Therapy*, vol. 9, no. 3, pp. 511–524, 2020.

[29] R. Wilson and A. Devaraj, "Radiomics of pulmonary nodules and lung cancer," *Translational Lung Cancer Research*, vol. 6, no. 1, pp. 86–91, 2017.

[30] H. Chen, W. Li, and Y. Zhu, "Improved window adaptive gray level co-occurrence matrix for extraction and analysis of texture characteristics of pulmonary nodules," *Computer Methods and Programs in Biomedicine*, vol. 208, no. 1, article 106263, 2021.

[31] J. Shi, Y. Ye, D. Zhu, L. Su, Y. Huang, and J. Huang, "Comparative analysis of pulmonary nodules segmentation using multiscale residual u-net and fuzzy c-means clustering," *Computer Methods and Programs in Biomedicine*, vol. 209, no. 1, article 106332, 2021.

[32] L. Yang, D. Gu, J. Wei et al., "A radiomics nomogram for preoperative prediction of microvascular invasion in hepatocellular carcinoma," *Liver Cancer*, vol. 8, no. 5, pp. 373–386, 2019.

Hindawi
Computational and Mathematical Methods in Medicine
Volume 2022, Article ID 3490463, 6 pages
https://doi.org/10.1155/2022/3490463

Research Article

Classification and Segmentation Algorithm in Benign and Malignant Pulmonary Nodules under Different CT Reconstruction

Zhiqian Lu,[1] **Feixiang Long**,[1] **and Xiaodong He**[2]

[1]*Department of Radiology, The People's Hospital of Xuancheng City, Anhui 242000, China*
[2]*Cancer Center, Department of Radiology, Zhejiang Provincial People's Hospital (Affiliated People's Hospital, Hangzhou Medical College), Hangzhou 310014, China*

Correspondence should be addressed to Xiaodong He; 15888815645@163.com

Received 22 December 2021; Revised 1 March 2022; Accepted 8 April 2022; Published 21 April 2022

Academic Editor: Kelvin Wong

Background and Objective. Effective segmentation of pulmonary nodules can effectively assist in the diagnosis of benign and malignant pulmonary nodules. We aim to explore the effectiveness of classification and segmentation algorithms in diagnosing benign and malignant pulmonary nodules under different CT reconstructions. *Methods*. The imaging data of 55 patients with chest CT plain scan in the Xuancheng People's Hospital were collected retrospectively. The data of each patient included lung window reconstruction, mediastinum reconstruction, and bone window reconstruction. The depth neural network and 3D convolution neural network were used to construct the model and train the classification and segmentation algorithm. The pathological results were the gold standard for benign and malignant pulmonary nodules. The classification and segmentation algorithms under three CT reconstruction algorithms were compared and analyzed by analysis of variance. *Results*. Under the three CT reconstruction algorithms, the classification accuracy of pulmonary nodule density types was 98.2%, 96.4%, and 94.5%, respectively. The Dice coefficients of all nodule segmentation were 80.32% ± 5.91%, 79.83% ± 6.12%, and 80.17% ± 5.89 %, respectively. The diagnostic accuracy between benign and malignant pulmonary nodules under different reconstruction algorithms was 98.2%, 96.4%, and 94.5%, respectively. There was no significant difference in the classification accuracy, Dice coefficients, and diagnostic accuracy of pulmonary nodules under three different reconstruction algorithms (all $P > 0.05$). *Conclusion*. The depth neural network algorithm combined with 3D convolution neural network has a good efficiency in identifying benign and malignant pulmonary nodules under different CT reconstruction classification and segmentation algorithms.

1. Introduction

The mortality of lung cancer ranks first in the world. It is one of the most malignant tumors threatening human health. For lung cancer, only early diagnosis and treatment can reduce mortality and prolong the survival time of patients [1–4]. Malignant pulmonary nodules often indicate the deterioration of disease progression, and more active and targeted treatment is needed to prevent the continuous deterioration of the disease. Therefore, accurate classification of benign and malignant pulmonary nodules can be an excellent adjuvant treatment of patients' diseases. High-resolution CT is the most commonly used means to detect pulmonary nodules accurately. With the more extensive application of high-resolution CT, the diagnostic burden of imaging doctors is increasing [5, 6]. Inexperienced imaging doctors are more likely to miss diagnosis and misdiagnosis.

In recent years, artificial intelligence (AI) technology has been widely used in various industries [7–9]. The application of AI-aided diagnosis system based on deep learning in imaging diagnosis of pulmonary nodules has made rapid progress, and the early lung cancer detection rate has been improved [10–12]. Applying AI technology to screen massive CT images and mark suspicious nodule lesions

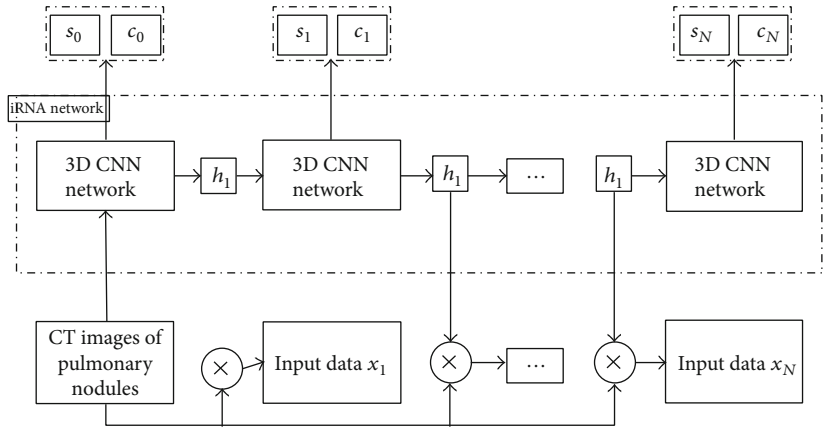

Figure 1: Model framework of pulmonary nodule density type classification and contour segmentation based on deep learning.

Table 1: Accuracy analysis of 55 pulmonary nodules density types under three different reconstruction algorithms (n/%).

Reconstruction algorithm	All nodules ($n = 55$)	Solid nodule ($n = 39$)	Subsolid nodule ($n = 16$)
Lung window	54/98.2	38/97.4	16/100.0
Mediastinal window	53/96.4	38/97.4	15/93.8
Bone window	52/94.5	37/94.9	15/93.8
χ^2 value	1.038	0.518	1.043
P value	0.595	0.772	0.593

Table 2: segmentation results of 55 pulmonary nodules under three different reconstruction algorithms (Dice coefficient) (%).

Reconstruction algorithm	All nodules ($n = 55$)	Solid nodule ($n = 39$)	Subsolid nodule ($n = 16$)
Lung window	80.32 ± 5.91	79.93 ± 5.74	82.62 ± 6.28
Mediastinal window	79.83 ± 6.12	79.28 ± 5.39	82.35 ± 6.49
Bone window	80.17 ± 5.89	80.05 ± 6.21	81.79 ± 6.56
F value	1.683	1.590	1.753
P value	0.281	0.237	0.315

preliminarily can help imaging doctors in tertiary hospitals, reduce workload, and improve diagnostic accuracy. This technology can also help grassroots imaging doctors and reduce the missed diagnosis rate of nodules [13].

CT imaging quality is affected by many factors, including radiation dose, reconstruction layer thickness, and reconstruction algorithm [14]. The early identification of benign and malignant pulmonary nodules can help doctors accurately diagnose and take appropriate clinical treatment measures. Therefore, this study intends to design a pulmonary nodule classification and segmentation algorithm which can be stable under different reconstruction algorithms. The 3D convolution neural network is used to mine the pulmonary nodules' imaging features fully. The recursive neural network integrating attention mechanism is used to effectively utilize pulmonary nodules' global and local context information [15, 16]. The two classification and segmentation tasks are used for joint learning, which complement each other to help the model further improve the effect to distinguish and evaluate the benign and malignant pulmonary nodules more accurately.

2. Material and Methods

2.1. General Data. A total of 55 patients with chest CT examinations in the Xuancheng People's Hospital from October 2018 to December 2020 were collected retrospectively, including 23 males and 32 females, aged 56.07 ± 10.09 years. Inclusion criteria: (1) pulmonary nodules were found; (2) chest CT plain scan images include three reconstruction algorithms: lung window reconstruction, mediastinum reconstruction, and bone reconstruction. Exclusion criteria: (1) excessive respiratory motion artifacts affect CT quality; (2) multiple pulmonary nodules.

2.2. Instruments and Methods. GE (Optima CT670) 64 slice spiral CT is adopted: tube voltage 120 kV, tube current 39 mAs, pitch 0.8 and layer thickness 5 mm; Philips (Brilliance) 16 slice spiral CT scanning: tube voltage 120 kV, tube current automatic adjustment, pitch 1, layer thickness 5 mm; the scanning range was from the upper edge of the sternoclavicular joint to the bottom of the lung and breath-holding scanning at the end of inhalation. The images of lung window reconstruction, mediastinum reconstruction, and bone window reconstruction were evaluated.

2.3. Construction of Pulmonary Nodule Model. Our study started with the features extracted from the model to build an algorithm model with a long-lasting effect. Multiple steps were used to enhance the features' representation ability and resist the impact of the change in the reconstruction algorithm. The specific framework of the model was shown in Figure 1.

The model design mainly starts from the following four points:

(1) Deep neural network is used instead of traditional machine learning to automatically learn features in

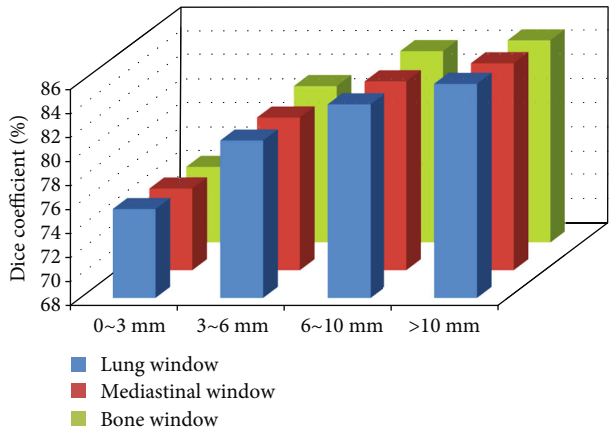

Figure 2: Dice coefficient in different diameter of pulmonary nodules.

a data-driven way to avoid the limitations of defining features based on rules in conventional machine learning

(2) Compared with the 2D convolutional neural network commonly used in natural images, the 3D convolutional neural network in this study can capture more spatial context information of pulmonary nodules

(3) A recurrent neural network with an attention mechanism is constructed, and the 3D convolution neural network replaces the matrix multiplication in the recurrent neural network. The process of subfocus observation of different regions of nodules in daily film reading is modeled as a time-series process by a recurrent neural network. Through continuous iteration, an attention map is generated at each iteration time, different local detail features of nodules are extracted, and multiregion features are fused

(4) The upper design of the model adopts the method of multitask learning to predict the nodule contour and the nodule density type simultaneously. In this way, the two tasks complement each other. While learning the nodule area, we can notice the impact of different density types, which can help the model further improve the recognition accuracy of the two tasks

2.4. Test Process. For the detection and qualitative diagnosis of pulmonary nodules by the imaging physician group, a senior resident shall first detect the nodules on the high-resolution thin-layer chest CT images and diagnose the benign possible or suspicious malignant nodes according to the size, density, shape, and relationship with the surrounding blood vessels and bronchus and then complete the examination by the deputy chief physician. The other two imaging physicians with senior professional titles combined with artificial intelligence and referred to the reviewed image report for nodule detection and identification. When they disagree, they combined with multiplanar reconstruction and discussed to obtain consistent results, which will be used as the gold standard for true nodule detection. The gold standard for diagnosing benign and malignant pulmonary nodules was the postoperative pathological results. The density, size, benign, and malignant of each nodule were recorded, respectively. The nodule was divided into solid nodule and ground glass nodule. In order to further explore the effect of deep learning model on contour segmentation, the maximum cross-sectional diameter of nodules is divided to obtain the effect of the model under different sizes of nodules. The size of the nodule was divided into diameter $<$ 3 mm and $\geq$3 mm.

2.5. Evaluation Index of Classification and Segmentation of Pulmonary Nodules. The average CT density classification accuracy index was used for pulmonary nodule density classification, and the average Dice coefficient of each pulmonary nodule was used for pulmonary nodule segmentation. The calculation formula of the Dice coefficient is as follows:

$$\text{Dice} = \frac{2 \times |\text{AI} \cap \text{Doc}|}{|\text{AI}| + |\text{Doc}|}, \quad (1)$$

where $|\text{AI} \cap \text{Doc}|$ represents the overlapping area between the system model segmentation and the gold standard and $|\text{AI}| + |\text{Doc}|$ represents the sum of the nodule area segmented by the model and the corresponding nodule area in the gold standard. When the result of model segmentation is consistent with the related consequence in the gold standard, the Dice coefficient is 1; when the two do not overlap, the Dice coefficient is 0.

2.6. Statistical Processing. In this study, SPSS 22.0 statistical software package was used for data analysis and processing; the accuracy of pulmonary nodule density classification and the Dice coefficient of segmentation were counted by SciPy 1.4.1 software. The accuracy of age and density classification and Dice coefficient conform to the normal distribution, expressed in $\bar{x} \pm s$; rate and frequency were used to describe the number of nodules. Analysis of variance was used to compare the classification accuracy and segmentation Dice coefficient of pulmonary nodules among three groups of different CT reconstruction algorithms. Inspection level $\alpha = 0.05$.

3. Result

3.1. Classification Results of Pulmonary Nodule Density Types under Three CT Reconstruction Algorithms. Under three different CT reconstruction algorithms, the classification accuracy of 55 CT nodules and the classification accuracy of solid and subsolid nodules were higher (Table 1). The difference was not statistically significant ($P > 0.05$).

3.2. Segmentation Results of Model Pulmonary Nodules under Three CT Reconstruction Algorithms. For lung reconstruction, mediastinal reconstruction, and bone reconstruction, there was no significant difference in Dice coefficients of all nodules, solid nodules and subsolid nodules under

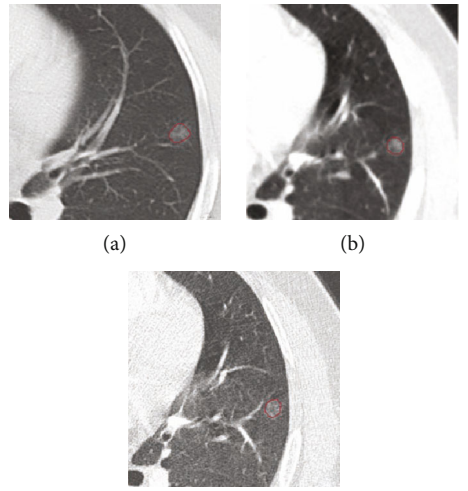

(a) (b) (c)

Figure 3: Segmentation of malignant pulmonary nodules under three reconstruction algorithms. (a) Lung window reconstruction. (b) Mediastinal reconstruction. (c) Bone window reconstruction.

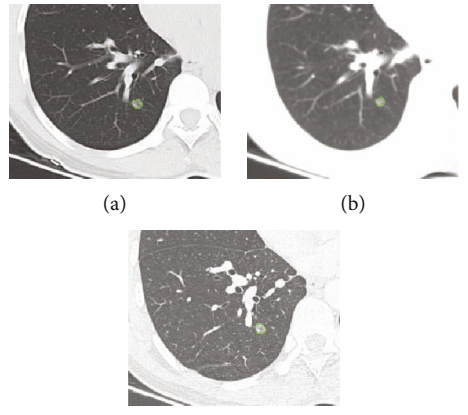

(a) (b) (c)

Figure 4: Segmentation of benign pulmonary nodules under three reconstruction algorithms. (a) Lung window reconstruction. (b) Mediastinal reconstruction. (c) Bone window reconstruction.

Table 3: Diagnostic accuracy under three different reconstruction algorithms (%).

Reconstruction algorithm	Sensitivity	Specificity	Accuracy
Lung window	96.6	100.0	98.2
Mediastinal window	93.1	100.0	96.4
Bone window	93.1	96.1	94.5
χ^2 value	0.424	2.026	1.038
P value	0.809	0.363	0.595

the three different reconstruction algorithms (all $P > 0.05$) (Table 2).

Under three different CT reconstruction algorithms, the Dice coefficient increased with the increase of the diameter of pulmonary nodules (Figure 2).

3.3. Results of Benign and Malignant Diagnosis of Model Pulmonary Nodules under Three CT Reconstruction Algorithms. From the postoperative pathological results, there were 29 cases of malignant pulmonary nodules (Figure 3) and 26 cases of benign pulmonary nodules (Figure 4). The results of three reconstruction algorithms for identifying benign and malignant pulmonary nodules are shown in Table 3. There was no significant difference of accuracy between benign and malignant pulmonary nodules under different reconstruction algorithms ($P > 0.05$).

4. Discussion

The early imaging signs of lung cancer are primarily pulmonary nodules. At present, the clinical diagnosis and evaluation of pulmonary nodules are generally through clinical data, imaging data, tumor markers, pathological biopsy, surgical treatment, etc. It is common to screen and diagnose pulmonary nodules by imaging methods [17, 18]. The chest plain CT images can clearly distinguish and judge pulmonary nodules' size, position, morphology, and internal characteristics [19]. It is of great significance to distinguish the

clinic's benign and malignant pulmonary nodules. Under different CT reconstruction algorithms, doctors' diagnoses vary widely. Thus, it is essential to observe the impact of images under different CT reconstruction algorithms on benign and malignant pulmonary nodule models and doctors' diagnoses [20–22]. The image in mediastinal reconstruction is smooth, the image in bone window reconstruction is sharp, and the image in lung window reconstruction is between the two. Different window reconstructions can diagnose various related diseases [23, 24].

In order to solve the instability of automatic segmentation of pulmonary nodules and classification of nodule density types under different CT reconstruction algorithms, a deep neural network model based on joint learning of pulmonary nodule segmentation and density type classification is proposed, which makes full use of the complementarity between the two tasks to promote each other [25]. At the same time, the model innovatively integrates many technologies such as a 3D convolution network, attention mechanism, and recurrent neural network to ensure that the model can thoroughly learn the local and global features of pulmonary nodules [26, 27]. The new method can carry out effective feature fusion to enhance the expression ability of the extracted features to improve the model's effectiveness for feature extraction under different image quality.

The test results of 55 pulmonary nodules in this study showed no significant difference in the classification accuracy of pulmonary nodules under different reconstruction algorithms ($P > 0.05$). There was no significant difference in the Dice coefficient of nodule segmentation under different reconstruction algorithms ($P > 0.05$). The model was stable under different CT reconstruction algorithms. The statistical results of pulmonary nodules grouped according to different sizes also show that the model effect improves with the increase of nodules. Except for nodules below 3 mm, the segmentation effect of the same group is stable under different reconstruction algorithms. The contours of benign and malignant nodules segmented by the model under different reconstruction algorithms are very similar, maintaining high consistency, and the difference is not statistically significant ($P > 0.05$). In addition, by analyzing the effect of models with different sizes of nodules, it is found that the poor segmentation effect is mainly concentrated on the micronodules with diameters less than 3 mm. The size of micronodules is small, and the boundary is not easy to determine, resulting in the deviation of the Dice coefficient index. However, with the increase of nodules, the effect of the model continues to improve, and the clinical analysis of larger nodules is of greater significance, indicating that the model meets the clinical needs. For the benign and malignant nodules, the models with different reconstruction algorithms had high sensitivity in diagnosing benign and malignant pulmonary nodules, and the difference was not statistically significant ($P > 0.05$).

5. Conclusions

In conclusion, the model constructed in this paper shows good performance in pulmonary nodule segmentation and density type classification and is stable under different CT reconstruction algorithms and has good diagnostic efficiency for benign and malignant pulmonary nodules, which shows that it has certain practical value in clinic. Due to the small scale of cases, this method has less classification of subsolid nodules and lacks certain validation. Future research can add data to verify the effectiveness of the model.

Data Availability

The data used to support the findings of this study are available from the corresponding author upon request.

Conflicts of Interest

All authors declare no conflicts of interest in this paper.

References

[1] B. J. Bartholmai, C. W. Koo, G. B. Johnson et al., "Pulmonary nodule characterization, including computer analysis and quantitative features," *Journal of Thoracic Imaging*, vol. 30, no. 2, pp. 139–156, 2015.

[2] D. Divisi, M. Barone, G. Zaccagna, and R. Crisci, "Fluorine-18 fluorodeoxyglucose positron emission tomography in the management of solitary pulmonary nodule: a review," *Annals of Medicine*, vol. 49, no. 7, pp. 626–635, 2017.

[3] M. C. B. Godoy, E. Odisio, M. T. Truong, P. M. de Groot, G. S. Shroff, and J. J. Erasmus, "Pulmonary nodule management in lung cancer screening: a pictorial review of lung-RADS version 1.0," *Radiologic Clinics of North America*, vol. 56, no. 3, pp. 353–363, 2018.

[4] X. Deng, Y. Liu, and H. Chen, "Three-dimensional image reconstruction based on improved u-net network for anatomy of pulmonary segmentectomy," *Mathematical Biosciences and Engineering*, vol. 18, no. 4, pp. 3313–3322, 2021.

[5] L. Gong, S. Jiang, Z. Yang, G. Zhang, and L. Wang, "Automated pulmonary nodule detection in ct images using 3d deep squeeze-and-excitation networks," *International Journal of Computer Assisted Radiology and Surgery*, vol. 14, no. 11, pp. 1969–1979, 2019.

[6] D. Groheux, G. Quere, E. Blanc et al., "FDG PET-CT for solitary pulmonary nodule and lung cancer: literature review," *Diagnostic and Interventional Imaging*, vol. 97, no. 10, pp. 1003–1017, 2016.

[7] Z. Tang and Z. Zhang, "The multi-objective optimization of combustion system operations based on deep data-driven models," *Energy*, vol. 182, pp. 37–47, 2019.

[8] Z. Han, K. Liu, Z. Li, and P. Luo, "A pre-check operator for reducing algorithmic optimisation time in image processing applications," *Enterprise Information Systems*, vol. 13, pp. 1–13, 2021.

[9] J. Shi, Y. Ye, D. Zhu, L. Su, Y. Huang, and J. Huang, "Automatic segmentation of cardiac magnetic resonance images based on multi-input fusion network," *Computer Methods and Programs in Biomedicine*, vol. 209, p. 106323, 2021.

[10] Z. Akkus, J. Cai, A. Boonrod et al., "A survey of deep-learning applications in ultrasound: artificial intelligence-powered ultrasound for improving clinical workflow," *Journal of the American College of Radiology*, vol. 16, no. 9, pp. 1318–1328, 2019.

[11] A. Esteva, A. Robicquet, B. Ramsundar et al., "A guide to deep learning in healthcare," *Nature Medicine*, vol. 25, no. 1, pp. 24–29, 2019.

[12] H. Chen, W. Li, and Y. Zhu, "Improved window adaptive gray level co-occurrence matrix for extraction and analysis of texture characteristics of pulmonary nodules," *Computer Methods and Programs in Biomedicine*, vol. 208, p. 106263, 2021.

[13] R. Poplin, A. V. Varadarajan, K. Blumer et al., "Prediction of cardiovascular risk factors from retinal fundus photographs via deep learning," *Nature Biomedical Engineering*, vol. 2, no. 3, pp. 158–164, 2018.

[14] A. W. Annen, D. D. Heston AL III, G. W. Dy, R. Bluebond-Langner, K. K. Jensen, and J. U. Berli, "Masculinizing genital surgery: an imaging primer for the radiologist," *AJR. American Journal of Roentgenology*, vol. 214, no. 1, pp. W27–W36, 2020.

[15] J. Mehl, A. Otto, J. B. Baldino et al., "The acl-deficient knee and the prevalence of meniscus and cartilage lesions: a systematic review and meta-analysis (crd42017076897)," *Archives of Orthopaedic and Trauma Surgery*, vol. 139, no. 6, pp. 819–841, 2019.

[16] B. Scheiderer, F. B. Imhoff, C. Kia et al., "LUCL internal bracing restores posterolateral rotatory stability of the elbow," *Knee Surgery, Sports Traumatology, Arthroscopy*, vol. 28, no. 4, pp. 1195–1201, 2020.

[17] M. Nardini and J. Dunning, "Pulmonary nodules precision localization techniques," *Future Oncology*, vol. 16, no. 16s, pp. 15–19, 2020.

[18] Y. Onishi, A. Teramoto, M. Tsujimoto et al., "Automated pulmonary nodule classification in computed tomography images using a deep convolutional neural network trained by generative adversarial networks," *BioMed research international*, vol. 2019, Article ID 6051939, 2019.

[19] S. Qiu, J. Sun, T. Zhou, G. Gao, Z. He, and T. Liang, "Spiculation sign recognition in a pulmonary nodule based on spiking neural p systems," *BioMed Research International*, vol. 2020, Article ID 6619076, 2020.

[20] J. Kiely, M. Kumar, and R. G. Wade, "The accuracy of different modalities of perforator mapping for unilateral DIEP flap breast reconstruction: a systematic review and meta-analysis," *Journal of Plastic, Reconstructive & Aesthetic Surgery*, vol. 74, no. 5, pp. 945–956, 2021.

[21] J. Kim, C. Park, H. S. Jeong et al., "The optimal combination of monochromatic and metal artifact reconstruction dual-energy ct to evaluate total knee replacement arthroplasty," *European Journal of Radiology*, vol. 132, p. 109254, 2020.

[22] J. Shi, Y. Ye, D. Zhu, L. Su, Y. Huang, and J. Huang, "Comparative analysis of pulmonary nodules segmentation using multiscale residual U-Net and fuzzy C-means clustering," *Computer Methods and Programs in Biomedicine*, vol. 209, p. 106332, 2021.

[23] H. Du, X. X. Tian, F. Q. Guo et al., "Evaluation of different surgical methods in treating recurrent patella dislocation after three-dimensional reconstruction," *International Orthopaedics*, vol. 41, no. 12, pp. 2517–2524, 2017.

[24] R. H. H. Wellenberg, E. T. Hakvoort, C. H. Slump, M. F. Boomsma, M. Maas, and G. J. Streekstra, "Metal artifact reduction techniques in musculoskeletal CT-imaging," *European Journal of Radiology*, vol. 107, pp. 60–69, 2018.

[25] Z. Han, Z. Li, K. Liu, and L. Yan, "Named data networking with neural networks for intelligent image processing information systems," *Enterprise Information Systems*, vol. 12, pp. 1–16, 2020.

[26] W. Zuo, F. Zhou, Y. He, and X. Li, "Automatic classification of lung nodule candidates based on a novel 3D convolution network and knowledge transferred from a 2D network," *Medical Physics*, vol. 46, no. 12, pp. 5499–5513, 2019.

[27] J. Dong, T. Fu, Y. Lin et al., "Hole-filling based on content loss indexed 3d partial convolution network for freehand ultrasound reconstruction," *Computer Methods and Programs in Biomedicine*, vol. 211, p. 106421, 2021.

Hindawi
Computational and Mathematical Methods in Medicine
Volume 2022, Article ID 4661156, 12 pages
https://doi.org/10.1155/2022/4661156

Research Article

Performance Index Based on Predicted Auditory Reaction Time Analysis for the Evaluation of Human-Machine Interface in Flight Control

Weiwei Yu,[1] **Dian Jin**,[1] **Xinliang Yang**,[2] **Feng Zhao**,[1] **Haiyang Wang**,[2] **and Ran Peng**[2]

[1]*School of Mechanical Engineering, Northwestern Polytechnical University, Xi'an, 710072, China*
[2]*Avionics Research Institute, Chinese Flight Test Establishment, Xi'an, 710089, China*

Correspondence should be addressed to Weiwei Yu; yuweiwei@nwpu.edu.cn and Dian Jin; d.jin@mail.nwpu.edu.cn

Received 8 October 2021; Revised 8 January 2022; Accepted 23 February 2022; Published 12 April 2022

Academic Editor: Kelvin Wong

With the rapid development of complex equipment, such as airplanes, the appropriate design of the human-machine interface is often upgraded, thus emerged many methods to evaluate whether such an upgrade is effective. Most researches focus on the time accumulation effect of the human state during the interaction to evaluate the interface. However, in the aviation application, the performance of the pilot's instantaneous reactions also reveals the design efficiency of the interface, since the difficulty level of obtaining the useful information would severely influence the reaction time in some voice command tasks or emergency situations. Besides, there are so many flight scenarios that are impossible to be simulated in experiments or in a laboratory environment. Also, voice commands are too numerous to be traversed simulated. This paper introduced predicted auditory reaction time as an index to evaluate human-machine interface design. The proposed method has two advantages. On the one hand, it effectively measures the pilot's auditory reaction time based on the eye movement tracking; thus, the data can be taken in flight task scenarios, and the experiment would not cause interference to the subjects. On the other hand, a prediction model is proposed, in which the pilot's reaction time under more generalized voice command can be estimated based on a small-size sample set.

1. Introduction

Human-machine (computer) systems refer to the system composed of humans and machines and fulfill some functions through the interaction between humans and machines [1]. With the rapid development of complex equipment, such as airplanes and remotely piloted aircraft (RPA), the appropriate design of the human-machine interface plays a crucial role in harnessing the powerful capabilities of equipment [2]. In common cases, the interface of upgraded equipment is designed or modified based on the original interface of the previous generation, while adding new functions. However, the simple interface modification or updates will not give full play to the capabilities of a new generation of equipment. Sometimes, the interface design may cause user failures to obtain critical information [3] or give rise to malfunctions of cognition and decision-making among operators, which may lead to accidents [4]. Thus, many methods called usability evaluation emerged, aimed at evaluating whether such an upgraded human-machine interface is effective.

There are methods based on analyzing the static attributes of the interface. In [5], the color and luminance contrast in information coding was discussed in Air Traffic Control (ATC) display systems. A prototype color palette that used color coding to prioritize display information while maintaining good legibility was presented. The Human Algorithm Knowledge-based layout Design method (HAKD) was proposed to deal with the problem of layout design [6]. HAKD took the evolutionary algorithm (e.g., genetic algorithm) as the algorithm foundation, in which human-provided artificial layout schemes (artificial solutions) and layout diagrams afford prior knowledge solutions, and the evolution algorithm produced novel algorithm

solutions. Thus, human intelligence, computer intelligence (evolution algorithm), and prior knowledge extracted from layout diagrams were fused for problem-solving.

However, the researches above paid more attention to the static attributes of the interface, and the dynamic factors of humans were seldom taken into consideration. Thus, researches based on the experiment which regarded human performance, either from the aspect of work performance evaluation or the mental workload evaluation, were adopted.

In performance evaluation, a cognitive walkthrough is one method. The developers of an interface walked through the interface in the context of core tasks that a typical user would accomplish. The actions and feedback of the interface were compared to the user's goals and knowledge, and discrepancies between the user's expectations and the steps required by the interface were noted [7]. With the development of technology, eye-tracking became one of the most precise and objective methods of usability studies [8] and was believed to be an efficient method to evaluate the design of the human-machine interface [9]. It was discovered that well-organized functional grouping resulted in shorter scan paths, covering smaller areas. An evaluation method called DEMIS was demonstrated [10]. Two effectiveness measures included the fixation-to-importance ratio (FIR) which represented attentional resources spent on an information source compared to the importance of the information source, and selective attention effectiveness (SAE) which incorporated FIRs for all information sources was proposed. Then, difficulties caused by a poor HMI design were evaluated by a focused interview based on the FIR evaluation.

Several researches are grounded on measuring the mental workload (MWL) of users to evaluate the user interface design. In engineering application, the NASA Task Load Index (TLX) was adopted as one of the indexes measuring the MWL [11]. It collected subjective workload scores based on a weighted average rating of six factors, which included mental demand, physical demand, temporal demand, own performance, effort, and frustration level. The results showed that the design style of the human-machine interface affected different factors of the operator's workload. Another multi-index evaluation method developed on performance measures, subjective rating, and physiological measure was used to evaluate MWL of operators [12]. It pointed out that interface design had a significant effect on operators' MWL in nuclear power plants. Same in the domain of nuclear power plant interface design, fuzzy comprehensive evaluation theory was adopted in [13] for assessment of interface designs. This method was validated in achieving the quick and accurate assessment of different display interfaces when considering the operators' MWL. In the domain of Air Traffic Control (ATC), [14] used operator's behavior and EGG/ERP to measure the cognitive load and also achieved the effective evaluation of the interface design.

Most of the previous methods based on operation performance or mental workload evaluation considered the time accumulation effect of the human state during the interaction. However, the performance of human instantaneous reactions also reveals the design efficiency of the interface, since the difficulty level of obtaining the useful information would severely influence the response time in some voice commands or emergency tasks. For example, in the application of the flight control interface, for some tasks, especially high maneuverability mission, after voice receiving commands, it is critical for pilots to understand the commands and perform quickly in highly dynamic flight scenarios. The reaction speed may affect the task performance of the whole mission [15]. Also, in the case of special situation handling during the flight, after receiving the auditory warning/alarming signal, the pilot has to obtain useful information from the interface as quickly as possible to avoid the accident [15]. Therefore, in the above application scenario, it is very necessary to propose the reaction time (RT) as one of the indexes to evaluate the user interface.

The pilot's RT is related to his proficiency; for example, expert pilots show less RT [16]. But for the same expert pilot, his RT for certain voice commands can reveal the accessibility of the useful information that the interaction interface provides to the user [17]. RT is commonly defined as the time interval between a stimulus and a reaction, which can be used as an index to evaluate the human-machine interface. In [18], RTs together with mental workload and subjective feedback were used to evaluate the agricultural machine user-centered interface. Significant differences were found in RT between two user interfaces, which showed that RT can be an index to measure the usability of an interface. Considering that the interaction interface may impact the user's efficiency of obtaining useful information, the user's response time for answering the questions related to the information presented on an interface was adopted to infer the situation awareness attained by the user. Higher response time was associated with lower situation awareness. Besides the study on auditory RT, the RT of visual warning, auditory warning, tactile warning, and any combination of these three types of signals were regarded as the indexes to assess the user's interface [19].

Although these studies have certain practical significance and provide good guidance to evaluate the design of a human-machine interface, most of the studies designed the experiment based on the virtual task or assumption task. For example, to evaluate auditory attention in a human-machine system, a choice RT experiment was organized, in which the user must give a response that corresponds to the stimulus [20]. In another research, to make ergonomics recommendations for multisensory interface design in control consoles, a signal (visual or auditory)-press button task was designed to evaluate the human-machine interface under different conditions by measuring RT and error percentages [21]. Gerhardt-Powals [17] created a simple firing task game. RT was obtained by recording the time interval between information receiving and key-pressing. Several principles based on the experiment are concluded to produce a "cognitive friendly" interface.

For the application of the human-machine interface in aviation, the flight deck is sophisticated and contains a lot of information [22]. The problem of human-machine interaction can be viewed as two powerful information processors attempting to communicate with

each other via a narrow-bandwidth, highly constrained interface [23]. Numerous experimental results indicate that the bandwidth of human perception is severely limited [24], which means that only limited information can be successfully acquired by users within a unit time. Moreover, the pilot's RT presents more task-related features. Different auditory commands or warning tones in different flight scenes and missions can seriously affect the information requirement of users. For example, in a conditionally automated driving experiment, the group of participants who received commands on limitations had a lower RT when the car approached the deer than the control group [25]. Therefore, it is particularly important to evaluate the human-machine interface in aviation considering different auditory commands in flight scenes as realistic as possible.

However, in the previous studies, either the experiment was not set under the task state or the experimental measurement of RT may disturb the subjects to complete the original task. Besides, different from other applications, flight tasks and scenarios are too complex to be simulated; for example, in high maneuverability missions, it is hard to generalize the proper voice command in experiments. Also, different from warning/alarm signals, voice commands are informative and too numerous to be traversed simulated. But it is always desired that the proposed method should be able to evaluate the interface design under more generalized situations based on a small-size experimental sample set.

This paper proposed predicted auditory RT as an index to evaluate the console interface of remotely piloted aircraft (RPA). Besides, the methods can be further applied in other domains, such as interface evaluation of airplanes and complex command and control systems. The work focused on the following three problems:

(1) The experiment method to measure and evaluate the auditory commands in the task state, which should keep the subject in a normal operating state and not influence the subject to execute the regular task

(2) The calculation method to predict the auditory RT of more generalized voice commands with a small-size sample set

(3) The analysis method to evaluate and analyze the interface design is based on auditory RT

We try to solve the above problems, and this paper was organized as follows: In Section 2, the architecture of the proposed approach was explained. Section 3 represents the method of auditory RT measurement, in which the experiment was organized in the pilot's flight task state. Section 4 was about the prediction method of voice command RT, in which the RT was estimated for more general voice commands based on the key words. Finally, the RT was used to evaluate two flight console interfaces in Section 5, which provided the idea of how to analyze the usability of the interface with RT. In Section 6, conclusions and future work are presented.

2. Architecture of Proposed Method

In the human reaction process, a stimulation induces a process in which the stimulus activates the sensory apparatus, which travels through the afferent nerve to the nerve center of the brain, through complex processing, and from the efferent nerve to the muscle, which contracts to perform the operation. Although this process is latent in the body, each step takes time. The sum time is called reaction time. RT consists of perception time (i.e., the time from the presence of the stimulus to the beginning of the action) and action time (i.e., the execution duration of action):

$$\mathrm{RT} = t_z + t_d, \tag{1}$$

where RT is the total reaction time, t_z is the perception time, and t_d is the action time. In terms of information acquisition and processing, perception time refers to the time of auditory information acquisition, while action time refers to the time of active visual information acquisition.

In a flight task, after the pilot receives a voice command, he/she does not produce the manual operation directly but obtains the related visual information first to gather useful information, then judges the situation based on the information and experience, and finally performs the action. Based on this phenomenon, eye movement tracking is adopted as a measuring means of RT in flight tasks. From the information perception aspect, the time interval between the ending time of voice command and human firstly obtaining the useful visual information indicates the time spent on processing auditory information, while the time interval between gaining first target information and all the useful visual information that have been acquired represents the reaction procedure of the information processing results. As this work uses RT to evaluate the information display interface, the manual operation time is not taken into account.

It is assumed that t_1 and t_2 represent the starting and ending times of a voice command. t_3 is the point-in-time on which the pilot firstly forms the fixation on the Area of Interests (AOIs) of the user interface. Because converting the voice command to useful visual information and achieving this information takes time, t_3 may not always equal to the point-in-time of the first target AOI t_4 for different interfaces. t_5 indicates the time that all target AOIs have been acquired by the pilot. The relationship of these time points in the sequence can be expressed as

$$\begin{aligned} t_z &= t_4 - t_2, \\ t_d &= t_5 - t_4. \end{aligned} \tag{2}$$

A pilot's RT represents the difficulty of obtaining multiple information under a certain command; thus, it can be used as an index to evaluate the rationality of the layout of multiple information in the interface.

The proposed approach mainly consists of three parts. The first part is to obtain the template data of RT for typical auditory commands based on eye movement tracking. The pilot was asked to do the normal flight task in this part, while

the typical voice commands were given randomly and eye movement data were recorded at the same time. Since the experiment was done without disturbing the pilot and flight task, all data were gathered in the task state. The second part developed the method of RT prediction based on small samples of experiments, which includes two steps. The first step is key word extraction, which extracts key words from original audio files. This step is constructed based on the fact that experienced pilots usually respond to the voice command according to the acquired key words so that he/she can give the response promptly. The combination of different key words will determine the pilot's RT to the command. The second step is to predict RT, where we trained a neural network that used the template data, which includes RT for typical commands and template key words, to predict RT of more general auditory commands. The significance of this prediction model is that it can estimate the RT for different commands without traversing all sample commands, since not all the flight scenes can be simulated in the simulator, and in some flight missions, the commands should be made according to the real task situation which is hard to be simulated. Moreover, the human-machine interface can be evaluated in more general cases. The workflow of our work is illustrated in Figure 1. The third part is to analyze the flight console interface based on the predicted RT of different voice commands.

This approach provides a new idea to predict the RT of voice command under the task state for the aviation application. Furthermore, the RT can be adopted as one of the indexes to evaluate the efficiency of a flight console interface, which offers perceptive information to users under various and complex tasks.

3. Auditory Reaction Time Obtaining Based on Eye Movement Tracking

In common cases, the interface of upgraded equipment is designed or modified based on the original interface of the previous generation. Assume that interface A is a new interface whose usability needs evaluation. However, since its usability has not been evaluated, we cannot measure it in a real scenario for the sake of safety. At the same time, it takes a lot of manpower and time to conduct experiments on all auditory commands, so we construct a prediction model to predict RT of more voice commands through experiments of a small number of commands which can be simulated. Suppose interface B is an old version interface, which has more pilot's RT data under voice commands. Through the comparison of the pilot's RT under each command, different interfaces can be compared and evaluated. For example, for combat missions, the interface that the pilot has smaller RT with combat commands is better; for search and rescue missions, the interface that the pilot has smaller RT with searching commands is better.

3.1. Experimental Scheme and Platform. The experiments are based on a search and rescue mission. All the experiments were done on the simulator of the RPA operation platform (as shown in Figure 2). The platform is composed of six modules, which are the integrated situation module, flight control module, CCD operation module, radar illumination module, voice command module, and eye movement tracking module. Different flight tasks can be simulated on the platform, such as "take-off," "climb," "cruise," "search target," and "flight return." In the experiment, while the RPA pilot executed certain flight tasks, the voice command module broadcasts voice commands according to the current flight situation, which was chosen from the command library including commonly used commands from the ground command center.

The eye movement tracking module recorded the RPA pilot's eye movement data at the same timeline with the voice command and flight parameters with Tobii Pro X3-120. Before the experiment, we used calibration software to calibrate the eye tracker. During the calibration process, we made sure that all the information on the screen was accessible to the pilot. For the collected eye movement data, the fixation time greater than 100 ms was selected as fixation points. In addition, multiple AOIs (Figure 3) can be obtained by dividing functional areas on the display, and eye movement points in corresponding AOI indicate that corresponding AOI information is obtained.

It is discovered that after receiving the auditory command or warning signals, instead of outputting the manual actions immediately, the pilot obtains related visual information firstly to gather useful information to know the current situation or to prepare for the next operation. Then, he finally performs the operation requested by voice command. Based on this discovery, it is reasonable to introduce eye movement tracking to evaluate the pilot's performance of response to the auditory command. Moreover, during the same flight task, to complete the proper operation, for the same command, AOIs (Area of Interests) that expert pilots pay attention to are the same, and these obtained AOIs are quite consistent for the expert pilots. However, different pilots may focus on the same group of AOIs when responding to one command; each pilot may not focus AOIs in the same order. For example, after the pilot got the voice command "encounter storm, altitude 6000," he/she can first obtain the "altitude" information or the "track" information.

Therefore, in this work, the auditory RT is defined as the time interval between the end of the voice command and the acquirement of all target AOIs. The target AOIs are obtained through experts' knowledge. For example, after the pilot got the voice command "encounter storm, altitude 6000," he needs to obtain the "altitude" information and the "track" information. But there is no requirement on the order of information acquisition. In this case, the experiment does not disturb the pilot's operation in flight mission, and the data are recorded in the flight task state.

The subject is an expert pilot, has good flying experience (three years of operating experience), does not wear glasses, and can master the simulation platform proficiently.

After each trial of the experiment, the pilot can have a short break to ensure that the RT is not affected by the fatigue state.

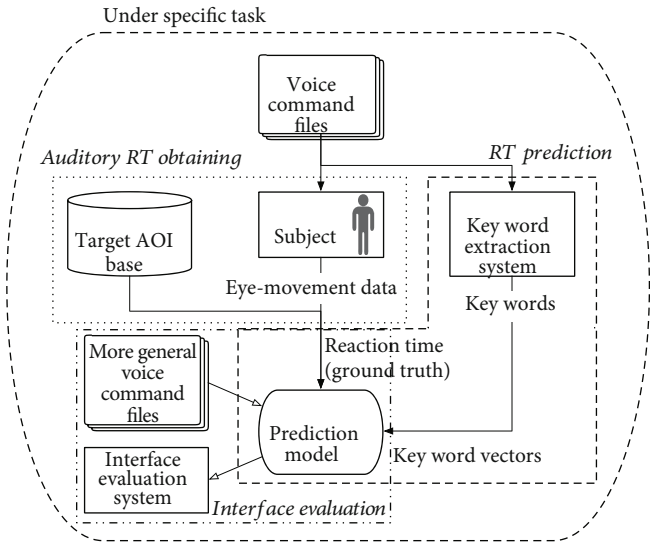

Figure 1: Architecture of the proposed method.

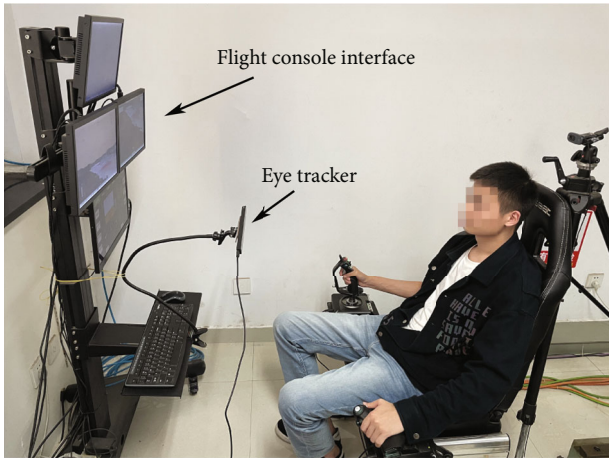

Figure 2: Flight mission simulation and reaction time measurement platform.

3.2. Auditory Reaction Time Obtaining. Through the measurement of action time, the ability of the human-machine interface to display mixed information to pilots is obtained. Performing a command often needs to access several pieces of information on current flight parameters, and this would require the pilot to acquire multiple information either within a single display or from multiple displays. According to SEEV theory [26], the expectation is an important factor affecting visual attention, so the pilot's visual attention should be properly considered and visual information should be input to the pilot in an appropriate way. A good human-machine interface should be reasonably planned; thus, the pilot can quickly get the information with little effort.

We take the flight task "cruise" as an example to illustrate how to gain the RT by eye movement data. The data obtaining process was as follows.

The pilot did a normal flight task in the simulated flight platform; then, he operated the aircraft to the required altitude and started the cruise task. During the cruise phase, the voice commands were sent to the pilot according to the real situation and flight scenes at irregular intervals. The platform can record the time t_{1i} when voice comment i was sent and the ending time t_{2i} of the command i. The pilot's eye movements were recorded with the same time label. The eye movement points were assigned into AOIs as shown in Figure 4, in which the red blocks were the predefined AOIs according to the functional area of the flight console interface, and the green lines indicated the eye movement trajectories from one AOI to the other. In this case, each fixation point was labeled with the functional information. After the end of voice command i, the time of the first AOI acquired by the pilot was recorded as t_{3i}, but this firstly obtained information may not be the required information prepared for the operation of commands. Thus, the time of the first target AOI acquired by the pilot was recorded as t_{4i}. When all the target AOIs had been gained by the pilot, the time was recorded as t_{5i}. The total RT of command i can be calculated by $\mathrm{RT}_i = t_{5i} - t_{4i}$.

4. Reaction Time Prediction

4.1. Extraction of Key Words in Voice Command. In the flight mission, when the voice command is given by the command center or ground station, the expert pilot usually responds to the obtained key words involved in command based on his experience. In this case, he can execute the command as soon as possible to handle the complex situation. For example, when there was command "no. 02 CCD on the target for 10 seconds," where "02" is the code number of his airplane, the pilot would pay his attention to the information of CCD view in the user interface according to the key word "CCD."

In the flight mission, because the voice commands given by the command center has very strict restrictions and is commonly broadcast with certain frequency and tones, the features of the same key words in different commands are

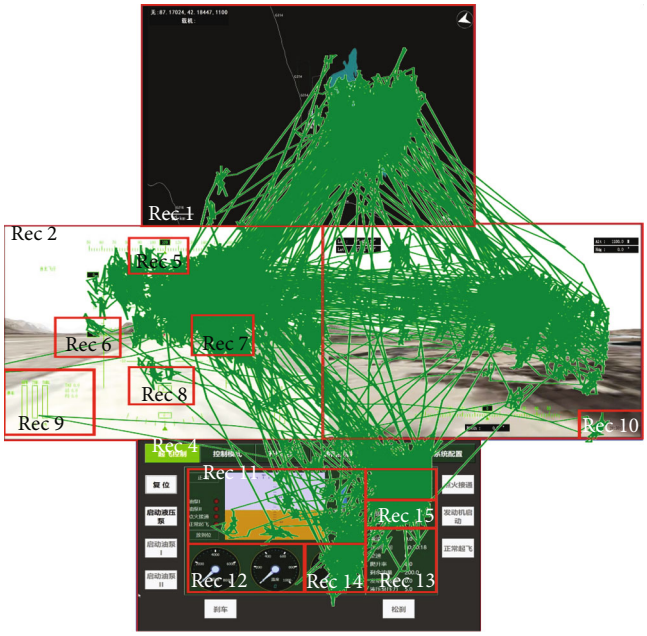

Figure 3: Eye movement trajectory responded to the voice command in flight task.

quite similar. Moreover, it is possible to collect the key words appearing in the voice command file based on the experiences of the expert pilot. Thus, the template base can be constructed to gather the extracted features of key words. Since the amount of information contained in different key words is different, which determines the difficulty level of information processing for the pilot, a thesaurus is established according to the word information content, which is also provided by the expert pilots. Then, the detected key words are classified according to the kind of thesaurus. In this case, the template base is stored according to the information category.

For any voice command during the flight task, the sliding window method and dynamic time warping (DTW) matching algorithm are adopted to automatically detect the input key words. The recognition method of voice command designed in this paper is illustrated in Figure 5. Besides the preprocessing of input voice command, the process mainly includes feature extraction of key words and template matching, which will be explained in the following parts.

4.1.1. Feature Extraction of Key Words in Voice Command. Before establishing the template base and recognizing the input speech, it is necessary to preprocess the speech signal to facilitate further processing, which commonly includes the processing procedure, such as sampling and quantization, preemphasis, framing, and windowing. The two most commonly used characteristic parameters are MFCC (Mel Frequency Cepstral Coefficient) and LPCC (cepstral linear predictive coding). Among them, MFCC is a feature parameter widely used in speech recognition. The extraction process of MFCC feature parameters [27] for key words in voice command adopted in this paper is described as the following steps:

(1) The preprocessing adopted in this work contains the procedure of preemphasis, framing, and windowing. The preemphasis filter is applied to a signal x using the first-order filter in the following equation with the filter coefficient α:

$$x_1(t) = x_0(t) - \alpha x_0(t-1). \tag{3}$$

After preemphasis, the signal is split into short time frames $x_2(n)$. Then, the Hamming window is applied to each frame aimed at increasing the continuity of the left and right ends of the frame. The chosen form is

$$w(n) = 0.54 - 0.46\cos\left(\frac{2\pi n}{N-1}\right), \tag{4}$$

$$x(n) = x_2(n)w(n), \tag{5}$$

where N is the window length, $0 \le n \le N$.

(2) The power spectrum of the voice command signal is calculated by Fourier transform:

$$P = \frac{|FFT(x_i)|^2}{N}, \tag{6}$$

where x_i is the i^{th} frame of x.

(3) Then, we can convert between Hertz (f) and Mel ($M(f)$) using the following equations:

$$M(f) = 2595\log_{10}\left(1 + \frac{f}{700}\right), \tag{7}$$

in which 2959 and 700 are empirical constants. The Mel scale is aimed at mimicking the nonlinear human ear perception of sound, by being more discriminative at lower frequencies and less discriminative at higher frequencies.

The energy spectrum is passed through a set of Mel scale triangular filter banks, and a filter bank with M filters is defined as

$$H_m(k) = \begin{cases} 0, & k < f(m-1), \\ \dfrac{2(k - f(m-1))}{(f(m+1) - f(m-1))(f(m) - f(m-1))}, & f(m-1) \le k \le f(m), \\ \dfrac{2(f(m+1) - k)}{(f(m+1) - f(m-1))(f(m) - f(m-1))}, & f(m) \le k \le f(m+1), \\ 0, & k \ge f(m+1), \end{cases} \tag{8}$$

where $\sum_{m=0}^{M-1} H_m(k) = 1$.

(4) At last, we have to obtain the Mel Frequency Cepstral Coefficients (MFCCs). The logarithmic energy output of each filter bank is calculated by the following equations:

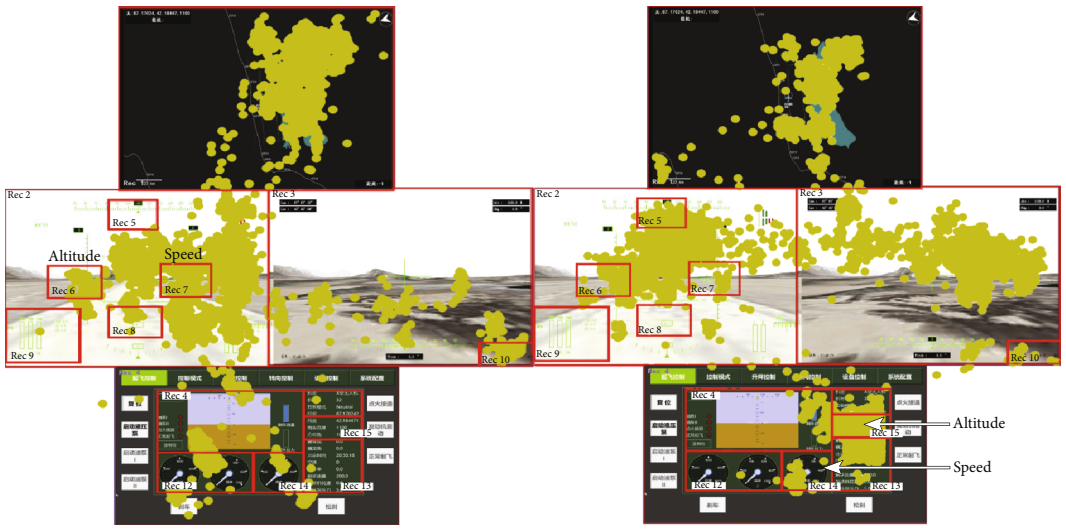

Figure 4: Flight console interface with eye movement: (a) interface A (new version); (b) interface B (old version).

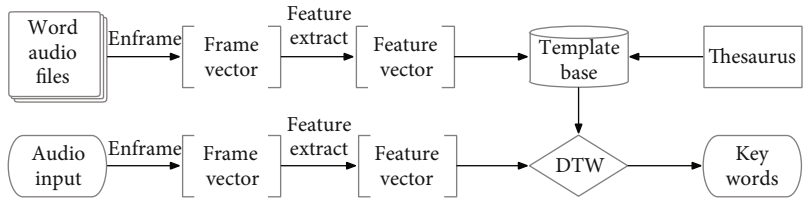

Figure 5: Proposed recognition method of key words in voice command.

$$s(m) = \ln\left(\sum_{k=0}^{N-1} |X(k)|^2 H_m(k)\right), \quad 0 \le m \le M. \tag{9}$$

Discrete Cosine Transform (DCT) is applied to decorrelate the filter bank coefficients and yields a compressed representation of the filter banks:

$$C(n) = \sum_{m=0}^{N-1} s(m) \cos\left(\frac{\pi n(m-0.5)}{M}\right), \quad n = 1, 2, \cdots, L, \tag{10}$$

where L refers to the order of the MFCC coefficient.

4.1.2. Key Word Template Matching. When using the template matching method for speech recognition, a single word is generally regarded as a recognition unit. In the training phase, the user said every word in turn, and each word's feature vector is extracted as a template in the template base. In the recognition phase, the similarity between the input speech feature vector series and each template in the template base is measured. The template owing the highest similarity is picked as recognition results.

However, it is impossible to simply compare the input parameter sequence with the corresponding reference template directly, because the speech signal has considerable randomness; even if the same person speaks the same word at different times and makes the same sound, it cannot have the same length of time. In template matching, these changes of time length will affect the measurement estimation and reduce the recognition rate. Therefore, the procedure of time scaling for the voice command signal is essential.

DTW is a nonlinear regularization technique which combines time regularization with distance measure calculation. For example, the test audio parameters are I-frame vector, and the reference template is a J-frame vector, $I \neq J$; then, dynamic time warping is to find a time warping function $j = \omega(i)$, which maps the time axis i of the test vector nonlinearly to the time axis j of the template and makes the function ω meet:

$$D = \min_{\omega(t)} \sum_{i=1}^{I} d[T(i), \quad R(\omega(i))], \tag{11}$$

where $d[T(i), R(\omega(i))]$ is the distance measurement between the i^{th} test vector $T(i)$ and the j^{th} vector $R(j)$. D is in the optimal time warping case. The cost function is

$$D[c(k)] = d[c(k)] + \min D[c(k-1)], \tag{12}$$

where $d[c(k)]$ is the cost of $c(k)$. Thus, the total cost function is the sum of the cost of the point itself and the cost of the best path to that point.

Table 1: Topic words.

Topic no.	1	2	3	4	5	6	7
Key word	CCD	Hover	Search target	Fast feed	Back	Direction	Climb (up) down
Topic no.	8	9	10	11	12	13	14
Key word	Attitude	Navigate	Right left	Team	Unknown	Quit	Time second

Table 2: Topic word vectors of 14 typical commands.

No.	Command	Topic word vector
1	No. 02 hover at navigation point	[0, 1, 0, 0, 0, 0, 0, 0, 1, 0, 0, 0, 0, 0]
2	Fast turn up	[0, 0, 0, 1, 0, 0, 1, 0, 0, 0, 0, 0, 0, 0]
3	All planes quit the mission and fly to the nearest airfield	[0, 0, 0, 0, 0, 0, 0, 0, 0, 0, 0, 0, 1, 0]
4	Fast turn down	[0, 0, 0, 1, 0, 0, 1, 0, 0, 0, 0, 0, 0, 0]
5	No. 01 11 o'clock direction target appears	[0, 0, 1, 0, 0, 1, 0, 0, 0, 0, 0, 0, 0, 0]
6	Fast turn left	[0, 0, 0, 1, 0, 0, 0, 0, 0, 1, 0, 0, 0, 0]
7	Fast turn right	[0, 0, 0, 1, 0, 0, 0, 0, 0, 1, 0, 0, 0, 0]
8	11 o'clock direction search targets	[0, 0, 1, 0, 0, 1, 0, 0, 0, 0, 0, 0, 0, 0]
9	Climb up to 1100	[0, 0, 0, 0, 0, 0, 1, 0, 0, 0, 0, 0, 0, 0]
10	Go back ten miles and return	[0, 0, 0, 0, 1, 0, 0, 0, 0, 0, 0, 0, 0, 0]
11	No. 02 CCD on the target for 10 seconds	[1, 0, 1, 0, 0, 0, 0, 0, 0, 0, 0, 0, 0, 1]
12	To landing altitude	[0, 0, 0, 0, 0, 0, 0, 1, 0, 0, 0, 0, 0, 0]
13	Contact target within 10 seconds	[0, 0, 1, 0, 0, 0, 0, 0, 0, 0, 0, 0, 0, 1]
14	Climb up to 1300, attention on fuel pressure	[0, 0, 0, 0, 0, 0, 1, 0, 0, 0, 0, 0, 0, 0]

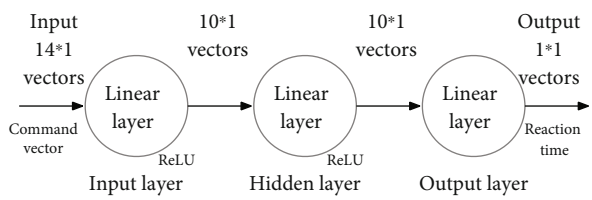

Figure 6: Structure of reaction time prediction model based on BP neural network.

Because DTW continuously calculates the distance between the two vectors to find the optimal matching path, two-vector matching is the normalized function with the minimum cumulative distance, which ensures the maximum acoustic similarity between them.

4.2. Key Word(s) Vectorization. When a pilot performs a task, his responding time to the voice command is actually determined by the combination of multiple key words in the command. He will pay attention to different combinations of key words to complete the flight target task.

According to the command template, the identified flight commands are converted into the input sample of the prediction model. The specific method is described as follows.

As it is difficult to determine the RT directly from the text information, it is necessary to preprocess the obtained text information. Inspired by the model of natural language processing, we extract key words from the possible appearing voice commands according to the experience of expert pilots. These words are divided into different topics based on the content similarity, and each topic is defined as one of the dimensions in the feature vector. Thus, the feature vectors corresponding to the commands are obtained. Then, topic words are selected according to the probability; that is, if a sentence appeared, several words that represent the sentence are selected as the topic words. For example, when the word "climb to 1000" is detected, there is a high probability that the sentence belongs to the category of "climb to XX," while the word "to" is detected, there is not a high probability that the command relates to the category of "climb to XX." Therefore, for this sentence, the topic word "climb" is chosen to represent the topic of the command, and this word covers most of the information of this sentence. Key words with high correlation, that is, words with a high probability of appearing together, words that are similar, or words that can be replaced with each other, are classified as one topic. Topic words are determined according to experimental results. Since the structure of voice command in flight scenes is specified and the command words are very standard, the voice command can be vectorized through these topic words. Here are some topic words used in the experiment presented in Table 1. For the real scene, there will be more topic words.

For example, if the above topic words appear in the voice command, the vector of the corresponding dimension is assigned as 1. If it does not appear, it is assigned as 0. Each command is vectorized according to the selected topic words.

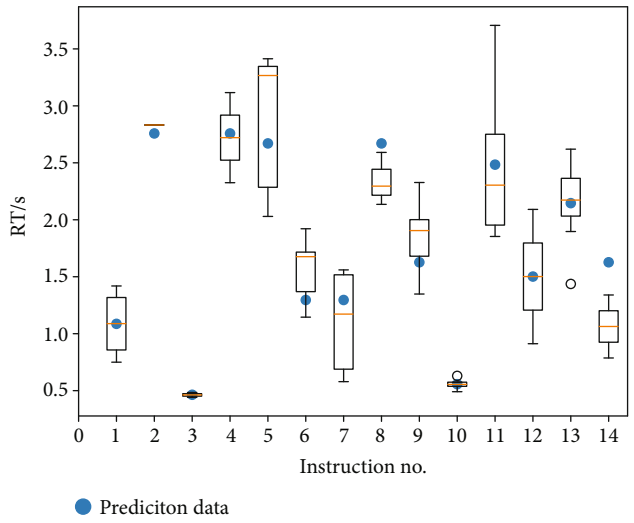

Figure 7: Reaction time prediction results for different voice instructions.

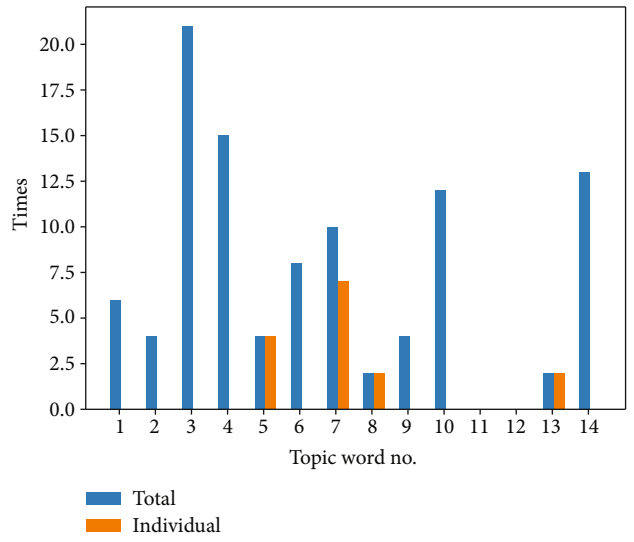

Figure 8: Training number of topic words appeared together or independently.

Some typical command vectors are presented in Table 2.

4.3. Reaction Time Prediction. So far, the problem of RT prediction can be regarded as a common prediction problem. That is, the command vector of each voice command is given to estimate the corresponding response time. Supervised learning algorithms can be used to solve this problem.

A BP neural network is constructed in this paper to achieve the prediction of RT. The neural network structure is shown in Figure 6. The input data is the vectorized voice command, and the output data is the RT. All the data obtained from the experiment are used to train the neural network.

4.4. RT Prediction Results and Analysis. In this paper, we gave an example of 14 voice commands used to train the

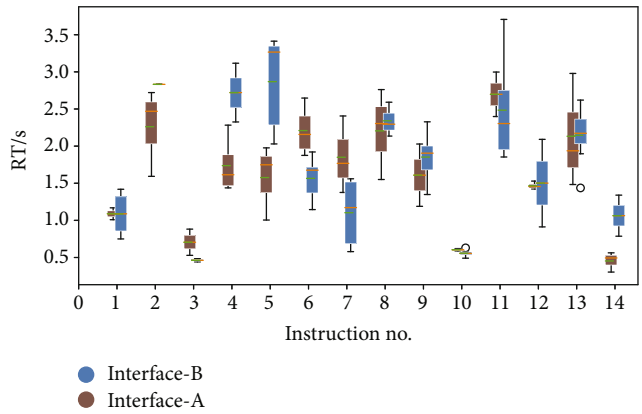

Figure 9: Results of pilot's reaction time experiments on interfaces A and B.

neural network to predict the RT. Prediction results are depicted in Figure 7. The boxes represent the measured RT data obtained from all the experiments. The yellow line represents the median value of all the experimental data, and the blue dots are the predictive value of the neural network for the commands.

Calculate accuracy δ_i for command i in cross-checking:

$$\delta_i = \frac{r_{pi} - \bar{r}_{ei}}{\bar{r}_{ei}}. \tag{13}$$

Total accuracy δ is computed as

$$\delta = \frac{\sum_{i=1}^{n}}{n}, \tag{14}$$

where r_{pi} represents the predicted RT for command i and $\bar{r}_e$ is the mean value of obtained RT for command i, while n represents the total number of commands.

In this example, the overall result has the prediction accuracy ($\delta = 0.904$), shown in Figure 7. For some commands, the prediction accuracy can hit up to 0.995. However, some only achieved 0.470. The reason can be explained by Figure 8. In the figure, the blue bars represent the number of times that those topic words are trained in the condition of the combination topic words that appeared in the voice command, while the orange bars represent the number of times that those topic words are trained individually. For example, in command "hover at navigation point," "hover" and "navigation" belong to a different topic category and were trained together. In command "climb up to 1100," "up" was trained independently, e.g., the command "contact target within 10 seconds" has a bad prediction performance (0.470), because the topic words in this command have not been individually trained. The command "climb up to 1100" performs well (0.995), because the topic word "up" is trained individually, which can achieve good prediction accuracy for the combination of words as well. In this example, topic words no. 11 and no. 12 do not appear in all 14 instructions, as shown in Table 2. However, in order to

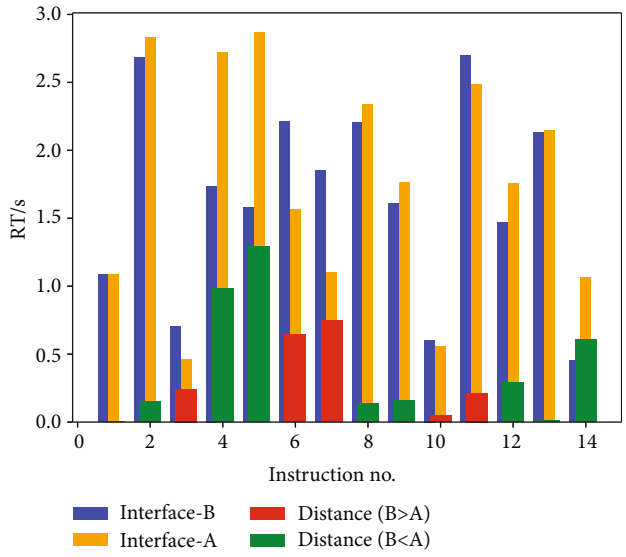

Figure 10: Reaction time comparison.

illustrate that our method can predict the reaction time of larger samples of instructions based on training more topic words, we keep these two topic words in Figure 8.

5. Interface Evaluation Based on Reaction Time Prediction

In this section, two flight console interfaces are evaluated based on the predicted voice command RT. Interface B is the original version of the RPA operation interface, while interface A is the updated version. The differences between the two versions are listed below:

(1) Interface A (Figure 4(a)) displayed speed and altitude information of RPA using the overlapping display on the front-view scene interface. For example, "speed" is shown in Rec 6 and "altitude" is shown in Rec 7. Rec indicates the previously defined AOI and is presented as a red rectangle in the figure. Yellow dots are recorded pilots' eye fixations during the flight task

(2) Interface B (Figure 4(b)) displayed speed and altitude information separately. For example, "speed" and "altitude" are depicted in Rec 14 and Rec 15, respectively, and they were shown independently on the flight parameter monitoring interface

Except for the "altitude" and "speed" information, other information on these two interfaces remains the same.

The operation platform is placed in a quiet and well-lit experimental environment; the expert pilot has good flying experience (three years of operating experience), does not wear glasses, and can master the simulation platform proficiently. Large head rotation during the execution of flying tasks is avoided to ensure the accuracy of eye tracker data.

With interface A, the pilot's RT experiments were conducted on 14 groups of voice commands, 8 times for each command. The total number of valid training RT data is 86. With interface B, the pilot's RT experiments were executed on the same 14 groups of commands, but 4 times for each command. After removing the measured RTs that are larger than 5 s as well as RT with a very large fluctuation range, which is generally caused by the accuracy of the eye tracker, the RT data from the experiment was obtained. Figure 9 presents all measured RT of each voice command for the two interfaces, respectively, in which the box depicts the measured RT data distribution, the orange line represents the median value for all the trials, and the dotted green line represents the mean value.

Table 3: AOIs for instructions.

Instruction	Interface A	Interface B	Comparison
4	f a s (t)	**f a s (t)**	Same
5	f t l	**f l**	A has t
6	**f t (a)**	f l t (a)	B has l
7	**f t**	f l t	B has l
14	f a (s)	**f a**	A has (s)

For both of the two cases, voice commands with nos. 1-8, 10, 11, 13, and 14 are training datasets, while nos. 9 and 12 are test sets (Table 2). RTs of voice command nos. 9 and 12 were predicted with the proposed model. The predicted error rate is 5.5% and 15.9% for instructions no. 9 and no.12, respectively, which refers to the mean value of RT of all trials. From the RT predicted results present in Figure 10, we can discover that for most instructions, the RTs of two interfaces are quite close. Distinctively, for instructions 4, 5, and 14, interface B performed better than interface A. For instructions 6 and 7, interface A performs better than interface B.

In Table 3, bold indicates that interface A or B performed better in this voice instruction. "f" represents that pilots obtained the visual information "front view," "a" represents "altitude," "s" is "speed," "t" is "track," "l" represents "CCD information," and "()" is this AOI appearing several times. It reveals that with interface B, pilots spend much time on "CCD information" (for example, instructions no. 6 and no. 7). The reason is that when the pilot needed CCD information to respond to the voice command, in interface A, the pilot uses his peripheral to roughly obtain the CCD information because the speed and altitude information is very close to the CCD view (CCD view is presented on the left interface in Figure 4). This can also be discovered by the fact that there are more fixation points formed on the CCD view of interface B compared with interface A. However, in interface B, these pieces of information are separated, which indicates that the pilot has to look at the CCD information intentionally to obtain it.

For voice command no. 4, the AOIs required by the pilot are the same in the two interfaces, while interface B shows better performance. In our case, this indicates that the speed and altitude information in interface B (displayed as overlay mode) can be much easier obtained by the pilot than interface A (displayed as digital numbers).

As the CCD information can be easier obtained by pilots with interface A, information display as interface A can be used in search and rescue missions. Because the altitude and speed information are relatively easier to be acquired with interface B, information presented like interface B can be used in high maneuverability missions.

6. Conclusions and Future Work

This paper proposed predicted auditory RT as an index to evaluate the flight console interface. The proposed architecture of the approach consisted of three parts RT measurement under samples of voice commands, prediction method to estimate RT under more general commands, and interface evaluation with RT prediction, which obtained the following achievement.

Firstly, the pilot's auditory RT is effectively calculated by eye movement tracking, which makes the experiment carried out in a flight task state, and the measurement would not influence the pilot to execute the normal task.

Secondly, the RT prediction model is built based on the extracted key words that appeared in commands. Then, a neural network is constructed, which made the RT under more generalized commands be estimated with small sample experiments. This can help to overcome the dilemma that some flight scenes are hard to be simulated and various voice commands are impossible to be traversed simulated.

Finally, the voice command RT is adopted as one aspect to evaluate the utilization of the new generation interface, which considers not only the time accumulation effect of the human state during the interaction but also instantaneous reactions to the input information of the interface.

This paper only presented the application in the evaluation of the flight console interface; in fact, the proposed approach can also be applied in other systems, such as the human-robot interface and operation interface of the command center. For further applications, there are still several works that need to be done in the future:

(1) The voice command library used in this paper is not large enough, a bigger dataset can be used to improve the prediction results, and more evaluation indexes could be used to evaluate the human-machine interface

(2) The features of instructions are not only included key words but semantic structure. The relationship between each key word can be considered, which may help to increase the RT prediction accuracy in a more general scenario

(3) The experiments were done under specific tasks, but our work actually can resolve the prediction problem under several different tasks. Thus, context information can be input into the prediction model to achieve the prediction under different tasks

(4) The target AOI base is based on experts' knowledge. However, while new technology emerges, new instructions will emerge, which means no target AOI knowledge to those instructions. Thus, an experimental method can be proposed to extract experts' knowledge

Data Availability

The data that support the findings of this study are available on request from the corresponding authors. The data are not publicly available due to privacy restrictions.

Conflicts of Interest

The authors declare that they have no conflicts of interest.

Acknowledgments

The study is supported by the Key Research and Development Program of Shaanxi and "111 project" (Grant no. B13044).

References

[1] G. Chao, "Human-computer interaction: process and principles of human-computer interface design," in *2009 International Conference on Computer and Automation Engineering*, pp. 230–233, Bangkok, Thailand, 2009.

[2] S. Sreetharan and M. Schutz, "Improving human–computer interface design through application of basic research on audiovisual integration and amplitude envelope," *Multimodal Technologies and Interaction*, vol. 3, no. 1, p. 4, 2019.

[3] D. A. Varakin, D. T. Levin, and R. Fidler, "Unseen and unaware: Implications of recent research on failures of visual awareness for human-computer interface design," *Human Computer Interaction*, vol. 19, no. 4, pp. 389–422, 2004.

[4] X. Wu, C. Xue, Y. Niu, and W. Tang, "Study on eye movements of infor-mation omission/misjudgment in radar situation-interface," in *International Conference on Engineering Psychology and Cognitive Ergonomics*, Lecture Notes in Computer Science (including subseries Lecture Notes in Articial Intelligence and Lecture Notes in Bioinformatics),, pp. 407–418, Springer, 2014.

[5] U. Ahlstrom and L. Arend, "Color usability on air traffic control displays," *Proceedings of the Human Factors and Ergonomics Society Annual Meeting*, vol. 49, no. 1, pp. 93–97, 2005.

[6] Z. W. Liu and H. F. Teng, "Human computer cooperative layout design method and its application," *Computers & Industrial Engineering*, vol. 55, no. 4, pp. 735–757, 2008.

[7] R. Jeffries, J. R. Miller, C. Wharton, and K. Uyeda, "User interface evaluation in the real world: a comparison of four techniques," in *Proceedings of the SIGCHI conference on Human factors in computing systems Reaching through technology - CHI '91*, pp. 119–124, New Orleans, Louisiana, USA, 1991.

[8] A. Brychtová, S. Popelka, and V. Vozenilek, "The analysis of eye movement as a tool for evaluation of maps and graphical outputs from GIS," in *Proceedings of the 19th International Conference on Geography and Geoinformatics: Challenge for Practise and Education*, pp. 154–162, Brno, Czech Republic, 2012.

[9] J. H. Goldberg and X. P. Kotval, "Computer interface evaluation using eye movements: methods and constructs,"

International Journal of Industrial Ergonomics, vol. 24, no. 6, pp. 631–645, 1999.

[10] J. S. Ha and P. H. Seong, "A human-machine interface evaluation method: a difficulty evaluation method in information searching (DEMIS)," *Reliability Engineering and System Safety*, vol. 94, no. 10, pp. 1557–1567, 2009.

[11] J. Akyeampong, S. Udoka, G. Caruso, and M. Bordegoni, "Evaluation of hydraulic excavator human-machine interface concepts using NASA TLX," *International Journal of Industrial Ergonomics*, vol. 44, no. 3, pp. 374–382, 2014.

[12] S. Yan, C. C. Tran, Y. Chen, K. Tan, and J. L. Habiyaremye, "Effect of user interface layout on the operators' mental workload in emergency operating procedures in nuclear power plants," *Nuclear Engineering and Design*, vol. 322, pp. 266–276, 2017.

[13] Y. Chen, S. Yan, and C. C. Tran, "Comprehensive evaluation method for user interface design in nuclear power plant based on mental workload," *Nuclear Engineering and Technology*, vol. 51, no. 2, pp. 453–462, 2019.

[14] L. Giraudet, J. P. Imbert, M. Bérenger, S. Tremblay, and M. Causse, "The neuroergonomic evaluation of human machine interface design in air traffic control using behavioral and EEG/ERP measures," *Behavioural Brain Research*, vol. 294, pp. 246–253, 2016.

[15] V. Ažaltovič, I. Škvareková, P. Pecho, and B. Kandera, "The correctness and reaction time of piloting the unmanned aerial vehicle," *Transportation Research Procedia*, vol. 51, pp. 342–348, 2020.

[16] S. Naeeri and Z. Kang, "Exploring the relationship between pilot's performance and fatigue when interacting with cockpit interfaces," in *IIE Annual Conference Proceedings*, pp. 1498–1503, 2018, https://www.proquest.com/scholarly-journals/exploring-relationshipbetween-pilots-performance/docview/2553578463/se-2?accountid=28284.

[17] J. Gerhardt-Powals, "Cognitive engineering principles for enhancing human-computer performance," *International Journal of Human Computer Interaction*, vol. 8, no. 2, pp. 189–211, 1996.

[18] A. K. Rakhra, M. K. Green, and D. D. Mann, "The influence of a user-centred design focus on the effectiveness of a user interface for an agricultural machine," *Agricultural Sciences*, vol. 11, no. 11, pp. 947–965, 2020.

[19] B. Li, W. Liu, X. Zhang, Z. Pan, and F. Zhao, "Effectiveness assessment of human-machine interface in driver assistance system," *Engineering*, vol. 197, pp. 567–574, 2013.

[20] R. J. Kosinski, "A literature review on reaction time," *Clemson University*, vol. 10, no. 1, pp. 337–344.

[21] K. W. Chan and A. H. Chan, "Spatial S-R compatibility of visual and auditory signals: implications for human-machine interface design," *Displays*, vol. 26, no. 3, pp. 109–119, 2005.

[22] W. C. Li, J. Zhang, T. Le Minh, J. Cao, and L. Wang, "Visual scan patterns reect to human-computer interactions on processing different types of messages in the ight deck," *International Journal of Industrial Ergonomics*, vol. 72, pp. 54–60, 2019.

[23] R. Jacob, "Eye movement-based human-computer interaction techniques: toward non-command interfaces," *Advances in human-computer interac-tion*, vol. 4, pp. 151–190, 1993.

[24] M. A. Cohen, D. C. Dennett, and N. Kanwisher, "What is the bandwidth of perceptual experience?," *Trends in Cognitive Sciences*, vol. 20, no. 5, pp. 324–335, 2016.

[25] Q. Meteier, M. Capallera, E. De Salis et al., "The effect of instructions and context-related information about limitations of conditionally automated vehicles on situation awareness," in *12th International Conference on Automotive User Interfaces and Interactive Vehicular Applications, ser. Automotive UI 2020* of *Association for Computing Machinery*, pp. 241–251, New York, NY, USA, 2020.

[26] C. Wickens, J. McCarley, K. Steelman-Allen, A. Sebok, J. Bzostek, and N. Sarter, "A model of attention capture and noticing on the flight deck," *In Proceedings of the Human Factors and Ergonomics Society*, vol. 53, no. 12, pp. 769–773, 2009.

[27] H. M. Fayek, "Speech processing for machine learning: filter banks, Mel-Frequency Cepstral Coe_cients (MFCCs) and what's in-between," 2016, https://haythamfayek.com/2016/04/21/speech-processing-for-machine-learning.html26.

Hindawi
Computational and Mathematical Methods in Medicine
Volume 2022, Article ID 6497754, 10 pages
https://doi.org/10.1155/2022/6497754

Research Article

Mechanical Analysis of Posterior Pedicle Screw System Placement and Internal Fixation in the Treatment of Lumbar Fractures

Shengkai Mu, Jingxu Wang, and Shuyi Gong

Shenyang Orthopedic Hospital, Shenyang, Liaoning 110044, China

Correspondence should be addressed to Shengkai Mu; msk2022@126.com

Received 19 January 2022; Revised 3 March 2022; Accepted 22 March 2022; Published 11 April 2022

Academic Editor: Kelvin Wong

Objective. Image segmentation technology is applied to separate a single vertebra from the three-dimensional model of the spine, so as to separate a single vertebra image with smaller error, higher degree of automation, and better results. The objectives are to study the biomechanical characteristics of posterior short-segment pedicle screw fixation by three-dimensional finite element method, analyze the mechanical characteristics of posterior pedicle screw rod fixation system under different factors, and demonstrate the feasibility of its application in the treatment of lumbar fracture. *Methods*. The authors searched the database for articles about the treatment of lumbar spine fracture, screw rod internal fixation system, and its mechanical parameters. The threshold segmentation method based on region segmentation method was used to segment the image, and the three-dimensional finite element model was used to analyze the biomechanical characteristics of different posterior internal fixation for lumbar spine fracture. *Results*. The posterior pedicle internal fixation system for the treatment of multilevel spinal fractures is a mature surgical technique and has fewer postoperative complications. Transpedicle fixation is effective and reliable. It can effectively restore the coronal and sagittal curvature of the vertebral body and restore the stability of the spine better. But the choice of internal fixation method should be individualized based on fracture type, identification of critical and secondary injury sites, and stability assessment. Only after mastering the biomechanical characteristics of the posterior screw rod system for the treatment of lumbar fracture, selecting the appropriate method, and fixing the appropriate movement unit can the best fixation be achieved. *Conclusion*. Threshold method is the most direct and simple image segmentation method. The core technology of thresholding is the selection of threshold, which will affect the final segmentation effect. The most common segmentation method is to calculate the segmentation threshold by histogram. The threshold method has less computation and good segmentation effect for the image with large contrast between background and target. Posterior pedicle screw rod system internal fixation has the advantages of less trauma, good reduction, reliable fixation, and less complications. The design, placement angle and depth of various internal fixation systems, and the number of fixed segments all show different mechanical characteristics. As long as we master the above characteristics, choose the appropriate method and fix the appropriate motor unit, and we can get the best fixation; it can be used as an effective treatment for lumbar fracture.

1. Introduction

Spinal fractures are not uncommon, and various types of spinal fractures have become a common orthopedic injury. In various kinds of spinal fractures, lumbar fractures have become a common and high incidence of spinal fracture due to their special anatomical and mechanical characteristics [1]. The spinal lumbar segment consists of five vertebrae, two adjacent vertebrae and the disc, joint protrusion, and ligament structures that connect them are known as the spinal function unit, also known as the movement segment. FSU is the smallest unit that can reflect the biological characteristics of the spine, and it is also the most basic unit for maintaining the stability of the spine [2]. The stability of the lumbar spine is the equilibrium state when the endogenous stabilizing factors of the motion segment interact with the external load. Lumbar spine fractures are mostly caused by direct or indirect violence, and the patients are accompanied by local pain and swelling. Lumbar spine fracture surgery is divided into anterior and posterior approaches, as well as long- and short-segment fixation methods. Most factors that cause spinal stenosis come from the front. The anterior decompression is relatively

complete, but the posterior internal fixation is more clearly exposed, and the internal fixation is more reliable.

The finite element method was proposed in 1943 to analyze the torsion gastric body, and then, it was applied in the design of aircraft and developed into the matrix displacement method. With the development of computer technology and software technology, the finite element method has also been continuously developed, from solid mechanics to biomechanics, fluid mechanics, magnetic and temperature fields, and other fields. In the field of biomechanics, it can be used to establish a three-dimensional finite element simulation model of the human body and perform corresponding stress and modal analysis on it. It is widely used in the analysis of biomechanics in the field of orthopedics [3]. The finite element method can simulate the mechanical changes of the spine by establishing a spine model and is a reasonable and effective tool in the study of spine mechanics [4]. This article uses three-dimensional finite element method to establish a lumbar fracture internal fixation model, conducts finite element analysis on the biomechanical characteristics of the injured vertebral body, and explores the posterior single-segment fixation and conventional short-segment fixation of the lumbar spine fracture. The biomechanical characteristics provide a basis for the choice of internal fixation for thoracolumbar fractures in clinical practice.

2. Materials and Methods

2.1. Vertebra Separation Based on Image Segmentation Method. Image segmentation refers to distinguishing different regions with special meanings in an image. These regions do not cross each other, and each region meets the consistency of a specific region. The features available for image segmentation include the following: image grayscale, color, texture, local statistical features, or spectral features. The difference in these features can be used to distinguish different target objects in the image. Medical image segmentation is to distinguish different regions with special anatomical functions in medical images, and each region meets regional consistency. Based on the threshold segmentation method in the area segmentation method, the image can be effectively segmented when the gray value or other characteristic values of different types of objects are very different [5]. The method of threshold segmentation is divided into single threshold segmentation and multithreshold segmentation. As we all know, there are large grayscale differences between bones and muscles, skin, and other soft tissues in CT images. For this reason, this article uses only a single threshold to segment bone images from the original data, that is, the tissue whose gray value is greater than the set threshold is the bone [6–8].

Let (fi, j) be the gray value of the pixel (i, j), and the binarization process can be carried out according to formula (1). Among them, T is the threshold of binarization, and the gray level of the image is $0{\sim}N$.

$$f(i,j) = \begin{cases} N & f(i,j) \geq T, \\ 0 & f(i,j) < T. \end{cases} \tag{1}$$

Figure 1 shows the gray value histogram of any one of the CT slice images of the spine. It can be seen from the histogram that the peak value of the maximum gray value is concentrated between the gray levels of 1170 to 1230. In the experiment, set the gray threshold to 1200. The effect before and after threshold segmentation is shown in Figures 2(a) and 2(b).

The lesion area will produce many isolated small dots and holes, and cracks will appear between the contour lines, as shown in Figure 2(b). In order to solve these problems, the method of mathematical morphology is introduced for filtering. Mathematical morphology image processing includes four basic operations or operations: dilation, erosion, opening, and closing. The experiment mainly adopts the opening operation (opening), that is, the process of corrosion first and then expansion. This operation can eliminate outliers, small objects, separate objects with fine points, and smooth large boundaries without significantly changing the target area. Its definition is shown in formula (2).

$$A \circ B = (A \Theta B) \oplus B. \tag{2}$$

In general, continuous opening operations can significantly improve the phenomenon of unsmooth target boundaries, small holes in the target area, and isolated noise in the background area in the image after the binarization operation. Figure 3 is the result of the opening operation. Compared with Figure 2(b), the scattered points, burrs, and small bridges in the original Figure 2(b) have been cleanly removed.

Perform noise removal on the original noisy CT image, perform a single threshold combined with morphological segmentation on the CT image, and retain only the spine part of the figure; perform three-dimensional reconstruction of the segmented results to obtain a three-dimensional model of the entire spine; use spatial superneighbors. Use domain algorithm to separate individual vertebra from the three-dimensional model of the spine, shown in Figure 4.

In response to the needs of virtual spine correction surgery, the research proposed a general process for processing CT image slice preprocessing. At the same time, according to the spatial superneighborhood algorithm, each single vertebra was automatically separated, and the separated single vertebra was in phase with the original vertebra. The ratio error is smaller, the degree of automation is higher, and the result is ideal. It has certain guiding significance for virtual spine correction surgery. It can be used for three-dimensional reconstruction of tissues and organs, medical image analysis, and the formulation of improved spine surgery plans.

2.2. Establishment of a Three-Dimensional Finite Element Model of Normal Thoracolumbar Spine and Fractures. Young male volunteers were selected, and X-ray films were taken before data acquisition to rule out pathological conditions of the spine. Use GE's LightSpeed 16-slice spiral CT to scan the spine T10~L2 continuously along the cross section. The scanning conditions are as follows: the scanning voltage is 120 kV, the scanning current is 300 mA, the layer thickness

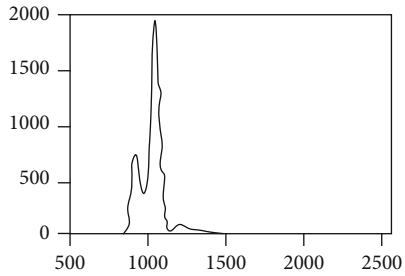

Figure 1: Example of histogram.

is 1.25 mm, and the layer interval is 0.625 mm. The scanned CT images are stored in the Dicom3.0 standard. The above-mentioned CT data in Dicom format was imported into Mimics 10.01 (Materialise, Belgium), and the three-dimensional model of the spine T10~L2 was established through operations such as threshold segmentation, dynamic area growth, and three-dimensional calculation, and the reverse engineering software Geomagic Studio was used for smooth processing. The finite element preprocessing software Hypermesh was used to supplement the establishment of intervertebral discs and corresponding ligaments. The area of the nucleus pulposus was about 43% of the total area of the intervertebral disc. The annulus fibrosus was simulated as a matrix containing fibers arranged obliquely 30°. Divide each part of the mesh and assign different material properties. Establish a normal model of T10~L2 segment. According to Denis spine fracture classification, a model of incomplete fracture of the upper part of the T12 vertebra was established [9–12]. The specific settings are as follows: remove the upper 1/2 cortical bone of the anterior middle part of the T12 vertebral body, and give the upper endplate and the upper 1/2 cancellous bone material properties of the anterior middle part after injury, shown in Figure 5.

2.3. Establishment of Three-Dimensional Finite Element Model of Single-Segment Fixation and Conventional Short-Segment Fixation through Injured Vertebra. Use the Pro/Engineer software to three-dimensionally reconstruct the internal fixation system used in spinal lumbar fracture surgery, and assemble it with the three-dimensional model of the spine from T10 to L2. Among them, due to the fracture of the upper part of the T12 vertebral body, the T11 and T12 vertebral bodies were fixed by a single-segment fixation model of the injured vertebra. The conventional short-segment internal fixation model fixes the T11 and L1 vertebral bodies across the segments. The screw placement and fixation methods refer to literature. The models of single-segment fixation and conventional short-segment fixation through injured vertebrae are shown in Figure 6.

A finite element analysis of transtraumatic and transtraumatic screw placement showed that transtraumatic screw placement was more effective in alleviating postoperative pain and improving spinal stability in the short and long term, although the operative time was longer and there was more intraoperative bleeding. In addition, transtraumatic screw placement may result in a lower rate of internal fixation failure.

2.4. Posterior Pedicle Screw System Internal Fixation for the Treatment of Lumbar Fractures. Pedicle internal fixation is suitable for patients with various unstable fractures and dislocations of the thoracolumbar spine or paraplegia: patients with spinal deformities, such as intervertebral disc degeneration, lumbar spondylolisthesis, and kyphosis. Dorsal midline incision is made with the diseased spine as the center, the position and direction of the pedicle screw are determined, the pedicle screw is inserted, the internal fixation device is placed, and the pedicle screw is reduced and fixed, as shown in Table 1.

The pedicle screw is a short-segment internal fixation system with superior biomechanical properties. Studies have shown that a posterior short-segment pedicle screw can transmit corrective forces to the three spinal columns through the posterior approach to the anterior part of the vertebral body. It is a mechanical tension fix with 6 degrees of freedom in three-dimensional space. Correct deformities and reduce fractures. The front, middle, and rear columns can be fixed at the same time. Effective anatomical reduction can be achieved even for difficult-to-reduce fractures. In addition, the feature of short-segment fixation avoids the impact of long-segment fixation on mobility and complications such as chronic low back pain and "flat back deformity." Effectively preserving motion segments can provide immediate stabilization of the spine, reduce the chance of nerve damage, and be safer and more reliable. Preoperative X-ray, CT or MRI examination can comprehensively evaluate and understand the fracture site, degree, type, spinal cord compression, attachment fracture, etc., and determine the method and scope of decompression.

After a lumbar fracture, the stability of the spine is destroyed and often accompanied by spinal cord nerve injury. The main factors that cause the spinal nerve compression are the bone mass behind the vertebral body and the compression of the upper edge of the injured vertebra due to the kyphosis angle and the displacement between the vertebral bodies [13]. The purpose of surgical treatment of lumbar fractures is to reconstruct the shape of the spinal canal, restore the stability of the spine, and eliminate the compression on the spinal cord. Restore the effective volume and stability of the spinal canal, and relieve the nerve compression in a timely and complete manner, which is conducive to the recovery of spinal nerve function. Removal of compressive material in front of the spinal cord, adequate decompression of the spinal canal, correction of deformities, reconstruction of spinal stability, and bone graft fusion have been recognized by most scholars. Thirty-five cases of thoracolumbar fractures were treated with posterior pedicle screw system internal fixation, of which 20 cases underwent intraoperative posterior decompression, and 8 cases underwent bone grafting of the diseased vertebrae through the pedicle. All 35 cases underwent bone grafting between the articular and transverse processes, and the average height (percentage) of the anterior and posterior edges of the injured vertebrae before and after the operation, the Cobb's angle, and the cross-sectional area of the spinal canal were measured. 35 cases of lumbar fractures were treated with posterior spinal canal decompression and nail-rod system

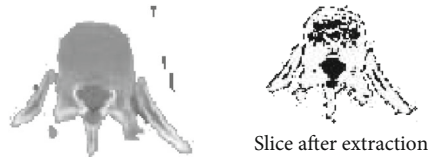

(a) Slice before extraction (b) Slice after extraction

Figure 2: Rendering before and after threshold segmentation.

Figure 3: Image after opening operation.

internal fixation, and satisfactory results were achieved, as shown in Figure 7.

2.5. Mechanical Experimental Study of Lumbar Internal Fixation. In 1988, Gurr et al. [14] compared the fixation effect of the Kaneda system with pedicle screws on the calf spine, and the results showed that the effect of the former fixation of 3 segments is equivalent to that of the latter fixation of 5 segments. Zdeblick et al. [15] and An et al. [16] compared several anterior internal fixation devices and found that the Kaneda system had the best stability. An et al. [17] proved through experiments that the use of a nut that prevents the screw from exiting will greatly enhance the fixing strength of the anterior internal fixation system. The posterior internal fixation system mainly includes pedicle screw and hook rod system. It is generally believed that the stiffness of the former is significantly higher than that of the latter. Lim et al. [18] confirmed through experiments that the axial torsional stability of the pedicle screw system is enhanced after the use of the transverse connecting rod, but the stability does not change significantly when subjected to other types of loads. Lynn et al. [19] found that the use of two transverse connecting rods can significantly increase the rotational and bending stiffness. There have been some studies on the pullout strength of pedicle screws. It is generally believed that the diameter of the pedicle screw is the most important factor. The larger the diameter of the screw, the higher the pullout strength. Another important factor that affects the strength of pedicle screw extraction is the shear strength of the pedicle and vertebral body, which is mainly related to the bone density of the cancellous bone and the torque when the screw is inserted. The lower the bone density, the lower the pull-out strength of the screw. Therefore, when the pedicle screw is located in an area with high bone density near the endplate, its extraction strength is relatively high. In the past, we mostly paid attention to the stability of the spine itself, ignoring the load-bearing effect of the internal fixation. When the fatigue strength of the internal fixation is lower than the breaking strength, it is necessary to effectively reduce the stress of the internal fixation. Cunningham et al. [20] used 12 kinds of pedicle screws to fix the vertebral body in the biomechanical experiment and found that the compressive strength and bending strength of all specimens were significantly lower than normal. It can be seen that if the stability of the anterior structure cannot be effectively reconstructed, the pedicle screw system will bear part or even all of the load originally borne by the anterior column. Clinical reports about broken nails and implant loosening after the treatment of thoracolumbar vertebral fractures with posterior pedicle screw system are not uncommon, most of which are cases of continuous damage to the anterior column, and if anterior bone grafting is performed at the same time, no such complications occurred. Cripton et al. [21] analyzed the load-sharing effect of the posterior lumbar internal fixation system and believed that the risk of damage to the posterior internal fixation system is great when severe anterior injury occurs, as shown in Figures 8 and 9.

3. Results

Biomechanical studies have shown that the posterior pedicle short-segment fixation has a firm three-column fixation function, which is a tension fixation in terms of spine mechanics. The short-segment pedicle internal fixation system can reconstruct the stability of the spine, restore the volume of the spinal canal, and provide a favorable external environment for the recovery of nerve damage. Fracture reduction is divided into direct reduction and indirect reduction. When the posterior screw rod is stretched longitudinally to restore the height of the spine and the posterior column, the posterior longitudinal ligament is stretched to achieve indirect reduction of the bone block in the spinal canal, and the rod is used for prereduction. Bent, angled pedicle screws and the lever force of expansion can restore the height of the anterior column. Whether it is a compression or burst fracture, as long as the anterior and posterior longitudinal ligaments are intact, most of the fracture fragments can be reduced satisfactorily through the expansion of the AF internal fixation system. During the operation, the fractured vertebrae should be determined under X-ray fluoroscopy, and the position, direction, depth, and reduction of the screw should be observed to prevent poor reduction and excessive expansion. When determining the position of the guide pin of the pedicle screw, the standard positive and lateral X-ray film is used to determine the position of the guide pin. If the positions of the screws on both sides are not symmetrical, the stresses received by the

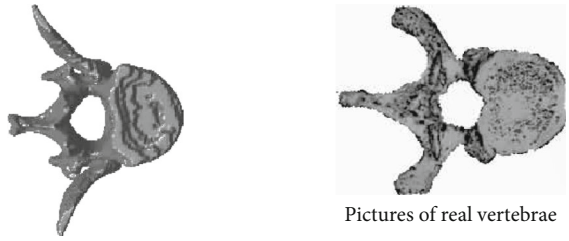

Reconstructed image of vertebrae (Top view)

Pictures of real vertebrae

(a) Reconstructed image of vertebrae (top view) (b) Pictures of real vertebrae

Figure 4: Single spine model.

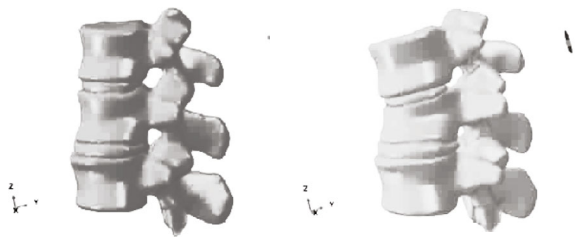

Normal lumbar spine model

Vertebral fracture model

(a) Normal lumbar spine model (b) Vertebral fracture model

Figure 5: Three-dimensional model of thoracolumbar T11-L1 segment.

Monosegmental fixation model

Short segmental fixation model

(a) Monosegmental fixation model (b) Short-segmental fixation model

Figure 6: 3D finite element fixation models of T10-L2 segment.

rod structures on both sides will be different, leading to complications such as bent or broken nails after surgery [22]. According to the patient's symptoms and signs, as well as the extent and extent of the kyphosis of the fracture, and the location and extent of spinal cord compression provided by the patient, select the decompression method and decompression range. Most of the posterior longitudinal ligaments with small fractures in the spinal canal are intact. Most of the fractures can be automatically reset by the force of expansion; for those with large fractures in the spinal canal that cannot be indirectly reset, the semilaminar or full-laminectomy is used. The blunt-head chisel strikes forward carefully to hit the fractured piece directly into the vertebral body to achieve the purpose of decompression. For large fractures in the spinal canal and obvious stenosis of the spinal canal, especially in patients with burst fractures of the lumbar spine, the anterior and posterior longitudinal ligaments have been damaged in most cases. Resection of the medial semi cortex and part of the facet joints of one or both sides of the pedicle, and then, decompress after reaching the front of the spinal canal; after distraction, the vertebral body of the injured vertebral body has the phenomenon of "hollow vertebral body" or cannot achieve distraction reduction. The anterior and middle columns lose their structural integrity. Without effective bone grafting, internal fixation fatigue, fracture, and collapse of the fractured vertebral body and loss of correction may occur in the late stage. Parker et al. [23] believe that the failure rate of internal fixation devices can reach 9% to 54% if only posterior

Table 1: Characteristics of pedicle internal fixation system.

	Characteristics of pedicle internal fixation system
Feature 1	Early reduction and internal fixation, fixed tightly
Feature 2	Short-segment fixation
Feature 3	Restore the normal physiological radian of the spine
Feature 4	Restore the cross-sectional area of the spinal canal, rebuild the stability of the spine, achieve effective and complete decompression, and relieve the strain on the spinal nerves. Promote the recovery of nerve function
Feature 5	Full bone graft fusion, high fusion rate of bone graft
Feature 6	Patients can get out of bed early

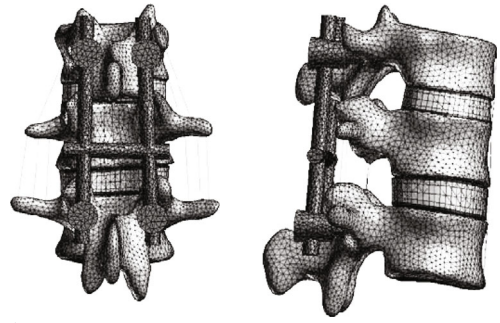

(a) Anteroposterior position (b) Lateral position

Figure 7: Finite element model of posterior decompression internal fixation.

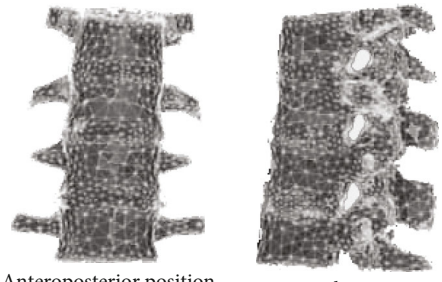

(a) Anteroposterior position (b) Lateral position

Figure 8: Anteroposterior and lateral view of finite element model of vertebral fracture.

fixation of burst fractures of the lumbar spine, without the support of the anterior column. Therefore, during the operation, it is necessary to focus on the decompression of the front of the spinal canal, as well as the recovery of the height of the diseased vertebrae and the bone mass. Therefore, we take the iliac bone from the body and implant the diseased vertebral body through the pedicle to restore its height as much as possible. At the same time, the lamina and spinous process removed during the operation are bitten into granules and placed on the transverse process and the small joints on the unopened side. Bone grafting was performed between the processes to achieve the purpose of spine stabilization. For the free bone fragments and intervertebral disc tissues in the spinal canal, all need to be removed with a small curette or nucleus pulposus forceps, fully decompressed, and at the same time, carefully protect the spinal nerve with nerve stripping paper.

At present, the clinical treatment of lumbar spine fractures mostly uses posterior pedicle screw internal fixation, which is beneficial to the recovery of lumbar spine function as soon as possible. With the increasing understanding of

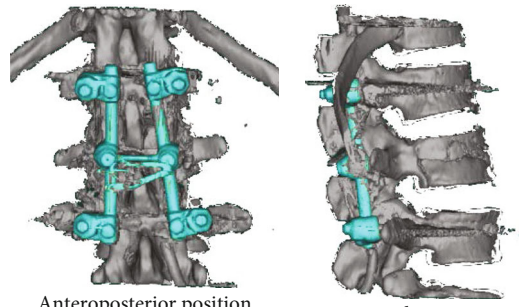

(a) Anteroposterior position (b) Lateral position

Figure 9: Schematic diagram of simulated pedicle screw placement.

the pathogenesis of spinal fractures, there is an urgent need for systematic and comprehensive biomechanical research on the spine. More and more scholars use the finite element analysis method to analyze the force of the spine under various loads. This method of biomechanical research through the finite element model is indispensable in the study of the biological characteristics of the spine. The important role of substitution not only provides strong guidance for the clinically carried out surgical internal fixation technology but also provides a scientific basis for the evaluation of surgical effects.

4. Discussion

4.1. The Rear Road Nail Bar System and the Front Road Cone Steel Plate System. Compared with the anterior vertebral plate system, the posterior screw and rod system has obvious mechanical advantages. The screw rod system firmly fixes the pedicle screw and the metal rod through a universal joint and can be adjusted in three dimensions in space, so as to achieve effective reduction and firm fixation of spinal fractures. The nail-rod system has the following characteristics: ① it has a long rod, which can fix longer segments and can fix multiple segments at the same time, which has obvious advantages in treating multisegment fractures; ② it can perform rod pretreatment according to the degree of fracture kyphosis. Bending can meet the correction requirements of different degrees and directions, but because the two rods are prone to asymmetry in the bending, the instability of the rotation direction is easy to occur; ③ it has irreplaceable advantages in spinal correction. AF is usually used for the fixation of single-segment vertebral fractures. For multisegment vertebral fractures, especially skip fractures, the application of AF is limited. The nail-rod combined pedicle internal fixation device can three-dimensionally correct multilateral fractures and displacements of the vertebral body through the expansion and rotation of the instrument. Especially for burst fractures of the vertebral body, it can effectively restore the height of the compressed vertebral body and fix the joints. The segment is short and reliable, in line with the principle of three-dimensional fixation of spinal fractures, shown in Table 2.

Table 2: The changes of Cobb angle before and after operation were compared between the two groups.

Group	Preoperative	Postoperative	After 1 year
Anterior	25.1 ± 8.9	3.4 ± 1.7	4.6 ± 1.6
Posterior	23.7 ± 7.6	3.2 ± 1.4	8.2 ± 2.1
T value	0.757	0.574	9.343
P value	0.452	0.567	0.001

With the development of internal fixation devices, pedicle screws can provide better fixation than the first posterior internal fixation devices such as Harrington rods and spinous process plates. In addition, posterior surgery has the advantages of simple operation and less trauma. Posterior pedicle screw internal fixation has become the most widely used surgical method for the treatment of thoracolumbar fractures in clinical practice, but some scholars [24] believe that this approach is more prone to kyphotic deformity compared with anterior surgery loss. Therefore, the selection of the surgical approach should be a reasonable choice by considering factors such as the type, location, nerve injury, and the skill and experience of the surgical operator (Figures 10 and 11).

4.2. Posterior Short-Segment and Single-Segment Pedicle Screw Internal Fixation. With the application of posterior short-segment transinjured vertebral nail placement in the treatment of lumbar fractures, some scholars have proposed posterior single-segment pedicle screw instrumentation (MPSI) in order to further reduce the number of fixed segments. For the treatment of thoracolumbar fractures, posterior single-segment pedicle screw internal fixation refers to the focus of the injured vertebrae and adjacent vertebral body segments. It is a development based on the placement of nails in the injured vertebrae. This surgical method mainly relies on a complete endplate. The residual bone on the side stretches the injured vertebrae to restore the original height and fix it. In clinical work, there is also a stabilization effect by only fixing the injured vertebrae and an adjacent normal vertebral body. The concept of fixing only one motion segment is different from the cross-segment pedicle screw internal fixation. McLain et al. [25] found that

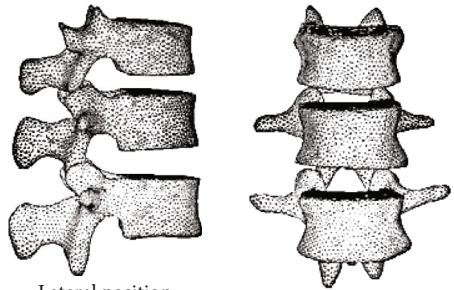

(a) Lateral position (b) Anteroposterior position

Figure 10: Finite element model of normal thoracolumbar vertebral body.

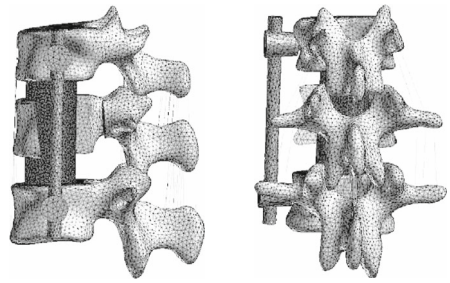

(a) Anteroposterior position (b) Lateral position

Figure 11: Finite element model of anterior internal fixation.

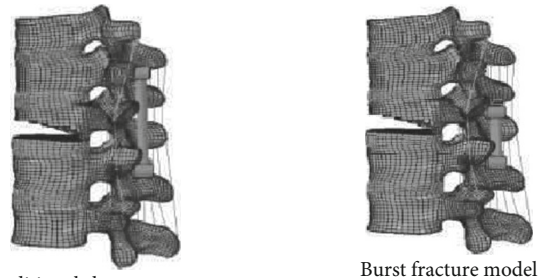

(a) Traditional short-segment pedicle screw fixation (b) Burst fracture model

Figure 12: Finite element model of spinal T10-L2 segment.

compared with short-segment fixation, it has the following advantages: one less fusion of the intervertebral space, which can maximize the preservation of the motion segment of the spine; the screw directly screwed into the injured vertebra can immediately open the injured vertebra, to better recover and maintain the height of the injured vertebral; because there are few fixed and fused segments, the degeneration of adjacent segments is reduced, and the postoperative vertebral body instability and loss of correction are minimized; to avoid long-term fixation of the contralateral intervertebral space and reduce regression Change; after posterior pedicle screw fixation, due to the stress shielding effect, most of the stress is transmitted through the posterior column screw. After single-segment fixation, the column torque is reduced, which can reduce the nail-rod stress load and reduce the probability of internal fixation damage. It can also reduce the rate of postoperative correction loss, especially in the treatment of flexion-traction fractures. The effect is more significant; the operation is small, the surrounding tissue is less peeled, the amount of bleeding is less [26–30], and the surgical trauma is reduced, and in most cases, there is no need to take the iliac bone for bone grafting, which avoids the problem of pain in the bone removal area [31] (Figure 12).

4.3. Finite Element Research. The biomechanical properties of the lumbar pedicle screw fixation system were evaluated by the finite element method. The results showed that,

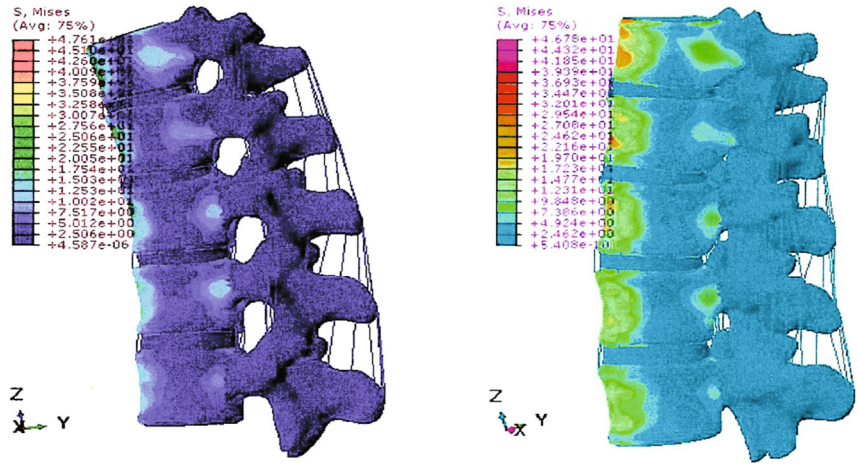

(a) Normal cone forward flexion force nephogram (b) Cloud image of normal pyramidal extension force

Figure 13: Stress nephogram of normal cone in forward and backward flexion.

compared with the traditional lateral pedicle screw fixation system with connecting device, the pedicle screw fixation system with connecting device increased the diagonal direction. It is more stable in flexion and extension; some studies have investigated the force transmission mechanism in the helical bone complex using finite element methods. The results show that the screw is subjected to a series of discrete loads within the vertebral body, resulting in local bending moments. The maximum stress on the screw acts on the screw base and threaded joints, which is consistent with the clinically observed screw fracture sites [32] (Figure 13).

5. Conclusion

The posterior pedicle internal fixation system for the treatment of multilevel spinal fractures is a mature surgical technique and has fewer postoperative complications. Transpedicle fixation is effective and reliable. It can effectively restore the coronal and sagittal curvature of the vertebral body and restore the stability of the spine better. But the choice of internal fixation method should be individualized based on fracture type, identification of critical and secondary injury sites, and stability assessment. Only after mastering the biomechanical characteristics of the posterior screw rod system for the treatment of lumbar fracture, selecting the appropriate method, and fixing the appropriate movement unit [33] can the best fixation be achieved.

Image segmentation technology is often used to meet the needs of virtual spine surgery. The commonly used segmentation techniques include "threshold method," "edge segmentation method," "region segmentation method," and some "theory specific segmentation methods." The threshold method is the most direct and simple method of image segmentation. According to the threshold, the image is divided according to the gray level. But the thresholding method is mainly for gray information, and if the image background is complex or there are multiple targets, it is difficult to ensure the segmentation effect. Threshold segmentation is often used in CT image processing. According to their own experience, doctors constantly adjust the threshold for segmentation until they achieve the desired effect.

Data Availability

The image data used to support the findings of this study have been deposited in the VerSe 2019 dataset (https://osf.io/nqjyw/).

Conflicts of Interest

The authors declare no conflicts of interest.

References

[1] S. Pneumaticos, G. K. Triantafyllopoulos, and P. V. Giannoudis, "Advances made in the treatment of thoracolumbar fractures: current trends and future directions," *Injury*, vol. 44, no. 6, pp. 703–712, 2013.

[2] A. A. White 3rd and M. M. Panjabi, "The basic kinematics of the human spine. A review of past and current knowledge," *Spine*, vol. 3, no. 1, pp. 12–20, 1978.

[3] T. Belytschko and C. A. Briggs, "Finite element stress analysisof an intervertebral disc," *Journal of Biomechanics*, vol. 974, no. 7, pp. 277–279, 1992.

[4] K. J. Cai, L. Z. Wang, J. Yao, and H. Gong, "The optimal elementsize, material property distributions and modeling methodsfor finite element modeling of lumbar vertebra," *Journal of Medical Biomechanics*, vol. 31, no. 2, pp. 135–141, 2016.

[5] A. J. Ramme, N. Devries, N. A. Kallemyn, V. A. Magnotta, and N. M. Grosland, "Semi-automated phalanx bone segmentation using the expectation maximization algorithm," *Journal of Digital Imaging*, vol. 22, no. 5, pp. 483–491, 2009.

[6] Y. Shi and R. C. Eberhart, "A modified particle swarm optimizer," in *IEEEInt'l Conf on Evolutionary Computation*, pp. 69–73, Anchorage, Alaska, 1998.

[7] D. Qiu, L. Zheng, J. Zhu, and D. Huang, "Multiple improved residual networks for medical image super-resolution," *Future Generation Computer Systems*, vol. 116, pp. 200–208, 2021.

[8] R. C. Eberhart and Y. Shi, "Comparing inertia weights and constrictionfactors in particle swarm optimization," in *Proceedings of the 2000Congress on Evolutionary Computation*, pp. 84–88, Piscataway, NJ, USA, 2000.

[9] J. Noailly, D. Lacroix, and J. A. Planell, "Finite element study of anovel intervertebral disc substitute," *Spine*, vol. 30, no. 20, pp. 2257–2264, 2005.

[10] A. Polikeit, L. P. Nolte, and S. J. Ferguson, "The effect of cementaugmentation on the load transfer in an osteoporotic func-tional spinal unit: finite-element analysis," *Spine*, vol. 28, no. 10, pp. 991–996, 2003.

[11] D. W. He, L. J. Wu, and Y. L. Chi, "Biomechanical finite elementanalysis of bone graft fusion of bilateral articular process-combined with spinous process preventing postoperativecorrection loss for thoracolumbar fracture surgery," *Yiyong Shengwu Lixue/Journal of Medical Biomechanics*, vol. 24, no. 3, pp. 193–210, 2009.

[12] J. Su, W. Z. Zhao, B. Z. Chen, B. Li, S. W. He, and X. Fan, "Establishing finite ele-ment contact model of human L1 ~ L5 lumbar segments," *Journal of Medical Biomechanics*, vol. 25, no. 3, pp. 200–205, 2010.

[13] T. Hashimoto, K. Kaneda, and K. Abumi, "Relationshipbetweentrau-maticspinalcancalstenosisandneurologicdeficit-sinthoracolum-barburstfractures," *Spine*, vol. 13, pp. 1268–1272, 1988.

[14] K. R. Gurr, P. C. McAfee, and C. M. Shih, "Biomechanical analysis of anterior and posterior instrumentation systems after corpectomy: a calf spine model," *JBJS*, vol. 70, no. 8, pp. 1182–1191, 1988.

[15] T. A. Zdeblick, K. E. Warden, D. Zou, P. C. McAfee, and J. J. Abitbol, "Anterior spinal fixators: a biomechanical in-vitro study," *Spine*, vol. 18, no. 4, pp. 513–517, 1993.

[16] H. S. An, T. H. Lim, J. W. You, J. H. Hong, J. Eck, and L. McGrady, "Biomechanical evaluation of anterior thoracolumbar spinal instrumentation," *Spine*, vol. 20, no. 18, pp. 1979–1983, 1995.

[17] J. W. You, H. S. An, and T. H. Lim, "Biomechanical Evaluation of Anterior Thoracolumbar Spinal Instrumentation[J]," *Journal of Korean Society of Spine Surgery*, vol. 2, no. 2, pp. 161–167, 1995.

[18] T. H. Lim, J. C. Eck, H. S. An, J. H. Hong, J. Y. Ahn, and J. W. You, "Biomechanics of transfixation in pedicle screw instrumentation," *Spine*, vol. 21, no. 19, pp. 2224–2229, 1996.

[19] G. Lynn, D. P. Mukherjee, R. N. Kruse, K. K. Sadasivan, and J. A. Albright, "Mechanical stability of horacolumbar pedicle screw fixation: the effect of crosslinks," *Spine*, vol. 22, no. 14, pp. 1568–1572, 1997.

[20] D. K. Ebelke, M. A. Asher, J. R. Neff, and D. P. Kraker, "Survivorship analysis of VSP spine instrumentation in the treatment of thoracolumbar and lumbar burst fracture," *Spine*, vol. 16, 8 Suppl, pp. S428–S432, 1991.

[21] P. A. Cripton, G. M. Jain, R. H. Wittenberg, and L. P. Nolte, "Load-sharing characteristics of stabilized lumbar spine segments," *Spine*, vol. 25, no. 2, pp. 170–179, 2000.

[22] M. K. Hsieh, L. H. Chen, C. C. Niu, T. S. Fu, P. L. Lai, and W. J. Chen, "Postoperative anterior spondylodiscitis after posterior pedical screw instrumentation," *The Spine Journal*, vol. 11, no. 1, pp. 24–29, 2011.

[23] J. W. Parker, J. R. Lane, E. E. Karalkovic, and R. W. Gaines, "Successfulshort-seg-mentinstrumentationandfusionforthoracolumbarspinalfrac-tures: aconsecutive 4•5-yearstudy," *Spine*, vol. 25, no. 9, pp. 1157–1170, 2000.

[24] P. W. Hitchon, J. Torner, K. M. Eichholz, and S. N. Beeler, "Comparison of anterolateral and posterior approaches in the management of thoracolumbar burst fractures," *Journal of Neurosurgery: Spine*, vol. 5, no. 2, pp. 117–125, 2006.

[25] R. F. McLain, J. K. Burkus, and D. R. Benson, "Segmental instrumentation for thoracic andthorac 01umbar fractures: prospective analysis of construct survival and five yearfollow up," *Spine*, vol. 1, no. 5, pp. 310–323, 2001.

[26] J. J. Verlaan, C. H. Diekerhof, E. Buskens et al., "Surgical treatment of traumatic fractures of the thoracic and lumbar spine: a systematic review of the literature on techniques, complications, and outcome," *Spine*, vol. 29, no. 7, pp. 803–814, 2004.

[27] X. Xinli, C. Zhang, F. Musharavati, T. A. Sebaey, and A. Khan, "UFSW tool pin profile effects on properties of aluminium-steel joint," *Vacuum*, vol. 192, no. 8, article 110460, 2021.

[28] X. Xu, C. Zhang, F. Musharavat, T. A. Sebaey, and A. Khan, "Dispersion of waves characteristics of laminated composite nanoplate," *Steel and Composite Structures*, vol. 40, no. 3, pp. 355–367, 2021.

[29] Z. Tang and Z. Zhang, "The multi-objective optimization of combustion system operations based on deep data-driven models," *Energy*, vol. 182, pp. 37–47, 2019.

[30] H. Bo, C. Zhou, H. Wang, and S. Chen, "Nonlinear tribodynamic model and experimental verification of a spur gear drive under loss-of-lubrication condition," *Mechanical Systems and Signal Processing*, vol. 153, article 107509, 2021.

[31] Q. L. Li, X. Z. Li, Y. Liu et al., "Treatment of thoracolumbar fracture with pedicle screws at injury level: a biomechanical study based on three-dimensional finite element analysis," *European Journal of Orthopaedic Surgery & Traumatology*, vol. 23, no. 7, pp. 775–780, 2013.

[32] B. S. Lonner, J. D. Auerbach, M. B. Estreicher et al., "Pulmonary function changes after various anterior approaches in the treatment of adolescent idiopathic scoliosis," *Journal of Spinal Disorders & Techniques*, vol. 22, no. 8, pp. 551–558, 2009.

[33] D. Qiu, S. Zhang, Y. Liu, J. Zhu, and L. Zheng, "Super-resolution reconstruction of knee magnetic resonance imaging based on deep learning," *Computer Methods and Programs in Biomedicine*, vol. 187, no. 12, article 105059, 2019.

Hindawi
Computational and Mathematical Methods in Medicine
Volume 2022, Article ID 9461236, 6 pages
https://doi.org/10.1155/2022/9461236

Research Article

A Comparative Study on the Diagnostic Value of CTA and MRA in Anterior Dislocation of Shoulder

Junhua Wu, Tao Zhang, Xuxue Li, Qian Dan, and Dezhou Zhang

Department of Radiology, Sichuan Provincial Orthopedic Hospital, Chengdu, Sichuan 610041, China

Correspondence should be addressed to Junhua Wu; wujunhua8686@126.com

Received 20 December 2021; Revised 27 January 2022; Accepted 14 March 2022; Published 11 April 2022

Academic Editor: Kelvin Wong

Objective. To investigate the diagnostic value of CTA and MRA in anterior dislocation of shoulder. *Methods*. The detection of inferior glenohumeral ligament injuries, anterior inferior labrum injuries, and bone and cartilage injuries by the two examination procedures was observed and compared with the results of arthroscopy or surgery on patients referred to our hospital owing to anterior dislocation of shoulder. *Results*. A total of 36 patients with shoulder injuries were gathered for this study. 32 cases with anterior inferior labrum tearings (27 cases detected by CTA and 30 cases by MRA), 24 cases with inferior glenohumeral ligament tearings (14 cases detected by CTA and 22 cases by MRA), 24 cases with inferior glenohumeral ligament tearings (14 cases detected by CTA and 22 cases by MRA), and 24 cases with inferior glenohumeral ligament tearings (14 cases detected by CTA and 22 cases by MRA) were detected. There were 30 bone and cartilage injuries, including 18 fractures (CTA identified 18), 10 bone contusions (CTA detected 0), and 5 cartilage damage (CTA detected 0) (CTA detected 0, MRA detected 5). *Conclusion*. The detection rate of MRA is better than that of CTA for inferior glenohumeral ligament injuries. For anterior inferior labrum injury, the detection rate of CTA and MRA was similar. CTA is more conducive to the detection of fracture blocks, while MRA is more advantageous for the observation of bone contusion and cartilage damage.

1. Introduction

The most prevalent type of shoulder damage (approximately 95 percent) is anterior dislocation [1]. The importance of accurate preoperative imaging assessment in the selection of surgical procedures and prognosis cannot be overstated. Due to its benefits in fracture display, MRI has been widely employed in clinic due to its high soft tissue resolution, and CT examination plays an important role in preoperative evaluation of shoulder joint damage. By injecting contrast agent into the articular cavity to open the capsule, direct arthrography of the shoulder can better show joint capsule and brachial ligament injury, labrum injury, bone, and cartilage damage. Currently, direct arthrography of the shoulder joint mainly includes CT arthrography and MR arthrography. In this study, CTA and MRA were performed on 36 patients admitted to our hospital for anterior dislocation of the shoulder, so as to explore the best preoperative imaging methods for patients with anterior dislocation of the shoulder.

2. Materials and Methods

2.1. The General Information. A total of 36 patients with anterior shoulder dislocation who visited our hospital from January 2018 to June 2020 were collected. The patients were informed of the significance and risks of the relevant examination and signed the informed consent. This study was reviewed and approved by the hospital ethics Committee. Among them, there were 27 males and 9 females, aged from 16 to 45 years old, with an average age of (24 ± 6) years, and a course of 1 to 32 months, with an average course of (5 ± 2) months. Among them, 21 cases were chronic repeated dislocation with no obvious pain or swelling of the shoulder joint and limited movement to varying degrees. The fear test of anterior instability of the shoulder joint was all positive. 15 cases were acute single dislocation with the main clinical symptoms of shoulder joint pain, swelling, and limited movement. All the 36 patients underwent CT arthrography and MR arthrography, 28 underwent shoulder arthroscopy exploration

and repair, and 8 underwent shoulder joint open surgery, with the findings of arthroscopy and open surgery as the gold standard.

2.2. Procedure. A 20-ml empty needle was used to prepare the contrast agent: 0.25 ml gadolinitic dextrine, 5 ml iodixanol, 5 ml lidocaine, and 5 ml 0.9% normal saline.

For CT arthrography, Siemens SOMATOM Definition AS 64 row multislice spiral CT from Germany was chosen. The patient was supine and had a forward-facing head. To ensure that the contrast agent injection into the articular cavity by fast spiral scanning, scanning parameters were as follows: voltage 120 kv, current 210-240 ma, collimating width 1.5 mm, and 0.75 1.0 mm raw data, which obtained thin-layer transverse images and spread to Siemens image postprocessing workstation for 3 d reconstruction.

For MR arthrography, after CT arthrography, the patient was rotated and abducted the shoulder joint three times, and then, MR arthrography was performed. MR angiography was performed using GE 1.5 T Signa explorer magnetic resonance scanner. Patients were randomly assigned to supine position and shoulder coil and underwent proton density-weighted fat suppressor image (PDWR-FS,TR/TE = 2517/58 ms), and T1-weighted image (T1WI,TR/TE = 450/13 ms), and T1-weighted fat suppressor image (T1wi-FS,TR/TE = 440/11 ms); sagittal T1WI-FS, horizontal T1WI-FS, and PDWR-FS were scanned; and the layers were 4 mm thick and 1 mm spaced.

2.3. Image Analysis and Statistics. All the image data were reviewed by 2 experienced MRI diagnostic physicians, and the osseous structure and soft tissue changes of the shoulder joint were carefully observed and analyzed, and the inconsistency of diagnosis was solved by negotiation. The main contents of observation include: (1) inferior glenohumeral ligament; (2) anterior lower lip; and (3) bone and cartilage. Observe the display of the above structures in each sequence and each azimuth, and record the imaging abnormalities.

SPSS17.0 software package was applied, and X^2 test was used for statistical analysis. $P < 0.05$ was considered statistically significant.

3. Results

In this group, 36 patients had 36 affected shoulders. With the exception of bone contusion (MRI is the gold standard for the diagnosis of bone contusion), the results of shoulder arthroscopy were the gold standard for all the other lesions (Table 1).

3.1. Inferior Glenohumeral Ligament Injury. The inferior glenohumeral ligament was injured in 24 of the 36 afflicted shoulders. 14 cases were detected by CT arthrography, and the transverse axial bone window revealed local discontinuity of the inferior glenohumeral ligament, reduced tension, retraction of the broken end, and leakage of some contrast agent through rupture on CT arthrography (Figure 1(a)), but 3 cases without the leakage of contrast agent (Figure 2(a)). 22 cases were detected by MR arthrography, and t1WI-FS in transverse and coronal positions showed good results (Figures 1(b) and 2(b)), showing local discontinuity of the inferior glenohumeral ligament, reduced tension, retraction of the broken end, and leakage of some contrast agent through rupture.

3.2. Anterior Inferior Labrum Injuries. There were 32 anterior inferior labrum injuries in the 36 affected shoulders, all of which were Bankart injuries. The transverse axial bone window revealed good outcomes (Figure 3(a)), with morphological alterations, nonunion or abnormalities of the anterior and inferior labial lips, local cracks, and contrast agent entrance being the most common symptoms. However, MR arthrography found 30 cases, and the transverse t1WI-FS showed promising results (Figure 3(b)). The results of MR arthrography for anterior and lower labial injuries were comparable to CT arthrography.

3.3. Bone and Cartilage Injury. 30 of the 36 affected shoulders had bone and cartilage injury, mainly manifested as osseous Bankart injury at the anterior lower margin of the glenoid cavity and Hill-Sachs injury at the outer upper margin of the humeral head. Eighteen fractures were detected by CT arthrography, showing local bone morphological changes; high-density bone fragments were separated and shifted (Figure 4(a)); In contrast, MR arthrography is less likely to detect fractures (Figure 4(b)).MPR three-dimensional imaging showed good results, and MR arthrography showed 8 fractures, showing local bone morphological changes; low signal bone fragments were separated and shifted; and various sequences in the horizontal axis showed good results. CT arthrography failed to show bone contusion (Figure 5(a)).There were 10 bone contusions, which all were detected by MR arthrography, showing high lamellar lipids and good lipid sequence in all directions (Figure 5(b)). There were 5 cartilage injuries, among which 0 were detected by CT arthrography (Figure 6(a)) and 5 by MR arthrography, showing gray hyaluronic defect on the articular surface. Gray-free cartilage tablets were seen in the articular cavity, and the t1WI-FS in the transverse axis showed good results (Figure 6(b)).

4. Discussion

Injuries to the inferior glenohumeral ligament and anterior inferior labrum are common pathological changes in anterior dislocation of the shoulder joint and are considered to be the most important causes of recurrent dislocation of the joint [2]. They can be accompanied by fractures of the external posterior humeral head and the anterior lower edge of the glenoid cavity, bone contusions, and articular cartilage injuries.

The labium is a fibrous cartilage that is dispersed around the bony joints, deepening the glenoid fossa and supporting the glenohumeral joints, comparable to the meniscus. The anterior labrum is frequently damaged by anterior dislocation or instability of the shoulder, which leads to repeated dislocation and instability of the anterior shoulder [3].

The upper glenobrachial ligament, middle glenobrachial ligament, and lower glenobrachial ligament strengthen the anterior articular capsule on the inner wall of the anterior

Table 1: Comparison of CT arthrography, MR arthrography, and surgical results on detecting lesions of anterior dislocation of shoulder.

Modalities	Inferior GHL injury	Bankart lesion	Bone and cartilage lesion		
			Fracture	Bone contusion	Cartilage injury
CTA	14	27	18	0	0
MRA	22	30	8	10	5
Surgical results	24	32	18	0	5
P value	0.008	0.423	<0.001	<0.001	0.011
Chi-square value	7.111	0.642	13.846	20.000	6.400

GHL = inferior glenohumeral ligament, CTA = computed tomography arthrography, and MRA = magnetic resonance arthrography. Table 1 shows that for lower glenohumeral ligament injury, fracture, bone contusion, and cartilage injury, CT arthrography and MR arthrography showed statistically significant differences ($P < 0.05$), while for Bankart injury of the anterior lower labial, CT arthrography and MR arthrography showed no statistically significant differences ($P > 0.05$).

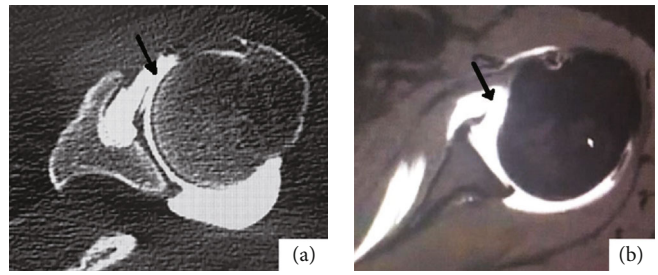

(a) (b)

Figure 1: Female, 24 years old, anterior dislocation of left shoulder for 5 months. (a) shows the bone window image on the horizontal axis of CTA of the left shoulder; as shown by the black arrow, anterior inferior glenohumeral ligament was torn, and part of contrast medium was leaked. (b) shows the T1WI-FS image in the transverse axis of the MRA of the left shoulder. The black arrow shows that the anterior ligament of the inferior glenohumeral ligament is torn, and the broken end is retracted.

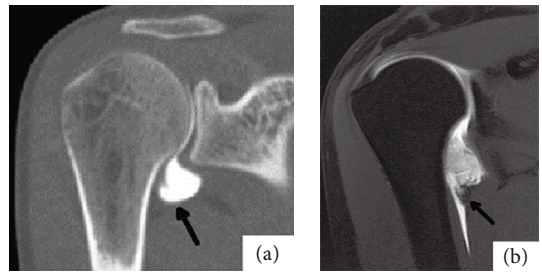

(a) (b)

Figure 2: Male, 24 years old, with recurrent anterior dislocation of right shoulder for 1 year. (a) shows the coronal bone window image of CTA in the right shoulder. The shape of the axillary capsule is irregular in arrow. (b) shows the right shoulder MRA coronal T1WI-FS image. The arrow shows the inferior glenohumeral ligament with nonunion of the fibers on the humerus side, retraction of the broken end, and partial contrast agent leakage.

articular capsule. The anterior inferior labrum, the anterior inferior glenoid ligament, and the anterior inferior articular capsule constitute the anterior inferior labrum-ligament complex, which is the most important functional device for the anterior stability of the shoulder [4]. In the case of anterior dislocation of the shoulder joint, the anterior inferior label-inferior glenohumeral ligament complex is the first to be injured, and the type of injury directly affects the surgical method and prognosis. For example, although the edge side of shoulder joint, after the former torn by arthroscopic shoulder joint capsule under repair, but the joint capsule body torn, humerus lateral joint capsule tearing, and severe joint capsule tearing are arthroscopic surgery taboo, you must repair by open surgery [5–8], therefore, preoperative accurate knowledge of joint capsule and dishes humerus ligament damage, the spoon lips injury situation, has important clinical value.

When below the humerus head forward dislocation, and edge of glenoid cavity before collision form shear stress, on the outside after the head of the humerus

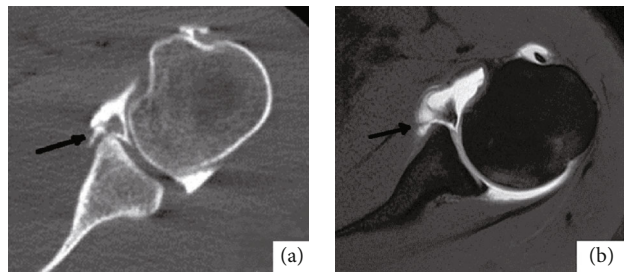

(a) (b)

Figure 3: Male, 29 years old, with recurrent anterior dislocation of left shoulder for half a year. (a) shows the bone window image in the transverse axis of the left shoulder CTA, and (b) shows the T1WI-FS image in the transverse axis of the left shoulder MRA. All the black arrows show local nonunion of the anterior lower lip and contrast agent entering the fissure.

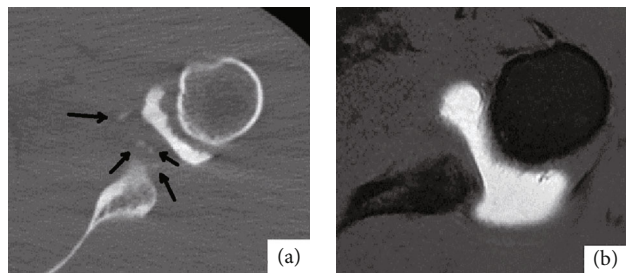

(a) (b)

Figure 4: Male, 27 years old, anterior dislocation of left shoulder for 3 months. (a) shows the transverse bone window image of CTA on the left shoulder. Black arrow shows that several high-density bone fragments can be seen beside the lower margin of the glenoid cavity. (b) shows the T1WI-FS image in the transverse axis of the left shoulder MRA, and no obvious bone fragments are seen beside the lower margin of the glenoid cavity.

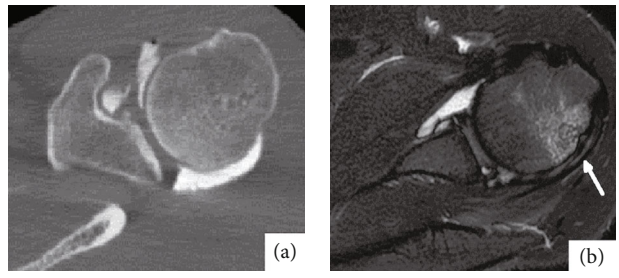

(a) (b)

Figure 5: Male, 23 years old, anterior dislocation of left shoulder for 1 month. (a) shows the transverse bone window image of CTA on the left shoulder. No obvious abnormalities were found in the morphology and density of the humerus. (b) shows the PDW-FS image of the left shoulder on the horizontal axis of MRA, and the signal of the patellar bone marrow edema outside and above the humeral head was shown in the white arrow.

and glenoid cavity edge of former can cartilage injury, bone contusion and fracture and cartilage slices or pieces of bone into the joint cavity forming loose bodies can cause irritation and traumatic osteoarthritis secondary to again and again, so it is necessary surgery to remove loose bodies [8–10].

In this study, it was found that MRA has more advantages for lower glenohumeral ligament injuries, because MRI itself has high resolution for soft tissue and can clearly display upper, middle, and lower glenohumeral ligaments and joint capsule structures [10–13]. The 22 cases detected by MRA all had partial contrast agent leakage through the rupture opening, whereas the three cases detected by CTA had no contrast agent leakage through the rupture opening, which could be due to uneven contrast agent distribution and partial fibrous adhesion between the broken ends of the torn inferior glenohumeral ligament. Following a CTA examination, shoulder joint

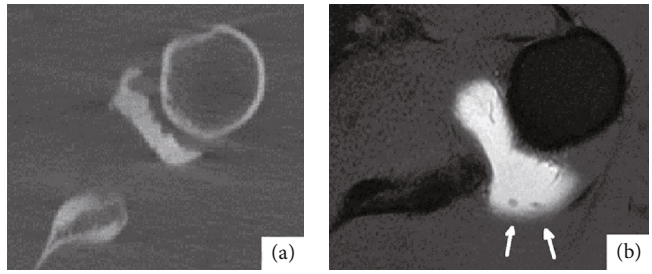

(a) (b)

Figure 6: Male, 19 years old, with anterior dislocation of the left shoulder for 2 months. (a) is the bone window image of CTA transverse axis of the left shoulder. No obvious free cartilage tablets were found in the joint capsule. (b) shows the T1WI-FS image of the left shoulder in the horizontal axis of MRA. White arrows show two free small cartilage tablets in the joint capsule.

mobility uniformizes the contrast agent distribution and separates the adhesion broken ends. As a result, during an MRA examination, contrast agent can be seen leaking through the rupture site. For anterior inferior labial injuries, both CTA and MRA have high detection rates, because the main component of the labial is fibrous cartilage, and normally, the transverse axis presents triangular low density or uniform low signal. When the labial is torn, the morphology of the labial changes and contrast agent enters into the tear, which is not difficult to determine [12–18]. Because of its thin-layer scanning and 3D reconstruction functions, CTA is more likely to discover small bone fragments than MRA, and white high-density bone fragments are easier to see on CT pictures than black low-density bone fragments on MRI images. Bone marrow edema is the most common symptom of bone contusion. The compression fat sequence of MRI (pdw-fs or t2wi-fs) has unique benefits for the diagnosis of bone marrow edema due to its high sensitivity and specificity [18–20] and is the best approach for the detection of bone marrow edema. As a result, MRA outperforms CTA when it comes to detecting bone marrow edema. The implementation of a predictive control method based on deep learning [21, 22] onto the orthopedic diagnosis of patients may prove to be an effective technique in the future. Due to the limitation of resolution, CTA shows poor cartilage structure, and the free cartilage slices with equal density are easy to be covered under the background of white contrast agent in the joint cavity. However, due to the good soft tissue resolution, hyaluronic cartilage rich in water shows equal or slightly higher gray signals in MRI images. MRA can directly observe articular cartilage. When cartilage has cracks or defects, the entry of high signal contrast agent will set off the contrast of the wound surface, and the gray-free cartilage tablets will not be difficult to show under the contrast of contrast agent in the articular cavity. Therefore, MRA is more advantageous than CTA for cartilage injury.

5. Conclusion

In conclusion, for the diagnosis of anterior dislocation of shoulder, MRA is superior to CTA. MRA plus CT examination is the best combination of preoperative imaging examination. If the patient cannot undergo MRA examination, CTA examination can be used as an alternative to provide some valuable diagnostic information.

Data Availability

Data available on request from the authors due to privacy/ethical restrictions.

Conflicts of Interest

The authors declare no conflict of interest for this paper.

References

[1] A. M. Beason, R. J. Koehler, R. A. Sanders et al., "Surgeon agreement on the presence of pathologic anterior instability on shoulder imaging studies[J]," *Orthopaedic Journal of Sports Medicine*, vol. 7, no. 8, p. 2325967119862501, 2019.

[2] J. H. Stevenson and T. Trojian, "MRI evaluation of shoulder joint pain," *Journal of Practical Radiology*, vol. 21, no. 9, pp. 940–942, 2005.

[3] C. S. Lee, S. M. Davis, C. McGroder et al., "Analysis of low-field MRI scanners for evaluation of shoulder pathology based on arthroscopy," *Orthopaedic Journal of Sports Medicine*, vol. 2, no. 7, article 2325967114540407, 2014.

[4] T. Liu, J. Ma, H. Cao, D. Hou, and L. Xu, "Evaluation of the diagnostic performance of the simple method of computed tomography in the assessment of patients with shoulder instability: a prospective cohort study," *BMC Med Imaging*, vol. 18, no. 1, 2018.

[5] J. H. Assunção, E. A. Malavolta, F. J. de Souza, M. E. C. Gracitelli, and A. A. Ferreira, "Anterior glenohumeral instability: systematic review of outcomes assessment used in brazil," *Revista Brasileira de Ortopedia*, vol. 54, no. 5, pp. 483–490, 2019.

[6] A. Bozzo, C. Oitment, P. Thornley et al., "Humeral avulsion of the glenohumeral ligament: indications for surgical treatment and outcomes—a systematic review [J].Orthop," *The Journal of Sports Medicine*, vol. 5, no. 8, p. 232596711772332, 2017.

[7] M. Jana and S. Gamanagatti, "Magnetic resonance imaging in glenohumeral instability [J].World," *Journal de Radiologie*, vol. 3, no. 9, pp. 224–232, 2011.

[8] A. J. Kompel, X. Li, A. Guermazi, and A. M. Murakami, "Radiographic evaluation of patients with anterior shoulder instability," *Current Reviews in Musculoskeletal Medicine*, vol. 10, no. 4, pp. 425–433, 2017.

[9] T. Chunyan and Z. Zhuo-Zhao, "Diagnostic value of MR imaging of shoulder joint for anterior and inferior shoulder capsular tear," *Magnetic Resonance Imaging*, vol. 3, no. 4, pp. 250–254, 2012.

[10] X. Lihua, F. Xianmiao, G. Yun et al., "Value of magnetic resonance shoulder arthrography in the evaluation of articular labrum injury," *Journal of Applied Medical Imaging*, vol. 19, no. 4, pp. 285–288, 2018.

[11] C. U. I. Zheng Zhuo-zhao and F. A. N. J. Guoqing, "Diagnostic value of MR imaging of shoulder joint for anterior labrum lesions," *Chinese journal of radiology*, vol. 40, no. 9, pp. 941–944, 2006.

[12] M. Jarraya, F. W. Roemer, H. I. Gale, P. Landreau, P. D'Hooghe, and A. Guermazi, "MR-arthrography and CT-arthrography in sports-related glenolabral injuries: a matched descriptive illustration," *Insights Into Imaging*, vol. 7, no. 2, pp. 167–177, 2016.

[13] N. I. Yang Chaoxiang and D. B. Caifang, "Application of magnetic resonance imaging in the diagnosis of shoulder joint diseases," *Journal of practical radiology*, vol. 19, no. 5, pp. 467–470, 2003.

[14] F. Fallahi, N. Green, S. Gadde, L. Jeavons, P. Armstrong, and L. Jonker, "Indirect magnetic resonance arthrography of the shoulder; a reliable diagnostic tool for investigation of suspected labral pathology," *Skeletal Radiology*, vol. 42, no. 9, pp. 1225–1233, 2013.

[15] J. K. Stewart, D. C. Taylor, and E. N. Vinson, "Magnetic resonance imaging and clinical features of glenoid labral flap tears," *Skeletal Radiology*, vol. 46, no. 8, pp. 1095–1100, 2017.

[16] S. Acid, T. Le Corroller, R. Aswad, V. Pauly, and P. Champsaur, "Preoperative imaging of anterior shoulder instability: diagnostic effectiveness of MDCT arthrography and comparison with MR arthrography and arthroscopy," *AJR. American Journal of Roentgenology*, vol. 198, no. 3, pp. 661–667, 2012.

[17] M. Yoneda, K. Izawa, S. Wakitani, S. Nakasato, K. Hayashida, and S. Nakagawa, "Diagnostic imaging of unstable superior glenoid labral detachment: a comparison between MR arthrography and unenhanced MRI," *Modern Rheumatology*, vol. 11, no. 2, pp. 140–144, 2001.

[18] M. Hantes and V. Raoulis, "Arthroscopic findings in anterior shoulder instability," *The Open Orthopaedics Journal*, vol. 11, no. 1, pp. 119–132, 2017.

[19] M. K. Mahmoud, Y. M. Badran, H. G. Zaki, and A. H. Ali, "One-shot MR and MDCT arthrography of shoulder lesions with arthroscopic correlation," *Egyptian Journal of Radiology and Nuclear Medicine*, vol. 44, no. 2, pp. 273–281, 2013.

[20] P. Baudi, M. Rebuzzi, G. Matino, and F. Catani, "Imaging of the unstable shoulder," *The Open Orthopaedics Journal*, vol. 11, no. 1, pp. 882–896, 2017.

[21] Z. Tang and Z. Zhang, "The multi-objective optimization of combustion system operations based on deep data-driven models," *Energy*, vol. 182, pp. 37–47, 2019.

[22] Z. H. Tang, Y. Y. Li, X. Y. Chai, H. Y. Zhang, and S. X. Cao, "Adaptive nonlinear model predictive control of NOx emissions under load constraints in power plant boilers," *Journal of Chemical Engineering of Japan*, vol. 53, no. 1, pp. 36–44, 2020.

Hindawi
Computational and Mathematical Methods in Medicine
Volume 2022, Article ID 4909294, 10 pages
https://doi.org/10.1155/2022/4909294

Research Article

A Novel Psychotherapy Effect Detector of Public Art Based on ResNet and EEG Imaging

Tingyi Tian,[1] **Le Wang**,[2,3] **Man Luo**,[1] **and Wei Zhu**[1]

[1]*School of Art and Design, Shanghai University of Engineering Science, Shanghai 201620, China*
[2]*Department of Design, National Taiwan Normal University, Taipei, Taiwan*
[3]*Product Design and Development Laboratory, Taiwan*

Correspondence should be addressed to Tingyi Tian; 07180011@sues.edu.cn

Received 18 January 2022; Revised 8 February 2022; Accepted 27 February 2022; Published 7 April 2022

Academic Editor: Kelvin Wong

Background and Objective. In view of the imperfection of the current public art evaluation system and practical utility detection system, this paper designs and invents a psychotherapy effect detector of public art based on ResNet network and EEG imaging. The detector includes sensor signal acquisition unit, signal storage and transmission unit, and human-computer interaction visualization unit. The detector is designed in order to test the psychotherapy effect of public art and quantify the public's evaluation of public art to improve the public art evaluation system. *Methods*. The EEG emotion dataset seed is used for feature extraction with DE, and the emotion is recognized by ResNet. Adam optimizer is used to classify the extracted DE through ResNet50 model. Each batch is set as 5 groups of data and is trained for 50 rounds, then the model is optimized, and the accuracy rate is 76.47%, which output the probability of good emotion through the model. We put the model optimized by ResNet into the intelligent module and visualize it with numerical value. *Results*. The detector designed by EEG data and ResNet50 optimization model has high accuracy. The results show that the error between the detector data and the questionnaire interview data is small, the average error is 2.77, and the accuracy is 97%. The closer the subject's emotion before the test is to neutral emotion, the closer the questionnaire result is to the test result of the tester, and the smaller the error is. The difference between the tester data and the survey questionnaire data is 0.2, which is in good agreement and has small error. It can be seen that the detector has high accuracy. *Conclusion*. Our proposed public art psychotherapy effect detector has good accuracy in detecting users' emotions. It can detect the group psychotherapy effect of public art and can classify and screen a large number of public arts in the city by quantitative methods. It provides support for further summarizing the practical utility of public art and provides a new way for the optimal design and follow-up evaluation of public art design.

1. Introduction

The development of public art today has developed greatly in both scale and quality. In recent years, public art has become an important part of people's living space because of its characteristics of multilevel, multistage, multiconnotation, multiform, and participation. More than 300 cities in North America will legislate for public art. With the complexity and diversification of social needs, public art research began to focus on exploring its effectiveness in the regulation and relief of spirit and emotion. Human participation in creative cultural activities is conducive to mental health and emotional regulation, as well as the transmission of health information and the enhancement of social tolerance [1]. Participatory art also has potential benefits for mental health [2]. Participation is not only a way to express and release but also a way for people to adjust their inner emotions and change space scenes. In the production of public art, it forms resonance based on human emotion [3]. This empathy and resonance are a means for public art to have an impact on people's spirit and psychology. Moreover, public art has the function of social psychological intervention. It stimulates the public's psychological reflection and acceptance through some art form. Many theoretical studies have

proved that public art has a certain effect on emotional regulation and psychotherapy.

The evaluation of public art psychotherapy effect has been a qualitative study in previous studies. Most are evaluated by artists, designers, or government departments and organizations that invest in public art. The feedback by public participation is basically in the form of interview, which is highly subjective. More subjective evaluation is not conducive to the establishment of evaluation system and the optimization of public art design principles. With the rapid development of artificial intelligence, emotion recognition computing technology can recognize the changes of emotion from the technical level and classify. Emotion is people's attitude experience and corresponding behavior response to objective things. It is also a psychological phenomenon mediated by individual needs, wishes, and other tendencies [4].

Therefore, identifying people's emotions when participating in public art can evaluate public art more objectively. In emotion recognition, micro expression information, language voice, posture expression, and physiological signals are important data sources [5]. Among these data sources, EEG signal is the most typical physiological signal, which is difficult to disguise and rich in information. EEG signal is the overall response of electrical activities of nerve cells in the cerebral cortex or scalp surface, which contains a lot of physiological and pathological information [6]. The fluctuation of emotion will have an impact on the physiological signals of the body and will inevitably have a corresponding impact on the brain waves [7]. Therefore, by collecting and analyzing EEG signals, we can intuitively and accurately judge the physiological and psychological state of the human body. Lin et al. [8] used convolutional neural network to collect a variety of human physiological parameters through wearable devices and tried to send different control commands to the manipulator according to the changes of emotion. Naima and Canny [9] detected human EMG, ECG, blood oxygen saturation, respiratory rate, and exercise status through wearable devices and used artificial intelligence technology to realize real-time monitoring of personal physical and mental health. Pan et al. [10] trained the model based on EEG signals and convolutional neural network to classify emotions. The key problem of EEG signal analysis is feature extraction. In emotion recognition, EEG signal features are mainly extracted from time-domain features [11], frequency-domain features [12], time-frequency-domain features [13], nonlinear dynamic analysis [14], spatial domain features [15], and so on. At the same time, in previous studies, sensor-based consciousness and emotion awareness basically realized an efficient and natural human-computer interaction [16]. However, there is little research on the application of this method in the field of public art.

This paper attempts to solve the problem that the public's evaluation on public art stays at the stage of large subjective factors, which is based on the research basis of emotion recognition and classification by the combination of artificial intelligence and sensors, so as to make it have an objective and quantitative evaluation method. Therefore, this paper proposes to collect EEG data, analyze the data through convolution neural network and ResNet model, and visualize human-computer interaction, so as to complete the detection of public art psychotherapy effect and achieve the objectivity of public art social evaluation at the same time. The public art psychotherapy effect detector designed in this paper not only provides a scheme for the measurement of the practical utility of public art but also provides a method for the evaluation of a large number of existing public art in the city, so as to promote the design of public art to have more practical effects.

2. Methodology

2.1. Residual Neural Network. Residual neural network [17] has achieved excellent results in many competitions in the field of visual recognition. We know that the greater the complexity of the model is, the higher the accuracy will be, but this does not mean that the more complex the model is, the higher the efficiency of improving the accuracy will be. "Moore's law" [18] also appears in deep learning, that is, with the increase of the number of layers of the model, it will cost more to improve the accuracy a little later. Because with the increase of the number of model layers, it is bound to bring huge consumption of computing resources, and there will be the problem of "gradient disappearance."

ResNet solves the problem of "gradient disappearance" [19] which is also an important reason why this paper uses ResNet for experiments. ResNet is developed on the basis of VGG19. It adds residual unit through short circuit mechanism, directly uses convolution with step size of 2 for down sampling, and replaces the full connection layer with Global Average Pooling (GAP) layer. In the ResNet model, two residual elements are mainly used, as shown in Figure 1. The build block on the left corresponds to the shallow network, while the bottleneck block on the right corresponds to the deep network. There are two paths for the input information. The first is identity mapping. Identity mapping ensures that the learned information is completely saved. If improvement is needed, it is carried out in the direct mapping, that is, $f(x)$ In. The better $f(x)$ changes the information between blocks, the better the performance of the model.

The purpose of residual structure is to make the neural network retain the ability of basic identity mapping. This ability can ensure that the network training results will not degrade with the stacking of networks. Assuming that the input parameter of the neural network is x, the target output is $h(x)$, and the internal structure of $H(x)$ may not be clearly expressed. ResNet allows the residual $f(x) = H(x) - x$ directly learned by the submodule to make the target output $F(x) + X$, which avoids the performance degradation and accuracy degradation caused by too many convolution layers. The structure on the right belongs to the shortcut connection. Through the shortcut operation before activating the function, add the output before this layer and the output after passing through the network of this layer, and send the added value to the activation function to obtain the total output of this layer. ResNet has a shortcut

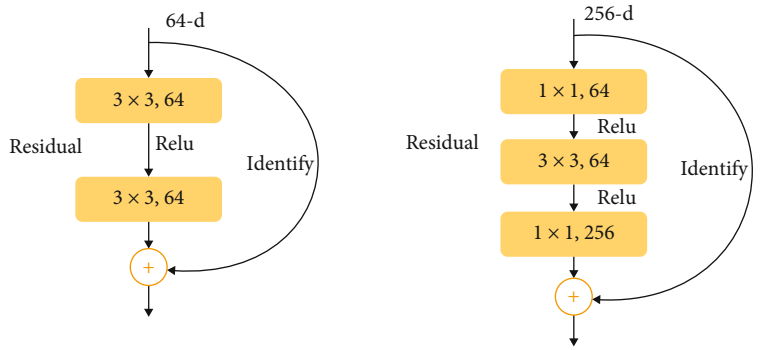

Figure 1: Two residual elements.

connection; assuming that the input is x, the output y is

$$y = F(x, \{W_i\}) + x. \tag{1}$$

The relationship between the normal data input and the output obtained by the neural network is as follows. Since there is an activation function ReLU in the middle, considering the double-layer weight, there are

$$F = W_z\sigma(W_1x). \tag{2}$$

Generally, the activation function ReLU is used to increase the nonlinearity and associate the weights $W1$ and $W2$ of the function and structure layers. Changing the number of channels can change the dimensions of the input data and output data of the signal. Here, when shorting, make a linear transformation WS for X, as follows:

$$F = W_z\sigma(W_1x). \tag{3}$$

In this paper, ResNet50 network model is selected for image feature extraction, precisely because ResNet network has long been widely used in image feature extraction in various fields, and the residual module in ResNet50 residual neural network can effectively solve the degradation problem with the deepening of the network, as well as the problem of insufficient learning ability of the model with shallow network layers and poor effect of feature extraction. Figure 2 is a structure diagram of ResNet50 network. The whole network structure is divided into 50 layers and consists of four large modules: the first large module has three small modules, the second large module has four small modules, the third large module has six small modules, and the fourth large module has three small modules, in which each small module is composed of three convolution cores. The convolution layer of the first layer and the full connection layer of the last layer of the network are added to constitute a 50-layer network structure.

2.2. EEG Sensor Data Acquisition. Emotion recognition of EEG signals mainly includes five basic steps [20], as shown in Figure 3.

EEG signal is an extremely weak physiological signal (with amplitude at microvolt level). In the acquisition process, it will not only be disturbed by EEG data acquisition equipment and external environment but also be affected by some physiological factors of the human body, such as eye electricity and electromyography [21]. At the same time, the current physiological and psychological state of the tester will also affect the acquisition of EEG signals. A large number of artifact signals will increase the difficulty of EEG signal analysis, and it is difficult to intuitively analyze the internal relationship with emotion. In order to facilitate the follow-up research, the collected signals are preprocessed. Through this preliminary processing, the signals with certain laws can be obtained [22].

2.3. Database. SEED [23] public database was used in this experiment [24]. This dataset has the largest number of EEG acquisition channels, with 62 channels of EEG collected from 15 subjects. Participants were asked to watch a video of positive/negative/neutral emotions for about four minutes each, and the corresponding electrical signals were recorded. The dataset has a longer duration used for emotionally stimulating videos, which is more conducive to the emotional expression of subjects, and its classification accuracy is higher than other public databases.

The database data were obtained by selecting 15 film clips (positive, neutral, and negative emotions) from the library as stimuli used in the experiment. Stimulants (film clips) were selected according to the following criteria: (a) the length of the entire experiment should not be too long to avoid subject fatigue; (b) the video can be understood without explanation; (c) the video should elicit a single target emotion. Each film clip lasts about four minutes, and each film clip is carefully edited to create coherent emotion and maximize emotional meaning [25]. There were 15 experiments in each experiment. There is a 5-second prompt before each clip, a 45-second self-assessment, and a 15-second break after each clip in a session. The order of presentation is arranged in such a way that two movie clips targeting the same emotion are not played consecutively. To get feedback, participants were told to report their emotional response to each film clip by completing a questionnaire immediately after watching each clip [26]. The detailed process is shown in Figure 4.

In the SEED database's "Preprocessed_EEG" folder, there are files that contain downsampled, preprocessed,

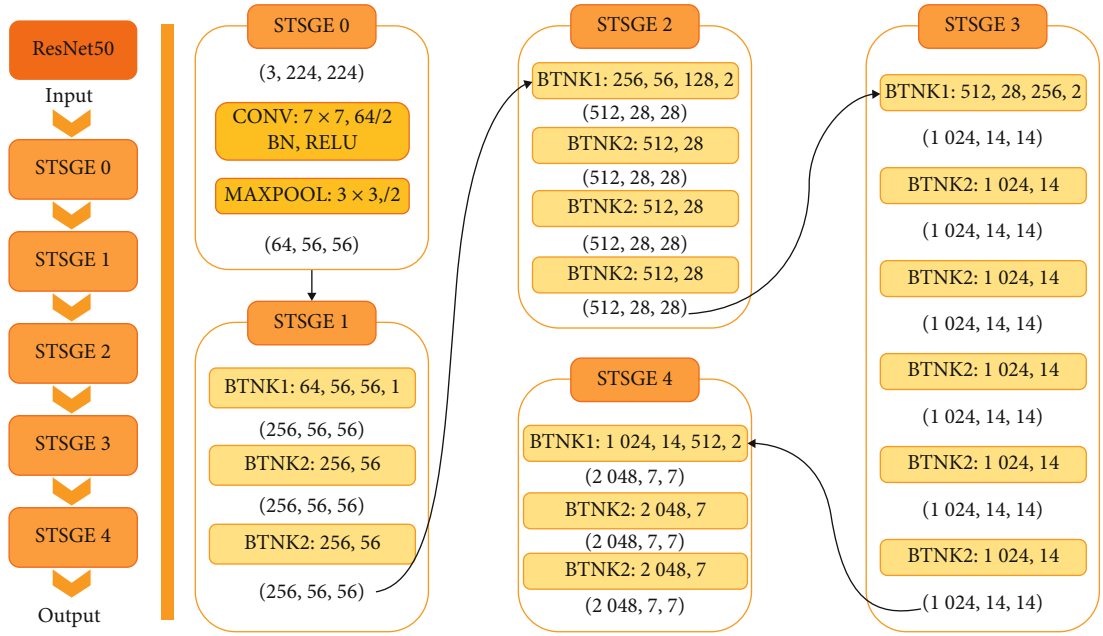

Figure 2: ResNet50 network architecture.

Figure 3: Main steps of EEG emotion recognition.

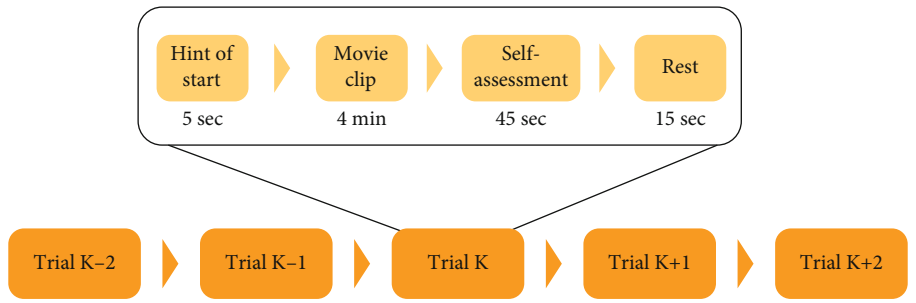

Figure 4: SEED data acquisition experiment process.

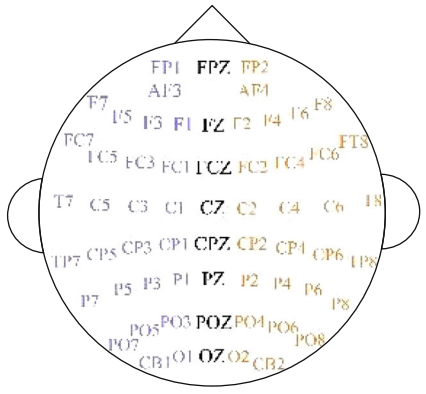

Figure 5: International standard 10-20 system 62-channel EEG.

and segmented versions (.mat) of EEG data in MATLAB. The data is downsampled to 200 Hz. A bandpass frequency filter of 0-75 Hz is applied. In this design, EEG segments corresponding to the duration of each film were extracted. There are 45 .mat files (MATLAB files), in which one file matches each experiment. Each subject underwent 3 experiments, with an interval of about 1 week. Each topic file contains 16 arrays. The 15 arrays contain segmented preprocessed EEG data (EEG_1 to EEG_15, channel × data) for 15 trials in one experiment. The array name tag contains the tag for the corresponding emotion tag (-1 for negative, 0 for neutral, and +1 for positive). The detailed order of channels is contained in the dataset, as shown in Figure 5.

SEED data is an EEG dataset used to analyze human emotion. The dataset collected and recorded the EEG signal data of 15 human subjects (7 males and 8 females) when

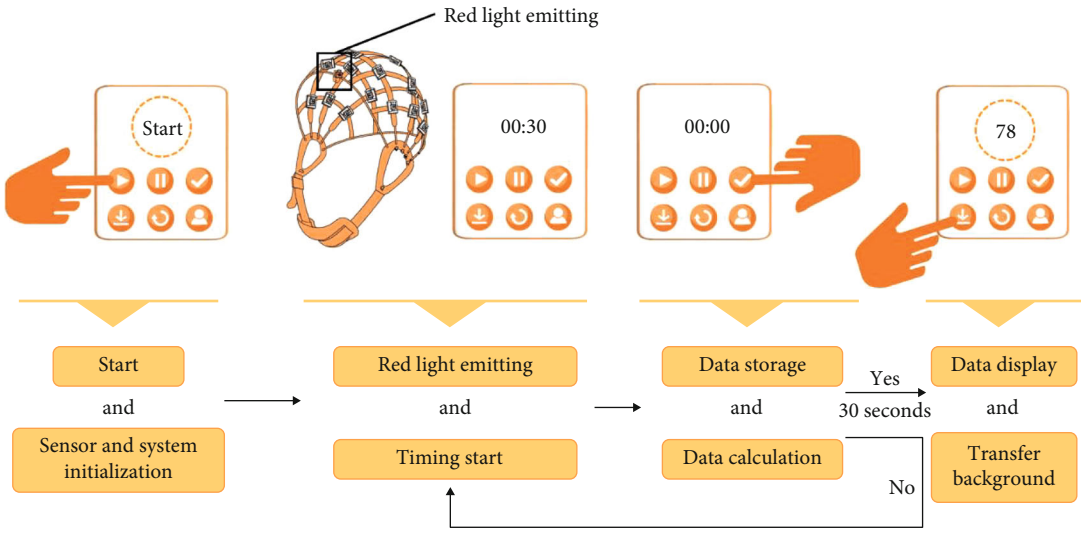

Figure 6: Workflow of detector.

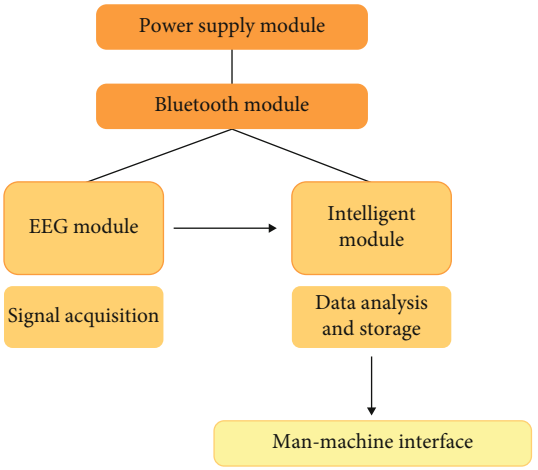

Figure 7: Sensor module system structure.

they watched videos with obvious emotional stimulation effect for about 4 minutes, so as to analyze the relationship between their emotional changes and EEG signal. In order to ensure the reliability of the test results, 15 subjects were tested in three different periods of time, watching 15 videos, respectively, in each test, and recording the changes of EEG signals. Related data were extracted by MATLAB software, and PS, DDE, DASM, RASM, ASM, and DCUA data were obtained. Previous studies have proved that DE (differential entropy) data has the highest accuracy in emotion recognition [24], so this paper adopts DE data in SEED data for modeling. DE can be expressed by the formula

$$h(X) = -\int_{-\infty}^{\infty} \frac{1}{\sqrt{2\pi\sigma^2}} e^{-(x-\mu)^2/2\sigma^2} \log\left(\frac{1}{\sqrt{2\pi\sigma^2}} e^{-(x-\mu)^2/2\sigma^2}\right) dx = \frac{1}{2}\log\left(2\pi e\sigma^2\right). \tag{4}$$

The time series X obeys the Gaussian distribution $n(\mu, \sigma^2)$. In order to remove the components irrelevant to emotion, the linear dynamic system (LDS) [25] method with a window length of 20 s is used to smooth the feature sequence. The data dimension is $62 \times N \times 5$, where 62 represents 62 regions of the brain, N is the length of EEG signal, and 5 represents the corresponding five bands (delta: 1-3 Hz, theta: 4-7 Hz, alpha: 8-13 Hz, beta: 14-30 Hz, and gamma: 31-50 Hz). In this paper, $N = 180$ is uniformly used, that is, the dimension of DE_LDS dataset is $62 \times 180 \times 5$. Finally, the data is unified to reshape a two-dimensional data 224×224. A total of 675 groups of sample data of DE_LDS were obtained. In order to train the model, 675 groups of data were randomly allocated according to the ratio of 9 : 1 between training set and test set, which get 607 training sets and 68 test sets. The model is trained on the training set and the accuracy of the model is tested on the test set.

2.3.1. Standardization. Before entering the model, the data needs to be standardized. In this paper, the minimax standardization method is used to unify the data at the same dimensional level [19]. The formula is as follows:

Pair and sequence $x_1, x_2, x_3, \cdots, x_n$:

$$y_i = \frac{x_1 - \min\{x_1, x_2, x_3, \cdots, x_n\}}{\max\{x_1, x_2, x_3, \cdots, x_n\} - \min\{x_1, x_2, x_3, \cdots, x_n\}}. \tag{5}$$

New sequence $y_1, y_2, y_3, \cdots, \in [0, 1]$.

2.3.2. Loss Function. In the classification task, the loss function mainly used in this paper is the categorical_crossentropy loss, which is defined as

$$C = -\frac{1}{n}\sum_x [y \ln a + (1-y)\ln(1-a)], \tag{6}$$

where "y" is the desired output and "a" is the actual output of the neuron.

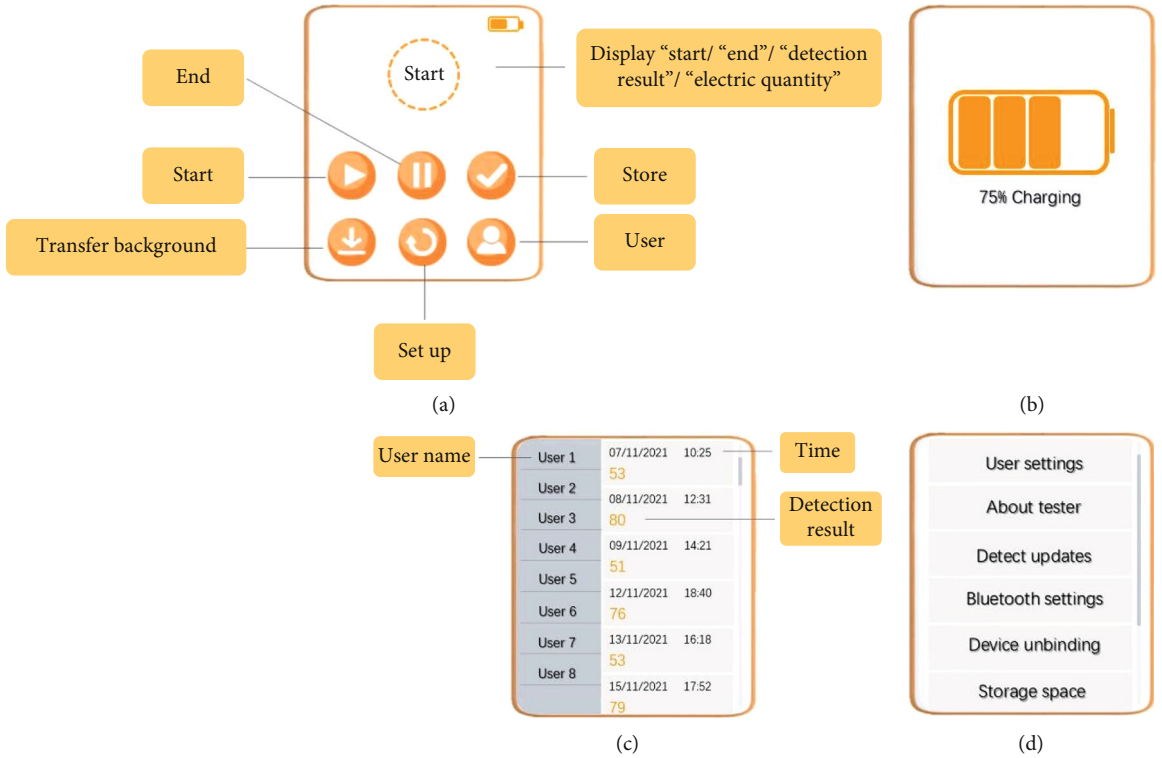

Figure 8: Human-machine interaction interface design description: (a) main interface; (b) charging interface; (c) user information interface; (d) system setting interface.

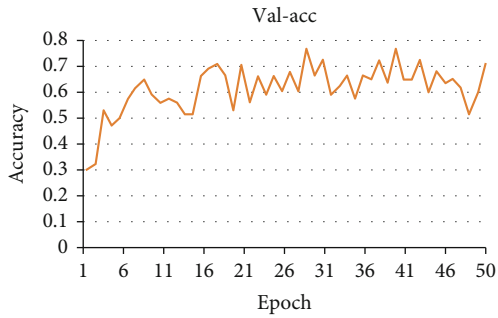

Figure 9: Variation of test accuracy with training epoch.

Table 1: List of selected public art projects.

Number	Name of public art
1	Siping Road "poetry one-way street"
2	Xinhua community public art
3	Public art of Caoyang Baixi Park
4	A move in Linfen community
5	Yangpu Binjiang public art "things outside the sky"

2.3.3. The Activation Function. Activation function is responsible for mapping the input of neurons to the output, which plays a very important role in the fitting of deep learning model. The activation functions mainly used in this paper include ReLU function and Softmax function.

The ReLU function is used in the hidden layer of the model to speed up the learning of the model. Its mathematical formula is as follows:

$$\mathrm{ReLU}(x) = \begin{cases} x & x > 0, \\ 0 & x <= 0. \end{cases} \tag{7}$$

Softmax function is used for the final output of the model. It maps the output of multiple neurons to the $(0, 1)$ interval to carry out multiclassification. Its mathematical formula is as follows:

$$\mathrm{Softmax}(x_i) = \frac{\exp(x_i)}{\sum_{j=1}^{n} \exp(x_j)}, \tag{8}$$

where "x_i" is the output value of the node and "n" is the number of output nodes, that is, the number of categories classified. Through the Softmax function, the output values of multiple classifications can be converted into probability distributions ranging from $[0, 1]$ to 1.

2.4. Human-Computer Interaction (HCI) Detection Design. In this design, EEG wearable devices are used to collect electrical signals from the brain. The sensor module is just like neurons on the human body, sensing the stimulation of external substances all the time. The specific measurement process of this design is as follows: it sets the whole measurement time for 60 s and controls the red light in the sensor to emit light at 200 Hz in the first 30 s, which starts collecting

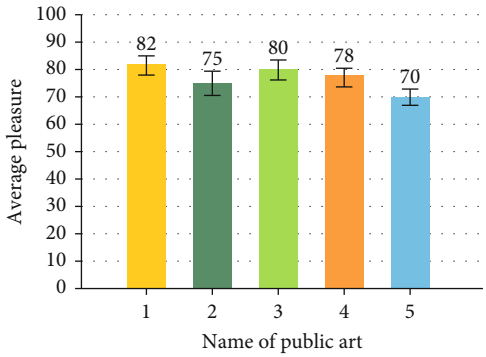

Figure 10: Survey results.

EEG signals at a sampling rate of 200 Hz, that is, collects a signal point every 5 ms and stores the brainwave signals. The working process of the last 30 s is that the EEG signal is transmitted to the human-machine interface module through Bluetooth, and the human-machine interface analyzes and visualizes the data collected by the sensor. The detection workflow is shown in Figure 6.

2.4.1. The Sensing Module. Sensor module is the basis of human-computer interaction and an important part. It includes power module, EEG sensor device, intelligent module, and Bluetooth module. The system structure is shown in Figure 7.

2.4.2. Human-Machine Interface. In the HCI interface, based on the intelligent module, the data samples were extracted from the difference entropy (DE) feature and analyzed in the emotion classification model module by preprocessing the collected data. The design established the emotion classification model module through the ResNet50 model and SEED public database to achieve the emotion classification and visual display to detect the user's emotional state. HCI interface is shown in Figure 8.

3. Results

3.1. ResNet50 Network Training. In this paper, Adam optimizer is used, and the learning rate is set as the default parameter. By entering the data into the model in batches, each batch is set as 5 groups of data, and a total of 50 rounds are trained. After each round, the accuracy test (accuracy) of the model is carried out through the test set, in which the accuracy changes with rounds, as shown in Figure 9.

The experimental results show that the model with the highest accuracy rate is the 39th round of training, and its accuracy rate can reach 0.7647. Therefore, the 39th round model is finally determined as the final model in this design. For better visualization, in the model, the higher the probability is set, the higher the pleasure is, which is a good emotion. The lower the probability is set, the lower the degree of pleasure is, which is a bad emotion, and the middle value is neutral emotion.

3.2. Human Testing Experiment. The detector can detect in the normal active state of nonstationary, but it is not suitable for detection in the state of running and vigorous exercise. Five public arts in Shanghai were selected for the test experiment, as shown in Table 1. These public arts chosen for the test are the works in Shanghai's 2019 and 2021 city space art season, which has the most reading volume on the WeChat official account. Before the experiment, 30 questionnaires were conducted on the pleasure degree generated by the five public art projects. The pleasure degree was set to 1-100. The higher the value is, the higher the pleasure degree is. A total of 28 valid questionnaires were collected and averaged. The survey results show that among the five public arts, public art no. 1 has the highest pleasure, with a value of 82. The public art is set in the community and has strong participation; public art no. 5 has the lowest pleasure with a value of 70. This public art is a large sculpture in Yangpu Binjiang Park. The pleasure degree of each public art project is shown in Figure 10.

Another 6 people were tested to wear the detector. The subjects were between 25 and 40 years old. The nature of work was civil servants, public institutions, teachers, financial industry, and computer industry, and everyone wore the detector one time in work or life before the experiment. They wore the detector once when appreciating or participating one of the five public arts selected in the experiment. The value displayed by the tester was 1-100. The higher the value is, the higher the pleasure is. The two rounds of test results are shown in Figure 11.

The experimental results show that the error between the test data and the questionnaire interview data is small, the average error is 2.77, and the accuracy is 97%; it shows that the accuracy of the tester is high. In the experiment, the closer the subjects' emotion before the test is to neutral emotion, the closer the questionnaire results are to the test results of the detector, and the smaller the error is. According to the data of the tester, the average pleasure improvement value of 6 subjects in public art no. 1 is 34.2, and the average pleasure improvement value of public art no. 5 is 22, with a difference of 12.2. The results of the questionnaire show that the average pleasure of no. 1 public art is 82 and that of no. 5 public art is 70 with a difference of 12. It can be seen that the error between the experimental results and the results of the questionnaire is small, and the difference is 0.2.

4. Discussion

In the past, public art was mainly evaluated from the perspective of designers, artists, and government investors. There are fewer evaluations from the public, and the evaluations mainly adopt the form of interview, which was highly subjective. And there is no measurable method to determine whether a large number of public arts in cities have practical utility. The public art psychotherapy effect detector based on ResNet network and EEG sensor designed in this paper can collect more objective people's feelings about public art and classify the good, neutral, and bad emotions generated by public art through emotion recognition, which evaluates

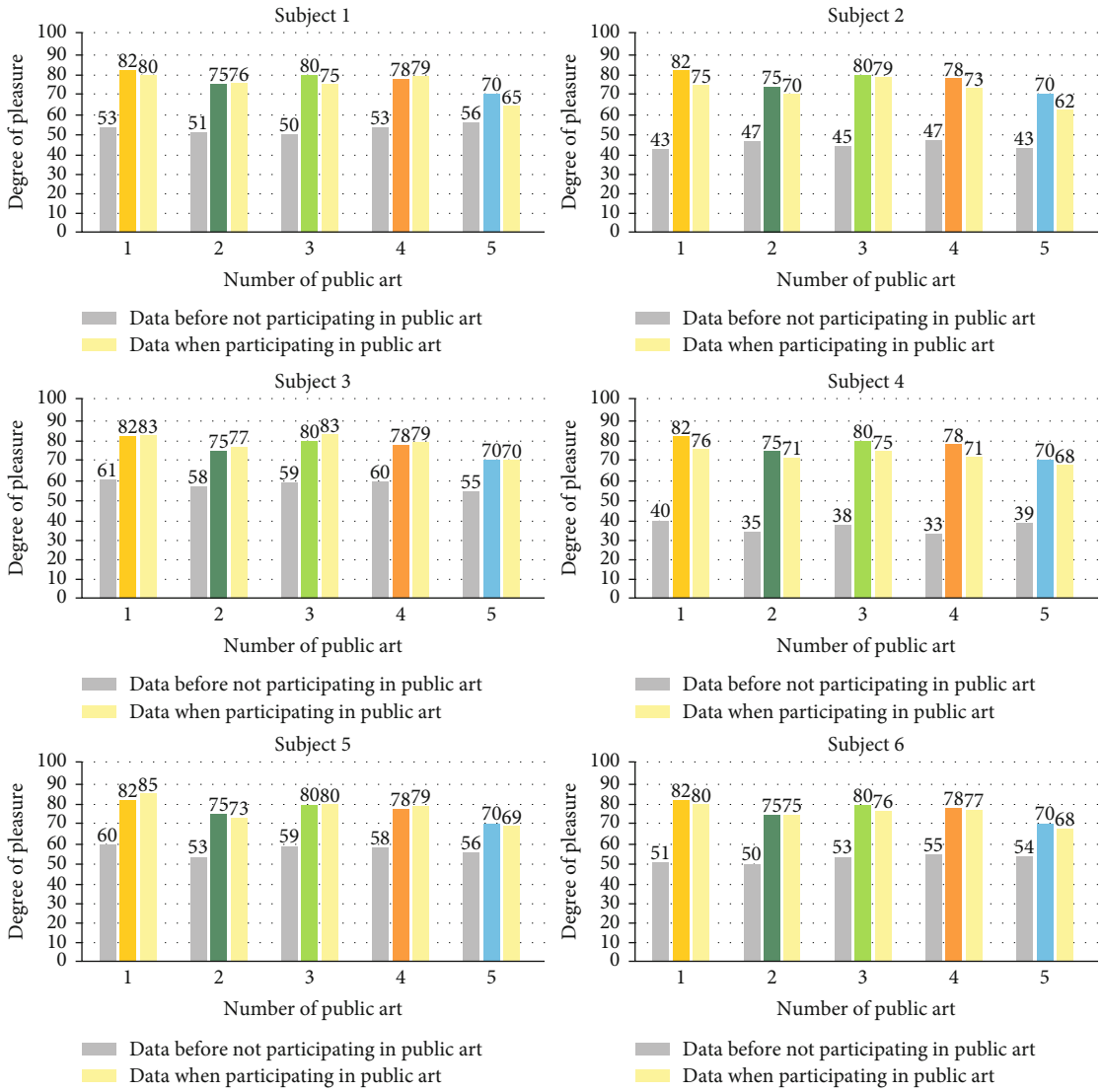

Figure 11: Results of two rounds of data of 6 subjects.

the public art psychotherapy effect at the same time. Therefore, it has certain innovation.

The model designed in this paper adopts SEED public data, which is optimized by ResNet50 model, ReLU function and Softmax function activation, and Adam optimizer. Finally, the intensive reading of model recognition reaches 76.47%.

The psychotherapy effect of public art can be tested by comparing the data wearing the detector in normal state with the data when participating in public art. Although individual differences and the emotional state before the test are variable factors, the detector shows high accuracy by comparing the test results of the same public art with the questionnaire results of different subjects, Therefore, the effects of different public art psychotherapy can be tested. In addition, by comparing the test results of different public arts with the questionnaire results of the same subjects, the detector also showed high accuracy. Therefore, the psychological healing effects of different public arts can be evaluated and analyzed, which has certain practicability.

The detector designed in this paper also has some limitations. First, the model training uses a public database, so the data acquisition of the detector needs to use the same acquisition channel as the data of SEED database. Second, this experiment analyzes EEG data, but other physiological data can also carry out emotion analysis, but multisensor will bring greater difficulty to data analysis. In the follow-up upgrading research of detector, we will try to use multisensor.

5. Conclusion

The development of efficient machine learning algorithms and the creation of ubiquitous wearable technologies make emotional interaction possible and have a quantifiable and detectable data acquisition method. The public art psychotherapy effect detector based on ResNet network and EEG sensor has good accuracy in detecting users' emotions and can detect the group psychotherapy effect of public art. Therefore, it can classify and screen a large number of public

arts in the city by quantitative methods. It provides support for further summarizing the practical utility of public art and provides a new way for the optimal design and follow-up evaluation of public art design.

Data Availability

Data are available on request from the authors due to privacy/ethical restrictions.

Consent

All human subjects in this study gave their consent for the participation in the research. Signed informed consent for publication was obtained from all authors.

Conflicts of Interest

The authors declare no conflicts of interest.

Acknowledgments

The authors thank all members who contributed to this research. The study was supported by the General Topics of Shanghai Philosophy and Social Sciences Planning in 2020 (2020BWY028) and supported by the Youth Scientific Research Team Cultivation Program of Shanghai University of Engineering Science (QNTD202109).

References

[1] D. Węziak-Białowolska, "Attendance of cultural events and involvement with the arts–impact evaluation on health and well-being from a Swiss household panel survey," *Public Health*, vol. 139, pp. 161–169, 2016.

[2] N. V. Mohatt, B. A. Hunter, S. L. Matlin, J. Golden, A. C. Evans, and J. K. Tebes, "From recovery-oriented care to public health: case studies of participatory public art as a pathway to wellness for persons with behavioral health challenges," *Journal of psychosocial rehabilitation and mental health*, vol. 2, no. 1, pp. 9–18, 2015.

[3] J. M. Palmer, "The resonances of public art: thoughts on the notion of co-productive acts and public art," *City & Society*, vol. 30, no. 1, pp. 68–88, 2018.

[4] X. T. Huang, *Introduction to Psychology*, Beijing: Peoples Education Press, 1991.

[5] G. Zhao, J. Song, Y. Ge, Y. Liu, L. Yao, and T. Wen, "Advances in emotion recognition based on physiological big data," *Computer Research and Development*, vol. 53, no. 1, pp. 80–92, 2016.

[6] Y. Li, *J.EEG signal analysis method and its application*, Beijing: Science Press, 2009.

[7] J. H. Chen, L. Li, and K. X. Qian, "Emotion recognition based on multiple physiological signals," *Journal of Biomedical Engineering Research*, vol. 25, no. 3, pp. 141–146, 2006.

[8] W. Q. Lin, "Emotion recognition and interaction application driven by physiological signal," *Hangzhou: Zhejiang University*, 2019.

[9] R. Naima and J. Canny, *The Berkeley Tricorder: Ambulatory Health Monitoring*, Piscataway, 2009.

[10] C. Pan, C. Shi, H. Mu, J. Li, and X. Gao, "EEG-based emotion recognition using logistic regression with Gaussian kernel and Laplacian prior and investigation of critical frequency bands," *Applied Sciences*, vol. 10, no. 5, pp. 1619–1642, 2020.

[11] N. Zhuang, Y. Zeng, L. Tong, C. Zhang, H. Zhang, and B. Yan, "Emotion recognition from EEG signals using multidimensional information in EMD domain," *Bio Med Research International*, vol. 2017, pp. 1–9, 2017.

[12] B. Xing, H. Zhang, K. Zhang et al., "Exploiting EEG signals and audiovisual feature fusion for video emotion recognition," *IEEE Access*, vol. 7, pp. 59844–59861, 2019.

[13] Z. Sun and C. C. Chang, "Structural damage assessment based on wavelet packet transform," *Journal of Structural Engineering*, vol. 128, no. 10, pp. 1354–1361, 2002.

[14] S. C. Li, H. Wang, H. B. Zhao et al., "Research on continuous detection method of EEG chaotic dimension complexity," *Chinese Journal of Biomedical Engineering*, vol. 28, no. 6, pp. 846–850, 2009.

[15] H. Chao, L. Dong, Y. L. Liu, and B. Lu, "Improved deep feature learning by synchronization measurements for multi- channel EEG emotion recognition," *Complexity*, vol. 2020, 15 pages, 2020.

[16] Y. Zhang, X. M. Ji, and S. H. Zhang, "An approach to EEG-based emotion recognition using combined feature extraction method," *Neuroscience letters*, vol. 633, pp. 152–157, 2016.

[17] C. Szegedy, S. Ioffe, V. Vanhoucke, and A. A. Alemi, "Inception-v4, Inception-Res Net and the Impact of Residual Connections on Learning," in *Thirty-first AAAI conference on artificial intelligence*, pp. 4278–4284, San Francisco, California, USA, 2016.

[18] C. Lattner, M. Amini, U. Bondhugula et al., "MLIR: a compiler infrastructure for the end of moore's law," 2020, https://arxiv.org/abs/2002.11054.

[19] K. He, X. Zhang, S. Ren, and J. Sun, "Deepresidual learning for im- age recognition," in *IEEE Conference on Computer Vision and Pattern Recognition*, pp. 770–778, Las Vegas, USA, 2016.

[20] M. Z. Ilyas, P. Saad, and M. I. Ahmad, "A survey of analysis and classifica- tion of EEG signals for brain-computer interfaces," in *2nd International Conference on Biomedical Engineering*, Penang, Malaysia, 2015.

[21] T. Liu and D. Yao, "Removal of the ocular artifacts from EEG data using a cascaded spatiotemporal processing," *Computer Methods and Programs in Biomedicine*, vol. 83, no. 2, pp. 95–103, 2006.

[22] M. Rajyalakshmi, T. V. Prasad, and V. C. Prasad, "Survey on EEG signal processing methods," *International Journal of Advanced Re- search in Computer Science and Software Engineering*, vol. 4, no. 1, pp. 84–91, 2014.

[23] W. Zheng and B. Lu, "Investigating critical frequency bands and channels for EEG-based emotion recognition with deep neural networks," *IEEE Transactions on Autonomous Mental Development*, vol. 7, no. 3, pp. 162–175, 2015.

[24] R. Duan, J. Zhu, and B. Lu, "Differential entropy feature for EEG-based emotion classification," in *6th International IEEE/EMBS Conference on Neural Engineering*, pp. 81–84, San Diego, 2013.

[25] L.-C. Shi and B.-L. Lu, "Off-line and on-line vigilance estimation based on linear dynamical system and manifold learning,"

in *Annual International Conference of the IEEE Engineering in Medicine and Biology*, pp. 6587–6590, Buenos Aires, Argentina, 2010.

[26] Z. H. Tang, Y. Y. Li, X. Y. Chai, H. Y. Zhang, and S. X. Cao, "Adaptive nonlinear model predictive control of NOx emissions under load constraints in power plant boilers," *Journal of Chemical Engineering of Japan*, vol. 53, no. 1, pp. 36–44, 2020.

Hindawi
Computational and Mathematical Methods in Medicine
Volume 2022, Article ID 9005792, 7 pages
https://doi.org/10.1155/2022/9005792

Research Article

The Effect of Acupuncture on Elbow Joint Sports Injuries Based on Magnetic Resonance Imaging

Weihua Yang[1] **and Fei Wang**[2]

[1]*Xinxiang University, Xinxiang Henan 453003, China*
[2]*Hainan General Hospital, Haikou Hainan 570311, China*

Correspondence should be addressed to Weihua Yang; xxxyyangweihua@126.com

Received 19 January 2022; Revised 2 March 2022; Accepted 23 March 2022; Published 4 April 2022

Academic Editor: Kelvin Wong

Purpose. Elbow joint injuries are extremely common in most athletes. Athletes' chronic elbow injuries can involve multiple complex anatomical structures related to orthopedics. Therefore, it is of great significance to explore the characteristics of magnetic resonance (MR) images of chronic sports injuries of the elbow joint and the influence of acupuncture treatment on MR images and clinical symptoms. *Methods*. A total of 60 elbow joints of 39 athletes from 15-25 years old were selected for coronal, sagittal, and axial MR scans to observe the image characteristics; 60 elbow joints were randomly divided into acupuncture group and control group and observed changes in MR images and clinical symptoms after acupuncture treatment. *Results*. After acupuncture treatment, the clinical symptoms were significantly improved. MR images showed that the elbow joint effusion was reduced, and the bone marrow edema was reduced. The effective rate of acupuncture treatment is as high as 100%, while the effective rate of the control group is only 40%. Acupuncture treatment has significantly improved the range of motion of the elbow joint. *Conclusion*. Acupuncture treatment can significantly relieve athletes' elbow joint pain and locking symptoms, improve joint range of motion, and is beneficial to recovery of special training and high-level competitive competitions. It is a sensitive, effective, and noninvasive method.

1. Introduction

With the continuous development of modern competitive gymnastics, athletes' injuries also occur frequently, which seriously affects the normal systematic training of athletes. Competitive gymnasts' injuries mostly occur in the wrist, ankle, and elbow joints, and the ankle joint has the highest injury rate. The elbow joint is one of the most important joints in the human body, and it is also the joint that experiences the greatest load, the most unstable and easy to be injured in the whole body joints [1]. Therefore, this paper analyzes and discusses the mechanism, prevention, treatment, and rehabilitation training of elbow joint injury and aims to provide theoretical basis for the teaching and training of competitive gymnastics.

Early diagnosis of sports injuries and how to extend the sports life span of athletes are the most fundamental tasks of sports medicine. The occurrence of sports injury diseases is not only different in pathogenesis but also in athletes' treatment and prognosis [2, 3]. Elbow injuries are extremely common among athletes in gymnastics, tennis, judo, weightlifting, badminton, javelin, skills, basketball, table tennis, and other sports. Athletes' chronic elbow injuries can involve multiple epiphyses, cartilage, synovium, ligaments, soft tissues, and other complex anatomy.

The elbow joint is the main weight-bearing joint of the human body and one of the vulnerable joints in daily life and sports competitions [4, 5], accounting for about 40% of all sports injuries. The ligaments around the elbow joint play an important role in maintaining the stability of the elbow joint. Its injuries are often complicated by elbow joint fractures, and other normal anatomical structures around the joint are destroyed and joint instability. If not treated properly, patients are prone to joint laxity and subsequent cartilage injury, traumatic osteoarthritis, and so on [6, 7]. Accurately determining the damage to the ligaments around

the elbow joint is very important for the treatment and prognosis of the patient.

The anatomical structure of the human elbow joint is complex. At present, the clinic mainly relies on routine X-ray examination of ankle injuries. With the development of clinical imaging technology, magnetic resonance imaging (MRI) has gradually been recognized and promoted [8–10]. Currently, the imaging technology has high resolution and noninvasiveness for soft tissues due to the characteristics of sex and nonradiation damage have been widely used in clinical examination of various system diseases of the human body [11]. Recently, clinical studies have found that the implementation of MRI diagnosis for patients with elbow joint ligament injury has a good diagnostic effect.

At present, conventional X-ray films have a clear diagnosis of fractures, but the evaluation of chronic elbow injuries in athletes is more limited, and certain types of epiphyseal injuries often cause difficulties in diagnosis and treatment [12–14]. MRI can clearly show cartilage, synovia, ligaments, soft tissues, and blood vessels. It is sensitive to show changes in bone marrow and can detect bone damage, osteomyelitis, aseptic necrosis, etc. early. Acupuncture treatment of elbow joint injury is mostly based on the local injury and combined with remote point differentiation.

2. Methods and Materials

2.1. Patient Demographics. This group of 39 athletes with chronic elbow joint sports injury has a total of 60 elbow joints, and there are 6 selection criteria: (1) Elbow pain, swelling, elbow joint dysfunction, or limited mobility; (2) X-ray films exclude pathological fractures; (3) criteria do not involve major nerve and blood vessel injury; (4) 15-25 years old; (5) uninterrupted treatment as prescribed; (6) complete follow-up obtained. Cases meeting the above inclusion criteria are eligible cases.

Among them are 36 right elbows and 24 left elbows; 31 males and 29 females (19.3 ± 6.1) years old; all are professional athletes, including 22 elbows for gymnastics, 15 elbows for tennis, 4 for weightlifting, and 4 for badminton. 3 elbow joints for javelin, judo, technique, basketball, and table tennis individually; course of disease (12.5 ± 24.8) months; follow-up time (12.2 ± 14.5) months. The 60 elbow joints were randomly divided into acupuncture group and control group according to age, gender, pain degree, and joint range of motion according to the random number table method. The acupuncture group had 30 elbow joints, and the control group had 30 elbow joints. There were 2 groups of symptoms, the signs and conditions were not significantly different after analysis, and they were comparable ($P > 0.05$), as shown in Figure 1.

2.2. Treatment Methods. Acupuncture is used in this study, and the skin is routinely disinfected by acupuncture points. When acupuncture Chize point, we use a 1.5-inch needle with the tip of the needle at an angle of 30° to the skin and quickly penetrate into the skin. Stop when there is a feeling of tightness and stagnation under the fingers. Insert the needle and then twist the needle body at a speed of 200 revolutions/min for 2 minutes; retract the needle to the subcutaneous position, and insert the needle tip to the left at an angle of 90° to the front and back midline of the elbow. We repeat the above operations.

Needle is penetrated backward and rightward, and the operation is the same as before. When acupuncture other points, quickly pierce the needle under the skin, and then slowly insert the needle with a twisting technique. When there is a feeling of tightness and stagnation under the fingers, stop the needle and insert the needle with the twisting technique for 2 minutes. We keep the needle for 30-60 minutes and row the needle every 15 minutes. Once a day, 15 times are a course of treatment. The interval between each treatment is 2 d. There are 4 courses of treatment. Control group: stop training with affected elbow and rest.

2.3. MR Scanning Method. All subjects used GE HD Excite 1.5 T MRI instrument to perform conventional sagittal, coronal, and axial multisequence, multiparameter scans, sagittal FRFSE T2WI fs (TR2000ms, TE60-80 ms), FSET1WI (TR500ms, TE20ms), STIR T2∗WI (TR2000ms, TE30ms), coronal FSE T1WI, PDWI (TR2000ms, TE20-30 ms), and axial FSE T1WI (TR1000ms, TE40ms).

2.4. Evaluation Procedures. After 4 courses of treatment, the two groups were uniformly evaluated for curative effect. The modified Hospital for Special Surgery (HSS) elbow score was used as the evaluation criterion for efficacy. (1) Cured: the local redness, swelling, and pain disappeared, and the range of motion of the joint returned to normal (the range of motion of the elbow joint was ≥110°); (2) significant effect: the local redness, swelling, and pain basically disappeared, there was no obvious restriction on activities of daily living, and the range of motion of the elbow joint was 90-110°; (3) improved: local swelling and pain are relieved, activities of daily living are mildly limited, and the range of motion of joints is 60-90°; (4) ineffective: local swelling and pain are not significantly improved, and activities of daily living are significantly improved limited, joint range of motion <60°. The overall efficacy includes cure, marked improvement, and improvement.

2.5. Statistical Analysis. We analyzed the data with SPSS11.0 statistical software and performed χ^2 test on the data.

3. Results

3.1. Comparison of MR Images Pre- and Postacupuncture Treatment. The first feature is the thickening of the elbow joint capsule ligament and synovial membrane, the joint space of the inner elbow can be seen larger than normal; the synovial membrane can also be seen unevenly thickened, the PDWI sequence shows high signal, synovial effusion, manifested as strip hypo-intensity signal on T1WI, and hyperintensity signal on T2WI. The specific image is shown in Figure 2(a).

The second feature is that the ulnar collateral ligament is interrupted by normal low signal in PDWI sequence. A few athletes can see low signal calcification of muscles and tendons. The ossification or calcification and the surrounding

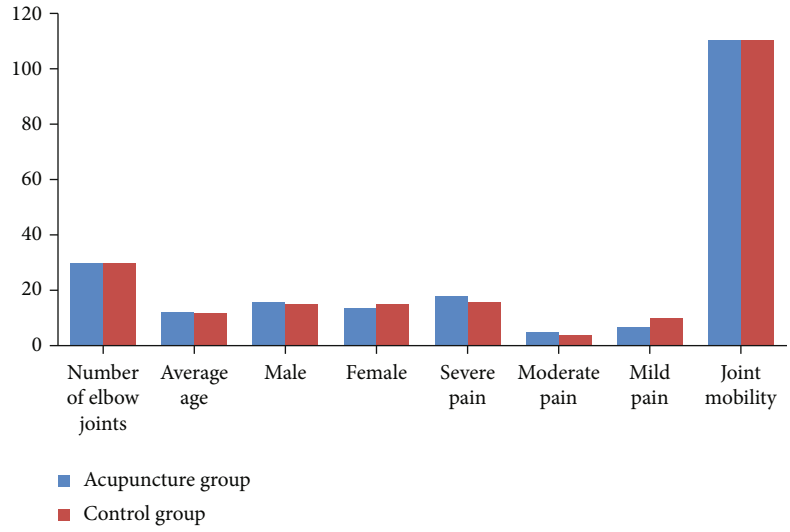

Figure 1: Comparison of symptoms and signs between the two groups.

soft tissue scars, inflammation, contracture, and incarceration can all cause elbow mobility disorder. The surrounding soft tissues are swollen, and uneven hyperintensity signals can be seen in the soft tissues on both T2WI and PDWI sequences. It is more common in elbow-ulnar pain syndrome, as shown in Figure 2(b).

The third feature is the cartilage injury of the capillary humerus and the internal epicondylitis of the humerus. The manifestations are the internal epicondyle of the humerus and the articular surface of the humerus. The cartilage signal is defective. And on the PDWI sequence, hyperintensity signals can be seen in the capillary cartilage of the humerus, the olecranon, and the coronoid process of the ulna, as shown in Figure 2(c).

After acupuncture treatment, MR images showed that the elbow joint effusion was reduced, the joint cavity effusion was reduced, the synovial sac was not significantly thickened, and the bone marrow edema was reduced, as shown in Figure 2(d).

3.2. Comparison of Clinical Manifestations before and after Treatment. Before treatment, 60 elbow joints had pain, of which 34 were obvious pain, 9 were moderate pain, and 17 were mild pain. The specific elbow joint training degree and bending degree are shown in Table 1.

Acupuncture treatment is divided into 4 courses. In order to better compare the effects of acupuncture treatment, we carefully recorded the changes in elbow joint mobility during the 4 courses, as shown in Figure 3.

It can be seen from Figure 3 that the elbow joint range of motion in the control group did not change much, while the acupuncture group increased the range of motion after 4 courses of treatment. Although it only increased by 0.5°, the range of motion has also increased a lot. It also affects the daily efficiency of athletes.

The follow-up time after acupuncture treatment was (12.2 ± 14.5) months. Among the 30 elbows in the acupuncture group, 21 elbow pain disappeared, 6 elbow joint pain basically disappeared, activities of daily living were not significantly restricted, the pain degree of 3 elbow joints was reduced, and the apparent rate was 100%. Of the 30 elbows in the control group, 4 elbow pain disappeared, 3 elbow joint pain basically disappeared, there was no obvious restriction in activities of daily living, 5 elbow joint pain was reduced, 18 elbow joint pain was not improved significantly, daily life activity capacity is obviously limited, and the apparent efficiency is 40%. The treatment efficiency of the acupuncture group and the treatment group is shown in Table 2.

Figure 4 shows the comparison of elbow joint treatment effects between the two groups, showing the specific number of elbow joints. We can easily conclude that the treatment effect of the acupuncture group is better than that of the control group.

4. Discussion

When the extension, flexion, and rotation of the elbow joint exceed a certain range of angles, or when the joint cannot perform any movement, it can cause injury. All joint surfaces are covered by articular hyaline cartilage. To evaluate articular cartilage, it is best to use GRE sequence or fat-saturated proton density-weighted image [15], while X-ray and CT cannot show articular hyaline cartilage. The medial collateral ligament of the elbow joint plays an important role in the movement of the elbow joint. Chronic elbow joint instability [16] mainly involves chronic injury of the elbow collateral ligament. MR can show the anatomy of the elbow collateral ligament and clearly distinguish the anterior medial collateral ligament. The anterior and posterior tracts of the medial collateral ligament at different flexion angles have been found to play a role, respectively, in the study [17].

Due to the abnormal range of the elbow joint's out-of-groove motion, excessive extension, flexion, twisting, and supporting load, the cartilage surface of the elbow joint is constantly squeezed, rubbed, and collided and gradually strained and injured. At the same time, traumatic osteochondritis can lead to secondary elbow joint

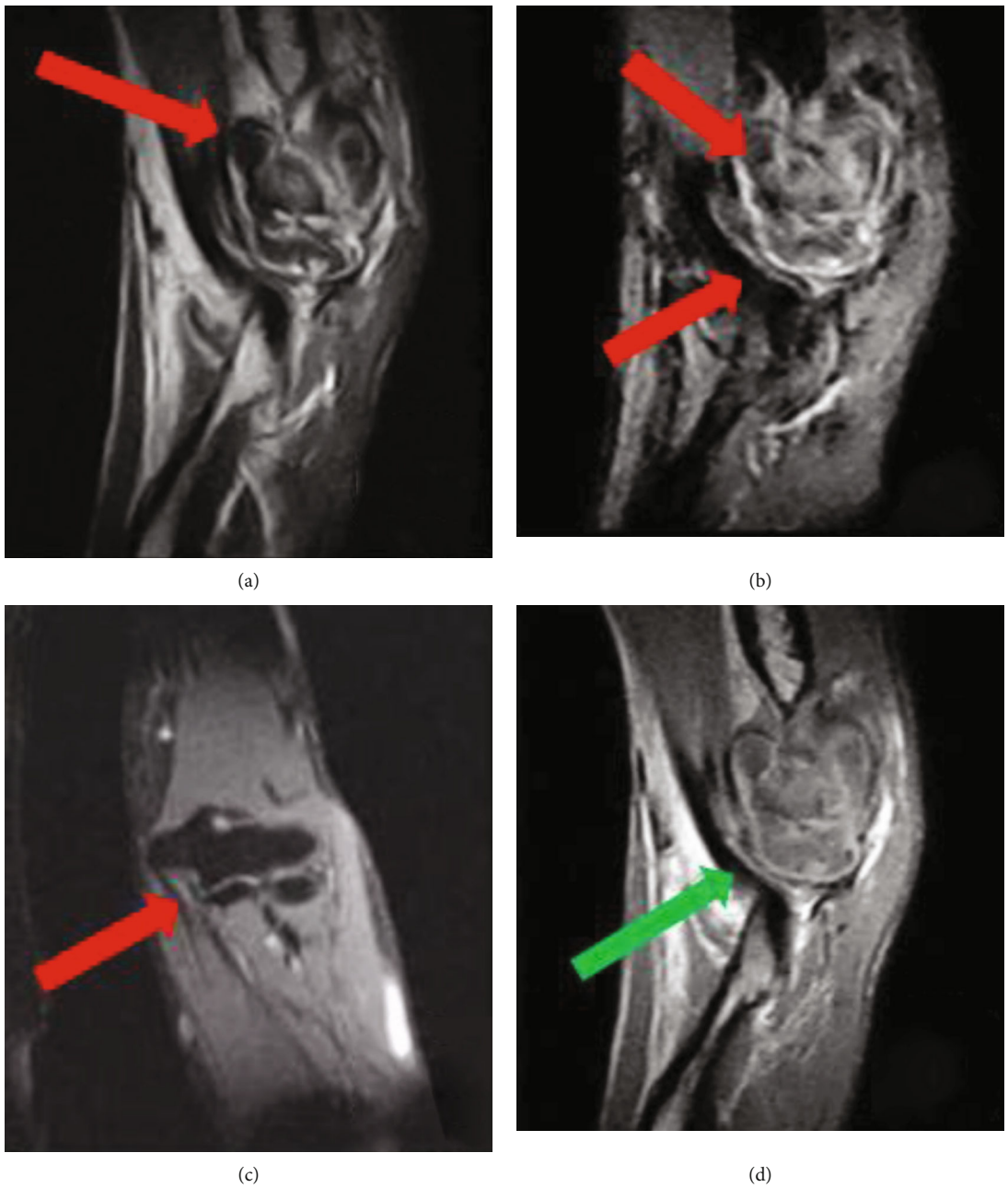

(a) (b) (c) (d)

Figure 2: MR images before and after acupuncture treatment based on (a) MR image of elbow joint injury feature one before treatment, (b) MR image of elbow joint injury feature two before treatment, (c) MR image of elbow joint injury feature three before treatment, and (d) MR image after acupuncture treatment. The red arrow represents the injury site before treatment, and the green arrow represents the recovery position after treatment.

Table 1: The degree of elbow joint training and the degree of bending before treatment.

Group	Trauma	No trauma	Participate in normal special training			Angle of elbow extension	The angle of the elbow joint
			Cannot	Impact	Obvious impact		
Acupuncture group	14	16	7	10	13	$14.9^{\circ} \pm 13.4^{\circ}$	$119.9^{\circ} \pm 13.4^{\circ}$
Control group	9	21	10	6	14	$15.1^{\circ} \pm 12.7^{\circ}$	$118.8^{\circ} \pm 9.9^{\circ}$

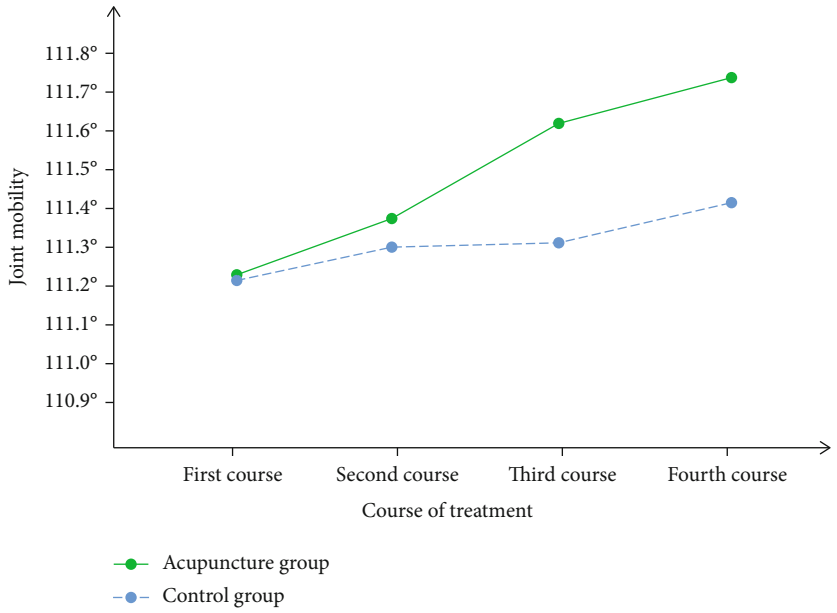

Figure 3: Changes in elbow joint range of motion in four courses.

Table 2: The treatment efficiency of acupuncture group and treatment group.

Group	Number of elbow joints	Treatment (%)	Effective (%)	Get better (%)	Invalid (%)	Total effective rate (%)
Acupuncture group	30	70.00	20.00	10.00	0.00	100.00
Control group	30	13.33	10.00	16.67	60	40.00

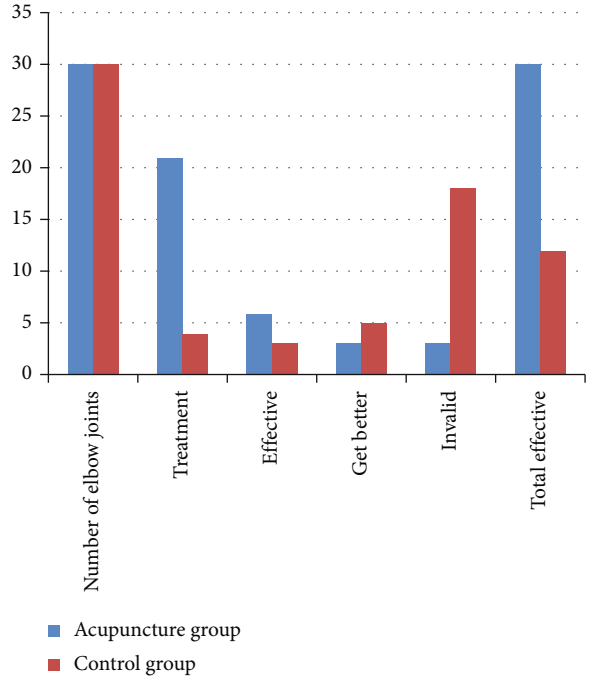

Figure 4: Comparison of elbow joint treatment effects between the two groups.

osteoarthropathy [18]. After the primary injury is healed, hematomas in the joint cavity gradually become organized, and the joint capsules and soft tissues around the joints such as muscles, tendons, ligaments, and other soft tissues contracture adhesion [19], there are joint extension and flexion disorders, joint swelling, and muscle atrophy.

Acupuncture treatment is based on different diseases and syndromes, and the treatment is based on syndrome differentiation, so that the local blood vessels are unobstructed, the muscles and bones are nourished, and the joints are flexible in flexion and extension. The treatment of this disease is based on the principles of dredging the meridians, relieving spasms, loosening adhesions, improving blood circulation in local tissues, relieving pain, and promoting joint function to normal [20]. Acupuncture treatment achieves the purpose of smoothing joints, relieving adhesions, improving joint function, and eliminating inflammation and edema [21, 22].

Although the acupuncture treatment method proposed in this paper has achieved a significant efficiency of 100%, there are still many problems and areas that can be improved [23].

First, we should expand the experimental cases. This paper only uses 39 cases of elbow joint injuries, but to draw more accurate conclusions, we need more cases to further prove our point [24].

Second, in MR images, three-dimensional factors are added [25]. The images in this paper are all two-dimensional, and there is a risk of ignoring important details of the elbow joint injury. Deep learning can be used for automatic diagnosis of the patient in future [26–29].

Third, we will study more common elbow injuries in the future. This paper mainly studies athletes' elbow joint

injuries, but in reality, the situation of ordinary people's elbow joint injuries is more complicated [30], and future research directions will work hard in this area.

5. Conclusion

The HSS scoring method was used before and after treatment in all cases. Pain and functions of daily living accounted for a significant proportion of the scores, indicating that attention should be paid to improving the overall function of the elbow joint and improving the activities of daily living of the affected limb. After more than 3 months of follow-up, the apparent efficiency of the acupuncture group reached 100%, indicating that the acupuncture treatment can restore joint flexion to the greatest extent.

In the examination of athletes' elbow injuries, especially those involving complex elbow joint injuries, MR examination can take full advantage of its noninvasive, reproducible, and high-resolution advantages of soft tissue structure, combined with multiple scan orientations, multiple scan parameters, and pass continuous. Scanning observation can make a comprehensive judgment. Not only that, MR examination can play a role in guiding treatment by evaluating the stability of trauma fractures and the stability after treatment. In addition, it is generally believed that MR examination can detect cartilage callus formation earlier than plain X-ray films, and it can also be used to monitor the healing of fractures.

Data Availability

The image data used to support the findings of this study have been deposited in the musculoskeletal radiographs (MURA) dataset (https://stanfordmlgroup.github.io/competitions/mura/).

Conflicts of Interest

The authors declare that they have no conflicts of interest.

Acknowledgments

The author would like to thank the staff and students of Hainan General Hospital and University for their help in processing the image scans obtained in this study.

References

[1] B. Swobodo and R. D. Scott, "Humeral hemiarthroplasty of the elbow joint in young patients with rheumatoid arthritis: a report on 7 arthroplasties," *Journal of Arthroplasty*, vol. 57, no. 6, pp. 157–160, 1999.

[2] S. Tyrdal and B. S. Olsen, "Hyperextension of the elbow joint: pathoanatomy and kinematics of ligament injuries," *Journal of Shoulder and Elbow Surgery*, vol. 7, no. 3, pp. 272–283, 1998.

[3] K. Wise and T. A. Mason, "Detection of movements of the human forearm during and after co-contractions of muscles acting at the elbow joint," *The Journal of Physiology*, vol. 508, no. 1, pp. 325–330, 1998.

[4] G. M. Kerkhoffs, V. Den, M. Bekerom, and L. A. Elders, "Diagnosis, treatment and prevention of ankle sprains: an evidence-based clinical guideline," *British Journal of Sports Medicine*, vol. 46, no. 12, pp. 854–860, 2012.

[5] A. Nazarenko, L. S. Beltran, and J. T. Bencardino, "Imaging evaluation of traumatic ligamentous injuries of the ankle and foot," *Radiologic Clinics of North America*, vol. 51, no. 3, pp. 455–478, 2013.

[6] S. Kuroda and K. Sakamaki, "Ulnar collateral ligament tears of the elbow joint," *Clinical Orthopaedics and Related Research*, vol. 208, 1986.

[7] J. Grondalen, W. Konermann, and G. Gruber, "Arthritis in the elbow joint of young rapidly growing dogs. III. Uninvited medical coronoid process of the ulna and osteochondritis dissents of the humeral condyle. Surgical procedure for correction and postoperative investigation," *Nordisk Veterinarymedicine*, vol. 31, no. 12, 1979.

[8] P. Melloni and R. Valls, "The use of MRI scanning for investigating soft-tissue abnormalities in the elbow," *European Journal of Radiology*, vol. 54, no. 2, pp. 303–313, 2005.

[9] A. K. Dewan, A. B. Chhabra, A. J. Khanna, M. W. Anderson, and L. M. Brunton, "MRI of the elbow: techniques and spectrum of disease," *The Journal of Bone and Joint Surgery-American Volume*, vol. 95, no. 14, 2013.

[10] G. Akansel, S. Dalbayrak, M. Yilmaz, H. Bekler, and A. Arslan, "MRI demonstration of intra-articular median nerve entrapment after elbow dislocation," *Skeletal Radiology*, vol. 32, no. 9, pp. 537–541, 2003.

[11] M. Libicher and J. Freyschmidt, "Radiologic imaging of the contracted elbow joint. Value of CT and MRI," *Der Orthopäde*, vol. 30, no. 9, pp. 593–601, 2001.

[12] J. Syed, A. R. Zamri, S. Jamaluddin, J. K. Ruben, and M. Gopindran, "Intra-articular entrapment of medial epicondyle fracture fragment in elbow joint dislocation causing ulnar neuropraxia: a *case report*," *Malaysian Orthopaedic Journal*, vol. 11, 2017.

[13] N. Nishioka, T. Kamishima, T. Masuko et al., "Intra-articular nodular fasciitis in the elbow joint, with an emphasis on MR imaging findings," *European Journal of Radiology Extra*, vol. 69, no. 1, pp. e33–e36, 2009.

[14] C. Kober, L. Gallo, H. F. Zeilhofer, and R. A. Sader, "Computer-assisted analysis of human upper arm flexion by 4D-visualization based on MRI," *International Journal of Computer Assisted Radiology and Surgery*, vol. 6, no. 5, pp. 675–684, 2011.

[15] W. D. Middleton and T. L. Lawson, *Anatomyand MRI of the Joints*, Raven Press, New York, 1989.

[16] S. Tyrdal and B. S. Olsen, "Combined hyperextension and supination of the elbow joint induces lateral ligament lesions," *Knee Surgery, Sports Traumatology, Arthroscopy*, vol. 6, no. 1, pp. 36–43, 1998.

[17] D. Ring and J. B. Jupiter, "Current concepts review - fracture-dislocation of the elbow," *The Journal of Bone & Joint Surgery*, vol. 80, no. 4, pp. 566–580, 1998.

[18] M. J. Tuite and R. Kijowski, "Sports-related injuries of the elbow: an approach to MRI interpretation," *Clinics in Sports Medicine*, vol. 25, no. 3, pp. 387–408, 2006.

[19] T. H. Pöyhiä, M. P. Koivikko, J. I. Peltonen, M. O. Kirjavainen, A. E. Lamminen, and A. Y. Nietosvaara, "Muscle changes in brachial plexus birth injury with elbow flexion contracture: an MRI study," *Pediatric Radiology*, vol. 37, no. 2, pp. 173–179, 2007.

[20] M. Costa, S. Owenjohnstone, and J. K. Tucker, "The value of MRI in the assessment of an elbow injury in a neonate," *The*

Journal of Bone and Joint Surgery. British Volume, vol. 83, no. 4, pp. 544–546, 2001.

[21] M. C. Ciccotti, J. D. Stull, P. S. Buckley, and S. B. Cohen, "Correlation of MRI to arthroscopy in the elbow: thrower's elbow and ulnar collateral ligament injury," *Sports Medicine and Arthroscopy Review*, vol. 25, no. 4, pp. 191–198, 2017.

[22] M. A. Wessely, K. L. Hurtgen-Grace, and J. M. Grenier, "Elbow MRI: Part 1. Normal imaging appearance of the elbow," *Clinical Chiropractic*, vol. 9, no. 4, pp. 198–205, 2006.

[23] J. J. Schreiber, H. G. Potter, R. F. Warren, R. N. Hotchkiss, and A. Daluiski, "Magnetic resonance imaging findings in acute elbow dislocation: insight into mechanism," *The Journal of Hand Surgery*, vol. 39, no. 2, pp. 199–205, 2014.

[24] T. Takizawa, S. Akizuki, Y. Yasukawa, H. Horiuchi, and I. Yamazaki, "4 investigation of throwing injury with cystic change on MRI," *Journal of Shoulder and Elbow Surgery*, vol. 7, no. 3, pp. 321–321, 1998.

[25] J. Wendy and S. Hurd, "Magnetic resonance imaging of the throwing elbow in the uninjured, high school-aged baseball pitcher," *The American Journal of Sports Medicine*, vol. 67, no. 2, pp. 241–250, 2011.

[26] X. Xinli, C. Zhang, F. Musharavati, T. A. Sebaey, and A. Khan, "UFSW tool pin profile effects on properties of aluminium-steel joint," *Vacuum*, vol. 192, no. 8, article 110460, 2021.

[27] X. Xu, C. Zhang, F. Musharavat, T. A. Sebaey, and A. Khan, "Dispersion of waves characteristics of laminated composite nanoplate," *Steel and Composite Structures*, vol. 40, no. 3, pp. 355–367, 2021.

[28] Z. H. Tang, Y. Y. Li, X. Y. Chai, H. Y. Zhang, and S. X. Cao, "Adaptive nonlinear model predictive control of NOx emissions under load constraints in power plant boilers," *Journal of Chemical Engineering of Japan*, vol. 53, no. 1, pp. 36–44, 2020.

[29] H. Bo, C. Zhou, H. Wang, and S. Chen, "Nonlinear tribodynamic model and experimental verification of a spur gear drive under loss-of-lubrication condition," *Mechanical Systems and Signal Processing*, vol. 153, article 107509, 2021.

[30] K. J. Stevens and E. G. Mcnally, "Magnetic resonance imaging of the elbow in athletes," *Clinics in Sports Medicine*, vol. 29, no. 4, pp. 521–553, 2010.

Hindawi
Computational and Mathematical Methods in Medicine
Volume 2022, Article ID 8498159, 6 pages
https://doi.org/10.1155/2022/8498159

Research Article

Prediction Model for Infectious Disease Health Literacy Based on Synthetic Minority Oversampling Technique Algorithm

Rongsheng Zhou,[1] **Weihao Yin**,[2] **Wenjin Li**,[1] **Yingchun Wang**,[1] **Jing Lu**,[1] **Zhong Li**,[1] **and Xinxin Hu**[1]

[1]*The Third People's Hospital of Hefei, Hefei Third Clinical College of Anhui Medical University, Hefei 230022, China*
[2]*Linyi Hospital of Traditional Chinese Medicine, Dezhou 251500, China*

Correspondence should be addressed to Zhong Li; henrylee711@163.com and Xinxin Hu; ssykjchxx@163.com

Received 24 December 2021; Revised 22 February 2022; Accepted 8 March 2022; Published 25 March 2022

Academic Editor: Kelvin Wong

Objective. Improving health literacy in infectious diseases is a direct manifestation of the solid advance in disease control and prevention. Our study is aimed at exploring applying synthetic minority oversampling technique (SMOTE) in the prediction assessment of whether residents and business employees have infectious disease health literacy. *Methods*. The Chinese resident infectious disease health literacy evaluation scale was used to investigate the associated variables. The screened variables were input variables and the presence or absence of infectious diseases health literacy as outcome variables. Logistic regression, random forest, and support vector machine (SVM) models were built in the data sets before and after treatment by the SMOTE algorithm, respectively, and the performance of the models was evaluated by receiver operating characteristic curves (ROC). *Results*. Logistic regression, random forest, and SVM achieved accuracies of 0.828, 0.612, and 0.654 before SMOTE algorithm processing, and the areas under the ROC curves (AUCs) of the three models were 0.754, 0.817, and 0.759, respectively. The accuracies were 0.938, 0.911, and 0.894 after SMOTE algorithm processing, and the AUCs of the three models were 0.913, 0.925, and 0.910, respectively. *Conclusions*. The random forest model based on the SMOTE has high application value in assessing whether residents versus enterprise employees have infectious disease health literacy.

1. Introduction

Infectious diseases are both transmissible and epidemic, posing a great danger to human health [1, 2]. With more developed transportation, logistics, and so on, the mobility and clustering of the population have increased, and the probability of all types of major infectious diseases spreading worldwide has risen dramatically. Once the infectious disease occurs, it quickly causes harm to the people's physical health and life safety. At the same time, it causes damage to social and personal properties even hinders social development [3, 4]. Health literacy is the ability of individuals to acquire or understand basic health information and services and use this information and services to make correct decisions to maintain and promote their health [5].

Infectious disease health literacy is part of health literacy. Health literacy and health status are closely linked. Low health literacy negatively impacts lifestyle, health service utilization, and adherence to interventions, resulting in high disease incidence and prevalence and poor disease outcomes [6]. The 2012 national health literacy surveillance results showed low health literacy among Chinese residents. Among the six categories of health problems, infectious disease prevention and treatment literacy was at a low level [7]. Infectious disease health literacy reflects residents' understanding and application to the initiation, prevention, and treatment of infectious diseases. The improvement of health literacy in infectious diseases is a direct manifestation of the solid advance in infectious disease control and prevention, and it is essential to control the spread of common infectious diseases, respond to large-scale infectious diseases, and enhance our ability to deal with public health crises [8]. High-level infectious disease health literacy among residents is both an objective need of the era and a powerful weapon to tackle

the unknown challenges facing future infectious disease prevention and control efforts [9].

In this study, several machine learning prediction models were developed using data from the China health literacy evaluation scale for infectious diseases of residents. The models were based on the synthetic minority oversampling technique (SMOTE), and the prediction effects were compared. It is hoped that the low health literacy population will be screened to inform the development of targeted interventions through an established prediction model that predicts the health literacy status of an individual or a group.

2. Material and Methods

2.1. General Data. Considering this study as a stratified sampling study, the sample size was calculated according to the following formula:

$$N = \frac{u_\alpha^2 \times p_0(1-p_0)}{\sigma^2} \times \text{deff}. \quad (1)$$

According to the 2014 analysis of health literacy survey on prevention of infectious diseases among urban and rural residents of Hefei, the health literacy level of infectious diseases among urban and rural residents of Hefei is 49.4%. Using this as a reference, $P = 0.494$, relative allowable error $r = 10\%$, then absolute allowable error $=10\% \times 49.4\% = 0.0494$, calculated sample size of 950 participants based on 95%CI $= 1.96$, design efficiency deff $= 1.5$.

2.2. Study Subjects. The study subjects were residents and enterprise employees in the Jiakai District of Hefei City, and the questionnaire release time was from February 5, 2020, to February 12, 2020. In this investigation, 1900 questionnaires were issued cumulatively, and 1874 were returned, and the effective rate of the questionnaire was 98.63%.

2.3. Research Method. The health literacy evaluation scale for infectious diseases among Chinese residents was used, and the first part of the scale consists of 22 items [10].

The health literacy evaluation scale for infectious diseases among Chinese residents was used. The first part of the scale consists of 22 items belonging to four dimensions: F1: basic knowledge and concept of infectious diseases (seven items, which mainly examine the individual's basic knowledge and concept on the infectious sources, transmission routes, and susceptible populations of common infectious diseases); F2: prevention of infectious diseases (7 entries that primarily examine an individual's knowledge of common infectious disease precautions); F3: management and treatment of infectious diseases (4 entries, mainly looking at the mastery of management and treatment of common infectious diseases); and F4: recognition of infectious disease (4 entries that primarily examine an individual's ability to discern common infectious agents and symptoms). Cronbach's a for the four dimensions was 0.654, 0.673, 0.562, and 0.638, with a construct validity of 0.8 for each item. The second part of the Chinese health literacy assessment scale for infectious diseases of residents, which consists of 6 items with genera measuring separate dimensions of responders' cognitive abilities, was not included in the analysis. F1 was set as the exogenous dependent latent variable (not affected by the other latent variables), based on expertise in infectious disease health literacy; F2, F3, and F4 were set as the internal dependent latent variables (influenced by other latent variables). The magnitude of the mutual effect between the four latent variables of the China health literacy assessment scale for infectious diseases among residents is the effect value. The direct effect between the two latent variables is termed the immediate effect. The effect produced through an intermediate variable is the indirect effect, and the sum of the immediate effect versus the indirect effect is the total effect. The flow chart of scale analysis is shown in Figure 1.

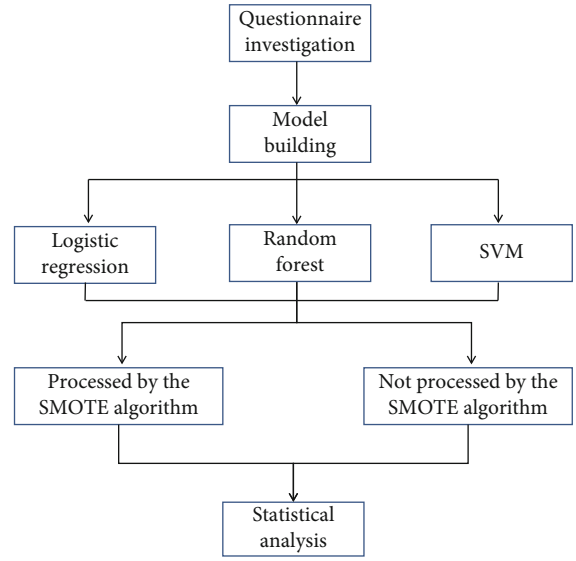

Figure 1: Flow chart of scale analysis.

2.4. Model Building. Python 3.7 software was used to establish the prediction model. Calling train_test_split in sklearn.model_selection and randomly split the data set into four parts: the first 3/4 as the training set was used to build the model, and the remaining 1/4 as the test set was used to evaluate the model performance. Logistic regression models were built in the training set with place of residence, educational level, occupational class, whether they had healthcare related work and monthly household income as input variables, and whether they had health literacy as predictor outcome, respectively, after univariate screening with random forest and support vector machine (SVM). Most machine learning algorithms' classification accuracy decreases substantially when the data become imbalanced [11–13]. Thus, the models were then applied in the test set to assess whether residents and business staff possess infectious disease health literacy.

SMOTE algorithm is an improved scheme based on the random oversampling algorithm (Figure 2). Because random oversampling adopts the strategy of simply copying samples to increase a few samples, it is easy to produce the problem

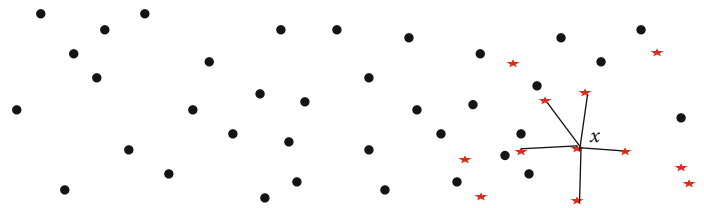

Figure 2: Schematic diagram of SMOTE algorithm.

Table 1: Univariate analysis of health literacy and health behavior of residents and employees of enterprises.

Items	Resident		Enterprise staff	
	Health literacy	Health literacy	Health literacy	Health literacy
Gender				
Male	36.33 ± 4.70	11.19 ± 1.65	36.42 ± 4.75	11.23 ± 1.66
Female	36.91 ± 4.49	11.33 ± 1.66	36.87 ± 4.41	11.27 ± 1.63
t	1.309	0.898	0.972	0.245
P	0.191	0.370	0.331	0.806
Degree of education				
Junior high school and below	33.00 ± 2.95	9.33 ± 0.95	33.29 ± 3.31	9.47 ± 1.10
Senior high school/vocational high school/technical secondary school	35.31 ± 3.11	11.33 ± 0.95	35.50 ± 3.39	11.34 ± 1.00
Junior college	38.31 ± 4.65	11.66 ± 0.25	38.27 ± 4.63	11.65 ± 1.24
Undergraduate	39.00 ± 4.35	13.00 ± 0.82	39.30 ± 4.27	12.88 ± 0.89
Postgraduate	43.33 ± 3.40	14.00 ± 0.84	43.53 ± 3.41	14.00 ± 0.82
F	67.406	217.531	65.143	196.757
P	<0.001	<0.001	<0.001	<0.001
Age				
16~20 years old	33.10 ± 2.98	9.48 ± 1.06	33.35 ± 2.82	9.46 ± 0.90
20~30 years old	35.59 ± 3.55	11.33 ± 1.22	34.87 ± 3.75	10.82 ± 1.52
30~40 years old	38.54 ± 4.64	11.88 ± 1.31	38.51 ± 4.70	11.84 ± 1.28
40~50 years old	39.82 ± 4.60	13.22 ± 0.96	39.25 ± 4.41	12.68 ± 1.28
>50 years old	34.51 ± 3.68	10.38 ± 1.43	35.85 ± 5.31	11.27 ± 2.10
F	47.862	107.497	28.792	48.625
P	<0.001	0.037	<0.001	<0.001

Table 2: Performance comparison of the 3 classification models applied to raw data.

Model	Recall	Accuracy rates	f-scores	Precision	AUC
Logistic	0.291	0.828	0.431	0.936	0.754
Random forest	0.349	0.612	0.448	0.932	0.817
SVM	0.419	0.654	0.497	0.938	0.759

of model overfitting, even if the information learned by the model is too specific and not general [14]. The basic idea of the SMOTE algorithm is to analyze a small number of samples, synthesize new samples, and add them to the data set according to the small number of samples, as shown in the figure below. The algorithm process is as follows:

(1) For each sample x in the minority class, the distance from it to all samples in the minority class sample set is calculated by taking the Euclidean distance as the standard, and its k-nearest neighbor is obtained

(2) A sampling ratio is set according to the sample imbalance ratio to determine the sampling magnification n. For each minority sample x, several samples are randomly selected from its k-nearest neighbors, assuming that the selected nearest neighbor is x_n

(3) For each randomly selected nearest neighbor x_n, a new sample is constructed with the original sample according to the following:

$$x_{\text{new}} = x + \text{rand}(0, 1) \times (\tilde{x} - x) \quad (2)$$

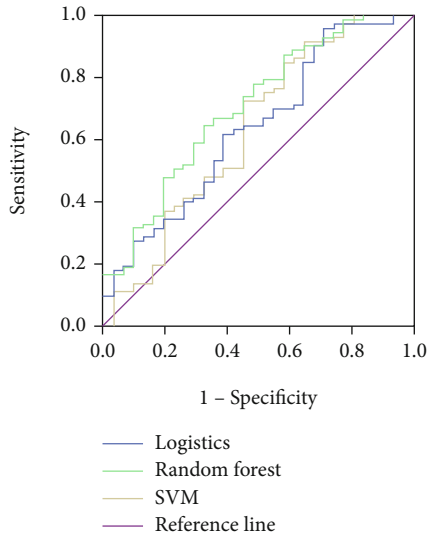

Figure 3: ROC curves of three classification models applied to the raw data.

Table 3: Performance comparison of 3 classification models applied to data processed by SMOTE algorithm.

Model	Recall	Accuracy rates	f -scores	Precision	AUC
Logistic	0.608	0.938	0.739	0.816	0.913
Random forest	0.732	0.911	0.817	0.855	0.925
SVM	0.741	0.894	0.806	0.851	0.910

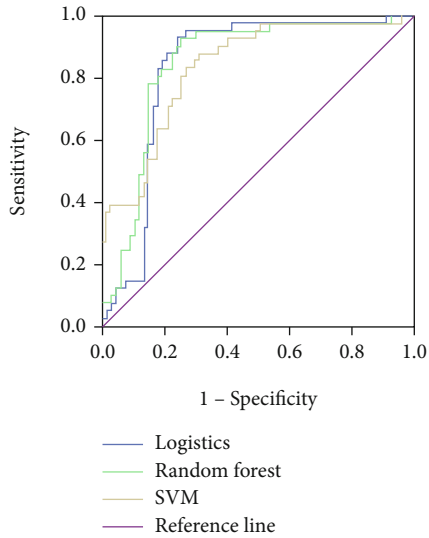

Figure 4: ROC curve of three classification models applied to data processed by the SMOTE algorithm.

To improve the classification accuracy of machine learning, this study again adopted the synthetic minority class oversampling technique for repeated sampling, so that the data tended to be balanced. This process employs R3.7, the software calls the synthetic minority oversampling technique (SMOTE) package, settings perc.over = 600, perc.under = 200, to generate new data. The previous modeling process was repeated in this new data one more time.

2.5. Statistical Processing. Model establishment and evaluation were implemented through the software Python 3.7: logistic regression model was built by applying logistic regression in sklearn.linear_model; random forest models were built applying the randomforestclassifier in sklearn.ensemble, n_estimators = 100; SVM model building by applying the SVC in sklearn.svm, $C = 100$, gamma = 0.001.

3. Result

3.1. Input Variable Filtering. Univariate screening of independent variables was performed prior to model building: a logistic regression model was constructed using the presence or absence of health literacy as the dependent variable and the nine factors included in the questionnaire as independent variables, with a test level of 0.05, and gender, education level, and age were screened out as input variables. Specific results are shown in Table 1.

3.2. Comparison of Performance of Each Classification Model on Raw Data without the SMOTE Algorithm. Logistic regression, random forest, and SVM models were trained on the training data set after one hot coding of the univariate filtered independent variables as input variables, with health literacy as the outcome variable or not. The random forest model was subjected to a grid search optimal n_estimators taken 100. The SVM model was subjected to a grid search optimal C taken 100 and gamma taken 0.001. Tests were performed in a test data set with the real situation. The precision of all three models exceeded 90%, but several other metrics were low, especially recall and f-scores. The greater the curve areas under the ROC curves (AUCs) in the receiver operating characteristic (ROC) plot indicates better model performance, and the higher the ROC curve for the random forest model than for the logistic and SVM models. Specific results are shown in Table 2 and Figure 3.

3.3. Comparison of Performance of Each Classification Model on Data Processed by the SMOTE Algorithm. After the raw data were processed with the SMOTE algorithm, the new data set was used with the same method to build a model and compare the performance. The precision of all three models decreased, but each of the other indexes increased significantly. The random forest model had a higher recall, f-scores, accuracy, and AUC than the other two models, and the specific results are shown in Table 3 and Figure 4.

4. Discussion

Health literacy is an essential measure of the state's basic level of public service and people's health. It is also considered a key factor influencing the prevention and management of chronic diseases [15]. Low-level health literacy severely negatively impacts overall national health and the

national health system. It has become a severe public health problem that has received extensive attention [16, 17]. Many factors associated with low-level health literacy are also associated with health disparities and may influence health outcomes. Infectious disease health literacy is an essential component of individual health literacy, which can be used both as a basis for developing regional infectious disease control and for assessing the outcomes of infectious disease control efforts [18, 19]. In this study, we trained three machine learning models based on the original data and the balanced data processed by the SMOTE algorithm, respectively, and compared their performances through the mediation results of the communicable diseases health literacy evaluation scale for Chinese residents, and finally proposed an effective prediction model to provide the basis for implementing measures such as monitoring and evaluation of infectious diseases health literacy.

Imbalanced sample refers to the fact that in classification problems; there are classes in the training sample with particularly large sample numbers and some classes with particularly small sample numbers [20]. When there is class imbalance in the data set, it can have a large impact on the classification sensitivity of machine learning. In fact, in the real world, data are unbalanced [21]. The class imbalance problem has a wide range of applications in many ways. In all described uses, minority classes have high sensitivity and its information is the goal. However, classification algorithms are attracted to most classes and ignore a few. Therefore, their predictions for minority populations are mostly less accurate.

SMOTE is a oversampling technique for imbalanced data sets, which is considered as a preprocessing step of learning algorithms and an effective and common method to deal with class imbalance [20, 22, 23]. After SMOTE resampling of the original data to balance the data, logistic regression, random forest, and SVM models were trained again on the new data set. The results showed that the random forest model had higher performance than the other two models in the prediction of infectious disease health literacy for both residents and business employees, which can provide some credit for the prediction of infectious disease health literacy as well as the later delivery of interventions. Compared with traditional logistic regression methods, random forests balance sample error through random feature selection and are more convincing results than logistic models fitted with only a single test sample. SMOTE is considered an effective and common method to deal with class imbalance but it also increases the cycle, which resulting in the decrease of computing performance [14, 22].

5. Conclusion

In summary, it is feasible to continuously improve residents' basic knowledge and concepts of infectious diseases, recognition, and prevention skills of infectious diseases by means of health education and health promotion approaches, which will lead to improved levels of infectious disease management and treatment. The random forest model based on the SMOTE has high application value in assessing whether residents versus enterprise employees have infectious disease health literacy.

Data Availability

The data presented in this study are available on request from the corresponding author.

Conflicts of Interest

The authors declare no conflict of interest.

Authors' Contributions

Rongsheng Zhou and Weihao Yin are co-first authors.

References

[1] J. H. Ellwanger, V. L. Kaminski, and J. A. B. Chies, "Emerging infectious disease prevention: where should we invest our resources and efforts?," *Journal of Infection and Public Health*, vol. 12, no. 3, pp. 313–316, 2019.

[2] A. K. Townsend, D. M. Hawley, J. F. Stephenson, and K. E. G. Williams, "Emerging infectious disease and the challenges of social distancing in human and non-human animals," *Proceedings of the Biological Sciences*, vol. 287, no. 1932, p. 20201039, 2020.

[3] N. I. Nii-Trebi, "Emerging and neglected infectious diseases: Insights, advances, and challenges," *BioMed Research International*, vol. 2017, Article ID 5245021, 2017.

[4] D The Lancet Infectious Diseases, "Infectious disease crisis in the Philippines," *The Lancet Infectious Diseases*, vol. 19, no. 12, p. 1265, 2019.

[5] L. Marciano, A. L. Camerini, and P. J. Schulz, "The role of health literacy in diabetes knowledge, self-care, and glycemic control: a meta-analysis," *Journal of General Internal Medicine*, vol. 34, no. 6, pp. 1007–1017, 2019.

[6] B. Smith and J. W. Magnani, "New technologies, new disparities: the intersection of electronic health and digital health literacy," *International Journal of Cardiology*, vol. 292, pp. 280–282, 2019.

[7] M. Zheng, H. Jin, N. Shi et al., "The relationship between health literacy and quality of life: a systematic review and meta-analysis," *Health and Quality of Life Outcomes*, vol. 16, no. 1, p. 201, 2018.

[8] D. Levin-Zamir and I. Bertschi, "Media health literacy, ehealth literacy, and the role of the social environment in context," *International Journal of Environmental Research and Public Health*, vol. 15, no. 8, p. 1643, 2018.

[9] S. Conard, "Best practices in digital health literacy," *International Journal of Cardiology*, vol. 292, pp. 277–279, 2019.

[10] X. Nie, Y. Li, C. Li, J. Wu, and L. Li, "The association between health literacy and self-rated health among residents of China aged 15-69 years," *American Journal of Preventive Medicine*, vol. 60, no. 4, pp. 569–578, 2021.

[11] C. W. Connor, "Artificial intelligence and machine learning in anesthesiology," *Anesthesiology*, vol. 131, no. 6, pp. 1346–1359, 2019.

[12] G. S. Handelman, H. K. Kok, R. V. Chandra, A. H. Razavi, M. J. Lee, and H. Asadi, "Edoctor: machine learning and the future

of medicine," *Journal of Internal Medicine*, vol. 284, no. 6, pp. 603–619, 2018.

[13] Z. Tang and Z. Zhang, "The multi-objective optimization of combustion system operations based on deep data-driven models," *Energy*, vol. 182, pp. 37–47, 2019.

[14] S. Sreejith, H. Khanna Nehemiah, and A. Kannan, "Clinical data classification using an enhanced smote and chaotic evolutionary feature selection," *Computers in Biology and Medicine*, vol. 126, p. 103991, 2020.

[15] S. A. Fleary, P. Joseph, and J. E. Pappagianopoulos, "Adolescent health literacy and health behaviors: a systematic review," *Journal of Adolescence*, vol. 62, pp. 116–127, 2018.

[16] E. S. Goldfarb and L. D. Lieberman, "Three decades of research: the case for comprehensive sex education," *The Journal of Adolescent Health*, vol. 68, no. 1, pp. 13–27, 2021.

[17] A. Matchanova, M. Babicz, L. D. Medina, P. L. Fazeli, D. E. Vance, and S. P. Woods, "Latent structure of health literacy and its association with health-related management and decision-making in hiv," *Psychology & Health*, vol. 36, no. 8, pp. 985–1002, 2021.

[18] J. Perazzo, D. Reyes, and A. Webel, "A systematic review of health literacy interventions for people living with hiv," *AIDS and Behavior*, vol. 21, no. 3, pp. 812–821, 2017.

[19] R. Reynolds, S. Smoller, A. Allen, and P. K. Nicholas, "Health literacy and health outcomes in persons living with HIV disease: a systematic review," *AIDS and Behavior*, vol. 23, no. 11, pp. 3024–3043, 2019.

[20] S. I. Popoola, B. Adebisi, R. Ande, M. Hammoudeh, K. Anoh, and A. A. Atayero, "SMOTE-DRNN: a deep learning algorithm for botnet detection in the internet-of-things networks," *Sensors (Basel)*, vol. 21, no. 9, p. 2985, 2021.

[21] J. H. Seo and Y. H. Kim, "Machine-learning approach to optimize smote ratio in class imbalance dataset for intrusion detection," *Computational Intelligence and Neuroscience*, vol. 2018, Article ID 9704672, 2018.

[22] L. Ma and S. Fan, "CURE-SMOTE algorithm and hybrid algorithm for feature selection and parameter optimization based on random forests," *BMC Bioinformatics*, vol. 18, no. 1, p. 169, 2017.

[23] S. Wang, Y. Dai, J. Shen, and J. Xuan, "Research on expansion and classification of imbalanced data based on SMOTE algorithm," *Scientific Reports*, vol. 11, no. 1, p. 24039, 2021.

Hindawi
Computational and Mathematical Methods in Medicine
Volume 2022, Article ID 9173913, 10 pages
https://doi.org/10.1155/2022/9173913

Research Article

Prognosis Model of Advanced Non-Small-Cell Lung Cancer Based on Max-Min Hill-Climbing Algorithm

Weizheng Fu,[1] **Qingsheng Kan**,[1] **Bin Li**,[2] **and Xiaoming Zhang**[3]

[1]*Department of Oncology, Suzhou Hospital of Anhui Medical University (Suzhou Municipal Hospital of Anhui Province), Suzhou 215002, China*
[2]*Department of Radiology, Suzhou Hospital of Anhui Medical University (Suzhou Municipal Hospital of Anhui Province), Suzhou 215002, China*
[3]*School of Basic Medical Sciences, Anhui Medical University, Hefei 230032, China*

Correspondence should be addressed to Xiaoming Zhang; zhxm@ahmu.edu.cn

Received 8 October 2021; Revised 12 December 2021; Accepted 7 March 2022; Published 25 March 2022

Academic Editor: Kelvin Wong

A safer and more effective treatment is need for the comprehensive treatment based on chemotherapy in patients with advanced non-small-cell lung cancer (NSCLC). The max-min hill-climbing (MMHC) is a common algorithm for disease prediction. This study is aimed at analyzing the efficacy of the MMHC algorithm in prognosis evaluation of advanced NSCLC. In this study, the prognosis model of lung cancer was first established by the MMHC algorithm. Then, according to the MMHC algorithm results, 40 patients with advanced NSCLC were divided into the research group and control group before anlotinib hydrochloride capsule combined with pemetrexed disodium chemotherapy. The diameter of solid tumor lesions, objective response rate (ORR), disease control rate (DCR), and progression-free survival (PFS) was compared between the two groups. The results showed that the MMHC model has a higher prediction accuracy of survival status of lung cancer patients. Under the guidance of the model, the research group has a smaller diameter of primary foci and metastatic foci, a higher ORR, DCR, and a longer PFS than the control group ($P < 0.05$). We can conclude that the MMHC algorithm can guide the maintenance treatment of advanced NSCLC, which is conducive to the prognosis judgment and treatment cost control.

1. Introduction

Lung cancer is a tumor with a very high degree of malignancy in clinical practice. Its mortality ranks the first among malignant tumors, and its incidence tends to rise year by year [1]. The non-small-cell lung cancer (NSCLC) accounts for more than 80% of all lung cancer patients, and about 50% of these patients have progressed to stage IIIB or IIIC at the time of treatment and have lost the best opportunity for surgery [2, 3].

At present, the clinical treatment of this disease mainly adopts the comprehensive treatment method based on chemotherapy. However, the effective rate of chemotherapy in most advanced NSCLC patients is very low, with the highest rate being only 20%-40% [4, 5]. Finding a safer and more effective treatment has become a hot topic in this field. Pemetrexed is often used to treat NSCLC clinically, with good therapeutic effect and less toxic and side effects [6]. In recent years, as a new tumor treatment method, molecular targeted therapy has been increasingly favored by doctors and patients. The drug inhibits the growth of tumor cells by precisely locating the carcinogenic sites [7]. Anlotinib is a new drug for targeted molecular therapy [8], but its safety and effectiveness remain to be further studied. If the prognosis of patients is poor, molecular targeted therapy cannot produce economic benefits. Therefore, it is of great significance to establish a predictive model suitable for clinical practice and considering multiple factors.

With the application of data mining technology in medical research, many scholars use machine learning methods for disease research [9–12]. Kim et al. [13] used the support vector machine to predict the 5-year survival of breast cancer patients. Chen et al. [14] used artificial neural network to establish the survival risk model of patients with NSCLC

in four medical institutions. The max-min hill-climbing (MMHC) is a classical Bayesian network structure learning algorithm proposed by Tsamartinos in 2006 [15]. This algorithm is a local optimization method and an improvement of depth first search. It uses feedback information to help generate solution decisions. In this study, we first established the prediction model by MMHC in previous case data. Then, the effects of 40 patients with advanced NSCLC who came to our hospital were predicted by the model. Finally, the actual curative effect was analyzed.

2. Materials and Methods

2.1. General Information. The previous data set was selected from the lung cancer patients diagnosed in our hospital in the recent five years. The prognosis model was built by the maximum and minimum hill-climbing algorithm (MMHC). A total of 40 patients with advanced NSCLC in our hospital from January 2019 to July 2020 were selected as the validate database. According to the prediction results of the MMHC model, the patients were divided into the research group and control group. The study was approved by the hospital ethics committee, and informed consent was obtained from patients and their families.

2.2. Inclusion and Exclusion Criteria. Inclusion criteria were as follows: (1) the histologic examination diagnosed with NSCLC and patients clinical staging for III B or above, (2) over 18 years of age, (3) patients with a performance status score of 0-2 according to the physical condition established by the Eastern American Cancer Society group, (4) with measurable lesions and the expected survival time is more than three months, (5) epidermal growth factor receptor (EGFR) or anaplastic lymphoma kinase- (ALK-) positive in enrolled patients, and (6) all subjects gave informed consent and signed informed consent.

Exclusion criteria were as follows: (1) patients with primary tumors other than lung cancer; (2) patients with severe heart, liver, kidney, and other organ dysfunction; (3) patients suffering from neuropsychiatric diseases and unable to cooperate with this study; (4) the tumor has invaded essential blood vessels or during the follow-up treatment is likely to have massive bleeding patients; (5) women during pregnancy or lactation; (6) patients with deep venous thrombosis or pulmonary embolism; and (7) patients with other diseases were seriously endangering the life safety of patients or affecting the conduct of this study.

2.3. Establishment of Prognosis Model of Lung Cancer

2.3.1. Feature Selection. According to tumor information and prognostic factors related to survival, 16 information variables including these factors were derived from the database: gender, marital status, location, affected side, pathological type, histological grading, tumor staging, degree of transfer, degree of diffusion, degree of lymph node accumulation, type of operation, radiotherapy or not, age of diagnosis, tumor size, number of lymph nodes, and examined number of positive lymph nodes. The last four variables were continuous, and the rest were discrete variables.

To improve the model's accuracy, the valuable features were selected from the above 16 information variables. Firstly, the chi-square test was passed in 12 variables ($P < 0.05$), which were marital status, histological grade, tumor stage, degree of metastasis, degree of diffusion, degree of lymph node accumulation, type of operation, radiotherapy or not, age of diagnosis, tumor size, number of lymph nodes examined, and positive number of lymph nodes. Then, the logistic regression analysis was used to filter the final characteristic variables. They were histological grade, tumor stage, diagnosis age, tumor size, number of examined lymph nodes, and number of positive lymph nodes. The screening results were shown in Table 1.

2.3.2. Data Discretization. Both the final choice characteristic variables were are continuous data. These data should be discretized by the equidistant method. The main idea of this study is let the value range of continuous variable X be $[X_{\min}, X_{\max}]$ and give the separable interval number "r" according to the prior knowledge. Since each interval is of equal width, the width of each interval is $d = X_{\max} - X_{\min}/r$. The value X_i of continuous variable X and discrete level $j\,(0 \le j \le r-1)$ satisfies the following equation:

$$\{X_i = X_{\min}, \mathrm{X_{min}} + \mathrm{j} \times \mathrm{d} < \mathrm{X_i} \le X_{\min} + (j+1) \times d, X_i = j + 1\, X_i = 0. \tag{1}$$

2.3.3. Modeling Method. In disease survival prediction, the traditional statistical model is challenging to calculate the posterior probability and cannot directly express the relationship between variables. In this study, the Bayesian network method was used to establish the prognosis model of lung cancer. Bayesian network is a directed acyclic graph with parameters, which is represented by two tuples (G, Θ), where $G = (V, E)$ is the directed acyclic graph of node relationship, which is called Bayesian network structure. Node set $V = \{X_1, X_2, \cdots, X_n\}$ is the random vector, and directed edge set $E = \{e_{ij} \mid X_i \longrightarrow X_j, i, j = 1, 2, \cdots, n\}$ is the dependence between variables. $\Theta = \{\Theta_1, \Theta_2, \cdots, \Theta_n\}$ represents the conditional probability of node X_i, which is called Bayesian network parameter. The parameter o of node X represents the conditional probability distribution of itself and its parent node set $\mathrm{Pa}(X_i)$, which is $\Theta = \mathrm{P}(X_i \mid Pa(X_i))$. In addition, any given Bayesian network satisfies the Markov condition; that is, $\forall X_i \in V$, and X_i are independent of all nondescendant nodes except its parent node set $\mathrm{Pa}(X_i)$. Therefore, the joint probability distribution of variable set $\mathrm{V} = \{X_1, X_2, \cdots, X_n\}$ can be decomposed into

$$\mathrm{P(V)} = \mathrm{P}(X_1, X_2, \cdots, X_n) = \prod_{i=1}^{n} P(X_i \mid Pa(X_i)). \tag{2}$$

The Bayesian network model uses a directed acyclic graph to represent the dependent and independent relationship between variables and uses conditional probability distribution to describe the dependent relationship between variables and their parent nodes. Therefore, the establishment of the Bayesian network model includes two parts: (1)

Table 1: Final characteristic variables filtered by logistic regression analysis.

Variable	B	Std. error	P	Exp	95% exp	
Histological grade	—	—	0.002	—	—	—
Tumor stage	—	—	0.011	—	—	—
Diagnosis age	0.058	0.012	0.001	0.931	0.921	0.962
Tumor size	0.015	0.006	0.012	0.978	0.962	0.989
Number of examined lymph nodes	0.048	0.013	0.003	1.049	1.013	1.084
Number of positive lymph nodes	0.187	0.062	0.004	0.821	0.731	0.947

determining the relationship between variables to find the network structure, namely, structure learning and (2) determining the conditional probability table of each node, namely parameter learning.

2.3.4. Structural Learning Methods. The MMHC algorithm is used to learn the structure of the Bayesian network. This algorithm combines the methods of dependency analysis and score search and is divided into two stages. The first stage is learning. In this stage, the MMPC algorithm is used to determine each node's candidate parent-child node set, and the undirected framework of Bayesian network structure is constructed. In the second stage, the greedy mountain climbing algorithm is used to search and score the framework of the network structure obtained and find the network structure which makes the scoring function the largest.

The MMPC algorithm uses the max-min heuristic strategy to determine the candidate parents and children (CPC) set of the target variable (T) from the given data set, which is divided into two stages. In the first stage, we define a correlation function to determine the conditional dependence of other variables and target variable T under a given CPC. The larger the function value indicates, the stronger the conditional dependence between variables; when the function value is zero, there is no dependency between variables: the independent piece. The max-min heuristic strategy selects the variable with the max-min relevance to the target variable t under the given CPC condition to enter the CPC. When all variables except the variables in the CPC are conditionally independent of the target variable T under the given CPC condition, the first stage stops. In the second stage, the variables in the candidate parent-child node-set CPC are tested, and wrong variables are removed. For the variable X in CPC, if there is a subset S of CPC such that Assoc (X, T,| S), then the variable X is removed from CPC.

The correlation function of variables X and T under given variable set Z is defined as

$$\mathrm{Assoc}(\mathrm{X}, \mathrm{T} \mid \mathrm{Z}) = 2\sum_{a,b,c} N_{ijk}^{abc} \ln \frac{N_{ijk}^{abc} N_k^c}{N_{ik}^{ac} N_{jk}^{bc}}, \tag{3}$$

where N_{ijk}^{abc} is the number of samples satisfying $X = a$,$T = h$, and $Z = c$ in data set D. The corresponding minimum correlation function is defined as

$$\mathrm{MinAssoc}(\mathrm{X}, \mathrm{T}, |\mathrm{Z}) = \min_{S \subseteq Z} Assoc(X, T \mid S), \tag{4}$$

where S is a subset of variable set Z.

2.4. Treatment Methods. The 40 patients in the validate database were predicted by the above MMHC algorithm. Among them, 20 cases predicted better curative effect and was defined as the research group. Another 20 patients with poor prognosis were defined as the control group. There was no significant difference in gender, age, TNM stage, tumor type, and follow-up time between the two groups ($P > 0.05$).

Both groups were given pemetrexed disodium (Qilu Pharmaceutical Co., Ltd.) by intravenous drip of 500 mg/m^2, 10 min/time, for 21 days for 1 treatment cycle. Prophylactic medication was as follows: 7 days before pemetrexed disodium infusion, folic acid 400 g/d was taken orally for 28 days, until the end of pemetrexed treatment. Intramuscular injection of vitamin B12 at 1 000 g/d 7 days before pemetrexed was performed at an interval of 9 weeks. Dexamethasone 4 mg was taken orally for 2 times per day before and after pemetrexed, respectively. CT examination was performed once every 2 cycles of chemotherapy to evaluate the efficacy, and chemotherapy was continued without tumor deterioration or severe adverse reactions. As the tumor worsens, the chemotherapy regimen is changed. Before chemotherapy, patients were given a 5-HT3 receptor antagonist to prevent vomiting, and on this basis, taking anlotinib hydrochloride capsule (Chia Tai Tianqing Pharmaceutical Group Co., Ltd.) orally once per day, with the initial dose of 12 mg/time. The regimen was taken orally before breakfast for 14 d consecutively, with 7 d withdrawal and 21 d as a cycle. If severe toxicity occurred during treatment, the dose of anlotinib was reduced to 10 mg/d or 8 mg/d.

2.5. Intelligent Image Segmentation and Diameter Measurement. After the tumor was segmented by artificial neural network, the long diameter of primary tumor and most extensive metastatic lesion was measured to compare the changes between two groups.

2.5.1. Image Preprocessing. CT image is polluted by noise and the image quality decreases. Wiener filter is a classical linear denoising filter. It is often used to recover useful signals from additive noise. It is a filtering method that combines degradation function and noise statistical characteristics. At the same time, the imprecise and fuzzy information of CT image are processed by fuzzy enhancement to enhance the image contrast.

2.5.2. Image Texture Feature Extraction. Texture is a visual feature that reflects the homogeneous phenomenon in the image and reflects the surface structure, organization, and arrangement attribute of the object surface that changes slowly or periodically. Because texture features can provide unique spatial diversity information of regional pixels, it is easy to distinguish between target and background, which is suitable for lung cancer lesion extraction. There are three salient features extracted in this study, namely, image inertia, mean, and entropy, which are obtained from formulas (5)–(7):

$$tf_1 = \sum_{i=1}^{N}\sum_{j=1}^{N}(i-j)\times p(i,j)^2, \tag{5}$$

$$tf_8 = \sum_{i=1}^{N}\sum_{j=1}^{N}\frac{p(i,j)}{M\times N}, \tag{6}$$

$$tf_{10} = \sum_{i=1}^{N}\sum_{j=1}^{N}(i-j)\times p(i,j)\times \lg\left[p(i,j)\right]. \tag{7}$$

2.5.3. Image Fractal Feature Extraction. Fractal feature is used to describe complex and irregular medical image features. Fractal dimension is an important parameter to describe the complexity, irregularity, and spatial distribution trend of nonlinear image, which is calculated by difference box dimension.

The specific steps are as follows: divide the $N \times N$ image into $s \times s$ blocks. $2 < s < N/2$, let $r = n/s$, each block contains a column $s \times s \times h$ of boxes, and H is the height of a single box. A 5×5 window is used to slide on the image with a moving range of r. assuming that the maximum gray value and the minimum gray value in the (i, j)-th block fall in the K and l boxes, respectively, the number of boxes required to cover the (i, j)-th block is calculated by formula (8), and the number of boxes required to cover the whole image is given by formula (9). At this time, the corresponding fractal dimension FD is given by formula (10). Select a group of S, and the fractal dimension FD can be obtained by linear fitting:

$$n_r(i,j) = l - k + 1, \tag{8}$$

$$N(r) = \sum_{i,j} n_r(i,j), \tag{9}$$

$$\mathrm{PD} = \frac{\log\left[N(r)\right]}{\log\left(1/r\right)}. \tag{10}$$

2.5.4. Artificial Neural Network. Artificial neural network has the ability of self-learning and self-adaptive. It can determine the potential law between the two by pretraining samples and prediction samples and calculate the new input sample data by using the rules formed in the training stage.

When using ANN to segment the image, all points in the image to be segmented are clustered into target and nontarget pixels, and the nontarget pixels are removed after accurate clustering, so as to obtain the target image. The specific steps are as follows.

(1) A c-layer neural network is set. For example, the input mode P is added to the input layer, the sum of y unit inputs in layer z is U_x^z, the output is U_j^k, and the combination weight from the j-th neuron in layer $z-1$ to the x-th neuron in layer z is W_{xy}. If the relationship function between input and output of each neuron is f, the relationship between variables is shown in formulas (11)–(13):

$$V_x^z = f(U_x^z), \tag{11}$$

$$U_x^z = \sum_y W_{xy} V_x^{z-1}, \tag{12}$$

$$\mathrm{f(h)} = \frac{1}{1+e^{-h}}. \tag{13}$$

(2) Define the error function E as the square sum of the difference between the expected output and the actual output, as shown in the formula (14). The ANN learning process is to find the minimum value of the error function. The gradient descent method of nonlinear programming is used to obtain the update ΔW_y^x of the weight W_y^x, as shown in the formula (15). ε is the learning rate, with a value of 0-1:

$$\mathrm{E} = \frac{1}{2}\sum_y \left(V_y^c - T_y\right)^2, \tag{14}$$

$$\Delta W_y^x = -\varepsilon\frac{\vartheta E}{\vartheta W_{xy}}. \tag{15}$$

(3) After more complex derivation operation, the modified weight is obtained. See the formulas (16) and (17) to complete the convergence of the algorithm:

$$W_{xy}^{\cdot} = W_{xy} - \varepsilon d_y^z V_y^{z-1}, \tag{16}$$

$$d_y^z = V_y^z\left(1 - V_y^z\right)\sum_p W_{xp} d_y^{z+1}. \tag{17}$$

In order to avoid over fitting, the formula (18) is used to obtain the upper limit of the number of hidden layers N_h, where N_i represents the number of neurons in the input layer, N_o represents the number of neurons in the output layer, N_s represents the number of training samples, the value range of α is 2-10, and the average value of input and output is used as the lower limit of the hidden layer:

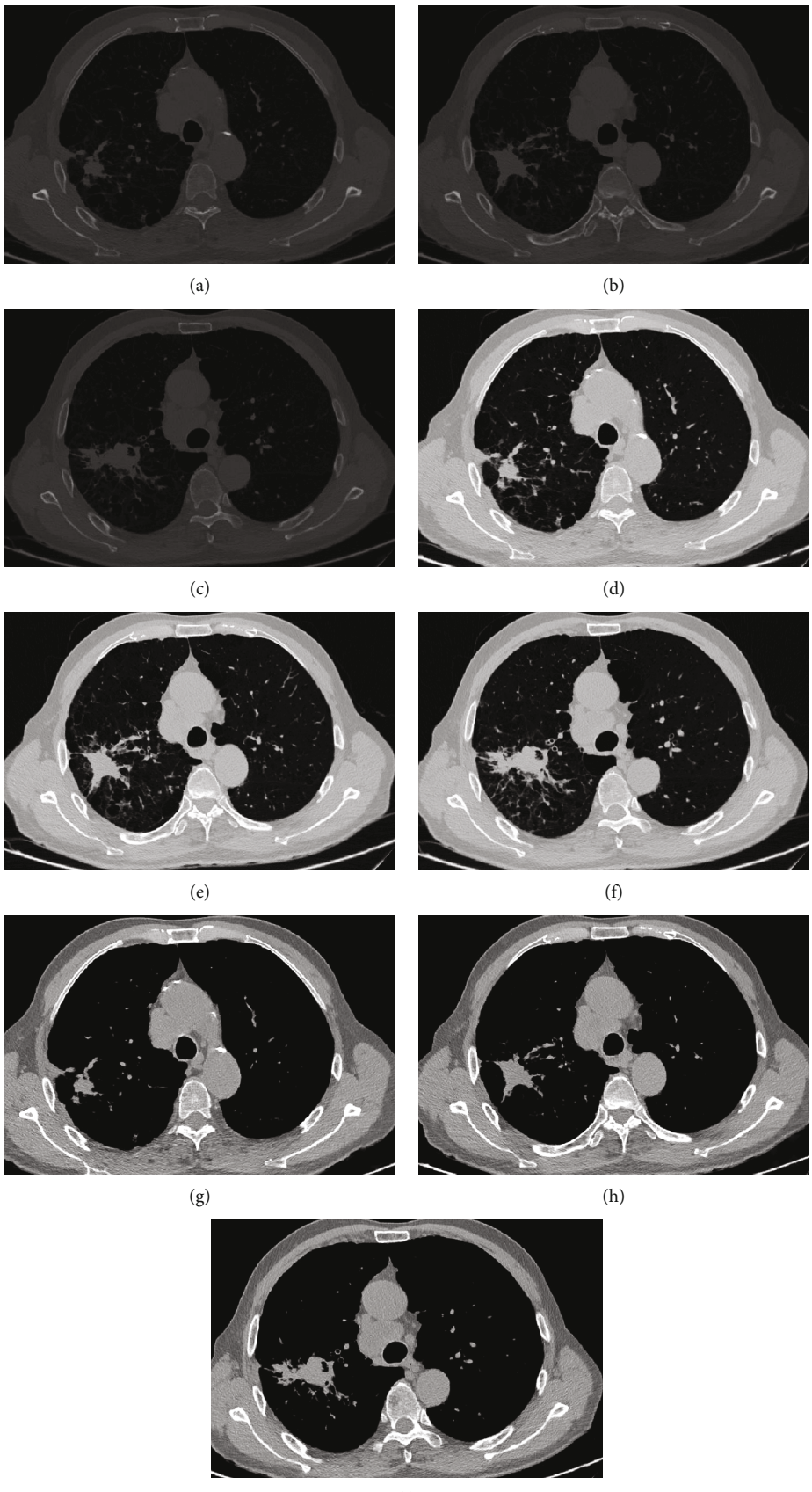

(a) (b) (c) (d) (e) (f) (g) (h) (i)

Figure 1: Image preprocessing of lung cancer. (a)–(c) gray image. (d)–(f) Wiener filtering. (g)–(i) Fuzzy enhancement.

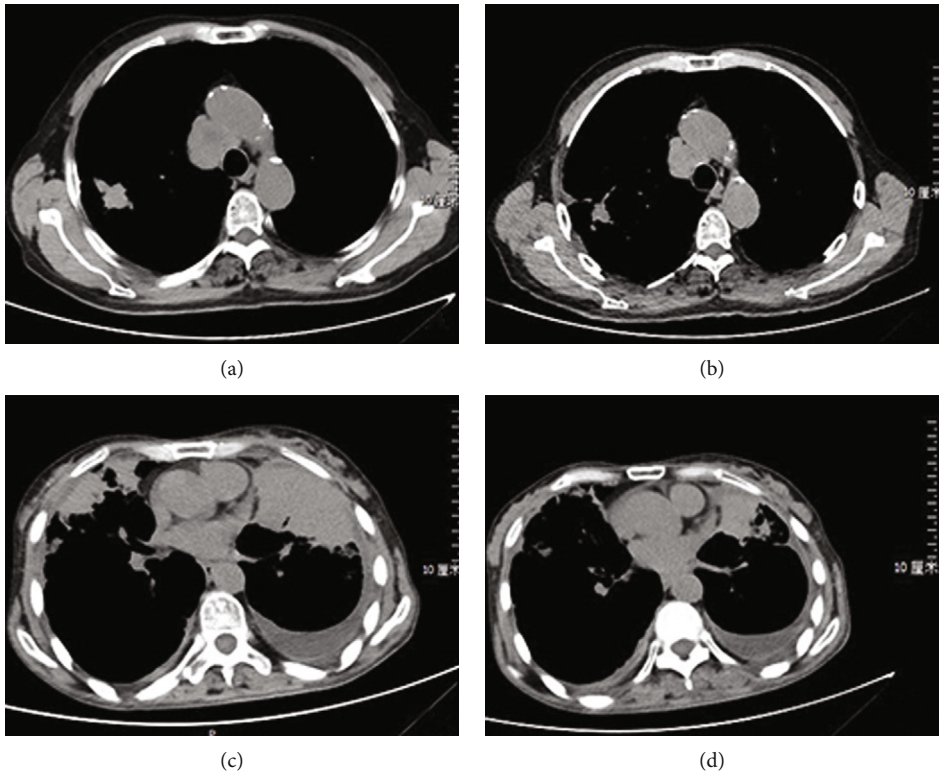

(a) (b) (c) (d)

Figure 2: CT observation before and after treatment in the two groups. (a) Control group before treatment. (b) Control group after treatment. (c) Research group before treatment. (d) Research group after treatment.

$$N_h = \frac{N_s}{\alpha(N_i + N_o)}. \tag{18}$$

2.6. Criteria for Clinical Efficacy. Patients were followed up until disease progression or intolerance. The RECIST was applied to evaluate the tumor regression of primary tumor after chemotherapy. Complete remission (CR) was as follows: all target lesions are undetectable and duration not less than four weeks. Partial remission (PR) was as follows: compared with the baseline level, the sum of the two diameters of all target lesions is reduced by more than 30%. Progression disease (PD) was as follows: baseline lesion long diameter increased not less than 20% or new lesions appeared. Stable disease (SD) was as follows: sum of the length of the long diameter of baseline lesions did not reach PR or increase did not reach PD:

$$\text{Disease control rate (DCR)} = (\text{CR} + \text{PR} + \text{SD})/\text{total cases}, \tag{19}$$

$$\text{Objective response rate (ORR)} = (\text{CR} + \text{PR})/\text{total cases}, \tag{20}$$

which compared the progress free survival (PFS) between them after treatment.

2.7. Statistical Methods. Use SPSS 20.0 statistical software. The measurement data were measured by mean ± standard deviation, and the count data was described by component ratio or rate (%) and using χ^2 test for comparison between groups.

3. Results

3.1. Intelligent Image Segmentation Results. The image preprocessing results are shown in Figure 1, in which Wiener filtering eliminates image noise, and the image contrast is significantly improved after fuzzy enhancement.

3.2. Measurement of the Maximum Diameter of Solid Tumor Lesions. After two courses of treatment, the maximum diameter of primary foci and metastatic foci in both groups was significantly reduced compared with that before treatment (Figure 2). The solid tumors in the research group shrank significantly, surpassing the control group. The difference was statistically significant ($P < 0.05$, Figures 3 and 4). The three-dimensional (3D) reconstruction results from the segmented images showed that the tumor volume in the research group was significantly reduced than in the control group (Figure 5).

3.3. Comparison of Clinical Efficacy between Two Groups. After treatment, the ORR and DCR of the control group were 20.0% and 75.0%; the ORR and DCR of the research group were 20.0% and 90.0%, respectively; the DCR of the research group was significantly higher than that of the conventional group ($P < 0.05$), see Table 2.

3.4. PFS Comparison between the Two Groups. After treatment, PFS in the research group was 7.1 months, significantly higher than the conventional group (4.8 months). The difference is statistically significant ($P < 0.01$), as shown in Figure 6.

4. Discussion

For patients with early NSCLC, surgical treatment is still the primary treatment, but the treatment of advanced NSCLC is still dominated by traditional radiotherapy and chemotherapy. However, with the in-depth research on the EGFR signaling pathway, a series of targeted drugs have been found, and corresponding targeted therapeutic drugs have been developed [16]. At present, the treatment of lung cancer has been upgraded to the level of molecular targeted therapy. The emergence of targeted drugs has prolonged the survival time of NSCLC patients, especially for patients with favorable EGFR mutations and ROS1 and ALK-positive patients, and improved the patients' clinical prognosis and life quality. The clinical efficacy of negative patients without modifications is still low, and there is also a phenomenon of targeted drug resistance in clinical. There is no unified treatment plan in clinical, and the effectiveness of ROS1 drug treatment is quite different [17]. Therefore, the development of new targeted therapeutic drugs has become a hot issue in this field.

Anlotinib can inhibit VEGF1, 2 ,and 3, α and β, platelet-derived growth factor receptor, fibroblast cell growth factor receptors-1, 2, 3, and 4, C-kit, and other targets. This drug plays a robust inhibitory effect and then plays a role in inhibiting tumor blood vessel growth and tumor growth [18, 19]. Related studies have found that anlotinib has certain advantages in the clinical efficacy and safety of treating patients with NSCLC. It can provide new therapies for refractory NSCLC patients who have failed multiline chemotherapy and drug resistance [20]. Pemetrexed is an antimetabolic drug that can block purine and pyrimidine synthase, thereby preventing cell proliferation and playing an antitumor effect. Pemetrexed has a good impact on various tumors, especially NSCLC and malignant mesothelioma [21, 22].

In this study, it was found that the DCR of anlotinib hydrochloride combined with pemetrexed could be effectively improved and prolong the PFS of the patients. After treatment, the patient's daily life, emotional control, activities, social/family life, and other scores were higher than before treatment, and the total score was also higher than before treatment. The results indicated that combined treatment has certain advantages in clinical efficacy and safety in treating patients with NSCLC. The consideration may be related to the following reasons. Firstly, anlotinib acts as a tumor suppressant through targeted inhibition of angiogenesis and cell proliferation-related kinases. Secondly, by using molecular targeting to treat patients with NSCLC, the body damage caused by chemotherapy is avoided, and the life quality of patients can be improved [23]. This study also found that combined treatment can increase the incidence of hand-foot syndrome in patients. Therefore, when using anlotinib to treat patients, attention should be paid to complications such as hand-foot syndrome to avoid serious consequences.

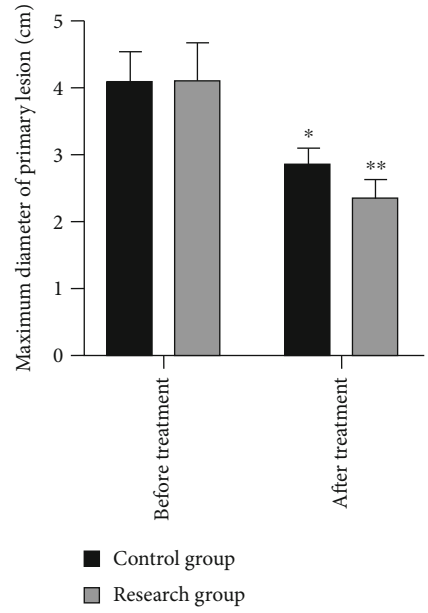

Figure 3: Comparison of maximum diameter of the primary lesion between the two groups before and after treatment. *Compared with the data before treatment, $P < 0.05$; **compared with the data before treatment, $P < 0.01$.

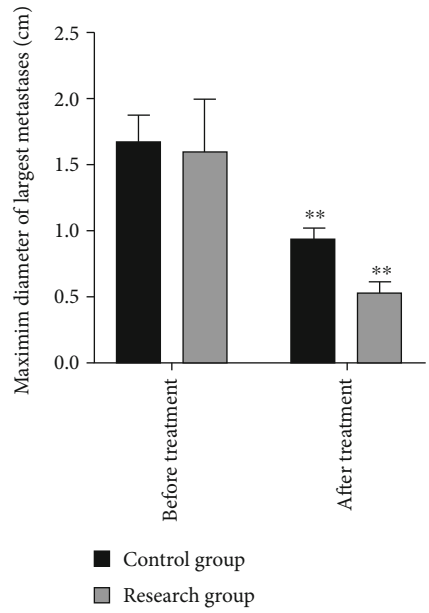

Figure 4: Comparison of maximum diameter of the largest metastases between the two groups before and after treatment. ** Compared with the data before treatment, $P < 0.01$.

The development of targeted drugs is expensive, which brings a severe economic burden to patients. If the curative effect is not exact, it is not worth the loss for the whole family. Therefore, the ideal way is to evaluate the prognosis of

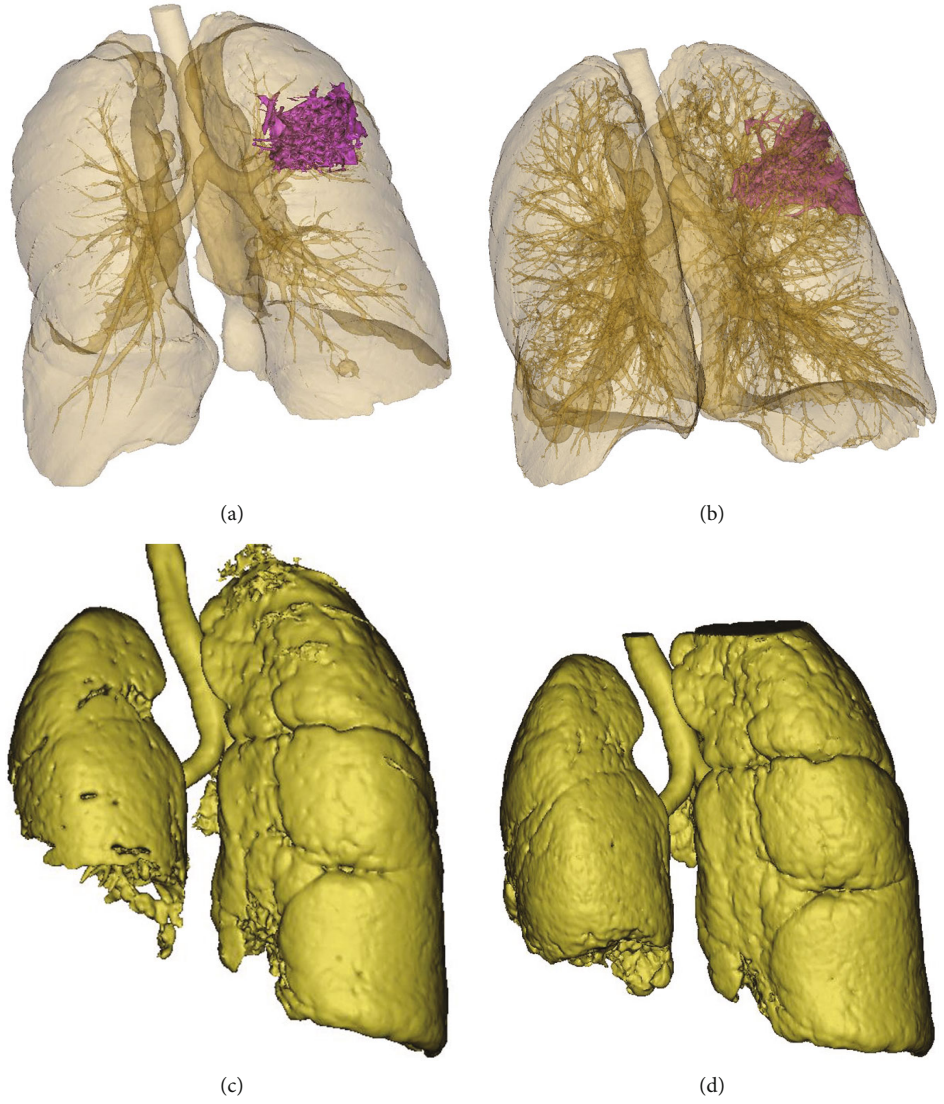

Figure 5: Three-dimensional reconstruction before and after treatment in the two groups. (a) Control group before treatment. (b) Control group after treatment. In the control group, the tumor volume decreased from 53.6 cm^3 to 48.1 cm^3 (5.5 cm^3). (c) Research group before treatment. (d) Research group after treatment. In the research group, the normal lung volume increased from 2139.0 cm^3 to 2327.4 cm^3, equivalent to the reduction of tumor volume by 188.4 cm^3.

Table 2: Comparison of clinical efficacy between two groups of patients.

Group	n	CR/case	PR/case	SD/case	PD/case	ORR/%	DCR/%
Control group	20	0	4	11	5	20.0	75.0
Research group	20	0	4	14	2	20.0	90.0*

*$P < 0.05$ vs. conventional group.

patients in advance. If the prognosis is good, the use of drugs is more reasonable. Based on the data collected in the past five years, this study established a prediction model using the MMHC algorithm. Then, we make a further prospective study using this model. Under the guidance of the model, the research group has a lower diameter of primary foci and metastatic foci, a higher ORR, DCR, and a longer PFS than the control group. The results further confirm the role of the MMHC algorithm in the precise treatment of NSCLC. In addition, many factors may influence the prognosis, mainly the histological grade, tumor stage, diagnosis age, tumor size, number of examined lymph nodes, and number of positive lymph nodes. The MMHC algorithm model is the result of a comprehensive analysis.

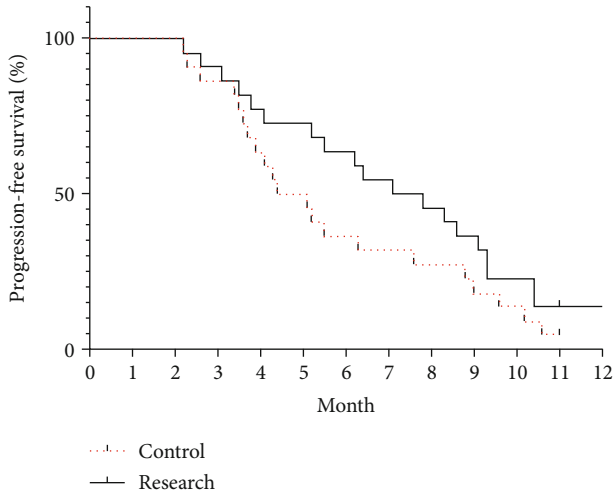

Figure 6: Progression-free survival curves for the two groups.

5. Conclusions

In summary, under the guidance of the MMHC algorithm modes, the combination of Anlotinib hydrochloride capsules and pemetrexed disodium chemotherapy in the treatment of advanced NSCLC is more effective, which is conducive to the prognosis judgment and treatment cost control. There are some shortcomings in this study. The sample of patients was small, which needs to be further improved in the future. In the future, we will apply more algorithms to predict the efficacy of drugs.

Data Availability

The data used to support the findings of this study are available from the corresponding author upon request.

Conflicts of Interest

The authors declared that there was no conflict of interest.

References

[1] Y. Mao, D. Yang, J. He, and M. J. Krasna, "Epidemiology of lung cancer," *Surgical Oncology Clinics of North America*, vol. 25, no. 3, pp. 439–445, 2016.

[2] M. Nagasaka and S. M. Gadgeel, "Role of chemotherapy and targeted therapy in early-stage non-small cell lung cancer," *Expert Review of Anticancer Therapy*, vol. 18, no. 1, pp. 63–70, 2018.

[3] T. Cufer and L. Knez, "Update on systemic therapy of advanced non-small-cell lung cancer," *Expert Review of Anticancer Therapy*, vol. 14, no. 10, pp. 1189–1203, 2014.

[4] D. Rocco, L. Della Gravara, C. Battiloro, and C. Gridelli, "The role of combination chemo-immunotherapy in advanced non-small cell lung cancer," *Expert Review of Anticancer Therapy*, vol. 19, no. 7, pp. 561–568, 2019.

[5] S. Gettinger, L. Horn, D. Jackman et al., "Five-year follow-up of nivolumab in previously treated advanced non-small-cell lung cancer: results from the ca209-003 study," *Journal of Clinical Oncology*, vol. 36, no. 17, pp. 1675–1684, 2018.

[6] Y. Y. Syed, "Anlotinib: first global approval," *Drugs*, vol. 78, no. 10, pp. 1057–1062, 2018.

[7] L. Liang, K. Hui, C. Hu et al., "Autophagy inhibition potentiates the anti-angiogenic property of multikinase inhibitor anlotinib through jak2/stat3/vegfa signaling in non-small cell lung cancer cells," *Journal of Experimental & Clinical Cancer Research*, vol. 38, no. 1, p. 71, 2019.

[8] G. Shen, F. Zheng, D. Ren et al., "Anlotinib: a novel multi-targeting tyrosine kinase inhibitor in clinical development," *Journal of Hematology & Oncology*, vol. 11, no. 1, p. 120, 2018.

[9] H. Chen, W. Li, and Y. Zhu, "Improved window adaptive gray level co-occurrence matrix for extraction and analysis of texture characteristics of pulmonary nodules," *Computer Methods and Programs in Biomedicine*, vol. 208, article 106263, 2021.

[10] Y. Liu, Q. Fang, A. Jiang, Q. Meng, G. Pang, and X. Deng, "Texture analysis based on u-net neural network for intracranial hemorrhage identification predicts early enlargement," *Computer Methods and Programs in Biomedicine*, vol. 206, article 106140, 2021.

[11] E. I. Mohamed, R. A. Meshref, S. M. Abdel-Mageed, M. H. Moustafa, M. I. Badawi, and S. H. Darwish, "A novel morphological analysis of DXA-DICOM images by artificial neural networks for estimating none mineral density in health and disease," *Journal of Clinical Densitometry*, vol. 22, no. 3, pp. 382–390, 2019.

[12] Z. Tang and Z. Zhang, "The multi-objective optimization of combustion system operations based on deep data-driven models," *Energy*, vol. 182, pp. 37–47, 2019.

[13] W. Kim, K. S. Kim, J. E. Lee et al., "Development of novel breast cancer recurrence prediction model using support vector machine," *Journal of Breast Cancer*, vol. 15, no. 2, pp. 230–238, 2012.

[14] Y. C. Chen, W. C. Ke, and H. W. Chiu, "Risk classification of cancer survival using ANN with gene expression data from multiple laboratories," *Computers in Biology and Medicine*, vol. 48, pp. 1–7, 2014.

[15] I. Tsamardinos, L. E. Brown, and C. F. Aliferis, "The max-min hill-climbing bayesian network structure learning algorithm," *Machine Learning*, vol. 65, no. 1, pp. 31–78, 2006.

[16] S. Tabchi, H. R. Kourie, and J. Kattan, "Adding checkpoint inhibitors to tyrosine kinase inhibitors targeting egfr/alk in non-small cell lung cancer: a new therapeutic strategy," *Investigational New Drugs*, vol. 34, no. 6, pp. 794–796, 2016.

[17] M. C. CE, G. K. Le AT, K. Jones et al., "Resistance mechanisms to targeted therapies inROS1+andALK+Non–small cell lung cancer," *Clinical Cancer Research*, vol. 24, no. 14, pp. 3334–3347, 2018.

[18] B. Lin, X. Song, D. Yang, D. Bai, Y. Yao, and N. Lu, "Anlotinib inhibits angiogenesis _via_ suppressing the activation of VEGFR2, PDGFR β and FGFR1," *Gene*, vol. 654, pp. 77–86, 2018.

[19] R. S. Heist, M. J. Guarino, G. Masters et al., "Therapy of advanced non-small-cell lung cancer with an sn-38-anti-trop-2 drug conjugate, sacituzumab govitecan," *Journal of Clinical Oncology*, vol. 35, no. 24, pp. 2790–2797, 2017.

[20] D. Wu, J. Nie, L. Dai et al., "Salvage treatment with anlotinib for advanced non-small cell lung cancer," *Thorac Cancer*, vol. 10, no. 7, pp. 1590–1596, 2019.

[21] R. Y. Kim, D. H. Sterman, and A. R. Haas, "Malignant mesothelioma: has anything changed?," *Seminars in Respiratory and Critical Care Medicine*, vol. 40, no. 3, pp. 347–360, 2019.

[22] J. H. Park, B. S. Kwon, S. J. Park et al., "Exceptional pemetrexed sensitivity can predict therapeutic benefit from subsequent chemotherapy in metastatic non-squamous non-small cell lung cancer," *Journal of Cancer Research and Clinical Oncology*, vol. 145, no. 7, pp. 1897–1905, 2019.

[23] Y. Sun, W. Niu, F. Du et al., "Safety, pharmacokinetics, and antitumor properties of anlotinib, an oral multi-target tyrosine kinase inhibitor, in patients with advanced refractory solid tumors," *Journal of Hematology & Oncology*, vol. 9, no. 1, p. 105, 2016.

Hindawi
Computational and Mathematical Methods in Medicine
Volume 2022, Article ID 3684700, 8 pages
https://doi.org/10.1155/2022/3684700

Research Article

Risk Prediction of Coronary Artery Stenosis in Patients with Coronary Heart Disease Based on Logistic Regression and Artificial Neural Network

Xiaobing Cheng,[1,2] **Weixing Han**,[1] **Youfeng Liang**,[1] **Xianhe Lin**,[1] **Juanjuan Luo**,[3] **Wansheng Zhong**,[2] **and Dong Chen**[2]

[1]*Department of Cardiology, The First Affiliated Hospital of Anhui Medical University, Hefei 230022, China*
[2]*Department of Cardiology, Hefei Third Clinical College, Anhui Medical University (Hefei Third People's Hospital), Hefei 230022, China*
[3]*Department of Pathophysiology, Gannan Medical College, Gannan 341000, China*

Correspondence should be addressed to Weixing Han; ayhwx57@163.com

Received 5 December 2021; Revised 16 January 2022; Accepted 28 February 2022; Published 19 March 2022

Academic Editor: Kelvin Wong

Objective. Coronary heart disease (CHD) is considered an inflammatory relative disease. This study is aimed at analyzing the health information of serum interferon in CHD based on logistic regression and artificial neural network (ANN) model. *Method*. A total of 155 CHD patients diagnosed by coronary angiography in our department from January 2017 to March 2020 were included. All patients were randomly divided into a training set ($n = 108$) and a test set ($n = 47$). Logistic regression and ANN models were constructed using the training set data. The predictive factors of coronary artery stenosis were screened, and the predictive effect of the model was evaluated by using the test set data. All the health information of participants was collected. Expressions of serum IFN-γ, MIG, and IP-10 were detected by double antibody sandwich ELISA. Spearman linear correlation analysis determined the relationship between the interferon and degree of stenosis. The logistic regression model was used to evaluate independent risk factors of CHD. *Result*. The Spearman correlation analysis showed that the degree of stenosis was positively correlated with serum IFN-γ, MIG, and IP-10 levels. The logistic regression analysis and ANN model showed that the MIG and IP-10 were independent predictors of Gensini score: MIG (95% CI: 0.876~0.934, $P < 0.001$) and IP-10 (95% CI: 1.009~1.039, $P < 0.001$). There was no statistically significant difference between the logistic regression and the ANN model ($P > 0.05$). *Conclusion*. The logistic regression model and ANN model have similar predictive performance for coronary artery stenosis risk factors in patients with CHD. In patients with CHD, the expression levels of IFN-γ, IP-10, and MIG are positively correlated with the degree of stenosis. The IP-10 and MIG are independent risk factors for coronary artery stenosis.

1. Introduction

Coronary heart disease (CHD) is a heart disease caused by various degrees of myocardial ischemia, which leads to narrowing or obstruction of blood vessels. The exact mechanism of CHD is not precise, and it is generally believed that its occurrence and development are related to genetic, environmental, and other factors [1–3]. Different types of immune cells play an essential role in forming early atherosclerotic plaque. These immune cells release effector molecules that can accelerate plaque formation. Therefore, atherosclerosis is considered an inflammatory relative disease and is the result of the joint action of various immune factors [4]. Different immune cells can cause multiple immune responses in the vascular wall, and inflammatory cytokines play an essential regulatory role in this process. Among them, T lymphocyte-induced pathological inflammatory response plays a crucial role in the progression of

atherosclerosis. Clinical studies have shown that T lymphocytes can be detected at all stages of atherosclerotic plaque formation [5]. Although T lymphocytes act as both proinflammatory and anti-inflammatory cytokines, it is noteworthy that most T lymphocytes in plaques are members of the Th1-cell family [6].

High expression of interferon-γ (IFN-γ) and its inducible C-X-C chemokinereceptor 3 (CXCR3) are detected in the arterial plaques of patients with coronary heart disease [7–9]. The serum CXCR3 chemokine level is high in patients with hypertension or aortic aneurysm. T-helper-1 (Th1-) related chemokines, including the monokine induced by interference (MIG/CXCL9), interfer-induced protein 10, (IP-10/CXCL10), and interference-induced t-cell alpha chemoattractant (I-TAC/CXCL11), are all induced by IFN-γ. These factors play a chemotactic role by interacting with CXCR3. CXCR3 chemokines (including MIG, IP-10, and I-TAC) may play a decisive role in developing atherosclerosis [10, 11]. Those studies have found an independent correlation between serum MIG level and carotid artery plaque, but no studies have reported whether the serum MIG level correlated with coronary artery stenosis.

Logistic regression and artificial neural networks (ANN) have been widely used in the biomedical field [12, 13]. This study is aimed at analyzing the health information of serum interferon in CHD based on logistic regression and the ANN model to provide a new method for the early diagnosis of CHD.

2. Material and Methods

2.1. General Data. From January 2017 to March 2020, 155 patients with coronary artery disease were randomly selected from the Third People's Hospital of Hefei, hospitalized due to palpitation, chest tightness, chest pain, etc. The diagnostic criteria for CHD were as follows: Patients with typical symptoms; the results of coronary angiography indicated that the lumen stenosis degree of one or more branched of coronary artery > 50%, or the left main artery stenosis degree > 50%. The exclusion criteria are as follows: patients with complicated aortic valve disease, variant angina pectoris, angina pectoris caused by coronary spasm, malignant tumor, infectious disease, autoimmune connective tissue disease, severe liver and kidney dysfunction, and a recent history of surgery or trauma.

A total of 155 patients with CHD were randomly divided into a training set ($n = 108$) and a test set ($n = 47$) according to a 10-fole crossover method. Logistic regression and ANN models were constructed using the training set data. The predictive factors of coronary artery stenosis were screened, and the predictive effect of the model was evaluated by using the test set data. The specific modeling steps are shown in Figure 1.

2.2. Serological Examination. For all the enrolled patients, 3 ml peripheral venous blood was extracted on admission or in the morning of the next day. After standing for one hour, the serum was centrifuged at 4000 rotation/min for 15 min. The upper serum was collected, divided into 0.6 ml centrifuge tubes, and placed in the refrigerator at -80°C for storage.

The ELISA was used to detect IFN-γ and MIG. The kit was provided by Endogen Company. IP-10 was detected by ELISA, and the kit was supplied by HyCult Biotechnology Company in the Netherlands. All three indicators were tested strictly according to the operation instructions. In addition, routine examinations of liver or renal function, blood lipid, or glucose were performed for all the enrolled patients. Cardiac color ultrasound examination was routinely performed, 12-lead electrocardiogram examination was performed, and the results were strictly recorded. With the written informed consent of all patients, the study plan was approved by the hospital ethics committee.

2.3. Grade of Coronary Artery Disease. Coronary angiography was performed with the participation of associate chief physicians qualified for coronary artery disease intervention. According to the number of diseased vessels, coronary angiography was divided into single-, double-, and multivessel diseases. Gensini score is a method to evaluate the severity of coronary artery disease. The more severe the CHD is, the higher the Gensini score.

The degree of lesion of each vessel was quantitatively assessed according to Gensini score: Luminal stenosis ≤ 25% was 1 point, 26%~50% was 2 points, 51%~75% was 4 points, 76%~90% was 8 points, 91%~99% was 16 points, and 100% was 32 points.

The coronary score coefficients of different segments were different. The score was multiplied by the lesion vessel coefficient, and the final score of the lesion was the sum of the branching scores of each patient. According to Gensini integral, there were three subgroups (Figure 2): 0 ~ 20 points (mild stenosis $n = 29$), 21~40 points (moderate stenosis $n = 52$), and >40 points (moderate stenosis $n = 27$).

2.4. Logistic Regression Model. As a logistic regression statistical model in which the most commonly used outcome variable is a dichotomous variable, the general form of logistic regression equation is often expressed as

$$\text{Logit}(P) = \text{Log}\left(\frac{P}{1-P}\right) = a + b_1x_2 + b_2x_2 + \cdots + b_mx_m, \quad (1)$$

where "a" is the constant, $b_1, b_2 \cdots, b_m$ is a regression coefficient, and $x_1, x_2, \cdots x_m$ is the predictor. Further calculation is expressed as

$$P = \frac{\exp\left(a + b_1x_2 + b_2x_2 + \cdots + b_mx_m\right)}{1 + \exp\left(a + b_1x_2 + b_2x_2 + \cdots + b_mx_m\right)}. \quad (2)$$

The logistic regression was used to determine the risk factors that significantly affected Gensini score.

2.5. Artificial Neural Network Model. ANN model is a computer structure and system based on modern neurobiological research, reflecting some human brain characteristics. The ANN uses training and learning methods to compare each neuron's actual output and expected output in the output

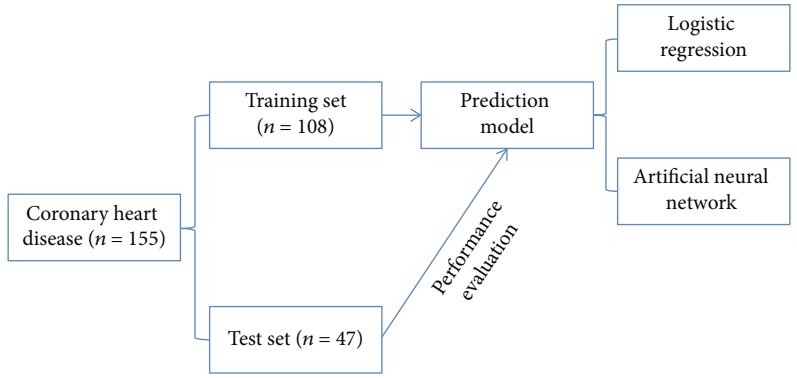

Figure 1: Modeling flow chart.

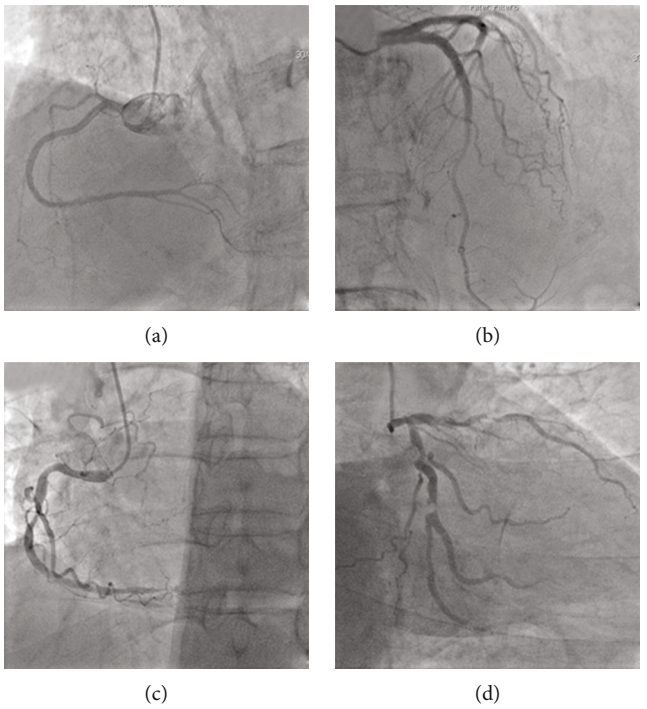

Figure 2: Different degrees of coronary artery stenosis. (a) There was no obvious stenosis in the right coronary artery. (b) 50% stenosis in the distal segment of anterior descending artery. (c) 80% stenosis in the middle segment of right coronary artery. (d) 95% stenosis in the middle segment of anterior descending artery, and 95% stenosis in the anterior and middle segments of circumflex branch.

layer to obtain the error between them. Then, according to the direction of reducing the error, each connection weight is modified from the output layer through each hidden layer and layer by layer and finally returns to the input layer. Thus, the accuracy of input pattern recognition is constantly improved, which can be used to predict the probability of occurrence.

2.6. Statistical Method. The data were analyzed by SPSS 23.0 software. Continuous variables were expressed as mean ± standard deviation or median ($P25$, $P75$). The t-test and one-way ANOVA were used. When the results of ANOVA showed statistically significant differences between each subgroup, the q' test was used for pairwise comparative analysis of the mean between the groups. The qualitative data were expressed as a percentage (%), and the qualitative data were compared by chi-square test. The Spearman correlation test was used for correlation analysis. Multivariate analysis was performed by logistic regression analysis.

3. Result

3.1. Comparison of General Clinical Data. There were no significant differences in gender, age, history of drinking and smoking history, history of diabetes and hypertension, body mass index (BMI), total cholesterol, triglyceride, low-density lipoprotein (LDL), non-HDL, myoglobin, IFN -γ, MIG, IP-10, with cysteamine acid, and systolic blood pressure between the training set and the test set ($P > 0.05$, Table 1 and Figure 3).

Table 1: Comparison of general clinical data.

Item	Training set ($n = 108$)	Test set ($n = 47$)	t/χ^2 value	P value
BMI (kg/m^2)	24.94 ± 2.03	21.34 ± 2.40	2.34	0.643
WC (cm)	85.02 ± 6.54	84.02 ± 8.39	1.68	1.231
TC (mmol/l)	4.78 ± 1.10	4.78 ± 2.01	1.76	1.012
TG (mmol/l)	1.99 ± 1.74	2.10 ± 0.88	1.34	0.810
HDL-C (mmol/l)	0.81 ± 0.26	0.79 ± 0.33	0.40	0.686
LDL-C (mmol/l)	3.21 ± 0.98	3.45 ± 0.78	2.32	0.076
SBP (mmHg)	125.23 ± 14.43	122.51 ± 13.24	1.11	0.271
DBP (mmHg)	85.26 ± 10.89	92.31 ± 10.11	1.67	0.991
Hcy (μmol/l)	14.00 ± 3.26	14.20 ± 3.21	0.35	0.725
hsCRP (mg/l)	1.60 ± 3.31	1.52 ± 3.16	0.14	0.889
IFN-γ (pg/ml)	97.5 ± 8.97	96.09 ± 8.31	0.92	0.359
MIG (pg/ml)	103 ± 10.10	104.11 ± 9.31	0.64	0.521
IP-10 (pg/ml)	109 ± 11.01	109.34 ± 10.35	0.18	0.857

Note: BMI: body mass index; WC: waist circumference; TC: total cholesterol; TG: triglyceride; HDL-C: high-density lipoprotein cholesterol; LDL-C: low-density lipoprotein cholesterol; SBP: systolic pressure; DBP: diastolic pressure; hsCRP: hypersensitive C-reactive protein; Hcy: homocysteine; Sdldl-c: small and dense low-density lipoprotein cholesterol; Sdldl-c/LDL-C: ratio of small, dense low-density lipoprotein cholesterol to low-density lipoprotein cholesterol.

3.2. Establishment of the Artificial Neural Network Model. In this study, according to the basic principle of ANN, the data of these influencing factors of 108 CHD patients in the training set were taken as input. The degree of coronary artery ISR corresponding to the patients was taken as output to construct and train the neural network, to realize the prediction effect of the model on coronary artery ISR (Figure 4).

3.3. Correlation Analysis of Serum Interferon with Coronary Artery Gensini Score. According to the Gensini score, patients in the training set were divided into three subgroups. The clinical variables correlation analysis showed that the three subgroups were significantly positively related with age, history of DM, hsCRP, BMI, and SBP; negatively correlated with high-density lipoprotein cholesterol; and significantly positively associated with the MIG and IP-10 serum levels (Table 2).

3.4. Logistic Regression Model Analysis. The multivariate logistic analysis took Gensini as dependent variables and introduces age, diabetes, IFN-γ, MIG, IP-10, and hsCRP into the logistic regression equation. Logistic regression analysis showed that MIG and IP-10 are predictors of Gensini's evaluation. MIG and IP-10 are independent risk factors of coronary artery disease. The results of Logistic regression analysis were shown in Table 3.

3.5. Distinction between Logistic Regression and Artificial Neural Network Model. The area under the curve of the logistic regression model in the training set is 0.805 (95% CI: 0.637-0.912), and the area under the curve of the ANN model in the training set is 0.847 (95% CI: 0.651-0.920). The area under the curve of the logistic regression model in the test set is 0.947 (95% *CI*: 0.899-0.963), while that in the ANN model is 0.958 (95% CI: 0.914-0.971). There was no statistically significant difference between the logistic regression and the neural network model ($P > 0.05$) (Figure 5).

4. Discussion

In this study, 108 patients with CHD were used as training set to establish logistic regression and ANN models to evaluate the detection factors of coronary artery stenosis and test sets verified the model's validity. According to Gensini integral in the training set, it could be divided into three subgroups, and the Spearman correlation analysis suggested IFN-γ, MIG, IP-10, and Gensini integral relationship [14–16]. Logistic regression analysis showed that MIG and IP-10 were independent risk factors for coronary artery stenosis. Therefore, serum IP-10 and MIG levels had potential clinical significance in diagnosing coronary atherosclerosis. Our results are similar to Gaballah et al. [17].

Coronary atherosclerotic heart disease is the leading cause of death and disability in humans worldwide. The pathophysiological mechanism of atherosclerosis remains unclear. Despite years of in-depth research in this field, rapid changes in treatment significantly reduced mortality and improved quality of life. The underlying cause of CHD is atherosclerosis, which is a chronic inflammatory disease. Th1 cells have been reported to be an important determinant of atherosclerosis progression. Their function is to secrete IFN-γ, promote the expression of adhesion molecules in endothelial cells and macrophages, and produce cytokines and chemokines [18]. As a decisive regulator of immune function, the IFN-γ has also become an essential factor in atherosclerosis [19, 20]. In recent years, many large-scale studies have proved that MIG is involved in

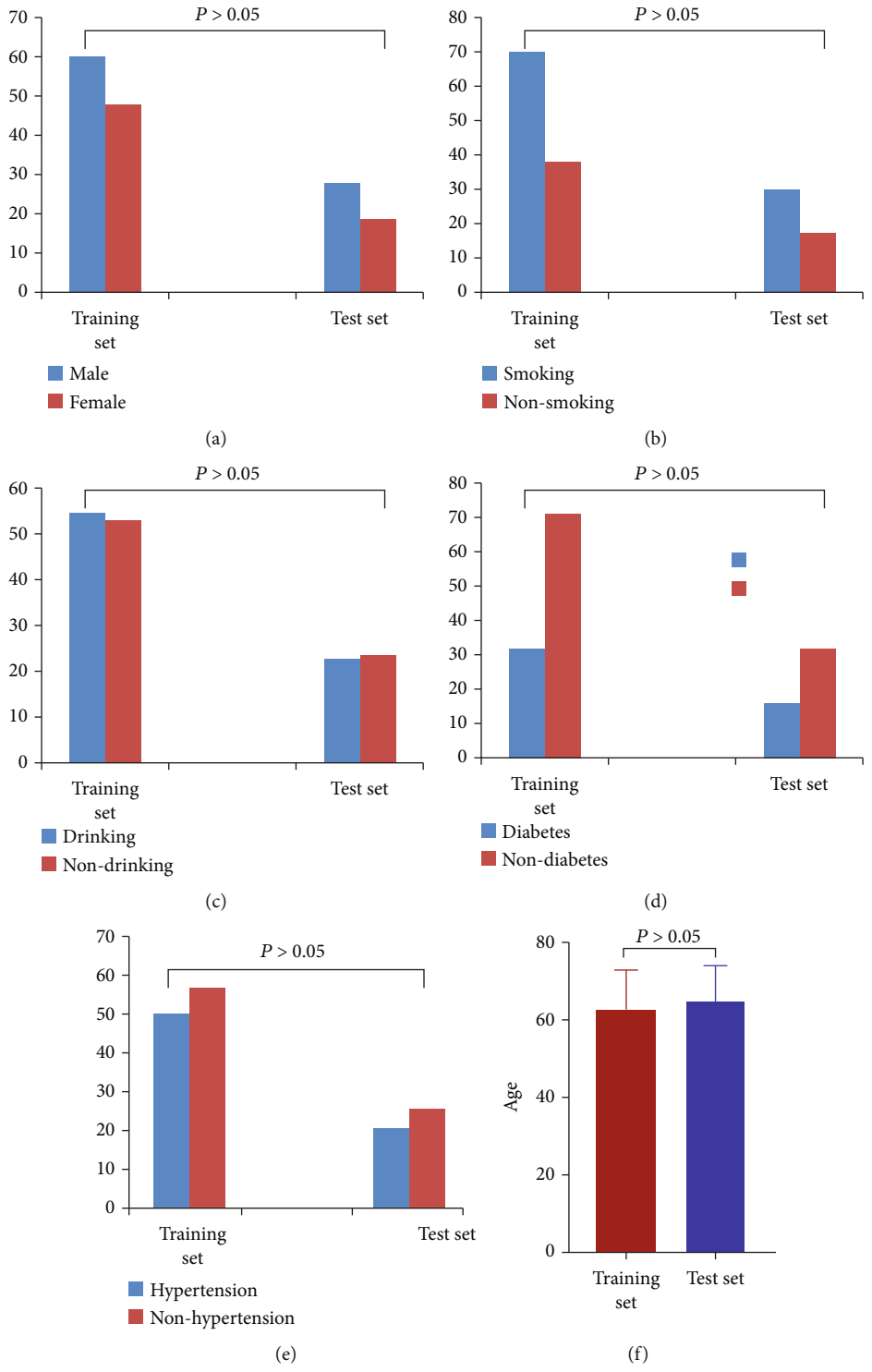

Figure 3: Comparison of gender, age, history of drinking and smoking, history of diabetes, and hypertension between training set and test set. There was no statistically significant difference between the two sets ($P > 0.05$).

atherosclerosis [21, 22]. In this study, IFN-γ in the CHD group was significantly higher. The IFN-γ also increased with the Gensini score, and the correlation analysis indicated a significant correlation with Gensini [8, 23]. The IFN-γ induces MIG and IP-10 secretion, and it has been previously reported that IFN-γ induces the co-localization of CXCR3 chemokines in human atherosclerotic plaques. Consistent with the results of this study, the mRNA levels of MIG, IP-10, and IFN-γ in CHD patients increased with the increase of Gensini. Th1-related chemokines, including interferon inducing mononuclear factor (MIG/CXCL9), IP-10/CXCL10, and interferon induction of T cell chemotactic

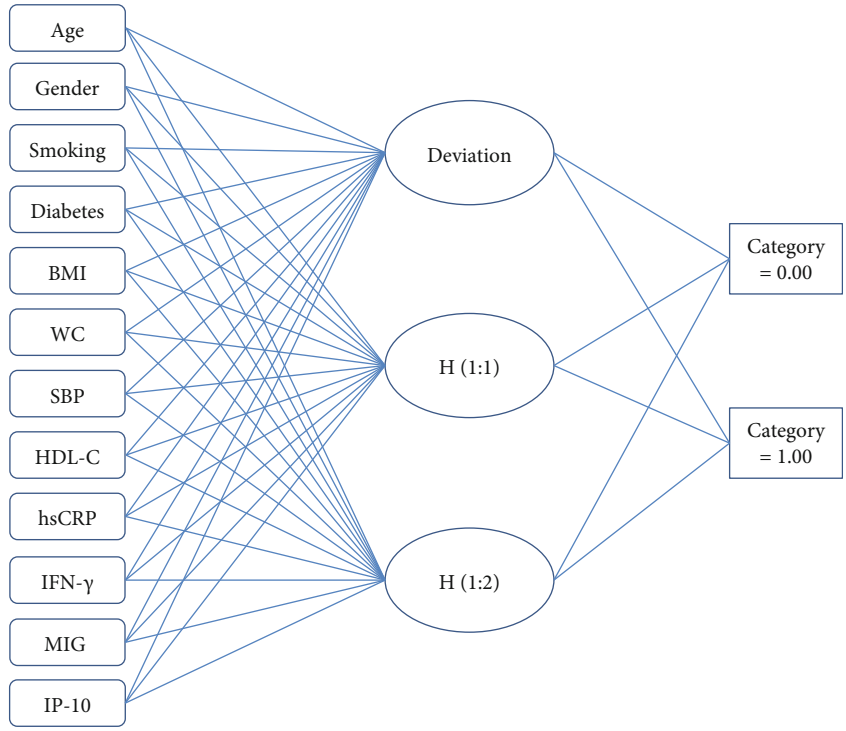

Figure 4: Multilayer perceptron artificial neural network.

Table 2: Correlation analysis between Gensini score and clinical variables.

Variable	Mild stenosis		Moderate stenosis		Severe stenosis	
	r	*P*	*r*	*P*	*r*	*P*
Age	0.492	<0.001	0.485	<0.001	0.563	<0.001
Male	0.102	0.21	0.087	0.237	0.132	0.322
Smoking	0.034	0.647	0.23	0.231	0.301	0.010
Diabetes	0.561	0.002	0.64	0.002	0.66	0.011
BMI	0.572	0.011	0.670	0.017	0.65	0.012
WC	0.211	0.12	0.302	0.13	0.201	0.003
SBP	0.679	<0.001	0.673	<0.001	0.621	<0.001
HDL-C	-0.173	0.030	-0.164	0.048	-0.201	0.023
hsCRP	0.052	0.541	0.053	0.491	0.544	0.332
IFN-γ	0.045	0.323	0.043	0.291	0.213	0.112
MIG	0.607	<0.001	0.794	<0.001	0.787	<0.001
IP-10	0.737	<0.001	0.772	<0.001	0.556	<0.001

Table 3: Analysis of risk factors of Gensini score.

Variable	β	*P*	OR	95% CI
Age	0.09	0.511	1.009	0.982–1.036
Diabetes	-0.257	0.550	0.774	0.333–1.795
IP-10	0.024	0.001	1.024	1.009–1.039
IFN-γ	-0.514	0.343	0.898	0.439–1.81
MIG	-0.100	<0.001	0.904	0.876–0.934
hsCRP	0.108	0.048	1.300	1.007–1.817

factor (I-TAC/CXCL11) will be induced by IFN-γ, probably in the process of the development of atherosclerosis play an important role, and vascular disease and atherosclerosis disease are often associated with carotid intimal thickening [24].

Like other IFN-γ-induced chemokines, IP-10 can produce different effects by binding CXCR3. These effects include the accumulation of CXCR3 T cells to the site of vascular injury, leading to intimal hyperplasia [25]. Chemokines can selectively induce the release of leukocyte cytokines and endothelial adhesion molecules and promote the accumulation of many inflammatory cells in the lesion site of atherosclerosis, triggering the inflammatory response [26]. At the same time, IP-10 can induce a variety of chemokines in vascular endothelial cells, macrophages, and smooth muscle cells, causing a variety of cascade effects, chemotaxis more inflammatory cells to the lesion site of atherosclerosis, and aggravates tissue damage. Peripheral blood mononuclear cells can produce high concentrations of MIG, IP-10, IFN-γ, mRNA and higher proportion of CXCR3+ cells and in mononuclear cell regulation of lymphoid cells in atherosclerotic lesions, migration, and retention using CXCR3 antagonists NBI-74330 treatment in mice, by blocking CXCR3+ T cells from circular migration to atherosclerotic plaques, thereby reducing the formation of atherosclerosis; therefore, these findings suggest that T cell-driven inflammation may play an important role in the progression of human atherosclerosis. In our study, we found that IP-10 was a predictor of Gensini assessment and an independent risk factor of coronary artery disease. In human and mouse models of atherosclerosis, IP-10 is involved in inflammation and angiogenesis in the mechanism of coronary atherosclerosis, making

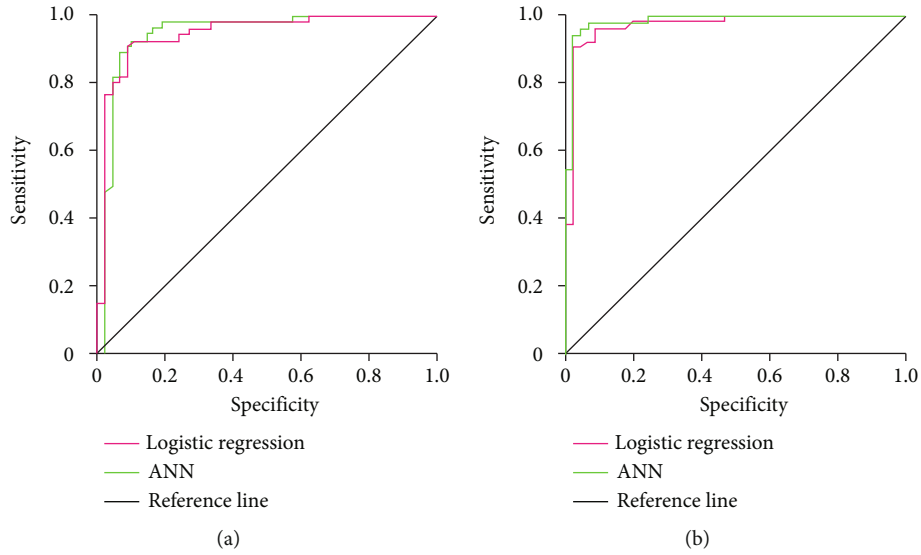

Figure 5: ROC curves of the logistic regression model and neural network model. (a) Degree of differentiation between the logistic regression model and neural network model in the training set. (b) Test the differentiation between logistic regression model and artificial neural network model.

it an attractive biomarker for coronary atherosclerosis. In people of European descent, IP-10 is associated with CHD, hypertension, and symptomatic heart failure [27, 28].

In this study, 155 patients with CHD were included to construct logistic regression and ANN models. The results showed that in the coronary heart disease group, serum MIG and IP-10 levels were positively correlated with Gensini score. The multiple regression showed that MIG and IP-10 were independent risk factors of coronary artery stenosis: MIG (95% CI: 0.876~0.934, $P < 0.001$) and IP-10 (95% CI: 1.009~1.039, $P < 0.001$). In addition, there was no significant difference between the neural network model and logistic regression model ($P > 0.05$). This means that MIG and IP-10 might be specific markers of coronary atherosclerosis. The results of this study have certain clinical significance. In addition, in the training and test sets, there was no statistically significant difference between the logistic regression model and ANN model in the area under the curve ($P > 0.05$). It shows that the logistic regression model and ANN model have good predictive efficiency in CHD.

However, there are several limitations to our study. First, the effectiveness of the prediction model is also affected by the number of variables, types, and sample size. In addition, this study is a single-center study, with fewer cases included and short observation time. In future studies, the number of population cases and multicenter participation will be further increased to further improve risk factors, to determine the application of MIG and IP-10 in coronary artery disease.

5. Conclusion

In summary, our results indicate the potential role of serum MIG and IP-10 in the progression of atherosclerosis. These findings also suggested that MIG may be a useful biomarker for the severity of coronary artery disease.

Data Availability

All data analyzed during this study are available from the corresponding author on reasonable request.

Conflicts of Interest

All authors declare no conflicts of interest in this paper.

Acknowledgments

This project is supported by the key topics of applied medicine research of Hefei Health and Family Planning Commission (Hwk2016zd009) and by the key project of Hefei Third People's Hospital (SYKZ202002).

References

[1] N. Behnamfar, M. J. Zibaeenezhad, H. Golmoghaddam, and M. Doroudchi, "d45ro+ memory t-cells produce il-17 in patients with atherosclerosis," *Cellular and Molecular Biology (Noisy-le-Grand, France)*, vol. 61, no. 8, pp. 17–23, 2015.

[2] S. F. Chang, S. F. Liu, C. N. Chen, and H. C. Kuo, "Serum ip-10 and il-17 from kawasaki disease patients induce calcification-related genes and proteins in human coronary artery smooth muscle cells in vitro," *Cell & Bioscience*, vol. 10, p. 36, 2020.

[3] I. Dhar, S. Siddique, E. R. Pedersen et al., "Lipid parameters and vitamin a modify cardiovascular risk prediction by plasma neopterin," *Heart*, vol. 106, no. 14, pp. 1073–1079, 2020.

[4] T. J. Guzik, N. E. Hoch, K. A. Brown et al., "Role of the t cell in the genesis of angiotensin II–induced hypertension and vascular dysfunction," *The Journal of Experimental Medicine*, vol. 204, no. 10, pp. 2449–2460, 2007.

[5] B. Yang, B. Xu, H. Zhao et al., "Dioscin protects against coronary heart disease by reducing oxidative stress and inflammation via Sirt1/Nnrf2 and p38 MAPK pathways," *Molecular Medicine Reports*, vol. 18, no. 1, pp. 973–980, 2018.

[6] G. Niccoli, R. A. Montone, V. Sabato, and F. Crea, "Role of allergic inflammatory cells in coronary artery disease," *Circulation*, vol. 138, no. 16, pp. 1736–1748, 2018.

[7] B. Fu, Y. Zhang, Q. Chen, Z. Guo, and N. Jiang, "Antibody microarray analysis of serum inflammatory cytokines in patients with calcific aortic valve disease," *Annals of Translational Medicine*, vol. 8, no. 12, p. 761, 2020.

[8] K. Liang, S. R. Dong, and H. Peng, "Serum levels and clinical significance of ifn-γ and il-10 in patients with coronary heart disease," *European Review for Medical and Pharmacological Sciences*, vol. 20, no. 7, pp. 1339–1343, 2016.

[9] Y. Liang, C. Yang, Q. Zhou et al., "Serum monokine induced by gamma interferon is associated with severity of coronary artery disease," *International Heart Journal*, vol. 58, no. 1, pp. 24–29, 2017.

[10] H. Wang, N. Zhang, G. Li, and B. Xu, "Proinflammatory cytokine ifn-γ, lncrna bancr and the occurrence of coronary artery disease,," *Life Sciences*, vol. 231, article 116510, 2019.

[11] Y. Xu and B. Shao, "Circulating lncrna ifng-as1 expression correlates with increased disease risk, higher disease severity and elevated inflammation in patients with coronary artery disease," *Journal of Clinical Laboratory Analysis*, vol. 32, no. 7, article e22452, 2018.

[12] E. I. Mohamed, R. A. Meshref, S. M. Abdel-Mageed, M. H. Moustafa, M. I. Badawi, and S. H. Darwish, "A novel morphological analysis of DXA-DICOM images by artificial neural networks for estimating bone mineral density in health and disease," *Journal of Clinical Densitometry*, vol. 22, no. 3, pp. 382–390, 2019.

[13] Z. Tang, Y. Li, X. Chai, H. Zhang, and S. Cao, "Adaptive nonlinear model predictive control of nox emissions under load constraints in power plant boilers," *Journal of Chemical Engineering of Japan*, vol. 53, no. 1, pp. 36–44, 2020.

[14] J. Karhu, T. I. Ala-Kokko, T. Vuorinen, P. Ohtonen, I. Julkunen, and H. T. Syrjälä, "Interleukin-5, interleukin-6, interferon induced protein-10, procalcitonin and C-reactive protein among mechanically ventilated severe community-acquired viral and bacterial pneumonia patients," *Cytokine*, vol. 113, pp. 272–276, 2019.

[15] N. O. Kurtovic and E. K. Halilovic, "Serum concentrations of interferon gamma (IFN-γ) in patients with psoriasis: correlation with clinical type and severity of the disease," *Medical Archives*, vol. 72, no. 6, pp. 410–413, 2018.

[16] H. R. Mozaffari, M. Molavi, P. Lopez-Jornet et al., "Salivary and serum interferon-gamma/interleukin-4 ratio in oral lichen planus patients: a systematic review and meta-analysis,," *Medicina*, vol. 55, no. 6, 2019.

[17] A. Gaballah, I. S. Naga, M. S. Zaghloul, H. M. Mostafa, and A. Noby, "Changes in the co-expressions of interleukin 29 (IL-29), IFN-inducible protein 10 (IP-10) and monokine induced by IFNγ (MIG) genes in chronic hepatitis c egyptian patients untreated and treated with DAAs," *Acta Virologica*, vol. 65, no. 2, pp. 141–148, 2021.

[18] A. H. Lichtman, C. J. Binder, S. Tsimikas, and J. L. Witztum, "Adaptive immunity in atherogenesis: new insights and therapeutic approaches," *The Journal of Clinical Investigation*, vol. 123, no. 1, pp. 27–36, 2013.

[19] K. E. Wilson, H. Demyanovich, L. H. Rubin, H. J. Wehring, C. Kilday, and D. L. Kelly, "Relationship of interferon-γ to cognitive function in midlife women with schizophrenia," *The Psychiatric Quarterly*, vol. 89, no. 4, pp. 937–946, 2018.

[20] X. Zhang, J. Xu, Z. Wu, W. Zhu, and S. Dong, "Development of a tree shrew-specific interferon-gamma assay," *Journal of Immunoassay & Immunochemistry*, vol. 39, no. 2, pp. 136–149, 2018.

[21] M. Sato, K. Hashimoto, Y. Kawasaki, and M. Hosoya, "Immune response after a single intravenous peramivir administration in children with influenza," *Antiviral Therapy*, vol. 23, no. 5, pp. 435–441, 2018.

[22] H. T. Yu, J. Lee, E. C. Shin, and S. Park, "Significant association between serum monokine induced by gamma interferon and carotid intima media thickness," *Journal of Atherosclerosis and Thrombosis*, vol. 22, no. 8, pp. 816–822, 2015.

[23] M. L. Martinez-Fierro, I. Garza-Veloz, M. R. Rocha-Pizaña et al., "Serum cytokine, chemokine, and growth factor profiles and their modulation in inflammatory bowel disease," *Medicine*, vol. 98, no. 38, article e17208, 2019.

[24] J. C. Youn, H. T. Yu, B. J. Lim et al., "Immunosenescent CD8 +T cells and c-x-c chemokine receptor type 3 chemokines are increased in human hypertension," *Hypertension*, vol. 62, no. 1, pp. 126–133, 2013.

[25] C. Li, W. Zong, M. Zhang et al., "Increased ratio of circulating t-helper 1 to t-helper 2 cells and severity of coronary artery disease in patients with acute myocardial infarction: a prospective observational study," *Medical Science Monitor*, vol. 25, pp. 6034–6042, 2019.

[26] S. Shokri, S. Mahmoudvand, R. Taherkhani, and F. Farshadpour, "Modulation of the immune response by middle east respiratory syndrome coronavirus," *Journal of Cellular Physiology*, vol. 234, no. 3, pp. 2143–2151, 2019.

[27] S. Zhang, Z. Q. You, L. Yang et al., "Protective effect of shenmai injection on doxorubicin-induced cardiotoxicity via regulation of inflammatory mediators," *BMC Complementary and Alternative Medicine*, vol. 19, no. 1, p. 317, 2019.

[28] D. Y. Sevgi, B. Bayraktar, A. Gündüz et al., "Serum soluble urokinase-type plasminogen activator receptor and interferon-γ-induced protein 10 levels correlate with significant fibrosis in chronic hepatitis b," *Wiener Klinische Wochenschrift*, vol. 128, no. 1-2, pp. 28–33, 2016.

Hindawi
Computational and Mathematical Methods in Medicine
Volume 2022, Article ID 4242069, 16 pages
https://doi.org/10.1155/2022/4242069

Research Article

A Novel Radiomics-Based Machine Learning Framework for Prediction of Acute Kidney Injury-Related Delirium in Patients Who Underwent Cardiovascular Surgery

Xin Xue,[1] **Wen Chen**,[2] **and Xin Chen**[1,2]

[1]*Department of Cardiothoracic Surgery, School of Medicine, Southeast University, Nanjing 210009, China*
[2]*Department of Thoracic and Cardiovascular Surgery, Nanjing First Hospital, Nanjing Medical University, Nanjing 210006, China*

Correspondence should be addressed to Xin Chen; stevecx@njmu.edu.cn

Received 8 November 2021; Revised 2 January 2022; Accepted 11 February 2022; Published 18 March 2022

Academic Editor: Kelvin Wong

Acute kidney injury (AKI) can be caused by multiple etiologies and is characterized by a sudden and severe decrease in kidney function. Understanding the independent risk factors associated with the development of AKI and its early detection can refine the risk management and clinical decision-making of high-risk patients after cardiovascular surgery. A retrospective analysis was performed in a single teaching hospital between December 1, 2019, and December 31, 2020. The diagnostic performance of novel biomarkers was assessed using random forest, support vector machine, and multivariate logistic regression. The nomogram from multivariate analysis of risk factors associated with AKI indicated that only LVEF, red blood cell input, and ICUmvat contribute to AKI differentiation and that the difference is statistically significant ($P < 0.05$). Seven radiomics biomarkers were found among 65 patients to be highly correlated with AKI-associated delirium. The importance of the variables was determined using the multilayer perceptron model; fivefold cross-validation was applied to determine the most important delirium risk factors in radiomics of the hippocampus. Finally, we established a radiomics-based machine learning framework to predict AKI-induced delirium in patients who underwent cardiovascular surgery.

1. Introduction

Notwithstanding that unprecedented progress has been made in understanding the pathogenesis and development of novel therapeutic strategies, cardiovascular disease remains the leading cause of morbidity and mortality in patients with renal dysfunction, especially acute kidney injury (AKI) [1]. AKI is a complex syndrome caused by multiple etiologies and characterized by a sudden and severe decrease in kidney function, presented with an increase in serum creatinine (SCr) or a reduction in urine output [2, 3]. In a recent study, more than half the patients hospitalized in the intensive care unit (ICU) ward developed AKI [4]. Note that increased AKI severity correlates positively with short- and long-term mortality after discharge [5, 6]. In addition, as established recently, the mortality risk increases significantly with AKI severity, reaching a rate of up to 40–60% [5, 7, 8]. The occurrence rate of AKI might be somewhat affected by differences in socioeconomic statuses [9]. Consequently, the severity of adverse events has become a worldwide medical burden. To the best of our knowledge, regardless of the underlying etiology, there are no effective treatments for AKI once it develops [10]. Clinically, AKI management refers to an early detection of its occurrence for the general critical care population with limited ongoing or recurrent renal injury, consequently providing supportive management of advanced renal dysfunction [11]. Considering the negative impact of AKI on short- and long-term outcomes, it is essential to explore novel methods to identify high-risk patients and diagnose subclinical AKI to improve patient outcomes. As previously described, the development of statistical predictive models for estimating the risk factors of AKI has become possible with the development of

clinical informatics and the increasing availability of electronic medical records [12]. Of note, multivariate logistic regression analysis is the most frequently used statistical algorithm to determine risk predictors for the short-term outcome [11]. Several underlying susceptibilities, procedures, or exposures have been identified as risk factors for the occurrence of postoperative AKI, such as older age, chronic kidney disease, comorbidities (e.g., diabetes and hypertension), sepsis, major surgery, and hemodynamic instability [13, 14].

An increasing body of evidence has suggested that AKI can significantly affect the brain tissue and function. Ischemic AKI can reportedly cause neuronal pyknosis and an increase in brain microgliomas. In addition, AKI can lead to brain microvascular protein leakage and increased vascular permeability, thereby increasing the risk of cerebrovascular diseases and the incidence of brain dysfunction. The incidence rate of stroke increased significantly with a glomerular filtration rate below 60 $ml \cdot min^{-1} \cdot 1.73\, m^{-2}$ and a Cr/Alb ratio greater than 30 mg/g. Moreover, the United States Renal Disease Database reported that the incidence rate of stroke in uremic people aged >65 years is 9%. The early symptoms in AKI patients with concomitant impaired brain tissue and function include fatigue, apathy, bradykinesia, and an inability to concentrate. In severe cases, delirium, confusion, and coma might occur. In addition, reduced autonomous behavior and slow movement have been documented in animal models of renal ischemia and bilateral nephrectomy.

Acute kidney injury might be associated with numerous brain and hippocampal complications, as it can alter the permeability of the blood–brain barrier. Although the pathogenesis of acute uremic encephalopathy is poorly understood, the potential underlying mechanism contributing to hippocampal involvement includes the release of multiple inflammatory mediators, which lead to hippocampal inflammation and cytotoxicity, neurotransmitter derangement, transcriptional dysregulation, and changes in the expression of apoptotic genes. Impairment of brain function, especially of a structure that has vital activity in learning and memory and is highly sensitive to renal ischemic injury, can ultimately lead to cognitive and functional complications in patients with AKI. Delirium is the most common clinically observed symptom after AKI, as it has a relatively high mortality rate (22%–76%). Liu et al. found that AKI leads to the release of soluble and cellular inflammatory mediators in the brain, which primarily target the hippocampus and increase brain microvascular protein leakage. They also found that severe AKI and bilateral nephrectomy can lead to more pronounced behavior changes than less severe AKI or the combination of sham AKI with surgery and anesthesia [15]. Therefore, early prediction and intervention of hippocampal changes caused by AKI are crucial in reducing patient mortality and improving the prognosis [16].

As it is clinically difficult to detect early hippocampal damage, the prognosis is generally poor once the injury occurs, and the associated mortality rate is high. Currently, there is a paucity of efficient and low-cost methods for detecting early hippocampal damage. The current clinical approach involves magnetic resonance imaging (MRI) examination of the hippocampus and qualitative assessment methods to observe morphological changes, with no quantitative analytical methods available. This study is aimed at establishing and validating a machine learning-based quantitative method for noninvasive hippocampal assessment through preoperative cranial computed tomography (CT) instead of magnetic resonance imaging for the early detection of AKI-related hippocampal damage and prompt clinical intervention.

However, early biochemical and clinical data have not been analyzed in studies that sought to predict the risk factors of AKI after surgery [17]. In addition, risk assessment before surgery is crucial to optimize strategies to prevent AKI and AKI-induced hippocampal changes to determine which patients require more intense motorizations after surgery. Overall, the present study seeks to determine the incidence and risk factors of AKI and AKI-associated hippocampal damages in patients who have undergone cardiovascular surgery.

2. Materials

2.1. Subjects. A retrospective cohort analysis was conducted in a teaching hospital. Patients (age ≥ 18 years) at risk of developing AKI after primary cardiovascular surgery were included in our current study. The exclusion criteria comprised patients with renal insufficiency, acute or chronic kidney disease, or preoperative hemodynamic instability; patients who underwent emergency operation; patients who developed postoperative urinary tract infection or were treated with nephrotoxic drugs or glucocorticoids before or after surgery; and patients without complete clinical data. All patients provided written informed consent before participation. The study was approved by the Medical Ethics Committee of the First Affiliated Hospital of Nanjing Medical University (KY20190404-03-KS-01) and complied with the requirements of the Declaration of Helsinki.

2.2. AKI Definition and Grouping Design. According to the Kidney Disease Improving Global Outcomes (KDIGO) workgroup [18], the AKI criteria comprise 50% increase in SCr measurements relative to the baseline, SCr increases of more than 0.3 mg/dl within a 48-h interval during 7 days, or urine volume less than 0.5 ml/(kg·h) for 6 h [19]. After cardiovascular surgery, patients who developed postoperative AKI were included in the AKI group, whereas those without AKI were included in the non-AKI group.

2.3. Delirium Definition and Grouping Design. According to the DSM-IV-TR criterion [20], the diagnostic criteria for delirium included the following: (A) disturbance of consciousness (i.e., reduced clarity of environmental awareness) with reduced ability to focus, sustain, or shift attention. (B) A change in cognition or the development of a perceptual disturbance that is not better accounted for by a preexisting, established, or evolving dementia. Other common features of delirium include sleep disorders (such as changes in sleep–wake cycles), changes in psychomotor activity, and

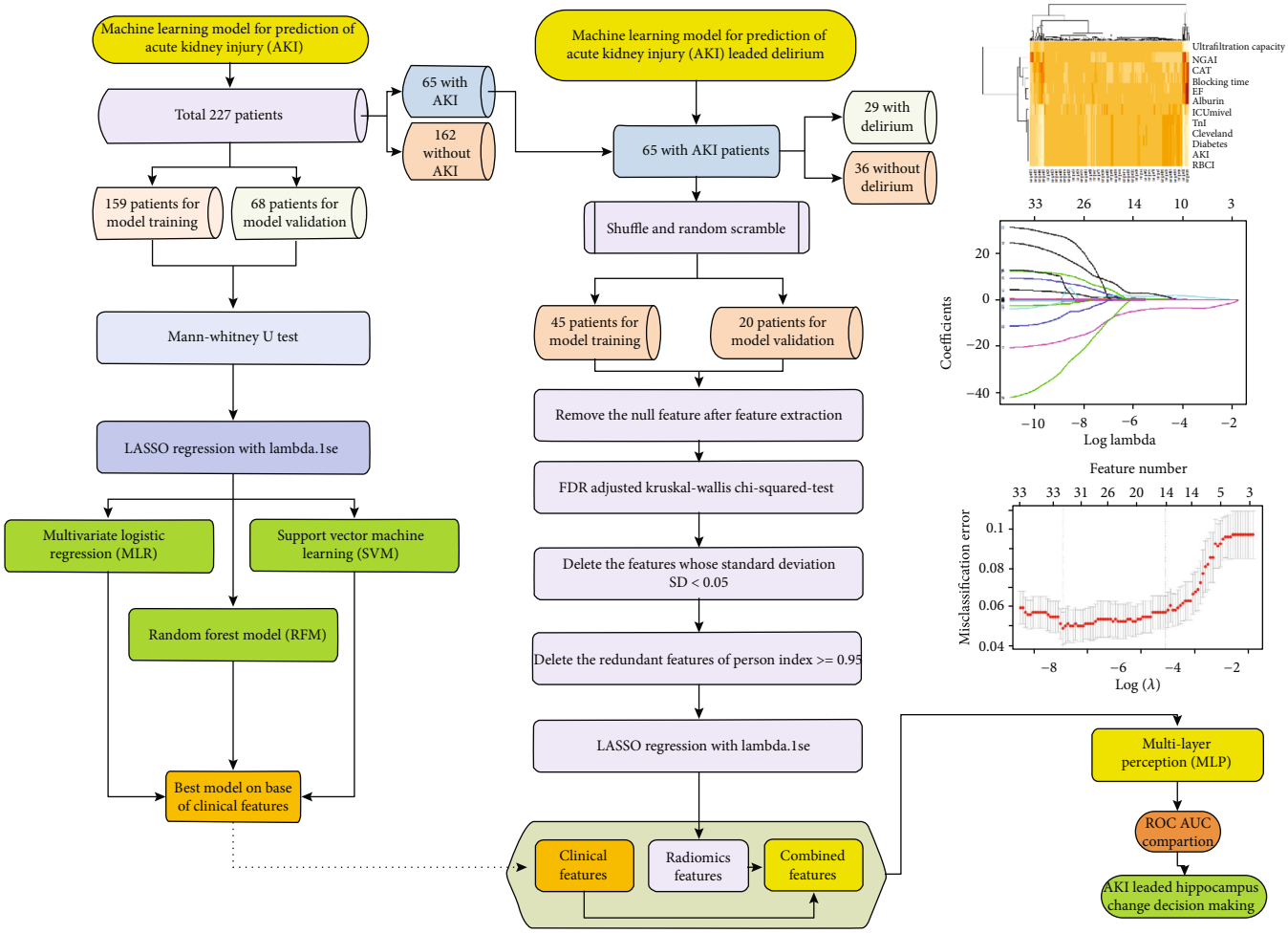

Figure 1: Machine learning analysis process of AKI and AKI-led delirium on clinical and CT radiomics parameters.

abnormal neurobehavioral symptoms. Delirium cases were divided into hyperactive type (HT), inhibited type (IT), and mixed type (MT). Patients with HT presented with a state of restlessness and high alertness to the surrounding environment. Patients with IT exhibited poor arousal, lethargy, and weakness. Because this type of delirium is nondestructive, the symptoms are usually undetectable. Patients expressing both phenotypes were classified as MT. Within 48 h of cardiovascular surgery, the included patients were examined by psychologists and classified using the abovementioned criteria.

3. Methods

3.1. Clinical Data Collection. Three hundred and twenty patients who underwent cardiovascular surgery from December 1, 2019, to December 31, 2020, were retrieved from hospital's electronic medical records. Finally, 227 patients were included in our study and separated into training and validation groups. The preoperative data mainly included demographic characteristics (age, gender), height, body weight, body mass index, smoking and drinking history, comorbidities (hypertension, diabetes, and cardiovascular disease), central venous pressure, left ventricular ejection fraction (LVEF), coronary arteriography, and clinical laboratory data (hemoglobin, albumin, hematocrit, baseline SCr, N-terminal pro-brain natriuretic peptide (NT-proBNP), neutrophil gelatinase-associated lipocalin (NGAL), fatty acid-binding protein (FABP), troponin I (TnI), and blood glucose). The intraoperative data comprised the cardiopulmonary bypass (CPB) time, type of surgery, extracorporeal circulation urine output, ultrafiltration volume, and red blood cell input (RBCI) on the surgery day. Finally, the postoperative data included the length of ICU stay, mechanical ventilation auxiliary time (MVAT), and continuous renal replacement therapy (CRRT) use.

3.2. Imaging Data Collection. All patients underwent brain CT before cardiovascular surgery; CT images with an axial slice thickness of 1 mm were retrospectively collected between December 1, 2019 and December 31, 2020. All study subjects were older than 18 years, and a normal hippocampus was confirmed before surgery. Figure 1 demonstrates the machine learning process adopted in the study and patient data distribution.

3.3. Image Preprocessing and Hippocampus Autosegmentation. After the brain CT images were obtained, a deep learning

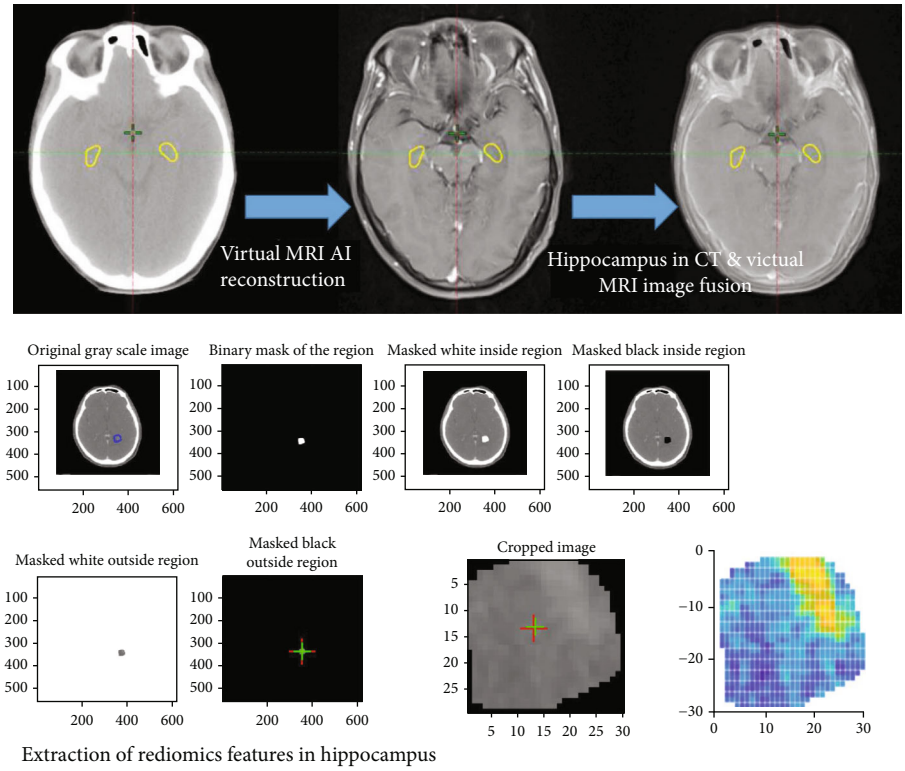

Figure 2: The process of automatically delineating the hippocampus ROI from CT and radiomics feature extraction.

method was applied to generate a visual MRI image set for hippocampus auto-segmentation, as reported by Li et al. [21]. The traditional CT image and artificial intelligence brain library were used to reconstruct the MRI image from the virtual image library closest to the patient's brain anatomy and to perform CT-MR image fusion through artificial intelligence methods. Accordingly, a virtual MRI could determine the location of the hippocampus from the CT image and delineate it. In addition, bias field correction was applied for virtual MRI image noise reduction and preprocessing. Regions of interest (ROIs) were used as the range for feature extraction of the hippocampus. To compensate for the effect of variable voxel size on image analysis, all CT images were resampled to pixel dimensions of 1 mm × 1 mm × 5 mm. To reduce the errors associated with manual delineation of the hippocampus and improve the delineation efficiency, a rigorously tested and internally developed delineation program based on artificial intelligence was used to delineate the hippocampus before and after the cardiovascular surgery. As enhanced CT is not routinely used in clinical practice, cases with only plain CT scans were also collected to delineate the hippocampus. According to the literature, the two images exhibit no statistical significance in delineating the volume and boundary of the hippocampus. The mean Dice similarity coefficient and average Hausdorff distance of the two image sequences were 0.90 and 1.6 mm, respectively. All above steps are explained in Figure 2, the process of automatically delineating the hippocampus ROI from CT and radiomics feature extraction.

3.4. Image Feature Extraction. Quantitative radiomics analysis was conducted on the hippocampus region. A total of 661 radiomics features characterizing the intensity and texture of the hippocampus were extracted. Wavelet transformation was performed on the hippocampus region to quantify the hippocampus in multiple dimensions.

The intensity features measured the gray-level distribution in the tumor region and quantified in terms of mean, energy, entropy, variance, skewness, and kurtosis. The texture features that characterized the tumor texture properties were based on the gray-level cooccurrence matrix (GLCM), gray-level size-zone matrix (GLSZM), gray-level run-length matrix (GLRLM), and neighborhood gray-tone-difference matrix (NGTDM), including homogeneity (GLCM), small-zone emphasis (GLSZM), short-run emphasis (GLRLM), and complexity (NGTDM). Details of the texture features, including the category and feature names, are provided in Table 1.

Wavelet selection was performed by selecting the high-frequency parts (H) or low-frequency parts (L) of the wavelet components of the tumor region at the very axis. Eight categories of wavelet features were acquired and labeled as HHH, HHL, HLH, LHH, LLL, LLH, LHL, and HLL. The HLH category features comprised texture features derived from the tumor region after high-frequency wavelet selection on the x-axis and z-axis and low-frequency wavelet selection on the y-axis.

3.5. Image/Clinical Feature Selection. To compensate for the accuracy of AD on hippocampus delineation, the texture analysis method was repeated two more times by performing morphological erosion and expansion of all pixels on the initial contour of the ROI. Only radiomics features that showed

Table 1: Characteristics of patients of risk factors associated with AKI after cardiovascular surgery ($N = 227$).

Variables	AKI group ($n = 66$)	Non-AKI group ($n = 161$)	$\chi^2/F/t/Z$	P value
Demographic				
Gender (male) (n [%])	39 (59.09)	82 (50.93)	1.293	0.256
Age ≥ 60 (year)	44 (66.67)	84 (52.17)	4.669	0.031
Height (cm) ($\bar{x} \pm s$)	164.12 ± 9.64	163.52 ± 8.63	0.477	0.634
Weight (kg) ($\bar{x} \pm s$)	66.89 ± 11.51	66.69 ± 10.71	0.988	0.323
BMI (kg/m^2) ($\bar{x} \pm s$)	1.797 ± 0.178	1.793 ± 0.169	0.146	0.884
Smoking history (n [%])	17 (25.75)	28 (17.39)	2.400	0.121
Drinking history (n [%])	8 (12.12)	9 (5.59)	2.198	0.138
Laboratory				
Hematocrit ($\bar{x} \pm s$) (%)	24.92 ± 3.89	25.08 ± 3.80	-1.425	0.155
Albumin (g/l) ($\bar{x} \pm s$)	38.25 ± 3.36	40.12 ± 3.40	-3.794	0.000
NGAL (ng/ml) (M [IQR])	82.3 (51.7, 153.7)	49.2 (34.9, 117.2)	-3.272	0.001
TnI (>0.5 ng/ml) (n [%])	12 (18.18)	24 (14.90)	0.327	0.568
FABP (>2.5 ng/ml) (n [%])	17 (25.75)	37 (22.98)	0.243	0.622
NT-prBNP (>300 pg/ml) (n [%])	20 (30.30)	24 (14.91)	2.079	0.149
Coronary angiography (n [%])	49 (74.24)	112 (69.56)	0.397	0.529
Clinical				
Hypertension (n [%])	33 (50.00)	76 (47.20)	0.180	0.671
Diabetes (n [%])	25 (37.88)	28 (17.39)	10.979	0.001
Anemia (n [%])*	25 (37.87)	20 (12.42)	19.086	0.000
LVEF ($\bar{x} \pm s$) (%)	58.43 ± 7.42	60.42 ± 5.39	-1.807	0.024
CVP (cmH_2O) ($\bar{x} \pm s$)	9.076 ± 3.400	8.621 ± 2.629	0.973	0.333
Type of surgery (n [%])			9.900	0.007
Coronary artery bypass surgery	19 (28.79)	38 (23.60)		
Valvuloplasty	29 (43.94)	103 (63.98)		
Combined surgery**	18 (27.27)	20 (12.42)		
CPB time (>120 minutes) (n [%])	34 (51.52)	45 (27.95)	11.456	0.001
Duration of surgery (>6 hours) (n [%])	40 (60.60)	69 (42.85)	5.908	0.015
Aortic occlusion time (minute) (M [IQR])	108 (83.5, 140.5)	97 (82.0, 129.0)	-1.670	0.095
Red blood cell input (n [%])	23 (34.85)	10 (6.21)	30.899	0.000
Urine output (ml) (M [IQR])	200 (100, 300)	200 (150, 350)	-1.619	0.105
Ultrafiltration volume (ml) (M [IQR])	1350 (800, 2250)	1500 (800, 2070)	-0.720	0.472
ICU length of stay (day) (M [IQR])	2 (1, 4)	1 (1, 2)	-5.4189	0.000
Mechanical ventilation time (hour) (M [IQR])	14 (10.0, 20.25)	11 (7.5, 14.0)	-3.822	0.000
CRRT (n [%])	2 (3.0)	0 (0.00)	Fisher's	0.246
Hospitalization time (day) ($\bar{x} \pm s$)	18.70 ± 5.52	15.78 ± 5.61	3.591	0.000

Notes: *Preoperative anemia was defined as a hemoglobin less than 110 g/l in female patients and 120 g/l in male patients; **Combined surgery was referred to a combination of two or more surgical operations. Abbreviations: BMI: body mass index; CPB: cardiopulmonary bypass; CVP: central venous pressure; CRRT: continuous renal replacement therapy; FABP: fatty acid-binding protein; IABP: intra-aortic balloon pump; ICU: intensive care unit; LVEF: left ventricular ejection fraction; M [IQR]: median [inter quartile range]; NGAL: neutrophil gelatinase-associated lipocalin; NT-prBNP: N-terminal probrain natriuretic peptide; TnI: troponin I.

a high correlation (>0.99) with the erosion and expansion of the ROI were used for further analysis.

Specific feature screening steps:

(1) After feature extraction, the null features were removed, and features that had no omics feature changes before and after the operation were deleted, leaving 714 features

(2) The MWU test was conducted to delete features unrelated to the result variable ($n = 103$), and 611 features were left. The study samples were divided into two groups (delirium and no delirium) according to our data. The Mann–Whitney U-test/Wilcoxon rank-sum test was used to compare the preoperative and postoperative hippocampal radiomics characteristics of different groups. The characteristics that

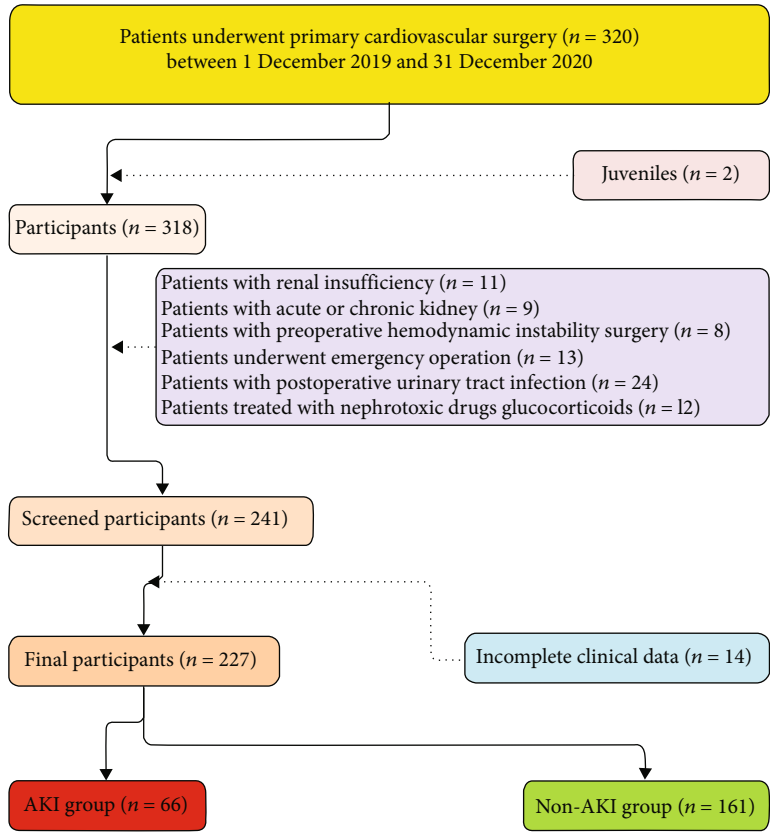

Figure 3: Flow chart representing the patient selection process and groups.

exhibited significant differences between the groups were screened. The MWU test excluded 107 features that exhibited no statistical differences within the group (FDR was used to obtain corrected P values).

(3) Variance/standard deviation analysis: the features whose standard deviation (SD) was less than 0.05 were deleted, resulting in 490 features

(4) Correlation detection: redundant features with a Pearson correlation index ≥ 0.99 were deleted, and features highly correlated with the classification results were retained. The number of feature variables was reduced from 491 to 163

(5) Finally, LASSO dimensionality reduction was performed, features were reduced from 163 to 7, and the smallest MSE was selected. As a result, the simplest predictive classification model obtained with one SD consisted of only eight variables

3.6. Image/Clinical Signature Construction. A radiomics signature and a clinical signature were built by summing the features multiplied by their coefficients. The prediction value of integration of radiomics and clinical features was tested using a multivariable logistic regression model. Finally, the prediction model's performance was assessed by calculating the AUC of the ROCs.

3.7. Image/Clinical Signature Validation. The signatures were established using a fourfold cross-validation approach. The patients were randomly separated into five folds. Three out of the four folds were used for feature selection at a λ value. The resulting signature was then tested on the other fold patients. The binomial deviance of fivefold cross-validation was used to select the best λ value for the least binomial deviance.

3.8. Statistical Analysis. Measured data were expressed as absolute numbers and percentages or mean ± standard deviation ($\bar{x} \pm s$) and interquartile ranges (25th and 75th percentiles) when applicable. Continuous variables were compared using the Mann–Whitney U test, and categorical variables were compared using the chi-square or Fisher's exact test. All calculations were performed using SPSS 22.0 Statistical Software (SPSS, Inc., Chicago, IL, USA) and MedCalc Statistical Sofware, version 19.0.4 (MedCalc Software bvba, Ostend, Belgium). Univariate logistic regression was conducted to screen potential risk factors significantly associated with AKI. The multivariate logistic regression analysis included factors that exhibited statistical significance during univariate analysis (P value < 0.05) to stratify postoperative AKI-related risk factors. The stepwise forward method was used for variable selection. Measures of effect were reported using odds ratios for both crude and adjusted analysis, followed by a 95% confidence interval, and a P value <

Table 2: Characteristics of patients with delirium and without delirium ($N = 66$).

	Delirium group ($N = 29$)		Nondelirium group ($N = 36$)			
	Average	sd	Average	sd	P value	q value
Age	62.364	11.054	62.097	11.214	0.543	0.283
Weight	64.927	9.093	64.758	9.845	0.784	0.682
Height	165.200	8.322	164.661	9.009	1.231	1.231
BMI	1.803	0.144	1.798	0.158	0.068	0.015
Hemoglobin	131.291	21.513	131.468	22.320	0.342	0.149
Hematocrit	25.182	3.087	24.710	3.400	0.743	0.614
Albumin	39.485	3.285	39.349	3.455	0.066	0.011
NGAL	130.778	67.210	130.911	66.236	0.593	0.361
TnI	0.348	0.836	0.479	1.606	0.055	0.005
FABP	1.580	2.959	1.721	3.103	0.784	0.716
NT-prBNP	376.628	501.617	408.349	568.687	0.124	0.038
LVEF	62.273	5.182	61.565	6.385	0.112	0.029
CVP	8.618	3.670	8.548	3.640	0.054	0.002
Type of surgery	2.164	1.290	2.129	1.263	0.342	0.164
CPB time	112.255	36.932	115.258	38.488	0.674	0.527
RBCI	0.487	1.527	0.529	1.524	0.634	0.413
Aortic occlusion time	73.155	28.342	76.218	29.587	0.894	0.855
Ultrafiltration volume	1820.982	1096.451	1858.935	1121.492	0.556	0.314
ICU length of stay	1.927	2.641	2.290	3.050	0.064	0.008
ICU mechanical ventilation time	12.825	13.227	14.974	17.253	0.321	0.126
Hospitalization time	17.576	8.069	18.237	7.965	0.667	0.493

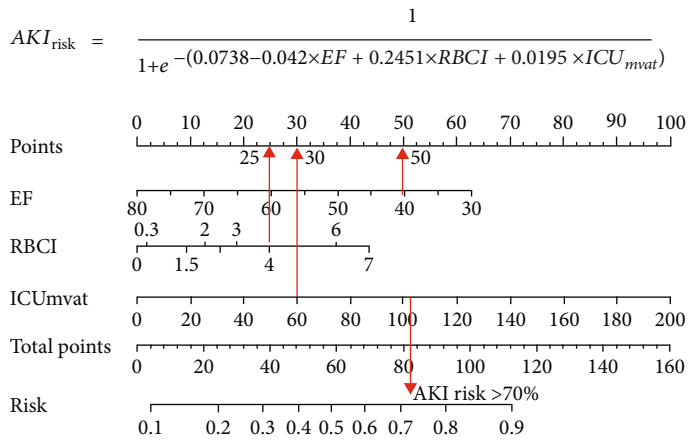

Figure 4: Nomogram from multivariate analysis of risk factors associated with AKI.

0.05 was used to determine statistical significance. Furthermore, the diagnostic performance of novel biomarkers was assessed by calculating the areas under the receiver-operator characteristic curves (AUC); pairwise comparison of ROC curves was performed for AKI risk and AKI-associated hippocampal changes and delirium.

4. Experimental Results and Discussion

4.1. Characteristics and Outcomes of Patients. Between December 1, 2019, and December 31, 2020, 320 patients were at risk of developing AKI in the cardiothoracic surgery department, and 227 patients were involved in the final study cohort. A flowchart of our study is provided in Figure 3. According to the KDIGO clinical practice guidelines, 66 patients were diagnosed with hospital-acquired AKI within a week after the cardiovascular surgery, of which 29 patients (43.94%) exhibited hippocampal changes and delirium. Surgical procedures in the AKI group included coronary artery bypass surgery ($n = 19$), valve replacement ($n = 29$), and a combination of two or more cardiovascular surgical operations ($n = 18$). Surgical procedures in the non-AKI group also included coronary artery bypass surgery ($n = 38$), valve replacement ($n = 103$), and a combination of

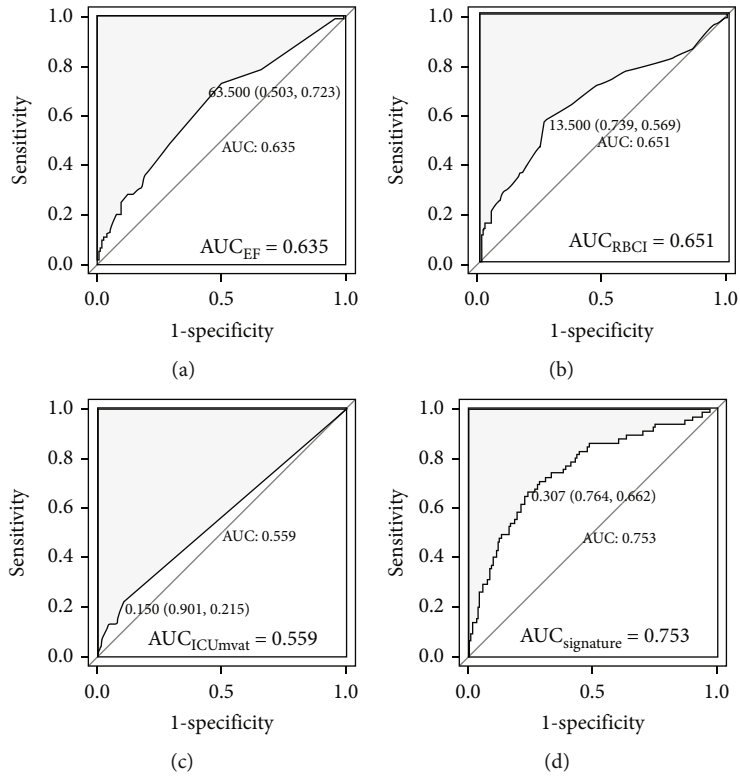

Figure 5: Diagnostic performance of novel biomarkers using receiver-operative characteristic curves of EF, RBCI, ICU_{mvat}, and clinical signature. (a–d) stands for the performance of novel biomarkers of EF, RBCI, ICUmvat, and clinical signature, respectively.

two or more cardiovascular surgical operations ($n = 20$). At the end of the study, two patients who required CRRT after valve replacement surgery or coronary artery bypass surgery survived. Of the four patients (1.76%) who died, three developed postoperative AKI, and the mortality rate in the AKI group was higher than that in the non-AKI group ($P \leq 0.01$). Detailed patient characteristics grouped according to the KDIGO workgroup are provided in Table 1. Detailed patient characteristics with and without delirium are provided in Table 2.

4.2. Univariate Logistic Regression Analyses of Risk Factors for AKI. Upon admission, the older patients, especially those older than 60 years, harbored a higher risk of AKI. As shown in Table 1, patients with preexisting complications were prone to AKI, such as diabetes. Patients with anemia were at an increased risk of AKI, especially those with low serum albumin levels. Conversely, no significant correlation was found between the other demographic and physiological variables in AKI patients ($P_s > 0.05$). To increase the diagnostic accuracy, novel biomarkers, including NGAL, TnI, FABP, and NT-proBNP, were also investigated in this setting. Univariate analysis revealed that the urinary NGAL level was higher in patients with AKI than those without ($P < 0.05$). In contrast, there were no significant differences among the serum levels of TnI, FABP, and NT-proBNP between patients with and without AKI. Additionally, there was no remarkable difference in the coronary angiography findings between patients with and without AKI ($P > 0.05$).

Table 3: Multivariate analysis of risk factors associated with AKI after cardiovascular surgery.

	Coefficients	St. error	Z	P value
Intercept	0.0738	2.4390	0.0300	0.9759
Diabetes	0.2187	0.1543	1.4170	0.1563
NGAL	0.0004	0.0007	0.4870	0.6260
TnI	-0.1471	0.1273	-1.1550	0.2480
Albumin	-0.0265	0.0527	-0.5030	0.6146
LVEF	-0.0420	0.0209	-2.0060	0.0449*
CPB time	-0.0001	0.0085	-0.0110	0.9912
Aortic occlusion time	0.0173	0.0109	1.5820	0.1137
RBCI	0.2451	0.1346	1.8210	0.0485*
Ultrafiltration capacity	0.0001	0.0002	0.6930	0.4882
ICUmvat	0.0195	0.0089	2.1920	0.0284*
Cleveland	0.2304	0.1421	1.6210	0.1050

Abbreviations: 95% CI: 95% confidence interval; CPB: cardiopulmonary bypass; ICU: intensive care unit; NGAL: neutrophil gelatinase-associated lipocalin; OR: odds ratio; SE: standard error. * P value < 0.05.

Analysis of routinely used intraoperative variables showed that an increased risk of AKI was associated with a combination of surgical operations, prolonged CPB therapy, longer duration of surgery, or erythrocyte transfusions on the day of surgery. Conversely, there were no significant differences in other intraoperative variables between patients with and without AKI, such as interval, aortic occlusion

Table 4: 5-fold cross-validation results of AUC after multiple logistic regression (MLR).

Signature	AUC	Precision	Recall	*F*-score	Accuracy	Delong test for AUC values
Training set						
Fold-1	0.633	0.696	0.320	0.438	0.773	
Fold-2	0.594	0.619	0.250	0.356	0.739	
Fold-3	0.635	0.667	0.340	0.450	0.757	$Z = 8.551$, $P \leq 0.01$
Fold-4	0.640	0.708	0.333	0.453	0.773	
Fold-5	0.662	0.639	0.426	0.511	0.757	
Average	0.633	0.666	0.334	0.442	0.760	
Testing set						
Fold-1	0.596	0.200	0.500	0.286	0.667	
Fold-2∗	0.817	0.385	0.833	0.526	0.804	
Fold-3	0.745	0.583	0.636	0.609	0.800	$Z = 6.321$, $P \leq 0.01$
Fold-4	0.609	0.214	0.500	0.300	0.689	
Fold-5	0.503	0.182	0.250	0.211	0.667	
Average	0.654	0.313	0.544	0.386	0.725	
Best model in validation set∗	AUC	Precision	Recall	*F*-score	Accuracy	
	0.753	0.667	0.277	0.391	0.934	

Table 5: AKI classification performance using clinical-based random forest (RF) model.

Signature	AUC	Precision	Recall	*F*-score	Accuracy	Delong test for AUC values
Training set						
Fold-1	0.957	0.714	0.909	0.800	0.889	
Fold-2	0.934	1.000	0.308	0.471	0.800	
Fold-3	0.927	1.000	0.636	0.778	0.909	$Z = 11.203$, $P \leq 0.01$
Fold-4	0.881	1.000	0.462	0.632	0.848	
Fold-5	1.000	1.000	1.000	1.000	1.000	
Average	0.940	0.943	0.663	0.736	0.889	
Testing set						
Fold-1	0.686	0.471	0.296	0.364	0.691	
Fold-2	0.665	0.522	0.231	0.320	0.718	
Fold-3	0.583	0.267	0.074	0.116	0.665	$Z = 9.674$, $P \leq 0.01$
Fold-4	0.659	0.485	0.308	0.376	0.706	
Fold-5∗	0.714	0.571	0.500	0.533	0.767	
Average	0.661	0.463	0.282	0.342	0.709	
Best model in validation set∗	AUC	Precision	Recall	*F*-score	Accuracy	Delong test for AUC values
	0.817	0.620	0.677	0.647	0.788	

time, urine output, and ultrafiltration volume ($P_s > 0.05$). Notably, postoperative AKI was associated with worse outcomes, such as prolonged mechanical ventilation auxiliary time, length of ICU stay, and hospitalization time.

4.3. Diagnostic Performance of Novel Biomarkers Using Random Forest, Support Vector Machine, and Multivariate Logistic Regression. When EF, RBCI, and ICUmvat were entered in the regression equation, ICUmvat had the largest impact on the entire model, followed by EF and RBCI. We assumed that when ICUmvat was equal to 60 h, EF was 40%, and RBCI was 4, yielding scores of 30, 50, and 25, respectively (the red arrow in Figure 4), and a total score of 105. A total score greater than 70% was obtained for the predicted risk of AKI using the above three variables. This approach is simple and can be easily implemented in clinical practice.

Figure 4 demonstrates the nomogram obtained from multivariate log regression analysis of risk factors associated with AKI, including EF, RBCI, and ICUmvat. We created a nomogram with these three variables for easy implementation during clinical practice. Meanwhile, the diagnostic performance of novel biomarkers EF, RBCI, and ICUmvat, and the clinical signature was assessed using ROC curves (Figure 5).

Prediction of AKI and AKI-related hippocampus changes after the cardiovascular surgery is demonstrated in

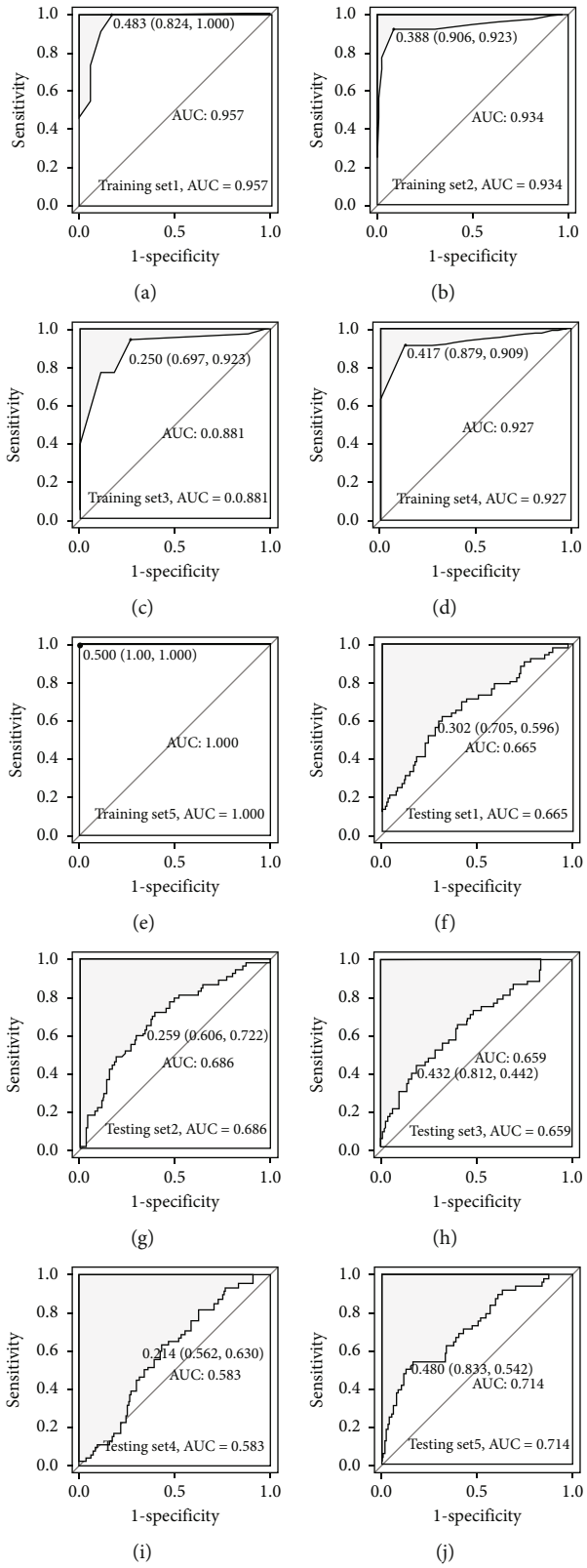

Figure 6: ROC curve of the 5 folds in training and testing sets and the best performance Signature of random forest (RF) model. The first row (a–e) represents the ROC calculated by 5 folds of the training set; the second row (f–j) represents the ROC calculated for 5 folds of the test set.

Table 6: The AKI classification performance using clinical-based support vector machine (SVM) model.

Signature	AUC	Precision	Recall	*F*-score	Accuracy	Delong test for AUC values
Testing set						
Fold-1	0.535	0.973	0.777	0.864	0.729	
Fold-2	0.500	1.000	0.767	0.868	0.696	
Fold-3	0.558	0.861	0.786	0.822	0.700	$Z = 2.551$, $P = 0.042$
Fold-4	0.548	0.938	0.777	0.850	0.724	
Fold-5	0.500	1.000	0.777	0.874	0.713	
Average	0.528	0.954	0.777	0.856	0.712	
Training set						
Fold-1	0.612	0.247	1.000	0.396	0.124	
Fold-2	0.769	0.865	0.776	0.818	0.867	
Fold-3	0.650	0.938	0.818	0.874	0.844	$Z = 5.551$, $P = 0.019$
Fold-4	0.808	0.849	0.776	0.811	0.889	
Fold-5*	0.615	0.938	0.776	0.849	0.778	
Average	0.731	0.882	0.778	0.826	0.849	
Best model in validation set*	AUC	Precision	Recall	*F*-score	Accuracy	Delong test for AUC values
	0.812	0.821	0.742	0.780	0.870	

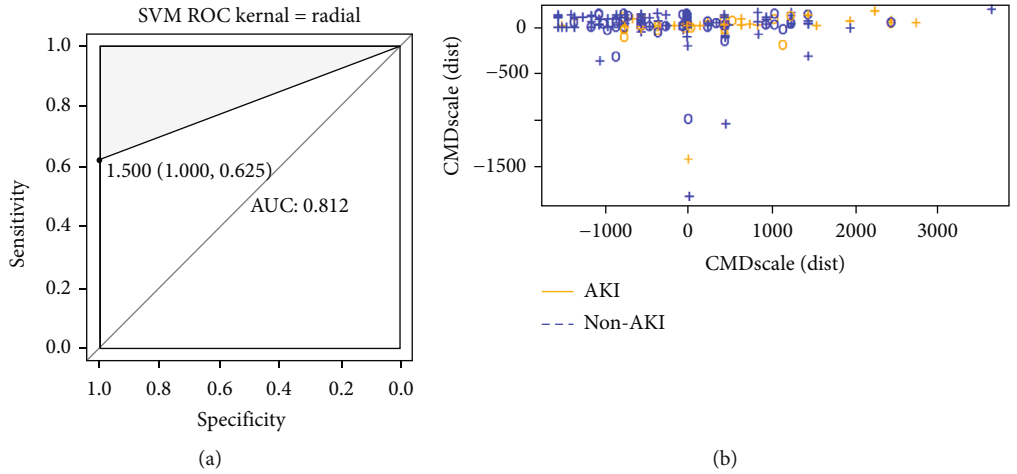

Figure 7: (a) The ROC curve of the best performance signature of SVM model, (b) which reflects the multidimensional scale transformation diagram of AKI and non-AKI.

Table 3. The AUC scores of the fivefold cross-validation after the application of multiple logistic regression, random forest, and support vector machine are summarized in Tables 4 and 5 (Figure 6) and Table 6 (Figure 7), respectively. The SVM model that performed the best during the fivefold cross-validation could distinguish AKI from non-AKI, as demonstrated in the heat map (Figure 8).

The "cmdscale" function can implement traditional multidimensional scaling, also known as principal coordinate analysis. It takes the interior point distance matrix as the input and outputs a series of points. Ideally, these points are two-dimensional or three-dimensional. The Euclidean distance between them produces the same distance matrix as the original; accordingly, the scatter plot of these points can objectively present the original distance.

4.4. Multilayer Perceptron-Based Prediction Model Establishment for AKI-Led Delirium. Before developing the predictive model, the collected data were randomly divided into training (70%) and validation (30%) datasets. The training dataset was used to construct predictive models using machine learning algorithms (multilayer perceptron (MLP) was mainly used here). Fivefold cross-validation was used to continuously adjust model's parameters to reduce the chance of overfitting and then verify and compare the final performance of each model in the validation dataset. AUC, sensitivity, specificity, and accuracy were used to compare different models. For modeling and statistical analysis, the Rstudio neural network package version 1.44.2 (https://cran.r-project.org/web/packages/neuralnet/index.html) and Python programming software version 3.9 (Python software,

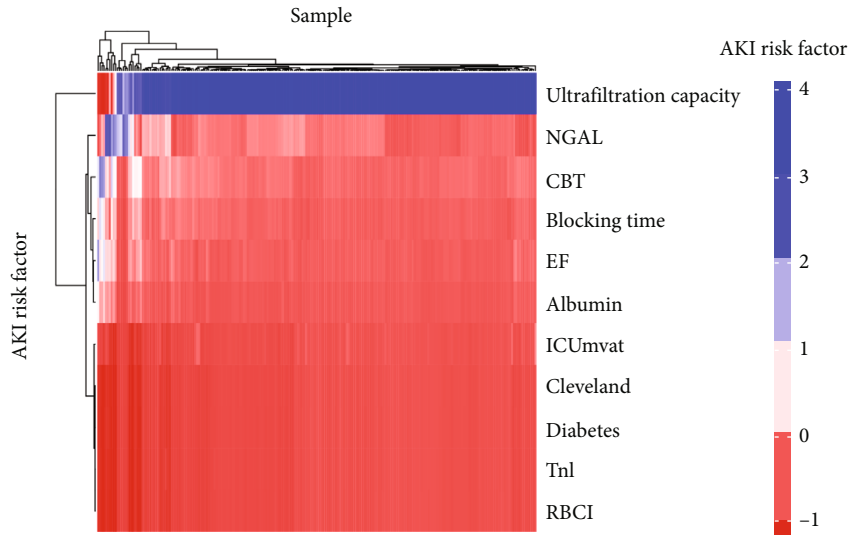

Figure 8: Heat map of the best performance signature of SVM model with the horizontal axis represents samples, and the vertical axis represents different predictors.

Table 7: Radiomics biomarker correction with AKI-led delirium.

	Delirium	
	OR	95% CI
GLCM∗315.4ClusterProminence	1.45	0.98-1.89
GLCM270.7Contrast	2.33	1.76-2.97
GLCM333.7InverseVariance	1.56	1.11-1.98
GLCM180.7Energy	2.67	2.03-3.19
GLCM225.1InformationMeasureCorr1	1.97	0.98-2.23
GLCM225.4Correlation	1.19	0.87-1.34
GLCM315.4Correlation	2.54	1.78-3.07

Notes: ∗GLCM: gray level cooccurrence matrices.

http://www.python.org/) were used. An MLP network with two hidden layers was built using the training dataset. Each hidden layer contained 11 neurons. The same network structure was used for the validation dataset, but the training weight parameters of each neuron were obtained after optimizing the training dataset. The softmax activation function was used in the final output layer before the network could output the final results.

Seven radiomics biomarkers were found in 65 patients to be highly correlated with AKI-related delirium (Table 7).

The importance of the variables was determined using the MLP model (Figure 9); fivefold MLP training and validation was applied to determine the most important delirium risk factors in the radiomics of the hippocampus. The MLP network structure and model performance are presented in Figures 10 and 11, respectively.

4.5. Discussion. Cardiac surgery-associated acute kidney injury (CSA-AKI) is a well-documented complication following cardiac surgery, associated with increased morbidity and mortality, prolonged hospital stay, and higher medical costs [22]. Much heterogeneity surrounds AKI incidence after cardiovascular surgery due to the differences in research objects, research methods, AKI definitions, diagnosis and treatment levels of medical centers, and selected models. Based on the KDIGO clinical practice guidelines, 66 patients in our present study were diagnosed with hospital-acquired AKI within a week after cardiovascular surgery, with an incidence rate of 29.07% (range 5%–30%), consistent with the literature [23, 24]. To appropriately manage CSA-AKI, a precise prediction model for identifying high-risk patients is required to optimize the postoperative treatment strategy.

To analyze numerous variables with nonlinearity and complex relationships associated with CSA-AKI development, an alternative and effective approach is required to develop precise prediction models. Over the years, machine learning has been applied in different areas of medicine, such as outcome prediction, diagnosis, medical image interpretation, and treatment [25, 26]. The advantage of this completely data-driven learning without reliance on rule-based programming is that machine learning constitutes a reasonable approach. Accordingly, in the present study, machine learning methods especially in predictive control techniques were applied to develop a model for the accurate prediction of CSA-AKI [27].

Previous studies have addressed the relationship between cardiac dysfunction and AKI risk in various clinical settings. For instance, in patients who underwent coronary artery bypass grafting and had preserved systolic function, preoperative $E/e' > 15$ was a strong independent predictor of AKI [28]. Moreover, among patients who underwent primary coronary intervention due to ST-segment elevation myocardial infarction, a high E/e' ratio was associated with an increased risk of AKI [29]. Another study showed that decreased LVEF was associated with a faster deterioration of the renal function [30]. Patients with heart failure who underwent coronary artery bypass surgery exhibited an increased risk for AKI postoperatively, even after adjustment for comorbidities, such as LVEF. Among patients with heart failure, having a severely reduced LVEF was associated with

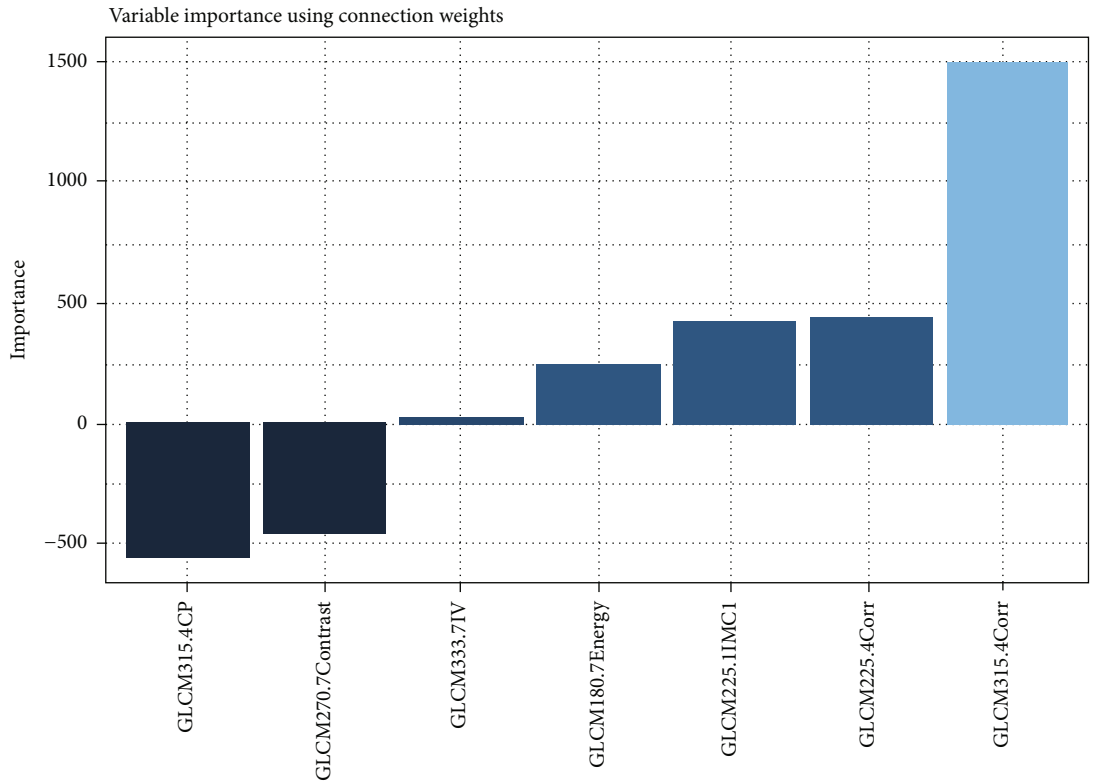

Figure 9: The importance of the variables determined by the MLP model; a 5-fold MLP training and testing was applied to determine the most important delirium risk factors in radiomics of the hippocampus.

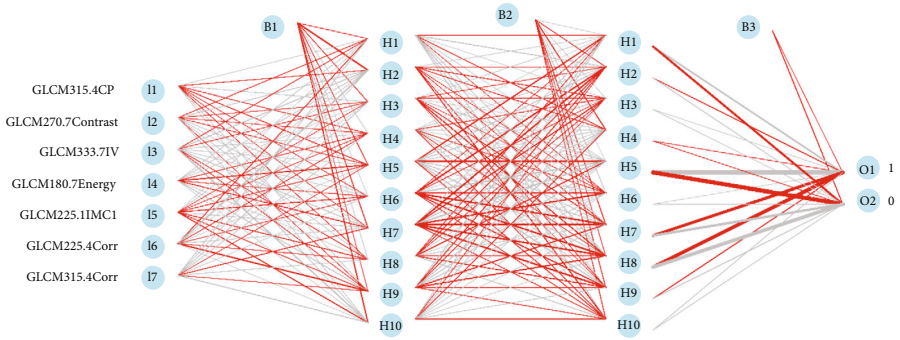

Figure 10: The MLP training network structure which includes two hidden layer.

AKI more than those with preserved LVEF [31]. The present study also supported these previous results. In addition, the present study showed that systolic and diastolic heart dysfunction, characterized by LVEF differences, was associated with AKI development in hospitalized patients. Therefore, echocardiographic monitoring of heart dysfunction can be added to the prediction models of AKI and possibly to real clinical practice to identify high-risk patients and improve outcomes.

Meanwhile, anemia has been reported as a potential modifiable risk factor for postoperative AKI [32, 33]. Anemia is associated with an increased AKI risk, mainly in the surgical setting [33]. However, preoperative anemia is associated with an increase in the probability of erythrocyte transfusion, risk of postoperative renal failure, and mortality, as more intraoperative blood transfusion implies more postoperative bleeding [34]. Accumulating evidence has demonstrated a dose-dependent association between the volume of red blood cells (RBCs) and AKI severity [35, 36]. Consistent with the literature, we found that erythrocyte transfusions on the surgery day were associated with an increased rate of AKI. A series of changes that RBCs experience during storage, including decreased deformability, increased fragility, progressive hemolysis, and accumulation of free hemoglobin and iron, have been proposed as mechanisms responsible for transfusion-associated AKI [37].

In addition, our analysis of intraoperative variables demonstrated that adult patients had a high incidence of AKI after CPB heart surgery and required a prolonged length of ICU or hospital stay; severe AKI could increase

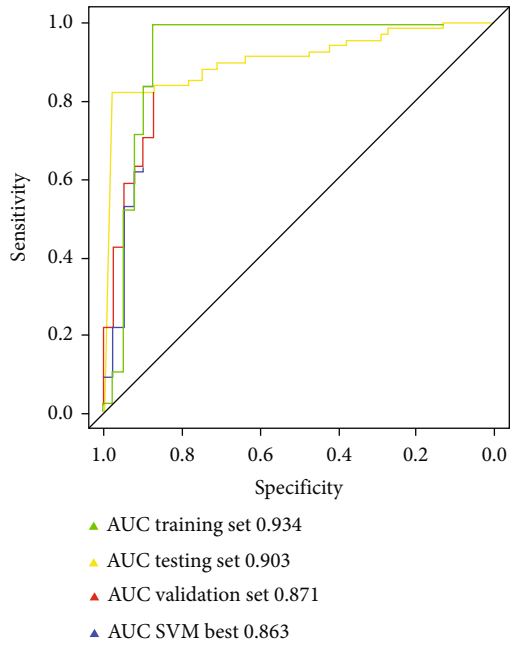

Figure 11: Prediction model compared MLP model performance in training, testing, and validation set with the best SVM model.

perioperative mortality by 3–8 times [38]. An increasing body of evidence has suggested that postoperative AKI occurrence is associated with short-term adverse outcomes [39, 40]. The present study showed that patients who developed AKI required invasive mechanical ventilation, higher mortality, prolonged length of ICU stay, and longer hospitalization time. Exposure to surgery and nephrotoxins is one of the specific modifiable factors, subsequently contributing to AKI development [5, 18, 41]. Additionally, AKI has been associated with increased in-hospital mortality and short- and long-term mortalities after discharge [6]. It has previously been reported that the long-term prognosis is still poor for AKI patients, even with complete recovery of the renal function [42]. Accordingly, it is important to explore the risk factors associated with short- and long-term outcomes of AKI patients.

As shown in Figure 5, the multivariate logistic regression method showed that the predictive performance of a single clinical or laboratory index for AKI was limited. The largest and smallest AUC values were found for RBCI (0.651) and ICUmvat (0.559), respectively, suggesting that although these indicators are effective in predicting AKI and are statistically significant during logistic regression, their predictive power is largely limited. However, the predictive performance was significantly enhanced when the three variables were integrated into a prediction model (AUC value 0.753). In addition, although the random forest-based prediction model yielded excellent performance in the training set, the AUC values ranged from 0.881 to 1 during training of the fivefold cross-validation model. However, in the subsequent validation dataset, the model's generalization ability was average, and the maximum AUC was only 0.714. This finding shows that the random forest model exhibits transitional fitting in the training set. The above findings suggest that the generalization of our model was average, with a lower performance yield than the multivariate logistic regression method. This observation is related to settings such as the number of random forest trees during the design of the random forest model. Pruning and pruning settings have always been challenging in machine learning, requiring constant trial and error to balance the training and validation datasets. The support vector machine-based model performed better than the above two methods, with an AUC value of 0.812 for the best model. When the simple neural network of MLP was used to predict the probability of delirium caused by AKI, although the number of hidden layers was 2 and the number of neurons in each layer was 10, the machine learning MLP model yielded excellent performance in the training and validation datasets. The average AUC reached 0.903, suggesting that our simple neural network is efficient for the two-class prediction models and yields excellent prediction results with a simpler network structure.

This study has some limitations. Our analysis used only single-center data, with a relatively small sample size. The performance of the machine learning algorithm might differ when applied to larger datasets with heterogeneous patient characteristics. As such, external validation is required to prevent overfitting. Future prospective studies are required to evaluate the application of machine learning-based predictive models during clinical practice to identify patients at high risk of AKI and improve outcomes.

5. Conclusion

Because of the high incidence of AKI, understanding the independent risk factors associated with the development of AKI and its early detection is helpful in the risk management and clinical decision-making of high-risk patients after cardiovascular surgery. A radiomics-based machine learning framework can predict AKI-related delirium in patients who have undergone cardiovascular surgery.

Data Availability

Data are available on request from the authors due to ethical restrictions of our patients' privacy.

Conflicts of Interest

There are no competing interests associated with the manuscript.

Acknowledgments

The authors express their gratitude to the editor and the reviewers for their useful comments and suggestions that helped improve the quality of this study. This work was supported by the Program of the National Natural Science Foundation of China (no. 81870193) and Jiangsu Provincial Key Medical Discipline (Laboratory) (ZDXKA2016021).

References

[1] B. Medić, B. RovIanin, G. B. Jovanović, S. Radojević-Škodrić, and M. Prostran, "Kidney injury molecule-1 and cardiovascular diseases: from basic science to clinical practice," *BioMed Research International*, vol. 2015, Article ID 854070, 10 pages, 2015.

[2] J. A. Kellum and J. R. Prowle, "Paradigms of acute kidney injury in the intensive care setting," *Nature Reviews. Nephrology*, vol. 14, no. 4, pp. 217–230, 2018.

[3] J. Gameiro, T. Branco, and J. A. Lopes, "Artificial intelligence in acute kidney injury risk prediction," *Journal of Clinical Medicine*, vol. 9, no. 3, p. 678, 2020.

[4] D. N. Cruz and C. Ronco, "Acute kidney injury in the intensive care unit: current trends in incidence and outcome," *Critical Care*, vol. 11, no. 4, p. 149, 2007.

[5] E. A. Hoste, S. M. Bagshaw, R. Bellomo et al., "Epidemiology of acute kidney injury in critically ill patients: the multinational AKI-EPI study," *Intensive Care Medicine*, vol. 41, no. 8, pp. 1411–1423, 2015.

[6] Y. B. Sun, Y. Tao, and M. Yang, "Assessing the influence of acute kidney injury on the mortality in patients with acute myocardial infarction: a clinical trail," *Renal Failure*, vol. 40, no. 1, pp. 75–84, 2018.

[7] N. Srisawat, F. E. Sileanu, R. Murugan et al., "Variation in risk and mortality of acute kidney injury in critically ill patients: a multicenter study," *American Journal of Nephrology*, vol. 41, no. 1, pp. 81–88, 2015.

[8] S. H. Howitt, S. W. Grant, C. Caiado et al., "The kdigo acute kidney injury guidelines for cardiac surgery patients in critical care: a validation study," *BMC Nephrology*, vol. 19, no. 1, p. 149, 2018.

[9] G. Igiraneza, V. Dusabejambo, F. O. Finklestein, and A. Rastegar, "Challenges in the recognition and management of acute kidney injury by hospitals in resource-limited settings," *Kidney International Reports*, vol. 5, no. 7, pp. 991–999, 2020.

[10] A. M. Uber and S. M. Sutherland, "Nephrotoxins and nephrotoxic acute kidney injury," *Pediatric Nephrology*, vol. 35, no. 10, pp. 1825–1833, 2020.

[11] G. S. Collins, J. B. Reitsma, D. G. Altman, and K. G. M. Moons, "Transparent reporting of a multivariable prediction model for individual prognosis or diagnosis (TRIPOD): the TRIPOD statement," *BMJ*, vol. 350, 2015.

[12] L. E. Hodgson, N. Selby, T. M. Huang, and L. G. Forni, "The role of risk prediction models in prevention and management of AKI," *Seminars in Nephrology*, vol. 39, no. 5, pp. 421–430, 2019.

[13] C. Ichai, C. Vinsonneau, B. Souweine et al., "Acute kidney injury in the perioperative period and in intensive care units (excluding renal replacement therapies)," *Annals of Intensive Care*, vol. 6, no. 1, 2016.

[14] N. Li, H. Qiao, J. F. Guo et al., "Preoperative hypoalbuminemia was associated with acute kidney injury in high-risk patients following non-cardiac surgery: a retrospective cohort study," *BMC Anesthesiology*, vol. 19, no. 1, p. 171, 2019.

[15] J. B. O'Neal, A. D. Shaw, and F. T. Billings, "Acute kidney injury following cardiac surgery: current understanding and future directions," *Critical Care*, vol. 20, no. 1, 2016.

[16] M. Liu, Y. Liang, S. Chigurupati et al., "Acute kidney injury leads to inflammation and functional changes in the brain," *Journal of the American Society of Nephrology*, vol. 19, no. 7, pp. 1360–1370, 2008.

[17] Y. Pan, W. Wang, J. Wang, and F. Ding, "Incidence and risk factors of in-hospital mortality from AKI after non-cardiovascular operation: a nationwide survey in China," *Scientific Reports*, vol. 7, no. 1, 2017.

[18] A. Khwaja, "KDIGO clinical practice guidelines for acute kidney injury," *Nephron. Clinical Practice*, vol. 120, no. 4, pp. c179–c184, 2012.

[19] Y. H. Choi, D. H. Lee, J. H. Oh et al., "Renal replacement therapy is independently associated with a lower risk of death in patients with severe acute kidney injury treated with targeted temperature management after out-of-hospital cardiac arrest," *Critical Care*, vol. 24, no. 1, 2020.

[20] European Delirium Association; American Delirium Society, "The DSM-5 criteria, level of arousal and delirium diagnosis: inclusiveness is safer," *BMC Medicine*, vol. 12, no. 1, 2014.

[21] W. Li, Y. Li, W. Qin et al., "Magnetic resonance image (MRI) synthesis from brain computed tomography (CT) images based on deep learning methods for magnetic resonance (MR)-guided radiotherapy," *Quantitative Imaging in Medicine and Surgery*, vol. 10, no. 6, pp. 1223–1236, 2020.

[22] W. Vandenberghe, S. Gevaert, J. A. Kellum et al., "Acute kidney injury in cardiorenal syndrome type 1 patients: a systematic review and meta-analysis," *Cardiorenal Medicine*, vol. 6, no. 2, pp. 116–128, 2016.

[23] R. Aksoy, T. Adademir, E. Yilmaz et al., "Is hypoalbuminemia a predictor for acute kidney injury after coronary bypass grafting in diabetes mellitus patients?," *Brazilian Journal of Cardiovascular Surgery*, vol. 34, no. 5, pp. 565–571, 2019.

[24] A. Lassnigg, D. Schmidlin, M. Mouhieddine et al., "Minimal changes of serum creatinine predict prognosis in patients after cardiothoracic surgery: a prospective cohort study," *Journal of the American Society of Nephrology*, vol. 15, no. 6, pp. 1597–1605, 2004.

[25] F. Jiang, Y. Jiang, H. Zhi et al., "Artificial intelligence in healthcare: past, present and future," *Stroke and Vascular Neurology*, vol. 2, no. 4, pp. 230–243, 2017.

[26] A. Rajkomar, J. Dean, and I. Kohane, "Machine learning in medicine," *The New England Journal of Medicine*, vol. 380, no. 14, pp. 1347–1358, 2019.

[27] P. Y. Tseng, Y. T. Chen, C. H. Wang et al., "Prediction of the development of acute kidney injury following cardiac surgery by machine learning," *Critical Care*, vol. 24, no. 1, p. 478, 2020.

[28] M. Hur, K. Nam, W. Y. Jo, G. Kim, W. H. Kim, and J. H. Bahk, "Association between elevated echocardiographic index of left ventricular filling pressure and acute kidney injury after off-pump coronary artery surgery," *Circulation Journal*, vol. 82, no. 3, pp. 857–865, 2018.

[29] N. Flint, N. Kaufman, A. Gal-Oz et al., "Echocardiographic correlates of left ventricular filling pressures and acute cardio-renal syndrome in ST segment elevation myocardial infarction patients," *Clinical Research in Cardiology*, vol. 106, no. 2, pp. 120–126, 2017.

[30] S. C. Chen, H. M. Su, C. C. Hung et al., "Echocardiographic parameters are independently associated with rate of renal function decline and progression to dialysis in patients with chronic kidney disease," *Clinical Journal of the American Society of Nephrology*, vol. 6, no. 12, pp. 2750–2758, 2011.

[31] D. Hertzberg, U. Sartipy, L. H. Lund, L. Rydén, J. W. Pickering, and M. J. Holzmann, "Heart failure and the risk of acute

kidney injury in relation to ejection fraction in patients undergoing coronary artery bypass grafting," *International Journal of Cardiology*, vol. 274, no. 274, pp. 66–70, 2019.

[32] S. Parida and A. S. Badhe, "Cardiac surgery-associated acute kidney injury," *Journal of Anesthesia*, vol. 27, no. 3, pp. 433–446, 2013.

[33] K. Karkouti, H. Grocott, R. Hall et al., "Interrelationship of preoperative anemia, intraoperative anemia, and red blood cell transfusion as potentially modifiable risk factors for acute kidney injury in cardiac surgery: a historical multicentre cohort study," *Canadian Journal of Anesthesia*, vol. 62, no. 4, pp. 377–384, 2015.

[34] G. Paone, "Anemia, transfusion, and outcome: both are bad… does it really matter which is worse?," *The Journal of Thoracic and Cardiovascular Surgery*, vol. 156, no. 1, pp. 75-76, 2018.

[35] Y. Y. Liu, F. S. Xue, H. X. Li, and G. Z. Yang, "Association between intraoperative blood product transfusions and acute kidney injury following cardiac surgery," *Perfusion*, vol. 33, no. 1, pp. 81-82, 2018.

[36] S. R. Rasmussen, K. Kandler, R. V. Nielsen, P. C. Jakobsen, M. Ranucci, and H. B. Ravn, "Association between transfusion of blood products and acute kidney injury following cardiac surgery," *Acta Anaesthesiologica Scandinavica*, vol. 64, no. 10, pp. 1397–1404, 2020.

[37] S. Amini, M. N. Najafi, S. P. Karrari et al., "Risk factors and outcome of acute kidney injury after isolated CABG surgery: a prospective cohort study," *Brazilian Journal of Cardiovascular Surgery*, vol. 34, no. 1, pp. 70–75, 2019.

[38] C. Ortega-Loubon, M. Fernández-Molina, Y. Carrascal-Hinojal, and E. Fulquet-Carreras, "Cardiac surgery associated acute kidney injury," *Annals of Cardiac Anaesthesia*, vol. 19, no. 4, pp. 687–698, 2016.

[39] M. E. O'Connor, C. J. Kirwan, R. M. Pearse, and J. R. Prowle, "Incidence and associations of acute kidney injury after major abdominal surgery," *Intensive Care Medicine*, vol. 42, no. 4, pp. 521–530, 2016.

[40] M. E. Grams, Y. Sang, J. Coresh et al., "Acute kidney injury after major surgery: a retrospective analysis of veterans health administration data," *American Journal of Kidney Diseases*, vol. 67, no. 6, pp. 872–880, 2016.

[41] K. Singbartl and J. A. Kellum, "AKI in the ICU: definition, epidemiology, risk stratification, and outcomes," *Kidney International*, vol. 81, no. 9, pp. 819–825, 2012.

[42] C. E. Hobson, S. Yavas, M. S. Segal et al., "Acute kidney injury is associated with increased long-term mortality after cardiothoracic surgery," *Circulation*, vol. 119, no. 18, pp. 2444–2453, 2009.

Hindawi
Computational and Mathematical Methods in Medicine
Volume 2022, Article ID 2037019, 9 pages
https://doi.org/10.1155/2022/2037019

Research Article

Intelligent Image Diagnosis of Pneumoconiosis Based on Wavelet Transform-Derived Texture Features

Zichen Wang, Maoneng Hu, Min Zeng, and Guoliang Wang

Department of Imaging, The Third Clinical College of Hefei of Anhui Medical University, The Third People's Hospital of Hefei, Hefei 230022, China

Correspondence should be addressed to Maoneng Hu; hfyxzk@126.com

Received 21 November 2021; Revised 22 December 2021; Accepted 28 February 2022; Published 17 March 2022

Academic Editor: Kelvin Wong

Objective. Early diagnosis and treatment of occupational pneumoconiosis can delay the development of the disease. This study is aimed at investigating the intelligent diagnosis of occupational pneumoconiosis by wavelet transform-derived entropy. *Method*. From June 2013 to June 2020, the high KV digital radiographs (DR) and computed tomography (CT) images from a total of 60 patients with occupational pneumoconiosis in our department were selected. The wavelet transform-derived texture features were extracted from all images, and the decision tree was used for feature selection. The support vector machines (SVM) with three kernel functions were selected to classify the two kinds of images, and their diagnostic efficiency was compared. *Result*. After eight times of wavelet decomposition, eight wavelet entropy texture features (feature set) were extracted, and six were selected to form the feature subset. The classification effect of linear kernel function SVM is better than those of other functions, with an accuracy of 84.2%. The diagnostic values of DR and CT for occupational pneumoconiosis were the same (kappa = 0.737, $P < 0.001$). The detection rate of CT for stage I of occupational pneumoconiosis was significantly higher than that of DR ($P = 0.031$). *Conclusion*. It is helpful to improve the early diagnosis level of pneumoconiosis by using SVM to make an intelligent diagnosis based on the wavelet entropy.

1. Introduction

Occupational pneumoconiosis is a systemic disease caused by diffuse fibrosis in lung tissue caused by long-term inhalation of productive dust and occupation during occupation activities [1–3]. Its pathogenesis is complex, and the primary process is as follows: when dust particles enter the upper respiratory tract and alveoli, about 2%~3% of them will eventually deposit in the alveolar wall; then, it will be phagocytized and digested by macrophages in human tissues; finally, the particles discharged from the body or transported to the lymphatic system [4]. When the human body inhales a large number of free silica particles, the latter accumulates in the alveolar wall [5]. Pneumoconiosis has the characteristics of occult and long incubation period, which can not be cured and can be aggravated year by year [6]. Although the incidence of pneumoconiosis is decreasing overall, the incidence rate of some special causes, such as asbestosis, is rising [7]. After a long period of inflammatory stimulation, pneumoconiosis is highly likely to develop into mesothelioma [8].

Early diagnosis and treatment of occupational pneumoconiosis can delay the development of the disease. At present, the diagnosis and staging of occupational pneumoconiosis in China are mainly based on the high KV X-ray and the posteroanterior digital radiography (DR) [9]. Computed tomography (CT) and magnetic resonance imaging (MRI) were also used to diagnose pneumoconiosis. However, due to the scanning time and resolution, MRI is difficult to be used as a routine examination method [10, 11]. Due to the complexity and diversity of X-ray manifestations of pneumoconiosis, it is challenging to master the classification criteria. The accuracy of early diagnosis of pneumoconiosis needs to be improved. The results show small shadows with different sizes, uneven distribution, and densities in pneumoconiosis patients' images, which show different texture characteristics from healthy people's

DR chest films. In medical images, the quantitative or qualitative changes of texture features often reflect the pathological changes of the body. Therefore, researchers try to use a variety of texture analysis techniques to analyze various medical imaging images and explore new ways of disease diagnosis and treatment. Due to the complexity of medical images and their textures, there is no general texture analysis method suitable for all kinds of medical images.

In recent years, wavelet transform has been widely used in image processing [12–15]. Because wavelet transform can concentrate the energy of the original image on a small number of wavelet coefficients and the decomposed wavelet coefficients have a high local correlation in the detail components of three directions, it provides favorable conditions for feature extraction. At present, some researchers have applied the features of energy and entropy based on wavelet transform to the texture analysis of ceramic tiles and textiles and achieved good results [16, 17]. As the city's occupational disease prevention and control hospital, our hospital has carried out the research and development of the accurate diagnosis of occupational pneumoconiosis with multimodal imaging. In this study, the value of wavelet entropy texture features for pneumoconiosis diagnosis was applied. The aim is to improve the early diagnosis and differential diagnosis of occupational pneumoconiosis.

2. Materials and Methods

2.1. Research Objects. A total of 120 imaging data were from the Department of Radiology, the Third People's Hospital of Hefei. All patients were male. Specifically, 60 were healthy persons received physical examination, and the rest were 60 patients with pneumoconiosis. All patients were male, aged 33-86 years, with an average of 52.18 ± 14.11 years. They had a dust exposure history of 4-30 years, with an average of 11.85 ± 6.76 years. The main symptoms were chronic cough, expectoration, chest pain, chest tightness, shortness of breath, dyspnea, etc.

2.2. Inspection Method. Digital X-ray imaging system (DXR vision) produced by Neusoft company was used for chest high KV DR examination. Take the standard chest posteroanterior position; imaging parameters were set as 120~140 kV, power $\geqq$ 20 kW, 4~8 mAs, exposure time $\leqq$ 0.1 s, focus $\leqq$ 1.2 mm, and focal film distance of 1.8 m. The patient's chest wall was close to the detector, the feet were naturally separated, and the arms rotate inward so that the scapula does not overlap with the lung field. The centerline was aligned with the height of the sixth thoracic vertebrae, and the exposure is conducted under a breath holding state after full deep inspiration.

The chest CT scan was performed with optima CT produced by GE company. The imaging parameters were 120 kV and 200 mAs. The patient was supine on the examination table with both arms raised. The patient was positioned at the level of sternal stalk notch. The chest was positioned in a positive position. The scanning range was 2-3 cm from the apex of the lung to the diaphragm. Thin layer scanning was used for the local lung field with suspected abnormalities or small lesions. The interval between layers was 1.25 mm, and the thickness was 1.25 mm. The bone algorithm was used for reconstruction.

Furthermore, the original image was saved in terms of DICOM. Then, the lung fields was extracted from the imaging data after image enhancement via the most significant between-class variance algorithm based on morphological reconstruction.

2.3. Wavelet Texture Features. The texture of the pneumoconiosis imaging data was different from those of the normal ones because there were a certain number of small shadows in the pneumoconiosis imaging data, which could not be found in the normal ones. Based on this, a diagnosis of pneumoconiosis could be made. This paper, therefore, performed wavelet decomposition based on db7 wavelet basis and calculated the entropy of wavelet coefficients as texture features. Furthermore, the definition and calculation process of wavelet entropy is as follows.

Assuming that N-level wavelet decomposition was performed, the K-th wavelet coefficient sequence of the $i\,(i = l, 2, \cdots, N)$ decomposition layer was recorded as $\{S_{ik} \mid (k = 1,2,3, \cdots)\}$. Meanwhile, let E_i be the energy of the i decomposition layer on the k scale; then,

$$E_i = \sum_{k=1} S_{ik}^2. \tag{1}$$

Use the total energy E of the image (that is, the sum of the energy E_i of each layer) to normalize the energy E of the i decomposition layer to obtain the relative energy P_i of the i decomposition layer, that is,

$$p_i = \frac{E_i}{E}. \tag{2}$$

According to Shannon's information entropy theory, the wavelet entropy H_i of the i decomposition layer was defined as

$$H_i = -p_i \ln p_i. \tag{3}$$

According to the size of the DR image, 8 wavelet decompositions were performed on the image, finally obtaining a feature vector composed of 8 wavelet entropy values:

$$H = [H_1, H_2, H_3, H_4, H_5, H_6, H_7, H_8]. \tag{4}$$

2.4. Feature Selection Based on Decision Tree. Since the wavelet transform was performed layer by layer on the same image, there would be a certain correlation between the texture features based on the wavelet transform, thus generating redundant features. In addition, there might be noise features interfering with the classification process of the classifier. Therefore, before using wavelet entropy for pneumoconiosis diagnosis and classification, the decision tree was first employed for feature selection.

The decision tree algorithm finds the feature with the best classification ability and divides the data into multiple

Table 1: Wavelet-based entropy from healthy people and patients with pneumoconiosis.

Wavelet entropy	Healthy	Pneumoconiosis	P value
T_1	-0.972	1.154	0.589
T_2	-1.795	3.532	0.176
T_3	-5.192	9.538	<0.001
T_4	-4.036	6.743	0.005
T_5	-2.629	4.341	0.031
T_6	-0.527	0.776	0.754
T_7	-0.254	0.385	0.887
T_8	-1.263	2.246	0.435

subsets. Each subset was divided by the feature with the best classification ability until the condition for the decision tree to stop growing was met. Therefore, the result of decision tree feature selection was those features considered to have the best classification ability in each subset. According to the criteria for judging the ability of feature classification, there were many growth algorithms for decision trees, such as the ID3 algorithm based on information entropy, the CART algorithm based on Gini index, the C4.5 algorithm based on information gain rate, and the C5.0 algorithm. Considering that wavelet entropy was all continuous features, this paper applied C5.0 algorithm decision tree to feature selection.

2.5. Support Vector Machine Classifier. From the perspective of data mining, disease diagnosis was a binary classification task; therefore, an appropriate classifier model should be selected for pneumoconiosis diagnosis via texture features of imaging data. The support vector machine (SVM) was a research direction in statistical learning. It was developed based on the theory of small sample statistics and possessed a positive generalization ability for high-dimensional spaces. What is more, for the second-class data classification problem, the basic idea of SVM was to find an optimal hyperplane via a kernel function to maximize the gap between the two categories. Furthermore, the performance of SVM is closely related to the choice of the kernel function. Accordingly, an SVM classifier with good generalization ability could obtain only by selecting a suitable kernel function and projecting the data into a suitable feature space.

There are many kernel functions of support vector machines, and there is no established standard to judge the applicability of kernel functions. Therefore, this study selected the following three kernel functions for comparative research.

(1) Linear kernel function:

$$K(x, y) = x \bullet y. \tag{5}$$

(2) Polynomial kernel function:

$$K(x, y) = (x \bullet y + 1)^q, q = 1, 2, \cdots, N. \tag{6}$$

(3) Gaussian kernel function:

$$K(x, y) = \exp\left\{-\frac{|x - y|^2}{2\sigma^2}\right\}. \tag{7}$$

Among them, x is the input feature vector, the category of which is $y \in \{0, 1\}$, and q is the degree of the polynomial. Moreover, in this paper, $q = 3$; the learning parameter σ^2 is used to determine the distance between sample vectors in the feature space in accordance with the empirical text, $\sigma^2 = 0.1$. Additionally, the output of the SVM is a decimal C between 0 and 1, and it is divided into two categories with a limit of 0.5. That is, a sample with $C \geq 0.5$ is diagnosed as a pneumoconiosis patient, while a diagnosis with $C < 0.5$ is a normal person.

2.6. Evaluation of the Classifier Model. When verifying the SVM model, considering the number of sample cases and the time of calculation, a 5-fold cross validation method was employed. Specifically, all imaging data were randomly divided into 5 subsets, each of which included 7 normal imaging data and 5 imaging data of pneumoconiosis patients. Furthermore, in a certain round of model verification, 4 sample subsets were used as the training set to train the model, and the remaining 1 sample subset was used as the test set to verify the model. Then, after 5 rounds of modeling-testing, the SVM output for classifying all imaging data was saved, and the classification accuracy, sensitivity, and specificity were calculated. What is more, the receiver operating characteristic (ROC) and the area under the curve (AUC) represented the average specificity of the classification results under various specificities or displayed the average sensitivity of the result under various sensitivities. Accordingly, it was used as a comprehensive index to evaluate the SVM classification results.

2.7. Observation Index. The total detection rate and the detection rate for variant stages of occupational pneumoconiosis were compared by high KV DR and CT and the detection of pulmonary complications.

2.8. Statistical Analysis. The normality of data was tested by the Kolmogorov-Smirnov method and Shapiro-Wilk method. If the P values were larger than or equal to 0.05, the data conform to normal distribution. The measurement data was expressed by $\bar{x} \pm s$, and the statistical analysis was conducted by a t-test. The count data was shown by the number of cases or percentage, and the statistical treatment was performed by a chi-square test. The consistency of the two imaging methods was tested by kappa consistency analysis: kappa $\leqq$ 0.4, poor consistency; 0.4 < kappa $\leqq$ 0.6, general consistency; 0.6 > kappa $\leqq$ 0.8, high consistency; and kappa > 0.8, good consistency.

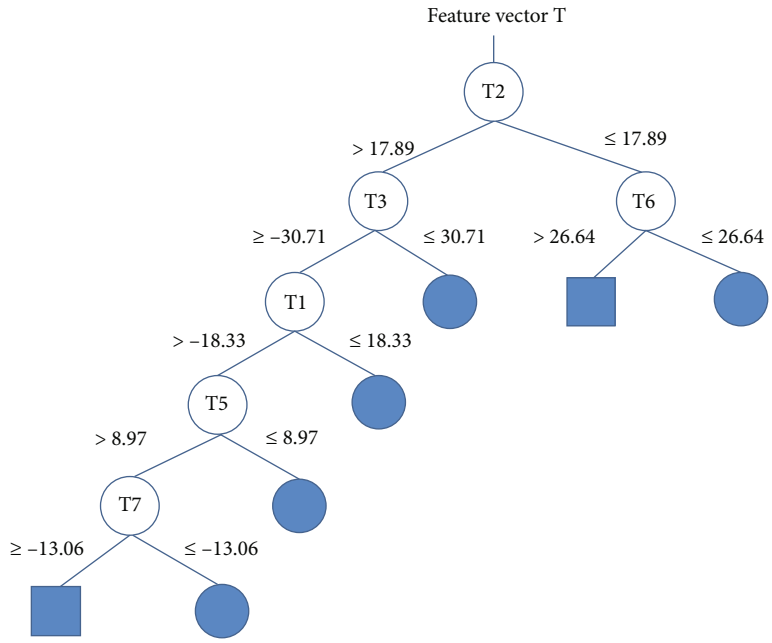

Figure 1: Decision tree used for feature selection.

Table 2: Classification results based on different SVM classifier models (%).

Kernel function	Accuracy (%)		Sensitivity (%)		Specificity (%)	
	Full set	Subset	Full set	Subset	Full set	Subset
Gaussian	78.3	82.5	68.3	73.3	88.3	91.6
Linear	75.8	84.2	61.6	75.0	90.0	93.3
Polynomial	75.8	80.8	60.0	71.6	91.6	90.0

3. Results

3.1. Wavelet Entropy Textural Features. Since some entropy values among the 8 wavelet entropy features showed a significantly skewed distribution with widely differing orders of magnitude across features, all features were log-transformed. They were approximately normally distributed and varied within an appropriate range. The log-transformed eigenvectors are denoted as $T = [T_1, T_2, T_3, T_4, T_5, T_6, T_7, T_8]$. Wavelet entropy results extracted from imaging data of 60 normal subjects and 60 pneumoconiosis patients are shown in Table 1.

3.2. Feature Selection. The decision tree constructed with the C 5.0 algorithm is shown in Figure 1. In this decision tree, a total of six features appear at the branches, and thus, the eigenvectors T are constructed from these six wavelet entropies.

$$T^* = [T_1, T_2, T_3, T_5, T_6, T_7]. \quad (8)$$

3.3. SVM Classification Results. The classification accuracy, sensitivity, and specificity of the SVM classifier models using Gaussian kernel, linear kernel, and polynomial kernel functions, respectively, are shown in Table 2. After feature selection, the classification performance of SVM classifiers with different kernel functions was all improved, indicating that the decision tree algorithm feature selection was helpful to eliminate noisy features and redundant features and improve the performance of classifiers.

From the ROC curves shown in Figure 2, the classification performance of SVM varies when selecting different kernel functions. The classification performance of SVM was related to both the selection of kernel function and the selection of features. Using the selected feature subset, when the linear kernel function of SVM was used, the classification performance was the best. The AUC is 0.90, and the classification accuracy is 84.2%.

3.4. Consistency Analysis. In all 60 cases under High KV DR detection: in 33 cases in stage I, with overall density grade 1 small shadow, distribution range is 2-4 lung areas; in 11 cases in stage II, with overall density grade 2-3 small shadows, distribution range is not less than 4 lung areas; in 8 cases in stage III, large shadow was found. In CT detection, in 40 cases in stage I, grade 1 small density shadow was found; in 12 cases in stage II, grade 2-3 small shadow with or without complications was found; in 8 cases in stage III, large shadow with related complications was found. Typical cases are shown in Figures 3 and 4.

The comparison and analysis of high KV DR and chest CT detection results showed that 51 cases (85.0%) had the same results for pneumoconiosis. Among them, 32 cases (53.0%) were consistent with stage I, 11 cases (18.3%) were consistent with stage II, and 8 cases (13.3%) were consistent with stage III. A kappa consistency test showed that kappa $= 0.737$ and $P < 0.001$. Details are shown in Figure 5.

3.5. Detection Rate of Different Stages. The gold standard was the diagnosis conclusion of the occupational

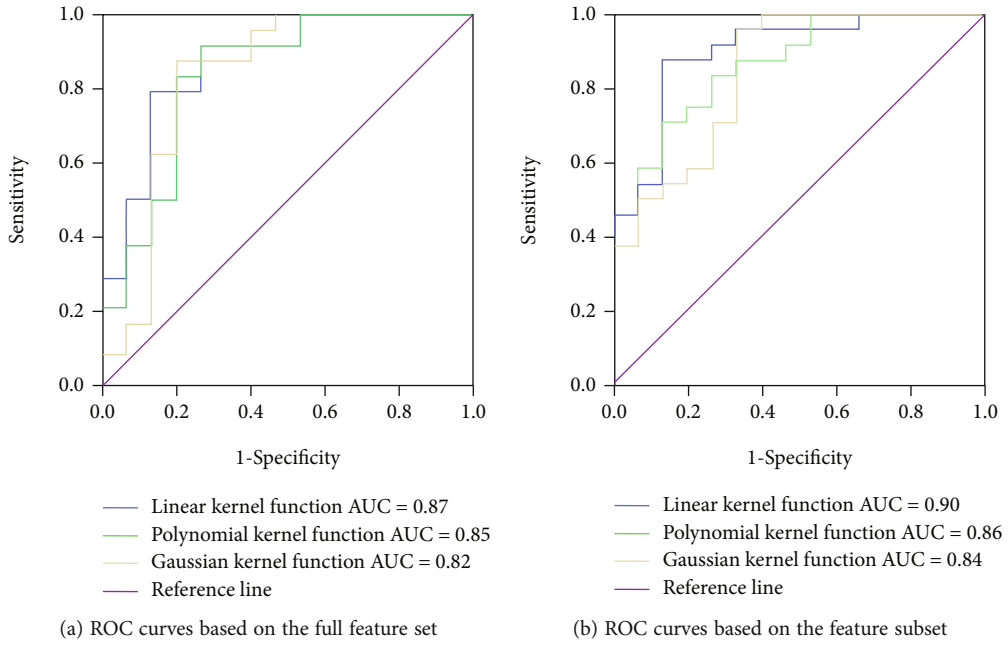

(a) ROC curves based on the full feature set

(b) ROC curves based on the feature subset

Figure 2: ROC curves of support vector machines for diagnosis of pneumoconiosis.

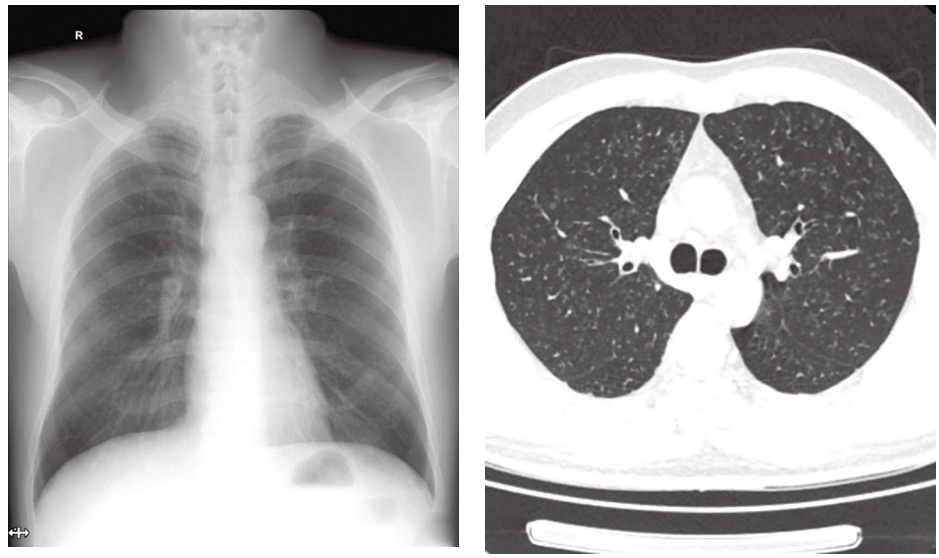

(a) (b)

Figure 3: Typical case from a patient with stage I of occupational silicosis. (a) High KV DR show increased and disordered lung markings; small dot shadow is not obvious. (b) CT shows diffuse miliary nodules in both lungs with ground glass-like changes.

pneumoconiosis expert group. There were 40 stage I cases, the correct detection rate was 80.0% in DR, and there were 7 cases of undetermined diagnosis and 1 case of misdiagnosis as stage III; the correct detection rate was 95.0% in CT, and 2 cases were misdiagnosed as stage III. There was a significant difference in the detection rate of pneumoconiosis between the two methods ($P = 0.031$). There were 12 stage II cases, the correct detection rate was 91.7% in DR, and 1 case was misdiagnosed as stage III; the correct detection rate was 100.0% in CT. There were 8 stage III cases; the correct detection rate in both DR and CT was 100.0%. Details are shown in Figure 6.

4. Discussion

Since the 1970s, chest radiograph-based computer-assisted diagnostic studies for pneumoconiosis have been successively carried out at home and abroad, and initial results have been achieved. Yu et al. [18] performed gray level histogram and gray level cooccurrence matrix analysis on DR images to diagnose 300 normal chest radiographs with 125 pneumoconiosis (containing stage III pneumoconiosis) chest radiographs with 87.7%-89.2% accuracy by SVM classifier. Chen et al. [19] evaluated the automated classification of abnormal small shadow on radiographs and calculated its

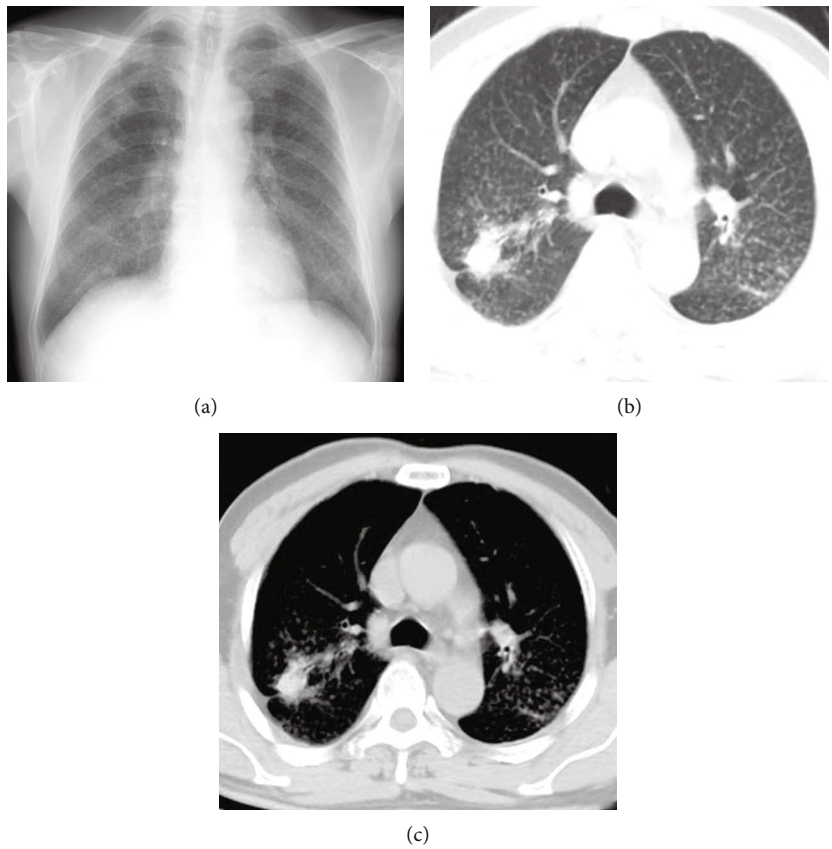

(a) (b) (c)

Figure 4: Typical case from a patient with stage II of occupational silicosis. (a) High KV DR shows scattered small nodules in both lungs, thickened hilum, smooth diaphragm surface, and sharp costophrenic angle. (b) Lung window of CT shows small nodules scattered in all the two lungs, partially fused into a mass; pleural adhesion and thickening were also found. (c) Mediastinal window of CT shows the obvious fusion adhesion between the nodule and pleura.

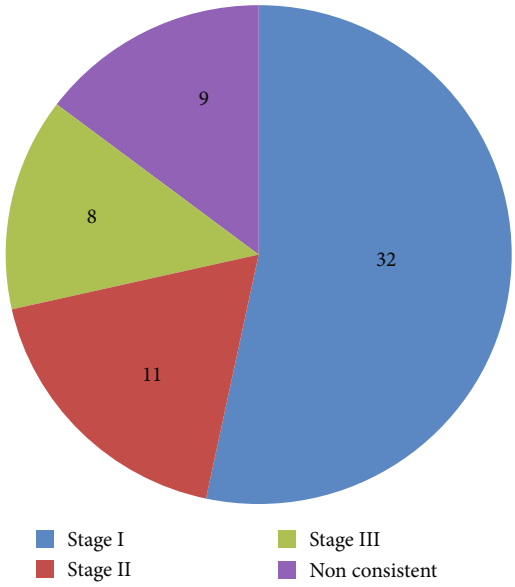

Figure 5: Consistency analysis of high KV DR and CT detection.

size and density. Compared with the expert identification results, the identification of small shadow results has a false detection rate of 19% and a missed detection rate of 28%. In this study, wavelet entropy texture features were used to diagnose pneumoconiosis which is challenging to diagnose clinically with an accuracy of 84.2% and an AUC of 0.90, demonstrating the value of wavelet entropy texture features in diagnosing early-stage pneumoconiosis using DR chest radiographs.

When using data mining technology to complete the classification task, the classifier algorithm and the selection of classification features are essential. Due to the complex and diverse classification tasks, there are no universal applicable classification algorithms and parameter setting of the algorithms or even uniform and definite selection criteria. For this reason, many researchers have compared multiple classification algorithms that are more widely used, such as neural networks and SVM. Based on the previous work, we selected SVM as a classifier model to compare the effect of different SVM kernel functions on classification results. The results show that SVM with a linear kernel has the best classification performance. The results illustrate that the choice of the SVM kernel function, as well as the setting of other parameters, is tailored to a specific classification task.

In terms of feature selection, effective feature selection can provide as much information as possible while reducing the number of features, resulting in classification algorithms with faster processing, simpler results, and even superior performance. There are many methods for feature selection,

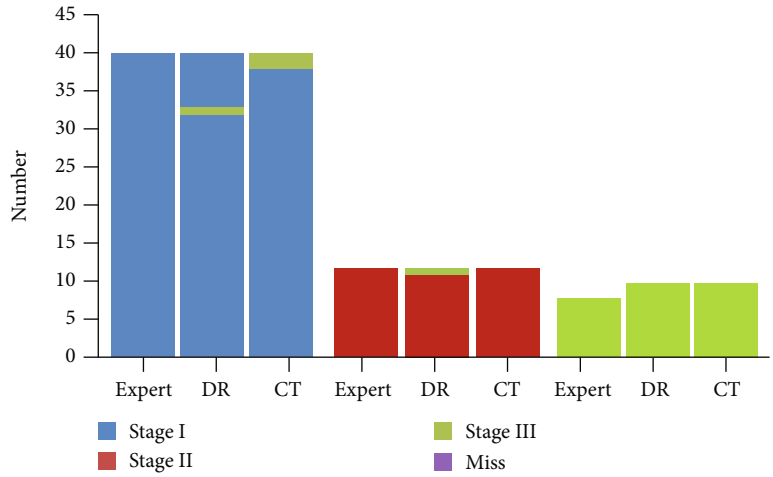

Figure 6: Different stages of occupational pneumoconiosis detected by DR and CT.

such as the relief method, rough set method, and simulated annealing algorithm. Decision tree algorithms are currently one of the most popular algorithms in data mining techniques with built-in feature selection capabilities. It determines the last enrolled feature by finding the best classification feature that splits the dataset into subsets and loops down until the conditions for the decision tree to stop growing are met. A decision tree is therefore a supervised feature selection method, the results of which are those features that are considered to best satisfy the classification requirements in each subset.

The main pathological changes of occupational pneumoconiosis were silicosis and pulmonary interstitial fibrosis. The main symptoms are chest pain, chest tightness, shortness of breath, and dyspnea. Its early detection and treatment can delay the development of the disease, alleviate the pain of patients, improve the quality of life, and prolong the survival period. Therefore, accurate diagnosis and staging of occupational pneumoconiosis are particularly important [20, 21].

With the rapid development of medical imaging, chest CT examination technology is gradually widely used in the diagnosis of occupational pneumoconiosis, and its advantages in the diagnosis of pneumoconiosis are gradually highlighted [22, 23]. The high KV DR is an imaging method that uses tube voltage above 120 kV to generate X-ray with high energy in order to obtain rich levels of imaging range. It is usually used for screening and diagnosis of occupational pneumoconiosis. In X-ray photography with voltage above 120 kV, Compton scattering effect dominates the absorption of X-ray in body tissues [24, 25]. The image density of each part of tissue structure is affected by atomic number and body thickness, and the density difference of bone, soft tissue, fat, and gas is reduced correspondingly, so it is commonly used in the general survey and diagnosis of occupational pneumoconiosis. However, the image contrast is reduced and the haze is increased while the rich layers are obtained. In addition, the selection and adjustment of exposure conditions, distance, posture, inspiratory state, artifact, and window technology during high KV DR will also affect the image quality.

The characteristic imaging manifestations of occupational pneumoconiosis are multiple nodular and striped shadows in the lung, enhanced and disordered lung markings, emphysema, thickening of interlobular septum, and some changes in the hilum [26]. However, some reports show that the accuracy of X-ray diagnosis of silicosis is low, and misdiagnosis and missed diagnosis are easy to occur [20]. In this group of data, it was found that 7 cases of stage I pneumoconiosis were not clearly detected in DR. However, the scattered miliary nodules could be observed in the same patient's CT images. The reasons may be as follows: firstly, the density of small nodules in stage I pneumoconiosis is low, and the density is small; secondly, due to the overlapping of ribs, mediastinum, heart, and large vessels and soft tissue, the lung field lesions in the covered part are not well displayed; finally, the image density resolution of DR is low, which can not fully display the shape and density characteristics of the lesions, which is not conducive to observation [27]. The greatest advantage of chest CT is high density resolution, and when CT is used to examine pneumoconiosis, doctors can perform tubular reconstruction and sagittal reconstruction to clearly show the structure of pulmonary lobules and the characteristic changes of pulmonary interstitial fibrosis, including interlobular septal thickening, subpleural line, nodules and honeycomb shadows in interlobular septum, cavities, and calcification in lesions. The lung window and mediastinal window can also be changed for further observation, so the chest CT is more sensitive for the stage I pneumoconiosis. But in the stage II and stage III cases, the diagnosis coincidence rate is very high; there is no significant difference in detection rate between the DR and CT, because the imaging performance of pneumoconiosis patients in this stage has been very obvious, with many lesions and wide range, being easy to observe and analyze, with comprehensive judgment. However, two patients were still diagnosed as stage III by CT and DR at admission, and the diagnosis results were corrected to stage I and stage

II, respectively, at discharge. The cause of misdiagnosis was considered that the patients were overstaged because of the imaging interference of pulmonary tuberculosis and pleural thickening. Therefore, it is suggested that in the diagnosis of occupational pneumoconiosis, we should have a higher ability of differential analysis of lung lesions in order to do a good job in differential diagnosis.

5. Conclusions

In summary, it is helpful to improve the early diagnosis level of pneumoconiosis by using SVM to make an intelligent diagnosis based on the wavelet entropy of the image. In addition, the chest CT is better than chest DR in the early diagnosis of occupational pneumoconiosis and complications; the combined application of the two imaging methods can improve the detection rate and accurate staging of occupational pneumoconiosis. Therefore, while the DR is a routine screening and diagnosis of occupational pneumoconiosis, the selective application of chest CT examination can play a good role in diagnosis and supplement.

Data Availability

The data presented in this study are available on request from the corresponding author.

Conflicts of Interest

The authors declare no conflict of interest.

Acknowledgments

The study was supported by the Hefei Independent Innovation Policy "Loan to Supplement" Fund Project (No. J2019Y06).

References

[1] Y. Fan, W. Xu, Y. Wang, Y. Wang, S. Yu, and Q. Ye, "Association of occupational dust exposure with combined chronic obstructive pulmonary disease and pneumoconiosis: a cross-sectional study in china," *BMJ Open*, vol. 10, no. 9, article e038874, 2020.

[2] L. Han, W. Yao, Z. Bian et al., "Characteristics and trends of pneumoconiosis in the Jiangsu Province, China, 2006-2017," *International Journal Environment Research Public Health*, vol. 16, no. 3, p. 437, 2019.

[3] J. Q. Zhao, J. G. Li, and C. X. Zhao, "Prevalence of pneumoconiosis among young adults aged 24-44 years in a heavily industrialized province of China," *Journal of Occupational Health*, vol. 61, no. 1, pp. 73–81, 2019.

[4] L. Kurth, A. S. Laney, D. J. Blackley, and C. N. Halldin, "Prevalence of spirometry-defined airflow obstruction in never-smoking working us coal miners by pneumoconiosis status," *Occupational and Environmental Medicine*, vol. 77, no. 4, pp. 265–267, 2020.

[5] J. Chiarchiaro, L. R. Tomsic, S. Strock et al., "A case series describing common radiographic and pathologic patterns of hard metal pneumoconiosis," *Respiratory Medicine Case Reports*, vol. 25, pp. 124–128, 2018.

[6] H. Altınöz, C. Çelikkalkan, G. D. Horasan, F. Hamşioğlu, N. Cengiz, and H. Orbay, "Socio-demographic and clinical characteristics of turkish workers with pneumoconiosis," *Central European Journal of Public Health*, vol. 24, no. 3, pp. 231–233, 2016.

[7] P. Shi, X. Xing, S. Xi et al., "Trends in global, regional and national incidence of pneumoconiosis caused by different aetiologies: an analysis from the global burden of disease study 2017," *Occupational and Environmental Medicine*, vol. 77, no. 6, pp. 407–414, 2020.

[8] H. Chen, N. Xu, F. Zhu, T. Ge, Y. Li, and J. Ge, "Malignant pleural mesothelioma and tuberculous empyema: Ct differential diagnosis," *Journal of Medical Imaging and Health Informatics*, vol. 7, no. 4, pp. 875–879, 2017.

[9] X. Wang, J. Yu, Q. Zhu et al., "Potential of deep learning in assessing pneumoconiosis depicted on digital chest radiography," *Occupational and Environmental Medicine*, vol. 77, no. 9, pp. 597–602, 2020.

[10] S. Berk, D. O. Dogan, C. Gumus, and I. Akkurt, "Relationship between radiological (x-ray/hrct), spirometric and clinical findings in dental technicians' pneumoconiosis," *The Clinical Respiratory Journal*, vol. 10, no. 1, pp. 67–73, 2016.

[11] L. Zhang, C. Wang, Q. Yan, T. Zhang, Z. Han, and G. Jiang, "Diagnostic and clinical application value of magnetic resonance imaging (MRI) for progressive massive fibrosis of coal worker pneumoconiosis: case reports," *Medicine (Baltimore)*, vol. 96, no. 20, p. e6890, 2017.

[12] Y. Ding, Y. Wei, S. Zhang, and S. Yu, "Reversible information of encrypted image based on feature difference detection and wavelet transform," *Contrast Media Mol Imaging*, vol. 2021, article 5483001, 6 pages, 2021.

[13] L. M. Hari, G. Venugopal, and S. Ramakrishnan, "Dynamic contraction and fatigue analysis in biceps brachii muscles using synchrosqueezed wavelet transform and singular value features," *Proceedings of the Institution of Mechanical Engineers. Part H*, vol. 236, no. 2, pp. 208–217, 2022.

[14] M. Zhou, B. D. Boyd, W. D. Taylor, and H. Kang, "Double-wavelet transform for multi-subject resting state functional magnetic resonance imaging data," *Statistics in Medicine*, vol. 40, no. 30, pp. 6762–6776, 2021.

[15] Z. Tang, Y. Li, X. Chai, H. Zhang, and S. Cao, "Adaptive nonlinear model predictive control of nox emissions under load constraints in power plant boilers," *Journal of Chemical Engineering of Japan*, vol. 53, no. 1, pp. 36–44, 2020.

[16] S. Khoje, "Appearance and characterization of fruit image textures for quality sorting using wavelet transform and genetic algorithms," *Journal of Texture Studies*, vol. 49, no. 1, pp. 65–83, 2018.

[17] H. Chen, W. Li, and Y. Zhu, "Improved window adaptive gray level co-occurrence matrix for extraction and analysis of texture characteristics of pulmonary nodules," *Computer Methods and Programs in Biomedicine*, vol. 208, article 106263, 2021.

[18] P. Yu, H. Xu, Y. Zhu, C. Yang, X. Sun, and J. Zhao, "An automatic computer-aided detection scheme for pneumoconiosis on digital chest radiographs," *Journal of Digital Imaging*, vol. 24, no. 3, pp. 382–393, 2011.

[19] X. Chen, J. -I. Toriwaki, and J. -I. Hasegawa, "Automated classification of pneumoconiosis radiographs based on recognition of small rounded opacities," *Systems and Computers in Japan*, vol. 21, no. 12, pp. 33–44, 1990.

[20] E. Okumura, I. Kawashita, and T. Ishida, "Computerized classification of pneumoconiosis on digital chest radiography artificial neural network with three stages," *Journal of Digital Imaging*, vol. 30, no. 4, pp. 413–426, 2017.

[21] O. Ulker, B. Yucesoy, O. Demir, I. Tekin, and A. Karakaya, "Serum and bal cytokine and antioxidant enzyme levels at different stages of pneumoconiosis in coal workers," *Human & Experimental Toxicology*, vol. 27, no. 12, pp. 871–877, 2008.

[22] E. K. Choi, H. L. Park, I. R. Yoo, S. J. Kim, and Y. K. Kim, "The clinical value of f-18 fdg pet/ct in differentiating malignant from benign lesions in pneumoconiosis patients," *European Radiology*, vol. 30, no. 1, pp. 442–451, 2020.

[23] C. Costa, G. Ascenti, E. Scribano et al., "CT patterns of pleuropulmonary damage caused by inhalation of pumice as a model of pneumoconiosis from non-fibrous amorphous silicates," *La Radiologia Medica*, vol. 121, no. 1, pp. 19–26, 2016.

[24] T. L. Fauber, T. F. Cohen, and M. C. Dempsey, "High kilovoltage digital exposure techniques and patient dosimetry," *Radiologic Technology*, vol. 82, no. 6, pp. 501–510, 2011.

[25] J. S. Jang, H. J. Yang, H. J. Koo et al., "Image quality assessment with dose reduction using high kVp and additional filtration for abdominal digital radiography," *Physica Medica*, vol. 50, pp. 46–51, 2018.

[26] M. U. Şener, C. Şimşek, Ş. Özkara, H. Evran, İ. Bursali, and A. Gökçek, "Comparison of the international classification of high-resolution computed tomography for occupational and environmental respiratory diseases with the international labor organization international classification of radiographs of pneumoconiosis," *Industrial Health*, vol. 57, no. 4, pp. 495–502, 2019.

[27] C. S. Guan, S. Yan, Z. B. Lv et al., "Ct imaging and pathological basis of linear shadow connecting pulmonary segmental artery to horizontal fissure," *Medicine (Baltimore)*, vol. 99, no. 29, p. e21239, 2020.

Hindawi
Computational and Mathematical Methods in Medicine
Volume 2022, Article ID 6499461, 6 pages
https://doi.org/10.1155/2022/6499461

Research Article

Preservation of Autologous Brachiocephalic Vessels with Assistance of Three-Dimensional Printing Based on Convolutional Neural Networks

Yu Yan[1], **Yan-Yan Su**[2] **and Zhong-Ya Yan**[1]

[1]*Department of Cardiovascular Surgery, The Second Affiliated Hospital of Anhui Medical University, Hefei, China*
[2]*Department of Anatomy, Anhui Medical University, Hefei, China*

Correspondence should be addressed to Zhong-Ya Yan; yan20197@163.com

Received 4 January 2022; Revised 21 February 2022; Accepted 1 March 2022; Published 17 March 2022

Academic Editor: Kelvin Wong

Background. Preservation of autologous brachiocephalic vessels in Stanford type A aortic dissection has good short-time outcomes. However, getting access to the details is not easy by conventional examination methods. This study is aimed at reconstructing the aortic arch model by three-dimensional (3D) printing based on convolutional neural networks (CNN) to understand the details for performing surgery. *Methods*. Three patients with type A aortic dissection from October 2017 to June 2018 were indicated for simplified Sun's procedure. Convolutional neural network (CNN) is used as a deep learning model, and the model was preset by transfer learning. The genetic algorithm (GA) was used to optimize the parameters. The aortic arch models were reconstructed using the segmented image. *Results*. The predicted damage area (mean 0.021 mm^2) of the model optimized by deep learning was consistent with the experimental results (mean 0.023 mm^2). Among the three patients, one patient died due to multiple organ failure and septic shock on the 11th day after surgery. The other two patients were cured, no reoperation was reported, and their cardiac functions were defined as class I during the 13 and 20 months of follow-up. *Conclusion*. It is feasible to use CNN to optimize the manufacturing of the aortic arch models.

1. Introduction

Stanford type A aortic dissection is a life-threatening disease that deteriorates rapidly. The incidence of this disease has been increasing in China [1]. Without medical intervention, the mortality rate of this disease increases by 1% each hour after its onset and reaches 30-50% within 48 hours [2, 3]. At present, Stanford type A aortic dissection is mainly treated by surgery. Among different surgical procedures, Sun's procedure (total aortic arch replacement combined with stented elephant trunk implantation) [4] applies to a variety of patients with complex changes in aortic arch morphology [5].

Although well accepted, this procedure is complicated because of its multiple anastomose. The autologous brachiocephalic vessel preserved Sun's procedure is one of the simplified procedures of conventional Sun's procedure, and it has excellent shot-term outcomes [6, 7]. Considering the requirement of comprehensive understanding of the details of patients' aortic arch (including the autologous brachiocephalic vessels) for applying the simplified procedure and the complex morphology of the aortic arch itself, the information obtained from conventional imaging examination before surgeries are relatively limited [8].

Convolutional neural networks (CNN) predictive analysis has been widely used in biomedical field [9–11]. Based on the patients' computed tomography angiography (CTA) data, we tried to reconstruct the aortic arch models using three-dimensional (3D) printing technology based on the CNN to make an accurate diagnosis and grasp the strict surgical indications of this simplified procedure properly.

2. Material and Methods

2.1. Case Information. From October 2017 to June 2018, there were three patients with type A aortic dissection who were indicated for simplified Sun's procedure, and the clinical data of patients are listed in Table 1.

2.2. Experimental Data Set. CT scan images of patients were selected with scanning thickness of 3.0 mm and reconstruction resolution of 512×512. Aortic CTA was performed, and the occurrence of type A aortic dissection was confirmed in each patient. First, we transformed the original CTA data into a rough 3D graphic of the aortic lumen, using 3D image processing software Mimics medical (21.0) (Materialise NV, Leuven, Belgium) (Figure 1). The transverse CT images were classified by combining the reconstructed sagittal and coronal positions. A total of 3/5 of the classified data was used for training, 1/5 for testing, and 1/5 for verification. The images were converted from DICOM format to PNG format.

2.3. Convolutional Neural Networks. The CNN used in this study includes convolution layer, full connection layer, and pooling layer. The convolutional layer is the basic structure of convolutional neural network, which can obtain local information of image by acting on local image region with a certain size of convolution kernel [12, 13]. The general form of the convolution layer is shown in the equation (1).

$$x_j^l = f\left(\sum_{k \in M_j} x_k^{l-1} * k_{jk}^l + b_j^l\right). \tag{1}$$

The pooling layer is essentially a "down-sampling" operation. Different from the convolutional layer operation, the pooling layer does not contain parameters to be learned. The general expression is as shown in the equation (2).

$$x_j^l = f\left(\beta_j^l \mathrm{down}\left(x_j^{l-1}\right) + b_j^l\right). \tag{2}$$

The full connection layer is generally located at the end of the network. Two-dimensional vector features obtained from the convolution layer and pooling layer are converted into one-dimensional vectors for classification, and the general expression is shown in the formula (3).

$$x_j^l = f\left(w^l x^{l-1} + b^l\right). \tag{3}$$

2.4. Transfer Learning. The parameter training of CNN requires a large number of training samples; so, this paper adopts transfer learning to solve the problem of insufficient training samples [14]. Transfer learning can solve the problem of learning small sample data with existing knowledge, thus improving the classification accuracy of small sample data sets by CNN [15]. Compared with traditional machine learning methods, transfer learning no longer needs enough and available training samples to obtain a good classification model nor does it require that the training samples and the new test samples used for learning meet independent homodistribution [16, 17].

In this study, based on the transfer learning strategy, the convolutional neural network is trained as a pretraining model. The weight parameters of the pretraining model are transferred to the training model. Finally, various parameters are fine-tuned and optimized, the whole network is trained on the training set to update the parameters, and finally, the new model weight is obtained. The specific process is shown in Figure 2.

2.5. Model Training and Validation. CNN trains the model, including image format conversion, random classification, training, and testing. The specific training diagram is shown in Figure 3. The genetic algorithm (GA) was used to optimize the parameters [18, 19]. To verify the optimized parameters, the optimized parameters after training were printed once, and the damaged area of the model was observed for comparison.

2.6. Operation Method. The optimized parameters were used to build a 3D model, and the aortic arch model was printed in 3D entity (Figure 4). After diagnosis and evaluation of the surgical indications in assistance of the 3D models, we run simplified Sun's procedure under hypothermic cardiopulmonary bypass with selective antegrade cerebral perfusion on all 3 patients. The procedure of the surgery is briefly illustrated in Figure 4(d).

3. Results

3.1. 3D Reconstruction Printing and Surgical Results. Three-dimensional reconstruction model of aortic arch tends to theoretical model (Figure 1(e)). The damaged area of the model printed with optimized parameters was 0.021 mm^2 (mean), which was not significantly different from the theoretical value (mean 0.023 mm^2). In addition, simplified Sun's procedure was applied as planned on each of the 3 patients, and the relevant information are also listed in Table 1. The aortic arch is replaced, a stented elephant trunk is implanted, the autologous brachiocephalic vessels are preserved, and the left subclavian artery is anastomosed to the left common carotid artery.

3.2. Postoperative Follow-Up Results. The intraoperative findings of the aortic arch were all consistent with the reconstructed models. Of these three patients, one patient (patient 1 in Table 1) died due to multiple organ failure and septic shock on the 11th day after surgery. The other 2 patients were cured, no reoperation was reported, and their cardiac functions were both defined as class I during the 13 and 20 months of follow-up, respectively.

4. Discussion

As one of the treatments for aortic dissection aiming at reconstruction of the aortic arch, simplified Sun's procedure has the similar cardiopulmonary bypass time, selective antegrade cerebral perfusion time, and short-time outcomes with that of conventional Sun's procedure [6]. The advantage of

Table 1: Clinical data of patients.

	Patient 1	Patient 2	Patient 3
Age (years)	67	54	48
Gender	Male	Male	Male
Hypertension	Yes	Yes	Yes
Initial symptom	Chest pain	Chest tightness	Chest pain
Time from onset to hospitalization (days)	1	3	1
CPB time (mins)	133	167	179
Aortic crossclamping time (mins)	64	82	99
SACP time (mins)	21	24	24
Concomitant procedure	Ascending aorta replacement	Bentall procedure	Bentall procedure

CPB: cardiopulmonary bypass; SACP: selective antegrade cerebral perfusion.

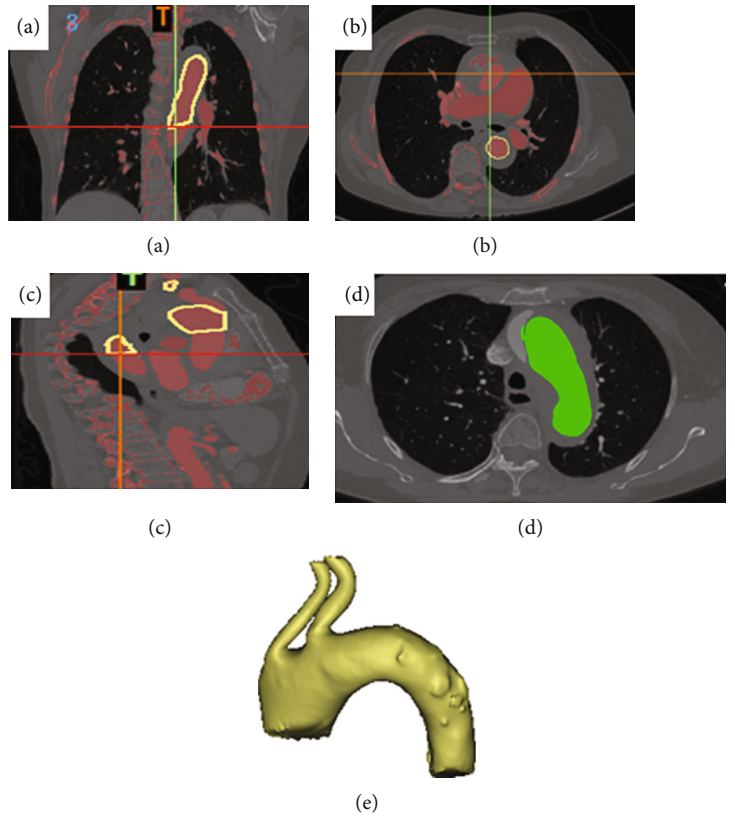

Figure 1: 3D reconstruction process diagram based on CNN model feature extraction. Coronal plane (a), horizontal plane (b), and sagittal plane (c). (d) CNN radiomic feature extraction. (e) 3D reconstruction model of the aortic arch.

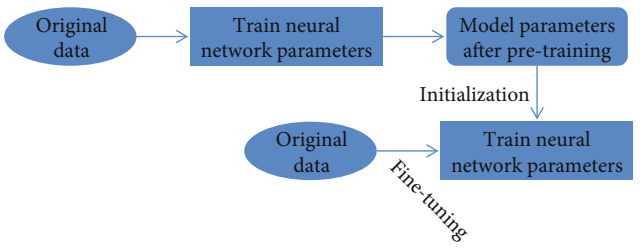

Figure 2: Illustration of model fine-tuning.

this simplified procedure is that it preserves the autologous brachiocephalic vessels of the patients, leading to a high long-term patency rate. In addition, the reduced anastomoses simplify the operation and reduce the related complications. What is more, the anastomosis of the aortic arch is applied between the left common carotid artery and the left subclavian artery in this procedure, and the relatively clear visualization of the anastomotic site combined with limited separation of the arch makes it more facilitated to do anastomosis. In this study, for the patient who died after surgery, the cause of death was not related to either the preservation of brachiocephalic vessels or the arch anastomosis in the

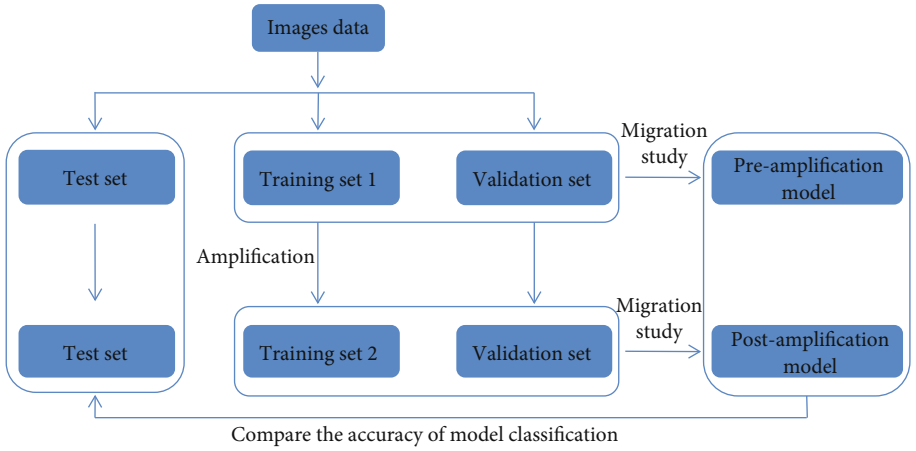

Figure 3: The workflow of model training.

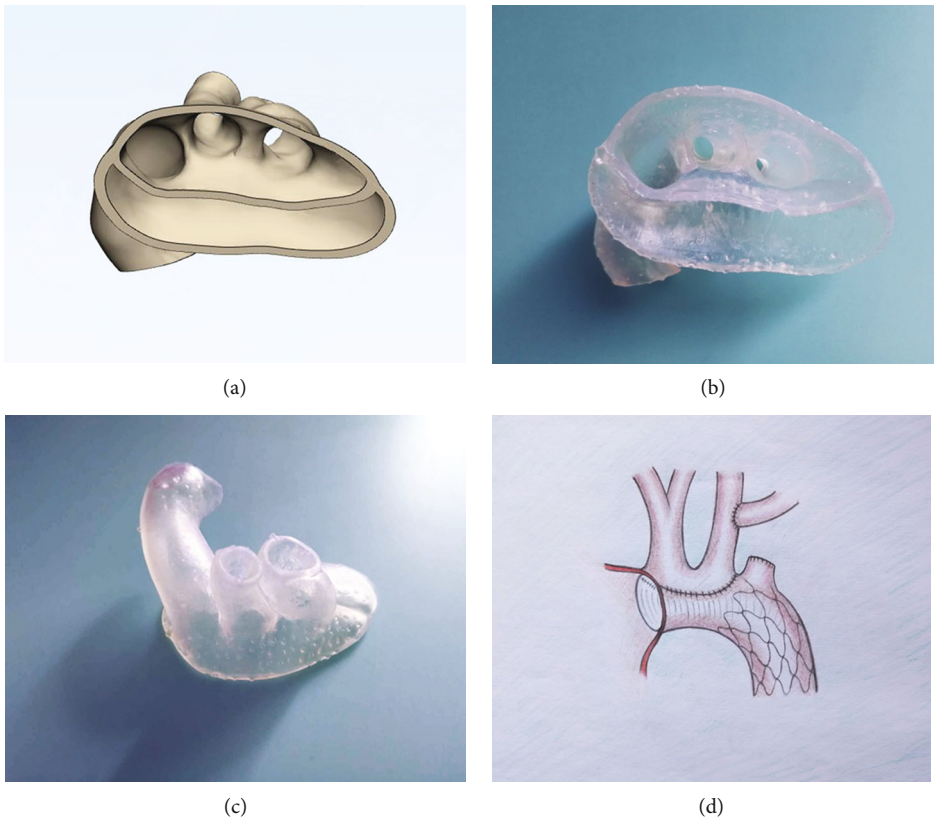

Figure 4: Preservation of autologous brachiocephalic vessels in the treatment for Stanford type A aortic dissection with assistance of three-dimensional (3D) printing. (a) Bottom view of the aortic arch in 3D image, no sign of dissection, or hematoma around the opening of the brachiocephalic vessels and the vessels themselves. (b) 3D printing model of the aortic arch (bottom view). (c) 3D printing model of the aortic arch (anterosuperior view). (d) Illustration of the surgical procedure, the aortic arch is replaced, a stented elephant trunk is implanted, the autologous brachiocephalic vessels are preserved, and the left subclavian artery is anastomosed to the left common carotid artery.

surgery. This patient had a long-term history of smoking. Therefore, it was difficult to control his postoperative pulmonary infection, which led to his multiple organ failure and septic shock.

Aortic dissection occurs and progresses rapidly, leaving a small window of time for clear diagnosis and development of a surgical plan. The diagnosis and the evaluation of surgical indications require precise understanding of the details of the aortic arch and the brachiocephalic vessels, as well as the openings of the branched vessels. Considering the limited cases and relatively fewer training of surgeons in low-volume heart centers like ours, the preoperative surgical plan

is particularly important for the application of such a complicated surgery. Preoperative aortic CTA examination is essential for the diagnosis of Stanford type A dissection and is also the fundamental basis for determining the preservation of autologous brachiocephalic vessels [20]. However, the flat image of CTA cannot fully satisfy us with enough details. In some patients with type A aortic dissection, before surgery, according to the CTA image, we planned to preserve the autologous brachiocephalic vessels, but it revealed that the opening of the vessels was slightly involved in the dissection during operation. In that situation, we had to perform conventional Sun's procedure instead of the simplified one, and the change of surgical procedure could increase the risk of surgery [21].

Compared with reconstructed CTA images on the screen, 3D printing models can be more helpful, since it allows us to intuitively view the entire internal conditions of the affected aortic arch and the branched vessels and let us better define the specific condition of the aortic lesions [22, 23]. Precision medicine is an important direction of future medical development. In this paper, CNN is used to train CT images. Transfer learning is applied to model training to solve the problem of small sample size. The GA was used to optimize, and the corresponding manufacturing parameters were obtained [24]. In our study, the model of 3D reconstruction based on image features extracted by the CNN algorithm is closer to the theoretical value. Therefore, it makes it possible for us to develop a surgical plan accurately and even to simulate the surgical procedure. As in this study, the intraoperative findings were all consistent with that of the reconstructed models of the patients; therefore, we could run these surgeries exactly as planned. In addition, two cured patients were followed up for 13 months. No reoperation was performed, and all patients had grade I cardiac function. Li et al. showed that the total endovascular repair for false lumen stent-graft implantation was feasible and minimally invasive [25], and the postoperative recovery of patient is similar to that of our patients.

After obtaining the CTA data, 3D reconstruction of images and model printing can be done within 6 hours; so, we do not need extra time, since it can be done simultaneously with preparation of the operation before surgery. The cost of 3D printing is about $ 150 per person, that is affordable to most of the patient, and it is free of charge in this study.

There are several limitations to our study. Given the small sample size and short follow-up time in this study, more information should be gained with more patients and longer time of follow-up in the future. In addition, the algorithm is too long, affecting the calculation time.

5. Conclusion

In summary, the application of 3D printing models based on the CNN is feasible and can be benefit to low-volume heart centers in performing Sun's procedure with preservation of autologous brachiocephalic vessels.

Data Availability

The data used to support the findings of this study are available from the corresponding author upon request.

Conflicts of Interest

The authors declare that they have no conflicts of interest.

References

[1] F. Fan, Q. Zhou, J. Pan et al., "Preliminary observation of chemokine expression in patients with Stanford type a aortic dissection," *Cytokine*, vol. 127, p. 154920, 2020.

[2] A. C. Braverman, "Aortic dissection: prompt diagnosis and emergency treatment are critical," *Cleveland Clinic Journal of Medicine*, vol. 78, no. 10, pp. 685–696, 2011.

[3] I. Mészáros, J. Mórocz, J. Szlávi et al., "Epidemiology and clinicopathology of aortic dissection," *Chest*, vol. 117, no. 5, pp. 1271–1278, 2000.

[4] L. Sun, R. Qi, J. Zhu, Y. Liu, and J. Zheng, "Total arch replacement combined with stented elephant trunk Implantation," *Circulation*, vol. 123, no. 9, pp. 971–978, 2011.

[5] Y. Zhu, B. Lingala, M. Baiocchi et al., "Type A aortic dissection–experience over 5 decades:," *Journal of the American College of Cardiology*, vol. 76, no. 14, pp. 1703–1713, 2020.

[6] J. M. Zhu, R. D. Qi, L. Chen et al., "Surgery for acute type A dissection using total arch replacement combined with stented elephant trunk implantation: preservation of autologous brachiocephalic vessels," *The Journal of Thoracic and Cardiovascular Surgery*, vol. 150, no. 1, pp. 101–105, 2015.

[7] Y. L. Zhong, R. D. Qi, W. G. Ma et al., "Frozen elephant trunk with modified en bloc arch reconstruction and left subclavian transposition for chronic type a dissection," *Journal of Thoracic Disease*, vol. 10, no. 9, pp. 5376–5383, 2018.

[8] Y. Wu, R. Jiang, P. Xu, G. Wang, J. Wang, and S. Yang, "Perioperative results and risk factors for in-hospital mortality in patients with Stanford type a aortic dissection undergoing sun's procedure - a single center study," *The Heart Surgery Forum*, vol. 21, no. 6, pp. E432–e437, 2018.

[9] E. I. Mohamed, R. A. Meshref, S. M. Abdel-Mageed, M. H. Moustafa, M. I. Badawi, and S. H. Darwish, "A novel morphological analysis of DXA-DICOM images by artificial neural networks for estimating bone mineral density in health and disease," *Journal of Clinical Densitometry*, vol. 22, no. 3, pp. 382–390, 2019.

[10] T. Cai and Z. Zhao, "Convolutional neural network-based surgical instrument detection," *Technology and Health Care*, vol. 28, no. S1, pp. 81–88, 2020.

[11] Z. Tang, Y. Li, X. Chai, H. Zhang, and S. Cao, "Adaptive nonlinear model predictive control of nox emissions under load constraints in power plant boilers," *Journal of Chemical Engineering of Japan*, vol. 53, no. 1, pp. 36–44, 2020.

[12] S. A. Agnes, J. Anitha, S. I. A. Pandian, and J. D. Peter, "Classification of mammogram images using multiscale all convolutional neural network (ma-cnn)," *Journal of Medical Systems*, vol. 44, no. 1, p. 30, 2019.

[13] N. Kriegeskorte and T. Golan, "Neural network models and deep learning," *Current Biology*, vol. 29, no. 7, pp. R231–r236, 2019.

[14] C. Cai, S. Wang, Y. Xu et al., "Transfer learning for drug discovery," *Journal of Medicinal Chemistry*, vol. 63, no. 16, pp. 8683–8694, 2020.

[15] Y. Xiao, F. Liang, and B. Liu, "A transfer learning-based multi-instance learning method with weak labels," *IEEE Trans Cybern*, vol. 52, no. 1, pp. 287–300, 2022.

[16] S. Belharbi, C. Chatelain, R. Hérault et al., "Spotting L3 slice in CT scans using deep convolutional network and transfer learning," *Computers in Biology and Medicine*, vol. 87, pp. 95–103, 2017.

[17] J. H. Lee, D. H. Kim, S. N. Jeong, and S. H. Choi, "Detection and diagnosis of dental caries using a deep learning-based convolutional neural network algorithm," *Journal of Dentistry*, vol. 77, pp. 106–111, 2018.

[18] D. Toubiana, R. Puzis, A. Sadka, and E. Blumwald, "A genetic algorithm to optimize weighted gene co-expression network analysis," *Journal of Computational Biology*, vol. 26, no. 12, pp. 1349–1366, 2019.

[19] M. Verotti, P. Di Giamberardino, N. P. Belfiore, and O. Giannini, "A genetic algorithm-based method for the mechanical characterization of biosamples using a MEMS microgripper: numerical simulations," *Journal of the Mechanical Behavior of Biomedical Materials*, vol. 96, pp. 88–95, 2019.

[20] T. Gudbjartsson, A. Ahlsson, A. Geirsson et al., "Acute type a aortic dissection - a review," *Scandinavian Cardiovascular Journal*, vol. 54, no. 1, pp. 1–13, 2020.

[21] P. Liu, B. Wen, C. Liu et al., "En bloc arch reconstruction with the frozen elephant trunk technique for acute type a aortic dissection," *Frontiers in Cardiovascular Medicine*, vol. 8, 2021.

[22] D. Ho, A. Squelch, and Z. Sun, "Modelling of aortic aneurysm and aortic dissection through 3D printing," *Journal of Medical Radiation Sciences*, vol. 64, no. 1, pp. 10–17, 2017.

[23] D. Spinelli, S. Marconi, R. Caruso, M. Conti, F. Benedetto, and H. W. De Beaufort, "3D printing of aortic models as a teaching tool for improving understanding of aortic disease," *The Journal of Cardiovascular Surgery*, vol. 60, no. 5, pp. 582–588, 2019.

[24] X. Shi, W. Long, Y. Li, and D. Deng, "Multi-population genetic algorithm with er network for solving flexible job shop scheduling problems," *PLoS One*, vol. 15, no. 5, article e0233759, 2020.

[25] X. R. Li, Y. H. Tong, X. Q. Li, C. J. Liu, C. Liu, and Z. Liu, "Total endovascular repair of an intraoperative stent-graft deployed in the false lumen of Stanford type a aortic dissection: a case report," *World Journal of Clinical Cases*, vol. 8, no. 5, pp. 954–962, 2020.

Hindawi
Computational and Mathematical Methods in Medicine
Volume 2022, Article ID 6428759, 7 pages
https://doi.org/10.1155/2022/6428759

Research Article

On the Effect of Electroacupuncture in Promoting Healing after High Tibial Osteotomy

XiangDong Tian[1], **Xia Li**[1], **LiQun Zhou**[2], **JiPing Zhao**[1], **XiaoMin Li**[3], **Ye Huang**[3] and **TianSong Ding**[3]

[1]*Dongzhimen Hospital, Beijing University of Chinese Medicine, Beijing 100700, China*
[2]*Wudang Medical Institute, Beijing University of Chinese Medicine, Beijing 100029, China*
[3]*The Third Affiliated Hospital, Beijing University of Chinese Medicine, Beijing 100029, China*

Correspondence should be addressed to LiQun Zhou; zhouliqun6080@126.com and JiPing Zhao; zjpbucm@outlook.com

Received 25 December 2021; Revised 15 January 2022; Accepted 7 February 2022; Published 17 March 2022

Academic Editor: Kelvin Wong

Purpose. To explore the clinical effect of electroacupuncture in promoting the healing of the osteotomy area after high tibial osteotomy. *Methods*. 50 patients with knee osteoarthritis who underwent open wedge high tibial osteotomy (OWHTO) were selected and randomly divided into the observation group and control group. The control group got the common postoperative treatment, and the observation group was added electroacupuncture from the 3rd day after the operation on the basis of the control group. The electroacupuncture acupoints were selected SP10, ST34, ST32, EX-LE2, ST40,KI6, KI3, SP6, and ST41, once a day, and 14 days were a course of treatment. And then we contrasted the index of the Lane-Sandhu X-ray score, the skin incision healing time, the swelling subsided time, Visual Analogue Scale (VAS), Western Ontario and McMaster Universities Osteoarthritis Index Score (WOMAC), and Lysholm in different time. *Results*. The Lane-Sandhu X-ray score of the observation group was better than that of the control group at all time points ($P < 0.05$), and the time to achieve bone healing was about 2 weeks earlier than that of the control group. The skin healing and swelling were the subsided time in the osteotomy area. Both were better than the control group, and the difference was statistically significant ($P < 0.05$). The VAS score, WOMAC score, and Lysholm score of the two groups were significantly improved compared with preoperatively, and the difference was statistically significant ($P < 0.05$). The improvement of the observation group's VAS score, WOMAC score, and Lysholm score at 1 week, 4 weeks, and 8 weeks after the end of the treatment course was better than that of the control group, and the difference was statistically significant ($P < 0.05$). *Conclusion*. Electroacupuncture can quicken the healing of bone tissue and surrounding soft tissues in the osteotomy area after high tibial osteotomy, and at the same time, it can help the relief of knee joint pain and improve knee joint function.

1. Introduction

Knee osteoarthritis (KOA) is a common cartilage degenerative disease which causes a high disability rate [1–4]. It usually occurs in the medial compartment, which often forms medial single-compartment knee osteoarthritis (MSCKOA) and leads to knee varus deformity [5, 6]. High tibial osteotomy (HTO) becomes more and more popular to be a treatment methods of medial compartment knee osteoarthritis, which can effectively relieve knee symptoms and improve knee joint function [7, 8]. Open wedge high tibial osteotomy (OWHTO) is the current mainstream osteotomy method, with a wide range of clinical applications [9].

Although the strong internal fixation of the osteotomy area is the guarantee for the success of the operation, the healed time of the osteotomy is also an important factor to finish the treatment of KOA. Nowadays, allograft bone is used to fill the area to speed up the healing of the fracture area. However, is there an effectively methods such as physical treatment to do it well? We used acupuncture to do it.

In traditional Chinese medicine, acupuncture and moxibustion have been studied [10–12] to promote fracture

Table 1: Comparison of general baseline data between the two groups.

Index	Observation group($n = 25$)	Control group($n = 25$)	Statistics	P value
Age ($\bar{x} \pm s$)	64.76 ± 6.07	64.84 ± 8.84	$t = -0.037$	0.970
Gender (male/female)	8/17	6/19	$X^2 = 0.397$	0.529
Affected limb (left/right)	11/14	12/13	$X^2 = 0.081$	0.777
BMI index $\left(\mathrm{kg/m^2}, \bar{x} \pm s\right)$	26.37 ± 3.38	28.92 ± 3.59	$t = -1.475$	0.147

healing to a certain extent. Electroacupuncture has less relevant reports on the effect of promoting the healing of the osteotomy area after high tibial osteotomy.

In the paper, electroacupuncture was used as an intervention treatment after tibial osteotomy to explore the effect of promoting the healing of the osteotomy area after high tibial osteotomy.

2. Methods

2.1. Patients. 50 patients with MSCKOA were treated in the Department of Minimally Invasive Arthritis of The Third Affiliated Hospital of Beijing University of Chinese Medicine from January 2020 to October 2020. The patients were randomly divided into the observation group and observation group using the randomized envelope method, 25 cases in each group. The difference in baseline data between the two groups was not statistically significant ($P > 0.05$).

The inclusion criteria were as follows: (1) patients with MSCKOA, (2) receiving high tibial osteotomy, (3) age 40 to 70 years old, (4) consciously able to cooperate with treatment, and (5) signed informed consent book.

The exclusion criteria were as follows: (1) knee osteoarthritis and destruction of lateral cartilage; (2) combined with knee gouty arthritis, rheumatoid arthritis, and other diseases; (3) combined with severe diabetes, hypertension and severe liver and kidney insufficiency, and other diseases; and (4) combined with chronic wasting diseases such as tuberculosis and tumors as shown by Table 1.

2.2. Treatment Methods

2.2.1. Control Group. Routine rehabilitation program begins after surgery. On the first day after the surgery, the patient underwent an ankle pump exercise. The day after the operation, a knee flexion and extension exercise were performed. The third day after the operation, patient began to walk to the ground with the help of a walker. Two weeks after surgery, the patient walked with the assistance of double crutches. At 8–10 weeks after the surgery, the patient walked autonomously.

2.2.2. Observation Group. On the basis of the treatment of the control group, electroacupuncture treatment was started on the 3rd day after operation. Acupoint selection is as follows: SP10, ST34, ST32, EX-LE2, ST40, KI6, KI3, SP6, and ST41. Acupuncture procedure is to get the patient's cooperation firstly and then mark the right acupuncture points; secondly, next step is to select 0.3×40 mm disposable acupuncture needles and then to puncture the needles that is 90° to the skin, and the depth is about 3 cm. After that, the pulse electroacupuncture device (Indy KWD-808-I Changzhou Indy Electronic Medical Equipment Co., Ltd., Su Xie Zhun 20152261330, Figure 1(a)) is connected with the end of the needles separately (Figure 1(b)), selects the stimulus intensity tolerated by the patient, and routinely retains the needle for 30 minutes, once a day. 14 days are a course of treatment.

2.3. Observation Indicators

2.3.1. Lane-Sandhu X-Ray Scoring. It is used to evaluate the healing of bone tissue in the osteotomy area.

2.3.2. Incision Healing Time and Lower Limb Swelling Time. The incision healing time and lower limb swelling time were used to evaluate the recovery of soft tissue after osteotomy. The lower limb swelling was evaluated by the difference between the circumference of the thigh and the calf and compared with the healthy limb.

2.3.3. VAS. It is used to evaluate knee joint pain, which is from 0 to 10 points. The larger the score, the more painful it is.

2.3.4. WOMAC. It is used to evaluate knee joint function. The higher the score, the worse the knee joint function.

2.3.5. Lysholm Scale. It is used to evaluate knee joint function. The lower the score, the worse the knee joint function.

2.4. Statistical Analysis. Statistical analysis was performed using SPSS22.0, measurement data were expressed as mean ± standard deviation, paired t-test was used for comparison within groups, two independent sample t-test was used for comparison between groups, and rank sum test was used if the data did not conform to the normal distribution. The count data was tested by the χ^2 test, and $P < 0.05$ was statistically significant.

3. Results

Both groups of patients successfully completed the operation without intraoperative complications. Both groups of patients completed the postoperative treatment and were followed up. There was no infection in the two groups after the operation, and no serious adverse reactions occurred after the operation.

The bone healing in the osteotomy area of the observation group was better than that of the control group at all time points ($P < 0.05$), and the time to achieve bone healing

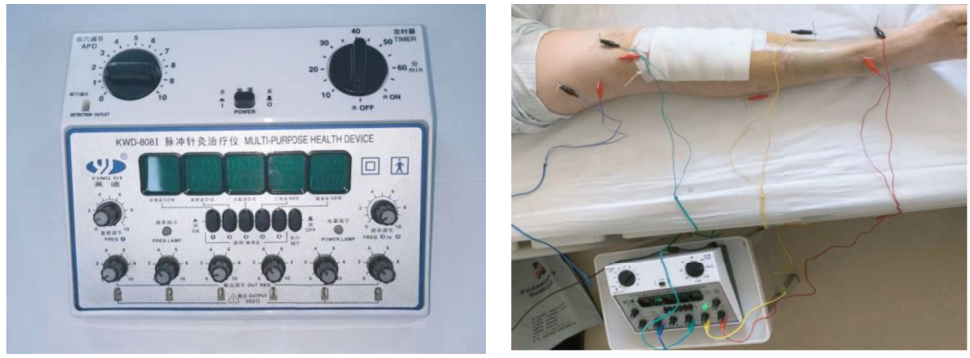

(a) (b)

Figure 1: (a) Electroacupuncture treatment instrument. (b) Schematic diagram of electroacupuncture treatment.

Table 2: Comparison of Lane-Sandhu X-ray scores of fracture healing between the two groups ($\bar{x} \pm s$, points).

Group	Number	4 weeks	8 weeks	10 weeks	12 weeks	14 weeks	F	P
Observation	25	2.08 ± 1.08	5.68 ± 1.38	8.72 ± 1.34	12.00 ± 0.00	12.00 ± 0.00	815.810	<0.001
Control	25	1.08 ± 0.70	3.92 ± 1.22	6.96 ± 1.27	9.16 ± 1.21	11.04 ± 6.76	245.814	<0.001
Z		-3.417	-3.976	-4.014	-6.310	-5.360		
P		0.001	<0.001	<0.001	<0.001	<0.001		

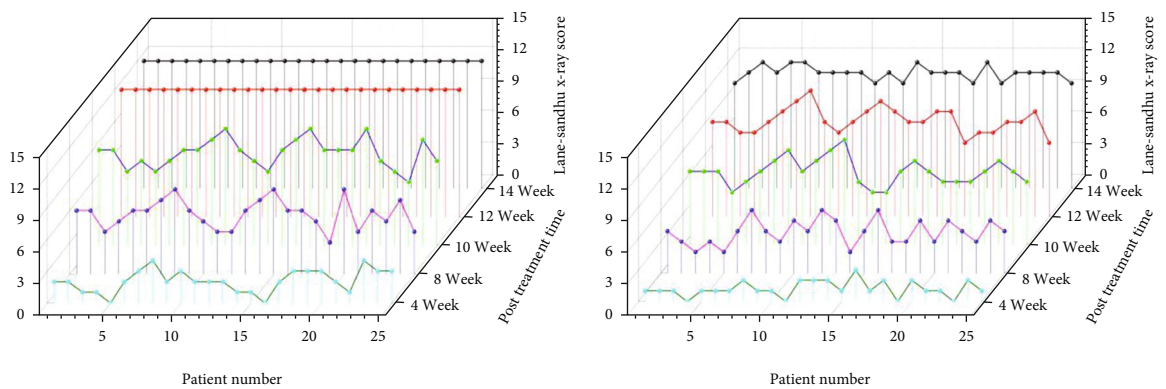

(a) (b)

Figure 2: (a) Results of Lane-Sandhu X-ray score in the observation group. (b) Results of Lane-Sandhu X-ray score in the control group.

was about 2 weeks faster than that of the control group as shown by Table 2 and Figure 2.

The skin healing time of the observation group and the time to reduce swelling were better than those of the control group, and the difference was statistically significant ($P < 0.05$) as shown by Table 3.

At 1 week, 4 weeks, and 8 weeks after the treatment, the VAS score, WOMAC score, and Lysholm score of the observation group and the control group were significantly improved compared with preoperatively, and the difference was statistically significant ($P < 0.05$); the VAS score of the observation group, WOMAC score, and Lysholm score was better than the control group at 1, 4, and 8 weeks after treatment ($P < 0.05$) as shown by Table 4 and Figures 3–5.

Table 3: Comparison of soft tissue healing between the two groups.

Group	Number of cases	Incision healing time	Swelling time
Observation group	25	10.88 ± 1.86	10.24 ± 1.81
Control group	25	13.40 ± 1.87	13.52 ± 2.04
t value		-4.782	-6.008
P value		<0.001	<0.001

4. Discussion

4.1. Healing Time of Fracture by Some Effective Methods. With the continuous advancement of the concept of

Table 4: Comparison of follow-up data between the two groups ($\bar{x} \pm s$, points).

Index	Point in time	Observation group ($n = 25$)	Control group ($n = 25$)	Statistics	P value
VAS	Preoperative	7.92 ± 1.04	7.52 ± 0.87	$z = -1.345$	0.179
	1 week after treatment	2.20 ± 0.96	3.08 ± 0.86	$z = -3.090$	0.002
	4 weeks after treatment	0.80 ± 0.71	1.48 ± 0.77	$z = -2.943$	0.003
	8 weeks after treatment	0.44 ± 0.51	1.04 ± 0.79	$z = -2.771$	0.006
	F value	371.121	436.465		
	P value	<0.001	<0.001		
WOMAC	Preoperative	117.92 ± 18.13	120.40 ± 17.70	$t = -0.489$	0.627
	1 week after treatment	95.15 ± 2.44	99.68 ± 3.66	$t = -5.135$	<0.001
	4 weeks after treatment	80.36 ± 2.29	87.12 ± 2.13	$t = -10.815$	<0.001
	8 weeks after treatment	73.96 ± 4.39	80.36 ± 2.31	$t = -6.450$	<0.001
	F value	184.189	144.782		
	P value	<0.001	<0.001		
Lysholm	Preoperative	48.68 ± 5.18	48.08 ± 4.00	$t = 0.459$	0.649
	1 week after treatment	78.80 ± 2.02	65.00 ± 4.61	$t = 13.709$	<0.001
	4 weeks after treatment	90.88 ± 1.86	83.80 ± 3.16	$t = 9.655$	<0.001
	8 weeks after treatment	92.20 ± 2.04	87.52 ± 2.79	$t = 6.776$	<0.001
	F value	760.937	755.786		
	P value	<0.001	<0.001		

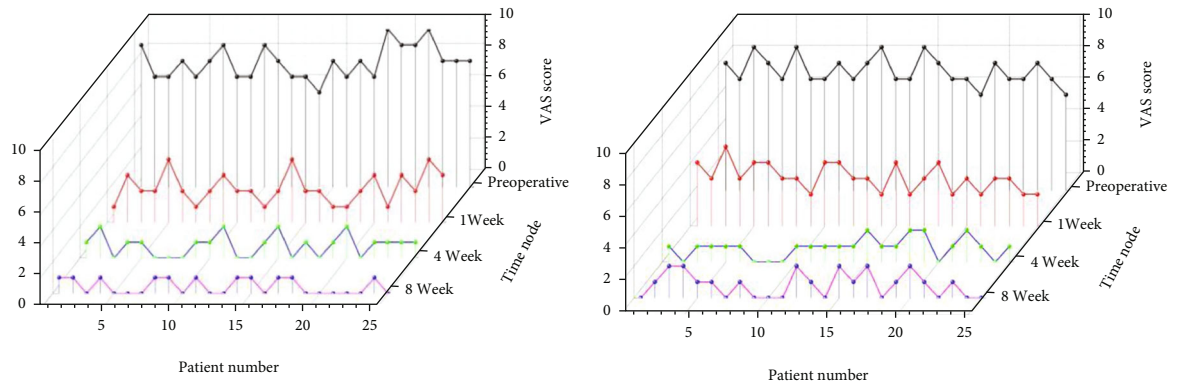

Figure 3: (a) Results of VAS score in the observation group. (b) Results of VAS score in the control group.

enhanced recovery after surgery (ERAS) and the search for comprehensive treatment methods to promote the rapid healing of the osteotomy area, the recovery of knee joint function and relieve pain has attracted more and more attention from clinicians. In order to seek rapid healing of the osteotomy area after THO, we have made efforts to do it.

We used strong internal fixation and bone grafting in the osteotomy area to promote the healing of the osteotomy as other surgeons do. Studies have shown that [13, 14] strong internal fixation materials can promote fracture healing and to make patients to walk as soon as possible, which is conducive to the recovery of lower limb function. Wedge-shaped osteotomy on the medial tibia will lead to a wedge-shaped bone defect area, and the larger the expansion angle, the larger the defect volume, which may increase the risk of nonunion of the osteotomy area. Therefore, it is necessary to perform bone grafting operation [15, 16] to avoid the risk of bone nonunion. However, how to promote the healing of the osteotomy area through other methods is still a big challenge.

4.2. Acupuncture in the Healing Time of Fracture. Acupuncture, as a traditional Chinese medicine therapy, has the functions of dredging the meridians, reconciling qi and blood, and promoting blood circulation [17]. Study [18] has found through animal experiments that acupuncture can improve the blood circulation in the fracture area, thereby promoting fracture healing. Du [19] found through clinical research that acupuncture can promote the deposition of minerals and trace elements at the fracture site and accelerate the

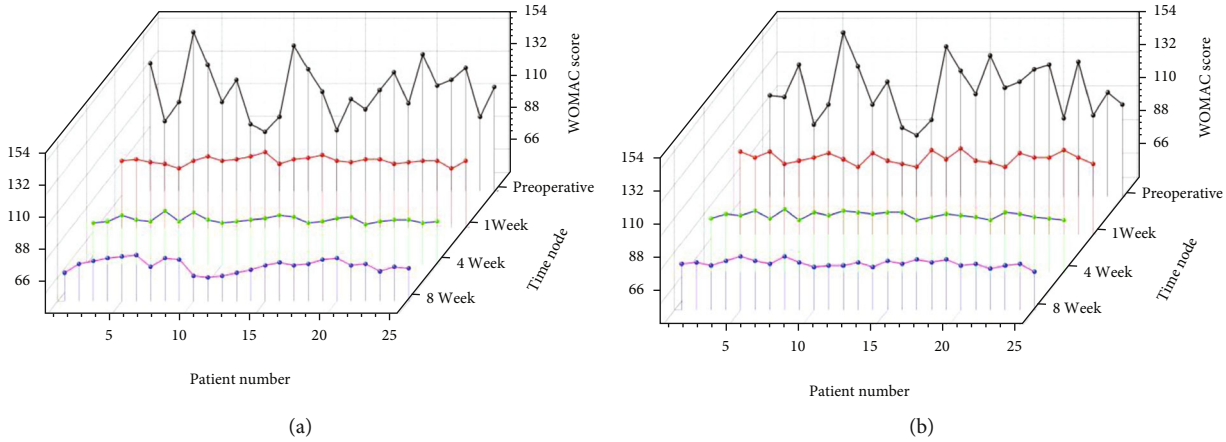

Figure 4: (a) Results of WOMAC score in the observation group. (b) Results of WOMAC score in the control group.

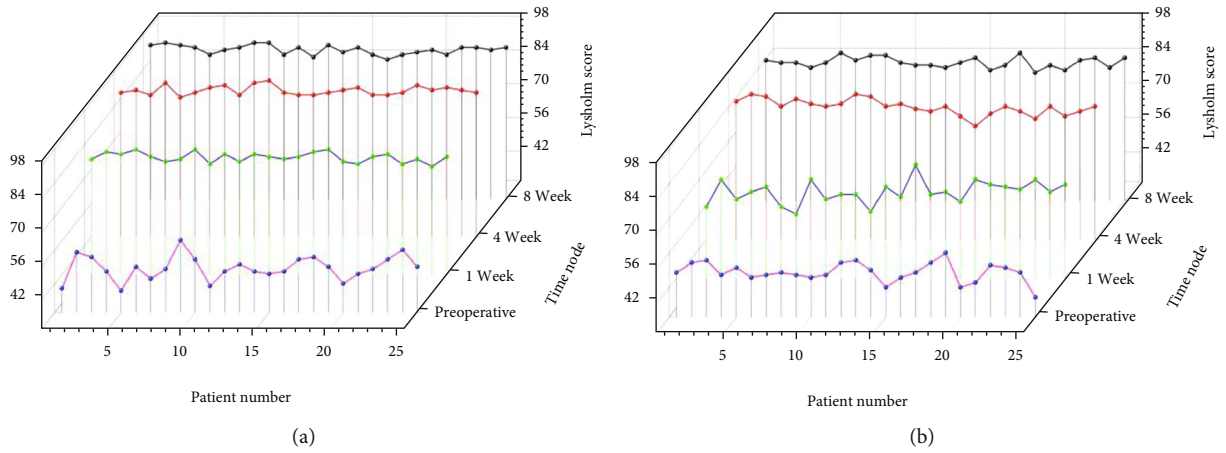

Figure 5: (a) Results of Lysholm score in the observation group. (b) Results of Lysholm score in the control group.

fracture healing process. Studies have also found that [20, 21] acupuncture can speed up fracture healing by regulating human hormone levels. In addition, acupuncture can also promote fracture healing by regulating the process of bone formation and bone destruction, activating the WNT/β-catenin signal pathway protein, and regulating the level of cell growth factors [22].

Electrical stimulation therapy is a type of physical therapy, which has been widely used in clinical practice [23, 24]. Studies have found that [25] electrical stimulation therapy can promote fracture healing by improving circulation and adding bone nutrition. Although the specific mechanism of electrical stimulation to promote fracture healing has not yet been uniformly concluded, relevant basic research and clinical studies have shown that the effect of electrical stimulation on promoting fracture healing is definite [26–28].

Studies have suggested that [29–31] the mechanism of electrical stimulation to promote fracture healing may be that osteoblasts are induced by electrical stimulation to produce a variety of bone growth factors, thereby accelerating fracture healing. Fitzsimmons et al. [32] found in a model study of electrical stimulation of bone tissue that short-term electrical stimulation can promote the secretion of insulin-like growth factor-II (insulin-like growth factor-II, IGF-II) by osteoblasts.

Studies have also found that [33] electrical stimulation can promote the expression of transforming growth factor-β (TGF-β), BMP2, and BMP4 in osteoblasts, thereby accelerating the process of fracture healing. Kuzyk et al. [34] believed that under the action of electrical stimulation, the originally closed microvessels opened, which enriched the local blood supply, stimulated the proliferation and differentiation of bone cells and chondrocytes, promoted the deposition of mineral calcium, and shortened the calcification time, and reduce osteoclast activity and bone resorption, increase the production of bone tissue matrix protein, and strengthen bone tissue [35].

In addition, the normal effect of the electromagnetic field can also speed up the fracture healing process. The bone structure integrity is heavily influenced by the material properties that are dependent on certain characteristics [36, 37]. Predictive control [38] of diagnosis can contribute to the healing effect.

5. Limitation of the Study

This study has its limitations, such as one of the barriers to demonstrating rapid healing of the fracture area in surgical and medical image diagnosis is plate occlusion limiting the evaluation of more points in the fracture area and having an impact on the data.

6. Conclusion

We found that electroacupuncture can significantly promote the healing of bone tissue and surrounding soft tissues in the osteotomy area after HTO, which also can speed up the relief of knee joint pain and improve knee joint function. As a clinically effective and simple and inexpensive treatment method, it is worthy to be clinical promotion.

Data Availability

Data are available on request from the authors due to privacy/ethical restrictions.

Ethical Approval

All human subjects in this study have given their written consent for the participation of our research.

Consent

Signed informed consent for publication was obtained from all authors.

Conflicts of Interest

The authors declare no conflict of interest.

Authors' Contributions

XiangDong Tian and Xia Li contributed equally to the work and should be considered as co-first authors.

Acknowledgments

The authors thank all members of hospitals who contributed to this research. This study was funded by the Third Affiliated Hospital of Beijing University of Chinese Medicine (No. BZYSY-QNJS-2019-JYB-JS-178).

References

[1] E. R. Vina and C. K. Kwoh, "Epidemiology of osteoarthritis: literature update," *Current Opinion in Rheumatology*, vol. 30, no. 2, pp. 160–167, 2018.

[2] D. J. Hunter, D. Schofield, and E. Callander, "The individual and socioeconomic impact of osteoarthritis," *Nature Reviews Rheumatology*, vol. 10, no. 7, pp. 437–441, 2014.

[3] A. E. Weber, I. K. Bolia, and N. A. Trasolini, "Biological strategies for osteoarthritis: from early diagnosis to treatment," *International Orthopaedics*, vol. 45, no. 2, pp. 335–344, 2021.

[4] H. Madry, C. N. van Dijk, and M. Mueller-Gerbl, "The basic science of the subchondral bone," *Knee Surgery, Sports Traumatology, Arthroscopy*, vol. 18, no. 4, pp. 419–433, 2010.

[5] B. T. Hanypsiak and B. S. Shaffer, "Nonoperative treatment of unicompartmental arthritis of the knee," *The Orthopedic Clinics of North America*, vol. 36, no. 4, pp. 401–411, 2005.

[6] H. Hempfling, K. Bohndorf, and F. Roemer, "Akuter, traumatischer versus chronischer knorpelschaden unter gutachterlichen gesichtspunkten," *Zeitschrift für Orthopädie und Unfallchirurgie*, vol. 146, no. 3, pp. 381–391, 2008.

[7] M. B. Santoso and L. Wu, "Unicompartmental knee arthroplasty, is it superior to high tibial osteotomy in treating unicompartmental osteoarthritis? A meta-analysis and systemic review," *Journal of Orthopaedic Surgery and Research*, vol. 12, no. 1, 2017.

[8] M. C. Loia, S. Vanni, F. Rosso et al., "High tibial osteotomy in varus knees: indications and limits," *Joints*, vol. 4, no. 2, pp. 98–110, 2016.

[9] J. Lu, S. Tang, Y. Wang et al., "Clinical outcomes of closing- and opening-wedge high tibial osteotomy for treatment of anteromedial unicompartmental knee osteoarthritis," *The Journal of Knee Surgery*, vol. 32, no. 8, pp. 758–763, 2019.

[10] M. Inoue, M. Nakajima, T. Hojo, M. Itoi, and H. Kitakoji, "The effect of electroacupuncture on osteotomy gap healing in a rat fibula model," *Acupuncture in Medicine*, vol. 31, no. 2, pp. 222–227, 2013.

[11] H. Fan, F. Ji, Y. Lin et al., "Electroacupuncture stimulation at CV4 prevents ovariectomy-induced osteoporosis in rats via Wnt-β-catenin signaling," *Molecular Medicine Reports*, vol. 13, no. 3, pp. 2485–2491, 2016.

[12] Y. Seval, K. Emre, Y. Erhan, K. Ahmet, G. Suleyman, and O. Mustafa, "Effect of acupuncture therapy on fracture healing in rats with femur fractures," *Journal of Traditional Chinese Medicine*, vol. 40, no. 2, pp. 275–283, 2020.

[13] J. D. Agneskirchner, D. Freiling, C. Hurschler, and P. Lobenhoffer, "Primary stability of four different implants for opening wedge high tibial osteotomy," *Knee Surgery, Sports Traumatology, Arthroscopy*, vol. 14, no. 3, pp. 291–300, 2006.

[14] K. Stoffel, G. Booth, S. M. Rohrl, and M. Kuster, "A comparison of conventional versus locking plates in intraarticular calcaneus fractures: a biomechanical study in human cadavers," *Clinical Biomechanics (Bristol, Avon)*, vol. 22, no. 1, pp. 100–105, 2007.

[15] M. P. van den Bekerom, T. W. Patt, M. Y. Kleinhout, H. M. van der Vis, and G. H. Albers, "Early complications after high tibial osteotomy: a comparison of two techniques," *The Journal of Knee Surgery*, vol. 21, no. 1, pp. 68–74, 2008.

[16] K. P. Valkering, M. P. van den Bekerom, F. M. Kappelhoff, and G. H. Albers, "Complications after tomofix medial opening wedge high tibial osteotomy," *The Journal of Knee Surgery*, vol. 22, no. 3, pp. 218–225, 2009.

[17] J. W. Chen, H. J. Wang, and X. F. Zheng, "Research progress on the mechanism of acupuncture and moxibustion in promoting fracture healing," *China Orthopedics and Traumatology*, vol. 33, no. 1, pp. 93–96, 2020.

[18] E. R. Magden, "Spotlight on acupuncture in laboratory animal medicine," *Veterinary Medicine: Research and Reports*, vol. 8, pp. 53–58, 2017.

[19] G. Du, Z. Chen, X. Qi et al., "Effects of acupuncture staging treatment on X-ray callus score and serum calcium, phosphorus and alkaline phosphatase in patients with middle and

lower tibial fractures," *China Journal of Traditional Chinese Medicine Science and Technology*, vol. 20, no. 5, 2013.

[20] O. Donoso, A. M. Pino, G. Seitz, N. Osses, and J. P. Rodríguez, "Osteoporosis-associated alteration in the signalling status of BMP-2 in human MSCs under adipogenic conditions," *Journal of Cellular Biochemistry*, vol. 116, no. 7, pp. 1267–1277, 2015.

[21] M. Shen, X. Qi, Y. Huang, Y. Lü, and W. Cai, "Effects of acupuncture on the pituitary-thyroid axis in rabbits with fracture," *Journal of Traditional Chinese Medicine*, vol. 19, no. 4, pp. 300–303, 1999.

[22] X. Zheng, G. Wu, Y. Nie, and Y. Lin, "Electroacupuncture at the governor vessel and bladder meridian acupoints improves postmenopausal osteoporosis through osteoprotegerin/RANKL/RANK and Wnt/β-catenin signaling pathways," *Experimental and Therapeutic Medicine*, vol. 10, no. 2, pp. 541–548, 2015.

[23] F. C. Atamaz, B. Durmaz, M. Baydar et al., "Comparison of the efficacy of transcutaneous electrical nerve stimulation, interferential currents, and shortwave diathermy in knee osteoarthritis: a double-blind, randomized, controlled, multicenter study," *Archives of Physical Medicine and Rehabilitation*, vol. 93, no. 5, pp. 748–756, 2012.

[24] L. A. Talbot, Z. Solomon, L. Webb, C. Morrell, and E. J. Metter, "Electrical stimulation therapies for active duty military with patellofemoral pain syndrome: a randomized trial," *Military Medicine*, vol. 185, no. 7-8, pp. e963–e971, 2020.

[25] S. Ehnert, K. Falldorf, A. K. Fentz et al., "Primary human osteoblasts with reduced alkaline phosphatase and matrix mineralization baseline capacity are responsive to extremely low frequency pulsed electromagnetic field exposure - Clinical implication possible," *Bone Reports*, vol. 3, pp. 48–56, 2015.

[26] C. T. Brighton, P. Shaman, R. B. Heppenstall, J. L. Esterhai Jr., S. R. Pollack, and Z. B. Friedenberg, "Tibial nonunion treated with direct current, capacitive coupling, or bone graft," *Clinical Orthopaedics and Related Research*, no. 321, pp. 223–234, 1995.

[27] A. Zeighami, F. Alizadeh, and M. Saviz, "Optimal currents for electrical stimulation of bone fracture repair: a computational analysis including variations in frequency, tissue properties, and fracture morphology," *Bioelectromagnetics*, vol. 40, no. 2, pp. 128–135, 2019.

[28] G. Scott and J. B. King, "A prospective, double-blind trial of electrical capacitive coupling in the treatment of non-union of long bones," *The Journal of Bone and Joint Surgery. American Volume*, vol. 76, no. 6, pp. 820–826, 1994.

[29] D. Hannouche, H. Petite, and L. Sedel, "Current trends in the enhancement of fracture healing," *Journal of Bone and Joint Surgery. British Volume (London)*, vol. 83-B, no. 2, pp. 157–164, 2001.

[30] H. Ito and Y. Shirai, "The efficacy of ununited tibial fracture treatment using pulsing electromagnetic fields: relation to biological activity on nonunion bone ends," *Journal of Nippon Medical School*, vol. 68, no. 2, pp. 149–153, 2001.

[31] J. T. Ryaby, "Clinical effects of electromagnetic and electric fields on fracture healing," *Clinical Orthopaedics and Related Research*, vol. 355, pp. S205–S215, 1998.

[32] R. J. Fitzsimmons, J. T. Ryaby, S. Mohan, F. P. Magee, and D. J. Baylink, "Combined magnetic fields increase insulin-like growth factor-II in TE-85 human osteosarcoma bone cell cultures," *Endocrinology*, vol. 136, no. 7, pp. 3100–3106, 1995.

[33] M. Nagai and M. Ota, "Pulsating electromagnetic field stimulates mRNA expression of bone morphogenetic protein-2 and -4," *Journal of Dental Research*, vol. 73, no. 10, pp. 1601–1605, 1994.

[34] P. R. Kuzyk and E. H. Schemitsch, "The science of electrical stimulation therapy for fracture healing," *Indian Journal of Orthopaedics*, vol. 43, no. 2, pp. 127–131, 2009.

[35] Z. Ahmed, "Dipolar cortico-muscular electrical stimulation: a novel method that enhances motor function in both - normal and spinal cord injured mice," *Journal of NeuroEngineering and Rehabilitation*, vol. 7, no. 1, 2010.

[36] X. Xu, C. Zhang, H. A. Derazkola, M. Demiral, A. M. Zain, and A. Khan, "UFSW tool pin profile effects on properties of aluminium-steel joint," *Vacuum*, vol. 192, no. 8, article 110460, 2021.

[37] X. Xu, C. Zhang, F. Musharavat, T. A. Sebaey, and A. Khan, "Dispersion of waves characteristics of laminated composite nanoplate," *Steel and Composite Structures*, vol. 40, no. 3, pp. 355–367, 2021.

[38] Z. H. Tang, Y. Y. Li, X. Y. Chai, H. Y. Zhang, and S. X. Cao, "Adaptive nonlinear model predictive control of NOx emissions under load constraints in power plant boilers," *Journal of Chemical Engineering of Japan*, vol. 53, no. 1, pp. 36–44, 2020.

Hindawi
Computational and Mathematical Methods in Medicine
Volume 2022, Article ID 9592970, 7 pages
https://doi.org/10.1155/2022/9592970

Research Article

Machine Learning-Based MRI LAVA Dynamic Enhanced Scanning for the Diagnosis of Hilar Lesions

Haijin Wang,[1,2] **Song Wang**,[3] **and Lihua Zhou**[1]

[1]*School of Nursing, Anhui Medical University, Hefei, China 230032*
[2]*Department of Hepatobiliary and Pancreatic Surgery, The First Affiliated Hospital of Anhui Medical University, Hefei, China 230022*
[3]*Medical imaging center, The Fourth Affiliated Hospital of Anhui Medical University, Hefei, China 230002*

Correspondence should be addressed to Lihua Zhou; 531879548@qq.com

Received 30 November 2021; Revised 3 January 2022; Accepted 26 January 2022; Published 24 February 2022

Academic Editor: Kelvin Wong

Objective. To explore the value of machine learning-based magnetic resonance imaging (MRI) liver acceleration volume acquisition (LAVA) dynamic enhanced scanning for diagnosing hilar lesions. *Methods*. A total of 90 patients with hilar lesions and 130 patients without hilar lesions who underwent multiphase dynamic enhanced MRI LAVA were retrospectively selected as the study subjects. The 10-fold crossover method was used to establish the data set, 7/10 (154 cases) data were used to establish the training set, and 3/10 (66 cases) data were used to establish the validation set to verify the model. The region of interest was extracted from MRI images using radiomics, and the hilar lesion model was constructed based on a convolutional neural network. *Results*. There were significant differences in respiration and pulse frequency between patients with hilar lesions and without hilar lesions ($P < 0.05$). The subjective scores of the images in the first three phases of dynamic enhanced scanning in the training set were higher than those in the validation set ($P < 0.05$). There was no significant difference between the training and validation set in the last three phases of dynamic enhanced scanning. *Conclusion*. Machine learn-based MRI LAVA dynamic enhanced scanning for diagnosing hilar lesions has high diagnostic efficiency and can be used as an auxiliary diagnostic method.

1. Introduction

Magnetic resonance imaging (MRI) has been widely used in clinical diagnosis because of its safety, no radiation, high soft tissue resolution, multidirectional, and multiparameter [1]. The anatomical structure of the hilar region is complex, and the incidence rate is high. Therefore, MRI has irreplaceable advantages as an essential method to check hilar lesions [2]. Liver acceleration volume acquisition (LAVA), as a new MRI imaging technology with high time resolution, can obtain images at different times. The dynamic enhancement features of lesions can be displayed in more frequent sequences, often used in dynamic enhancement imaging. However, this sequence is greatly influenced by the patients' respiratory movement, which largely determines the quality of MRI [3].

Hilar lesions need to consider the anatomical location, scope, and relationship with peripheral blood vessels of the tumor [4]. Therefore, it is essential to obtain clear and high-quality images of hilar hepatic without artifacts. Radiomics is a noninvasive method for identifying quantitative imaging indicators to predict critical clinical outcomes [5, 6]. This technology combines imaging and machine learning to extract high-throughput quantitative features from clinical images [7]. In recent years, studies have shown that convolutional neural network (CNN) machine learning based on deep learning architecture can automatically perform image classification by providing supervised input-output data [8–11]. However, there are few reports about applying this model in the imaging examination of hilar lesions.

The purpose of this study was to explore the value of machine learning-based MRI LAVA dynamic enhanced

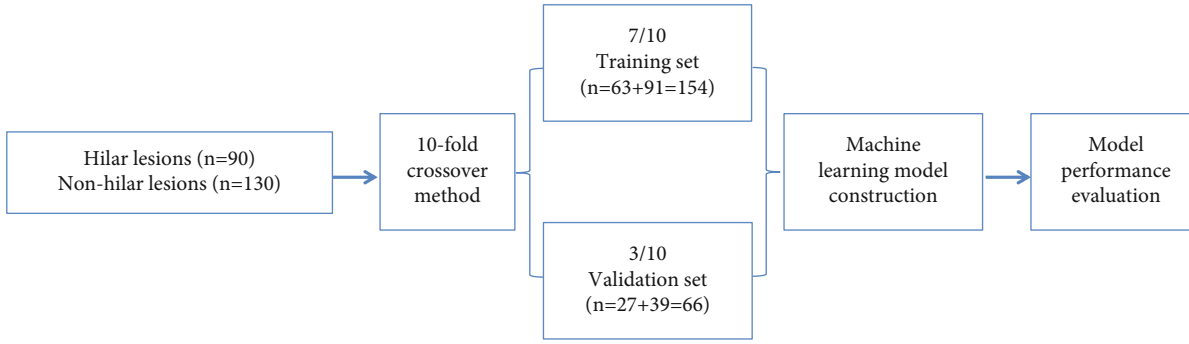

Figure 1: Modeling flow chart.

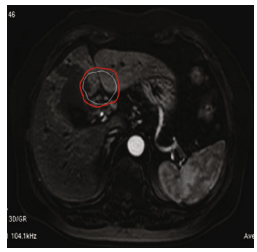

Figure 2: Capture of hilar region of interest for MRI.

scanning for the diagnosis of hilar lesions to provide clinicians with an auxiliary diagnostic method for hilar lesions.

2. Materials and Methods

2.1. General Information. A random sampling method was used to select 90 patients with hilar lesions clinically found from July 2019 to October 2019 who underwent multiphase dynamic enhanced MRI LAVA examination. In addition, 130 patients without hilar lesions who underwent this examination were selected.

Inclusion criteria are as follows: (1) Patients had no contraindications for MRI examination, and all underwent multiphase LAVA dynamic enhanced scanning for the first time. (2) Patients can cooperate with examination, with no mental diseases. (3) Before the examination, all patients were truthfully informed about the content of this study, obtained and signed informed consent.

Exclusion criteria are as follows: (1) patients allergic to contrast agents; (2) patients with underlying severe diseases; (3) patients with vague mental consciousness and lack of cognitive ability; and (4) patients having a cardiac pacemaker or metal implant.

A 10-fold crossover method was used to establish a data set for all 220 patients. 7/10 data ($n = 154$ cases) established a training set, including 82 males and 72 females, aged 19-81 years, with an average of (51.5 ± 14.9) years. A validation set was established in 3/10 data ($n = 66$ cases), including 36 males and 30 females, aged 18-81 years, with an average of (52.0 ± 16.6) years. Then, the machine learning model was constructed, and its performance was evaluated. The modeling flow chart is shown in Figure 1.

2.2. Scanning Method. The images were obtained in the GE Signa HDx 3.0 T MRI system, body phased-array surface coil. The scanning sequence included axial T1WI, axial iso phase inversion, coronal T2WI, axial fat compression T2WI, DWI ($b = 800$ s/mm^2), magnetic resonance cholangiography (MRCP), and LAVA multiphase dynamic enhancement sequence. The scanning process is as follows: After plain scanning, 0.1 mmol/kg (gadolinium spray meglumine, GD-DTPA) was injected through the cubital vein mass at a flow rate of 2.0 mL/s, followed by injection of 20 mL normal saline, and dynamic scanning was performed in six phases (phase A1-A6). 10 s after the contrast agent injection, the patients were instructed to hold their breath for about 15-20 s for stage A1 scan. After each scan, patients were instructed to take a deep breath, followed by stage a2-a5 scan at 55, 90, 120, 180, 240, and 360 s. The holding time for each phase was 15-20 s.

2.3. MRI Interception. After preprocessing the experimental images, the image was segmented into regions of interest (ROI). The tumor was separated from other tissues by a circle corresponding to the size of the hilar tumor to calibrate the tumor region. The ROI images were collected using radiomics (Figure 2).

2.4. Data Collection. Typical CNN consists of a convolution layer and pooling layer. The basic structure of the convolutional neural network is shown in Figure 3. The convolution layer can directly conduct convolution operations with two-dimensional data, read images, and identify their features. As the core of CNN, the convolution layer is used to extract the features of input data. The convolution layer extracts local information from the data sampled regularly, and each convolution layer is composed of multiple filters. After the convolution, an activation graph describing the existing degree of features in the data is generated [12]. In general, the output of the JTH filter in the one-dimensional convolution layer is

$$x_j^l = \mathrm{ReLU}\left(\sum_{i \in D} x_i^{l-1} * w_{ij}^l + b_j^l\right) \quad (1)$$

In machine learning, regularization is used to train set observations to prevent overfitting. For the cost function $J($

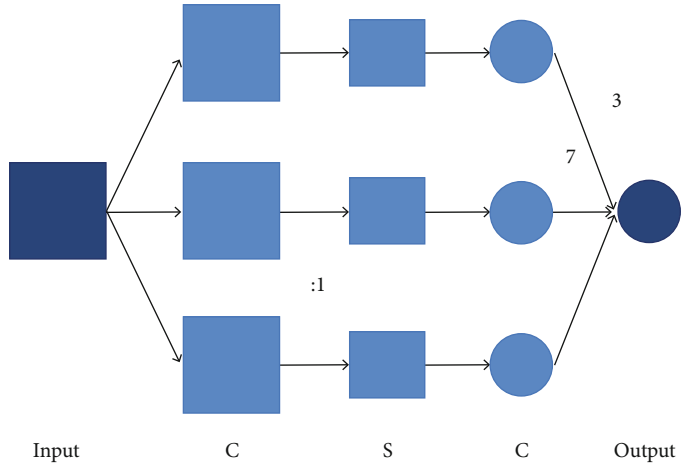

Figure 3: Schematic diagram of convolutional neural network.

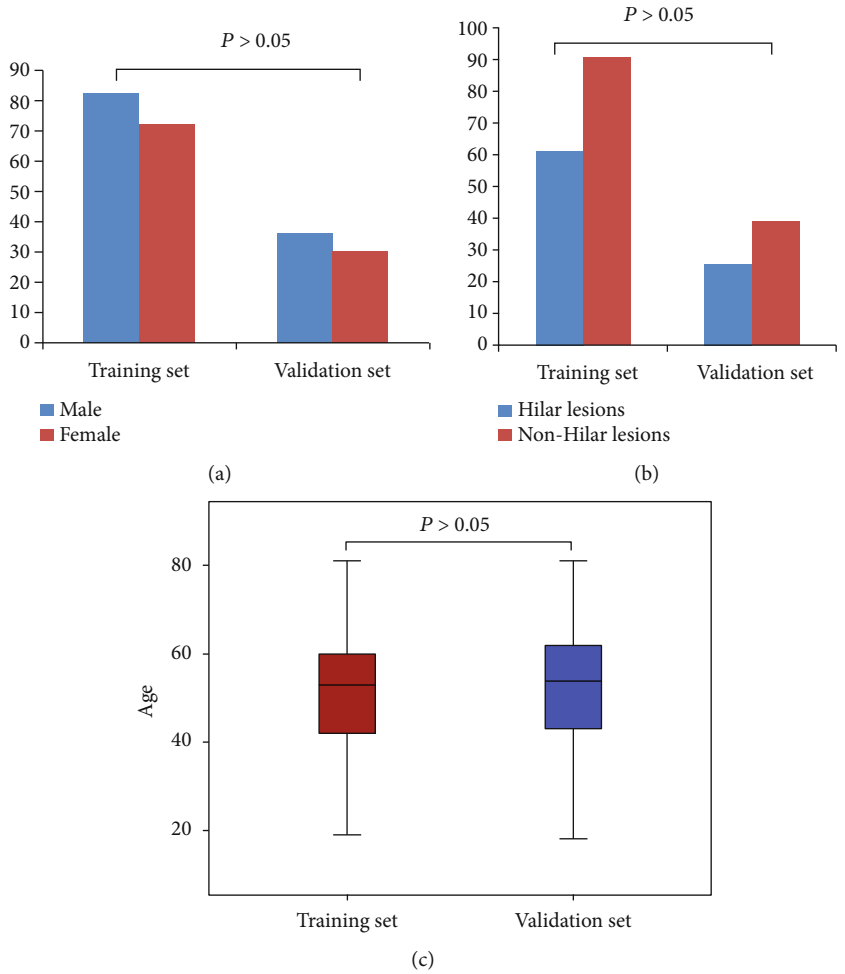

Figure 4: General data comparison of patients in training and test sets. There were no significant differences in gender (a), proportion of hilar lesions (b), and age (c) between the training set and the validation set ($P > 0.05$).

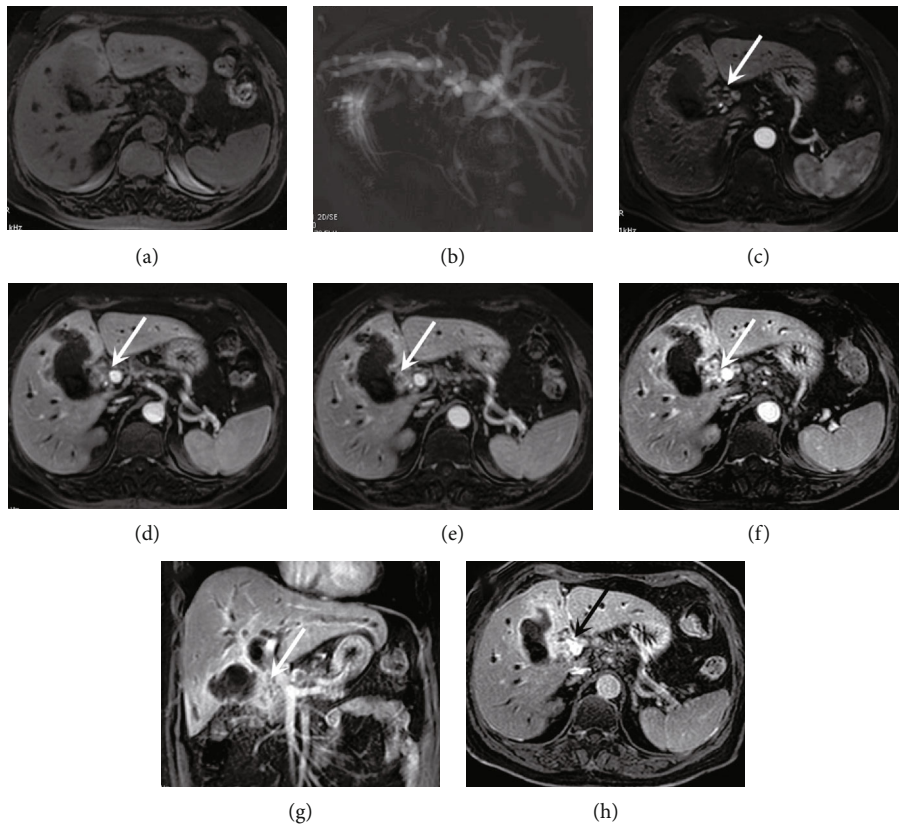

Figure 5: MRI LAVA dynamic enhanced scanning showed clear hilar features. A 72-year-old female patient presented with hilar infiltrating cholangiocarcinoma. The patient had good breath-holding coordination, clear images at all stages, and no noticeable respiratory artifacts. Plain scan showed irregular thickening of the bile duct wall (a), MRCP image showed significant dilation of the intrahepatic bile duct (b), and images of LAVA dynamic enhancement showed irregular thickening of the hilar bile duct wall with "progressive enhancement" (c–h, arrow).

Table 1: The respiratory and pulse scores of patients with hilar lesions in two set.

Group	n	Respiration (times/min)	Pulse (times/min)
Training set	63	18.56 ± 1.37	76.89 ± 6.12
Verification set	27	19.53 ± 1.59	81.42 ± 6.95
t value		2.932	3.089
P value		0.004	0.003

$\theta;\quad X, y)$, with grid parameter θ, the function corresponding to the J-th layer of the training set is

$$\widehat{J}(\theta; x, y) = J(\theta; x, y) + \lambda_1 \|w\|_1 + \|w\|_2. \quad (2)$$

2.5. Evaluation Index. The image quality of the training set and validation set was graded by two attending physicians. The dynamic enhanced scan's six-phase images (phases A1-A6) were evaluated separately as follows: 1 point: the image was clear and without any motion artifact; 2 points: the image is clear, with a few motion artifacts; 3 points: there are certain motion artifacts, the image is still clear, the lesions can be displayed, and their enhancement features are not affected; 4 points: the motion artifact was obvious, the image was not clear, and the lesion could be displayed to a certain extent, but it had a great influence on the diagnosis; 5 points: the motion artifact was significant, the image was not clear, and could not be used for diagnosis.

2.6. Statistical Analysis. SPSS 20.0 statistical software was used to analyze and process relevant data. Independent sample t-test was used for measurement data comparison, and an independent sample nonparametric statistical Mann–Whitney rank-sum test was used for image scoring. $P < 0.05$ was considered statistically significant.

3. Results

3.1. General Conditions. There were no significant differences between the training set and the validation set in gender, age, and proportion of hilar lesions ($P > 0.05$), as shown in Figure 4. There were significant differences in respiration and pulse frequency between these two sets ($P < 0.05$, Table 1).

3.2. Image Quality Score. Patients with good breath-holding coordination during dynamic enhanced scan showed clear, dynamic enhancement characteristics of hilar lesions and liver parenchyma, which could meet the diagnostic requirements (Figure 5). For patients with poor breath-holding coordination, the image artifacts were heavier or even

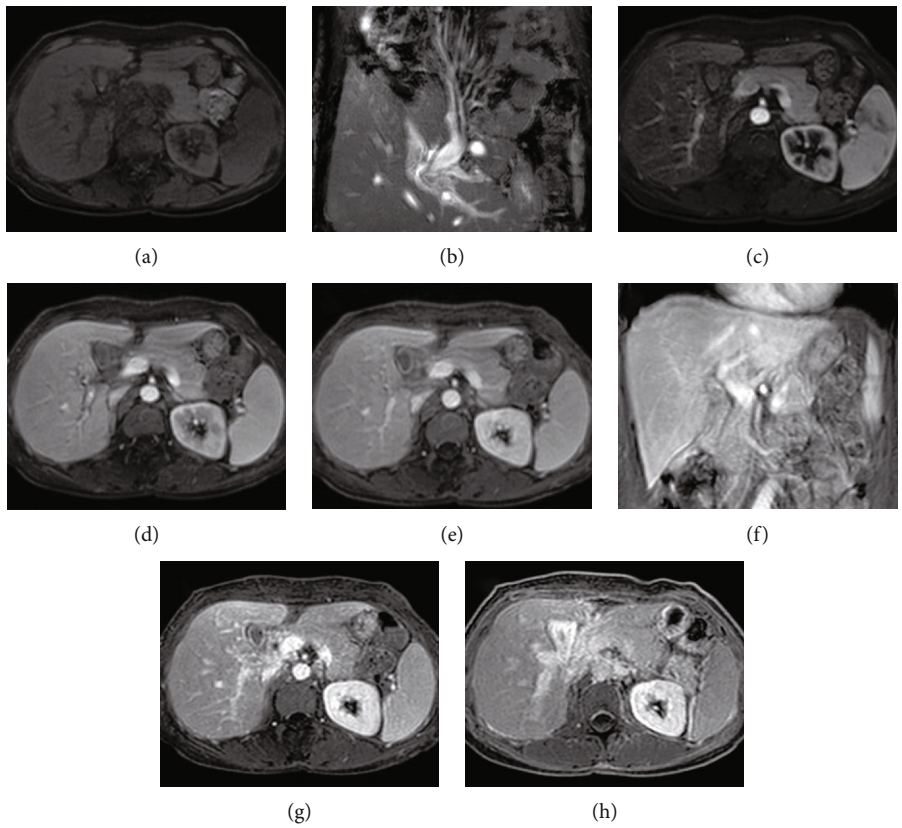

Figure 6: MRI LAVA dynamic enhanced scanning showed unclear hilar features. A 53-year-old female patient with hilar cholangitis had poor breath-holding coordination, and some phase images were not clearly displayed due to the presence of respiratory artifacts. Scan and T2WI coronary (a and b), no obvious abnormal changes; LAVA dynamic enhanced early periods image quality display fair, no obvious respiratory motion artifact (c–h); hepatic portal vein in the bile duct wall thickening of mild change, late to enhance image has the obvious respiratory motion artifact, hepatic portal vein display is not clear, cannot be used for diagnosis.

completely deformed, which could not meet the diagnostic needs (Figure 6). The image data in the training set were integrated into the CNN model to obtain the scoring results of important features (Table 2). The number of image cases with 1 score and the image quality in first three stages (A1-A3) was statistically significant ($P < 0.05$). The number of image cases and the image quality in last three stages (A4-A6) were not statistically significant ($P > 0.05$).

Table 2: Image quality score of patients with hilar lesions in two sets.

Phase	Training set ($n = 63$)					Verification set ($n = 27$)					P value
	1	2	3	4	5	1	2	3	4	5	
A1	61	2	0	0	0	18	8	1	0	0	<0.001
A2	58	5	0	0	0	20	5	2	0	0	0.026
A3	60	3	0	0	0	19	7	1	0	0	0.004
A4	40	22	1	0	0	17	7	2	0	1	0.193
A5	37	19	5	0	2	18	5	2	0	2	0.588
A6	32	20	7	1	3	12	9	2	2	2	0.629

4. Discussion

Hilar lesions are a widespread disease, especially cholangiocarcinoma [13]. At present, dynamic enhanced sequence MRI LAVA is the best imaging method for diagnosing and differential hilar lesions [14]. By obtaining dynamic enhanced multiphase images, more accurate information about blood perfusion of hilar lesions can be provided. Since most patients have different degrees of anxiety, anxiety inferiority complex, and other corresponding negative emotions, a 3.0 T MRI abdominal scan is performed in a dark and closed environment. In addition, patients must be coordinated with regular breath and breath-holding during the dynamic enhanced scan, and the whole examination process takes a long time and is difficult to coordinate. These negative emotions will affect the coordination degree of patients' examination and the accuracy of scanning site structure image and lead to various uncomfortable symptoms such as dizziness, palpitation, and nausea. Eventually, the diagnosis and treatment effect is not good [15]. Therefore, there is still a specific risk of misdiagnosis in the traditional diagnostic methods.

Radiomics based on machine learning can build models according to the information provided by the training sets and then predict the input sample information. In recent years, radiomics has been widely used in diagnosing brain dysfunction and lung cancer by MRI [16, 17]. Combining radiomics with disease imaging can mine the underlying

information of related images, which can be applied to individual diagnosis and prognosis assessment [18]. This study showed that the respiratory and pulse scores of patients in the training group with hilar lesions were lower than those in the without hilar lesions group ($P < 0.05$), which indicates that the machine learning model has better prediction reliability and is effective in improving diagnostic efficiency. Our results are similar to previous studies [19]. Liu et al. assisted in the preoperative classification of HCC based on MRI radiomics. They found that the radiomics model based on unsupervised learning descent mode had a good predictive performance in the identification of pathological classification [20]. Zhang et al. established a model based on machine learning to intercept the region of interest of primary liver cancer tumors in CT images. Their results showed that the features of high-throughput images could be effectively extracted, and the prediction model had good identification efficiency in different pathological types [21].

As one of the essential factors for the success of MRI LAVA dynamic enhancement, respiratory coordination determines the length of examination to a certain extent and determines the quality of diagnostic images [22]. However, in a convolutional neural network based on deep learning architecture, many high-dimensional and quantitative image features are extracted from MRI images at high throughput for analysis [23, 24]. The results show that the image quality of the training set is better than that of the verification set in the first three phases (A1-A3 phase), which indicates that the model can effectively extract practical features, verify the validity of the model, and improve the image quality. The image quality of the last three phases (A4-A6) did not improve. The possible reasons are analyzed as follows: (1) Due to the experimental scanning method of end-expiratory breath-holding, patients are more prone to involuntary movement in the late stage of breath-holding with the extension of breath-holding time. In addition, the total time of the six dynamic scans was longer than that of the available scans, which would significantly increase the possibility of motion artifacts in the later stage of breath-holding. (2) The imaging time of each phase of the LAVA dynamic enhancement scan sequence is shorter, so the influence of patients' respiratory movement on the LAVA dynamic enhancement sequence is more significant than that of the conventional sequence. In general, machine learning-based MRI LAVA dynamic enhanced scanning has good predictive efficacy in MRI diagnosis of hilar lesions.

There are some limitations to our study. Machine learning needs to extract feature parameters from images during classification and recognition and then carry out targeted analysis, which may miss some critical information and reduce the model's accuracy [25, 26]. In addition, the sample of this study was a single-center retrospective study, which needs further verification in the prospective study of a large multicenter sample.

5. Conclusion

In conclusion, machine learning-based MRI LAVA dynamic enhanced scanning in this study has stable and reliable results of LAVA dynamic enhancement examination for patients with hilar lesions. The imaging quality has been improved, providing an auxiliary means for clinicians to diagnose.

Data Availability

The data used to support the findings of this study are available from the corresponding author upon request.

Conflicts of Interest

All authors declare no conflicts of interest in this paper.

Acknowledgments

The study was supported by the National Natural Science Foundation of China (No. 81571308) and scientific research fund of Anhui Medical University (No. 2020xkj046).

References

[1] Y. Anzai, S. Minoshima, and V. S. Lee, "Enhancing value of MRI: a call for action," *Journal of Magnetic Resonance Imaging*, vol. 49, no. 7, pp. e40–e48, 2019.

[2] T. Yousaf, G. Dervenoulas, and M. Politis, "Advances in MRI methodology," *International Review of Neurobiology*, vol. 141, no. 1, pp. 31–76, 2018.

[3] L. Lu, K. Xu, C. Han et al., "Comparison of 3.0T MRI with 3D LAVA sequence and digital subtraction angiography for the assessment of accessory hepatic veins in Budd-Chiari syndrome," *Journal of Magnetic Resonance Imaging*, vol. 45, no. 2, pp. 401–409, 2017.

[4] A. F. Correa, H. Yankey, T. Li et al., "Renal hilar lesions: biological implications for complex partial nephrectomy," *Urology*, vol. 123, no. 1, pp. 174–180, 2019.

[5] R. J. Gillies, P. E. Kinahan, and H. Hricak, "Radiomics: images are more than pictures, they are data," *Radiology*, vol. 278, no. 2, pp. 563–577, 2016.

[6] S. Rizzo, F. Botta, S. Raimondi et al., "Radiomics: the facts and the challenges of image analysis," *European Radiology Experimental*, vol. 2, no. 1, p. 36, 2018.

[7] P. Lambin, R. T. H. Leijenaar, T. M. Deist et al., "Radiomics: the bridge between medical imaging and personalized medicine," *Nature Reviews. Clinical Oncology*, vol. 14, no. 12, pp. 749–762, 2017.

[8] F. Lu, F. Wu, P. Hu, Z. Peng, and D. Kong, "Automatic 3d liver location and segmentation via convolutional neural network and graph cut," *International Journal of Computer Assisted Radiology and Surgery*, vol. 12, no. 2, pp. 171–182, 2017.

[9] A. Zaitcev, M. R. Eissa, Z. Hui, T. Good, J. Elliott, and M. Benaissa, "A deep neural network application for improved prediction of HbA_{1c} in type 1 diabetes," *IEEE Journal of Biomedical and Health Informatics*, vol. 24, no. 10, pp. 2932–2941, 2020.

[10] B. Hu, C. Zhou, H. Wang, and S. Chen, "Onlinear tribodynamic model and experimental verification of a spur gear drive under loss-of-lubrication condition," *Mechanical Systems and Signal Processing*, vol. 153, article 107509, 2021.

[11] Z. Tang, Y. Li, X. Chai, H. Zhang, and S. Cao, "Adaptive nonlinear model predictive control of nox emissions under load constraints in power plant boilers," *Journal of Chemical Engineering of Japan*, vol. 53, no. 1, pp. 36–44, 2020.

[12] P. Sodmann, M. Vollmer, N. Nath, and L. Kaderali, "A convolutional neural network for ecg annotation as the basis for classification of cardiac rhythms," *Physiological Measurement*, vol. 39, no. 10, article 104005, 2018.

[13] S. Rizvi, S. A. Khan, C. L. Hallemeier, R. K. Kelley, and G. J. Gores, "Cholangiocarcinoma – evolving concepts and therapeutic strategies," *Nature Reviews. Clinical Oncology*, vol. 15, no. 2, pp. 95–111, 2018.

[14] R. Okamoto, O. Miyazaki, H. Aoki et al., "Mediastinal and hilar soft tissue mass-like lesions in congenital unilateral pulmonary vein atresia: a retrospective review of seven pediatric patients," *Pediatrics International*, vol. 62, no. 11, pp. 1234–1240, 2020.

[15] A. Orlacchio, F. Chegai, S. Fabiano et al., "Role of mri with hepatospecific contrast agent in the identification and characterization of focal liver lesions: pathological correlation in explanted livers," *La Radiologia Medica*, vol. 121, no. 7, pp. 588–596, 2016.

[16] C. Lai, Y. Chen, T. Wang et al., "A machine learning approach for magnetic resonance image–based mouse brain modeling and fast computation in controlled cortical impact," *Medical & Biological Engineering & Computing*, vol. 58, no. 11, pp. 2835–2844, 2020.

[17] L. Huang, Y. Rong, X. Tang, K. Yi, J. Wu, and F. Wang, "Circular RNAs are promising biomarkers in liquid biopsy for the diagnosis of non-small cell lung cancer," *Frontiers in Molecular Biosciences*, vol. 8, no. 1, article 625722, 2021.

[18] L. Balyen and T. Peto, "Promising artificial intelligence-machine learning-deep learning algorithms in ophthalmology," *The Asia-Pacific Journal of Ophthalmology*, vol. 8, no. 3, pp. 264–272, 2019.

[19] W. Cao, F. Li, J. Gong et al., "Liver acquisition with acceleration volume acquisition gadolinium-enhanced magnetic resonance combined with T2 sequences in the diagnosis of local recurrence of rectal cancer," *Journal of X-Ray Science and Technology*, vol. 24, no. 6, pp. 855–863, 2016.

[20] X. Liu, F. Khalvati, K. Namdar et al., "Can machine learning radiomics provide pre-operative differentiation of combined hepatocellular cholangiocarcinoma from hepatocellular carcinoma and cholangiocarcinoma to inform optimal treatment planning?," *European Radiology*, vol. 31, no. 1, pp. 244–255, 2021.

[21] J. Zhang, Z. Huang, L. Cao et al., "Differentiation combined hepatocellular and cholangiocarcinoma from intrahepatic cholangiocarcinoma based on radiomics machine learning," *Annals of Translational Medicine*, vol. 8, no. 4, p. 119, 2020.

[22] K. I. Ringe, C. von Falck, H. J. Raatschen, F. Wacker, and J. Hinrichs, "Evaluation of transient respiratory motion artifact at gadoxetate disodium-enhancedMRI-influence of different contrast agent application protocols," *PLoS One*, vol. 13, no. 7, article e0200887, 2018.

[23] V. Renganathan, "Overview of artificial neural network models in the biomedical domain," *Bratislavské Lekárske Listy*, vol. 120, no. 7, pp. 536–540, 2019.

[24] S. M. Anwar, M. Majid, A. Qayyum, M. Awais, M. Alnowami, and M. K. Khan, "Medical image analysis using convolutional neural networks: a review," *Journal of Medical Systems*, vol. 42, no. 11, p. 226, 2018.

[25] M. Bagherian, E. Sabeti, K. Wang, M. A. Sartor, Z. Nikolovska-Coleska, and K. Najarian, "Machine learning approaches and databases for prediction of drug-target interaction: a survey paper," *Briefings in Bioinformatics*, vol. 22, no. 1, pp. 247–269, 2021.

[26] A. K. Triantafyllidis and A. Tsanas, "Applications of machine learning in real-life digital health interventions: review of the literature," *Journal of Medical Internet Research*, vol. 21, no. 4, article e12286, 2019.

Hindawi
Computational and Mathematical Methods in Medicine
Volume 2022, Article ID 7156598, 7 pages
https://doi.org/10.1155/2022/7156598

Research Article

3D-Slicer Software-Assisted Neuroendoscopic Surgery in the Treatment of Hypertensive Cerebral Hemorrhage

Rongfang Liao, Longmao Liu, Bo Song, Xinhong Wan, Shuo Wang, and Jianhong Xu

The Second People's Hospital of Jingdezhen City, Jiangxi Province 333000, China

Correspondence should be addressed to Rongfang Liao; 53628377@qq.com

Received 13 December 2021; Revised 23 January 2022; Accepted 31 January 2022; Published 18 February 2022

Academic Editor: Kelvin Wong

Objective. To explore the 3D-slicer software-assisted endoscopic treatment for patients with hypertensive cerebral hemorrhage. *Methods*. A total of 120 patients with hypertensive cerebral hemorrhage were selected and randomly divided into control group and 3D-slicer group with 60 cases each. Patients in the control group underwent traditional imaging positioning craniotomy, and patients in the 3D-slicer group underwent 3D-slicer followed by precision puncture treatment. In this paper, we evaluate the hematoma clearance rate, nerve function, ability of daily living, complication rate, and prognosis. *Results*. The 3D-slicer group is better than the control group in various indicators. Compared with the control group, the 3D-slicer group has lower complications, slightly higher hematoma clearance rate, and better recovery of nerve function and daily living ability before and after surgery. The incidence of poor prognosis is low. *Conclusion*. The 3D-slicer software-assisted endoscopic treatment for patients with hypertensive intracerebral hemorrhage has a better hematoma clearance effect, which is beneficial to the patient's early recovery and reduces the damage to the brain nerve of the patient.

1. Introduction

Hypertensive intracerebral hemorrhage [1–4] is the most serious complication in the development of hypertensive disease. It has a high disability rate and fatality rate. This disease is very common in neurosurgery and has a great impact on the patient's quality of life and ability of daily living [5–7]. Relevant data point out that the incidence of men is higher than that of women and the patients are in poor mood.

Nowadays, the population is seriously aging, and the number of patients with hypertensive cerebral hemorrhage is gradually increasing. Surgical treatment is often used. In the past, the operation was a craniotomy, which was not effective. It is prone to infection and rebleeding after the operation. With the improvement of medical technology, the 3D-slicer software [8–11] is gradually improved and has a higher clinical application rate. Compared with craniotomy, the use of 3D-slicer software to assist endoscopic treatment has the characteristics of simple operation and high safety [12–15].

At present, domestic neuroendoscopic surgery for hypertensive cerebral hemorrhage mostly uses traditional body surface projection method to locate, but it is often difficult to accurately grasp the width and depth of the hematoma, which affects the effect of the operation. The 3D-slicer is an open source software that has attracted much attention in surgical auxiliary applications in recent years [16]. The software can perform three-dimensional reconstruction of hematoma before surgery, calculate the volume of hematoma, and design surgery through virtual reality and augmented reality technology. The puncture path plays a better auxiliary positioning value.

With the continuous development of imaging examination technology and surgical technology, clinically based on the clinical characteristics of the patient, head computed tomography (CT) [17–19] is used to check the location, size, degree of edema of the surrounding brain tissue, and whether there is cerebral edema. We rely on the results of the examination to remove the hematoma from the patient [20]. In this study, the effect of precision puncture treatment of hypertensive cerebral hemorrhage with 3D-slicer software was analyzed in order to improve the prognosis of patients and improve the treatment effect.

2. Methods and Materials

2.1. Structure of This Study. The overall structure of this study is shown in Figure 1. A controlled experiment is used to verify the efficacy of the 3D-slicer software in assisting neuroendoscopic surgery in the treatment of hypertensive cerebral hemorrhage.

2.2. Sample Data. The study period was from October 2017 to July 2020. 120 patients with hypertensive cerebral hemorrhage who came to our hospital were selected and randomly divided into control group and 3D-slicer group with 60 cases in accordance with the random number table method.

The ratio of men to women in the control group and the 3D-slicer group and the location of cerebral hemorrhage are shown in Figure 2. There was no statistically significant difference between the two groups of patients in general data such as gender, age, and bleeding site ($P > 0.05$). The age distribution and average age are shown in Table 1.

2.3. Selection Criteria. The inclusion criteria were as follows: ① all were diagnosed by head CT; ② none of them could undergo craniotomy; and ③ all met the indications for puncture and drainage surgery.

The exclusion criteria were ① patients with cerebral herniation; ② patients with severe coma and unconsciousness; ③ patients with cerebral hemorrhage caused by other diseases; and ④ patients with unstable vital signs.

2.4. Study Population

2.4.1. Control Group. In neural endoscopic surgery for hypertensive cerebral hemorrhage using conventional chord-to-body surface positioning, select the largest slice of hematoma, measure the linear distance from the puncture point to the anterior or posterior midpoint, that is, the chord distance, and convert it to the cranial body surface. In this research, we are to determine the puncture point. During the operation, the puncture is perpendicular to the center of the false hematoma projection, and the puncture is withdrawn after reaching the estimated depth. Through the transparent working sheath, the endoscope is introduced to remove the hematoma.

2.4.2. 3D-Slicer Group. In order to evaluate the method of the 3D-slicer technique, we deliberately simplified the method to the flowchart shown in Figure 3. We specifically introduce the subsequent puncture treatment. After routine anesthesia, a disposable cranial cone with a diameter of 4 mm is used to penetrate the scalp tissue, skull, and dura of the patient, and a soft channel drainage tube with a needle core is inserted according to the set puncture route. After reaching the ideal depth, remove the needle core, and you can see the dark red blood flowing out. Finally, we aspirate the hematoma with a needle tube, suture and fix the drainage tube, and connect a sterile drainage bag.

2.5. Evaluation Index

2.5.1. Hematoma Clearance Rate. The operation time, intraoperative blood loss, hospitalization time, and hematoma clearance rate were calculated for the two groups of patients. Head CT was used to calculate the hematoma clearance rate. The calculation method is as shown in Equation (1).

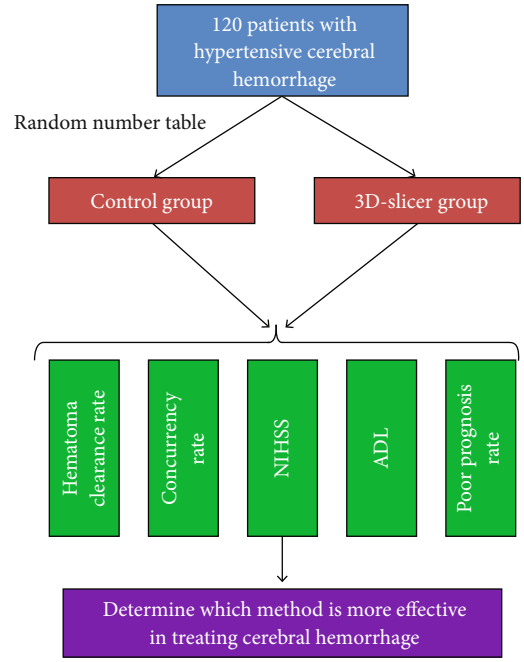

Figure 1: The overall structure of the full text.

$$H = \frac{P - V_3}{P} \times 100\% \quad (1)$$

In Equation (1), H represents the hematoma clearance rate, P represents the hematoma volume before operation, and V represents the hematoma volume 3 days after operation.

2.5.2. Complications. In this paper, we mainly observe and count the occurrence of postoperative infection, rebleeding, cerebral infarction, and stress ulcer and calculate the incidence of complications. The calculation method is shown in Equation (2).

$$C = \frac{I + R + CR + SC}{T} \times 100\% \quad (2)$$

In Equation (2), C represents the complications, I represent the infection, R represents the rebleeding, CR represents the cerebral infarction, SC represents the stress ulcer, and T represents the total number of cases.

2.5.3. Neurological Function Evaluation. The National Institutes of Health Stroke Scale (NIHSS) [21, 22] was used to evaluate the neurological function of patients before and 3 and 6 months after the operation. The total score was 42 points. The higher the score represents the more severe the neurological deficit.

2.5.4. Evaluation of Daily Living Ability. The ability of daily living (ADL) [23, 24] was used to evaluate the ability of daily

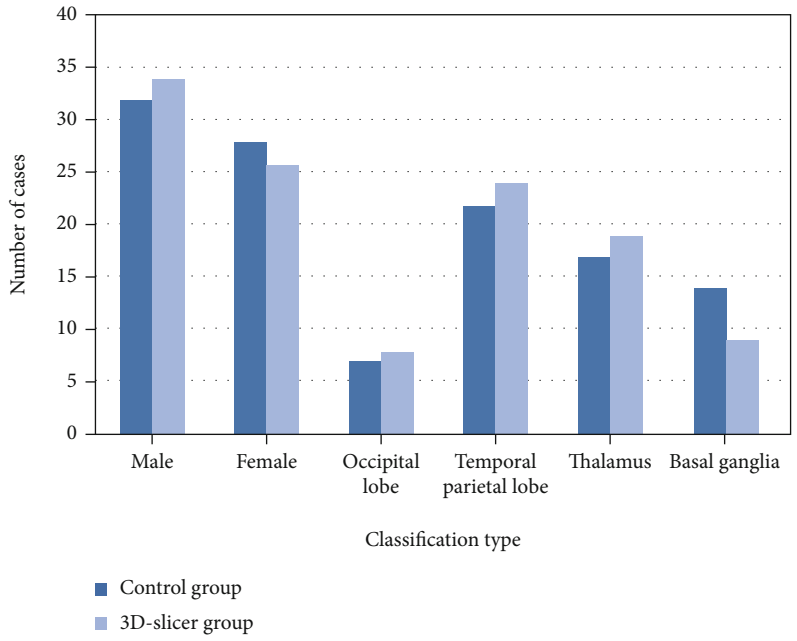

Figure 2: The distribution of men and women in the two groups and the location of cerebral hemorrhage.

Table 1: Age distribution and average age.

Group	Age range	Average age
Control group	43-82	61.2 ± 1.7
3D-slicer group	45-83	62.1 ± 1.2

living of the two groups of patients before and after 3 and 6 months. The total score was 100 points. The higher the score represents the stronger the ability of daily living.

2.5.5. Poor Prognosis. The two groups were followed up for 3 months to compare the poor prognosis of the two groups, and the Glasgow Outcome Scale (GOS) [25, 26] was used to evaluate. One is divided into death from illness (I); 2 is divided into plant survival (PS); 3 is divided into severe disability (SM) which is conscious and needs care in daily life; 4 points in mild disability but can live independently; 5 is divided into good recovery and normal life accompanied by mild defect. The calculation of poor prognosis (P) is shown in Equation (3).

$$P = \frac{I + \mathrm{PS} + \mathrm{SM}}{T} \tag{3}$$

In Equation (3), T represents the total number of cases.

2.6. Statistical Methods. We use SPSS 21.0 statistical software for the analysis. Measurement data with normal distribution and uniform variance are expressed as mean ± standard deviation. The comparison between groups adopts independent sample t test. The comparison of grade grouping data adopts group design and two sample comparison. The rank sum test (Wilcoxon two-sample comparison method) is based on test level: $\alpha = 0.05$, two-sided test.

3. Results

3.1. Head CT. Figure 4 shows the head CT before and after the operation. The red arrow points to the hematoma.

It can be seen from Figure 4 that through the 3D-slicer software, the hematoma can be located more efficiently and the therapeutic effect of cerebral hemorrhage can be improved.

3.2. Comparison of Hematoma Clearance Rate. Table 2 shows the comparison of operation time, intraoperative blood loss, hospital stay, and hematoma clearance rate between the two groups.

It can be seen from Table 2 that the 3D-slicer group is stronger in terms of operation time, intraoperative blood loss, hospitalization time, and hematoma clearance rate. Therefore, the use of 3D-slicer to treat hypertensive cerebral hemorrhage is worthy of clinical promotion.

3.3. Complications. The overall proportion of postoperative infection, rebleeding, cerebral infarction, and stress ulcer in the 3D-slicer group was significantly lower than that in the control group, as shown in Figure 5.

3.4. Evaluation of the Nerve Function and Ability of Daily Living. There was no statistically significant difference between the two groups of patients in the preoperative nerve function and ability of daily living; 3 and 6 months after surgery, the nerve function and ability of daily living of the two groups were better than those before operation, and the 3D-slicer group had neurological function. The improvement of daily living ability was higher than that of the control group, and the difference was statistically significant, as shown in Table 3.

3.5. Comparison of Poor Prognosis. The incidence of poor prognosis in the 3D-slicer group was lower than that in the

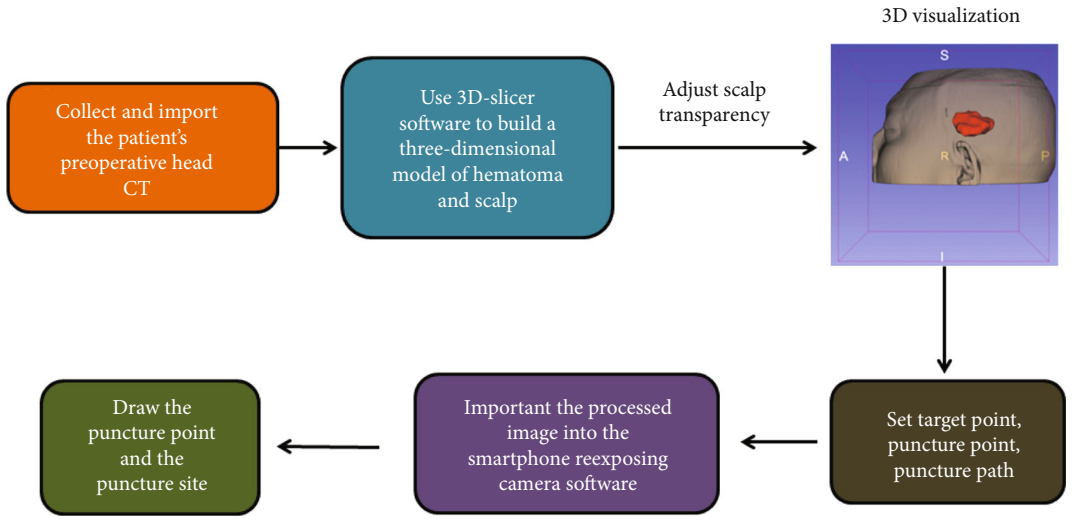

Figure 3: Specific steps assisted by the 3D-slicer software.

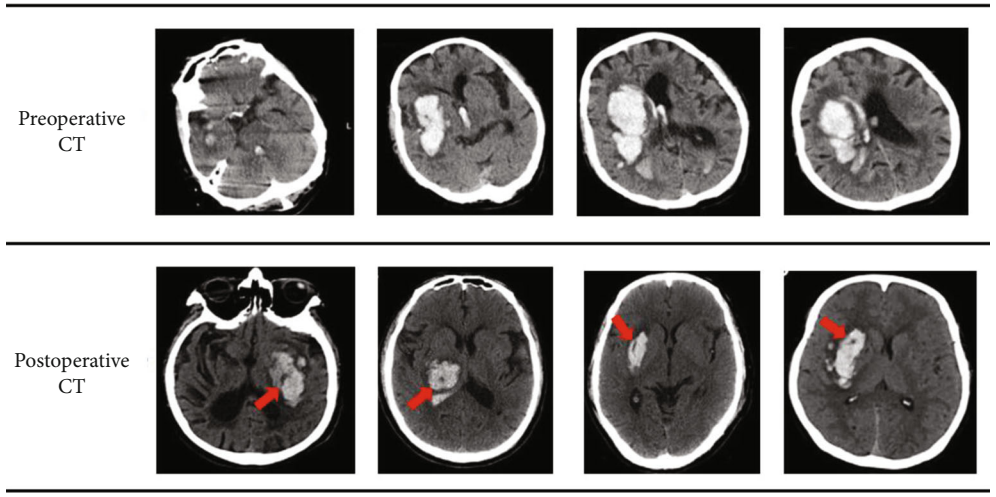

Figure 4: Head CT before and after surgery.

Table 2: Comparison of operation time, intraoperative blood loss, hospital stay, and hematoma clearance rate.

Type	Control group	3D-slicer group
Operation time (min)	91.4 ± 10.8	62.0 ± 8.9
Intraoperative blood loss (ml)	110.2 ± 11.8	52.0 ± 12.4
Hospital stay (day)	23.4 ± 2.3	17.5 ± 2.4
Hematoma clearance rate (%)	77.9	97.8
t	7.458	7.846
P	0.007	0.006

control group, and the difference was statistically significant ($P < 0.05$), as shown in Figure 6.

4. Discussion

At present, CT equipment has been quite popular in domestic medical units, especially the emergence of spiral CT. Volume scanning can provide more abundant internal information of the human body [27], but the limited two-dimensional information is still used. With the development of computer technology, many image postprocessing software continue to emerge.

The 3D-slicer software allows us to use the original DICOM format data of CT and MRI to reconstruct the tissues and organs of the human body. It is compatible with Windows, Lunix, and MAC operating systems and can run smoothly on personal computers with relatively simple operation.

At present, the surgical treatment of cerebral hemorrhage is basically to remove hematoma under the microscope. The advantage of removing hematoma under a craniotomy microscope is thorough removal, but the operation time is longer and the amount of bleeding is high, which requires higher requirements for the surgeon and requires strong microneurosurgical skills [28, 29]. Because the surgical trauma is large, the patient is bedridden for a long time, there are many complications, and the prognosis is poor,

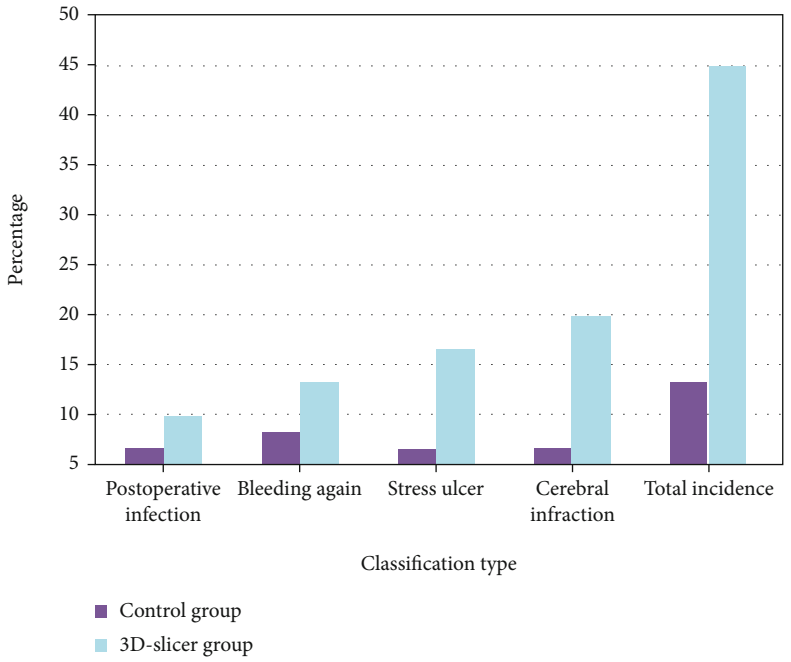

Figure 5: Comparison of complications between the two groups.

Table 3: Comparison of nerve function and ability of daily living.

Group	Nerve function			Ability of daily living		
	Preoperative	3 hours after surgery	6 hours after surgery	Preoperative	3 hours after surgery	6 hours after surgery
Control group	24.57	18.47	15.22	50.76	71.84	82.33
3D-slicer group	23.98	13.41	8.75	51.33	80.62	92.74

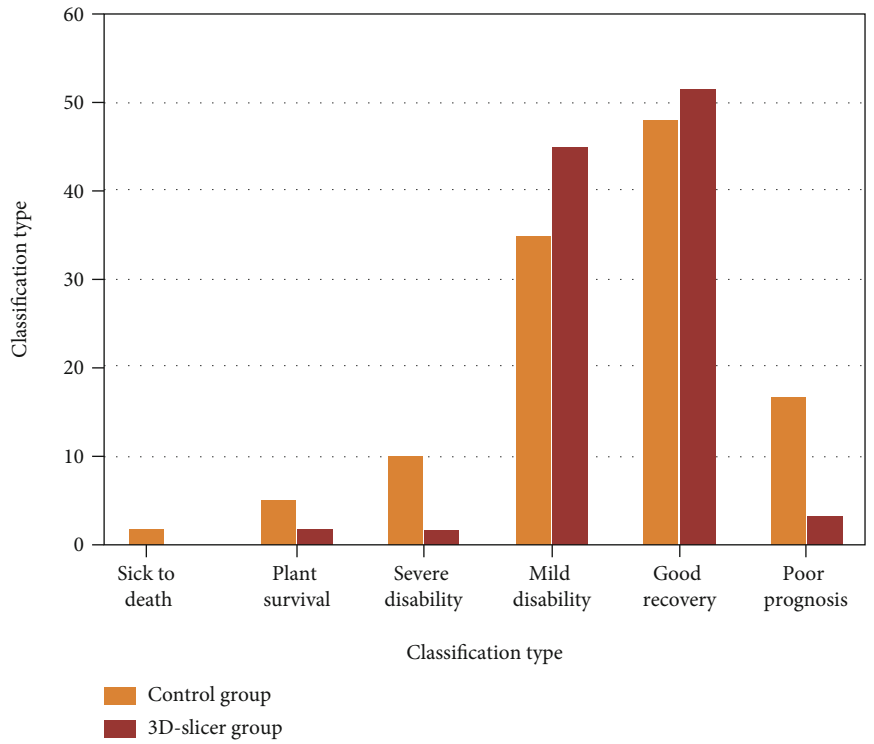

Figure 6: Comparison of poor prognosis.

which seriously increases the medical burden. Under the guidance of the concept of precision neurosurgery in the early stage, we learned and introduced the minimally invasive method of endoscopic removal. This technique can be used to open the craniotomy with a small incision, insert the puncture device to the center of the hematoma, guide the introducer to the ideal position, introduce the endoscope and suction device, and suck the hematoma.

The 3D-slicer software technology is widely used in the treatment of hypertensive cerebral hemorrhage. It assists neuroendoscopic minimally invasive surgery to effectively guarantee the quality of treatment and reduce complications. Endoscopic minimally invasive surgery has the advantages of fewer traumas, shorter operation time, less blood loss, higher hematoma clearance, less damage to the brain nerves of the patient, and fewer complications.

The 3D-slicer software may also be applied to study bone structure that is heavily influenced by the material properties on CT due to its different bone properties, which could be measured by various techniques [30, 31]. The implementation of a predictive control method [32] onto the diagnosis of patients using the 3D-slicer would enhance the effectiveness and efficiency of the technique.

5. Conclusion

Through the comparison of experimental data, the 3D-slicer group is better than the control group in various indicators, and the difference between the groups is statistically significant ($P < 0.05$). Compared with the control group, the 3D-slicer group has lower complications and hematoma. The clearance rate is slightly higher, the recovery of nerve function and daily living ability before and after surgery is better, and the incidence of poor prognosis is lower.

In summary, the 3D-slicer software-assisted endoscopic treatment for patients with hypertensive intracerebral hemorrhage has a better hematoma clearance effect, which is beneficial to the patient's early recovery and reduces the damage to the patient's brain nerve.

Data Availability

Data is available upon request from the corresponding author.

Ethical Approval

All human subjects in this study have given their written consent for the participation of our research.

Conflicts of Interest

The authors declare no conflict of interest for this paper.

References

[1] M. Kaneko, K. Tanaka, T. Shimada, K. Sato, and K. Uemura, "Long-term evaluation of ultra-early operation for hypertensive intracerebral hemorrhage in 100 cases," *Journal of Neurosurgery*, vol. 58, no. 6, pp. 838–842, 1983.

[2] S. Suzuki, R. E. Kelley, B. K. Dandapani, Y. Reyes-Iglesias, W. D. Dietrich, and R. C. Duncan, "Acute leukocyte and temperature response in hypertensive intracerebral hemorrhage," *Stroke; a Journal of Cerebral Circulation*, vol. 26, no. 6, pp. 1020–1023, 1995.

[3] S. T. Chen, S. D. Chen, C. Y. Hsu, and E. L. Hogan, "Progression of hypertensive intracerebral hemorrhage," *Neurology*, vol. 39, no. 11, pp. 1509–1514, 1989.

[4] G. Ooneda, Y. Yoshida, K. Suzuki, and T. Sekiguchi, "Morphogenesis of plasmatic arterionecrosis as the cause of hypertensive intracerebral hemorrhage," *Virchows Archiv. A, Pathological Anatomy and Histopathology*, vol. 361, no. 1, pp. 31–38, 1973.

[5] A. Wolf, A. Coros, J. Bierer et al., "Quantitative evaluation of vision-related and health-related quality of life after endoscopic transsphenoidal surgery for pituitary adenoma," *Journal of Neurosurgery*, vol. 127, no. 2, pp. 409–416, 2017.

[6] W. S. Rainer Wirtz, F. K. Albert, M. Schwaderer et al., "The benefit of neuronavigation for neurosurgery analyzed by its impact on glioblastoma surgery," *Neurological Research*, vol. 22, no. 4, pp. 354–360, 2000.

[7] M. Ronne-Engstr and E. AbuHamdeh, "Surgical site infections in standard neurosurgery procedures-a study of incidence, impact and potential risk factors," *British Journal of Neurosurgery*, vol. 17, no. 9, pp. 58–61, 2014.

[8] X. Guoqiang, S. Wei, and C. Shangjun, "Application of 3D-slicer software in neuroendoscopic surgery for hypertensive intracerebral hemorrhage," *Chinese Journal of Minimally Invasive Neurosurgery*, vol. 86, no. 7, pp. 75–82, 2017.

[9] A. F. Botero-Ospina, S. I. Duque-Vallejo, and J. F. Ochoa-Gómez, "Touchless control module for diagnostic images at the surgery room using the leap motion system and 3D slicer software," *Revista Facultad De Ingenieria*, vol. 82, no. 82, pp. 40–46, 2017.

[10] A. M. B. S. D. Neves, L. F. S. Toschi, and C. J. Feldman, "Curvature characterization of cochlea using CT-based ear atlas and 3D slicer software," *Brazilian Congress on Biomedical Engineering*, vol. 46, no. 8, pp. 95–97, 2019.

[11] G. Domínguez, H. Miguel, and R. P. Cristina, "Morphological and volumetric assessment of cerebral ventricular system with 3D slicer software," *Journal of Medical Systems*, vol. 40, no. 6, pp. 1–8, 2016.

[12] D. D. Oge, M. A. Topcuoglu, R. Gocmen, and E. M. Arsava, "The dynamics of hematoma surface regularity and hematoma expansion in acute intracerebral hemorrhage," *Journal of Clinical Neuroscience*, vol. 74, pp. 160–163, 2020.

[13] L. A. Beslow, R. N. Ichord, S. E. Kasner et al., "ABC/XYZ estimates intracerebral hemorrhage volume as a percent of total brain volume in children," *Stroke; a Journal of Cerebral Circulation*, vol. 41, no. 4, pp. 691–694, 2010.

[14] M. Stamplecoski, J. Fang, M. K. Kapral, and F. L. Silver, "Abstract T MP103: long-term outcomes of elderly patients with intracerebral hemorrhage and atrial fibrillation," *Stroke*, vol. 45, suppl_1, pp. 1053–1074, 2014.

[15] S. Kauffmann, R. Chabanne, A. Coste et al., "Favorable outcome of rivaroxaban-associated intracerebral hemorrhage reversed by 4-factor prothrombin complex concentrate," *A & A Case Reports*, vol. 4, no. 11, pp. 151–154, 2015.

[16] X. J. Chen, L. Xu, H. X. Wang, F. Wang, Q. Wang, and R. Kikinis, "Development of a surgical navigation system based on 3D slicer for intraoperative implant placement surgery," *Medical Engineering & Physics*, vol. 41, pp. 81–89, 2017.

[17] N. Miura, A. Nakahara, M. Kagawa, K. Kitamura, and N. Kobayashi, "A study of hypertensive intracerebral hemorrhage. (II)–Sequential CT examination and classification (author's transl)," *No Shinkei Geka*, vol. 6, no. 7, pp. 635–645, 1978.

[18] K. Nishitani, T. Izumidani, and M. Uno, "Less invasive surgery for hypertensive intracerebral hemorrhage," *Surgery for cerebral stroke*, vol. 23, no. 4, pp. 317–323, 1995.

[19] J. H. Kim, K. Y. Park, and J. K. Kang, "Clinical observation and CT findings of hypertensive intracerebral hemorrhage," *Journal of Cancer Therapy*, vol. 46, no. 2, pp. 241–245, 1980.

[20] T. Wang, Q. J. Zhao, and J. W. Gu, "Neurosurgery medical robot re-mebot for the treatment of 17 patients with hypertensive intracere-bral hemorrhage," *International Journal of Medical Robot*, vol. 15, no. 5, p. e 2024, 2019.

[21] C. M. Cheung, T. H. Tsoi, and S. F. K. Hon, "Using the National Institutes of Health Stroke Scale (NIHSS) to predict the mortality and outcome of patients with intracerebral hemorrhage," *International Journal of Stroke*, vol. 14, no. 5, pp. 367–370, 2008.

[22] C. Celik, J. Aksel, and B. Karaoglan, "Comparison of the Orpington Prognostic Scale (OPS) and the National Institutes of Health Stroke Scale (NIHSS) for the prediction of the functional status of patients with stroke," *Disability & Rehabilitation*, vol. 28, no. 10, pp. 609–612, 2006.

[23] E. E. Hrens, K. Amris, and A. G. Fisher, "Performance-based assessment of activities of daily living (ADL) ability among women with chronic widespread pain," *Pain*, vol. 150, no. 3, pp. 535–541, 2010.

[24] K. Sheikh, D. S. Smith, and T. W. Meade, "Repeatability and validity of a modified activities of daily living (ADL) index in studies of chronic disability," *International Rehabilitation Medicine*, vol. 1, no. 2, pp. 51–58, 1979.

[25] G. M. Teasdale, L. E. L. Pettigrew, and J. T. L. Wilson, "Analyzing outcome of treatment of severe head injury: a review and update on advancing the use of the Glasgow outcome scale," *Journal of Neurotrauma*, vol. 15, no. 8, pp. 587–597, 1998.

[26] L. E. L. Pettigrew, J. T. L. Wilson, and G. M. Teasdale, "Assessing disability after head injury: improved use of the Glasgow outcome scale," *Journal of Neurosurgery*, vol. 89, no. 6, pp. 939–943, 1998.

[27] S. J. Strååt, *Verification of High Energy Photon Therapy Based on PET/CT Imaging of Photonuclear Reaction*, vol. 24, no. 4, 2012Doctoral dissertation, Department of Physics, Stockholm University, 2012.

[28] Y. R. Yadav, V. Parihar, and S. Ratre, "Microneurosurgical skills training," in *11th neuroendoscopic fellowship training program*, vol. 34no. 4, pp. 56–60, Jabalpur MP India, 2015.

[29] H. Kanaya, "Development in neurosurgical approaches to hypertensive intracerebral hemorrhage in Japan," *Intracerebral Hematomas*, vol. 42, no. 1, pp. 486–490, 1992.

[30] X. Xinli, C. Zhang, F. Musharavati, T. A. Sebaey, and A. Khan, "UFSW tool pin profile effects on properties of aluminium-steel joint," *Vacuum*, vol. 192, no. 8, article 110460, 2021.

[31] X. Xu, C. Zhang, F. Musharavat, T. A. Sebaey, and A. Khan, "Dispersion of waves characteristics of laminated composite nanoplate," *Steel and Composite Structures*, vol. 40, no. 3, pp. 355–367, 2021.

[32] Z. H. Tang, Y. Y. Li, X. Y. Chai, H. Y. Zhang, and S. X. Cao, "Adaptive nonlinear model predictive control of NOx emissions under load constraints in power plant boilers," *Journal of Chemical Engineering of Japan*, vol. 53, no. 1, pp. 36–44, 2020.

Hindawi
Computational and Mathematical Methods in Medicine
Volume 2022, Article ID 9251225, 9 pages
https://doi.org/10.1155/2022/9251225

Research Article

Electrocardiogram Signal Classification in the Diagnosis of Heart Disease Based on RBF Neural Network

Yan Fang,[1,2,3] **Jianshe Shi**,[4] **Yifeng Huang**,[5] **Taisheng Zeng**,[1,2,3] **Yuguang Ye**,[1,2,3] **Lianta Su**,[1,2,3] **Daxin Zhu**,[1,2,3] **and Jianlong Huang**[1,2,3]

[1]*Faculty of Mathematics and Computer Science, Quanzhou Normal University, Quanzhou 362000, China*
[2]*Fujian Provincial Key Laboratory of Data Intensive Computing, Quanzhou 362000, China*
[3]*Key Laboratory of Intelligent Computing and Information Processing, Fujian Province University, Quanzhou 362000, China*
[4]*Department of General Surgery, Huaqiao University Affiliated Strait Hospital, Quanzhou, Fujian 362000, China*
[5]*Department of Diagnostic Radiology, Huaqiao University Affiliated Strait Hospital, Quanzhou, Fujian 362000, China*

Correspondence should be addressed to Yuguang Ye; chinaye@163.com and Jianlong Huang; robotics@qztc.edu.cn

Received 28 July 2021; Revised 29 September 2021; Accepted 26 October 2021; Published 30 January 2022

Academic Editor: Simon Fong

Heart disease is a common disease affecting human health. Electrocardiogram (ECG) classification is the most effective and direct method to detect heart disease, which is helpful to the diagnosis of most heart disease symptoms. At present, most ECG diagnosis depends on the personal judgment of medical staff, which leads to heavy burden and low efficiency of medical staff. Automatic ECG analysis technology will help the work of relevant medical staff. In this paper, we use the MIT-BIH ECG database to extract the QRS features of ECG signals by using the Pan-Tompkins algorithm. After extraction of the samples, K-means clustering is used to screen the samples, and then, RBF neural network is used to analyze the ECG information. The classifier trains the electrical signal features, and the classification accuracy of the final classification model can reach 98.9%. Our experiments show that this method can effectively detect the abnormality of ECG signal and implement it for the diagnosis of heart disease.

1. Introduction

Cardiac diseases are likely to occur in all age groups [1]. Surgery for cardiac diseases is difficult and risky. Conservative treatment is often used for nonessential cardiac diseases, which results in high recurrence probability and high diagnostic efficiency.

Electrocardiogram (ECG) detection is currently the most effective and direct way to detect ECG signals [2]. At present, the diagnosis of cardiac diseases is mainly determined by medical doctors and clinicians through manual detection and ECG analysis. The related ECG automatic analysis technology can provide effective help for the diagnosis of medical workers, which can help to improve the efficiency of diagnosis.

Based on the above problems, this paper proposes an automatic ECG analysis technology, which uses Pan-Tompkins algorithm, uses ECG data in MIT-BIH ECG database to extract the features of ECG QRS complex, and uses K-means clustering to filter the data after cutting the samples. Then, RBF neural network is used to train the classifier for the extracted ECG features. This method can effectively judge the abnormalities of ECG signals.

ECG is a diagnostic technology that records the electrocardiography activities of the heart in a certain time unit through the chest of biological objects. It collects and records the electrodes connected to the skin of specific parts of biological objects and preserves the relevant contents in a certain form [3].

In the process of detection, several electrodes are usually placed on human limbs. These electrodes must appear in pairs, as shown in Figure 1, which is called lead. In this paper, the LL+RL electrode combination, known as one- or

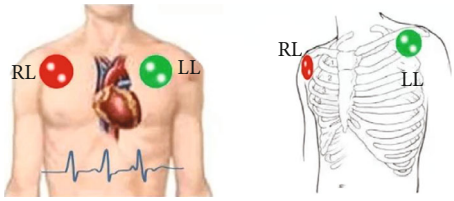

Figure 1: A schematic diagram of one or two human leads in registering ECG signals.

two-lead electrocardiograms, is used. This method is often used in one diagnosis [4]. This method coincides with the fast diagnosis direction in this paper.

Each electrode in the test result will get a corresponding ECG signal map. In this paper, the LA signal data is unified.

Although the ECG signal has a very obvious periodicity, due to the diversity of noise and random factors caused by external factors, it has become a difficult research problem for the diagnosis of ECG abnormalities [5]. Therefore, on the basis of previous studies by various scholars and experts [6], we use the compromise Pan-Tompkins paper [7] to denoise and extract features for the QRS wave group of ECG signal, use K-means algorithm [8] to cluster the sample wave group, select the similar ECG signal, and then use the radial basis function neural network to extract the ECG signal. The algorithm trains the feature classifier and achieves the expected results.

2. Methods

2.1. Feature Extraction

2.1.1. Object Survey. To analyze ECG signal, the most necessary step is to extract its QRS wave group. The QRS complex reflects changes in depolarization potential and time of the left and right ventricles. Considering the robustness and stability, the QRS wave group is finally selected in this paper [9].

ECG signal has periodicity. Compared with other electrical signals such as brain wave and muscle wave, ECG signal belongs to a kind of wave which is easy to detect and distinguish features.

The QRS wave group is a detailed description of potential changes in ventricular depolarization (Figure 2). In the ECG signal graph, after P wave ends, Q wave enters PR interval, and then, Q wave shows a downward trend, R wave quickly goes up, and S wave immediately goes down. These three waves correspond to the connected waves, which are collectively referred to as the QRS wave group in this paper.

Another very important reason for choosing the QRS wave group is that the QRS wave group is the most obvious corresponding signal in ECG signal. The correct choice of the QRS wave group is the next step to complete the selection of other signal waves.

It is obvious from Figure 2 that R wave is the narrowest and the largest of all waveforms.

T wave corresponds to the process of repolarization of human ventricular muscle; the process of cardiac depolarization corresponds to P wave, so it makes blunt circular image; PR corresponds to the process of transmission; in ideal state, there is no potential change, that is, the ECG signal is flat. The period of QT corresponds to a process of human ventricular contraction [10]. Therefore, the heart rate can be effectively detected by the change of the interval of QT. The size of the period of QT is proportional to the speed of human heart rate [11].

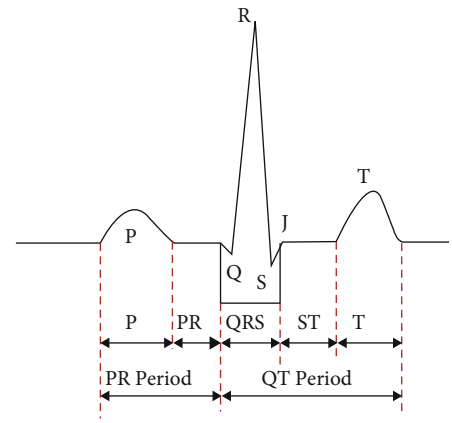

Figure 2: Schematic diagram of an ECG cycle.

In normal ECG signal cycle, P wave and T wave have no obvious characteristics. If we want to distinguish them clearly, we need to detect them by the position of the QRS wave group.

2.1.2. Contrastive Selection. There are many related literatures about the extraction and detection methods of the QRS wave group. The main methods are focused on wavelet transform [9], neural networks [12], classical Pan-Tompkins algorithm, and its improved algorithm [13]. The improved wavelet algorithm of notch filter [14] is added.

The accuracy of wavelet transform method is high, but the disadvantage is that its calculation steps are very tedious, so the time efficiency is not high. Secondly, the redundancy of data will increase in the process of wavelet transform. Although the neural network is a very accurate method, the performance of a neural network depends on its training model. This process is very long, and different training samples produce different training results. The above characteristics make it not suitable for practical applications. The algorithm provided in a real-time ECG filter for portable mobile medical systems [15] does not need model training, and the corresponding process of the method is more convenient and efficient than that of the wavelet transform method, which belongs to a compromise scheme.

To the best of our knowledge, this paper considers and presents the advantages and disadvantages of each method. To implement a real-time QRS detection algorithm, we adopted the RBF neural network to perform ECG classification [7].

2.1.3. Extraction Process. Some mature and extremely complex algorithms are proposed in references, including low-pass filtering, high-pass filtering, differential, square,

integral, adaptive threshold, and search. Based on references, this paper only gives a brief description of the implementation process.

(1) Noise Reduction. However, due to the different equipment and environment, different noises will be introduced in the acquisition process of electrical signals, which will inevitably affect the final judgment, so the processing of noise in ECG data is the core content of data preprocessing.

High-pass filter method and low-pass filter method are used in this process. The purpose is to filter out the noise in the electrical signal, so as to improve the signal-to-noise ratio of the electrical signal.

The main noise in ECG signal is power frequency interference and baseline drift [15]. Power system and other interference signals are called power frequency interference; the frequency is generally concentrated in 50 Hz. Skin contact, human breathing, etc. will produce the so-called baseline drift; the frequency is generally concentrated in 0.05 Hz to 2 Hz. The frequency of the QRS wave group mainly concentrates on 5 Hz to 11 Hz.

Taking T as sampling period, the cutoff frequency of low-pass filter is 11 Hz, and the difference equation can be expressed as follows:

$$y(nT) = 2y(nT-T) - y(nT-2T) - 2x(nT-6T) + x(nT-12T) + x(nT). \quad (1)$$

The cutoff frequency of the high-pass filter is 2 Hz, and the difference equation can be expressed as

$$y(nT) = y(nT-T) - x(nT) + 32x(nT-16T) + x(nT-32T). \quad (2)$$

(2) Amplification. R wave in the QRS wave group is the steepest wave in an ECG signal cycle. In order to distinguish QRS waves from other ECG signals conveniently, the corresponding differential method is needed to amplify the steep slope characteristics of QRS wave groups. The specific difference equation is as follows:

$$y(nT) = x(nT) - x(xT-2T). \quad (3)$$

The high-frequency characteristics can be enhanced by a nonlinear square function, whose equation can be expressed as

$$y(nT) = [x(nT)]^2. \quad (4)$$

(3) Threshold Dynamic Adjustment and Search. Threshold dynamic adjustment and search belong to the core part of the algorithm, through which to search the peak value of ECG signal, through a certain equation to update the threshold, and combined with backtracking detection, bidirectional discrimination, and other content to detect. The process of this method is complex, which has been described in detail in paper [7]. Using the method provided by it, the final detection can be completed.

2.2. Data Preprocessing

2.2.1. Pretreatment Basis. K-means clustering method is also called the K-means clustering algorithm. Firstly, the sample objects are randomly selected, then the selected objects are regarded as the center of the clustering process, and then other object samples are also put into the model to calculate the distance between each object sample and the cluster center sample selected randomly. The nearest center sample will assign it to. When the condition that the object is fully allocated is satisfied, it is recalculated. The process is repeated to meet the conditions and stop the computation. The termination condition of this paper is the minimum center change, that is, the number of cluster center changes is the smallest, and the clustering is stopped.

There is no best method for K value in theory. Only when clustering, we try to make manual selection repeatedly. But in the process of this step, K is taken as 2 to screen the corresponding segments of these clusters.

Based on the results of feature extraction, this paper will adopt the interception-clustering filtering method [16] for sample preprocessing.

2.2.2. Truncation Process. In the above, the QRS wave group of samples has been extracted with high accuracy, so according to the information of extracted feature points, samples can be effectively truncated for subsequent clustering screening, so as to improve the accuracy of classification results (Figure 3).

Normally, the heartbeat of normal people is the lowest once a second and the highest is twice a second. The corresponding heartbeat time of the heart rate is its corresponding ECG cycle. The converted range is about 600 ms to 1000 ms. The equation is as follows.

$$T = \frac{r}{t_h}, \quad (5)$$

where T is the period corresponding to ECG, R is the heart rate, and t_h is the number of heartbeats in the corresponding time of heart rate.

Let R wave correspond to R_i, Q wave correspond to Q_i, and S wave correspond to S_i, where $i = 1, 2, 3, 4 \cdots N$, N is the total set of R waves in the sample.

$$\begin{cases} Q_i - Q_{i-1} = T\ (i \neq 0), \\ Q_{i+1} - Q_i = T\ (i \neq N), \\ Q_{i+1} - Q_i = T\ (i \neq N), \\ R_i - R_{i-1} = T\ (i \neq 0), \\ R_{i+1} - R_i = T\ (i \neq N), \\ S_i - S_{i-1} = T\ (i \neq 0), \\ S_{i+1} - S_i = T\ (i \neq N). \end{cases} \quad (6)$$

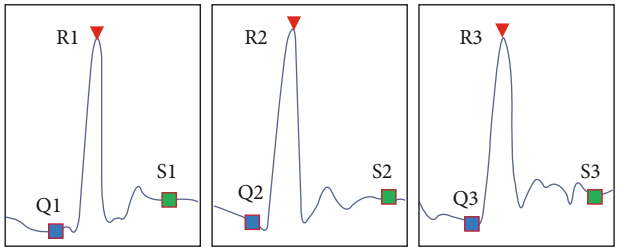

Figure 3: Examples of the same sample truncation results in the QRS wave group.

If the corresponding time limit of the QRS wave group is t_{QRSi} with units in milliseconds, it can be inferred.

$$60 \le t_{QRSi} \le 100. \tag{7}$$

Heart rate can be effectively detected by T wave and QRS wave group. Let T wave correspond to T_i, where $i = 1, 2, 3, 4, \cdots, N$, N is the total set of R waves in the sample.

$$r_t = T_i - Q_i. \tag{8}$$

The feature extraction has been carried out above, and the experimental data are analyzed. The $R_i + 500$ ms corresponding to R wave are truncated separately and saved as truncated samples, which will be used for the next clustering analysis. The data content stored in each row corresponds to an interval intercepted in this paper.

2.2.3. Screening Process. Suppose the input sample is $S = x_1, x_2, \cdots, x_m$ and m are the width of the cut sample, and the centers of the initial K samples are set to $\mu_1, \cdots, \mu_K$, respectively. For any sample $x_i (i = 1, 2, \cdots, m)$, according to the Euclidean distance equation, the nearest class of the center can be computed. Let D be the width of the truncated sample. The equation is as follows:

$$\operatorname{dist}(x_i, x_j) = \sqrt{\sum_{d=1}^{D} (x_i d - x_j d)^2}. \tag{9}$$

In the process of continuous iteration, we need to substitute a condition to stop iteration. As mentioned above, the method of error sum and criterion function is adopted to stop iteration. The function model is as follows:

$$J = \sum_{k=1}^{K} \sum_{x_i \epsilon C_k} \operatorname{dist}(x_i, Ce_k). \tag{10}$$

When the value of $\triangle J$ is less than the threshold set, the iteration stops.

In the case of this experiment, the number of samples in the cluster corresponding to the normal class is much larger than that of the abnormal cluster, so the abnormal data is eliminated directly. The screening process has been completed.

2.3. Feature Selection

2.3.1. Selection Process. Assuming that the number of data bars is n and the dimension is d, the method can be summarized as follows:

(1) The filtered data are composed of d rows and n column matrix M'

(2) Subtract all rows of M' from the average of the row

(3) Calculate the covariance matrix M' and the required value

(4) Arrange the eigenvectors

(5) Constituting a new matrix P, the matrix P is the result of reducing the dimension

For the covariance matrix, the sample size is assumed to be n, the average is X, the standard deviation is s, and the variance is s^2. The details are as follows:

$$\bar{X} = \frac{\sum_{i=1}^{n} X_i}{n}, \tag{11}$$

$$s = \sqrt{\frac{\sum_{i=1}^{n} (X_i - \bar{X})^2}{n-1}}. \tag{12}$$

$$s^2 = \frac{\sum_{i=1}^{n} (X_i - \bar{X})^2}{n-1}. \tag{13}$$

By computing the correlation by covariance, the following definitions are given:

$$\operatorname{cov}(X, Y) = \frac{\sum_{i=1}^{n} (X_i - \bar{X})(Y_i - \bar{Y})}{n-1}. \tag{14}$$

In fact, this paper solves a problem with multiple dimensions, so it needs to calculate multiple covariances. To achieve this process, a matrix is needed to organize the data, so a covariance matrix is defined:

$$C_{n\times n} = (c_{i,j}, c_{i,j} = \operatorname{cov}(\operatorname{Dim}_i, \operatorname{Dim}_j)). \tag{15}$$

Covariance matrix can be used:

$$M' = \begin{pmatrix} \operatorname{cov}(x,x) & \operatorname{cov}(x,y) & \operatorname{cov}(x,z) \\ \operatorname{cov}(y,x) & \operatorname{cov}(y,y) & \operatorname{cov}(y,z) \\ \operatorname{cov}(z,x) & \operatorname{cov}(z,y) & \operatorname{cov}(z,z) \end{pmatrix}. \tag{16}$$

Then, the eigenvalues and eigenvectors are calculated according to the actual situation to complete the corresponding operation of dimensionality reduction.

2.4. Classifier Design

2.4.1. Method Selection. The supervised classifier based on RBF neural network is adopted in this paper. Compared with the traditional BF method, it has the advantages of fast

learning, strong autonomy, linear output, and good classification effect [17]. Therefore, this method is chosen as the implemented classifier in this paper.

2.4.2. Implementation Process. In general, the Euclidean distance between any point in space and another point, i.e., the distance between x and x_c, is recorded as a monotone equation:

$$k(|x - x_c|). \tag{17}$$

The function commonly used in the model is Gauss Radial Basis Kernel Function [3], which can be expressed in the form of

$$k(|x - x_c|) = \exp\left\{\frac{-||x - x_c||^2}{2\sigma^2}\right\}. \tag{18}$$

In the above equations, x_c is defined as the midpoint of the kernel function and σ is the parameter of the width of the function, which is used to control the range of the function.

RBF neural network is actually a hierarchical structure, which includes three parts: input, hiding, and output. The transformation from input to hidden level is nonlinear, while the change from hidden to output level is linear. The output layer sums and outputs the output weights of the hidden layer. Let n be the total number of samples, and the given training sample is expressed as

$$X_n = \{x_{n1}, x_{n2}, \cdots, x_{n,m-1}, x_{nm}\}, (n = 1, 2, \cdots, N). \tag{19}$$

The output after learning is defined as

$$Y_n(n = 1, 2, \cdots, N). \tag{20}$$

The base function is defined as $\varphi(x, x_i)$ above. The output of the base function is expressed as the output corresponding to the hidden unit i, and the corresponding center point of the base function can be expressed as

$$i_n = \{i_{n1}, i_{n2}, \cdots, i_{n,m-1}, i_{nm}\}, (n = 1, 2, \cdots, N). \tag{21}$$

We set the initial value:

$$c_{jn} = \min n + \frac{\max N - \min N}{2n} + (j - 1)\frac{\max N - N}{n}, (j = 1, 2, \cdots, n). \tag{22}$$

The corresponding width is defined as

$$d_n(n = 1, 2, \cdots, N). \tag{23}$$

The calculation method of width can be expressed as

$$d_n = \sqrt{\frac{1}{N}\sum_{k=1}^{N}\left(x_n^k - c_{jn}\right)}. \tag{24}$$

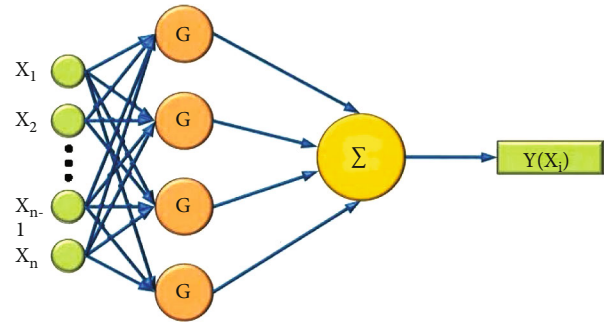

Figure 4: Supervised classifier based on RBF neural network for classification of ECG signals at different cycles.

The corresponding weight can be expressed as

$$\omega_n(n = 1, 2, \cdots, N). \tag{25}$$

The overall structure of the neural network is shown in Figure 4.

To sum up, the following summaries can be made:

(1) Initialization of parameters: according to Equation (20), the iteration ε jump-out accuracy is given

(2) When the output is generated, the RMS value of root mean square error is calculated. O_k represents the vector of expected output. The RMS equation is as follows:

$$\text{RMS} = \sqrt{\frac{\sum_{i=1}^{N}\sum_{k=1}^{n}(O_k - Y_k)}{nN}}. \tag{26}$$

When RMS $\leq \varepsilon$, the training is completed and the model is generated. Instead, it uses Equation (3)

(3) The adjustment parameters are recalculated and output; skip to Equation (2)

3. Experimental Method

3.1. Implementation Process

3.1.1. Brief Description. The implementation process of this paper can be summarized as follows. The flowchart is shown in Figure 5.

(1) Input the sample model group and extract the feature by using the algorithm of paper [7]

(2) All samples are processed into truncated samples according to their characteristics

(3) Cluster analysis, eliminating abnormal truncated samples

(4) Dimension reduction and feature selection

(5) Classifier training and testing after training

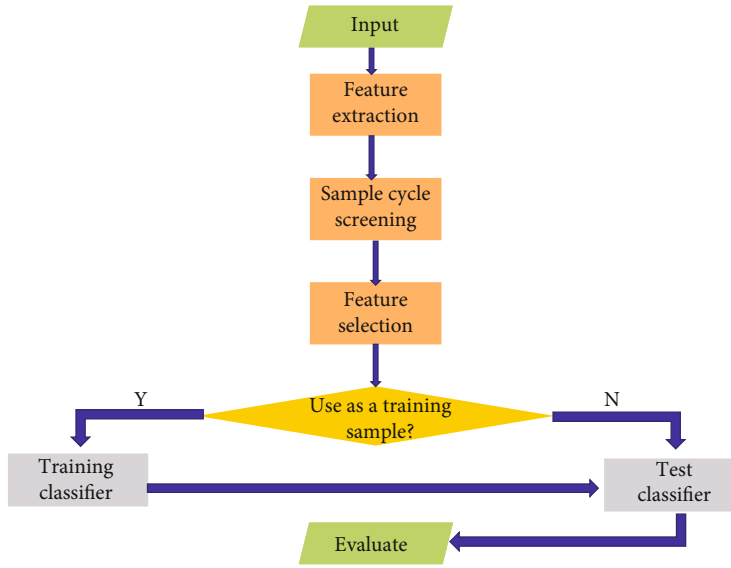

Figure 5: Procedural flowchart of method implementation.

(6) Classification and evaluation are obtained through analysis

3.1.2. Flowchart.

3.2. Experimental Process

3.2.1. Description. When the training is completed, the classification of ECG signals using this method can be summarized as follows. The flowchart is shown in Figure 6 and detailed as follows:

(1) Input the sample model group and extract the feature by using the algorithm of paper [7]

(2) Samples are processed into truncated samples according to their characteristics

(3) Cluster analysis, eliminating abnormal truncated samples

(4) Dimension reduction and feature selection

(5) Classifier is used to classify score, and the output is normal when the threshold is reached; otherwise, it is abnormal

3.2.2. Schematic Diagram.

4. Results

4.1. Data Sources. The experimental data in this paper are from the MIT-BIH ECG database [18], which is provided by MIT and is often used to study arrhythmia and other heart symptoms. The files in the database are composed of three parts: the header file which stores the sampling rate and the length of the data, the data file which stores the ECG data in the binary format, and the annotation file which stores the detailed description. The most important value of the latter is the actual position of each wave in the data file, which can be used to check the reliability of feature extraction. The corresponding feature extraction algorithm [7] that was previously proposed is relatively mature, and its reliability can reach 99.3%. Even if there is abnormal feature extraction content, it can be basically eliminated through the above screening process, so there is no more excessive research on reliability.

4.2. Classification Criteria. As for the classification of ECG signals, the American Association for the Advancement of Medical Instruments (AAMI) has drawn up the relevant rule paper [19], which classifies ECG [20] beats into normal N-type, supraventricular abnormal signal S-type, abnormal signal V-type caused by ventricular abnormalities, F-type, fusion signal, which may contain a variety of abnormalities, and Q-type, which cannot be classified. Type U refers to the unreadable type; in addition, there are U, X, O types which do not belong to the category of ECG signals. In summary, in fact, except for the N-type, which includes the normal ECG signal type, the other basic types belong to the abnormal category. Therefore, the core of classification of ECG is how to distinguish the normal ECG signal accurately.

4.3. Experimental Results

4.3.1. First Experiment. In this paper, 8000 sample models are used to identify abnormal ECG signals, including the above-mentioned situations, of which 5000 are used for training and 3000 for testing. The confusion matrix is shown in Table 1.

The results show that the accuracy of normal ECG signal detection can reach *99.71%*, abnormal ECG signal detection can reach *97.50%*, and comprehensive accuracy can reach *98.77%*.

4.3.2. Crossover Experiment. In order to verify the accuracy of the method, this paper subsequently carried out cross-validation [21] of the method. In the form of cross-

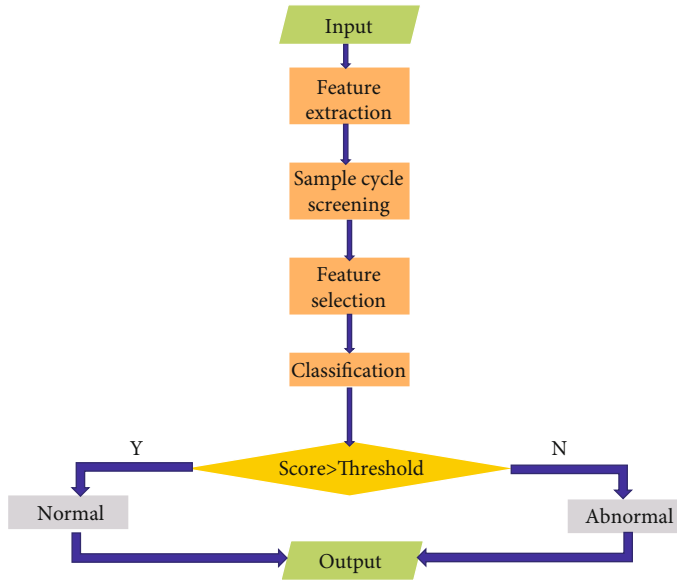

Figure 6: Procedural flowchart of our method.

validation, this paper selected 10-fold cross-validation, 5-fold cross-validation, and 2-fold cross-validation, respectively. There are two main reasons for conducting crossover experiments; one is to verify the accuracy, and the other is to study the influence of training quantity on test results.

According to the ideal state, the more training samples, the higher the final classification accuracy of the training model, and the limited number of actual samples; and because the interference of other factors does not necessarily meet the final results of this theory, this paper is only used for the accuracy of detection methods for crossover experiments.

Firstly, a 2-fold crossover experiment was conducted. For 8000 samples, 4000 samples were used for training and 4000 samples were used for testing. The results show that the accuracy of normal ECG signal detection can reach *99.96%*, abnormal ECG signal detection can reach *96.76%*, and comprehensive accuracy can reach 98.70%. The confusion matrix of the classification results is shown in Table 2.

Subsequently, 5-fold crossover experiment was carried out. For 8000 samples, 6400 samples were used for training and 1600 samples were used for testing. The results show that the accuracy of normal ECG signal detection can reach *99.79%*, abnormal ECG signal detection can reach *97.89%*, and comprehensive accuracy can reach 99.00%. The confusion matrix is shown in Table 3.

Finally, a 10-fold crossover experiment was conducted. For 8000 samples, 7200 samples were used for training and 800 samples for testing. The results show that the accuracy of normal ECG signal detection can reach *99.78%*, abnormal ECG signal detection can reach *97.61%*, and comprehensive accuracy can reach 98.88%. The confusion matrix [22] is shown in Table 4.

4.3.3. Comparative Experimental Evaluation. In the comparative experiment, the technology is replaced by other methods in the feature extraction stage and classifier selection stage, and the cross experiments are carried out, respectively.

Table 1: Confusion matrix for initial experimental results.

		Prediction		
		Normal	Abnormal	Total
Actual	Normal	1716	5	1721
	Abnormal	32	1247	1279
	Total	1748	1252	3000

Table 2: Twofold confusion matrix for cross-experimental results.

		Prediction		
		Normal	Abnormal	Total
Actual	Normal	2425	1	2426
	Abnormal	51	1523	1574
	Total	2476	1524	4000

In the stage of feature extraction, wavelet transform method and neural network extraction method [23] are used to replace them, while in the stage of classifier selection BF neural network method is used to replace them. The method used in this paper does not optimize it, only using the corresponding algorithm provided by other people in the network resources to carry out relevant comparative experiments. From this, we can get the replacement method as shown in Table 5.

It can be seen that besides using wavelet transform in the process of feature extraction, the accuracy of other methods is different from that of the methods proposed in this paper.

5. Discussion

In this paper, the classification of ECG signals is implemented by machine learning [24]. Firstly, the feature extraction is carried out according to the relevant methods provided in Section 2.1 of this paper. Then, according to

Table 3: Fivefold confusion matrix for crossover experimental results.

		Prediction		
		Normal	Abnormal	Total
Actual	Normal	934	2	936
	Abnormal	14	650	664
	Total	948	652	1600

Table 4: 10-fold confusion matrix for crossover experimental results.

		Prediction		
		Normal	Abnormal	Total
Actual	Normal	464	1	465
	Abnormal	8	327	335
	Total	471	329	800

Table 5: Method replacement consolidation table.

Substitution selection	Our method	BF neural network
The method in this paper	Method 1	Method 4
Wavelet transform	Method 2	Method 5
BF neural network	Method 3	Method 6

the result of feature extraction, the samples are truncated, the samples are clustered and analyzed, some special truncated samples are eliminated, and the process of data prepossessing is completed. After the screening, the sample features are selected and the PCA is used. A method is used to reduce the dimension; and the first training of the classifier is carried out afterwards. Next, three cross experiments of 2-fold, 5-fold, and 10-fold are carried out, and the results are good. Finally, some methods in the process are replaced by comparative experiments, and finally, the corresponding methods in this paper are realized.

This paper focuses on the supplement to this field, which is also the innovation of this paper. Although there are a variety of corresponding technical methods in the research literature in this field, with the upgrading and development of information technology, it is inevitable to supplement many contents in this field, so the research content of this paper is of great significance.

6. Conclusion

According to the comprehensive test results, the detection accuracy of normal ECG signals can reach *99.74%*, the detection of abnormal ECG signals can reach 97.53%, and the comprehensive accuracy rate can reach *98.98%*. Although there is room for improvement in the detection of abnormal ECG signals, this does not affect the good classification effect that this method can show in the classification study of ECG signals. However, the recognition accuracy of abnormal ECG signals can still continue to be improved, and we will further study this in the future.

The following research direction of this paper is to develop the entity system through the above methods and consider combining it into telemedicine-related technology and mobile medical technology. Secondly, the methods used in the research process will still optimize the parameters [25]. When new and better technical heart diagnostics techniques appear, the new methods will be incorporated into or applied to the existing approach in the future. The current type of approach in our paper has strong clinical potential in cardiac diagnosis and treatment.

Data Availability

The experimental data in this paper are from the MIT-BIH ECG database.

Conflicts of Interest

The authors declare no conflicts of interest.

Authors' Contributions

Yan Fang and Jianshe Shi contributed equally to this paper.

Acknowledgments

This research is supported by Science and Technology Program of Quanzhou (No. 2021CT0010). The authors also acknowledge the support by Fujian Provincial Key Laboratory of Data-Intensive Computing, Fujian University Laboratory of Intelligent Computing and Information Processing, and Fujian Provincial Big Data Research Institute of Intelligent Manufacturing. This work is supported by the Education and Scientific Research Project for Young and Middle-Aged Teachers of Fujian Province (No. JAT190511).

References

[1] M. Kruska, I. El-Battrawy, M. Behnes, M. Borggrefe, and I. Akin, "Biomarkers in cardiomyopathies and prediction of sudden cardiac death," *Current Pharmaceutical Biotechnology*, vol. 18, no. 6, pp. 472–481, 2017.

[2] S. Y. Ko, K. M. Wang, W. C. Lian, and C. H. Kao, "A portable ECG recorder. IEEE," in *2012 2nd International Conference on Consumer Electronics, Communications and Networks (CECNet)*, pp. 3063–3067, Yichang, China, 2012.

[3] C. Li, C. Zheng, and C. Tai, "Detection of ECG characteristic points using wavelet transforms," *IEEE Transactions on Biomedical Engineering*, vol. 42, no. 1, pp. 21–28, 1995.

[4] D. M. Krikler, "Heart disease: a textbook of cardiovascular medicine," *Mayo Clinic Proceedings*, vol. 59, no. 9, pp. 652-653, 2008.

[5] D. A. Winter, P. M. Rautaharju, and H. K. Wolf, "Measurement and characteristics of over-all noise content in exercise electrocardiograms," *American Heart Journal*, vol. 74, no. 3, pp. 324–331, 1967.

[6] Z. Tang, G. Zhao, and T. Ouyang, "Two-phase deep learning model for short-term wind direction forecasting," *Renewable Energy*, vol. 173, pp. 1005–1016, 2021.

[7] J. Pan and W. J. Tompkins, "A real-time QRS detection algorithm," *IEEE Transactions on Biomedical Engineering*, vol. BME-32, no. 3, pp. 230–236, 1985.

[8] K. Krishna and M. Narasimha Murty, "Genetic K-means algorithm," *IEEE Transactions on Systems, Man, and Cybernetics, Part B (Cybernetics)*, vol. 29, no. 3, pp. 433–439, 1999.

[9] H. Zhang, "An improved QRS wave group detection algorithm and Matlab implementation," *Physics Procedia*, vol. 25, pp. 1010–1016, 2012.

[10] J. P. Barnes and P. R. Johnston, "Application of robust generalised cross-validation to the inverse problem of electrocardiology," *Computers in Biology & Medicine*, vol. 69, pp. 213–225, 2016.

[11] L. Arnold, J. Page, D. Attwell, M. Cannell, and D. A. Eisner, "The dependence on heart rate of the human ventricular action potential duration," *Cardiovascular research*, vol. 16, no. 10, pp. 547–551, 1982.

[12] H. Turabieh, "A hybrid ANN-GWO algorithm for prediction of heart disease," *Operations Research*, vol. 6, no. 2, pp. 136–146, 2016.

[13] J. A. Abraham, "An improved algorithm for network reliability," *IEEE Transactions on Reliability*, vol. 28, no. 1, pp. 58–61, 1979.

[14] G. Luo, "Wavelet notch filter design of spread-spectrum communication systems for high-precision wireless positioning," *Circuits Systems & Signal Processing*, vol. 31, no. 2, pp. 651–668, 2011.

[15] J. Li, G. Deng, W. Wei, H. Wang, and Z. Ming, "Design of a real-time ECG filter for portable mobile medical systems," *IEEE Access*, vol. 5, pp. 696–704, 2017.

[16] S. J. McNaughton, "Serengeti Grassland Ecology: the role of composite environmental factors and contingency in community organization," *Ecological Monographs*, vol. 53, no. 3, pp. 291–320, 1983.

[17] J. H. Flowers and N. Wilcox, "The effect of flanking context on visual classification: the joint contribution of interactions at different processing levels," *Perception & Psychophysics*, vol. 32, no. 6, pp. 581–591, 1982.

[18] G. B. Moody and R. G. Mark, "The impact of the MIT-BIH arrhythmia database," *IEEE Engineering in Medicine & Biology Magazine*, vol. 20, no. 3, pp. 45–50, 2002.

[19] Association for the Advancement of Medical Instrumentation, *ANSI /AAMI EC57: 2012, Testing and Reporting Performance Results of Cardiac Rhythm and ST Segment Measurement Algorithms*, Association for the Advancement of Medical Instrumentation, Arlington, 2012.

[20] M. Thomas, M. K. Das, and S. Ari, "Automatic ECG arrhythmia classification using dual tree complex wavelet based features," *AEU - International Journal of Electronics and Communications*, vol. 69, no. 4, pp. 715–721, 2015.

[21] R. Kohavi, "A study of cross-validation and bootstrap for accuracy estimation and model selection," *International joint conference on artificial intelligence*, vol. 14, 1995.

[22] J. T. Townsend, "Erratum to: theoretical analysis of an alphabetic confusion matrix," *Perception & Psychophysics*, vol. 10, no. 4, pp. 256–256, 1971.

[23] "Multi-view convolutional neural network with leader and long-tail particle swarm optimizer for enhancing heart disease and breast cancer detection," *Neural Computing and Applications*, vol. 32, no. 19, pp. 15469–15488, 2020.

[24] S. H. Jambukia, V. K. Dabhi, and H. B. Prajapati, "Classification of ECG signals using machine learning techniques: a survey," in *2015 International Conference on Advances in Computer Engineering and Applications*, pp. 714–721, Ghaziabad, India, 2015.

[25] Z. H. Tang, Y. Y. Li, X. Y. Chai, H. Y. Zhang, and S. X. Cao, "Adaptive nonlinear model predictive control of NOx emissions under load constraints in power plant boilers," *Journal of Chemical Engineering of Japan*, vol. 53, no. 1, pp. 36–44, 2020.

Hindawi
Computational and Mathematical Methods in Medicine
Volume 2022, Article ID 8501948, 13 pages
https://doi.org/10.1155/2022/8501948

Research Article

Propofol Anesthesia Depth Monitoring Based on Self-Attention and Residual Structure Convolutional Neural Network

Yachao Wang,[1] Hui Zhang,[1] Ying Fan,[2] Peng Ying,[2] Jun Li,[2] Chenyao Xie,[1] and Tingting Zhao[2]

[1]*Dept. Anesthesiol, First People's Hospital Xiaoshan, Hangzhou, Zhejiang, China*
[2]*Department of Anesthesiology, Shulan (Hangzhou) Hospital Affiliated to Zhejiang Shuren University Shulan International, China*

Correspondence should be addressed to Tingting Zhao; tingting.zhao@shulan.com

Received 26 October 2021; Revised 24 November 2021; Accepted 4 January 2022; Published 29 January 2022

Academic Editor: Kelvin Wong

Background and Objective. To study the new method of selecting CNN+EEG index values, based on self-attention and residual structure of convolutional neural network, to deeply monitor propofol anesthesia. *Methods*. We compare nine index values, select CNN+EEG, which has good correlation with BIS index, as an anesthesia state observation index to identify the parameters of the model, and establish a model based on self-attention and dual resistructure convolutional neural network. The data of 93 groups of patients were selected and randomly grouped into three parts: training set, validation set, and test set, and compared the best and worst results predicted by BIS. *Result*. The best result is that the model's accuracy of predicting BLS on the test set has an overall upward trend, eventually reaching more than 90%. The overall error shows a gradual decrease and eventually approaches zero. The worst result is that the model's accuracy of predicting BIS on the test set has an overall upward trend. The accuracy rate is relatively stable without major fluctuations, but the final accuracy rate is above 70%. *Conclusion*. The prediction of BIS indicators by the deep learning method CNN algorithm shows good results in statistics.

1. Introduction

In clinical anesthesia operations, as the depth of propofol anesthesia increases, explicit memory and implicit memory disappear one after another [1]. The patient still has implicit memory in the case of innocuous stimulus and unconsciousness. Different patients require different anesthesia operations. In the operation under epidural anesthesia (intraspinal anesthesia), in order to eliminate the nervousness of the patient, we avoid leaving unpleasant memories to the patient, and eliminate implicit memory [2]. For those who have poor general conditions and cannot tolerate deep intravenous general anesthesia (such as old age and shock). They should be anesthetized (composure) to at least 2 points on the OAA/S score to eliminate explicit memory [3].

The sedation stage during surgery is an important part of general anesthesia. Correct selection of the observation indicators for the sedation stage is an important step in anesthesia monitoring [4]. The static depth observation index includes BIS index, Narcotrend index, and entropy the index [5]. The entropy index can characterize the complexity of the signal and reflect the difference of signals in different states. The calculation process is relatively simple and has attracted more and more attention. The BIS monitor is currently the most authoritative anesthesia status monitor [6]. The BIS index is obtained by the BIS monitor and has a high degree of recognition in clinical anesthesia operations at home and abroad. However, its algorithm has high complexity and rich subparameters, which affects the reaction time of the indicator in a certain period of time. It is an indicator of the depth of sedation identified by the US FDA to monitor sedation. Studies show a good correlation of BIS with the concentration of multiple anesthetic drugs. However, the BIS is insensitive to the monitoring of the nociceptive stimuli and cannot respond immediately to the instantaneous changes in the EEG signals. Entropy index analysis of the complexity or "order" of the EEG was performed. As the anesthesia depth increases, the EEG data becomes more

predictable or contains more "order," with more order representing less complexity and a lower entropy index. However, when the depth of anesthesia was shallow, EEG data decreased order and irregularity increased. Unlike the BIS algorithm, the entropy index does not depend on the absolute frequency and amplitude range of the EEG, which is based on the analysis of the physiological condition of the measured patients. EMG signals need to be filtered from their data analysis in BIS monitoring, but entropy index monitoring is useful and in some cases more sensitive to the evaluation of awareness levels or analgesia than EEG. However, its algorithmic complexity is high and its subparameters are rich, which affects the reaction time of this index in a certain period of time. The BIS was used as a value indicating the depth of sedation. However, this value can change significantly in a short period of time due to interference from other instruments in the operating room (such as high-frequency electrical surgery), the effect of EMG on the patient frontal muscle and medication, and changes in the surgical position. Anesthesiologists often use this value to determine that it is true or false.

1.1. Reply to Solve. The field of anesthesia has significant advantages in the development and application of machine learning technology: various computer control systems, such as monitors, drug infusion systems, and anesthesia electronic medical record systems can be directly connected to each patient to collect a large amount of high-fidelity data in real time. Monitoring the depth of anesthesia has always been a key issue for anesthesiologists [7]. Insufficient depth of anesthesia leading to intraoperative awareness may have serious psychological effects on the patient, and overdose of anesthetic may prolong the recovery time of anesthesia and even cause irreversible damage to the patient [8]. Objective, noninvasive, and reliable monitoring of the depth of anesthesia is a challenge for clinical anesthesia.

Therefore, this paper proposes a new method of analyzing propofol anesthesia from two aspects of nine parameter indicators and BIS subparameters, based on self-attention and residual structure of the convolutional neural network.

First, we use Butterworth filter and other methods to preprocess the EEG signal and then use the manual feature extraction method mentioned in related theories to extract the sample entropy, sort entropy, frequency spectrum, and a ratio from the EEG signal. We analyze the characteristics of BIS parameters. BIS parameters are suitable for anesthesia monitoring, combined with a new method of convolutional neural network based on self-attention and residual structure to build a model, and combine different EEG signal parameters with machine learning algorithms to evaluate the anesthesia status can accurately quantify the patient's anesthesia status. This method does not need to refer to the age of the patient and the anesthetic drugs used and can reliably predict the depth of anesthesia. Compared with a single feature, this model can accurately estimate the depth of anesthesia with a higher prediction probability. The experimental results evaluated on the data set show that the method proposed in this paper provides better performance compared with ranking entropy, the ratio, and other traditional methods.

2. Related Work

2.1. Entropy Index

2.1.1. Sample Entropy. The sample entropy (Sampan) was proposed by Richman and Moorman. The sample entropy can represent the complexity of a finite time series [9]. The larger the value of sample entropy, the more irregular the signal is reflected. Given a time series $x(i)$, $1 \le i < \mathrm{N}$ can reconstruct it into $N - m + 1$, a vector $x_m(i)$, which is defined as

$$x_m(i) = \{x(i), x(i+1), \cdots, x(i+m-1)\}, i = 1, 2, \cdots, N - m. \tag{1}$$

Let d be the distance between the vector $x_m(i)$ and $x_m(j)$ the formula as follows:

$$d_{ij}^m = d\left[x_i^m, x_j^m\right] = \max\left(|x(\mathrm{i}+k) - x(j-k)|\right), k = 0, 1, \cdots, m-1. \tag{2}$$

$C_i^m(r)$ is the probability of $x_m(j)$ within the distance r of $x_m(i)$, which is calculated as

$$C_i^m(r) = \frac{n_i(m, r)}{N - m + 1}, i = 1, N - m. \tag{3}$$

Among them, $n_i(m, r)$ is the number of vectors x_j similar to x_i, where $d(x_i, x_j) \le r$. When the embedding dimension is equal to m, the total number of template matches is

$$A(m, r) = \frac{\sum_{i=1}^{N-m} C_i^m(r)}{N - m}. \tag{4}$$

Let $m = m + 1$, and repeat the above steps, the sample entropy of this time series can be expressed as

$$SampEn(r, m, N) = -\mathrm{Ln}\frac{A(m+1, r)}{A(m, r)}. \tag{5}$$

Ln is the natural logarithm. The sample entropy is affected by three parameters r, m, and N. N is the length of the time series, r is the threshold for determining the similarity of the pattern, and m is the length of the comparison sequence. In this paper, we set $N = 500$, $r = 0.2$, and $m = 2$, and the selection of parameters can be based on Bruhn's paper.

2.1.2. Sort Entropy. Sorting entropy (PeEn) provides a simple and robust method for estimating the depth of anesthesia with low computational complexity. It quantifies the number of regularities in the EEG signal and takes into account the time sequence of these values. Given a time series $x_N = [x_1, x_2, \cdots x_N]$ with N points, x_N can be constructed as

$$x_N = \{x(i), x(i+\tau), \cdots, x(i+(m-1)\tau)\}, i = 1, 2, \cdots, N-(m-1)\tau, \tag{6}$$

where τ is the time delay and m represents the embedding dimension. Then, you can rearrange x_i in increasing order:

$$\{x(i+(j_1-1)\tau \le x(i+(j_2-1)\tau) \le \cdots \le x(i+(j_m-1)\tau)\}. \tag{7}$$

The sequence of length m has $J = m!$ permutations. Each vector x_i can be mapped to one of the permutations $J = m!$ Next, the probability p_j of the jth permutation can be defined as

$$P_j = \frac{n_j}{\sum_{j=1}^{m!} n_j}. \tag{8}$$

Among them, n_j is the number of occurrences of the j th arrangement. The sort entropy can be defined as

$$\mathrm{PE} = \frac{\sum_{j=1}^{m!} P_j \log P_j}{\log(m!)}. \tag{9}$$

The calculation of sort entropy depends on the length of the time series N and the time lag of m, where $N = 500$, $m = 4$, and $\tau = 1$. The choice of parameters can be based on the paper by Su et al.

2.1.3. Wavelet Entropy. Wavelet entropy is based on wavelet transform with multiple scales and directions. Choosing the appropriate wavelet base, the original signal will be generated according to different scales, where $C_j(k)$ is the decomposition coefficient of each scale j [10]. The wavelet energy E_j of the signal is defined as follows:

$$E_j = \sum_{k=1}^{L_j} \left|C_j(k)\right|^2, \tag{10}$$

where L_j represents the number of coefficients under each decomposition scale. Therefore, the total energy of the signal can be expressed as

$$E_{\text{total}} = \sum_j E_j = \sum_j \sum_{k=1}^{L_j} \left|C_j(k)\right|^2. \tag{11}$$

Then, we divide the wavelet energy by the total energy to get the relative wavelet energy at each scale j:

$$P_j = \frac{E_j}{E_{\text{total}}} = \frac{\sum_{k=1}^{L_j} \left|C_j(k)\right|^2}{\sum_j \sum_{k=1}^{L_j} \left|C_j(k)\right|^2}. \tag{12}$$

Finally, the wavelet entropy can be calculated from the above:

$$S = -\sum_j P_j \log\left(P_j\right). \tag{13}$$

2.1.4. Band Ratio. The α ratio, β ratio, and (β-α) ratio is also used to monitor the depth of anesthesia. The α ratio is the logarithmic relative power of two different frequency bands, which can be calculated in the following way:

$$\alpha_{\text{ratio}} = \log \frac{E_{30-42.5\text{hz}}}{E_{6-12\text{hz}}}. \tag{14}$$

The formula for β ratio and (β-α) ratio is as follows:

$$\begin{aligned} \beta_{\text{ratio}} &= \log \frac{E_{30-42.5\text{hz}}}{E_{12-21\text{hz}}}. \\ (\beta\text{-}\alpha)_{\text{ratio}} &= \log \frac{E_{6-12\text{hz}}}{E_{11-21\text{hz}}}. \end{aligned} \tag{15}$$

Among them, α_{ratio}, β_{ratio}, and $(\beta\text{-}\alpha)_{\text{ratio}}$ represent α ratio, β ratio, and (β-α) ratio, respectively, and $E_{30-42.5\text{hz}}$, $E_{6-12\text{hz}}$, and $E_{11-21\text{hz}}$, representing the spectral energy of the 30-42.5 Hz, 6-12 Hz, and 11-21 Hz frequency bands, respectively.

2.2. Time Collar Characteristics. Time-frequency analysis is a powerful tool that can decompose a signal into time and frequency components. Therefore, it provides a means for analyzing nonstationary signals (such as brain electrical signals). In the analysis of this kind of signal, people are often interested in the changes in frequency components over time, which is particularly important when analyzing sleep EEG [11]. In sleep EEG, many events (such as sudden waking) are measured by amplitude and the sudden change of frequency characteristics.

Short-time Fourier transform (STET) is the simplest form of time-frequency analysis. Usually, people only consider the squared amplitude of the STFT, and this squared amplitude is called a spectrogram. In order to calculate the short-time Fourier transform, the signal of interest is evenly divided into multiple short-term overlapping parts, and then, the data of each part is windowed and Fourier transformed. The result is a set of Fourier transforms at different points in time that reveals the changes in these spectral properties from one segment to another, which is the evolution of frequency over time. The time-frequency resolution of STFT is directly determined by the size of the window length: the smaller the window length, the higher the time resolution, and the lower the frequency resolution; the larger the window length, the lower the time resolution and the higher the frequency resolution. By increasing the size of the window length, the frequency resolution can be improved at the expense of reducing the time resolution [12]. It should also be noted that a longer window length may violate the quasistationarity assumption required by the Fourier transform.

Therefore, in addition to analyzing the stationarity of the previous signal, issues related to time and frequency resolution should also be considered. Due to its simplicity and ease

of implementation, STFT has been widely used in sleep EEG analysis.

2.3. Common Feature Extraction Methods of EEG Signals. In some past studies of EEG signals, in terms of feature extraction methods, they can be divided into two different categories. The first is the method of extracting features based on manual design. This method requires prior knowledge of EEG analysis to extract the corresponding features. These methods first extract the most common features, such as the time domain, frequency domain, and time-frequency domain features of a single-channel EEG waveform. Then, we apply traditional machine learning algorithms, such as support vector machine (SVM), random forest, and neural network and train the model for the application you want to implement based on the extracted features [13]. The BIS monitor is currently the most authoritative anesthesia status monitor. The BIS index is obtained by the BIS monitor and has a high degree of recognition in clinical anesthesia operations at home and abroad. It integrates multiple EEG parameters into a single indicator, including α ratio, synchronization speed ratio (SFS), median frequency (MPF), and edge frequency (SEF). Narcotrend index compares and analyzes the data accumulated by itself and automatically classifies the extracted EEG signals to judge different states of anesthesia. However, the complexity of its algorithm is relatively high, which affects the reaction time of the indicator in a certain period of time.

Although these methods have achieved reasonable performance, they also have some limitations and require certain prior knowledge of sleep analysis. The second is a method based on automatic feature extraction (for example, deep learning algorithms), in which the machine automatically extracts relevant features (for example, CNN extracts time-invariant features from the original EEG signal).

2.4. Automatically Extracted EEG Signal Features. Most of the features are extracted manually, which requires a certain degree of expertise. In recent years, based on deep learning, the method of automatically learning features from EEG signals has become popular, and there are also many methods of automatic sleep stage classification based on deep learning [14].

Due to the powerful ability of deep learning to automatically learn features from data and the amazing progress of deep networks in many fields, people are interested in applying it to automatic sleep stage classification. Using various deep learning techniques to classify sleep stages, the results obtained have made significant progress. CNN is a classic algorithm of deep learning technology, and it is also often used for sleep stage classification tasks. The weight sharing mechanism of the convolutional layer makes the learned features have shift invariance, reduces the complexity of the model, and improves the generalization ability of the model. Therefore, it is usually used as a supplement to other network types, such as CNN and DNN. Independent CNN has also been used to learn the sequential features of sleep, usually in an end-to-end manner in the network [15].

2.5. Evaluation Indicators. Previously, that is, the sample entropy (SampEn), sorting entropy (PeEn), wavelet entropy, α ratio, β ratio, and (β-α) ratio, synch fast slow (SFS), median frequency (MPF), spectral edge frequency (SEF), BIS, and CNN+BIS, nine kinds of anesthesia state observation indicators are introduced and parameters are selected. In order to compare the relationship between these nine indicators and BIS, the correlation coefficient was calculated.

The correlation coefficient is a measure of the correlation between two time series $x(t)$ and $y(t)$. The formula is as follows:

$$\mathrm{COR}(t) = \frac{\mathrm{cov}\ (x(t), y(t))}{\sqrt{\mathrm{var}\ (x(t)\ \mathrm{var}\ y(t))}}. \tag{16}$$

In the formula, cov $(x(t), y(t))$ is the covariance of $x(t)$ and $y(t)$; var $(x(t))$ is the variance of $x(t)$; and var $(y(t))$ is the variance of $y(t)$.

The correlation coefficient describes the degree of correlation among the variables $x(t)$ and $y(t)$. The value range of COR (t) is $[-1, 1]$. If $\mathrm{COR}(t) > 0$, then there is a positive correlation between $x(t)$ and $y(t)$. However, when $\mathrm{COR}(t) < 0$, there is a negative correlation between $x(t)$ and $y(t)$. This study uses the absolute value of COR (t), namely $|\mathrm{COR}\,(t)|$ to measure the two indicators the degree of correlation between the two indicators. When the $|\mathrm{COR}\,(t)|$ value is greater than 0.8, it is highly correlated, 0.5 to 0.8 is moderately correlated, 0.3 to 0.5 is low correlated, and less than 0.3 indicates no correlation.

In addition, in order to compare the relationship between these 9 indicators and BIS indicators, we calculated the 9 indicator values of the EEG data of 20 patients and then calculated the correlation between them and the CNN+BIS indicators. The statistics of specific relevance are shown in Table 1.

According to the results in the table, the average correlation coefficients of ApEn, α ratio, SampEn, SFS, and CNN+EEG and BIS indicators are all higher than 0.6, indicating that these 6 indicators and BIS indicators have a high correlation during anesthesia. Among them, the correlation coefficient between CNN+EEG and BIS is the largest; indicating that among these nine indicators, CNN+EEG and BIS have the best correlation. Therefore, the parameters with better correlation with the BIS index are selected as the observation index of anesthesia state to carry out the parameter identification of the model.

3. Experiment

3.1. Research on Metabolic Model Based on Deep Learning

3.1.1. Model Construction Ideas. Sheiner's PKPD model consists of two parts, namely, the PK model and PD model. However, the model parameters are greatly affected by individual differences, so there are still some differences between the theoretical model and the actual drug metabolism model. In response to these problems, this paper proposes a scheme of using deep learning algorithms to replace the traditional

Table 1: Correlation coefficients between different indicators and BIS indicators.

Index	SampEn	PeEn	WE	α_{ratio}	β_{ratio}
COR	0.608 ± 0.31	0.621 ± 0.28	0.394 ± 0.36	0.687 ± 0.20	0.596 ± 0.33
Index	$(\beta\text{-}\alpha)_{\text{ratio}}$	SFS	MPF	SEF	CNN+EEG
COR	0.564 ± 0.22	0.607 ± 0.22	0.035 ± 0.44	0.342 ± 0.36	0.717 ± 0.14

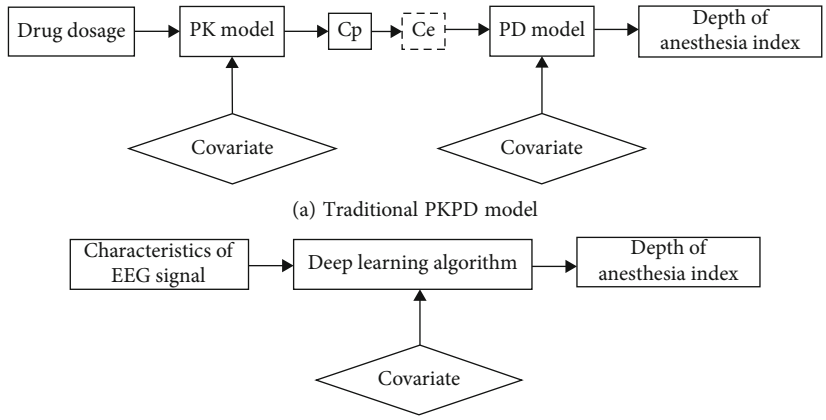

(a) Traditional PKPD model

(b) Metabolic model based on deep learning

Figure 1: Conceptual diagram of the model.

PKPD model. The concept of the model is shown in Figure 1.

Figure 1 is a conceptual diagram of the traditional PKPD model and the metabolic model based on deep learning. Among them, Figure 1(a) is a conceptual diagram of the traditional PKPD model. Among them, Ce represents the effect chamber concentration and Cp represents the blood drug concentration [16]. The covariates are the four physiological parameters of height, weight, gender, and age. Figure 1(b) is a conceptual diagram of a metabolic model based on deep learning, where the input of the model is the feature index and covariate extracted from the EEG signal, and the output of the model is the depth of anesthesia index. In the end, the basis for judging the quality of the model training is the degree of fit between the index values output by the model and the actual index values.

3.1.2. Introduction to CNN Algorithms. The concept of CNN was proposed by Yann at New York University in 1998. CNN is a deep learning algorithm, which has been widely used in image recognition and other fields. The structure of CNN mainly includes the input layer and hidden layer. The hidden layer is the focus of the CNN network. The hidden layer generally includes a pooling layer, a convolutional layer, and a fully connected layer. The convolutional layer and the pooling layer are unique to CNN [17].

Convolution operation is the focus of CNN. Under the action of the convolution kernel, the input data is subjected to convolution operation. Then, we add the deviation term to the obtained result, which can be input into the excitation function, and the value of the upper neuron can be obtained. The value at the (i, j) position on the upper layer is output by the lth convolution kernel on the s layer, which can be expressed as

$$x_{i,j} = f\left(w(s)_j \bullet I(i,j) + d\right), \tag{17}$$

where $I(i, j)$ is the feature of the convolutional layer, f is the activation function; $w(s)_j$ is the jth convolution kernel on the s layer, and d is the deviation term.

3.1.3. Optimize the Network. Convolution can optimize the complexity of the network through the following two parts in the calculation:

(1) Sparse connection in the previous network, the layer connection of neurons is generally fully connected. However, on the CNN, sparse connections are used between layers. This is because in CNN, there is a strong correlation between the two neighboring layers, so the next layer only needs to be connected to the previous layer, that is, local connection. This will not lead to the occurrence of information loss, and can reduce the size of the CNN structural parameters. The sparse connection between two adjacent layers is shown in Figure 2

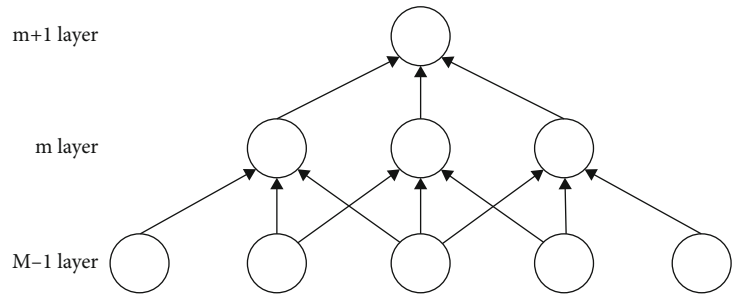

Figure 2: Sparse connection of two adjacent layers.

In Figure 2, the m layer is the hidden layer, and the $m-1$ layer is the input layer. According to the above thoughts, it can be seen that the $m-1$ layer only needs to be connected to the m layer.

(2) For weight sharing in CNN, filter parameters are shared [18]. That is to say, each convolution kernel performs convolution operation on the overall receptive field. The parameters of each convolution kernel have bias terms and weight coefficients. The weight sharing is shown in Figure 3

It can be seen from Figure 3 that the number of neurons in layer m is 3. In the figure, the weights of the lines connecting different positions are shared. You can use gradient descent to learn the shared weights without any changes. The advantage of weight sharing is that it has nothing to do with the location of feature extraction when extracting features. And the number of weight parameters of CNN can be reduced to a greater extent.

After the convolution operation, the maximum pool sampling method is used to reduce the size. By finding the largest feature parameter in this range, and then downsampling, new features are obtained. The features that have undergone downsampling still retain the effective information, and the reduction of the dimensionality is conducive to training. Setting the size of the pooling core to $m \times m$, the method can be expressed as

$$f(x) = \max\left(x_{(i,i+m)(j,j+m)}\right). \tag{18}$$

Finally, the prediction result is output through the fully connected layer. The input of the fully connected layer is the feature output by the CNN, and the output is the value corresponding to the sample to be predicted. Then, the CNN output is

$$y_r = f(w \bullet y_{r-1} + b). \tag{19}$$

3.1.4. Autoencoder. Autoencoder (AE) can be understood as a system that tries to restore its original input; as shown in Figure 4, it is a type of neural network. The blue dashed box is the AE model, which consists of two parts, an encoder f and a decoder g. The encoder converts the input signal x into a hidden representation Y, and the decoder restores y to the output signal x', which is the reconstructed x.

$$\begin{aligned} y &= f(x), \\ x' &= g(y) = g(f(x)). \end{aligned} \tag{20}$$

The purpose of the autoencoder is to recover the input x as much as possible. In fact, the network usually focuses on the encoding of the intermediate layer or the mapping from input to encoding. In other words, when the forced code y is different from the input x, the system can also restore the original signal x; then, the code Y already carries all the information of the original data, which is an effective representation of the automatic learning of the original data.

3.1.5. Self-Attention Mechanism. Data will be generated during the learning process. As the amount of data increases, it is particularly important to clean, analyze, and model these data. In the modeling process, accelerating the training of the model can save a lot of time and cost. Therefore, some scholars proposed the self-attention mechanism based on the attention mechanism of the human brain and successfully applied it in the field of natural language processing [19]. The idea of this model comes from the attention mechanism. The self-attention mechanism can realize parallel computing more easily than the attention mechanism. Its basic structure is shown in Figure 5.

First, we multiply the input text information by the corresponding weights to obtain $q1$, $k1$, and $v1$. The calculation process is as follows:

$$\begin{aligned} q(i) &= W^q x(i), \\ k(i) &= W^k x(i), \\ v(i) &= W^v x(i), \end{aligned} \tag{21}$$

Among them, W^q, W^k, and W^v correspond to the weight matrices of q, k, and v, respectively; $i = [0, N]$, and N is the size of the sample value. We perform the dot product operation on the obtained qi and ki, then normalize the result,

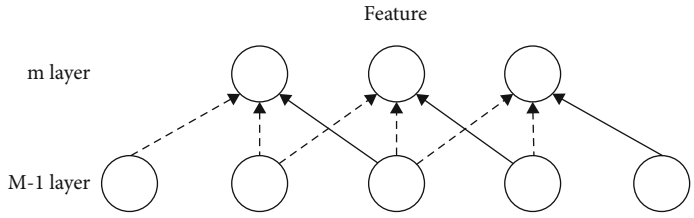

Figure 3: Schematic diagram of weight sharing.

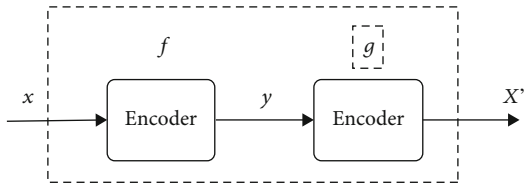

Figure 4: Self-encoder structure.

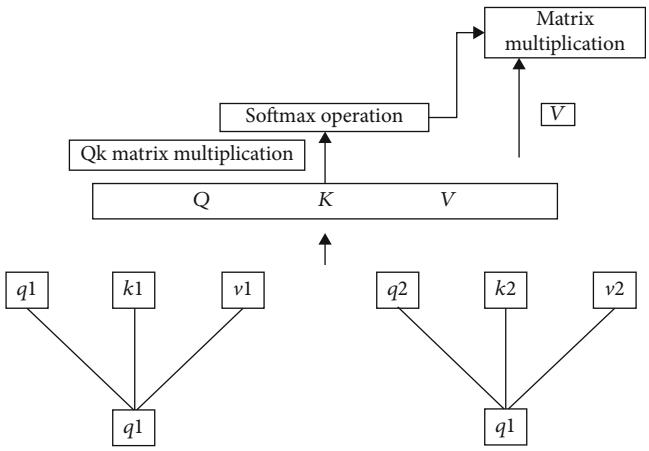

Figure 5: Self-attention mechanism model.

and finally multiply the corresponding weight $v(i)$ to get the output content, namely,

$$\begin{aligned}\alpha(1,i) &= \frac{q(i)\bullet k(i)}{\sqrt{d}},\\ \tilde{\alpha}(1,i) &= \exp\left(\alpha(1,i)\right)/\sum_j \exp(\alpha(1,j)),\\ b(i) &= \sum_i \tilde{\alpha}(1,i)v(i).\end{aligned} \tag{22}$$

It can be seen from the calculation result of $b(i)$ that the result value of each $b(i)$ is related to the entire input sequence, which is also one reason why the self-attention mechanism can speed up the calculation in parallel. The above calculation process is expressed as a matrix:

$$\text{self-Attention}(Q,K,V) = \text{softmax}\left(\frac{QK^T}{\sqrt{d_k}}\right)V. \tag{23}$$

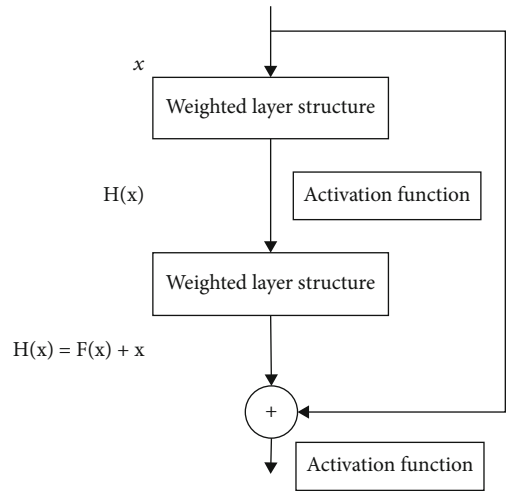

Figure 6: Residual network structure.

Among them, Q, K, and V are matrices formed by concatenating each of the above $q(i)$, $k(i)$, and $v(i)$. Therefore, another reason for the acceleration of the calculation speed is that the essence of the attention mechanism is matrix calculation.

3.1.6. Residual Network. With the continuous development of deep learning, the depth of the network is getting larger and larger. Although the accuracy of the model has been improved, a series of problems have arisen, such as gradient explosion and gradient disappearance. Initializing the weight parameters is particularly important. A reasonable weight value can prevent the parameters from entering the activation function saturation region, thereby reducing the problems of gradient disappearance and gradient explosion. However, the method of randomly initializing parameters is inefficient. He et al. [20] and others proposed a deep residual model (residual network (ResNet)), which not only solves the problem of gradient disappearance caused by deep networks but also solves the problem of network degradation. At the same time, the accuracy of the model has been improved. The basic residual structure is shown in Figure 6:

x is the information input, $H(x)$ is the characteristic information output, $F(x)$ is the residual, and its expression is

$$F(x) = H(x) - x. \tag{24}$$

The information input x can be directly connected to the back access layer, so that the back access layer can learn the

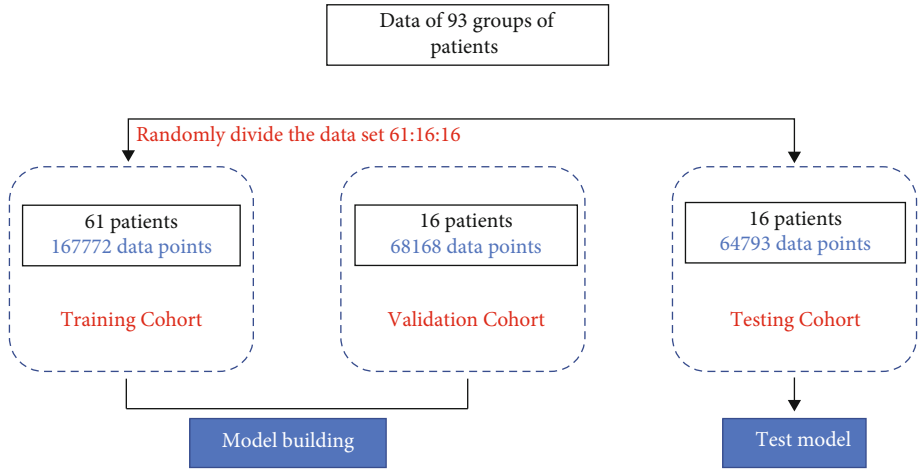

Figure 7: Division of the data set.

Table 2: Data set characteristics.

	Training cohort	Validation cohort	Testing cohort
Quantity	61	16	16
Weight (kg)	68.8 ± 10.2 (54-87)	67.2 ± 9.5 (55-81)	74.4 ± 8.8 (59-93)
Gender (male/female)	46/17	11/4	11/4
Age	55.4 ± 12.1 (22-83)	49 ± 11.5 (36-72)	57.3 ± 10.4 (24-78)
Height (cm)	167.4 ± 5.2 (158-180)	166.5 ± 5.3 (162-178)	169.7 ± 4.6 (160-180)

Table 3: Parameter settings of each layer of CNN.

Layer	Layer type	Nuclear model	Stride	Number of zero-padded turns	Output feature map size	Number of output feature maps
1	Convolutional layer 1	3 × 3	1	1	24 × 24	16
2	Pooling layer 1	2 × 2	2	—	12 × 12	16
3	Convolutional layer 1	3 × 3	1	1	12 × 12	32
4	Pooling layer 1	2 × 2	2	—	6 × 6	32
5	Convolutional layer 1	3 × 3	1	1	6 × 6	64
6	Pooling layer 1	2 × 2	2	—	3 × 3	64
11	Output layer	—	—	—	—	1

dual layer, so this connection is also called a shortcut connection. The residual structure increases the depth of the model through identity mapping. The basic operation is

$$x_L = x_l + \sum_{i=1}^{L-1} F(x_i, w_i). \tag{25}$$

x_l is the information representation of the features of the Lth depth unit. When the residual value is 0, the residual network is equivalent to performing identity mapping, so as to ensure that the training accuracy of the model will not decrease. In fact, due to the complexity and diversity of the data, the residual value will not be 0, which is equivalent to the model is constantly stacking layers to better learn new features.

3.2. Parameter Setting of Each Layer. This paper uses the method of combining multiple convolutional layers, pooling layers, and superimposing the output of the fully connected layer to train the input data to be trained. In the setting of the training parameters of the CNN model, the learning rate is 0.01, and the ReLU function is used as the excitation function of each convolutional layer [21]. In the setting of the pooling layer, the maximum pool sampling method is used to reduce the output of the convolutional layer. We use

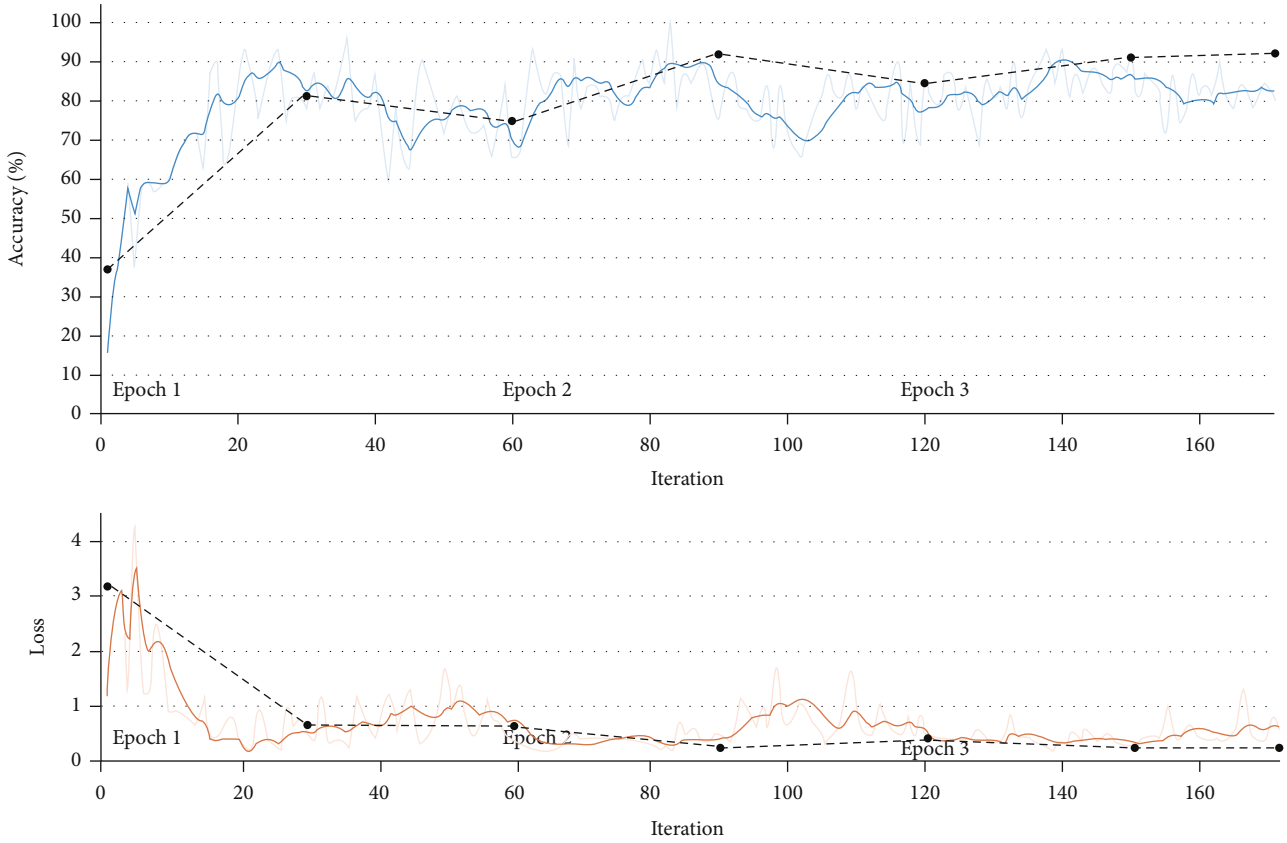

Figure 8: The optimal result of CNN tracking BIS on the test set.

SoftMax regression to output the predicted anesthesia state value.

In the model training, data from 93 groups of patients were used. First, it is divided into three parts: training set, validation set, and test set by random grouping. The grouping results are as follows: the training set includes 61 patient data (167772 data points in total), the validation set includes 16 patient data (68168 data points in total), and the test set includes 16 patient data (64793 data points in total), such as Figure 7. The specific data set characteristics are shown in Table 2.

In the part of the deep learning algorithm, a two-dimensional regressor is used. At this time, it is necessary to convert the one-dimensional EEG feature sequence into a two-dimensional matrix as the image format. Taking into account the s parameters as characteristic indicators and the four physiological parameters of height, weight, age, and gender, 48 indicator data were selected for combination in the same period, and they were sequentially combined into 576 numerical sequences. Then, we reshape 576 one-dimensional sequences into 24×24 two-dimensional matrices as the samples to be trained.

The sample set to be trained is used as the input of CNN, and the parameter settings and output of each layer are shown in Table 3:

3.3. Evaluation Indicators. In this paper, goodness of fit, mean square error, and average percentage error are used to evaluate the simulation prediction results. The calculation formula is as follows:

$$R^2 = 1 - \frac{\mathrm{SSE}}{\mathrm{SST}}, \tag{26}$$

$$\mathrm{RMSE} = \sqrt{\frac{\sum_{i=1}^{n}(e_i - \bar{e})}{n}}, \tag{27}$$

$$\mathrm{MAPE} = \sum_{i=1}^{n}\left|\frac{\mathrm{observed}_t - \mathrm{predicted}_t}{\mathrm{observed}_t}\right| \times \frac{100}{n}. \tag{28}$$

The meaning of these metrics is described as follows: The R^2 coefficient in (26) is the goodness of fit of the model output, and the range is $(0, 1)$. When the value of the goodness of fit is larger, it means that the result predicted by the model is closer to the true value; that is, the drug metabolism model obtained by training is more accurate [22–25]. Among them, SST is the sum of squared deviations, and SSE is the sum of squared residuals; RMSE in the Equation (27) is the mean square error of the training result. If its value is small, it means that the error of the training result is small. Among them, e_i is the test sample value, and $\bar{e}$ is the average value of e; MAPE in the Equation (28) is the average percentage error.

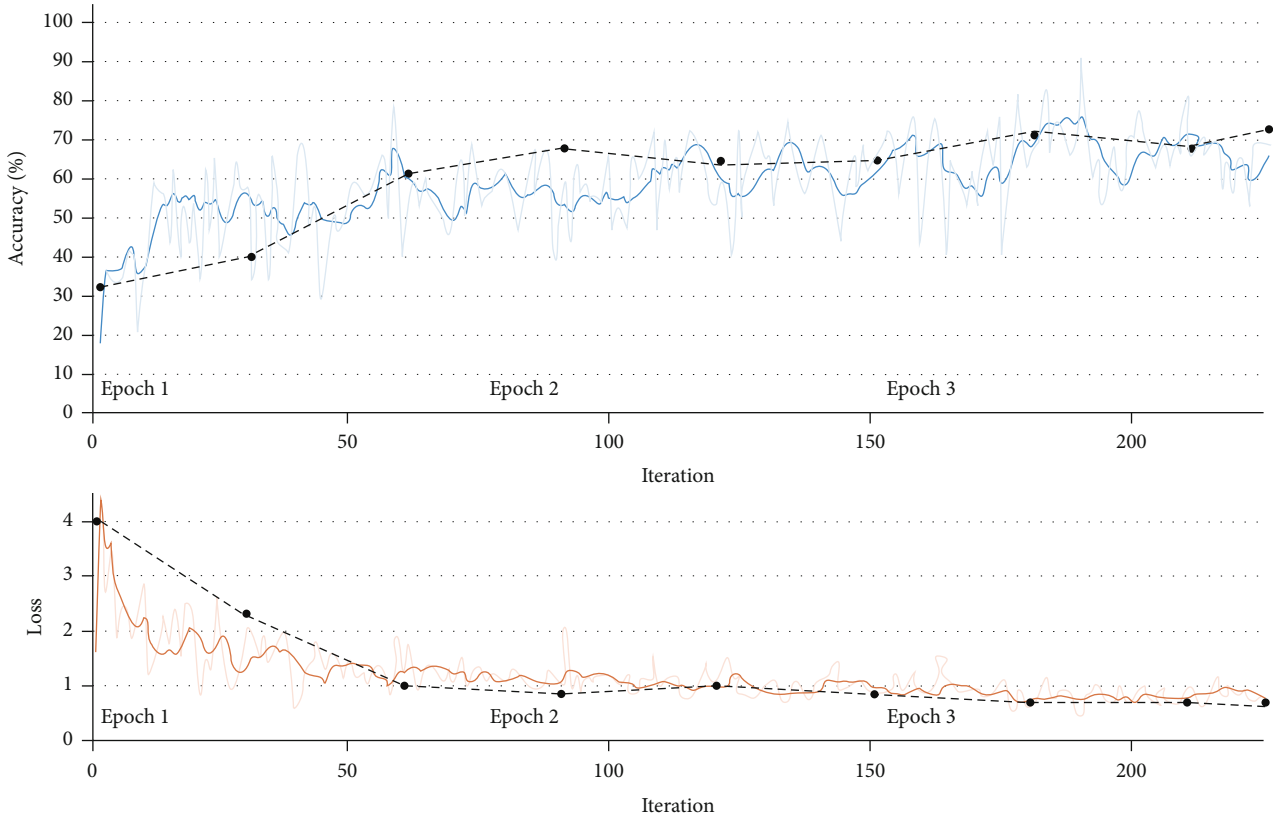

Figure 9: The worst result of CNN tracking BIS on the test set.

4. Results

We use the CNN network to construct the drug metabolism model. We take the 8 characteristic parameters of SPE, ApEn, SampEn, SFS, α ratio, SEF95, MPF, SpEn, height, weight, age, gender, and BIS indicators extracted from the clinical EEG data of the patient as the input of the network model for training. Model training adopts a 5-fold cross-validation method, and the best and worst results of BIS prediction are shown in Figures 3–7 and Figures 3–8.

Figures 8 and 9, respectively, show the best and worst results of CNN model tracking BIS on the test set. Among them, the lighter solid line is the result of each iteration, the darker solid line is the result of smoothing the iteration result, and the black dashed line is the result of each verification. After every 30 iterations, the prediction results are verified once.

The curves in Figures 8 and 9, respectively, show the trend of the iterative verification accuracy of the CNN model on the test sample and the error trend with the number of iterations.

According to Figure 8, the whole process is displayed in 3 time periods, and each time period is iterated 57 times, a total of 171 iterations. The accuracy and error are verified every 30 iterations. It can be seen that as the number of iterations continues to increase; the accuracy of CNN in predicting BLS on the test set is generally on the rise, eventually reaching more than 90%. The overall error shows a gradual decrease and eventually approaches zero.

Figure 9 is also displayed in three time periods; each time period is iterated 75 times, a total of 225 iterations. The accuracy and error are verified every 30 iterations. It can be seen that as the number of iterations continues to increase, and the accuracy of the model for predicting BIS on the test set is generally on the rise. The accuracy rate is relatively stable without major fluctuations, but the final accuracy rate is above 70%.

Further, we analyzed the results of several representative data samples and drew the corresponding curves, as shown in Figure 10. It can be seen intuitively from Figure 10 that through the training of the CNN model, a better BIS curve prediction can be achieved.

It can be seen intuitively from Figure 10 that through the training of the CNN model, a better BIS curve prediction can be achieved. Figure 10(a) is a BIS prediction tracing curve of a 39-year-old man, Figure 10(b) is a BIS prediction tracing curve of a 28-year-old woman, and Figure 10(c) is a BIS prediction of a 70-year-old man. Figure 10(d) shows the BIS prediction tracking curve of a 65-year-old female. According to the comparative analysis of different ages, the fit of the drug metabolism model based on the CNN training model has a certain relationship with the age of the patient. The fit is better in the young and middle-aged, and the fit is poor in the old. From the comparative analysis of different periods of anesthesia, it can be seen that in the induction period of anesthesia, the fitting effect of the predicted results is poor, and there is a relatively large deviation from the actual BIS value. At the same time, when the data fluctuates

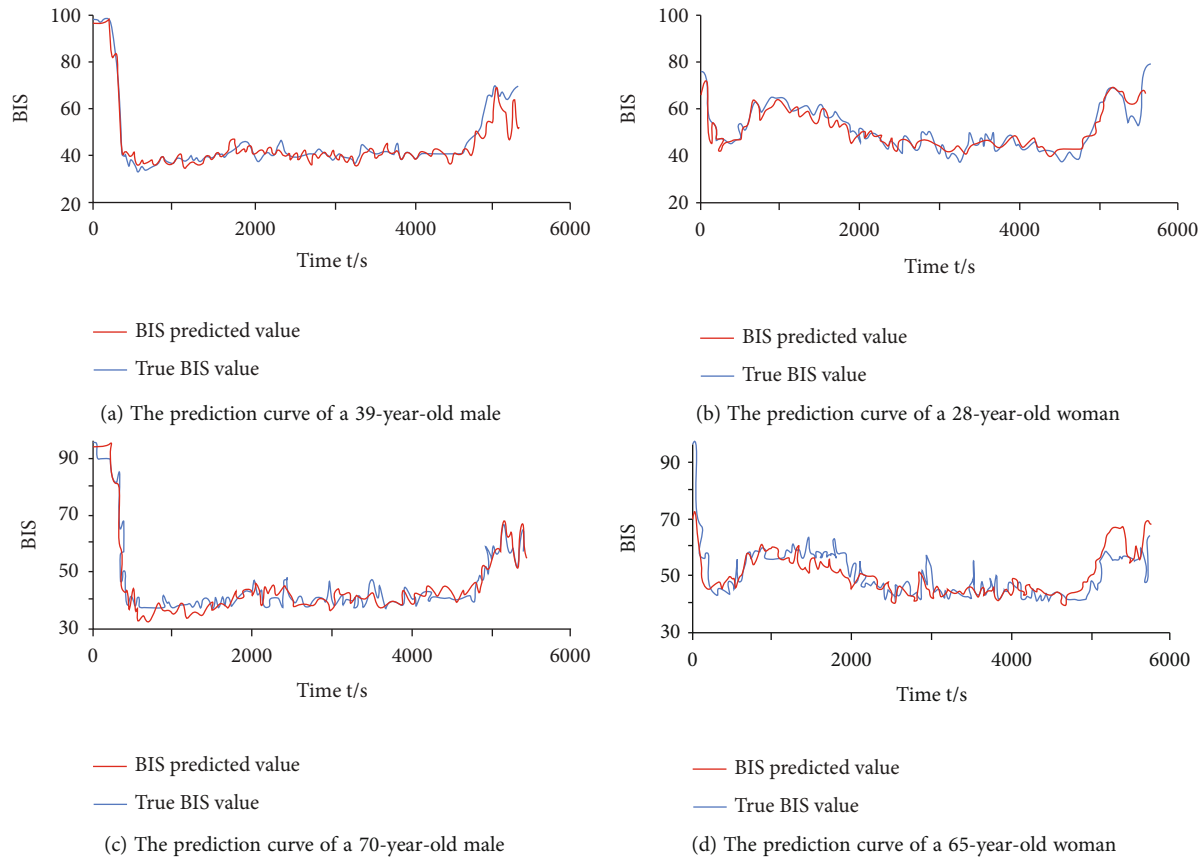

Figure 10: Predictive tracking curve of 4 patients.

Table 4: CNN's prediction result evaluation table.

Period of anesthesia	R^2 (%)	RMSE	MAPE (%)
Induction period	81.65 ± 9.5	7.1 ± 1.5	10.5 ± 3.0
Maintenance period	85.28 ± 8.8	5.2 ± 0.8	8.8 ± 2.5
Recovery period	80.33 ± 9.2	6.7 ± 1.2	9.8 ± 3.1
Whole paragraph	84.97 ± 8.4	5.5 ± 1.0	9.1 ± 2.8

greatly, the predicted effect of the model is not good. But as a whole, the prediction results are within the range available in statistics.

In order to make the predictable result of the model more accurate, the prediction results data of each stage of anesthesia were counted. This paper mainly uses R^2 coefficient, RMSE, and MAPE to evaluate the prediction results. The statistical results are shown in Table 4.

It can be obtained from Table 4 that in the prediction results of the controlled object based on the CNN training model, the maximum goodness of fit value of the test data set is 93.34 (%), and the smallest is 66.72 (%). The maximum RMSE value is 6.89, the minimum is 4.04, the maximum MAPE value is 14.73 (%), and the minimum is 3.99 (%).When analyzing the different stages of anesthesia, it was found that the predictive model performed the most stable in the maintenance phase and slightly worse in the induction and recovery phases. But on the whole, the predictive effect is within the range available in statistics.

5. Discussion

The analytical ability of machine learning algorithms is extremely high, which is superior to classical statistics. In recent years, great breakthroughs have been made in the imaging diagnosis of pulmonary nodules [22], and while maintaining good sensitivity with higher specificity than traditional methods, [23] deep learning algorithms also have good prospects in the sedation monitoring of anesthesia. For the small- and medium-sized surgery of ASAI-II can obviously assist the anesthesiologist to make the appropriate judgment to reduce the work intensity; but for the patients with ASAIII-IV undergoing large surgery, the use of vasoactive drugs is more complicated due to the drastic hemodynamic changes, and how to improve the sensitivity and stability of the analysis under this conditions is the direction of our next study At the same time, it is necessary to pay attention to the shortcomings of artificial intelligence itself, such as the inability to empathize with the patient, the inability to understand the patient's acceptance of anesthesia and surgical methods, and the trust in intelligent medical care degree [24]. It is very difficult for anesthesiologists to

understand the internal mechanisms of machine learning. Although the machine learning algorithm has been successful in various trials, it is difficult for clinicians to judge whether there will be errors inside the "black box," so it may be difficult for the machine learning algorithm to gain the clinician's reliance. Finally, the necessary premise of machine learning algorithms is to collect a large amount of high-fidelity physiological monitoring data from patients [25]. If the data is incomplete, unstable, biased, or even wrong in the training process, it may produce wrong results and mislead the doctor to make wrong judgments.

Therefore, it is necessary to ensure that a large amount of high-quality data is available to promote the success of machine learning in terms of adaptive control [26]. At present, the most reasonable way to introduce artificial intelligence and machine learning into anesthesia practice is still to manage the use of a closed-loop control system of drugs during routine operations of patients to maintain a stable anesthetic drug maintenance [27]. However, artificial intelligence has entered the field of anesthesia as a stepping stone, which brings challenges to the future development of anesthesiologists, as well as opportunities for professional development. It can effectively reduce the workload of anesthesiologists and give doctors more time and energy to focus on the impact of the progress of the surgery on patients. Of course, AI cannot completely replace anesthesiologists; anesthesiologists have to be prepared for the change of work philosophy [28].

6. Conclusion

With the advent of the "big data" era, artificial intelligence technology and the information industry will play a huge role in promoting the development of human health. More and more machine learning technologies may enter perioperative medicine, affect clinical decision-making, and improve patient's prognosis. The intelligent machine algorithm's assessment of patients and precise control of anesthesia will provide patients with a more comfortable anesthesia experience. In-depth monitoring of anesthesia is of great significance to improving the quality of anesthesia and ensuring the safety and rehabilitation of patients during the surgical period. Systematically, we review the EEG signal analysis algorithm, first compare the advantages and disadvantages of these parameters in clinical application, then propose the ranking entropy index algorithm with excellent denoising ability, and introduce the reverse mapping neural network to correct and optimize the EEG double frequency index, anesthesia trend, and ranking entropy index, so order to more accurately realize anesthesia depth monitoring. This paper introduces deep anesthesia monitoring as a deep CNC learning algorithm. A combination of index parameters extracted from the EEG signals and BIS index data was used as input for training. The results show that its prediction of BIS indicators reflects better statistical results. This paper introduces a deep learning method CNN algorithm. The index parameter combination extracted from the EEG signal and the BIS index data is used as input for training. The results show that its prediction of BIS indicators reflects better results in statistics.

Data Availability

All data analyzed during this study are available from the corresponding author upon request.

Conflicts of Interest

The authors declare no conflicts of interest.

Authors' Contributions

Yachao Wang and Tingting Zhao contributed equally to the work.

References

[1] D. Kai li, *Clinical observation of short-term memory and attention after awakening patients under intravenous anesthesia*, vol. 3, Wannan Medical College, 2020.

[2] F. Jianhua, "Observation of nausea and vomiting in general anesthesia patients in the anesthesia recovery room and resuscitation nursing countermeasures," *Chinese Community Physician*, vol. 34, no. 13, pp. 154-155, 2018.

[3] "Detrimental effects of general anaesthesia on young primates: are we closer to understanding the link?," *British Journal of Anaesthesia*, vol. 126, no. 3, pp. 575–577, 2021.

[4] Y. Yi feng and F. Zhidong, "The application research progress of anesthesia depth monitoring indicators in perioperative anesthesia," *Modern Medicine and Health*, vol. 37, no. 12, pp. 2026–2029, 2021.

[5] D. Qiu, Y. Cheng, X. Wang et al., "Gradual back-projection residual attention network for magnetic resonance image super-resolution," *Computer Methods and Programs in Biomedicine*, vol. 208, article 106252, 2021.

[6] K. K. L. Wong, G. Fortino, and D. Abbott, "Deep learning-based cardiovascular image diagnosis: a promising challenge," *Future Generation Computer Systems*, vol. 110, pp. 802–811, 2020.

[7] W. You ran, C. Li h, and Y. l. Ge, "Application progress of deep learning in anesthesiology research," *Journal of Clinical Anesthesiology*, vol. 37, no. 7, pp. 762–764, 2021.

[8] D. A. Hashimoto, E. Witkowski, L. Gao, O. Meireles, and G. Rosman, "Artificial intelligence in anesthesiology: current techniques, clinical applications, and limitations," *Anesthesiology*, vol. 132, no. 2, pp. 379–394, 2020.

[9] L. Jun, Y. q. Zhou, C. Shao bin, X. Tian H, C. Xiao, and X. Fei, "Research on the depth evaluation index of anesthesia consciousness based on sample entropy and decision tree," *Journal of Biomedical Engineering*, vol. 32, no. 2, pp. 434–439, 2015.

[10] D. Qiu, L. Zheng, J. Zhu, and D. Huang, "Multiple improved residual networks for medical image super-resolution," *Future Generation Computer Systems*, vol. 116, pp. 200–208, 2021.

[11] R. Shalbaf, H. Behnam, J. W. Sleigh, A. Steyn-Ross, and L. J. Voss, "Monitoring the depth of anesthesia using entropy features and an artificial neural network," *Journal of Neuroscience Methods*, vol. 218, no. 1, pp. 17–24, 2013.

[12] Q. Liu, Y. F. Chen, S. Z. Fan, M. F. Abbod, and J. S. Shieh, "A comparison of five different algorithms for EEG signal analysis in artifacts rejection for monitoring depth of anesthesia," *Biomedical Signal Processing and Control*, vol. 25, pp. 24–34, 2016.

[13] "Prediction of bispectral index during target-controlled infusion of propofol and remifentanil," *Anesthesiology*, vol. 128, no. 3, pp. 492–501, 2018.

[14] D. Qiu, Y. Cheng, and X. Wang, "Progressive U-Net residual network for computed tomography images super-resolution in the screening of COVID-19," *Journal of Radiation Research and Applied Science*, vol. 14, no. 1, pp. 369–379, 2021.

[15] H. Jiangshan, W. Gao, S. Jing, and W. L. Wang, "Research on medical image data management method based on convolutional neural network and long short-term memory network," *Medicine and Society*, vol. 33, no. 6, pp. 84–89, 2020.

[16] P. Morissette, S. Polak, A. Chain et al., "Combining an *in silico* proarrhythmic risk assay with a tPKPD model to predict QTc interval prolongation in the anesthetized guinea pig assay," *Toxicology and Applied Pharmacology*, vol. 390, p. 114883, 2020.

[17] H. Zhang Shi, D. Du Sheng, J. Zhen, and T. R. Li, "Medical entity relationship extraction based on deep neural network and self-attention mechanism," *Computer Science*, vol. 48, no. 10, pp. 77–84, 2021.

[18] Z. Tang, G. Zhao, and T. Ouyang, "Two-phase deep learning model for short-term wind direction forecasting," *Renewable Energy*, vol. 173, pp. 1005–1016, 2021.

[19] O. Firat, K. Cho, and Y. Bengio, "Multi-way, multilingual neural machine translation with a shared attention mechanism," *Computer Science and Exploration*, 2016, http://arxiv.org/abs/1601.01073.

[20] K. He, X. Zhang, S. Ren, and J. Sun, "Deep residual learning for image recognition," in *Proceedings of the IEEE Conference on Computer Vision and Pattern Recognition*, pp. 770–778, 2016.

[21] G. Lin and W. Shen, "Research on convolutional neural network based on improved Relu piecewise activation function," *Procedia Computer Science*, vol. 131, pp. 977–984, 2018.

[22] W. Ye, W. Gu, X. Guo et al., "Detection of pulmonary ground-glass opacity based on deep learning computer artificial intelligence," *Biomedical Engineering Online*, vol. 18, no. 1, p. 6, 2019.

[23] R. M. Perl, R. Grimmer, T. Hepp, and M. S. Horger, "Can a novel deep neural network improve the computer-aided detection of solid pulmonary nodules and the rate of false-positive findings in comparison to an established machine learning computer-aided detection?," *Investigative Radiology*, vol. 56, no. 2, pp. 103–108, 2021.

[24] Y. Gu, Z. Liang, and S. Hagihira, "Use of multiple EEG features and artificial neural network to monitor the depth of anesthesia," *Sensors*, vol. 19, no. 11, pp. 2499–2510, 2019.

[25] S. Kendale, P. Kulkarni, A. D. Rosenberg, and J. Wang, "Supervised machine-learning predictive analytics for prediction of postinduction hypotension," *Anesthesiology*, vol. 129, no. 4, pp. 675–688, 2018.

[26] Z. H. Tang, Y. Y. Li, X. Y. Chai, H. Y. Zhang, and S. X. Cao, "Adaptive nonlinear model predictive control of NOx emissions under load constraints in power plant boilers," *Journal of Chemical Engineering of Japan*, vol. 53, no. 1, pp. 36–44, 2020.

[27] C. W. Connor, "Artificial intelligence and machine learning in anesthesiology," *Anesthesiology*, vol. 131, no. 6, pp. 1346–1359, 2019.

[28] R. Pirracchio, M. J. Cohen, I. Malenica et al., "Big data and targeted machine learning in action to assist medical decision in the ICU," *Anaesthesia Critical Care & Pain Medicine*, vol. 38, no. 4, pp. 377–384, 2019.

Hindawi
Computational and Mathematical Methods in Medicine
Volume 2022, Article ID 7193902, 10 pages
https://doi.org/10.1155/2022/7193902

Research Article

Patellar Height after High Tibial Osteotomy of the Distal Tibial Tuberosity: A Retrospective Study of Age Stratification

Tiansong Ding,[1] Yetong Tan,[2] Xiangdong Tian,[2] Zhipeng Xue,[2] Sheng Ma,[2] Yuanyi Hu,[2] Ye Huang,[1] and Xiaomin Li[1]

[1]*Beijing University of Chinese Medicine, Beijing 100029, China*
[2]*Minimal Invasive Joint Department, The Third Affiliated Hospital of Beijing University of Chinese Medicine, No. 51 Anwai Xiaoguan Street, Chaoyang District, Beijing 100029, China*

Correspondence should be addressed to Xiangdong Tian; c083@bucm.edu.cn

Received 7 November 2021; Revised 6 December 2021; Accepted 11 January 2022; Published 27 January 2022

Academic Editor: Kelvin Wong

Objective. To explore the effect of age stratification on patellar height after single-plane high tibial osteotomy of the distal tibial tuberosity (DTT-HTO). *Methods*. A retrospective analysis was performed on 110 knee joints undergoing DTT-HTO. Patients were divided into three groups according to age: under 60 years old, 28 cases; 60 to 70 years old, 61 cases; and over 70 years old, 21 cases. All patients were followed up for no less than 12 months, and at each follow-up, short-leg radiographs and whole-leg radiographs were taken. The values of the Caton-Deschamps index (CDI) and Blackburne-Peel index (BPI) of single-short-leg radiographs and the femoral-tibial angle (FTA) and weight-bearing line ratio (WBLR) of whole-leg radiographs were measured before and at the last follow-up. The Lysholm score before and at the last follow-up and the visual analogue scale (VAS) score before and 3 days after surgery and at the last follow-up were calculated. The frequency of classification of the normal-height patella, patella alta, and patella baja before and after surgery was recorded. *Results*. There were no significant differences in CDI and BPI preoperatively or postoperatively among the three groups ($P > 0.05$), and there were no statistically significant differences in FTA and WBLR. There were no significant differences in CDI, BPI, FTA, or WBLR between the three groups before and after the operation ($P > 0.05$). The Lysholm score increased from 48.84 ± 10.10 before surgery to 91.96 ± 3.082 after surgery ($P < 0.05$); the VAS score decreased from 8.23 ± 0.99 before surgery to 1.93 ± 0.953 at 3 days after surgery and 1.07 ± 0.53 at the last follow-up ($P < 0.01$). No significant difference was observed in the incidence of each patellar height classification between the three groups preoperatively and postoperatively. *Conclusion*. Patellar height is not influenced by DTT-HTO. The age of patients is not a limiting factor for the selection of this surgical procedure. Without affecting the height of the patella, DTT-HTO can effectively reduce pain in the knee joint, restore the function of the knee joint, and delay the progression of patellar arthritis.

1. Introduction

High tibial osteotomy is one of the surgical methods for treating medial compartment knee osteoarthritis. Traditional HTO is divided into closing-wedge high tibial osteotomy (CWHTO) and open-wedge high tibial osteotomy (OWHTO), and both procedures can effectively correct the coronal weight-bearing line of the knee joint, transfer the lower limb alignment from the medial compartment of the knee joint to the lateral compartment, increase the stress area of the tibiofemoral joint, and reduce the pressure of the medial compartment to relieve medial compartment knee pain and help patients recover walking function [1–13]. The mechanical properties of a biostructure depend on its Young's modulus (E). Therefore, it is likely that a harder substance has a larger E [14]. For instance, the value of E for bone is 14 GPa. However, HTO can also affect the postoperative bone structure of the patellofemoral joint, resulting in patella alta or patella baja compared to the preoperative situation. Therefore, measurement methods [15] such as CDI [16] and BPI [16] are often used to test whether the height of the patella changes.

Table 1: Characteristics of the three groups.

	<60 years ($n = 28$)	60~70 years ($n = 61$)	>70 years ($n = 21$)	Value	P
Sex					
Male	8	15	5	$\chi^2 = 0.197$	0.906
Female	20	46	16		
Knee					
Left	20	33	15	$\chi^2 = 3.458$	0.178
Right	8	28	6		
Duration of disease (years)	8.50 ± 1.972	8.85 ± 2.056	9.29 ± 2.935	$F = 0.747$	0.476
BMI (body mass index) (kg/m^2)	26.40 ± 3.046	26.38 ± 3.195	25.89 ± 2.586	$F = 0.224$	0.800
BMD t-score					
≤-2.5 (%)	2	9	6	$\chi^2 = 5.508$	0.239
>-2.5~≤-1.5 (%)	5	15	6		
>-1.5 (%)	19	37	9		
Varus deformity (°)	8.71 ± 2.088	9.16 ± 2.099	9.62 ± 2.519	$F = 1.043$	0.356
Duration of follow-up (months)	20.86 ± 5.707	21.64 ± 4.401	24.05 ± 4.78	$F = 2.815$	0.064

There are different opinions about the effect of HTO on patellar height, but a consensus has already been reached regarding whether high tibial osteotomy above the tibial tuberosity can affect patellar height [6, 12, 17–20]. This was confirmed by previous retrospective clinical studies of DTT-HTO conducted by our team [9]. Patellar height disorder can lead to cartilage degeneration of the patellofemoral joint, loss of function, knee pain, and recurrent patellofemoral dislocation. The pressure on the patellofemoral joint increases during the bending of the patella baja; therefore, the possibility of patellofemoral joint degeneration increases [2]. Patellar instability is often associated with patellar alta, and long-term patellar instability can lead to knee pain, functional limitations, and osteoarthritis. The inability causes the patella to move outward when knee flexural activity, especially during the first 30°, is unable to pull the patella [21]. Because of the patella alta state, the contact area between the patella and the femur decreases, the pressure increases, and the patellofemoral joint wear increases, resulting in patellofemoral chondromalacia [22].

Current literature reports that HTO is suitable for young, active knee osteoarthritis patients with high functional needs. In previous studies, 60 years [23–25] or 65 years [26] was the age limit often used as the inclusion criterion for HTO surgical indicators. This may be due to the influence of certain variables (such as osteoporosis) that change with age on the outcome of surgery. However, it has been found that a number of knee osteoarthritis (KOA) patients aged over 60 or 65 years old also achieve good clinical efficacy by HTO in clinical practice. They often experience relief from knee pain in a short period of time and gradually recover walking, going up and down the stairs, flexion and extension functions, and so on. More research on the effect of HTO on patellar height has focused on the choice of surgical procedures; some studies have challenged the age limitation in HTO inclusion criteria, but no literature has been found on the effect of age on patellar height after HTO. The purpose of this study was to observe the influence of age on patellar height after DTT-HTO and to explore whether the age restriction can be broken and whether more surgical options can be provided to patients with KOA.

2. Methods

2.1. Patients. A retrospective study of 128 patients who received DTT-HTO in the Third Affiliated Hospital of Beijing University of Chinese Medicine from August 2016 to June 2020 was conducted. Except for the 18 cases that were removed according to the inclusion and exclusion criteria, a total of 110 patients aged 51 to 82 were divided into three groups according to age: under 60 years old, 28 cases; 60 to 70 years old, 61 cases; and over 70 years old, 21 cases. There was no significant difference in demographics or parameters among the three groups (Table 1). Inclusion criteria are as follows: (1) medial compartment arthritis of grade k-L: ≥3, lateral: ≤1; (2) follow-up time ≥ 12 months; and (3) image data that were completed and that comprised approximately 30° flexion knee lateral radiographs and whole-leg radiographs before and at the last follow-up. Exclusion criteria are as follows: (1) rotational angles existing between the medial femoral condyle and the lateral femoral condyle in one of the lateral radiographs and (2) patients suffering from types of arthritis other than KOA.

2.2. Operative Procedure. Starting from 1 cm below the midpoint of the medial joint line, an incision of approximately 5 cm was made downward to separate the skin, subcutaneous, deep fascia, muscle, and periosteum in turn to expose the tibial bone surface (Figure 1(a)), avoiding harming the patellar tendon and pes anserinus. A Kirschner wire was inserted from the distal tibial tubercle to 0~1 cm below the tibiofibular fornix at an angle of 30° to 45° to the vertical line of the longitudinal axis of the tibia. The position of the

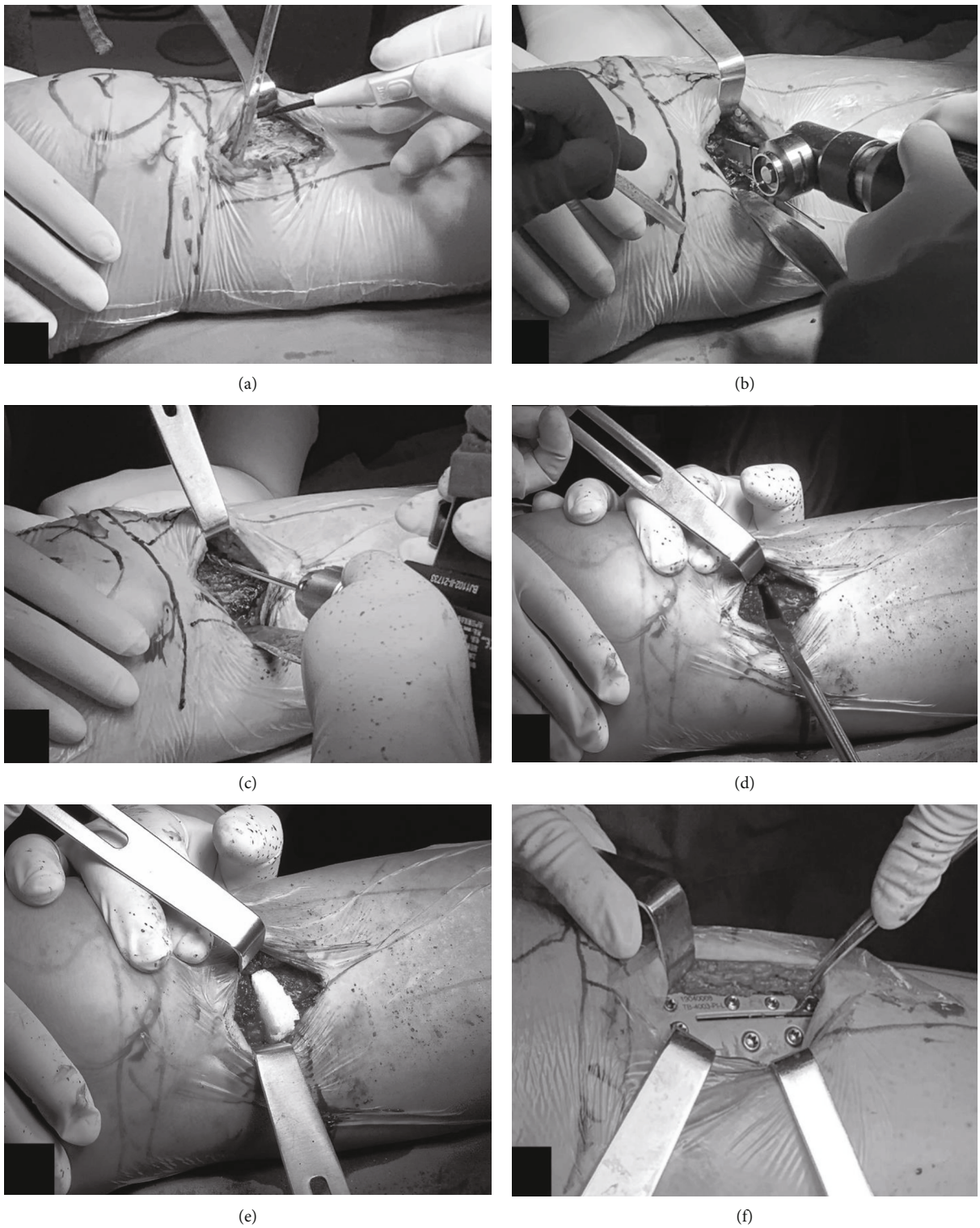

(a) (b) (c) (d) (e) (f)

Figure 1: Intraoperative operation of DTT-HTO. (a) Exposure of the tibial bone surface. (b) The medial tibia was sawed by a bone saw along the Kirschner wire route. (c) Use of a Kirschner wire to drill holes from the osteotomy area to the opposite side to weaken the lateral bone cortex. (d) Opening up the osteotomy area with the bone knife. (e) Implantation of bone substitutes. (f) Placement of the guide plate and its fixation with screws.

Kirschner wire was observed on the C-arm, and a bone saw cut the medial tibia off along the Kirschner wire (Figure 1(b)), leaving 1 cm of cortical bone on the lateral side of the tibia. The lateral cortex was loosened by drilling holes from the osteotomy area to the lateral residual cortex (Figure 1(c)). The assistant performed valgus and rotation stress on the operative limb, and the surgeon used a bone knife to open it up (Figure 1(d)) to change the lower limb

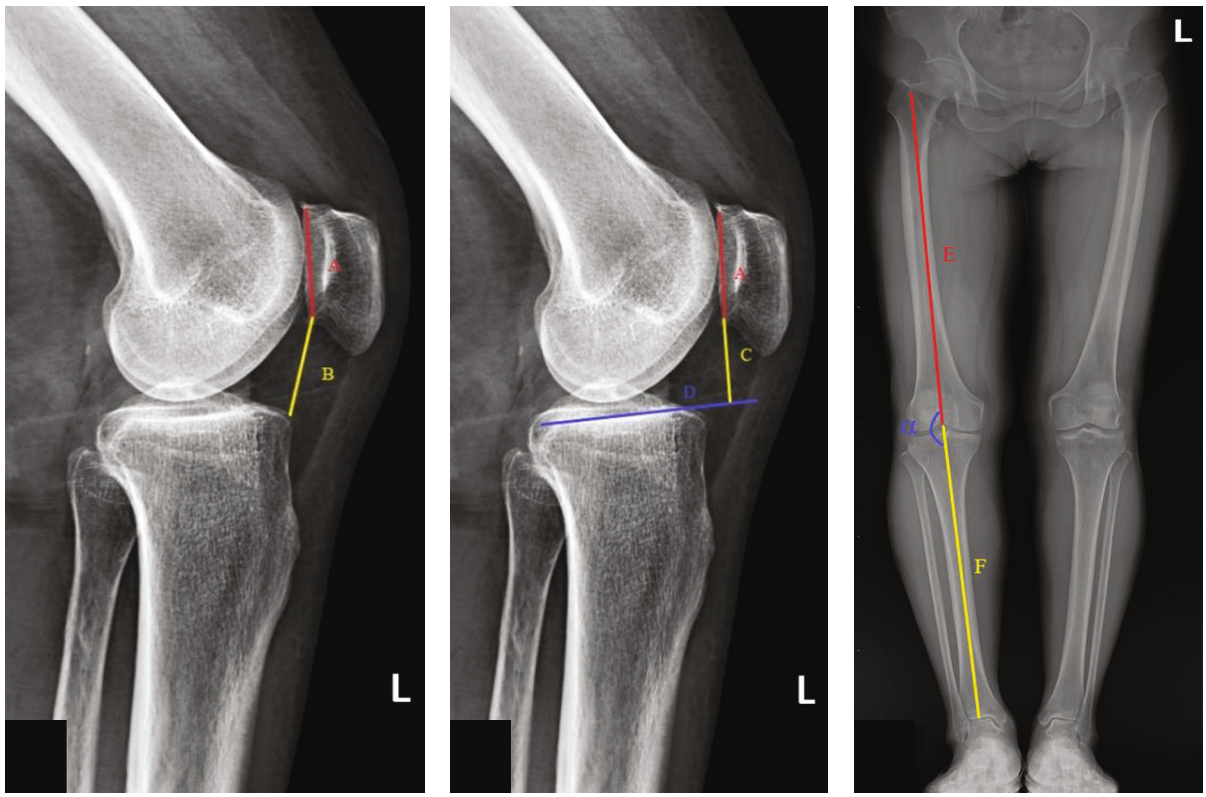

(a) (b) (c)

Figure 2: Methods of image measurement. (a) CDI = B/A. (b) BPI = C/A. (c) FTA = α.

alignment. C-arm fluoroscopy showed that the WBL passed lateral to the lateral tibial intercondylar eminence at the Fujisawa point. Bone substitutes were implanted (Figure 1(e)), a guide plate and screws were inserted (Figure 1(f)), and the wound was finally sewn up.

Ankle pump exercises were performed in bed on the first day after surgery, and patients were allowed to step on the ground with the aid of a walker on the third postoperative day. The patients advanced to walking with two crutches two weeks after the surgery and with a single crutch four weeks after the surgery. Walking without auxiliary devices was achieved 8 to 12 weeks after the surgery.

2.3. Radiological Measurements. All patients were photographed before surgery and at the last follow-up to observe the fixation of the guide plate and screws and the changes in CDI, BPI, FTA, and WBLR. All images were taken by the same technician and the same machine (GE Definium 6000 DR) and were independently measured by two project team members.

The Caton-Deschamps index is the ratio between the length from the lowest point of the patellar articular surface to the anterior tip of the tibial tuberosity and the patellar joint surface (B/A). BPI is the ratio of the vertical distance from the lowest point of the patellar articular surface to the medial tibial plateau line (D) to the patellar articular surface (C/A). FTA is the angle (α) formed by the anatomical axis of the femur (F) and tibia (G) at the center of the knee joint (Figure 2). WBLR is the distance from the intersection of the lower limb alignment and the tibial plateau to the medial edge of the tibial plateau (H) divided by the width of the tibial plateau (I) (Figure 3). The CDI and BPI were measured on lateral radiographs in mild degrees of flexion (30°). FTA and WBLR were gauged on non-weight-bearing lateral radiographs.

2.4. Clinical Evaluation. The Lysholm score was used to assess the knee status before and at the last follow-up, including gait, function, pain, swelling, and stability. The visual analogue scale (VAS) was used to assess the degree of pain before and 3 days after surgery and at the last follow-up, with a score ranging from 0 to 10. The frequencies of the normal-height patella, high patella, and low patella in the three groups were compared before and after the operation.

2.5. Statistical Analysis. All the collected data were analyzed using SPSS (version 25.0; SPSS, China). A paired t-test was used to analyze the CDI, BPI, FTA, and WBLR in the groups. Single-sample analysis of variance was used between the groups. A paired t-test was used to compare the preoperative and postoperative Lysholm scores, and repeated-measure ANOVA was used to detect the changes in VAS scores before surgery, 3 days after surgery, and at the last follow-up. The chi-square test was used to compare the changes in patellar height classification in the three groups before and after surgery.

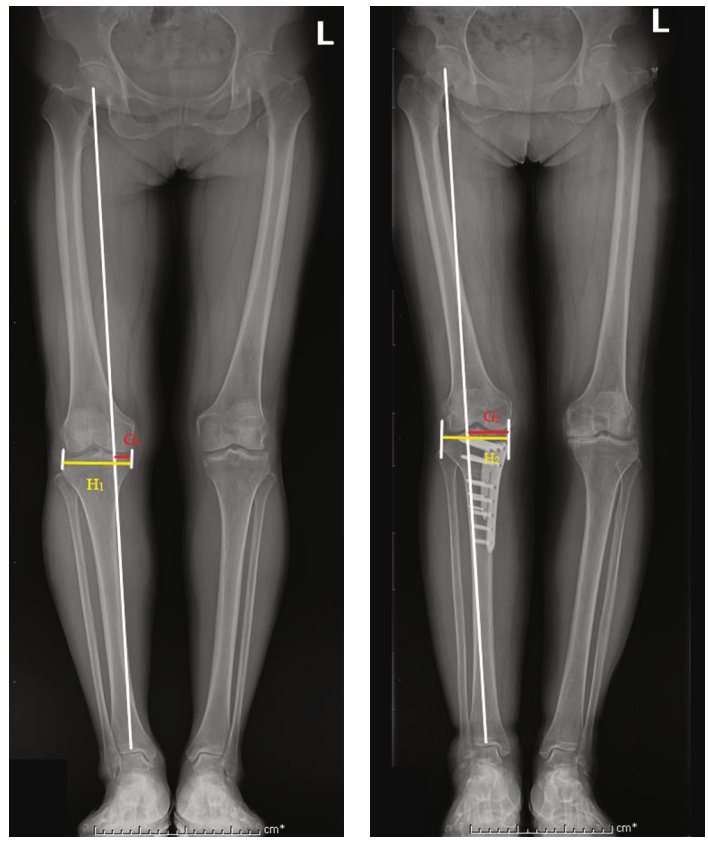

(a) (b)

Figure 3: Method of WBL. (a) $WBLR_1 = H_1/I_1$. (b) $WBLR_2 = H_2/I_2$.

3. Results

There were no significant differences in CDI and BPI preoperatively or postoperatively among the three groups ($P > 0.05$), and the differences in FTA and WBLR were statistically significant ($P < 0.05$). No significant differences were observed in CDI, BPI, FTA, or WBLR between the three groups before and after surgery ($P > 0.05$) (Table 2).

The Lysholm score of the knees increased from 48.84 ± 10.10 before the operation to 91.96 ± 3.082 at the last follow-up ($P < 0.05$). The VAS score decreased from 8.23 ± 0.99 before surgery to 1.93 ± 0.953 on the third postoperative day and 1.07 ± 0.53 at the last follow-up ($P < 0.01$) (Table 3).

The incidences of the normal patella, patella alta, and patella baja (CDI < 0.8 was taken as the standard) were 53.57%, 17.86%, and 28.57%, respectively, in the <60-year-old group before surgery and 50.00%, 17.86%, and 32.14%, respectively, at the last follow-up. The incidences of the three types of patellar heights in the 60~70-year-old group were 52.50%, 14.75%, and 32.79%, respectively, before surgery and 47.54%, 14.75%, and 37.70%, respectively, at the last follow-up. The incidences of the three types of patellar heights before surgery in the >70-year-old group were 52.50%, 14.75%, and 32.79%, and these incidences were 47.54%, 14.75%, and 37.70%, respectively, at the last follow-up. There were no significant differences among the three groups preoperatively and postoperatively (Table 4).

One patient in the <60-year-old group, five patients in the 60~70-year-old group, and one patient in the >70-year-old group had a suspicious low patella after knee surgery (0.6 < CDI < 0.8). Decreases in patellar height were not observed after surgery in the three groups (CDI < 0.6) (Table 5).

4. Discussion

4.1. Influence of HTO on Patellar Height in Previous Literature. CWHTO has a long history. Disadvantages of bone mass on the tibiofibular joint and the risk of common fibular nerve injury have caused it to be surpassed by OWHTO, which can avoid these problems and control the osteotomy angle and WBL more accurately and easily; however, bone substitutes are needed, and the healing speed declines in the osteotomy area because of cortical bone [4]. The patellar tendon is the lower part of the quadriceps femoris muscle, starting from the lower margin of the patella and ending at the tuberosity of the tibia [27]. Classical OWHTO was performed through the superior tibial tuberosity. Expansion of the osteotomy area resulted in the distal displacement of the tibial tuberosity and increased tensile stress of the patellar tendon, which pulled the patella to the distal end of the limb and led to changes in the height of the patella [5]. On this basis, the greater the osteotomy angle, the more obvious the patellar height decrease [13].

Table 2: Changes in imaging indicators in the three groups ($\bar{x} \pm s$).

	Groups	Preoperative	Postoperative	t	P
CDI	<60 years	0.88 ± 0.11	0.88 ± 0.121	-0.113	0.911
	60~70 years	0.87 ± 0.15	0.85 ± 0.156	1.569	0.122
	>70 years	0.90 ± 0.132	0.89 ± 0.131	1.333	0.197
F		0.422	0.537		
P		0.657	0.586		
BPI	<60 years	0.85 ± 0.124	0.87 ± 0.126	-0.854	0.401
	60~70 years	0.89 ± 0.128	0.88 ± 0.131	1.986	0.052
	>70 years	0.90 ± 0.08	0.91 ± 0.071	-0.285	0.779
F		1.256	0.812		
P		0.289	0.447		
WBLR	<60 years	0.18 ± 0.084	0.55 ± 0.089	-23.184	<0.01
	60~70 years	0.18 ± 0.138	0.59 ± 0.10	-20.136	<0.01
	>70 years	0.19 ± 0.089	0.61 ± 0.041	-19.481	<0.01
F		0.029	0.713		
P		0.972	0.492		
FTA	<60 years	182.96 ± 2.063	172.39 ± 3.919	15.884	<0.01
	60~70 years	183.57 ± 2.171	171.02 ± 3.359	25.800	<0.01
	>70 years	183.48 ± 2.112	170.62 ± 2.459	18.605	<0.01
F		0.830	2.046		
P		0.439	0.134		

Table 3: Preoperative and postoperative score changes of the affected knee ($\bar{x} \pm s$).

	Preoperative	Third postoperative day	Last follow-up	Value	P
Lysholm	48.84 ± 10.10	—	91.96 ± 3.082	$t = -36.662$	<0.01
VAS	8.23 ± 0.99	1.93 ± 0.953	1.07 ± 0.53	$F = 1461.907$	<0.01

Table 4: Changes in the frequency of patellar height classification ($n = 110$, %).

		Normal patella	Patella alta	Patella baja	χ^2	P
<60 years	Preoperative	15 (53.57)	5 (17.86)	8 (28.57)	0.093	0.954
	Postoperative	14 (50.00)	5 (17.86)	9 (32.14)		
60~70 years	Preoperative	32 (52.50)	9 (14.75)	20 (32.79)	0.357	0.837
	Postoperative	29 (47.54)	9 (14.75)	23 (37.70)		
>70 years	Preoperative	11 (52.38)	5 (23.81)	5 (23.81)	0.155	0.926
	Postoperative	12 (57.14)	5 (23.81)	4 (19.05)		

Contracture of the patellar tendon after osteotomy may also result in a decrease in the height of the patella [28].

CWHTO avoids osteotomy above the tibial tuberosity. In the meta-analysis of 28 trials included by Cheng et al. [29], no significant change in patellar height was seen after CWHTO. Tigani et al. [6] measured the patellar height after OWHTO and CWHTO by CDI and found that the patellar height of OWHTO decreased more significantly during at least 1 year of postoperative follow-up. Even in OWHTO, biplanar descending OWHTO (osteotomy line at the distal tibial tuberosity) did not affect patellar height compared with biplanar ascending OWHTO (osteotomy line at the proximal tibial tuberosity) [7]. Warner et al. [5] performed subtubercle osteotomy in the treatment of MCOA combined with the Ilizarov technique. They found that the height of the patella (CDI) in 72 knees did not change significantly after the operation and that the patellofemoral relationship was normal. Next, Bayam et al. [8] combined STO with the fixator-assisted nailing technique to perform orthopedic procedures on 32 knee joints, and the study confirmed that the patellar height was not affected during at least 30 months of follow-up. In a large number of clinical studies, it has been

Table 5: Outcomes of patellar height in the three groups ($n = 110$, cases).

	Preoperative	Postoperative	
<60 years	Normal patella	Normal patella	
		+	-
	+	14	1
	-	0	13
	Patella alta	Patella alta	
		+	-
	+	5	0
	-	0	23
	Patella baja	Patella baja	
		+	-
	+	8	0
	-	1	19
60~70 years	Normal patella	Normal patella	
		+	-
	+	27	5
	-	2	27
	Patella alta	Patella alta	
		+	-
	+	9	0
	-	0	52
	Patella baja	Patella baja	
		+	-
	+	18	2
	-	5	36
>70 years	Normal patella	Normal patella	
		+	-
	+	10	1
	-	2	8
	Patella alta	Patella alta	
		+	-
	+	5	0
	-	0	16
	Patella baja	Patella baja	
		+	-
	+	3	2
	-	1	15

confirmed that whether the osteotomy line passes through the tibial tuberosity is one of the evaluation criteria for the change in patellar height, and subtubercle osteotomy can effectively avoid this [3–5, 7–12].

Some studies [2] have shown that open-wedge proximal tibial osteotomy can significantly increase the pressure on the patellofemoral articular cartilage at 30°, 60°, and 90° knee flexion and accelerate the degeneration of the patellofemoral articular cartilage. Sim et al. [30] found that patellar height decreased after OWHTO, and single-photon emission computed tomography and conventional computed tomography (SPECT/CT) were used to capture the contact stress of the patellofemoral joint. The results showed that the contact stress increased in 7.1% of the knees, the articular cartilage of the patella and femoral trochlea significantly deteriorated, and the grade of patellofemoral arthritis was elevated.

4.2. Influence of Age on Radiological and Clinical Outcomes after HTO. Although some studies on HTO have included age as a criterion, it should not be used as a mandatory screening criterion for the treatment of older KOA patients. One study found that radiological outcomes in patients receiving OWHTO were not affected by age, and clinical outcomes (HSS, KSS) were affected by cartilage status rather than age per se [31]. Kuwashima et al. [32] found that, compared with the preoperative KSS score, only the functional activity score showed differences in the group aged ≥65 years and ≤64 years, while differences in the symptom score, satisfaction score, and expectation score were not statistically significant. Kohn et al. [33] found that the improvement of pain symptoms (VAS score) and functional status (Lysholm score) of knees after HTO showed no significant difference between the young group and the old group. They believed that the postoperative efficacy of HTO patients was determined not by their age but by the state of knee soft tissue. Goshima et al. [34] divided OWHTO patients into two groups, older than 65 years old and younger than 65 years old, and conducted follow-up for up to 24 months. It was concluded that age did not affect the clinical and imaging results after HTO. To enhance the medical image analysis, superresolution image enhancement of the medical scans may be applied based on techniques such as deep learning [35].

4.3. The Effect of DTT-HTO on Patellar Height in This Study. DTT-HTO was simple to perform and effectively avoided patellar lowering or elevation. Seven of 110 knee joints decreased from the normal-height patella ($0.8 < \text{CDI} < 1.2$) to the low patella ($\text{CDI} < 0.8$) in the image measurement data, but the overall height of the patella was not affected ($P > 0.05$), which may be related to measurement errors. The authors reviewed the factors affecting patellar height, including knee function, scarring on the patellar ligament, contracture [28], and the motion of the quadriceps femoris [12, 36]. Therefore, preoperative protection of the knee joint, avoidance of accidental injury of the patellar ligament during the operation, and postoperative rehabilitation exercise can contribute to the recovery of knee joint function. Other various algorithms can be used to improve medical imaging procedures [37]. The bone structure integrity is heavily influenced by the material properties that are dependent on certain characteristics [38, 39].

4.4. Relationship of Patellar Height to Osteoporosis. Aging is one of the predisposing factors of osteoporosis; current international literature mainly considers the group aged >60 or 65 years as the high-risk population of osteoporosis [40]. Other operations of HTO, such as OWHTO, performed osteotomy above the tibial tuberosity, where there is abundant cancellous bone. Affected by the position of the osteotomy line, the supporting stress of internal fixation

was mainly concentrated above the tibial tuberosity. If the patient with KOA also has osteoporosis, the screws, inserted to fix the guide, have the potential to cut cancellous bone under body gravity, resulting in bone loss and biomechanical environment disorder in the patellofemoral joint. DTT-HTO can avoid this happening effectively.

4.5. Limitation. The limitations of our study are as follows. (1) The short follow-up time made it impossible to explore the long-term effect of DTT-HTO on patellar height. (2) The observation indicators mainly focused on the image measurement method, and the results had errors. (3) Other factors contributing to the changes in body mechanisms associated with aging have not been explored more broadly. (4) The influence of osteoporosis on HTO has not been further studied.

5. Conclusion

DTT-HTO did not change the height of the patella at different ages, WBL and FTA were corrected, pain was relieved, and function was recovered. Based on the clinical trial results of this study, patients should not be forced to give up their choice of HTO simply because of their age. We recommend that the inclusion criteria for HTO be improved to provide more surgical options and benefit elderly KOA patients.

Abbreviations

KOA: Knee osteoarthritis
DTT-HTO: Distal tibial tuberosity high tibial osteotomy
CDI: Caton-Deschamps index
BPI: Blackburne-Peel index
VAS: Visual analogue scale
FTA: Femoral-tibial angle
WBLR: Weight-bearing line ratio
CWHTO: Closing-wedge high tibial osteotomy
OWHTO: Open-wedge high tibial osteotomy.

Data Availability

Data are available on request from the authors due to privacy/ethical restrictions.

Ethical Approval

All human subjects in this study have given their written consent for participation in our research.

Consent

Signed informed consent for publication was obtained from all authors.

Conflicts of Interest

The authors declare no conflict of interest.

Authors' Contributions

XDT designed the study. TSD collected the data and wrote the manuscript. YTT, SM, YYH, and ZPX performed the surgery. YH and XML collected the data and discussed the results. All authors read and approved the final manuscript.

Acknowledgments

The authors thank all members of the Third Affiliated Hospital of Beijing University of Chinese Medicine who contributed to this research. This study was funded by the Third Affiliated Hospital of Beijing University of Chinese Medicine (No. BZYSY-QNJS-2019-JYB-JS-178).

References

[1] T. O. Smith, D. Sexton, P. Mitchell, and C. B. Hing, "Opening- or closing-wedged high tibial osteotomy: a meta-analysis of clinical and radiological outcomes," *The Knee*, vol. 18, no. 6, pp. 361–368, 2011.

[2] K. Stoffel, C. Willers, O. Korshid, and M. Kuster, "Patellofemoral contact pressure following high tibial osteotomy: a cadaveric study," *Knee Surgery, Sports Traumatology, Arthroscopy*, vol. 15, no. 9, pp. 1094–1100, 2007.

[3] S. G. Gooi, C. X. Y. Chan, M. K. L. Tan, A. K. S. Lim, K. Satkunanantham, and J. H. P. Hui, "Patella height changes post high tibial osteotomy," *Indian J Orthop*, vol. 51, no. 5, pp. 545–551, 2017.

[4] J. S. Shim, S. H. Lee, H. J. Jung, and H. I. Lee, "High tibial open wedge osteotomy below the tibial tubercle: clinical and radiographic results," *Knee Surgery, Sports Traumatology, Arthroscopy*, vol. 21, no. 1, pp. 57–63, 2013.

[5] S. J. Warner, D. P. O'Connor, and M. R. Brinker, "Subtubercle osteotomy for medial compartment osteoarthritis of the knee using Ilizarov technique: survival analysis and clinical outcomes," *The Journal of Bone and Joint Surgery. American Volume*, vol. 100, no. 1, 2018.

[6] D. Tigani, D. Ferrari, P. Trentani, G. Barbanti-Brodano, and F. Trentani, "Patellar height after high tibial osteotomy," *International Orthopaedics*, vol. 24, no. 6, pp. 331–334, 2001.

[7] M. Krause, T. C. Drenck, A. Korthaus, A. Preiss, K. H. Frosch, and R. Akoto, "Patella height is not altered by descending medial open-wedge high tibial osteotomy (HTO) compared to ascending HTO," *Knee Surgery, Sports Traumatology, Arthroscopy*, vol. 26, no. 6, pp. 1859–1866, 2018.

[8] L. Bayam, M. Erdem, D. Gulabi, A. C. Erdem, A. C. Uyar, and A. Kochai, "Clinical and radiological outcomes of high tibial osteotomy with combined fixator-assisted nailing and subtubercle tibial osteotomy," *Acta Orthopaedica et Traumatologica Turcica*, vol. 54, no. 1, pp. 89–96, 2020.

[9] C. Han, X. Li, X. Tian et al., "The effect of distal tibial tuberosity high tibial osteotomy on postoperative patellar height and patellofemoral joint degeneration," *Journal of Orthopaedic Surgery and Research*, vol. 15, no. 1, p. 466, 2020.

[10] R. D. A. Gaasbeek, H. Sonneveld, R. J. van Heerwaarden, W. C. H. Jacobs, and A. B. Wymenga, "Distal tuberosity osteotomy in open wedge high tibial osteotomy can prevent patella infera: a new technique," *The Knee*, vol. 11, no. 6, pp. 457–461, 2004.

[11] P. D. Longino, T. B. Birmingham, W. J. Schultz, R. F. Moyer, and J. R. Giffin, "Combined tibial tubercle osteotomy with

medial opening wedge high tibial osteotomy minimizes changes in patellar height: a prospective cohort study with historical controls," *The American Journal of Sports Medicine*, vol. 41, no. 12, pp. 2849–2857, 2013.

[12] H. El-Azab, P. Glabgly, and J. Paul, "Patellar height and posterior tibial slope after open- and closed-wedge high tibial osteotomy: a radiological study on 100 patients," *The American Journal of Sports Medicine*, vol. 38, no. 2, pp. 323–329, 2010.

[13] R. Gaasbeek, R. Welsing, M. Barink, N. Verdonschot, and A. van Kampen, "The influence of open and closed high tibial osteotomy on dynamic patellar tracking: a biomechanical study," *Knee Surgery, Sports Traumatology, Arthroscopy*, vol. 15, no. 8, pp. 978–984, 2007.

[14] K. K. L. Wong, "Three-dimensional discrete element method for the prediction of protoplasmic seepage through membrane in a biological cell," *Journal of Biomechanics*, vol. 65, no. 65, pp. 115–124, 2017.

[15] L. Sun, Q. Kong, Y. Huang et al., "Automatic segmentation and measurement on knee computerized tomography images for patellar dislocation diagnosis," *Computational and Mathematical Methods in Medicine*, vol. 2020, Article ID 1782531, 2020.

[16] C. Ihle, M. Ahrend, L. Grünwald, A. Ateschrang, U. Stöckle, and S. Schröter, "No change in patellar height following open wedge high tibial osteotomy using a novel femur-referenced measurement method," *The Knee*, vol. 24, no. 5, pp. 1118–1128, 2017.

[17] J. Amzallag, N. Pujol, A. Maqdes, P. Beaufils, T. Judet, and Y. Catonne, "Patellar height modification after high tibial osteotomy by either medial opening-wedge or lateral closing-wedge osteotomies," *Knee Surgery, Sports Traumatology, Arthroscopy*, vol. 21, no. 1, pp. 255–259, 2013.

[18] D. Qin, W. Chen, J. Wang et al., "Mechanism and influencing factors of proximal fibular osteotomy for treatment of medial compartment knee osteoarthritis: a prospective study," *The Journal of International Medical Research*, vol. 46, no. 8, pp. 3114–3123, 2018.

[19] S. I. Bin, H. J. Kim, H. S. Ahn, D. S. Rim, and D. H. Lee, "Changes in patellar height after opening wedge and closing wedge high tibial osteotomy: a meta-analysis," *Arthroscopy*, vol. 32, no. 11, pp. 2393–2400, 2016.

[20] R. F. LaPrade, F. B. Oro, and C. G. Ziegler, "Patellar height and tibial slope after opening-wedge proximal tibial osteotomy: a prospective study," *The American Journal of Sports Medicine*, vol. 38, no. 1, pp. 160–170, 2010.

[21] N. A. Watson, K. R. Duchman, N. M. Grosland, and M. J. Bollier, "Finite element analysis of patella alta: a patellofemoral instability model," *The Iowa Orthopaedic Journal*, vol. 37, pp. 101–108, 2017.

[22] K. K. Middleton, S. Gruber, and B. E. Shubin Stein, "Why and where to move the tibial tubercle: indications and techniques for tibial tubercle osteotomy," *Sports Medicine and Arthroscopy Review*, vol. 27, no. 4, pp. 154–160, 2019.

[23] G. Papachristou, S. Plessas, J. Sourlas, C. Levidiotis, E. Chronopoulos, and C. Papachristou, "Deterioration of long-term results following high tibial osteotomy in patients under 60 years of age," *International Orthopaedics*, vol. 30, no. 5, pp. 403–408, 2006.

[24] I. J. Koh, M. S. Kim, S. Sohn et al., "Predictive factors for satisfaction after contemporary unicompartmental knee arthroplasty and high tibial osteotomy in isolated medial femorotibial osteoarthritis," *Orthopaedics & Traumatology, Surgery & Research*, vol. 105, no. 1, pp. 77–83, 2019.

[25] C. Bastard, G. Mirouse, D. Potage et al., "Return to sports and quality of life after high tibial osteotomy in patients under 60 years of age," *Orthopaedics & Traumatology, Surgery & Research*, vol. 103, no. 8, pp. 1189–1191, 2017.

[26] K. Trieb, J. Grohs, B. Hanslik-Schnabel, T. Stulnig, J. Panotopoulos, and A. Wanivenhaus, "Age predicts outcome of high-tibial osteotomy," *Knee Surgery, Sports Traumatology, Arthroscopy*, vol. 14, no. 2, pp. 149–152, 2006.

[27] M. Kazemi, Y. Dabiri, and L. P. Li, "Recent advances in computational mechanics of the human knee joint," *Computational and Mathematical Methods in Medicine*, vol. 2013, Article ID 718423, 27 pages, 2013.

[28] J. M. Wright, B. Heavrin, M. Begg, G. Sakyrd, and W. Sterett, "Observations on patellar height following opening wedge proximal tibial osteotomy," *The American Journal of Knee Surgery*, vol. 14, no. 3, pp. 163–173, 2001.

[29] X. Cheng, F. Liu, F. Xiong, Y. Huang, and A. C. Paulus, "Radiographic changes and clinical outcomes after open and closed wedge high tibial osteotomy: a systematic review and meta-analysis," *Journal of Orthopaedic Surgery and Research*, vol. 14, no. 1, p. 179, 2019.

[30] J. A. Sim, Y. G. Na, B. K. Lee, and B. H. Lee, "Alignment changes after open-wedge high tibial osteotomy result in offloading in the patellofemoral joint: a SPECT/CT analysis," *Knee Surgery, Sports Traumatology, Arthroscopy*, 2020.

[31] J. H. Song, S. I. Bin, J. M. Kim, and B. S. Lee, "Cartilage status, rather than chronologic age, determines the outcomes of open wedge high tibial osteotomy: a cartilage status-matched cohort study," *Arthroscopy*, vol. 37, no. 9, pp. 2915–2922, 2021.

[32] U. Kuwashima, K. Okazaki, K. Iwasaki et al., "Patient reported outcomes after high tibial osteotomy show comparable results at different ages in the mid-term to long-term follow-up," *Journal of Orthopaedic Science*, vol. 24, no. 5, pp. 855–860, 2019.

[33] L. Kohn, M. Sauerschnig, S. Iskansar et al., "Age does not influence the clinical outcome after high tibial osteotomy," *Knee Surgery, Sports Traumatology, Arthroscopy*, vol. 21, no. 1, pp. 146–151, 2013.

[34] K. Goshima, T. Sawaguchi, D. Sakagoshi, K. Shigemoto, Y. Hatsuchi, and M. Akahane, "Age does not affect the clinical and radiological outcomes after open-wedge high tibial osteotomy," *Knee Surgery, Sports Traumatology, Arthroscopy*, vol. 25, no. 3, pp. 918–923, 2017.

[35] M. Zhao, X. Liu, H. Liu, and K. Wong, "Super-resolution of cardiac magnetic resonance images using Laplacian pyramid based on generative adversarial networks," *Computerized Medical Imaging and Graphics*, vol. 80, p. 101698, 2020.

[36] K. W. Nha, A. Dorj, J. Feng et al., "Application of computational lower extremity model to investigate different muscle activities and joint force patterns in knee osteoarthritis patients during walking," *Computational and Mathematical Methods in Medicine*, vol. 2013, Article ID 314280, 9 pages, 2013.

[37] Z. H. Tang, Y. Y. Li, X. Y. Chai, H. Zang, and S. Cao, "Adaptive nonlinear model predictive control of NOx emissions under load constraints in power plant boilers," *Journal of Chemical Engineering of Japan*, vol. 53, no. 1, pp. 36–44, 2020.

[38] X. Xinli, C. Zhang, F. Musharavati, M. Demiral, A. M. Zain, and A. Khan, "UFSW tool pin profile effects on properties of

aluminium-steel joint," *Vacuum*, vol. 192, no. 8, article 110460, 2021.

[39] X. Xinli, C. Zhang, and H. A. Derazkola, "Dispersion of waves characteristics of laminated composite nanoplate," *Steel and Composite Structures*, vol. 40, no. 3, pp. 355–367, 2021.

[40] I. R. Reid, "A broader strategy for osteoporosis interventions," *Nature Reviews. Endocrinology*, vol. 16, no. 6, pp. 333–339, 2020.

Hindawi
Computational and Mathematical Methods in Medicine
Volume 2022, Article ID 3452348, 6 pages
https://doi.org/10.1155/2022/3452348

Research Article

Construction of Prediction Model of Deep Vein Thrombosis Risk after Total Knee Arthroplasty Based on XGBoost Algorithm

Yuhuan Chen and Yingqing Jiang

Department of Orthopedics, The First Affiliated Hospital of Soochow University, Suzhou 215006, China

Correspondence should be addressed to Yingqing Jiang; jiangyingqing2021@163.com

Received 19 November 2021; Revised 14 December 2021; Accepted 31 December 2021; Published 25 January 2022

Academic Editor: Kelvin Wong

Objective. Based on the XGBoost algorithm, the prediction model of the risk of deep vein thrombosis (DVT) in patients after total knee arthroplasty (TKA) was established, and the prediction performance was compared. *Methods*. A total of 100 patients with TKA from January 2019 to December 2020 were retrospectively selected as the study subjects and randomly divided into a training set ($n = 60$) and a test set ($n = 40$). The training set data was used to construct the XGBoost algorithm prediction model and to screen the predictive factors of postoperative DVT in TKA patients. The prediction effect of the model was evaluated by using the test set data. An independent sample T-test was used for comparison between groups, and the χ^2 test was used for comparison between counting data groups. *Results*. The top five items were combined with multiple injuries (35 points), time from injury to operation (28 points), age (24 points), combined with coronary heart disease (21 points), and D-dimer 1 day after operation (16 points). In the training set, the area under the curve of the XGBoost algorithm model was 0.832 (95% CI: 0.748-0.916). *Conclusion*. The model based on the XGBoost algorithm can predict the incidence of DVT in patients after TKA with good performance.

1. Introduction

Total knee arthroplasty (TKA) is an effective method for the treatment of end-stage knee osteoarthritis, which can significantly relieve the pain in patients and promote functional recovery [1]. Deep vein thrombosis (DVT) is one of the common complications of limb fractures in the perioperative period, which can lead to pulmonary embolism and postthrombotic syndrome. The rate of sudden death caused by pulmonary embolism is as high as 34%, which seriously affects the prognosis and life of patients [2]. DVT is a venous reflux disease caused by blood coagulation in the deep vein due to various reasons. There are three factors in patients with DVT: slow blood flow, hypercoagulability, and venous wall injury [3]. Previous studies showed that the overall incidence of DVT was 69.9% per patient postoperatively [4]. Therefore, the early diagnosis and treatment of DVT are extremely important.

In recent years, the extreme Gradient Boosting (XGBoost) model has become one of the common tools for solving classification problems due to its high efficiency, flexibility, and accuracy [5]. The XGBoost model is widely used in statistics, data mining, machine learning, and artificial intelligence, because of its low input data requirements, automatic variable selection, and low computational complexity. Especially in the medical field, the XGBoost model can make use of historical case data to build models for classification and predictions [6]. Direct prediction of postoperative indicators with clinical data and specific algorithms is helpful for doctors to make reasonable and effective judgments and further guide the follow-up medical work.

In recent years, a large number of studies have reported high-risk factors related to DVT [7], but there are few studies on predicting DVT after TKA by the XGBoost model. Therefore, the purpose of this study is to explore the risk factors for DVT in patients after TKA. The prediction model

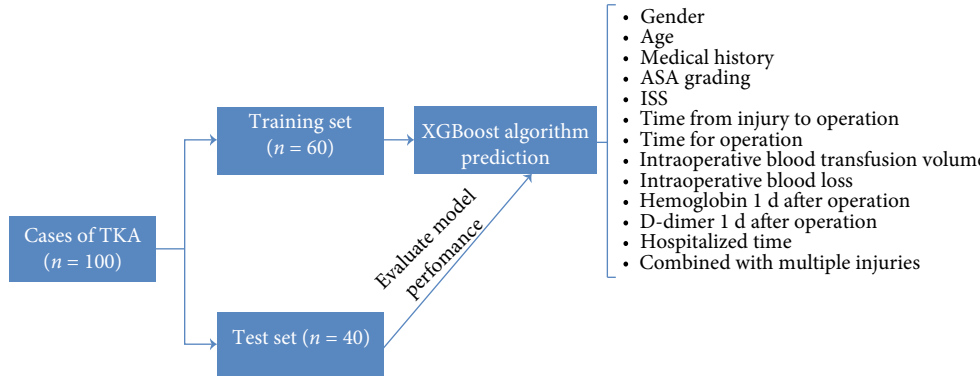

Figure 1: Modeling flow chart.

based on the XGBoost algorithm is aimed at providing reliable theoretical guidance for the early intervention of DVT after TKA.

2. Materials and Methods

2.1. General Information. From January 2019 to December 2020, 100 patients with TKA who met the inclusion and exclusion criteria were selected as research objects.

Inclusive criteria are patients younger than 80 years old who received unilateral TKA for the first time and without cognitive impairment and able to cooperate with the researcher and patients with stable condition at discharge without postoperative complications and who informed and agreed to participate in the study.

Exclusion criteria are patients with severe cardiovascular and cerebrovascular diseases and malignant tumors, patients with mental disorders who are unable to cooperate, patients with hip and ankle joint deformities that affect knee joint function, patients who have undergone TKA surgery or bilateral TKA surgery at the same time, and recent participants in other researches.

2.2. Research Queue. All patients with TKA were randomly divided into a training set ($n = 60$) and a test set ($n = 40$). The training set was used to construct the XGBoost algorithm prediction model, and the test set data was used to evaluate the prediction effect of the XGBoost model. According to the ultrasound results of both lower limbs after the operation, the patients in the training set were divided into a DVT group and a non-DVT group.

2.3. Indicators and Standards of Observation. Collecting baseline data include age, gender, previous medical history (hypertension and coronary heart disease), American Society of Anesthesiologists (ASA) classification, injury severity score (ISS), time from injury to operation, operation time, intraoperative blood transfusion volume, intraoperative blood loss, hemoglobin 1 day after operation, D-dimer 1 day after operation, hospital time, and combined with multiple injuries.

ISS<16 is a minor injury, $16 < \text{ISS} \leq 25$ is a moderate injury, and ISS > 25 is a severe injury [8]. According to the ASA classification, patients' condition was divided into five grades: Grade I: healthy; Grade II: suffering from systemic disease, with good compensatory function; Grade III: severe systemic disease, daily functions are limited within the scope of compensation; Grade IV: compensatory function is not complete, and daily function is lost; Grade V: the condition is serious and life-threatening [9].

2.4. Treatment Method. The risk assessment of thromboembolism was carried out regularly for all patients after operation. To prevent DVT, patients without contraindications of anticoagulation were injected subcutaneously with low molecular weight heparin sodium 0.4 mL every day. At the same time, the plantar vein pump was performed twice a day for 20 minutes each time. One day after the operation, blood samples were collected from all patients, and the D-dimer, blood routine, and coagulation were monitored. Ultrasound examination of veins of lower limbs was performed 3-5 days after the operation. Positive patients were given low molecular heparin calcium 0.4 mL twice a day, and the plantar venous pump was stopped for DVT treatment. All patients stopped using anticoagulants 12 hours before operation and started using anticoagulants 12 hours after operation.

2.5. Research Outcomes and Predictors. The outcome of the study was that DVT occurred in TKA patients 3-5 days after the operation. The inner diameter of the deep vein of lower limbs was observed from bottom to top along with the operation site, and DVT was diagnosed if the following phenomena occur: The lumen below the embolic site is enlarged, and the venous lumen cannot be closed. There is a solid echo with unequal intensity in the lumen. When the occlusion is complete, pulse and color Doppler show a small amount or no blood flow signal.

2.6. XGBoost Algorithm Model. The XGBoost algorithm is an optimized distributed gradient computing integration algorithm. The idea of this algorithm comes from the gradient lifting iterative decision tree algorithm. Based on the gradient lifting iterative decision tree algorithm, a second-order Taylor function is added to classify the data, which is specifically completed by the following:

Goal function:

$$\frac{\wedge}{y_i} = \sum_{k=1}^{K} f_k(x_i), \quad f_k \in F, \tag{1}$$

where $i = 1, 2, \cdots, n$, n is the number of samples, F is the set corresponding to all regression trees, and f_k is the function in F.

The regular term is the damage function of the model:

$$\Omega(f_k) = \gamma T + \frac{1}{2}\lambda \|w\|^2, \quad l\left(y_{i3}\hat{y}_i\right). \tag{2}$$

The second-order Taylor function is introduced to approximately expand the loss function, and the objective function is optimized to be closer to the actual value to improve the prediction accuracy:

$$o = l(y, y_i) + \sum_{k=1}^{k} \beta(f_k), \tag{3}$$

where $l(y, y_i)$ is a model for integrating data standardization, O represents the difference between the predicted value of the last formula and the recorded value of the actual data, and β represents the normalized processing coefficient, which is used to calculate the positive value after data weighting to prevent data confusion. Formulas (1) and (2) are fused by superposition calculation of multiple data, and the predicted values of iterative samples of data are substituted into the loss function, and the calculation results are multiplied by the normalization coefficient. The final simplified formula of the XGBoost algorithm is as follows:

$$o^t = \sum_{i=1}^{N} \left(y_i, y^{t-1} + g_i f_i(x_i) + \frac{1}{2} h_i y_i(x_i) \right) + \beta(f_i). \tag{4}$$

2.7. Statistical Methods. Single-factor analysis of variance was used to train the clinical data of the DVT group and the non-DVT group. SPSS20.0 software was used for the statistical analysis of the data. The independent sample T-test was used for comparison between groups, and the χ^2 test was used for comparison between counting data groups.

3. Results

3.1. Process of Model Establishment. 100 patients with TKA were randomly divided into the training set ($n = 60$) and test set ($n = 40$). The training set was used to construct the XGBoost algorithm prediction model, and the test set data was used to evaluate the prediction effect of the model. According to the ultrasound results of both lower limbs after operation, the patients in the training set were divided into the DVT group ($n = 24$) and the non-DVT group ($n = 36$). The predictive factors included all the items of observed indicators. Figure 1 shows the specific modeling process.

3.2. Clinical Data of Patients in Training Set and Test Set. There was no significant difference between the training set and the test set in terms of gender, age, complications, ASA grade, ISS, time from injury to operation, operation time, intraoperative blood transfusion volume, intraoperative blood loss, hemoglobin 1 day after operation, D-dimer 1 day after operation, hospitalized time, and combined with multiple injuries. In addition, there was no significant difference in diabetes mellitus and hyperlipidemia, ASA grade, ISS, operation time, intraoperative blood transfusion volume, intraoperative blood loss, and hospitalized time between the DVT group and the non-DVT group. There were statistically significant differences between the two groups in terms of gender, age, hypertension, coronary heart disease, time from injury to operation, hemoglobin, D-dimer at 1 day after operation, and combined with multiple injuries (Figure 2, Table 1).

3.3. Establishment of XGBoost Algorithm Model. By integrating the data in the training set into the XGBoost algorithm model, we have obtained important feature scoring results. The top five items were combined with multiple injuries (35 points), time from injury to operation (28 points), age (24 points), combined with coronary heart disease (21 points), and D-dimer 1 day after operation (16 points). In addition, the other three items were combined with hypertension (14 points), hemoglobin 1 day after operation (11 points), and gender (9 points), as shown in Figure 3.

3.4. Calibration Degree of XGBoost Algorithm Model. As shown in Figure 4, in the training set, the area under the curve of the XGBoost algorithm model was 0.832 (95% CI: 0.748-0.916).

4. Discussion

With the change of population structure, the number of elderly patients with TKA is increasing [10]. DVT is a common complication after orthopedic surgery. Previous studies showed that the incidence of postoperative DVT was as high as 57%-62%, and the incidence of DVT was 0.5%-44% even with routine prevention [11]. Bawa et al. showed that patients with hypercoagulability diagnoses were at a higher risk of postoperative DVT [12]. Tateiwa et al. found that the total incidence of DVT was 62.5% in 88 patients with TKA. Among the 55 patients with DVT, the incidence of distal DVT was 96.4%, and that of proximal DVT was 3.6% [13]. These results were similar to those of our study. The reason may be that TKA has caused great damage to tissues and blood vessel walls and caused more hemorrhage. In addition, patients with postoperative pain often stay in bed for braking, which further aggravates blood stasis and increases the risk of DVT. Therefore, for TKA patients, it is necessary to attach great importance to the occurrence of DVT and strengthen the screening and prevention of thrombosis.

Clinical studies have found that DVT after TKA is a risk factor for poor prognosis and death [14]. However, the risk factors leading to DVT are still inconclusive. According to the analysis of hip fracture patients, it is found that the average time interval between operation and hospitalization for patients with DVT after the operation was 9.45 days, while

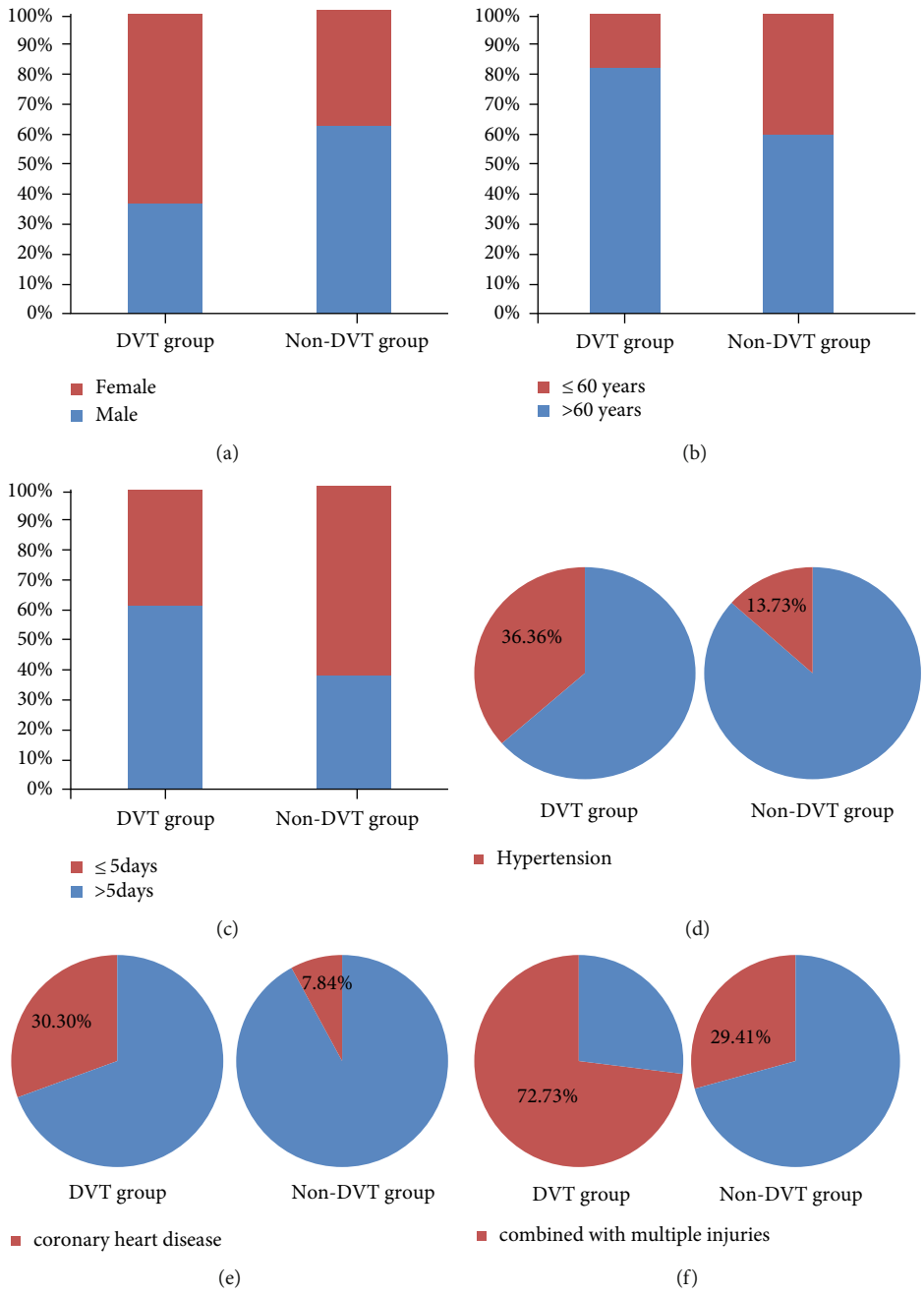

Figure 2: Comparison of clinical data between the DVT group and the non-DVT group in the training set. There were significant differences ($P < 0.05$) between the DVT and non-DVT groups in gender (a), age (b), time from injury to operation (c), hemoglobin (d), coronary heart disease (e), and combined with multiple injuries (f).

Table 1: Comparison of clinical data between the DVT group and the non-DVT group in the training set 1 day after operation (mean ± SD).

Index	DVT group	Non-DVT group	t value	P value
Hemoglobin (g/L)	107.25 ± 16.33	118.39 ± 17.52	2.922	<0.05
D-dimer (mg/L)	6.24 ± 4.87	2.66 ± 3.21	4.065	<0.001

that for patients without DVT was 1.06 days [15]. In this study, we found that the time from injury to operation over 5 days was an independent risk factor for DVT after TKA. This result is similar to previous studies [16]. This may be due to the long-term braking, traction, or pain after the operation, which leads to prolonged stay in bed, muscle atrophy, and hypercoagulability which then leads to the formation of DVT. Therefore, patients should be admitted to the hospital as soon as possible after being injured. Surgery should be performed as soon as possible when conditions permit to reduce the risk of DVT.

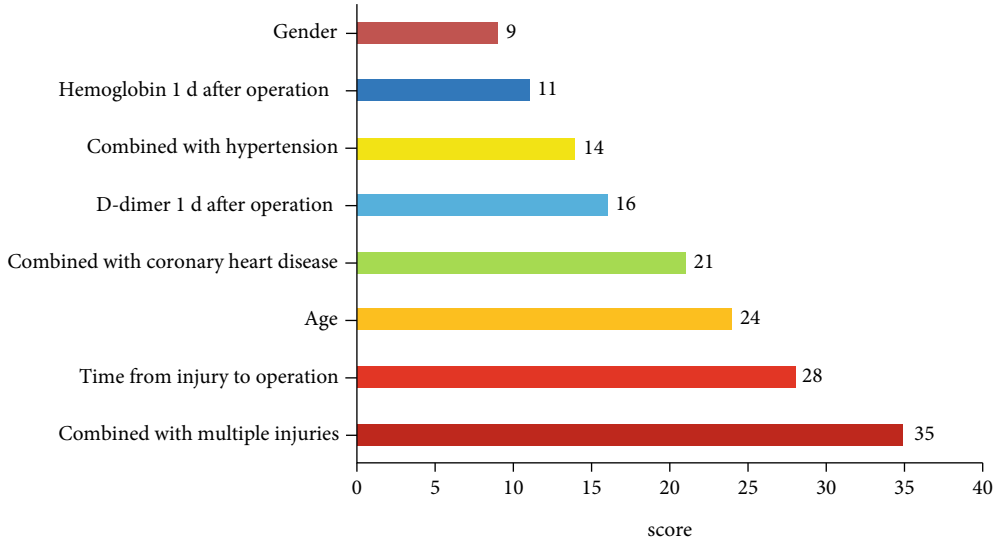

Figure 3: Score of important features in XGBoost algorithm model.

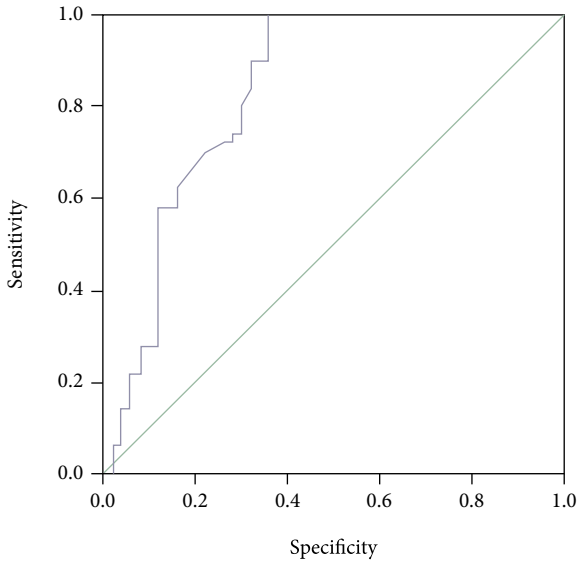

Figure 4: The receiver operation characteristic (ROC) curves of XGBoost algorithm model.

Patients over 60 years have decreased physical function, easily damaged intima of blood vessels, and decreased elasticity of blood vessels and blood circulation, which increases the risk of DVT. Nybo and Hvas provided that age is a risk factor for DVT [17]. Gómez-Jabalera et al. demonstrated that age over 60 years was an independent risk factor for DVT in patients after fracture operation, and it was highly specific for predicting DVT [18]. These were also consistent with our study. However, some scholars believe that the incidence of DVT has nothing to do with age. This may be due to the timely screening of DVT after injury [11]. In addition, we also found that coronary heart disease was an independent risk factor for DVT after TKA. Our results are consistent with those of previous scholars [19]. The reason may be that coronary atherosclerosis in patients with coronary heart disease leads to vascular endothelial damage, promotes platelet adhesion and aggregation, and accelerates the coagulation process, thus leading to the increased risk of postoperative DVT. D-dimer is the simplest degradation product of fibrin, and the increase of mass concentration can reflect the existence of hypercoagulability in the body, which is a nonspecific sign of thrombosis. It has been widely applied to the diagnosis and prognosis of clinical thrombotic diseases. Our study found that D-dimer was an independent risk factor for DVT after TKA, which was consistent with previous studies [20].

Davagdorj et al. built a model of noncommunicable diseases caused by smoking based on the XGBoost framework, which can realize a more accurate prediction [5]. In addition, in the diagnosis of chronic kidney disease, Ogunleye and Wang proved that the XGBoost model has a great advantage in prediction accuracy [21]. The XGBoost algorithm model established in this study has high sensitivity and specificity in predicting DVT in patients after TKA operation. Various algorithms have their own advantages and disadvantages. We will try to use new algorithms to evaluate the prognosis of the disease in the future [22, 23].

There are some limitations to our study. This study was a retrospective study of a small single-center sample, which needs further verification in the prospective study of a large multicenter sample. Secondly, there are not enough influencing factors in the analysis, and there was no hierarchical analysis of these factors. In addition, although the XGBoost algorithm model has unique advantages in dealing with high-dimensional variables, complex interactions among variables, and nonlinear relationships, the effectiveness of the prediction model will also be limited by the nature, number, type, and sample of variables.

5. Conclusion

The model based on the XGBoost algorithm can predict the occurrence of DVT in patients after TKA with good prediction performance. The items including combined with

multiple injuries, time from injury to operation, age, coronary heart disease, and D-dimer at 1 day after operation can be used as predictive indicators of DVT after TKA.

Data Availability

The data used to support the findings of this study are available from the corresponding author upon request.

Conflicts of Interest

All authors declare no conflicts of interest in this paper.

References

[1] A. M. Schwartz, K. X. Farley, G. N. Guild, and T. L. Bradbury Jr., "Projections and epidemiology of revision hip and knee arthroplasty in the United States to 2030," *The Journal of Arthroplasty*, vol. 35, no. 6, pp. S79–s85, 2020.

[2] H. Meng, Y. Zhu, J. Zhang et al., "Incidence and risk factor for preoperative deep vein thrombosis (DVT) in isolated calcaneal fracture, a prospective cohort study," *Foot and Ankle Surgery*, vol. 27, no. 5, pp. 510–514, 2021.

[3] J. M. Lurie, C. Y. M. Png, S. Subramaniam et al., "Virchow's triad in "silent" deep vein thrombosis," *Journal of Vascular Surgery. Venous and Lymphatic Disorders*, vol. 7, no. 5, pp. 640–645, 2019.

[4] M. J. Chang, M. K. Song, M. G. Kyung, J. H. Shin, C. B. Chang, and S. B. Kang, "Incidence of deep vein thrombosis before and after total knee arthroplasty without pharmacologic prophylaxis: a 128-row multidetector ct indirect venography study," *BMC Musculoskeletal Disorders*, vol. 19, no. 1, p. 274, 2018.

[5] K. Davagdorj, V. H. Pham, N. Theera-Umpon, and K. H. Ryu, "XGBoost-based framework for smoking-induced noncommunicable disease prediction," *International Journal of Environmental Research and Public Health*, vol. 17, no. 18, pp. 6513–6522, 2020.

[6] S. K. Devana, A. A. Shah, C. Lee, A. R. Roney, M. van der Schaar, and N. F. SooHoo, "A novel, potentially universal machine learning algorithm to predict complications in total knee arthroplasty," *Arthroplast Today*, vol. 10, no. 1, pp. 135–143, 2021.

[7] M. A. Alsheef, A. M. Alabbad, R. A. Albassam et al., "Pregnancy and venous thromboembolism: risk factors, trends, management, and mortality," *BioMed Research International*, vol. 2020, Article ID 4071892, 6 pages, 2020.

[8] S. M. Galvagno Jr., M. Massey, P. Bouzat et al., "Correlation between the revised trauma score and injury severity score: implications for prehospital trauma triage," *Prehospital Emergency Care*, vol. 23, no. 2, pp. 263–270, 2019.

[9] K. M. Knuf, C. V. Maani, and A. K. Cummings, "Clinical agreement in the American Society of Anesthesiologists physical status classification," *Perioperative Medicine*, vol. 7, no. 1, pp. 1–6, 2018.

[10] M. Weber, F. Völlner, A. Benditz et al., "Total knee arthroplasty in the elderly," *Orthopade*, vol. 46, no. 1, pp. 34–39, 2017.

[11] F. Bengoa, G. Vicencio, D. Schweitzer, M. J. Lira, T. Zamora, and I. Klaber, "High prevalence of deep vein thrombosis in elderly hip fracture patients with delayed hospital admission," *European Journal of Trauma and Emergency Surgery*, vol. 46, no. 4, pp. 913–917, 2020.

[12] H. Bawa, J. W. Weick, D. R. Dirschl, and H. H. Luu, "Trends in deep vein thrombosis prophylaxis and deep vein thrombosis rates after total hip and knee arthroplasty," *The Journal of the American Academy of Orthopaedic Surgeons*, vol. 26, no. 19, pp. 698–705, 2018.

[13] T. Tateiwa, T. Ishida, T. Masaoka et al., "Clinical course of asymptomatic deep vein thrombosis after total knee arthroplasty in Japanese patients," *Journal of Orthopaedic Surgery*, vol. 27, no. 2, 2019.

[14] M. Sloan, N. Sheth, and G. C. Lee, "Is obesity associated with increased risk of deep vein thrombosis or pulmonary embolism after hip and knee arthroplasty? A large database study," *Clinical Orthopaedics and Related Research*, vol. 477, no. 3, pp. 523–532, 2019.

[15] Y. H. Cho, Y. S. Byun, D. G. Jeong, I. H. Han, and Y. B. Park, "Preoperative incidence of deep vein thrombosis after hip fractures in Korean," *Clinics in Orthopedic Surgery*, vol. 7, no. 3, pp. 298–302, 2015.

[16] B. F. Zhang, X. Wei, H. Huang et al., "Deep vein thrombosis in bilateral lower extremities after hip fracture: a retrospective study of 463 patients," *Clinical Interventions in Aging*, vol. - Volume 13, pp. 681–689, 2018.

[17] M. Nybo and A. M. Hvas, "Age-adjusted D-dimer cut-off in the diagnostic strategy for deep vein thrombosis: a systematic review," *Scandinavian Journal of Clinical and Laboratory Investigation*, vol. 77, no. 8, pp. 568–573, 2017.

[18] E. Gómez-Jabalera, S. Bellmunt Montoya, E. Fuentes-Camps, and J. R. Escudero Rodríguez, "Age-adjusted D-dimer for the diagnosis of deep vein thrombosis," *Phlebology*, vol. 33, no. 7, pp. 458–463, 2018.

[19] K. Kaikita, K. Hosokawa, J. R. Dahlen, and K. Tsujita, "Total thrombus-formation analysis system (t-tas): clinical application of quantitative analysis of thrombus formation in cardiovascular disease," *Thrombosis and Haemostasis*, vol. 119, no. 10, pp. 1554–1562, 2019.

[20] J. Gregson, S. Kaptoge, T. Bolton et al., "Cardiovascular risk factors associated with venous thromboembolism," *JAMA Cardiology*, vol. 4, no. 2, pp. 163–173, 2019.

[21] A. Ogunleye and Q. G. Wang, "XGBoost model for chronic kidney disease diagnosis," *IEEE/ACM Transactions on Computational Biology and Bioinformatics*, vol. 17, no. 6, pp. 2131–2140, 2020.

[22] Z. Tang, Y. Li, X. Chai, H. Zhang, and S. Cao, "Adaptive nonlinear model predictive control of nox emissions under load constraints in power plant boilers," *Journal of Chemical Engineering of Japan*, vol. 53, no. 1, pp. 36–44, 2020.

[23] N. Li, P. Luo, C. Li, Y. Hong, M. Zhang, and Z. Chen, "Analysis of related factors of radiation pneumonia caused by precise radiotherapy of esophageal cancer based on random forest algorithm," *Mathematical Biosciences and Engineering*, vol. 18, no. 4, pp. 4477–4490, 2021.

Hindawi
Computational and Mathematical Methods in Medicine
Volume 2022, Article ID 6868483, 10 pages
https://doi.org/10.1155/2022/6868483

Research Article

Computed Tomography Image Segmentation of the Proximal Colon by U-Net for the Clinical Study of Somatostatin Combined with Intestinal Obstruction Catheter

Chunpeng Dou, Kuiwu Li, and Liang Wang

The First Department of General Surgery, Fuxin Centre Hospital, Fuxin 123000, China

Correspondence should be addressed to Chunpeng Dou; douchunpeng@163.com

Received 22 July 2021; Revised 30 August 2021; Accepted 23 October 2021; Published 18 January 2022

Academic Editor: Kelvin Wong

Objective. U-Net technology is implemented for image segmentation to diagnose cases of intestinal obstruction. To evaluate the application value of somatostatin combined with transanal intestinal obstruction decompression catheter in the treatment of distal colonic malignant intestinal obstruction and to explore the therapeutic effect of somatostatin on acute abdomen surgery in patients with intestinal obstruction. *Methods*. After the segmentation technique, a retrospective analysis of 30 patients with acute and complete distal colonic malignant obstruction treated by surgery was divided into a control group and an observation group according to a random number table. The treatment efficiency, clinical symptoms, disappearance time after treatment, and the incidence of complications were compared between the two groups of patients. *Results*. The image segmentation using U-Net can effectively assist in the medical diagnosis of the colon. Our study found that patients with combined treatment with somatostatin and anal intestinal obstruction catheter were relieved of preoperative abdominal pain and abdominal distension; compared with the abdominal circumference at the time of admission, the abdominal circumference was significantly reduced. Abdominal examination was performed 3 days after comprehensive treatment, and combined with computed tomography (CT), we observed that the measured maximum transverse diameter of the proximal colon was significantly smaller than that before treatment. Before treatment, all patients were divided into a control group and a treatment group. After treatment, the symptoms of the two groups of patients were alleviated. The treatment effective rate of the observation group was 93.3%, and the treatment effective rate of the control group was 73.3%. The effective rate was significantly higher than that of the control group, and the difference was statistically significant. *Conclusions*. Through the use of image segmentation technology, somatostatin treatment of early inflammatory bowel obstruction after acute abdomen surgery can effectively improve the treatment efficiency of patients, shorten the disappearance of clinical symptoms, reduce the incidence of complications, and have a significant therapeutic effect, which is worthy of clinical application. Somatostatin combined with enteral obstruction catheter treatment is safe and effective for elderly patients with acute distal large bowel malignant intestinal obstruction. It has a higher completion rate of laparoscopic surgery and a first-stage anastomosis power, which reduces the risk of perioperative period and reduces the patient's financial burden.

1. Introduction

Many computer vision tasks require intelligent segmentation of images to understand the content of the image and make it easier to analyze each part. Today's image segmentation technology uses deep learning models to accurately understand the real world, which was unimaginable ten years ago. Image segmentation uses a computer to distinguish the content of an image, which is a very challenging task in a computer vision system. Semantic segmentation is to classify all pixels in an image, and pixels with the same semantics are segmented. In recent years, there has been an increasing demand for image segmentation in industries such as smart medical care, autonomous driving, indoor navigation, human-computer interaction, virtual or augmented reality, robotics, image

beautification, and smart agriculture. More and more products need to be based on depth. The learned image segmentation algorithm serves as technical support.

In the field of smart medicine, medical image analysis has become a hot research topic. Brain tumor is an abnormal tissue caused by uncontrollable factors that cause cell canceration and proliferation. It seriously threatens human life and health. It is one of the main research contents of the medical scientific research team. Segmentation diagnosis of brain tumors in brain MRI images to determine the exact location of areas such as edema, enhancement, and necrosis plays a key role in later diagnosis and treatment, causing systemic inflammatory response syndrome, sepsis, and even organ dysfunction, making the condition more complicated [1–3]. The traditional brain tumor segmentation method is based on the knowledge of anatomy and pathology by radiologists, with the help of specific software to perform manual segmentation and label the data. This method is time-consuming and labor-intensive, the correct rate of annotation varies due to personal ability, and there is instability. Therefore, traditional brain tumor segmentation methods are difficult to meet the needs of clinical use in terms of segmentation speed and segmentation accuracy. It is particularly important to realize fast and accurate brain image segmentation with the help of a computer.

Intestinal obstruction is susceptible to gastrointestinal flora imbalance. Inadequate treatment or drug-resistant flora can be complicated by bacterial and endotoxin translocations, causing intestinal infections and systemic inflammatory response syndrome and sepsis, and even more, insufficiency of organs makes the condition more complicated [1–3]. How to correct the imbalance of intestinal flora as soon as possible, so that patients can recover quickly, is an important research question. In the past, clinically often highly targeted antibiotics were used to kill or inhibit intestinal pathogenic bacteria. It is expected that probiotic bacteria in the intestinal tract can grow rapidly, but the result is often counterproductive, resulting in the emergence of drug-resistant pathogenic bacteria or serious double infections. Microecological preparations, also known as microecological regulators, are produced with the development of intestinal nutritional support [4–6]. The human intestine is a huge and complex microecosystem, and the balance between its various floras is of great significance to the health and recovery of the disease. Studies have shown that the probiotics inherent in the live intestinal tract can be applied, supplemented with prebiotic preparations (which can inhibit the growth of pathogenic bacteria and promote the growth of probiotics), to achieve the restoration of intestinal flora balance.

Somatostatin is a clinically widely used neurohormone. It is mainly used for hemorrhage caused by liver cirrhosis and has a certain effect on upper gastrointestinal bleeding. Its main role is to inhibit the secretion of growth hormone, glucagon, insulin, and other hormones. In addition, it also affects the absorption of the gastrointestinal tract and nutritional functions. After intravenous injection of somatostatin, it can be quickly metabolized in the liver of the patient, 70% excretion can be achieved within hours, and the effect is fast. The application of intestinal obstruction symptoms is mainly to inhibit the secretion and stasis of gastrointestinal fluids of patients and relieve abdominal distension and abdominal pain symptoms. Relevant research shows that the number of patients with intestinal obstruction treated with somatostatin within 48 hours of emergency treatment is significantly lower than that if patients who are not treated with somatostatin which can effectively improve the intestinal surgical conditions of patients [7, 8]. Somatostatin treatment can effectively reduce the accumulation of digestive juice in the intestine by more than 50%. It can not only reduce the edema of the intestinal lining and maintain the integrity of the intestinal mucosa but also promote the blood circulation of the patient, thereby shortening the treatment time and facilitating the recovery of the patients' health [9, 10].

Computed tomography (CT) examination is fast and has high resolution. With the development of CT technology, thin-layer volume scanning and various image postprocessing techniques have significantly improved the diagnostic performance of CT and are widely used in the diagnosis of intestinal obstruction diseases. Therefore, in this study, CT images can help to analyze the condition of patients with intestinal obstruction.

The traditional conservative treatment methods for intestinal obstruction are fasting, gastrointestinal decompression, and parenteral nutrition support. Among them, gastrointestinal decompression is often performed through the nasogastric tube. Traditional nasogastric tube decompression can only drain the liquid in the stomach cavity, but the fluid in the intestinal cavity cannot be fully drained, causing a large amount of gas and liquid to accumulate in the intestine, causing the intestinal wall to expand and edema, and then blood flow is blocked, affecting the intestine road function recovery. An intestinal obstruction decompression tube is used to insert the catheter through the nasal cavity and esophagus with the aid of gastroscope or X-ray and then suck the stomach contents into the small intestine. The intestinal obstruction decompression tube can more easily pass through the pylorus and enter the intestinal cavity. Intestinal decompression relieves intestinal edema and restores blood flow when decompression is sufficient, laying a good foundation for restoring intestinal function [11].

Therefore, we envisage that if the microecological preparation and the intestinal obstruction decompression tube are jointly applied, the microecological preparation will be injected into the intestinal cavity near the obstruction through the decompression tube after the intestinal tube is fully decompressed, which can effectively inhibit the growth of pathogenic bacteria and prevent it in time. Or correct the intestinal flora imbalance, reduce the application rate of antibiotics, and timely monitor the changes of intestinal flora and endotoxin levels through the drainage fluid, and provide experimental basis for clinicians to choose the timing of surgery. It can also effectively improve the symptoms and signs of patients with intestinal obstruction, improve the cure rate of patients, and shorten the length of hospital stay and has important clinical significance for the prognosis of patients with intestinal obstruction

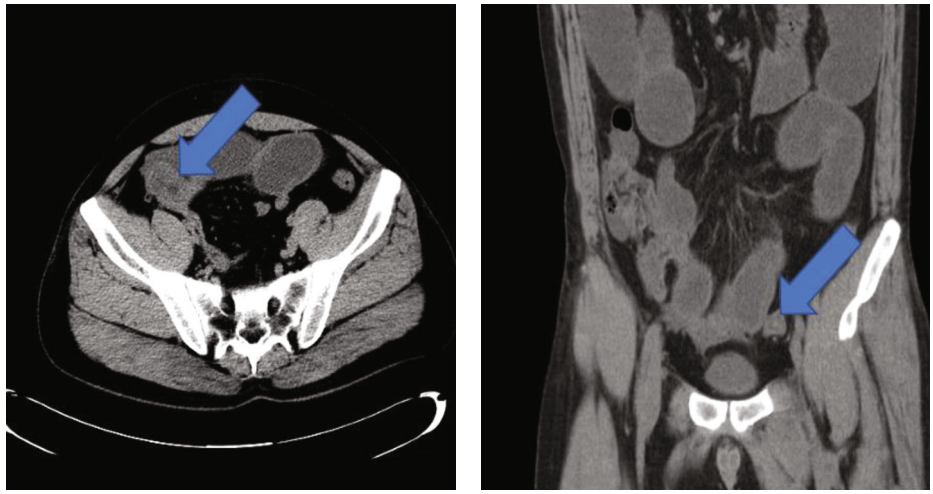

(a) (b)

Figure 1: CT image of patient's intestinal obstruction: front view (a); side view (b). The images depict the location of the patient's intestinal obstruction.

[12, 13]. Intestinal obstruction is a common acute abdomen in gastrointestinal surgery.

With the increasing incidence of colorectal cancer, there are more and more patients with acute mechanical intestinal obstruction caused by colorectal cancer. Most patients also have complications such as dehydration, electrolyte disturbance, and hypoproteinemia, which increase the risk of emergency surgery. Traditional surgical treatment methods include palliative tumor resection and proximal colostomy or only colostomy, which requires a second surgery to close the stoma or second-stage tumor resection, which increases the patient's hospital stay and hospitalization costs. Recent studies have shown that somatostatin can delay the progression of malignant intestinal obstruction and effectively improve the clinical symptoms of patients [14, 15]. The safety and effectiveness of transanal intestinal obstruction catheter for the treatment of colorectal malignant intestinal obstruction have been confirmed [16, 17].

2. Materials and Methods

2.1. Image Segmentation Based on Full Convolutional Network. A fully convolutional network (FCN) replaces the fully connected layer in the convolutional network structure with a fully convolutional layer, predicts the category of pixels from the extracted feature map, and realizes pixel-level classification or segmentation. The full convolutional network can input images of any scale, which solves the problem of repeated calculation of adjacent pixels. But the shortcoming of the full convolutional network is that the training result is still insufficiently accurate, and secondly, the spatial law is ignored.

U-Net uses the symmetrical connection structure of the codec, which performs well in the field of medical image segmentation. The model structure is shown in Figures 1–3. There are many variant structures of U-Net, such as the combination with modules such as ResNet. V-net has made improvements on the basis of U-Net, using 3D convolution; improving the objective function to the Dice coefficient; using random nonlinear transformation and histogram matching as new data enhancement methods; and adding the residual module increases convergence. DenseNet is applied to a fully convolutional network as a segmentation network. This structure can achieve optimal results without pretraining and postprocessing of conditional random fields, as shown by Figure 4.

SegNeW performs low-dimensional encoding on the input image and then uses the direction invariance of the decoder to restore the image. This will generate segmented images on the decoder side. SegNet and FCN are similar in structure but different in sample mode. FCN uses deconvolution upsampling, while SegNet records the coordinate position of the maximum value during the pooling process. During the upsampling process, the value of the feature map is mapped to the corresponding position, and the feature values of other positions of the new feature map are set to zero. During the sampling process of DeconvNet, both the encoder part and the SegNet adopt the structure of VGG16. The difference between DeconvNet and SegNet is that the network finally adds two fully connected layers.

The above four network structures are similar, and they are both the structure of the encoder and the decoder. The encoder part is a combination of the convolutional layer and the pooling layer. The decoder is an upsampling process. Different network structures mainly differ in upsampling methods. The sampling method of FCN is to add to the feature map after deconvolution. U-Net is the same as the sampling method of FCN. DeconvNet maps the feature value to the new feature according to the position of maximum pooling in the sampling process. In the figure, SegNet is the same as DeconvNet.

One of the main purposes of Deeplab is to perform image segmentation while helping control signal extraction, thereby reducing the number of samples and the amount

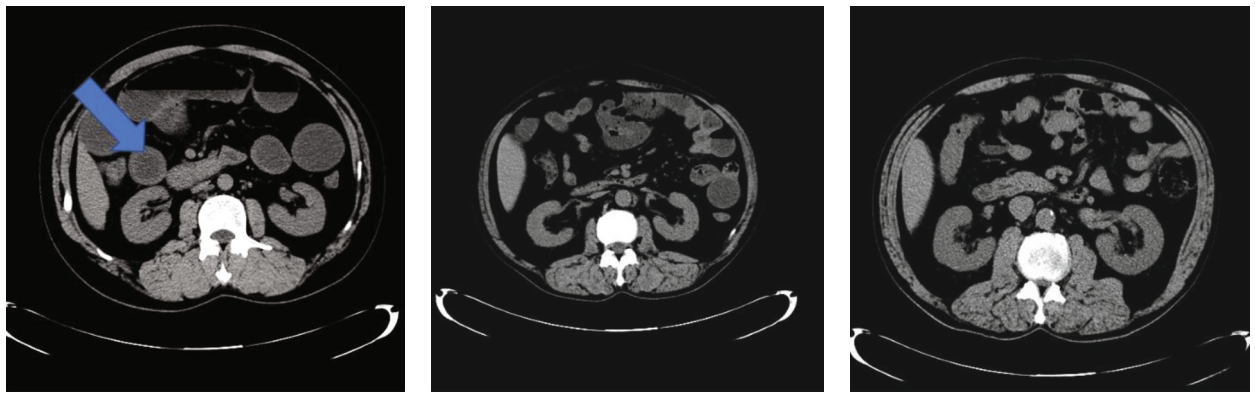

(a) (b) (c)

Figure 2: CT image of the largest diameter of the proximal colon: before surgery (a); 3 days after surgery (b); 7 days after surgery (c). Note that the arrow indicates the location of the patient's intestinal obstruction.

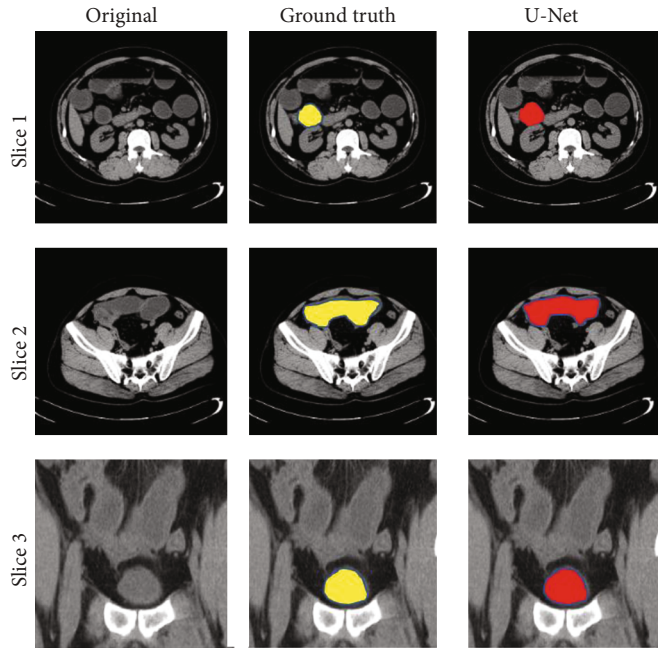

Figure 3: Visualization of the results of organ segmentation in patients with intestinal obstruction.

of data that the network must process. Another purpose is to support multiscale contextual feature learning-to-gather features from images of different scales. Deeplab uses ImageNet pretrained residual neural network for feature extraction. Deeplab uses hole convolution instead of ordinary convolution. The different expansion rate of each convolution enables the residual neural network to capture multiscale contextual information. Deeplab is composed of three parts: hole convolution, which can expand or contract the convolution filter; residual neural network; and Microsoft's deep convolution network, which can pass parameters in thousands of layers of neural networks without losing the parameter characteristics. The powerful representation ability of residual neural network promotes the application of computer vision, such as target detection and face recognition; passive spatial pyramid, used to provide multiscale information, uses a set of convolutions with different expansion rates to capture long-term context. The passive spatial pyramid also uses global average pooling (GAP) to incorporate image-level features and add global contextual information.

2.2. Patient Information. Thirty patients with colorectal cancer with incomplete intestinal obstruction who underwent surgical treatment in colorectal and anal surgery in our hospital from September 2010 to November 2016 were selected. The following are the inclusion criteria: (1) preoperative clinical manifestations such as abdominal distension, abdominal pain, and intestinal obstruction. Standing abdominal plain films

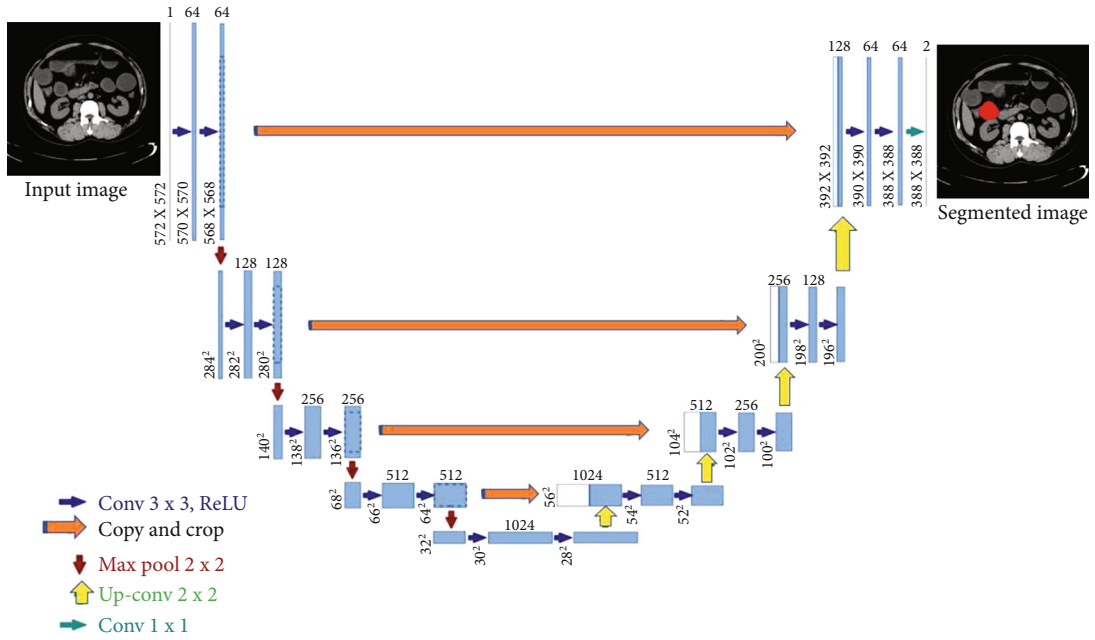

Figure 4: U-Net network model structure diagram.

show intestinal dilation and gas-liquid plane. Colonoscopy or abdominal CT diagnosis of colorectal cancer meets the diagnostic criteria for obstructive colorectal cancer, and patients with colorectal cancer were confirmed by postoperative pathology. According to the random number table method, it was divided into an observation group and a control group. The observation group was given Nengquansu combined with PEG for perioperative intestinal preparation, and the control group was given traditional liquid diet and senna leaves for intestinal preparation (observation group: 15 cases, 8 males and 7 females; age 54~77 years old; obstruction site: 4 cases of rectal obstruction, 6 cases of sigmoid colon obstruction, 3 cases of descending colon obstruction, two cases of colonic splenic flexion obstruction, and 15 cases in the control group, 6 males and 9 females; age 56 to 75 years old; obstruction sites: 5 cases of rectal obstruction, 6 cases of sigmoid colon obstruction, 3 cases of descending colon obstruction, and one case of obstruction of splenic flexure of the colon). Patients with severe heart, liver, and kidney diseases and malignant tumors were excluded. The difference in baseline indicators between the two groups was not statistically significant ($P > 0.05$) and was comparable.

2.3. Research Methods. In the intestinal preparation method, the observation group started oral administration of Nengquansu 1 can/d in the first week before surgery, 2/3 in the morning and 1/3 in the afternoon; meanwhile, 1 bag/d of PEG was taken orally every afternoon from the beginning of the week before the operation, two bags were taken orally 1 d before surgery. The control group was given a conventional liquid diet, and at the same time, senna extracts were given (1 g) before surgery (10 g/d); fasting 1 d before surgery, 20 g of senna extracts was given. All patients were not with enema. In the preoperative nutrition scoring method, the European Nutrition Risk Screening Table NRS-2002{4} was used as a nutrition scoring tool to evaluate the preoperative nutritional status of the two groups. NRS-2002 includes two parts: preliminary screening and final screening, and is finally divided into 4 grades: none, mild, moderate, and severe according to the patient's disease severity and nutritional status, which are counted as 0, 1, 2, and 3 points, respectively. Note that ≥3 points indicate that they are at risk of malnutrition and need nutritional support.

The control group was treated with conservative treatment methods, such as fasting before surgery, decompressing the gastrointestinal tract of the patient, correcting the patient's acid-base balance disorder and water and electrolyte disorder, and intravenously injecting dexamethasone and anti-infection according to the patient's specific situation. Treatment, such as taking cephalosporin antibiotics, was used. The observation group was treated with intravenous somatostatin for 3 to 12 days of continuous treatment. The dose was 6 mg each time. When somatostatin was infused, it was injected into 50 ml of 0.9% saline or 5% glucose injection before infusion. Care should be taken to control the rate of infusion to keep it at 2 ml per hour and continue treatment for 3 to 12 days.

2.4. Research Indicators

2.4.1. Postoperative Clinical-Related Indicators. The operation time, hospitalization time, tolerance of solid food postoperatively, postoperative anal exhaust time, and postoperative complications were observed in the two groups.

2.4.2. Immunological Test Index. The levels of T-lymphocyte subsets (CD3+, CD4+, CD8+, and CD4+/CD8+) and immunoglobulin (Ig G, Ig M) of patients were detected 1 day

before operation and 7 days after operation. The content of serum Ig G was measured by radioimmunoassay, and the content of serum Ig M was measured by enzyme-linked immunoassay. The operation process is strictly in accordance with the instructions of the kit. The percentages of CD3+, CD4+, and CD8+ were measured by flow cytometry (US BD). We took 2 ml of peripheral venous blood in an anticoagulation tube, added 50 μl of anticoagulated whole blood and 20 μl of fluorescent antibody, mixed and placed at room temperature for 30 min, and added 450 μl of hemolysin, mixed and placed at room temperature for 15 min. We then used the automatic analysis software to set the test acquisition conditions. After the quality control is passed, the sample analysis is performed, and the detection percentages of CD3+, CD4+, CD8+, and CD4+/CD8+ are reported.

2.4.3. Observation Index. The effectiveness of treatment, the time of disappearance of clinical symptoms, and the incidence of complications after treatment were compared between the two groups. The evaluation criteria for the effectiveness of treatment are as follows [18–20]:

(1) Cure: the clinical symptoms such as abdominal swelling, abdominal pain, nausea, and retching disappeared. The abdominal X-ray examination revealed that the intestinal effusion and gas disappeared, which was regarded as cured.

(2) Effective: clinical symptoms such as abdominal swelling, abdominal pain, and nausea and retching have been greatly relieved. The abdominal X-ray examination found that the symptoms of intestinal obstruction have been relieved and are considered effective.

(3) Invalid: in the patient's clinical symptoms, there was no relief or even signs of aggravation. The abdominal X-ray examination showed no improvement in the symptoms of intestinal obstruction, which was regarded as ineffective. Total effective rate = (cured + effective) cases/total cases × 100%.

Clinical symptom relief includes abdominal pain relief, time for defecation and defecation, and gastrointestinal decompression. Complications include abdominal infection and peritoneal effusion.

2.5. Statistical Processing. SPSS17.0 was used for data analysis, and the count data was expressed in the form of mean ± standard deviation (mean ± SD). The comparison between the two groups used Student's t-test analysis (T value test), and the comparison between multiple groups used single factor variance (one-way ANOVA followed by Dunnett's test), and the count data uses a chi-square test, which has certain statistical significance.

3. Results

3.1. Preoperative Treatment. After continuous somatostatin pumping and decompression tube treatment through anorectal obstruction for 4 to 10 days, the average (5.6 ± 1.2) days were compared with the abdominal circumference at admission (100%), and the abdominal circumference before surgery was significantly reduced; it is 81 ± 2.3% ($P \leq 0.001$). Abdominal CT examination 3 days after comprehensive treatment measured the maximum transverse diameter of the proximal colon to be 2.8 ± 0.3 cm, which was significantly smaller than 6.2 ± 0.5 cm before treatment ($P \leq 0.001$). In the somatostatin group, after 4 to 7 days and an average of 4.2 ± 1.1 days of treatment, compared with the abdominal circumference at admission (100%), the abdominal circumference before surgery was reduced to 88 ± 1.3% ($P = 0.01$); abdominal CT examination was performed 3 days after treatment to measure the maximum transverse diameter of the proximal colon was 4.6 ± 0.5 cm, which was less than 6.3 ± 0.6 cm before treatment ($P = 0.02$).

3.2. Surgical Treatment. All 30 patients underwent surgery. Of these, 13 patients underwent exploratory laparotomy due to unsatisfactory relief of abdominal distension, and the remaining 17 patients underwent laparoscopic exploratory surgery. Of all the patients, 10 patients completed radical surgery with one-stage anastomosis, including 7 patients who underwent laparoscopic surgery. In the remaining 20 cases, the colon was still significantly dilated and edema during operation, and the tumor was excised and the proximal colostomy was performed.

All patients had no complications such as anastomotic leakage, postoperative bleeding, and abdominal infection. All patients in the somatostatin treatment group underwent surgical treatment, and only 5 patients underwent radical tumor resection and one-stage anastomosis during operation. None of the 5 patients underwent anastomosis under laparoscopy, and 1 of 5 patients developed intestinal fistula 6 days after surgery. He was discharged after placing an irrigation tube for continuous irrigation treatment. The bloating relief time of the observation group was 2.3 ± 0.5 d, the abdominal pain relief time was 2.1 ± 0.4 d, and the voluntary exhaust time was 2.2 ± 0.1 d; the control group was 3.5 ± 0.7 d, 3.3 ± 0.7 d, and 3.5 ± 0.6 d. The indicators in the research group were significantly lower than those in the control group, and there was a significant difference between the two groups ($P < 0.05$).

3.3. Computed Tomography Image Analysis. In order to more intuitively show the effect of somatostatin on patients with intestinal obstruction, this study selected a medical image before and after surgery for comparison and interpretation. Figure 1 is a CT image of the patient's intestinal obstruction before surgery, and Figure 2 is a CT image of the maximum diameter of the proximal colon before and after the patient's operation.

3.4. Segmentation Result. In this paper, a deep neural network structure is proposed, which is an image segmentation model based on a feature mining network. The innovation lies in three aspects: the first is the feature correction unit, which corrects the feature along the direction that is beneficial to the segmentation result. The second is the macro information mining unit, which uses multiscale convolution kernels to scan small-scale features to obtain more spatial location information. The third is the semantic information

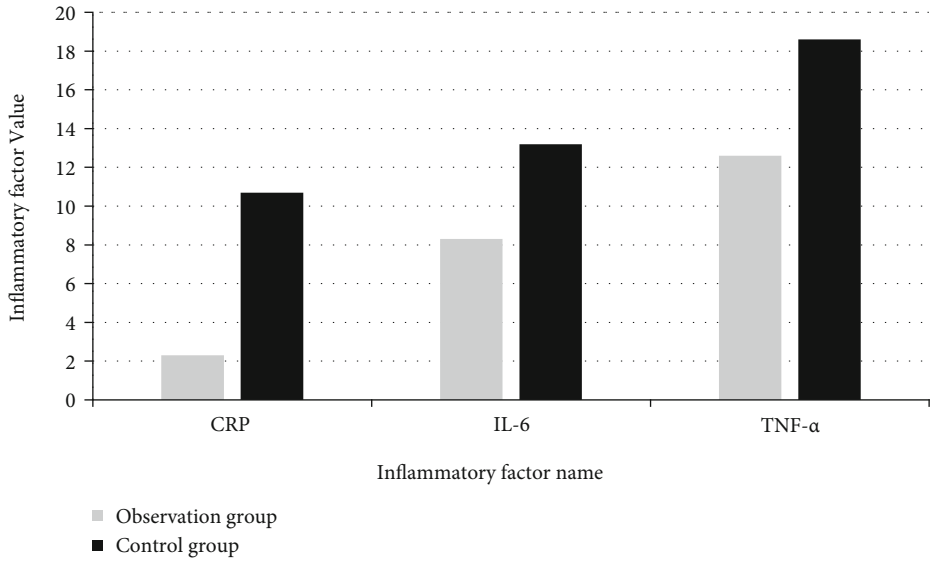

Figure 5: Statistics of changes in inflammatory factors.

mining unit, which uses two branches to dig deeper and more detailed features. Experiments show that all three innovations can improve segmentation performance. The segmentation results are as shown in Figure 3.

3.5. Comparative Analysis of the Treatment Results of the Two Groups of Patients. The levels of CRP, IL-6, and TNF-α in the observation group were significantly lower than those in the control group. There was a significant difference between the groups ($P < 0.05$). The statistic chart of changes in inflammatory factors is shown in Figure 5.

After treatment, the symptoms of the two groups of patients were alleviated. The treatment effective rate of the observation group was 93.3%, and the treatment effective rate of the control group was 73.3%; we note that $P < 0.05$. The comparison statistical table is shown in Table 1.

Compared with the control group, the disappearance time of clinical symptoms of the two groups of patients was lower than that of the control group, and the patients recovered faster, with statistical significance ($P < 0.05$). The comparison statistical table is shown in Table 2.

The complication rates of the two groups of patients were compared, the incidence of complications in the observation group was significantly lower than the control group, the effect was better, and the difference was statistically significant ($P < 0.05$). The comparison statistical table is shown in Table 3.

Table 1: Comparison of the treatment efficiency of the two groups of patients.

Group (n)	Cure	Effective	Invalid	Total efficiency (%)
Observation group (15)	9	5	1	93.3%
Control group (15)	7	4	4	73.3%
χ^2				4.8118
P				0.0283

4. Discussion

Early inflammatory bowel obstruction puncture occurs late in abdominal surgery and is a mechanical intestinal obstruction [21]. The cause of early postoperative inflammatory bowel obstruction is usually caused by prolonged exposure of the intestinal canal or inflammation in the abdominal cavity during the patient's abdominal surgery. The pathogenic mechanism is relatively complex, and most of them are multifactors acting at the same time. Common factors include inflammation, sympathetic nerve inhibition, release of neurotransmitters, hormones, and the use of narcotic drugs, analgesic drugs, etc. [22–24]. Inflammation can cause intestinal edema and hyperemia in patients, leading to intestinal adhesions and formation of intestinal obstruction. There are still no effective preventive measures at present, and the risk is high after surgery. The principle of treatment is generally fasting, correction of water and electrolyte disturbances, and acid-base balance disorders. Drug treatment is generally given adrenal corticosteroids to promote edema resolution, and antisense treatment with antibiotics is also required [25, 26].

Malignant intestinal obstruction caused by distal colon cancer accounts for 88% to 97% of the lower colorectal obstruction [27], and 7% to 28% of colon cancer patients have intestinal obstruction as the first symptom. In recent years, the incidence of colon cancer has increased year by year [28], and the number of patients with acute intestinal obstruction has increased year by year. The main cause of intestinal obstruction is the accumulation of digestive juices in the proximal digestive tract. Therefore, the key to nonsurgical treatment of intestinal obstruction is to reduce the secretion of digestive juice and reduce the accumulation of fluid in the digestive tract. Somatostatin not only inhibits

Table 2: Comparison of clinical symptoms disappearing time between two groups.

Group (n)	Abdominal pain relief time (d)	Exhaust time (d)	Gastrointestinal decompression (md/d)
Observation group (15)	3.16 ± 1.39	2.66 ± 1.45	254.33 ± 236.07
Control group (15)	5.88 ± 1.84	4.78 ± 1.97	605.29 ± 245.78
τ	6.46.5	4.7470	5.6407
P	0.001	0.001	0.001

Table 3: Comparison of the incidence of complications between the two groups.

Group (n)	Celiac infection	Ascites	Incidence (%)
Observation group (15)	1	2	20.0%
Control group (15)	2	4	40.0%
χ^2			8.5227
P			0.0035

the secretion of various hormones but also reduces the secretion of digestive juices.

Combined application of somatostatin therapy on the basis of total parenteral nutrition can reduce digestive juice secretion by more than 90%. The reduction of digestive juice can reduce intestinal wall edema, improve the condition of intestinal mucosal epithelial ischemia and hypoxia, and reduce capillary permeability [29–31]. Somatostatin can also inhibit the proliferation of tumor cells to a certain extent. In the last century, Japanese scholars reported for the first time the use of transanal obstruction decompression catheter for decompression and drainage of the proximal colon. At present, domestic and foreign scholars tend to use metal stents to expand or place trans-anal intestinal obstruction catheters to relieve the obstruction for a limited period of laparoscopic radical surgery. Compared with intestinal metal stents, transanal obstruction catheters are less expensive, and the probability of perforation and postoperative pain is also lower. It does not cause strong compression of the tumor, so the possibility of tumor spread is reduced.

In this study, after two groups of patients underwent gastric tube decompression, the fluid accumulation in the proximal digestive tract decreased. Combined use of somatostatin therapy can further reduce the secretion of digestive juice and relieve the pressure of obstructive bowel segment. All patients were able to obtain symptom relief before surgery, and the abdominal circumference was significantly reduced, and the degree of intestinal dilatation was also significantly reduced. Elderly patients with long-term intestinal obstruction mostly have intestinal wall congestion and edema and poor blood flow and more often have complications such as anemia, hypoproteinemia, and electrolyte disturbance important. Transanal obstruction catheter can effectively reduce the accumulation of fluid in the proximal large intestine, reduce the edema and expansion of the intestinal canal, and also be used to repeatedly clean the enema to achieve the purpose of preoperative preparation to clean the intestine. Research has shown that the success rate of intestinal obstruction catheter for colorectal cancer complicated with first-stage anastomosis is 84% to 98%, and postoperative incision infection rate and hospitalization time are significantly better than traditional emergency surgery. In this study, the first-stage anastomosis rate and laparoscopic completion rate after treatment with somatostatin and anorectal obstruction catheter were significantly higher than those with somatostatin treatment alone, and there were no serious complications after surgery.

In summary, the use of somatostatin in the treatment of early inflammatory bowel obstruction after acute abdomen surgery can effectively improve the treatment efficiency of patients, reduce the disappearance time of clinical symptoms, have a lower complication rate, and have a significant therapeutic effect, which is worthy of clinical application.

5. Conclusion

With the continuous development of modern medical imaging technology, the information contained in the images is becoming more and more abundant. At the same time, the increasing number of tumor patients has also increased the workload of doctors in diagnosis. It takes a lot of time to read an image of a patient, and it is very important to accurately obtain the tumor information in the image to make a clinical diagnosis of the patient. However, because the results produced in the process of manual tumor segmentation will produce different results due to the doctor's experience and medical background and even the final diagnosis results will be inconsistent, the emergence of auxiliary diagnosis can use the high-performance computing server and depth. Learning technology helps doctors complete tumor segmentation and accelerates the doctor's diagnosis process. This paper mainly introduces the basic concepts and principles of tumor segmentation, traditional segmentation methods, and segmentation methods based on deep learning. This thesis focuses on improving the accuracy of tumor segmentation (especially for smaller tumors) and the interpretability of tumor segmentation in tumor segmentation and improving the quality of medical aided diagnosis.

In conclusion, somatostatin combined with transanal obstruction catheter is safe and effective for the treatment of elderly patients with malignant intestinal obstruction in the distal colon. After a period of treatment, the patient's symptoms can be effectively relieved, and the conditions for surgical treatment can be created. Subsequent surgical treatment has a higher completion rate of laparoscopic surgery and a first-stage anastomosis power, which reduces

the incidence of postoperative complications and alleviates patient's hospital stay and financial burden.

Data Availability

The image data used to support the findings of this study have been deposited in the CVC-Clinic dataset (http://www.cvc.uab.es/CVC-Colon/index.php/databases/).

Conflicts of Interest

The authors declare that they have no conflicts of interest.

Acknowledgments

The authors appreciate the research data and the patient information provided by Fuxin Centre Hospital.

References

[1] K. Caglayan, I. Oner, Y. Gunerhan, P. Ata, N. Koksal, and S. Ozkara, "The impact of preoperative immunonutrition and other nutrition models on tumor infiltrative lymphocytes in colorectal cancer patients," *American Journal of Surgical Pathology*, vol. 204, no. 4, pp. 416–421, 2012.

[2] S. A. Mousavi, H. Karami, and H. Saneian, "Congenital duodenal obstruction with delayed presentation: seven years of experience," *Archives of Medical Research*, vol. 5, no. 5, pp. 1023–1027, 2016.

[3] D. Huang, Z. Sun, J. Huang, and Z. Shen, "Early enteral nutrition in combination with parenteral nutrition in elderly patients after surgery due to gastrointestinal cancer," *International Journal of Clinical and Experimental Medicine*, vol. 8, no. 8, pp. 13937–13945, 2015.

[4] O. Kherad, S. Restellini, M. Martel, and A. N. Barkun, "Polyethylene glycol versus sodium picosulfalte bowel preparation in the setting of a colorectal cancer screening program," *Candian Journal of Gasteroenterology*, vol. 29, article 350587, p. 7, 2015.

[5] A. Erdog, Y. D. Putra-Limasale, and D. Keskin, "_In vitro_ characterization of a liposomal formulation of celecoxib containing 1,2-distearoyl- _sn_ -glycero-3-phosphocholine, cholesterol, and polyethylene glycol and its functional effects against colorectal cancer cell lines," *Journal of Pharmaceutical Sciences*, vol. 102, no. 10, pp. 3666–3677, 2013.

[6] O. Algın, E. Ozmen, and M. R. Metin, "Bouveret syndrome: evaluation with multidetector computed tomography and contrast-enhanced magnetic resonance cholangiopancreatography," *Journal of Trauma and Emergency Surgery Current.*, vol. 19, no. 4, pp. 375–379, 2013.

[7] A. Li, F. Li, and Y. Fang, "Application of oral gastrografin in gastroenterography in judgment of the opportunity of operation in simple mechanical small bowel obstruction," *Journal of Clinical Surgery*, vol. 8, pp. 557–559, 2012.

[8] O. Catano, "Das fäzeszeichen: ein CT-befund bei dünndarmobstruktion," *Radiologe*, vol. 37, no. 5, pp. 417–419, 1997.

[9] D. Ufnagel, S. Rajaee, and F. H. Millham, "How many sunsets? Timing of surgery in adhesive small bowel obstruction," *Journal of Trauma-injury Infection and Critical Care*, vol. 74, no. 1, pp. 181–189, 2013.

[10] X. L. Sun, T. G. Wen, and L. Yang, "MSCT analysis of small bowel feces sign," *Journal of Clinical Radiology*, vol. 1, pp. 108–111, 2016.

[11] L. P. Ye, X. W. Wu, and J. M. Xu, "Clinical study on the etiologic diagnosis method of small bowel obstruction," *Chinese Journal of Digestion*, vol. 35, no. 4, pp. 221–224, 2015.

[12] V. E. Pricolo and F. Curley, "CT scan findings do not predict outcome of nonoperative management in small bowel obstruction: retrospective analysis of 108 consecutive patients," *International Journal of Surgery*, vol. 27, pp. 88–91, 2016.

[13] I. Millet, P. Taourel, and A. Ruyer, "Value of CT findings to predict surgical ischemia in small bowel obstruction: a systematic review and meta-analysis," *European Radiology*, vol. 25, no. 6, pp. 1823–1835, 2015.

[14] W. K. Xu, D. Li, and J. P. Sha, "Comparison of clinical diagnosis between CT and abdominal X-ray film on intestinal obstruction," *Modern Diagnosis and Treatment*, vol. 11, pp. 122-123, 2017.

[15] S. D. Deshmukh, D. S. Shin, and J. K. Willmann, "Non-emergency small bowel obstruction: non-emergency small bowel obstruction: assessment of CT findings that predict need for surgery," *European Radiology*, vol. 21, no. 5, pp. 982–986, 2011.

[16] Y. H. Liu, "Significance of piasma levei of advanced giycation end products in evaiuation of patients'condition after operations for intestinai obstruction," *Chinese General Practice*, vol. 11, pp. 1280–1283, 2015.

[17] E. Delabrousse, J. Lubrano, and N. Sailley, "Small-bowel bezoar versus small-bowel feces: CT evaluation," *American Journal of Roentgenology*, vol. 191, no. 5, pp. 1465–1468, 2008.

[18] J. H. Abu-hmeidan, H. A. Bismar, and A. M. Hamid, "Small bowel feces sign in association with occlusive mesenteric ischemia," *Acta Radiologica Short Reports*, vol. 3, no. 7, pp. 204798161454014–204798161454014, 2014.

[19] A. Lamazza, E. Fiori, and A. V. Sterpetti, "Endoscopic placement of a covered stent to arrest bleeding from obstructing colorectal cancer," *Techniques in Coloproctology*, vol. 21, no. 11, pp. 901–903, 2017.

[20] S. Oguro, T. Funabili, and K. I. Hosoda, "64-slice multidetector computed tomography evaluation of gastrointestinal tract perforation site: detectability of direct findings in upper and lower GI tract," *European Radiology*, vol. 20, no. 6, pp. 1396–1403, 2010.

[21] J. N. Roan and M. H. Wu, "Esophageal perforation caused by external air-blast injury," *Journal of Cardiothoracic Surgery*, vol. 5, no. 1, pp. 130–132, 2010.

[22] C. Tran, D. S. Fink, and M. Kunduk, "Minimally invasive management of tracheoesophageal fistula with T-tube," *The Laryngoscope*, vol. 125, no. 8, pp. 1911–1914, 2015.

[23] W. Memon, Y. J. Khattak, T. Alam, L. M. Sconfienza, M. Awais, and S. S. M. Anwar, "MDCT of small bowel obstruction: how reliable are oblique reformatted images in localizing point of transition?," *Gastroenterology Research and Practice*, vol. 2014, Article ID 815802, 7 pages, 2014.

[24] R. Guppta, P. Mittal, and A. Mittal, "Spectrum of MDCT findings in bowel obstruction in a tertiary care rural hospital in northern India," *Journal of Clinical and Diagnostic Research*, vol. 10, no. 11, p. TC01-TC04, 2016.

[25] W. W. Mayosmith, J. Wittenberg, and G. L. Benett, "The CT small bowel faeces sign: description and clinical significance," *Clinical Radiology*, vol. 50, no. 11, pp. 765–767, 1995.

[26] Y. Fang, F. Cao, and J. Li, "A study on the surgery timing for adhesive small bowel obstruction," *Chinese Journal of General Surgery*, vol. 30, no. 2, pp. 108–110, 2015.

[27] D. Lazarus, "Frequency and relevance of the "small-bowel feces" sign on CT in patients with small-bowel obstruction," *American Journal of Roentgenology*, vol. 183, no. 5, pp. 1361–1366, 2004.

[28] X. W. Yang, Y. Zheng, and Z. Z. Fan, "CT findings and the values of faces sign and bezoars in small bowel obstruction," *Diagnostic Imaging and Interventional Radiology*, vol. 21, pp. 361–364, 2012.

[29] A. Datye and J. Hersh, "Colonic perforation after stent placement for malignant colorectal obstruction – causes and contributing factors," *Minimally Invasive Therapy & Allied Technologies*, vol. 20, no. 3, pp. 133–140, 2011.

[30] H. J. Lee, S. P. Hong, J. H. Cheon et al., "Long-term outcome of palliative therapy for malignant colorectal obstruction in patients with unresectable metastatic colorectal cancers: endoscopic stenting versus surgery," *Gastrointestinal Endoscopy*, vol. 3, pp. 259–263, 2011.

[31] Z. Tang, G. Zhao, and T. Ouyang, "Two-phase deep learning model for short-term wind direction forecasting," *Renewable Energy*, vol. 173, pp. 1005–1016, 2021.

Hindawi
Computational and Mathematical Methods in Medicine
Volume 2022, Article ID 4312117, 7 pages
https://doi.org/10.1155/2022/4312117

Research Article

Prediction of Lung Infection during Palliative Chemotherapy of Lung Cancer Based on Artificial Neural Network

Wei Guo, Guoyun Gao, Jun Dai, and Qiming Sun

The Second People's Hospital of Wuhu, Wuhu, Anhui 230032, China

Correspondence should be addressed to Jun Dai; daijun772167@163.com and Qiming Sun; 2829584305@qq.com

Wei Guo and Guoyun Gao contributed equally to this work.

Received 7 October 2021; Revised 24 November 2021; Accepted 14 December 2021; Published 10 January 2022

Academic Editor: Kelvin Wong

Lung infection seriously affects the effect of chemotherapy in patients with lung cancer and increases pain. The study is aimed at establishing the prediction model of infection in patients with lung cancer during chemotherapy by an artificial neural network (ANN). Based on the data of historical cases in our hospital, the variables were screened, and the prediction model was established. A logistic regression (LR) model was used to screen the data. The indexes with statistical significance were selected, and the LR model and back propagation neural network model were established. A total of 80 cases of advanced lung cancer patients with palliative chemotherapy were predicted, and the prediction performance of different model was evaluated by the receiver operating characteristic curve (ROC). It was found that age ≥ 60 years, length of stay ≥ 14 d, surgery history, combined chemotherapy, myelosuppression, diabetes, and hormone application were risk factors of infection in lung cancer patients during chemotherapy. The area under the ROC curve of the LR model for prediction lung infection was 0.729 ± 0.084, which was less than that of the ANN model (0.897 ± 0.045). The results concluded that the neural network model is better than the LR model in predicting lung infection of lung cancer patients during chemotherapy.

1. Introduction

At present, lung cancer is still the leading cause of death globally [1–3]. Patients with advanced lung cancer who have multiple systemic metastases are less likely to receive palliative chemotherapy, because there is no indication for targeted therapy after gene detection. Palliative chemotherapy is also the use of traditional chemotherapy drugs, but the purpose is not to treat cancer but to reduce the clinical symptoms of lung cancer patients. Palliative chemotherapy can prolong the life of patients and help them recover their daily life. Therefore, the drug dose of palliative chemotherapy will be lower than that of general chemotherapy [4–6].

In the study of complications and causes of death in cancer patients, infection-related causes of death are as high as 76% [7–9]. The causes of infection in patients with lung cancer during chemotherapy are complex, and there are various risk factors affecting the disease [10, 11]. There may be an interaction between some risk factors and multicollinearity, which seriously interferes with the prediction of infection [12]. With the development of artificial intelligence technology, the artificial intelligence (AI) algorithm represented by deep learning is gradually applied in various medical fields and has achieved better diagnostic energy efficiency [13–16]. Among them, the back propagation (BP) neural network model is widely used to establish a prediction model in medical diagnosis [17].

The study analyzed 80 patients with lung cancer who were hospitalized for chemotherapy, established a specific prediction model by using the risk factors that affect the lung infection during palliative chemotherapy, and made an evaluation and prediction of the possible infection in patients with lung cancer. According to the prediction results, the individual status and whether preventive intervention measures should be taken can improve patients' treatment effect and quality of life.

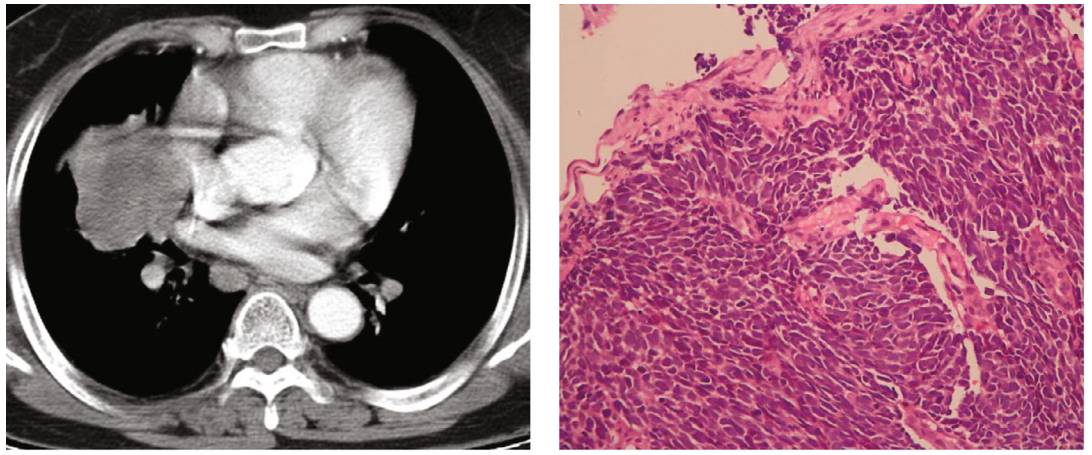

(a) (b)

Figure 1: The CT image (a) and pathology (b) from a patient with small-cell lung cancer.

2. Materials and Methods

2.1. General Information. The data collection time was from January 2019 to December 2019. All hospitalized patients with advanced lung cancer confirmed by clinical, imaging, and pathology were collected in this period. The cases collected in the study were approved by the ethics committee of the Second People's Hospital of Wuhu, and all patients were informed to sign informed consent.

The following are the inclusion criteria: (1) the diagnosis of lung cancer was supported by imaging and pathological results (Figure 1), (2) palliative chemotherapy was used, (3) estimated survival time of patients was greater than three months, and (3) there is no communication barrier with medical staff.

The following are the exclusion criteria: (1) serious complications, (2) serious physical diseases, (3) mental diseases, and (4) application for withdrawal from the study.

Finally, 80 patients were selected as the research objects. They were 56 male and 24 female patients, aged 46-86 (68.32 ± 9.45) years. In the TNM stage, there are 13 cases of IIIA stage, 27 cases of IIIB stage, 32 cases of IIIC stage, and 8 cases of IV stage. There were 7 cases of small-cell lung cancer, 30 cases of adenocarcinoma, 37 cases of squamous cell carcinoma, and 6 cases of other cancers.

2.2. Source of Data. The chemotherapy patients diagnosed as lung cancer by tissue and cytology were randomly selected by a stratified sampling method from January 2016 to December 2018. The demographic characteristics are shown in Table 1. The hospital history data should be unified and detailed, and the information collected includes age, sex, smoking index (-
smoking index = number of smoking per day × number of years of smoking), TNM stage, pathological classification, basic diseases, chemotherapy cycle, chemotherapy plan, invasive operation, lung cancer surgery history, radiotherapy history, leukocyte and albumin, adverse reactions after chemotherapy, hormone that should be used, antibiotics, and hospitalization time.

Table 1: Demographic characteristics of 400 patients with lung cancer.

Observation items	Features
Age	67.4 ± 15.2
Gender (male/female)	279/121
Cytological type (case)	
Small cell	38
Adenocarcinoma	152
Squamous cell carcinoma	176
Other	34
TNM staging	
IIIA	65
IIIB	131
IIIC	164
IV	40
Nosocomial infection (cases)	
Infected	76
Noninfected	354

2.3. Criteria of Pulmonary Infection. According to the diagnostic criteria of nosocomial pulmonary infection formulated by the American Thoracic Association, the selected patients had at least two or more of the following manifestations: (1) there were fever, cough, and expectoration after and chemotherapy; (2) fever, cough, and expectoration had occurred before chemotherapy, and the symptoms were aggravated after chemotherapy; (3) the pulmonary rales become more and more after chemotherapy; and (4) chest X-ray showed new or progressive infiltration.

2.4. Back Propagation Neural Network. ANN is divided into three layers: input layer, hidden layer, and output layer. Figure 2 is the schematic diagram of the neural network. Perceptron is the basic unit of neural network. It is composed of weight W, offset B, and transfer function $g(x)$.

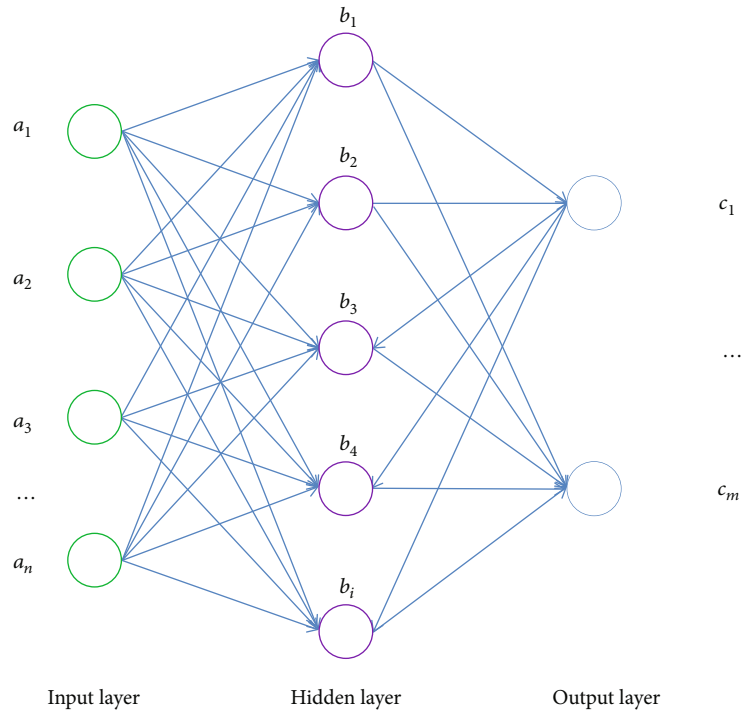

Figure 2: Schematic diagram of BP neural network algorithm.

The ANN algorithm is deduced and trained to obtain the training results.

We set the input layer as a_1, the hidden layer as $b_2 b_3 \cdots b_{n-1}$, and the output layer as c_n. We let the value of each perceptron in the input layer be $a_{1n}(n = 1, 2, 3 \cdots)$, and the other layers are similar. We set the weight w_{ab}^k as the weight between the a-th sensing unit of layer K and the b-th sensing unit of layer $K + 1$. The bias is b'. According to the perceptron principle, the bias can be used as a perceptron with a weight of 1 and a signal of b' in the upper layer. Therefore, bias b' is not considered in the following derivation.

The implemented neural network model has preoutput, back propagation, updating weights, and other parameters (Figure 3). The brief steps are as follows.

(Step 1) We set the input signal received by each unit of the input layer as $x_1 x_2 x_3 \cdots x_n$ and assign a random value to w. According to the above process, a set of calculation results can be obtained at the output layer.

(Step 2) The error between the predicted value and the real value is calculated in reverse, and the relationship between the final error and the initial weight is calculated.

(Step 3) Use stochastic gradient descent to find the minimum value of error E.

(Step 4) By iterating and updating W, the training is completed and the prediction results are obtained.

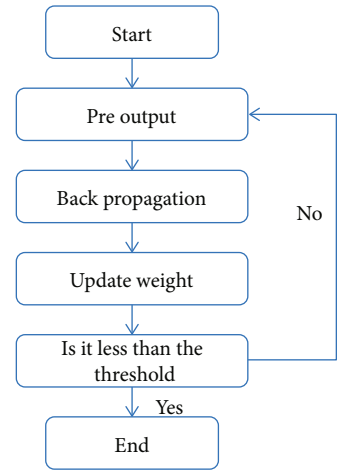

Figure 3: BP neural network algorithm flow.

For Step 1, the input value reaches the value $\sum_{i=1} w_{i1}^1 a_{1i}$ of the first neural unit b_{21} of the hidden layer b_2 through weight calculation, and the input signal value of b_{21} is $g(\sum_{i=1} w_{i1}^1 a_{1i})$ through the transfer function $g(x)$.

$$\text{The output layer is } c_{nj} = g\left(\sum_{i=1} w_{ij}^{n-1} b_{(n-1)i}\right).. \quad (1)$$

For Step 2, set the label as $d_{mi}(i = 1, 2, 3 \cdots)$ and substitute the hidden layer unit c_{nj_n} to obtain the relationship E between the error and the initial weight.

Table 2: Multivariate analysis of risk factors of infection in patients with lung cancer during chemotherapy.

Factor	β	SE	Wald	P	OR	95% CI
Age ≧ 60 years	0.718	0.242	9.235	0.004	2.079	0.279-3.182
Length of stay ≧ 14 d	1.349	0.381	14.526	<0.001	3.674	2.138-4.943
Surgery history	0.192	0.064	8.927	0.035	1.207	1.039-1.274
Combined chemotherapy	0.593	0.158	6.142	0.008	1.536	1.123-2.149
Myelosuppression	-1.452	0.017	11.472	<0.001	0.261	0.225-0.493
Diabetes	0.674	0.135	7.243	0.006	1.894	1.492-2.768
Hormone application	0.269	0.114	3.125	0.022	1.347	1.193-1.752

According to Step 4,

$$E = \frac{1}{2}\sum_{j_n=1}\left(d_{nj_n - c_{nj_n}}\right)^2 \tag{2}$$

set

$$k = \sum_{j_{n-1}=1} w_{j_{n-1}j_n}^{n-1} b_{(n-1)_{j_{(n-1)}}},$$
$$\frac{\delta E_i}{\delta w_{ij}^{n-1}} = \frac{\delta E_i \delta c_{ni} \delta k}{\delta c_{ni} \delta k \delta w_{ij}^{n-1}}, \tag{3}$$

and then the function (4) can be obtained

$$\frac{\vartheta E_i}{\vartheta w_{ij}^{n-1}} = -c_{ni} b_{(n-1)i}(d_{ni} - c_{ni})(1 - c_{ni}), \tag{4}$$

and the weight w_{ij}^{n-1} can be updated to obtain function

$$\left(w_{ij}^{n-1}\right)^* = w_{ij}^{n-1} - \eta^* \sum_{i=1} \frac{\vartheta E_i}{\vartheta w_{ij}^{n-1}}. \tag{5}$$

2.5. Statistical Analysis. In this study, considering that the number of neurons is too large and the sample size is high, the infection of lung cancer during chemotherapy was taken as the dependent variable, and the univariate and multivariate logistic regression (LR) analysis was carried out to establish the prediction model. The LR and artificial neural network (ANN) prediction models were established, respectively, using the 400 patients from January 2016 to December 2018. The test set was the 80 patients from January 2019 to December 2019. The Z test was used to compare the area under the receiver operator characteristics (ROC) curve with 0.5 to test whether the model has predictive value; the Z test was used to compare the area under the ROC curve of the model to evaluate the predictive effect of the model. The construction of LR model and the drawing of ROC curve are completed by SPSS software; the ANN model is constructed by MATLAB software, and the simulation and verification of test samples are carried out.

3. Results

3.1. Logistic Regression Analysis. From the univariate and multivariate conditional logistic regression analysis, seven indexes have statistical significance: age ≧ 60 years, length of stay ≧ 14 d, lung cancer surgery history, combined chemotherapy, myelosuppression, diabetes, and hormone application (Table 2). In multivariate analysis, the cut point value of classification was 0.5, and the maximum number of iterations was 20. The LR model was established by using the partial maximum likelihood forward method. The expression was follows:

$$\begin{aligned}\text{Logit}(P) = {} & -0.482 + 0.718\,(\text{age}) + 1.3749\,(\text{length of stay}) \\ & + 0.192\,(\text{surgery history}) \\ & + 0.593\,(\text{combined chemotherapy}) \\ & - 1.452\,(\text{myelosuppression}) + 0.674\,(\text{diabetes}) \\ & + 0.269\,(\text{hormone application}).\end{aligned} \tag{6}$$

3.2. ANN Analysis. According to the influence degree of input influencing factors on the network, the following sequence diagram was made (Figure 4). The influence degree was high to low: myelosuppression, length of stay, age, diabetes, combined chemotherapy, surgery history, and hormone application. Taking the above seven independent variables as input elements and pulmonary infection as output elements, a three-layer feedforward artificial BP neural network (ANN) model is directly constructed. In the input layer, there were 7 neural nodes; in the hidden layer, there were 7 changeable nodes (hyperbolic tangent transfer function); in the output layer, pulmonary infection occurred during chemotherapy (softmax transfer function). The transfer function of hidden layer was Tansig, the transfer function of output layer was Purelin, the target error is 0.01, the learning rate is 0.1, and LM optimization algorithm is used for network training.

3.3. Model Prediction. The area under the ROC curve of ANN was 0.897, which was larger than that of the LR regression model (0.729), indicating that the ANN model has higher predictive ability than the traditional LR model (Figure 5). The results showed that the accuracy, sensitivity, and Youden's index of the ANN model were higher than those of the LR model, but the specificity of the ANN model was lower than that of the LR model (Table 3).

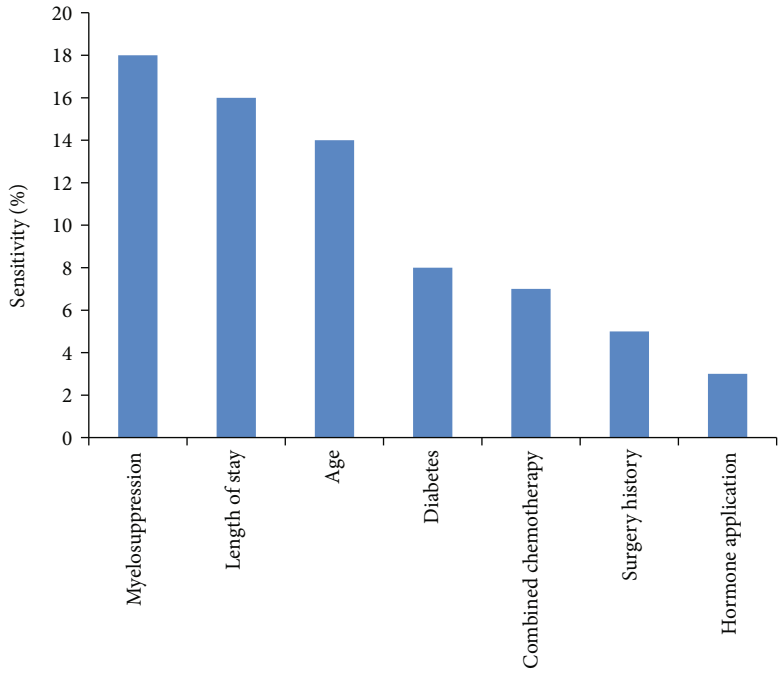

Figure 4: Sensitivity analysis of ANN input variables.

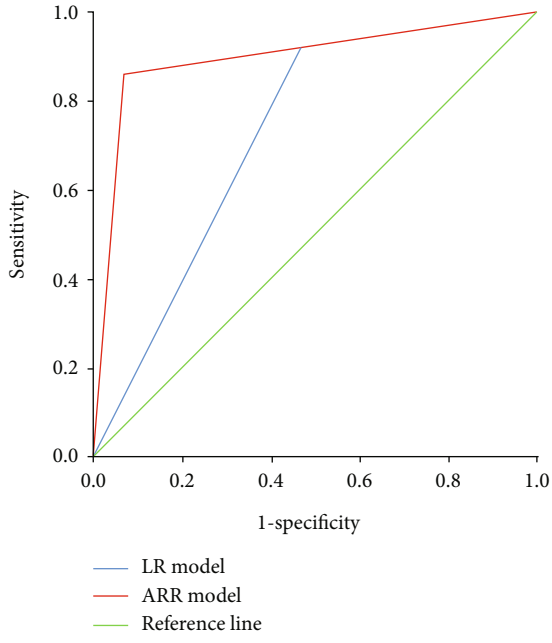

Figure 5: ROC curve of ANN and LR model for predicting pulmonary infection.

Table 3: Evaluation indexes of the ANN model and logistic model.

Model	AUC	Sensitivity	Specificity	Youden's index
LR	0.729 ± 0.084	53.3	92.3	45.6
ANN	0.897 ± 0.045	93.3	86.2	79.5

4. Discussion

The causes of infection in patients with lung cancer during chemotherapy are complex, and there are various risk factors of infection [18, 19]. Nosocomial infection not only affects treatment and rehabilitation, prolongs hospital stay, and increases medical costs but also significantly affects prognosis and even endangers life. Most of them were elderly patients with age-related organ dysfunction, low immunity, high incidence of multiple diseases, and being easy to complicate with all kinds of hospital infection. The incidence of nosocomial infection was 19.0% (76/40), which was similar to that reported in a domestic literature. Further analysis showed that age ≧ 60 years, length of stay ≧ 14 d, surgery history, combined chemotherapy, myelosuppression, diabetes, and hormone application were risk factors of infection in lung cancer patients during chemotherapy [20].

This study attempts to establish a specific mathematical model by using the risk factors of infection during chemotherapy, evaluating and predicting the possible infection of elderly patients with lung cancer, and evaluating and exploring a new method to predict individual disease. LR is simple and easy to use. It is the most commonly used method to predict the disease status with precise classification. However, it requires that the data meet certain conditions; that is, the dependent variable is a classification variable, the independent variables are independent of each other, and there is no obvious collinearity and interaction, so it is difficult to predict the infection of individual patients effectively. ANN has no requirements for the distribution and type of variables. It is good at dealing with nonlinear, fuzzy, and noisy data. It provides a new way to solve complex medical problems and has been paid more and more attention by medical workers in disease prediction. Relevant research shows that the BP neural network is much better than the traditional Cox regression and LR model for data fitting [21–23].

In this study, the risk factors screened by conditional LR regression analysis were used to establish LR and ANN prediction models, and test samples were used to test. The results show that the accuracy, sensitivity, and Youden's index of the ANN model are better than those of the LR model. In this study, the ROC curve was used to evaluate the predictive effect of the three models. The ROC curve can directly observe the relationship between sensitivity and specificity. The larger the area under the curve, the greater the accuracy of the diagnostic test. The results showed that the area under the ROC curve of the LR prediction model was 0.729 ± 0.084. The area under the ROC curve of the BP neural network was 0.897 ± 0.045, which indicated that the ANN prediction model had better prediction and discrimination performance than the LR prediction model. The data fitting of ANN was better than that of the traditional LR prediction model.

Accurate prediction of lung infection in lung cancer patients undergoing chemotherapy is helpful to improve the treatment effect of patients. Once it is determined that some patients are prone to pulmonary infection, we should pay more attention in clinical work and implement intervention nursing measures. It mainly includes the following: (1) the long-term bedridden patients should help to take the semireclining position during the day, guide effective cough and expectoration, and carry out respiratory function exercise, so as to prevent the occurrence of pneumonia; (2) when eating, the patient should take the sitting position and lie flat after eating for 1 hour to avoid aspiration; (3) encourage patients to exercise in bed and turn over regularly; (4) for patients with nutritional risk, the reasons of loss of appetite or inability to eat should be evaluated in time, and the pretreatment before chemotherapy and the observation and treatment of side effects after chemotherapy should be done well; (5) the ward environment, air circulation, and air conditioning should be deeply cleaned before use, to prevent the spread of bacteria through the air; (6) strict aseptic technical operation should be performed, according to the norms of the implementation of a variety of pipe care; and (7) strengthen oral care and guide patients to gargle after meals, and observe whether there are food residues in the mouth and the changes of oral mucosa.

Because this study is a retrospective study, the definition of patients with infection mainly depends on the doctor's diagnosis, course of disease records, imaging examination, and access to the test sheet in the case with specimen records, including sputum, blood, urine specimens, and pleural effusion. There are still some cases of antibiotic use. Because there are no precise diagnosis and no relevant laboratory and imaging evidence, it cannot determine whether antibiotics in this patient is preventive or therapeutic. This may lead to information limitations and bias, resulting in defects in the established prediction model.

5. Conclusions

This study analyzed infection risk factors in patients with lung cancer during palliative chemotherapy. The ROC curve shows that the area under the ROC curve of ANN is more significant than that of LR, which indicates that the prediction ability of ANN is higher than that of the traditional LR model. In the future, more deep learning algorithms [24–26] will be used for predictive analysis of lung cancer.

Data Availability

The data used to support the findings of this study are available from the corresponding author upon request.

Conflicts of Interest

The authors declare that there was no conflict of interests.

Authors' Contributions

Wei Guo and Guoyun Gao contributed equally to this work.

Acknowledgments

We would like to thank all patients who have participated in the experiment. Their support for the survey provided satisfactory data for this study.

References

[1] Y. Mao, D. Yang, J. He, and M. J. Krasna, "Epidemiology of lung cancer," *Surgical Oncology Clinics of North America*, vol. 25, no. 3, pp. 439–445, 2016.

[2] F. Nasim, B. F. Sabath, and G. A. Eapen, "Lung cancer," *The Medical Clinics of North America*, vol. 103, no. 3, pp. 463–473, 2019.

[3] A. Steven, S. A. Fisher, and B. W. Robinson, "Immunotherapy for lung cancer," *Respirology*, vol. 21, no. 5, pp. 821–833, 2016.

[4] W. A. Ghandourh, "Palliative care in cancer: managing patients' expectations," *Journal of Medical Radiation Sciences*, vol. 63, no. 4, pp. 242–257, 2016.

[5] V. T. Janmaat, E. W. Steyerberg, A. van der Gaast et al., "Palliative chemotherapy and targeted therapies for esophageal and gastroesophageal junction cancer," *Cochrane Database of Systematic Reviews*, vol. 2017, no. 11, article CD004063, 2017.

[6] M. Matzo, "Palliative chemotherapy," *The American Journal of Nursing*, vol. 116, no. 6, pp. 59–62, 2016.

[7] S. Hong, Y. Mok, C. Jeon, S. H. Jee, and J. M. Samet, "Tuberculosis, smoking and risk for lung cancer incidence and mortality," *International Journal of Cancer*, vol. 139, no. 11, pp. 2447–2455, 2016.

[8] K. Sigel, A. Makinson, and J. Thaler, "Lung cancer in persons with HIV," *Current Opinion in HIV and AIDS*, vol. 12, no. 1, pp. 31–38, 2017.

[9] K. Suresh, J. Naidoo, C. T. Lin, and S. Danoff, "Immune checkpoint immunotherapy for non-small cell lung cancer: benefits and pulmonary toxicities," *Chest*, vol. 154, no. 6, pp. 1416–1423, 2018.

[10] C. Bottura, L. Arcêncio, H. M. A. Chagas, P. R. B. Evora, and A. J. Rodrigues, "Frailty among non-elderly patients undergoing cardiac surgery," *Arquivos Brasileiros de Cardiologia*, vol. 115, no. 4, pp. 604–610, 2020.

[11] K. Gutsmiedl, M. Krause, I. Bighelli, J. Schneider-Thoma, and S. Leucht, "How well do elderly patients with major depressive disorder respond to antidepressants: a systematic review and

single-group meta-analysis," *BMC Psychiatry*, vol. 20, no. 1, p. 102, 2020.

[12] L. Yang, H. Y. Xu, and Y. Wang, "Diagnostic and therapeutic strategies of lung cancer patients during the outbreak of 2019 novel coronavirus disease (COVID-19)," *Zhonghua Zhong Liu Za Zhi*, vol. 42, no. 4, pp. 292–295, 2020.

[13] M. Zhao, Y. Wei, Y. Lu, and K. K. L. Wong, "A novel u-net approach to segment the cardiac chamber in magnetic resonance images with ghost artifacts," *Computer Methods and Programs in Biomedicine*, vol. 196, article 105623, 2020.

[14] M. Zhao, X. Liu, H. Liu, and K. K. L. Wong, "Super-resolution of cardiac magnetic resonance images using laplacian pyramid based on generative adversarial networks," *Computerized Medical Imaging and Graphics*, vol. 80, article 101698, 2020.

[15] Z. Tang, Y. Li, X. Chai, H. Zhang, and S. Cao, "Adaptive nonlinear model predictive control of nox emissions under load constraints in power plant boilers," *Journal of Chemical Engineering of Japan*, vol. 53, no. 1, pp. 36–44, 2020.

[16] S. Deb, Z. Tian, S. Fong, R. Wong, R. Millham, and K. K. L. Wong, "Elephant search algorithm applied to data clustering," *Soft Computing*, vol. 22, no. 18, pp. 6035–6046, 2018.

[17] F. Ruan, X. Ding, H. Li, Y. Wang, K. Ye, and H. Kan, "Back propagation neural network model for medical expenses in patients with breast cancer," *Mathematical Biosciences and Engineering*, vol. 18, no. 4, pp. 3690–3698, 2021.

[18] N. Lutwak and C. Dill, "Meeting elderly patients' nonmedical needs," *Health Affairs*, vol. 36, no. 3, pp. 580-581, 2017.

[19] K. Shigli, S. S. Nayak, R. A. Kusurkar, and S. Chari, "Use "latches" to communicate with elderly patients," *Special Care in Dentistry*, vol. 40, no. 4, pp. 390–392, 2020.

[20] H. Zhang, C. Xie, and Y. Huang, "Treatment and outcome of a patient with lung cancer infected with severe acute respiratory syndrome coronavirus-2," *Journal of Thoracic Oncology*, vol. 15, no. 5, pp. e63–e64, 2020.

[21] J. C. Gore, "Artificial intelligence in medical imaging," *Magnetic Resonance Imaging*, vol. 68, pp. A1–A4, 2020.

[22] D. A. Hashimoto, E. Witkowski, L. Gao, O. Meireles, and G. Rosman, "Artificial intelligence in anesthesiology: current techniques, clinical applications, and limitations," *Anesthesiology*, vol. 132, no. 2, pp. 379–394, 2020.

[23] D. Hassabis, D. Kumaran, C. Summerfield, and M. Botvinick, "Neuroscience-inspired artificial intelligence," *Neuron*, vol. 95, no. 2, pp. 245–258, 2017.

[24] Z. Tang, G. Zhao, and T. Ouyang, "Two-phase deep learning model for short-term wind direction forecasting," *Renewable Energy*, vol. 173, no. 72, pp. 1005–1016, 2021.

[25] K. K. L. Wong, "Bridging game theory and the knapsack problem: a theoretical formulation," *Journal of Engineering Mathematics*, vol. 91, no. 1, pp. 177–192, 2015.

[26] K. K. Wong, "A geometrical perspective for the bargaining problem," *PLoS One*, vol. 5, no. 4, article e10331, 2010.

Hindawi
Computational and Mathematical Methods in Medicine
Volume 2022, Article ID 5297580, 8 pages
https://doi.org/10.1155/2022/5297580

Research Article

Biostatistics of VHL-Gene Transfection in the Health Informatics Analysis of Renal Cell Carcinoma

Yunxiang Gong, Degang Wang, and Wengang Wang

Department of Urology Surgery, Fuxin Centre Hospital, Fuxin 123000, China

Correspondence should be addressed to Yunxiang Gong; gyxpalaces@163.com

Received 21 July 2021; Revised 26 August 2021; Accepted 28 September 2021; Published 7 January 2022

Academic Editor: Kelvin Wong

Objective. In this paper, we study the role of the VHL gene in regulating the proliferation and apoptosis of renal cell carcinoma, as well as the safety and transfection efficiency of ultrasound microbubble gene transfection technology. *Method*. We use kidney cancer cell lines as an in vitro research object and apply ultrasound microbubble gene transfection technology to transfect the VHL gene into kidney cancer cell line (786-0). The proliferation and apoptosis of cells were measured to clarify the inhibitory effect of the VHL gene in renal cell carcinoma. After that, pEGFP-VHL was transfected using ultrasonic microbubble and liposome gene transfection techniques, respectively, and the transfection efficiency was measured by immunofluorescence. *Results*. Compared with untreated and 786-0 cells that are transfected with empty vector, the expression level of VHL gene mRNA in 786-0 cells that are transfected with pcDNA3.1-VHL was significantly increased, and the cell growth inhibition rate was significantly higher. The rate of apoptosis increased significantly. Transfection efficiency of the pEGFP-VHL gene after transfection of 786-0 cells for 48 h: control group 0, liposome group (35.55 ± 2.77) %, ultrasound microbubble group (18.27 ± 2.83) %, and two transfection methods on cells. There is no significant difference in the impact of vitality. *Conclusion*. VHL gene expression can significantly inhibit the proliferation ability of renal cancer cell line 786-0 and promote its apoptosis. VHL gene is a potential target for gene therapy of kidney cancer.

1. Background

Renal cell carcinoma that is abbreviated as RCC, referred to as kidney cancer, accounts for 2-3% of all adult malignant tumors. Renal cancer deaths worldwide are more than 100,000 cases per year [1]. The incidence of kidney cancer involves multiple genes, of which the Von Hippel-Lindau (VHL) gene is most closely related to kidney cancer. VHL gene has the functions of regulating transcription, regulating cell cycle, and stabilizing cell growth-related genes.

The VHL gene suppresses the formation of the transcription elongation factor Elongin complex through pVHL and regulates the expression of cell growth-related genes. pVHL is also related to cell proliferation, apoptosis, and tumor infiltration and metastasis. VHL gene mutation, deletion, and hypermethylation are closely related to the occurrence of renal cell carcinoma. Research has found [2] that the VHL gene-hypoxia-inducible factor-hypoxia response gene pathway (VHL-HIF-HRG pathway) plays an important role in kidney cancer.

VHL disease involves multiple systemic lesions, including kidney cancer, hemangioblastoma, pheochromocytoma, pancreas, and epididymal cyst. Among them, the incidence of kidney cancer is as high as 28-45%. Lalif [3] successfully cloned the VHL gene in 1993 and confirmed that the root cause of VHL disease is VHL gene inactivation, and VHL exists in more than 98% of VHL diseases. The gene is inactivated. The total length is about 15 kb and encodes 4.7 kb long mRNA. The protein product produced by the VHL gene encoding is called protein VHL (pVHL).

The molecular weight of the VHL protein is 28 -30 KD, including 213 amino acids, called p30 or pVHLL protein; the VHL gene can also encode a protein with a molecular weight of 19 KD, called pl9 or pVHLS protein. The pl9 protein has a

similar function to the p30 protein. It is an isomer that is transcribed at the second transcription start site of the VHL gene. It is not clear why pl9 protein is produced. pVHL30 and pVHL 19 have different localizations in cells, and their functions have not yet been fully clarified. VHL19 is mainly located in the nucleus, which has a higher affinity for the nucleus than pVHL30. In the cytoplasm, pVHL30 is connected by tiny tubes, allowing mRNA to be specifically expressed in tissues. The homologous VHL has also been identified in mice, worms, and fruit flies [4].

The main biological feature of kidney cancer is the abundance of blood vessels. Angiogenesis requires four steps: degradation of extracellular matrix, migration of vascular endothelial cells, proliferation of endothelial cells, and vascular shaping. The process of angiogenesis requires the participation of a series of cytokines. These factors are called angiogenic factors. Due to the abnormality of the VHL gene, the VHL-HIF-HRG signaling pathway is continuously activated, causing tumor cells to synthesize and secrete a large amount of angiogenic factors. VHL is closely related to the formation of renal tumor blood vessels. The VHL-HIF-HRG pathway provides new targets for the treatment of kidney cancer in multiple links [5]. At present, the molecular biological mechanism of kidney cancer is continuously deepened, and molecular targeted therapy must be paid more and more attention.

VHL-HIF-HRG pathway provides a new target for the treatment of kidney cancer in multiple links. Humans control the growth of tumors by blocking the expression of downstream target genes of HIF-a, such as VEGF, PDGF, and TGF-a. A variety of molecular-targeted therapeutic drugs have come out in succession [6]. However, these drugs target the downstream target genes in the VHL-HIF-HRG pathway, and the VHL gene is the starting point of the VHL-HIF-HRG pathway. The VHL gene itself can be used as a target gene for gene therapy. Taking VHL as a target, transfecting it into renal cancer cells with appropriate methods, increasing the expression of the VHL gene, and correcting the apoptosis defects of tumor cells are very important treatment strategies.

Renal cancer cells lacking the VHL gene can form normal-sized tumors in nude mice, and the tumors formed after the introduction of wild-type VHL genes become significantly smaller, and even do not form tumors. Jacob et al. [7] reported that the introduction of VHL gene into arterial endothelial cells through adenovirus can effectively inhibit the proliferation of endothelial cells. However, how to transfer the VHL gene safely, efficiently, specifically, and stably to tumor target cells for gene therapy is an urgent problem to be solved. In recent years, ultrasound has attracted much attention. Studies by scholars at home and abroad have shown that microbubble contrast agents can be promoted by ultrasound-mediated microbubble rupture method [8]. The safe and effective targeted transfer of the target gene may become a new method of gene therapy SI. Through the in-depth study of VHL gene and the development of gene transfection technology, gene therapy for kidney cancer with VHL gene as a target has bright prospects.

2. Methodology

2.1. Experimental Subjects. The human kidney cancer cell line 786-0 is universal, suitable for this experiment, and provides experimental objects for universal kidney cancer gene therapy.

2.2. Sources of pcDNA3.1(+), pcDNA3.1-VHL, and pEGFP-VHL. The eukaryotic expression vector pcDNA3.1(+) was from Beijing Promega Biotechnology Co., Ltd. Recombinant plasmid pcDNA3.1-VHL was constructed and identified by Tianjin Saier Biological Company. The pEGFP-VHL fusion gene expression vector was constructed and identified by Tianjin Saier Biological Company.

2.3. Experimental Cells. 786-0 cells were trained in RPMI1640 medium consisting 100 g/ml penicillin >100 g/ml streptomycin and 10% fetal bovine serum in a 37°C, 5% CO_2 incubator.

2.4. Cell Transfection. Cell transfection procedures are as follows.

(1) Experiment grouping and experiment preparation:

   (a) The experiment is categorized as (1) control group, (2) pcDNA3.1 (+) group, and (3) pcDNA3.1-VHL group

   (b) Transfection using ultrasonic microbubble gene transfection method

   (c) The parameters of the ultrasonic gene transfection therapy instrument are power 1.2 W, frequency 1000 Hz, and irradiation time 30 s. Ultrasonic microbubble concentration is 1×106/ml; after preparing ultrasonic microbubble contrast agent with sterile double distilled water, remember count the microbubble concentration and take out the required volume according to the desired final concentration

   (d) Preparation of the microbubble contrast agent/pcDNA3.1(+) mixture: mix pcDNA3.1(+) 10 g/well with SonoVue microbubble 100 g/well, let stand on ice for 20 minutes, and then it can be used for transfection

   (e) Preparation of cDNA3.1-VHL mixture of microbubble contrast agent: mix pcDNA3.1(+) 10 g/well with SonoVue microbubble 100 g/well, let stand on ice for 20 minutes, and then it can be used for transfection

(2) The 786-0 cells in good growth state were cultured the day before transfection, $(0.5 - 2) \times 105$ cells/well, 2 ml per well without antibiotic medium, and cells per well when transfected the next day grows to 70-80%

(3) After washing the cells with PBS, we prepare a cell suspension without serum medium, 300 g/well, making the cell density 1×107 cells/ml

(4) Add the above mixture according to the requirements of each group, that is, pcDNA3.1(+) group plus microbubble contrast agent cDNA3.1(+) mixture, pcDNA3.1-VHL group plus microbubble contrast agent/pcDNA3.1-VHL mixture. Simultaneously give ultrasound irradiation under the above conditions. The control group only added serum-free medium. After continuing the culture for 6 hours, discard the old culture medium and add the normal culture medium at the same time and place it in a 37°C incubator to continue the culture

2.5. RT-PCR Analysis

2.5.1. RNA Extraction. After 48 h after transfection, aspirate the culture medium in each group of culture flasks, add 1 ml Trizol to make them even without passing through the bottom of the culture flask, let stand for 5 min, and shake the culture flask around. Blow the cells repeatedly with a pipette and then move to a 1.5 ml Eppendorf tube. We included 200 μl of chloroform, mix well by inversion, centrifuge at 14000 rpm, 4°C for 15 min. We aspirate supernatant into a new Eppendorf tube add 600 g of -20C precooled isopropanol to each tube. Centrifuge at l4000 rpm, 4 C for 10 min, discard the supernatant. Add 1 ml of 75% ethanol to each tube, pop up the pellet, centrifuge at 12000 rpm for 10 min, and discard the supernatant. Repeat step f-times. Leave to dry for 5 minutes at room temperature. Add 20 ml RNase-free water to each tube and dissolve for 5 min. After the precipitate is completely dissolved, remove 1 ml of each tube. The UV luminosity is A260 and A280 respectively.

2.5.2. Using mRNA for RT-PCR Reaction

(a) Based on the genetic information of VHL, Primer Premier 5.0 software was used to design RT-PCR primers for VHL. The primer sequences are as follows:

VHL upstream primer: 5′-TACCGAGTGTATACTC TGAAAG-3′.

Downstream primer: 5′-GCTCCTGTGTCAGCCGCTC C-3′.

3-actin upstream primer: 5′-CGTGACATTAAGGAGA AGCTG-3′.

Downstream primer: 5′-CTAGAAGCATTTGCGGTGG AC-3.

(b) Take 5ug RNA and perform reverse transcription reaction using MMLV reverse transcriptase and related reagents

2.6. Flow Cytometry to Detect Apoptosis. 48 h after transfection, we start the detection of apoptosis; aspirate the cell culture solution, wash the cells once with IxPBS solution, aspirate the PBS solution, add digestion solution (0.1% trypsin, 0.02% EDTA) 500 m, and act until the cell morphology changes. When the gap increases, we aspirate the digestion solution to stop digestion; we repeatedly blow the cells with Ixbinding buffer 200 and transfer cell suspension to a centrifuge tube; take 100 g of the cell suspension to a 1.5 ml centrifuge tube and add Annexin-VR-PE 10^1, after flicking and mixing, avoid light and ice bath for 20-30 min; we add Ixbinding buffer 380^1, then add 7-AAD 10 g, flick and mix; and finally, we detect it on flow cytometer.

2.7. MTT Detection Cell Value-Added Ability. We set up untreated group, pcDNA3.1 (+) group, and pcDNA3.1-VHL group, and each group has 3 complex wells. Digest the cells with 0.25% trypsin, centrifuge, inoculate 0.5×104 cells/well in a 96-well culture plate, 200 cell suspension per well, 3%, 5% CO_2 incubator incubate overnight. When the degree of normal cell adhesion and fusion was 70~80%, the treatment group was subjected to the abovementioned ultrasound microbubble transfection conditions. After continuing to cultivate for 6 hours, discard the old culture medium and add the normal culture medium at the same time and place it in a 37°C incubator to continue the culture. Remove the culture plate, add MTT 5 mg/ml to each well, and place in 5% CO_2 incubator for 4 hours.

We took away the culture plate, add 150^11 DMSO to each well to stop the reaction, shake for 10 min, and dissolve the purple crystals. The microplate reader measures the absorbance value (A570 value) of each well with a wavelength of 570 nm. Measure every 12 hours, record the result, and draw a curve.

2.8. Detection of Transfection Efficiency. There are the following categories: control group, pEGFP – VHL + liposome group, and PEGFP – VHL + ultrasound microbubble group. 786-0 cells were cultured in RPMI1640 with 100 g/m 1 penicillin, 100 g/ml streptomycin, and 10% fetal bovine serum in a 37°C, 5% CO2 incubator, whereby the cells used were all in the logarithmic growth phase. VHL cells in good growth state were cultured in 24-well plates and transfected when the cells grew to 70-80%. pEGFP – VHL + ultrasonic microbubble group: the pEGFP-VHL plasmid was transfected into 786-0 using the ultrasonic microbubble method. In the control group, only 1640 serum-free medium was added. After culturing for 48 hours, observe the transfection efficiency of the cells.

2.9. The Effect of Transfection. Our procedures are as follows:

(1) A control group (medium and cells), a zero-adjusting group (medium), a liposome + pcDNA3.1 (+) group, an ultrasonic microbubble + pcDNA3.1 (+), and three complex wells in each group

(2) Digest the cells with 0.25% trypsin, centrifuge, inoculate 0.5×104 cells/well in a 96-well culture plate, 200 g of cell suspension per well, and only add the equivalent in the zero-adjusting group amount of culture medium

(3) When the normal growth and fusion degree of the adherent cells are 70% to 80%, the liposome +

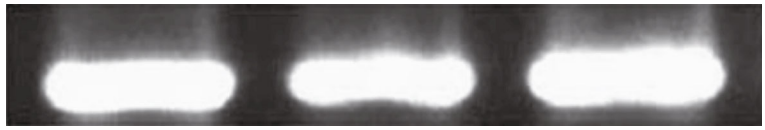

Figure 1: RT-PCR detection of VHL gene mRNA expression in 786-0 cells based on (a) control group, (b) pcDNA3.1 (+) group, and (c) pcDNA3 1-VHL group.

pcDNA3.1 (+) group and ultrasonic microbubbles + pcDNA3.1 (+) are transfected

(4) Liposome + pcDNA3.1(+) group: the liposome can transfect pcDNA3.1(+) vector 786-0

(5) Ultrasound microbubbles + pcDNA3.1(+) group: the pcDNA3.1(+) vector was transfected with 786-0 using the ultrasonic microbubbles method

(6) Put the culture plate in 37°C, 5% CO_2 incubator for 48 h, add 20 g of MTT to each well, continue culturing for 4 h, discard the supernatant, add 150 g DMSO to each well to stop the reaction, and shake for 10 min

2.10. Statistics. Data are statistically processed based on SPSS 12.0 software. Each analysis has at least three results. We used the mean ± standard deviation, using t test. $P < 0.05$ was considered to be significant and statistically significant.

3. Results

3.1. Semiquantitative Analysis of VHL Gene Expression. Results of RT-PCR analysis demonstrated that the relative IOD values of the mRNA levels of 786-0 cells untreated, transfected with pcDNA3.1(+) and transfected with pcDNA3.1-VHL, were 0.25 ± 0.03, 0.27 ± 0.05, and 0.73 ± 0.04, respectively. Compared with untreated and transfected 786-0 cells with pcDNA3.1(+), the expression level of VHL gene mRNA in 786-0 cells transfected with pcDNA3.1-VHL was significantly increased ($P < 0.05$): untreated and transfected. We note the similarity in expression level of VHL mRNA in 786-0 cells infected with pcDNA3.1 (+) ($P > 0.05$), as shown by Figure 1.

3.2. Flow Cytometry to Detect Apoptosis. The results of flow cytometry demonstrated that the apoptosis rates of 786-0 cells untreated, transfected with pcDNA3.1(+) and transfected with pcDNA3.1-VHL after 48 h of transfection, were 0.14%, 0.29%, and 22.74, respectively (Figures 2 and 3). Compared with untreated and transfected 786-0 cells with pcDNA3.1(+), the apoptosis rate of 786-0 cells transfected with pcDNA3.1-VHL was significantly increased. There are no significant difference in the apoptotic rate between untreated and 786-0 cells transfected with pcDNA3.1(+). It indicated that after transfection of VHL gene, the apoptosis rate of 786-0 cells increased.

Figure 3 shows that 48 hours after transfection, the apoptotic rate of each group was detected using a loss cytometer. FL1 (abscissa) is Annexin-VR-PE fluorescence signal value to detect phosphatidylserine; FL2 (ordinate) is 7-AAD fluorescence signal value to detect DNA. (1) Phosphatidylserine in the normal cell membrane is inside the membrane, and Annexin-V-R-PE cannot stain it; the cell membrane is intact, 7-AAD cannot be stained, and the corresponding points are distributed in the Q3 area. (2) The phosphatidylserine outside H, Annexin-VR-PE staining of the apoptotic cell membrane was positive; but the cell membrane was intact, 7-AAD could not be stained, and the corresponding points were distributed in the Q4 area. (3) Late apoptotic cells, necrotic cells, and other cell membranes of dead cells were broken, Annexin-VR-PE and 7-AAD could be stained, and the corresponding points were distributed in the Q2 area. The data were from at least three independent experiments. There was a difference at $P < 0.05$. Figure 3 demonstrated that 48 hours after transfection, the apoptosis rate of each group is from at least three independent experiments.

3.3. MTT to Detect Cell Growth. The proliferation curve (Figure 4) showed that there was no difference between untreated and transfected pcDNA3.1(+) 786-0 cell growth curves ($P > 0.05$), indicating that the cell proliferation characteristics after transfection with empty vector were not affected. The growth curve of 786-0 cells transfected with pcDNA3.1-VHL is below the two. There is a significant difference in cell proliferation ability between the pcDNA3.1-VHL group and the untreated group and the transfected pcDNA3.1(+) group (PV0.05). This indicates that the cell value of 786-0 cells transfected with the VHL gene is significantly reduced.

3.4. Detection of Transfection Efficiency by Different Transfection Methods. Liposome-mediated gene transfection is currently the most commonly used in vitro transfection method. We compared the efficiency of ultrasound microbubble-mediated gene transfection and liposome transfection. 48 hours after transfection, the transfection efficiency of pEGFP-VHL can be observed using a fluorescence microscope. Based on Figure 5, the transfection efficiency of the ultrasound microgroup ($18.27\% \pm 2.83\%$) was lower than that of the liposome group ($35.55\% \pm 2.77\%$). The transfection efficiency of the ultrasound microbubble group was improved within a certain range (Figure 5).

3.5. MTT Test on Cell Viability. We used ultrasound microbubble-mediated gene transfection and liposome transfection to transfect the empty vector into 786-0 cells. After 48 hours, the MTT experiment was used to examine

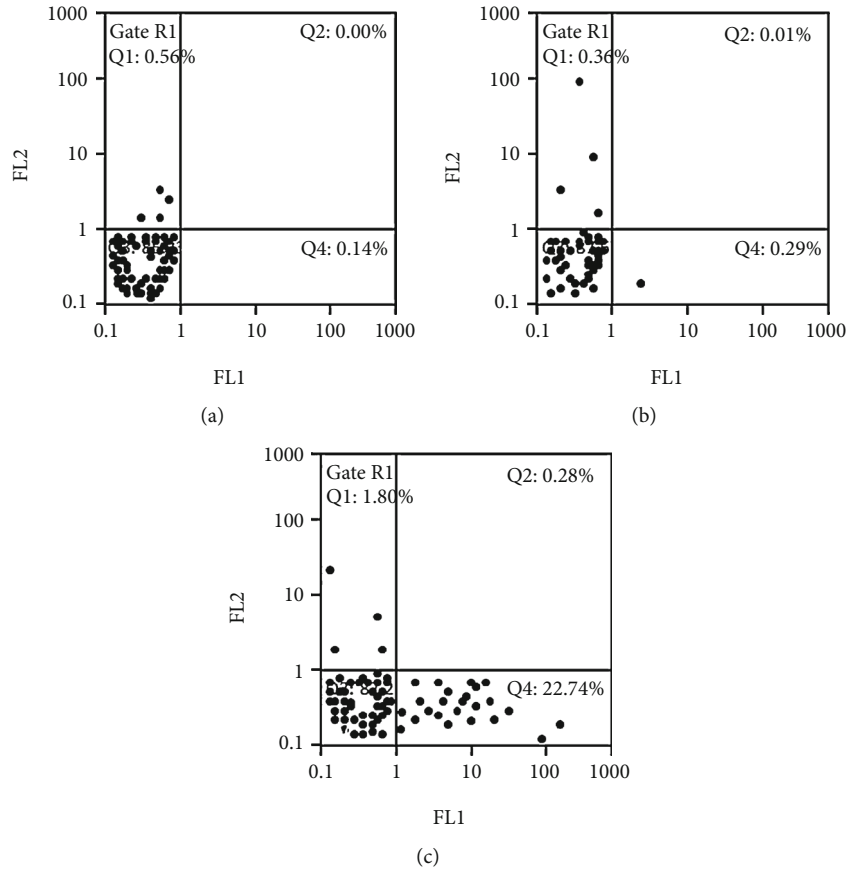

Figure 2: 48 hours after transfection, the apoptotic rate of each group was detected using a loss cytometer. (a) Control group. (b) pcDNA3.1 (+) group. (c) pcDNA3 1-VHL group.

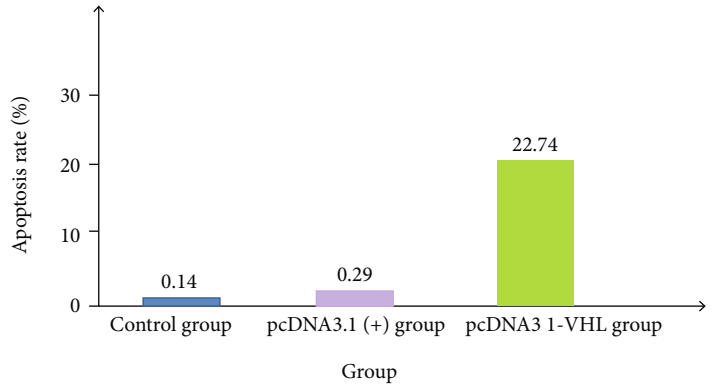

Figure 3: Apoptosis rate of each group 48 h after transfection.

the effect of two transfection methods on cell viability. Based on Figure 6, there was no significant difference in the effect of the two transfection methods on cell viability. The ultrasound microbubble group: 95.47% ± 8.04%, the liposome group: 90.63% ± 9.52%. 48 hours after transfection of 786-0 cells, the MTT experiment was used to examine the effects of the two transfection methods on cell viability. No significant difference exists between ultrasound microbubble group and the liposome group on cell viability.

4. Discussion

Kidney cancer is a common tumor in urology [9]. It is regrettable that about 30% of patients have reached the late stage after the diagnosis. The current treatment methods are mainly surgery plus biological therapy and radiotherapy and chemotherapy [8]. Renal cell carcinoma has poor sensitivity to radiotherapy and chemotherapy, especially for patients with advanced stage, metastasis, or recurrence.

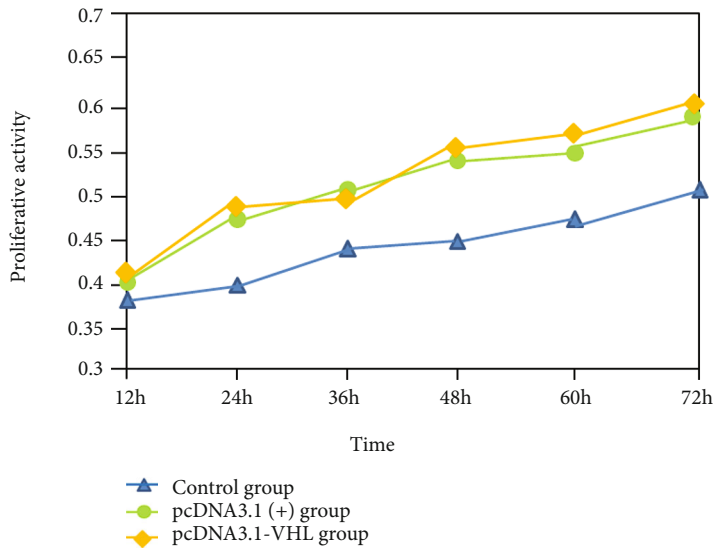

Figure 4: MTT detects the activity changes of cells at 12 h, 24 h, 36 h, 48 h, 60 h, and 72 h after 786-0 transfection.

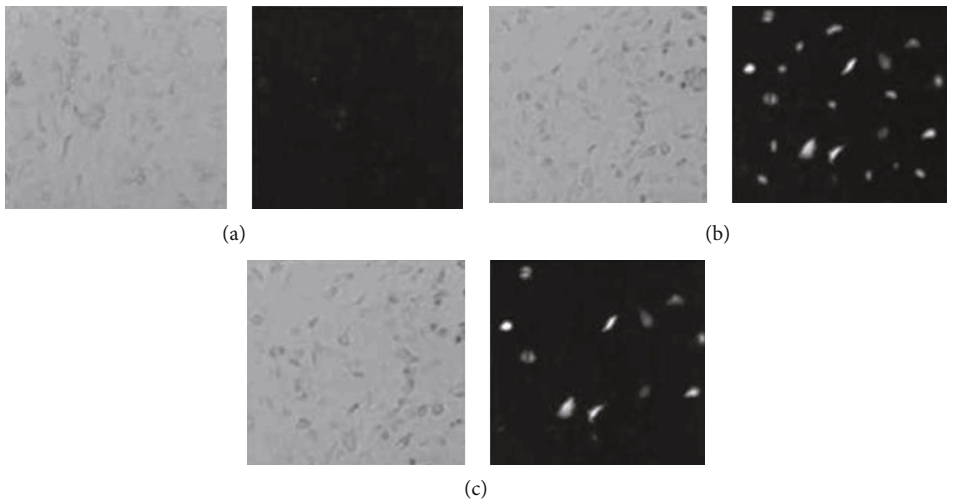

Figure 5: 48 hours after transfection, observe the distribution of GFP fluorescence in each group under a fluorescence microscope. (a) Control group. (b) Liposome group. (c) Ultrasound microbubble group.

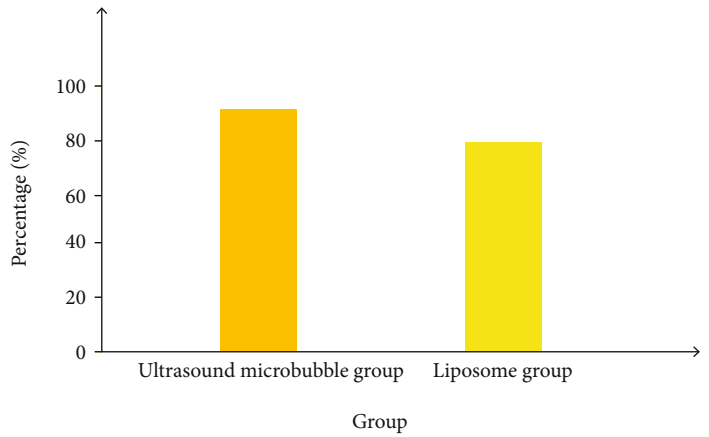

Figure 6: Comparison of transfection of empty vector with ultrasonic microbubble method and liposome method.

Finding a more effective treatment method has very important clinical significance for improving the treatment effect of kidney cancer [10].

Finding a more effective treatment method has very important clinical significance for improving the treatment effect of kidney cancer. Similar to other malignant tumor cells, apoptosis defects are a distinctive feature of kidney cells, showing an imbalance between proliferation and apoptosis and resistance to chemotherapy drugs [11]. It contains three exons and is located in the 3p25-26 region. Encoding product VHL protein (pVHL), pVHL includes two domains a and 0. pVHL and Elongin B-C and CUL2 proteins form a VBC (VHL·ElonginB/C-CUL2) complex. The VBC complex participates in the degradation of various proteins in the human body and belongs to the E3-ubiquitin protease system. In this system, pVHL specifically recognizes and binds substrate molecules through the 0 domain and binds to and presents substrate molecules through a domain to ElonginB/C, and VHL gene inactivation leads to the loss of these functions, which is conducive to the occurrence and development of tumors. Studies have shown that VHL gene mutations and hypermethylation are widespread in kidney cancer and are related to clinical stage, histological type, and lymph node metastasis.

70-80% of sporadic renal cell carcinomas have VHL gene inactivation [12]. Shiao [13] and other studies have shown 75 patients with renal cell carcinoma mainly clear cell carcinoma (60 cases). Using immunohistochemistry to detect the level of VHL protein, the expression level of VHL protein in 49 patients (65%) decreased significantly. Further research is needed. At present, there are few experimental studies on the VHL gene in vitro, adding tumor suppressor genes in tumor cells and analyzing the changes, which is helpful to reveal the molecular mechanism of tumor development.

Studies have found that increasing the expression of the VHL gene in tumor cells can effectively inhibit the proliferation of tumor cells and increase the sensitivity of tumor cells to radio chemotherapy [14]. We transfected the VHL gene into renal cancer cell line 786-0, using the RT-PCR method at the transcription level. At the same time, the growth activity of cells after transfection was detected by the MTT method. The selected 786-0 cell line itself is a cell line lacking the normal VHL gene, and the VHL gene is underexpressed. The results showed that after transfection, the expression level of the VHL gene in the 786-0 cell line was greatly increased at the transcription level [15]. MTT test showed that after VHL gene transfection, the growth activity of 786-0 was significantly inhibited. The apoptosis rate increased significantly. Compared with the transfected VHL gene, kidney cancer cell lines that were not transfected with the VHL gene had low expression of the VHL gene, cell growth activity was not inhibited, and cell apoptosis rate was low. This result is consistent with the results of Shiao et al.'s study on kidney cancer specimens. It further confirmed the important role of the VHL gene in the occurrence and development of human kidney cancer, and provided an experimental basis for gene therapy of kidney cancer. Seek new intervention targets and strategies for effective treatment of kidney cancer [16].

The issues caused by renal cell carcinoma are raised by more than 126% from 1950 to the present, and the annual mortality rate has increased by 37% [17]. The adverse reactions of this immunotherapy are obvious, and the effect is limited. Most kidney cancer patients overexpress VEGF, EGF, PDGF, TGF2a, and other growth factors due to VHL gene mutation and abnormal growth of tumor tissues resulting in HIF-related transcriptional activation. We activate Raf/MEK/ERK and PBK/Akt/mTOR pathways through autophosphorylation of receptor tyrosine kinases, causing uncontrolled cell division, proliferation, and transformation, stimulating neovascularization, and promoting tumor growth and metastasis [13]. The expressed growth factors and tumor-related molecular pathways can be used as targets for targeted therapy [18–20].

We applied ultrasound microbubble gene transfection technology and liposome gene transfection technology to transfect pEGFP-VHL into 786-0 cells, which we then measured the transfection rate by immunofluorescence [21]. The empty vector gene was transfected into renal cancer cell lines by the above two methods, respectively, and the effect of the two transfection methods on cell viability was detected by the MTT method [22]. The transfection efficiency of ultrasound microbubbles-mediated genes in vitro was still significantly lower than that of liposome-mediated gene transfection, but the transfection efficiency was improved to a certain extent compared with the blank control group. We prove that ultrasonic microbubble technology is safe and effective. We applied ultrasound microbubble method to transfect VHL plasmid into human kidney cancer cell lines, applied RT-PCR [10] method to detect the expression of the VHL gene, MTT to detect cell proliferation ability, and flow cytometer to detect apoptosis rate. The MTT test showed that the cell growth of the ultrasound microbubble group was significantly inhibited, the use of deep learning models is better for the research of this article [23], the flow cytometry test showed that the apoptosis rate of the ultrasound microbubble group increased [24, 25], and the experiment was repeated many times to show consistency in the results. It proves that the ultrasonic microbubbles transgene technology is stable and effective. Machine predictive control techniques [26] may be utilized in diagnosis of kidney cancer based on the biostatistics of VHL-gene transfection.

5. Conclusion

Ultrasound microbubbles gene transfection method can increase the transfection efficiency of the VHL gene into 786-0 cells within a certain range. Compared with liposome-mediated transfection, the two transfection methods had no significant difference in cell viability. The transfection efficiency of ultrasonic microbubbles with ultrasonic irradiation is still low, ultrasound microbubbles to promote gene transfection still have many problems, and such technique requires further research.

Data Availability

Data Availability Statement The image data used to support the findings of this study have been deposited in the cancer genome atlas (TCGA) (https://portal.gdc.cancer.gov/).

Ethical Approval

There is no ethics approval required for this paper.

Conflicts of Interest

The authors declare that they have no conflicts of interest.

Acknowledgments

The authors thank the staff of the Department of Urology of Fuxin Central Hospital for their help in preparing the data set.

References

[1] P. H. Patel, R. S. Chaganti, and R. J. Motzer, "Targeted therapy for metastatic renal cell carcinoma," *British Journal of Cancer*, vol. 94, no. 5, pp. 614–619, 2006.

[2] W. C. Hahn and R. A. Weinberg, "Rules for making human tumor cells," *New England Journal of Medicine*, vol. 347, no. 20, pp. 1593–1603, 2002.

[3] F. Latif, "Disease tumor suppressor gene," *Science*, vol. 260, pp. 1317–1320, 1993.

[4] M. Kim, Y. Yan, K. Lee, M. Sgagias, and K. H. Cowan, "Ectopic expression of von Hippel-Lindau tumor suppressor induces apoptosis in 786-O renal cell carcinoma cells and regresses tumor growth of 786-O cells in nude mouse," *Biochemical and Biophysical Research Communications*, vol. 320, no. 3, pp. 945–950, 2004.

[5] B. L. Petrella, J. Lohi, and C. E. Brinckerhof, "Identifcation of membrarle type-1 matrix metalloproteinase as a target of hypoxia-inducible factor-2 alpha in van Hippel-Lindau renal cell carcinoma," *Onconene*, vol. 24, no. 6, pp. 1043–1052, 2005.

[6] M. J. Ratain, T. Eisen, W. M. Stadler et al., "Phase II placebo-controlled randomized discontinuation trial of sorafenib in patients-with metastatic renal cell carcinoma," *Clinical Oncology*, vol. 24, no. 16, pp. 2505–2512, 2006.

[7] T. Jacob, E. Ascher, A. Hingorani, Y. Gunduz, W. Yorkovich, and P. Seth, "Yon Hippel-Lindan gene therapy: a novel strategy in limiting endothelial cell proliferative activity. Annals," *Vascular Surgery*, vol. 15, no. 1, pp. 1–6, 2001.

[8] S. Mehier-Humbert and R. H. Guy, "Physical methods for gene transfer: improving the kinetics of gene delivery into cells," *Advanced Drug Delivery Reviews*, vol. 57, no. 5, pp. 733–753, 2005.

[9] H. T. Cohen and F. J. McGovern, "Renal-cell carcinoma," *New England Journal of Medicine*, vol. 353, no. 23, pp. 2477–2490, 2005.

[10] W. G. Kaelin, "Molecular basis of the VHL hereditary cancer syndrome," *Nature Reviews Cancer*, vol. 2, no. 9, pp. 673–682, 2002.

[11] W. M. Linehan, "Editorial: molecular targeting of VHL gene pathway in clear cell kidney cancer," *Journal of Urology*, vol. 170, no. 2, pp. 593-594, 2003.

[12] Y. H. Shiao, A. Forsti, L. Egevad, L. M. Anderson, P. Lindblad, and K. Hemminki, "VHL down-regulation and differential localization as mechanisms in tumorigenesis," *Kidney International*, vol. 64, no. 5, pp. 1671–1674, 2003.

[13] I. Lentacker, B. G. de Geest, R. E. Vandenbroucke et al., "Ultrasound-responsive polymer-coated microbubbles that bind and protect DNA," *Langmuir*, vol. 22, no. 17, pp. 7273–7278, 2006.

[14] A. J. Pantuck, A. Zisman, and A. S. Belldegrun, "The changing natural history of renal cell carcinoma," *Journal of Psychiatry*, vol. 166, no. 5, pp. 1611–1623, 2001.

[15] M. D. Hughson, Z. He, S. Liu, J. Coleman, and W. B. Shingleton, "Expression of HIF-1 and ubiquitin in conventional renal cell carcinoma: relationship to mutations of the von Hippel-Lindau tumor suppressor gene," *Cancer Genetics and Cytogenetics*, vol. 143, no. 2, pp. 145–153, 2003.

[16] X. Gao, K. S. Kim, and D. Liu, "Nonviral gene delivery: what we know and what is next," *The AAPS Journal*, vol. 9, no. 1, pp. E92–104, 2007.

[17] J. P. Christiansen, B. A. French, A. L. Klibanov, S. Kaul, and J. R. Lindner, "Targeted tissue transfection with ultrasound destruction of plasmid-bearing cationic microbubbles," *Ultrasound in Medicine & Biology*, vol. 29, no. 12, pp. 1759–1767, 2003.

[18] S. L. Huang, "Liposomes in ultrasonic drug and gene delivery," *Advanced Drug Delivery Reviews*, vol. 60, no. 10, pp. 1167–1176, 2008.

[19] L. Huang, L. Yin, B. Liu, and Y. Yang, "Design and error evaluation of planar 2DOF remote center of motion mechanisms with cable transmissions," *Journal of Mechanical Design*, vol. 143, no. 1, 2021.

[20] B. Hu, C. Zhou, H. Wang, and L. Yin, "Prediction and validation of dynamic characteristics of a valve train system with flexible components and gyroscopic effect," *Mechanism and Machine Theory*, vol. 157, p. 104222, 2021.

[21] L. B. Feril, R. Ogawa, K. Tachibana, and T. Kondo, "Optimized ultrasound-mediated gene transfection in cancer cells," *Cancer Science*, vol. 97, no. 10, pp. 1111–1114, 2006.

[22] M. Duvshani-Eshet and M. Machluf, "Therapeutic ultrasound optimization for gene delivery: a key factor achieving nuclear DNA localization," *Journal of Controlled Release*, vol. 108, no. 2-3, pp. 513–528, 2005.

[23] Z. Tang, G. Zhao, and T. Ouyang, "Two-phase deep learning model for short-term wind direction forecasting," *Renewable Energy*, vol. 173, pp. 1005–1016, 2021.

[24] H. Qi and M. Ohh, "The von Hippel-Lindau tumor suppressor protein sensitizes renal cell carcinoma cells to tumor necrosis factor induced cytotoxicity by suppressing the nuclear factor-dB-dependent anti-apoptotic pathway," *Cancer Research*, vol. 63, pp. 7076–7080, 2003.

[25] S. Ananth, B. Knebelmann, and W. Gruning, "Transforming growth factor betalis a target for the von Hipper Landau tumor suppressor and a critical growth factor for clear cell renal carcinoma," *Cancer Research*, vol. 59, no. 9, p. 2, 1999.

[26] Z. H. Tang, Y. Y. Li, X. Y. Chai, H. Y. Zhang, and S. X. Cao, "Adaptive nonlinear model predictive control of NOx emissions under load constraints in power plant boilers," *Journal of Chemical Engineering of Japan*, vol. 53, no. 1, pp. 36–44, 2020.

Hindawi
Computational and Mathematical Methods in Medicine
Volume 2021, Article ID 4980718, 8 pages
https://doi.org/10.1155/2021/4980718

Research Article

Long-Term Assessment of Rehabilitation Treatment of Sports through Artificial Intelligence Research

Chaofan Zeng,[1] Ying Huang,[2] Longer Yu,[1] Qingmei Zeng,[3] Bijun Wang,[3] and Yi Xu[4]

[1]*Guangzhou Institute of Technology, Guangzhou, Guangdong 510075, China*
[2]*Guangdong Foreign Trade School, Guangzhou, Guangdong 510520, China*
[3]*Rehabilitation Department, The Fifth Affiliated Hospital, Southern Medical University, Guangzhou 510900, China*
[4]*Guangdong Eco-Engineering Polytechnic, Guangzhou, Guangdong 510520, China*

Correspondence should be addressed to Yi Xu; xuyi13631436589@163.com

Received 8 October 2021; Revised 21 November 2021; Accepted 26 November 2021; Published 22 December 2021

Academic Editor: Kelvin Wong

Background. Artificial intelligence (AI) technology has been incorporated into all walks of life, especially the integration of machine learning and health management has achieved very significant progress and results. It is very necessary to analyze personalized sports health management services and long-term assessment of health issues in the era of AI. *Methods*. This paper explores AI + personalized sports management service system design ideas, system operation process, management stage design, taking common chronic diseases, and diabetes as examples. 150 patients were divided into an observation group and a control group, and the blood glucose, blood pressure, blood lipid, and knowledge awareness rate were compared. *Results*. The blood glucose, blood pressure, and blood lipid levels of the observation group all reduced, and the awareness rate of diabetes knowledge increased, which proved that the AI research has great value in sports rehabilitation research coupled with long term health assessment and is worth further research. *Conclusion*. The AI research proposed in this paper is of far-reaching practical significance in helping the transformation and upgrading of the sports health management service industry, promoting the innovative development of sports health management service supply, and promoting national fitness and national health.

1. Introduction

In the past 20 years, population aging, cancer rejuvenation, and subhealth have become the focus of public health concerns [1]. The elderly have been suffering from osteoporosis and cardiovascular and cerebrovascular diseases for a long time. Lymphoma, gastric cancer, and other cancer patients are more common in young and middle-aged people, and most of them are found in the middle and late stages, and the mortality rate increases year by year. The distribution of China's population health status shows that only 5% are healthy people and 80% are subhealthy people, of which about 300 million are obese people [2, 3].

Long-term subhealth causes chronic diseases. The number of deaths caused by chronic diseases has accounted for 86% of the total deaths in the country 6%, and the burden of chronic diseases accounts for nearly 70% of the total disease burden. Chronic diseases have become a health crisis that people cannot ignore.

In 2018, China entered the first year of AI and became a new generation of AI innovation development test area. Nearly 30 provinces, cities, and regions issued relevant planning documents or issued supporting policies to promote the development of the AI industry. AI leaders, benchmarking companies, and specialized small and medium-sized enterprises produce a series of smart products with different functions such as sports wearable smart devices, online health management services, and real-time monitoring of health data. Residents can use these smart products to monitor and understand their own health status, help residents

self-health information query function and exercise monitoring, evaluation, promotion, and provide personalized health management services for residents [4–7].

China's sports health management service already has AI products and technology penetration, but it is not deep enough. The theoretical research on the application of AI in sports health management services is still very weak, and social development is in urgent need of sports health management services. Therefore, the research on the design of personalized sports health management service system in the era of AI will help the transformation and upgrade of sports health management service industry. To promote the innovative development of sports health management services, promote national fitness and national health, and provide a reference for the healthy development of China.

Personalized sports health management is a process of comprehensive monitoring, analysis, evaluation, and management of residents' physical health [8]. Through effective personalized sports fitness guidance and behavioral intervention, the purpose of improving residents' health levels and self-health management capabilities is achieved, thereby a new sports service process that promotes the health of athletes [9].

2. Methodology

2.1. AI + Personalized Sports Management Services

2.1.1. System Design Ideas. As can be seen from Figure 1, based on the sports health management service monitoring-evaluation-intervention-promotion, the AI + personalized sports health management service system is constructed. The four service links of health information management system, sports health assessment management, fitness guidance and intervention, and sports health promotion use AI equipment or technology to achieve fast, convenient, and scientific fitness management.

First, wearable smart products are used to monitor the true and reliable health data of residents, and a sports health cloud information system is established; then, residents and sports managers collect personal or group monitoring health cloud data and initially diagnose the health status of residents or groups through APP software or smart instruments and conduct sports health assessment to build sports health assessment management; then, individual residents or groups use scientific sports fitness projects, methods, or means to conduct fitness guidance and behavior intervention strategies in smart fitness venues.

Finally, residents can use the online knowledge base or interactive communication between sports health managers, to obtain feedback information for self-health management, to achieve health promotion. In order to build an AI sports health management service system, the entire system design idea not only helps residents' self-health information query function and exercise monitoring, evaluation, and promotion but also facilitates sports health managers to use intelligent platform data more flexibly, targeting different ages and different groups of people, individuals, or groups of different ranges customize personalized physical and health exercise programs.

We build a sports health management service system and use the sports health cloud management system to act on community sports health management services, athlete sports health management services, corporate sports health management services, sports health management services for the elderly, pregnancy and health management services, youth sports health management services, chronic disease sports health management services, physical health management services in eight areas, provide AI technology sports guidance, and form a series of health management service systems. A series of health management service systems have been continuously improved and improved, and on the contrary, the efficiency of sports health management service links has been promoted.

2.1.2. System Operation Flow. As can be seen from Figure 2, the operation process of the AI + personalized sports management service system is relatively complicated and cumbersome. The system subverts the traditional sports health management model, builds a new sports health management system of the Internet of Things and cloud computing, and adopts a vertical structure layered and horizontal cross-domain, vertical layered to complete the real-time health data recording of fitness people, information transmission, file collection, storage, calculation, processing, and security of collected data, to achieve the formation of various application programs and user reports on data and information transformation. Horizontal cross-domain interconnection, sharing, and collaborative processing with various clouds truly realizing the dynamic multidimensional management of national sports health records throughout the life cycle, providing sports health managers with dynamic data of health records, and providing real-time sports for users or residents health management services provides online sports service platforms for sports health instructors.

2.1.3. Management Stage Design. From Figure 3, the sports health management service link is divided into six links: sports health information collection system, sports health status assessment and prediction, sports health management plan formulation, sports health intervention, sports health promotion, and sports health evaluation; the size is included in the systematic management stage, the refined management stage, and the individualized management stage; according to the different work priorities, the sports and health managers who undertake the above work can be divided into social sports instructors, fitness management consultants, and personal trainers.

Residents then communicate, maintain, promote, and improve sports health management through the network with sports managers. Healthy residents or subhealthy residents can all self-monitor, self-control, self-discover problems, and self-analyze problems through intelligent software or network platforms. In the form of self-seeking solutions, when residents find that the exercise effect is not obvious, they can consult with online sports managers in time to obtain the most favorable fitness prescription. All of this can be done through AI software or instruments, bringing great convenience to residents, enhancing residents'

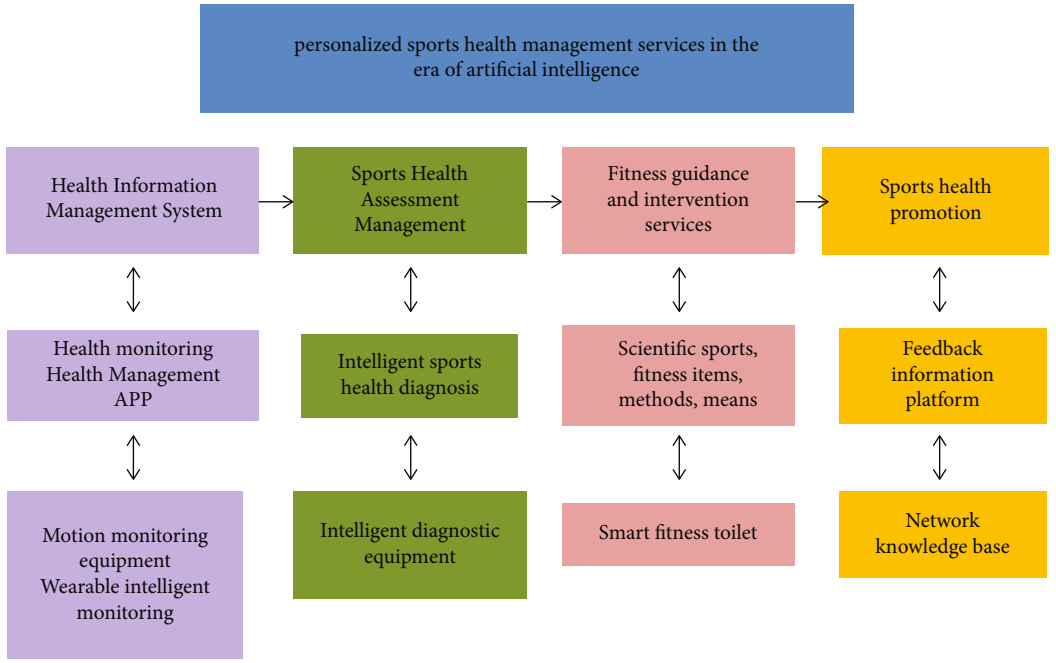

Figure 1: Design framework of AI + personalized sports management service system.

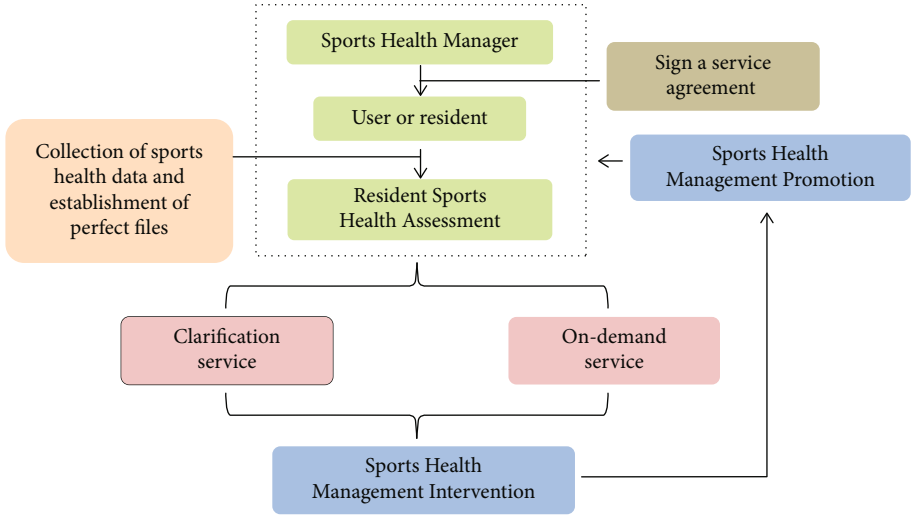

Figure 2: Operation flow chart of AI + personalized sports management service system.

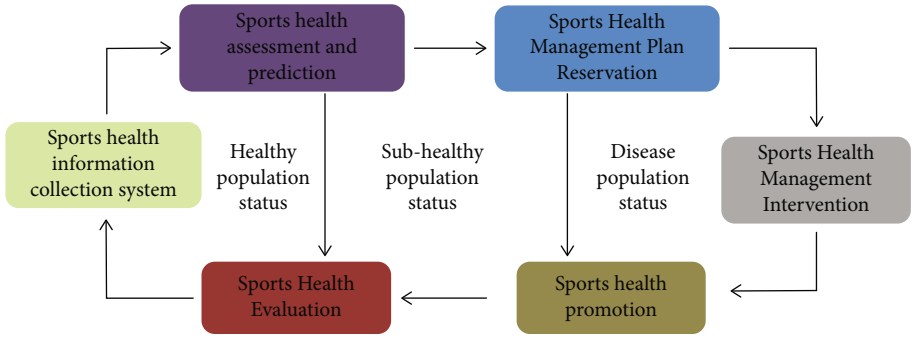

Figure 3: Design diagram of AI + personalized sports health service management stage.

knowledge and ability of active sports health management, saving time and effort, and bringing scientific and technological progress to the application of AI technology to the field of sports.

2.2. Implementation Path of Long-Term Sports Health Management Services in the Era of AI

2.2.1. Implementation Path of Self-Help Sports Health Service in the Unit of Family or Hospital. As can be seen from Figure 4, the self-service sports health service in the family unit is a resident health management information platform built by a third-party health operation organization, which provides remote sports health management information operation services for family members, forming a self-service sports fitness management service application based on family places system and application system of physical therapy and fitness management service with hospital as a place.

The family self-help sports health service application platform is a sports health information operation service organization that provides family members with sports prescriptions, technical guidance and consultation, and other information services. Provide self-service health online services to family members through mobile sports APP applications, WeChat, websites, or smart devices, including health file services, sports consulting services, sports fitness services, sports fitness assessment and guidance, and sports effect evaluation.

The physical therapy fitness management service application platform takes the hospital as a place, performs reasonable and effective rehabilitation physical therapy for the sick, and combines medical and physical therapy to build a physical medicine management contact service station. Specific operation steps establish an electronic medical record database, combine the online fitness guidance platform with medical treatment, provide fitness guidance and help needs, and provide people with online professional fitness coaches in a timely and effective manner to guide people in fitness exercises and improve the accuracy of guidance and efficiency and formulate effective exercise prescriptions.

In the process of sports rehabilitation, through the medical evaluation service, the changes in the disease can be evaluated to avoid physical damage caused by improper exercise. And to determine whether sports services are beneficial to patients' health and disease recovery, so that sports services can timely adjust exercise programs, assessment, and promotion processes according to patients' own diseases or health conditions.

2.2.2. The Implementation Path of Sports Health Management Services in Athletes. It can be seen from Figure 5 that under the unified leadership of the athlete, the sports health management service uses the intelligent equipment or instruments to carry out sports health testing, sports classroom teaching, extracurricular sports activities, sports training, and competition as the main content of the health management system. The specific tasks of athletes' sports health management: health information collection-student sports health management files-student sports health management information analysis and evaluation-personalized sports health guidance, intervention-re-collection-re-evaluation-re-guidance, and intervention management model. That is to pass first collect and manage students' health information through smart software or the Internet and establish student electronic health management accounts and files. The athlete carries out health education and carries out health education on nutrition knowledge, sports fitness knowledge, and sports safety knowledge related to physical health through elective courses, networks, lectures, and reports. Then evaluate the students' health status, formulate fitness and health management programs in physical education classrooms, extracurricular sports activities, sports training, and competitions, and intervene and guide the students' health status.

2.2.3. Implementation Path of Personalized Sports Health Management Services in the Community. Under the leadership of the city and municipal people's government, community sports health management services are led by the streets, and the neighborhood committees are coordinated to establish a sports health management team as a guide to carry out physical fitness tests and sports health events for community residents. Health education system with sports health skills transmission and sports health knowledge dissemination as the main content.

Specific tasks of community sports health management: mainly establish and improve the electronic health files of residents under the jurisdiction of the community health service center and regularly update the data of dynamic changes, which is not only convenient for statistical analysis of data but also convenient for community sports instructors and communities. Medical staff and community residents log in to view the health information of community residents. Second, for community residents, health records are entered into the community sports online health management system. To some extent, the community sports online health management system is a kind of basic public sports and health service with public welfare. For community sports instructors and community medical staff, the entry of health records into the community sports online health management system is conducive to their effective monitoring of health-risk groups.

2.3. Value of AI Research on Sports Rehabilitation Research

2.3.1. General Materials. This study selected 130 diabetic patients, divided into two groups according to the random number method, the observation group was given health management, and the control group was given general management, 75 cases each. In the observation group, there were 37 males and 38 females; the average age was (61.25 ± 2.85) years, with an age range of 54 to 72 years; the average course value was (6.02 ± 0.35) years, and the course of disease was 7 months to 12 years. In the control group, there were 38 males and 37 females; the average age was (61.28 ± 2.87) years old, with an age range of 55-72 years; the average

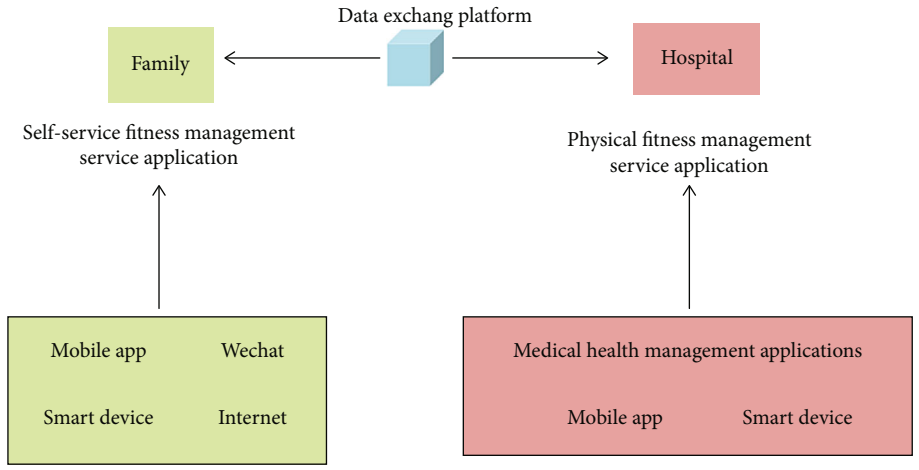

Figure 4: Roadmap for the implementation of self-service sports and health services by families.

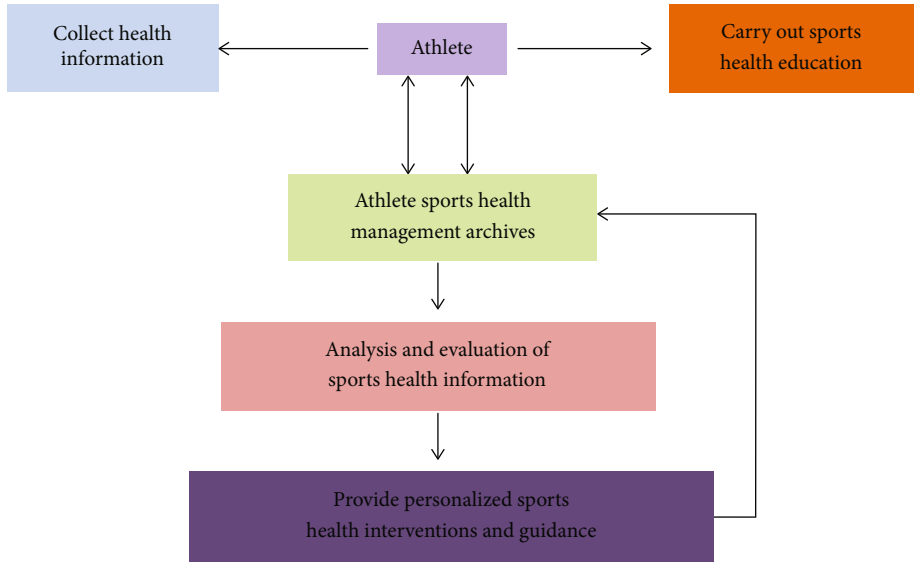

Figure 5: Implementation road map of athletes sports health service management.

course value was (6.06 ± 0.37) years, and the course of disease ranged from 8 months to 12 years.

2.3.2. Comparative Experimental Methods. Control method: give general management, that is, inform patients to take medicines according to doctor's orders and develop good living habits, moderate exercise, etc.

Observation group method: give health management for 6 months, as follows:

(1) *Establish a Health Management Team.* The main members are composed of nurses, and doctors and head nurses provide corresponding guidance. Participating members are trained in diabetes-related knowledge and can only be employed if they have passed the training

(2) *Investigating the Health Status.* The nursing staff should collect the patient's health information (awareness of the disease, lifestyle, medication, psychological status, etc.), then assess the health risk factors based on the collected information, and then be the inspected person formulate an individualized intervention plan

(3) *Health Management Methods.* Nursing staff can carry out health management by regularly conducting health lectures, distributing relevant knowledge manuals, establishing WeChat groups, monthly telephone calls, or follow-up visits

(4) *Health Management Content.* (a) Health education: choose appropriate language according to the patient's cultural level to explain disease-related knowledge, such as pathogenesis, inducing factors, clinical manifestations, complications manifestations, and preventive measures and then let them understand and improve recognition knowledge

has a significant promoting effect, and then inform patients that diabetes is a lifelong disease. Any treatment method cannot cure the disease. Only drugs can be used to control blood sugar levels, which, in turn, reduce the harm to physical functions, which is conducive to improving the patient's medication. Compliance and develop good habits. (b) Reasonable diet: make reasonable adjustments according to the patient's diet and focus on low-calorie, low-cholesterol, low-fat, low-salt, low-sugar, high-quality protein, and high-fiber, and abide by the principle of a small number of meals. (c) Exercise guidance: inform patients to exercise at least 5 times a week, mainly aerobic exercise, such as brisk walking, yoga, and square dance, can reduce the body weight while improving immunity, at the same time, it can further improve the insulin sensitivity. It is necessary to pay attention to the combination of work and rest during exercise, observe the step-by-step principle, and exercise intensity should be tolerated. (d) Take medicine according to the doctor's instructions: once again emphasize to the patient the importance and necessity of taking the medicine on time and on demand, which is conducive to controlling the disease and preventing the occurrence of complications, and at the same time, explaining the medicine-related knowledge to the patient, such as the method of taking, dosage, and effect, in turn, it plays a role in raising awareness; in addition, it is forbidden to change drugs and increase or decrease the dose of drugs at will

2.3.3. Observation Indicators. Observation and evaluation of systolic blood pressure, diastolic blood pressure, fasting blood glucose, 2 h postprandial blood glucose, glycated hemoglobin, total cholesterol (TC), triglyceride (TG), low-density lipoprotein (LDL-C), high-density lipoprotein (HDL-C), blood sugar, blood pressure, blood lipid, and knowledge awareness rate.

The knowledge awareness rate selection questionnaire is evaluated. The evaluation content includes 6 questions such as pathogenesis, clinical manifestations, etiology, treatment, and complications. It is designed as 25 multiple choice questions, each question has 5 options, and each option score is 0 to 4 points, the total score is 0 to 100 points; of which 80 to 100 points indicate complete awareness, 60 to 79 points indicate partial awareness, and less than 60 points indicate no awareness; the format of knowledge awareness rate is as follows.

$$\text{Awareness rate} = \frac{\text{Fully aware} + \text{Partially aware}}{\text{Total number of cases}}. \quad (1)$$

3. Results

3.1. Comparison of Blood Pressure Levels. The data in Table 1 shows that before intervention, and there was no statistically significant difference in systolic and diastolic blood pressure between the observation group and the control group ($P > 0.05$); after intervention, the systolic and diastolic blood pressure of the observation group was lower than that of the control group, and there was a statistical difference Academic significance ($P < 0.05$). It shows that AI has research value in the rehabilitation treatment of diabetes and can reduce systolic and diastolic blood pressure.

3.2. Comparative Analysis of Blood Sugar Levels. The data in Table 2 shows that before the intervention, there was no statistically significant difference between the observation group and the control group's fasting blood glucose, 2 h postprandial blood glucose, and glycated hemoglobin ($P > 0.05$); after intervention, the observation group's fasting blood glucose, postprandial 2 h blood glucose, and glycated hemoglobin were lower than those in the control group, and the difference was statistically significant ($P < 0.05$). In the observation group receiving AI health management, blood glucose levels have decreased significantly.

3.3. Comparative Analysis of Blood Lipid Levels. The data in Table 3 shows that before intervention, there was no significant difference in TC, TG, LDL-C, and HDL-C between the observation group and the control group ($P > 0.05$); after intervention, TC, TG, and LDL-C are lower than the control group, HDL-C is lower than the control group, and the difference is statistically significant ($P < 0.05$).

3.4. Comparative Analysis of Blood Sugar, Blood Pressure, Blood Lipids, and Knowledge Awareness Rate. The data in Table 4 shows that the observation awareness rate is higher than that in the control group, and the difference is statistically significant ($P < 0.05$). The observation group is receiving AI health management on diabetes pathogenesis, clinical manifestations, etiology, treatment, and complications.

4. Discussion

Diabetes is one of the more common chronic diseases in the clinic, with a high morbidity rate [10]. If it is not effectively treated in time, it can have a serious impact on the health of the patient. At present, there is no complete cure for the disease in the clinic, only by taking drugs to play a role in controlling the disease and have a positive effect on reducing the incidence of complications [11]. However, due to the low awareness of disease-related knowledge in some patients, it is easy to cause repeated fluctuations in blood glucose levels, and the predisposing factors are poor eating habits and lifestyle habits. (1) Have not taken medicine according to doctor's instructions. Some scholars have shown that good metabolic control for diabetic patients is conducive to avoiding the appearance of chronic complications and has a significant promoting effect on life extension. Therefore, it is very important to find suitable intervention methods in the clinic [12].

Smart technology has been applied to nearly 20 industries such as shopping malls, hotels, banks, museums, hospitals, and teaching and will be used in various fields of society in the future [13].

At present, wearable smart devices such as smart bracelets, smart sports shoes, smart glasses, and smart shirts in

Table 1: Comparison of blood pressure levels of the two patients.

Group	Number of cases	Systolic blood pressure		Diastolic blood pressure	
		Before intervention	After intervention	Before intervention	After intervention
Observation group	75	146.47 ± 10.46	125 ± 5.24	92.44 ± 4.67	80.24 ± 1.03
Contrast group	75	145.64 ± 10.27	129 ± 6.75	94.21 ± 4.35	87.55 ± 2.77
t value	—	0.021	7.012	0.024	21.471
P value	—	0.991	0.001	0.936	0.001

Table 2: Comparison of blood glucose levels of the two patients.

Group	Fasting blood glucose (mmol/L)		2 h blood glucose after meal (mmol/L)		Glycated hemoglobin (%)	
	Before intervention	After intervention	Before intervention	After intervention	Before intervention	After intervention
Observation group ($n = 75$)	10.68 ± 3.11	8.66 ± 0.99	14.21 ± 3.46	7.46 ± 1.52	9.11 ± 2.03	6.31 ± 0.67
Contrast group ($n = 75$)	9.96 ± 2.86	7.46 ± 1.02	13.19 ± 2.76	8.76 ± 1.98	9.31 ± 1.33	6.96 ± 0.77
t value	0.072	7.786	0.012	5.963	0.068	13.256
P value	0.939	0.001	0.943	0.001	0.996	0.001

Table 3: Comparison of blood lipid levels between the two patients.

Group	TC		TG		LDL-C		HDL-C	
	Before intervention	After intervention	Before intervention	After intervention	Before intervention	After intervention	Before intervention	After intervention
Observation group ($n = 75$)	4.75 ± 1.33	2.33 ± 0.34	1.86 ± 0.68	0.96 ± 0.03	2.78 ± 0.75	1.67 ± 0.16	1.24 ± 0.68	2.04 ± 0.89
Contrast group ($n = 75$)	4.86 ± 0.68	7.46 ± 1.02	1.55 ± 0.65	1.26 ± 0.36	2.33 ± 0.64	2.19 ± 0.52	1.35 ± 0.86	1.46 ± 0.85
t value	0.195	14.468	0.194	4.671	0.167	14.003	0.427	4.613
P value	0.855	0.001	0.821	0.001	0.864	0.001	0.876	0.001

Table 4: Comparison of blood glucose, blood pressure, blood lipid, and knowledge awareness levels of the two patients.

Group	Number of cases	Fully aware	Partially aware	Do not know	Awareness rate (%)
Observation group	75	56	17	2	97.33
Contrast group	75	50	14	11	85.33
X^2 value	—	—	—	—	7.134
P value	—	—	—	—	0.007

the sports and fitness industry have become indispensable sports products for residents' fitness. It can monitor user's health data in real time and timely feedback on sports effects, so that residents can know your own health status accurately [14, 15]. Deep learning can be used for automatic diagnosis of the patient in future [16–19]. China has used the intelligent physical fitness test system to complete the student's physical fitness test files, exercise risk prediction, scientific new fitness training, and fitness effect monitoring and other technical means to provide basis and services for the prevention, intervention, and improvement of athlete's health. The APP software is used to monitor the pace, calories, cadence, heart rate, etc. in real time during the fitness exercise and make the most suitable exercise intensity fitness management service plan in time. These intelligent products will inevitably lead the sports health management service to personalization and provide convenient conditions to meet individual needs.

5. Conclusion

Through AI, we can effectively study the value of sports rehabilitation research. After investigation, it is found that diabetes is a metabolic disease, not only the phenomenon of elevated blood sugar but also abnormal performance of blood pressure and blood lipids. Therefore, it is necessary

to implement a long-term health management of patients clinically to achieve control of blood sugar levels and improve blood pressure and blood lipids. Health management is mainly carried out from the aspects of education, diet, sports, and medical treatment. The premise is to establish a management team, through the training of group members, to improve the comprehensive quality of nursing staff, and then better the provision of services by patients has a positive effect on improving the quality of care and patient satisfaction.

Data Availability

The image data used to support the findings of this study have been deposited in the diabetes dataset (https://www.kaggle.com/naveenkhasa/pima-indian-diabetes-dataset).

Conflicts of Interest

The authors declare that there are no conflicts of interest.

Acknowledgments

This research was supported by data from Guangzhou Institute of Technology, Guangdong School of Foreign Trade, Rehabilitation Department of the Fifth Hospital Affiliated to Southern Medical University, and Guangdong Ecological Engineering Vocational and Technical College.

References

[1] B. A. Kobrinskii, O. G. Grigoriev, and A. I. Molodchenkov, "Artificial intelligence technologies application for personal health management," *IFAC-PapersOnLine*, vol. 52, no. 25, pp. 70–74, 2019.

[2] S. Mohan, P. S. Rao, and V. Chindam, "Artificial intelligence based health management of host system," *U.S. Patent 10,089,203*, vol. 24, no. 62, pp. 43–49, 2018.

[3] B. Sathyasri, M. Antobennet, and S. Bhuvaneshwari, "Artificial intelligence based e-health management system," *International Journal of Pure and Applied Mathematics*, vol. 119, no. 15, pp. 31–44, 2018.

[4] J. Bae, "Development and application of a web-based expert system using artificial intelligence for management of mental health by Korean emigrants," *Journal of Korean Academy of Nursing*, vol. 43, no. 2, pp. 203–275, 2013.

[5] L. I. Can-Dong, X. Ji-Liang, and L. Huang-Wei, "Health management of traditional Chinese medicine and artificial intelligence," *China Journal of Traditional Chinese Medicine and Pharmacy*, vol. 46, no. 4, pp. 37–42, 2019.

[6] K. Matsumoto, F. Ren, and Y. Takasaka, "Psychoms: a mental health patient management and variance analysis system using artificial intelligence," *Information an International Interdiplinary Journal in English Japanese & Chinese*, vol. 56, no. 4, pp. 89–93, 2006.

[7] C. Bennett, "Artificial intelligence for diabetes case management: the intersection of physical and *mental health*," vol. 99, no. 43, pp. 112–123, 2018.

[8] S. L. Chen, M. Craig, and R. Callan, "Use of artificial intelligence methods for advanced bearing health diagnostics and prognostics," *Aerospace Conference IEEE*, vol. 38, no. 4, pp. 240–246, 2008.

[9] D. Palmer, "Artificial intelligence in healthcare management," *Healthcare Informatics: the business magazine for information and communication systems*, vol. 7, no. 3, p. 54, 1990.

[10] T. A. Arcury, R. A. Bell, B. M. Snively et al., "Complementary and alternative medicine use as health self-management: rural older adults with diabetes," *The Journals of Gerontology Series B: Psychological Sciences and Social Sciences*, vol. 61, no. 2, pp. S62–S70, 2006.

[11] S. H. Roman and M. I. Harris, "Management of diabetes mellitus from a public health perspective," *Endocrinology and Metabolism Clinics of North America*, vol. 26, no. 3, pp. 443–474, 1997.

[12] Y. Heianza, S. Hara, Y. Arase et al., "Low serum potassium levels and risk of type 2 diabetes: the Toranomon Hospital Health Management Center Study 1 (TOPICS 1)," *Diabetologia*, vol. 54, no. 4, pp. 762–766, 2011.

[13] Y. Heianza, Y. Arase, S. Kodama et al., "Trajectory of body mass index before the development of type 2 diabetes in Japanese men: Toranomon Hospital Health Management Center Study 15," *Journal of Diabetes Investigation*, vol. 6, no. 3, pp. 289–294, 2015.

[14] S. Goyal, P. Morita, G. F. Lewis, C. Yu, E. Seto, and J. A. Cafazzo, "The systematic design of a behavioural mobile health application for the self- management of type 2 diabetes," *Canadian Journal of Diabetes*, vol. 40, no. 1, pp. 95–104, 2016.

[15] P. En-Chun, Z. Qin, and L. I. Yuan, "Cross- sectional survey on the health management of hypertension and diabetes mellitus patients conducted by medical staff in primary health service centers," *Chinese General Practice*, vol. 9, no. 2, pp. 52–56, 2014.

[16] K. K. L. Wong, G. Fortino, and D. Abbott, "Deep learning-based cardiovascular image diagnosis: a promising challenge," *Future Generation Computer Systems*, vol. 110, pp. 802–811, 2020.

[17] H. Long, Y. Lairong, L. Bei, and Y. Yang, "Design and error evaluation of planar 2DOF remote center of motion mechanisms with cable transmissions," *Journal of Mechanical Design*, vol. 143, no. 1, article 013301-1-12, 2021.

[18] H. Bo, Z. Changjiang, W. Hongbing, and Y. Lairong, "Prediction and validation of dynamic characteristics of a valve train system with flexible components and gyroscopic effect," *Mechanism and Machine Theory*, vol. 157, article 104222, 2021.

[19] Z. Tang, G. Zhao, and T. Ouyang, "Two-phase deep learning model for short-term wind direction forecasting," *Renewable Energy*, vol. 173, pp. 1005–1016, 2021.

Hindawi
Computational and Mathematical Methods in Medicine
Volume 2021, Article ID 9533573, 5 pages
https://doi.org/10.1155/2021/9533573

Research Article

Multislice Spiral Computed Tomography Postprocessing Technology in the Imaging Diagnosis of Extremities and Joints

Weihua Yang[1] **and Fei Wang**[2]

[1]*Xinxiang University, Xinxiang, Henan 453003, China*
[2]*Hainan General Hospital, Haikou, Hainan 570311, China*

Correspondence should be addressed to Weihua Yang; xxxyyangweihua@126.com

Received 7 October 2021; Revised 5 November 2021; Accepted 19 November 2021; Published 13 December 2021

Academic Editor: Kelvin Wong

Objective. To improve the clinical detection rate of bone and joint fractures of the extremities and to explore the value and significance of the application of multislice spiral computed tomography (MSCT) postprocessing technology in diagnosis. *Methods*. 80 patients with bone and joint fractures of the extremities admitted to the hospital were selected as the research objects. The patients received X-ray digital radiography (DR) plain film examination and then MSCT examination. At the same time, multiplane reconstruction (MPR) and surface shadow display (SSD) and volume rendering three-dimensional imaging (VRT) technology and other postprocessing technologies compare the differences in the detection rate of limbs and joint fractures between the two inspection methods. *Results*. A total of 100 fractures were found in 80 patients. The detection rate of X-ray DR was 69%. After MSCT postprocessing technology, the detection rates of MPR, SSD, and VRT were 96%, 98%, and 99%, respectively. The accuracy of MSCT postprocessing technology in diagnosing extremity bone and joint fractures was significantly higher than that of DR, and the difference between groups was statistically significant. *Conclusion*. MSCT postprocessing technology for patients with extremity bone and joint fractures has a good effect. It is not only noninvasive but also has a high detection rate. It can significantly reduce the missed and misdiagnosed rate and provide detailed imaging data for the formulation of clinical treatment plans.

1. Introduction

Bone and joint fractures of extremities are a common type of fracture in clinical practice, which seriously endanger the health of patients [1–3]. At present, many patients with extremity bone and joint fractures are diagnosed by X-ray film [4, 5] to determine whether the patient has extremity bone and joint fractures. X-ray examination is the first choice in clinical imaging. However, X-ray plain film examination has certain limitations for occult fractures. Suspicious fractures are prone to missed and misdiagnosed situations, which delays the clinical treatment of patients with limb bone and joint fractures.

The implementation of multilayer spiral computed tomography (MSCT) scanning and three-dimensional reconstruction technology for patients with extremity bone and joint fractures can help to quickly and accurately diagnose the damage of extremities and joints [6–9] and provide more detailed imaging data for the clinical treatment of patients. The effective use of multislice spiral CT postprocessing technology can establish three-dimensional images and intuitively feedback the images of the patient's limbs and joint fractures.

Fractures of the limbs and joints can easily affect the life and work of patients [10]. In the past, digital radiographs were mostly used in clinical examinations, but due to the overlap of structures, they can only observe the lesions from a single angle, and often fail to clearly show the lesions, leading to missed and misdiagnosed small or hidden fractures, which is not conducive to clinical guidance follow-up treatment. In addition, patients with limb bone and joint fractures are affected by factors such as pain and dysfunction during the filming, and the position of the film is not accurate, which makes it impossible to clearly display the anatomical structure of the affected area. Compared with

digital X-ray radiographs, MSCT postprocessing technology has a short scanning time and a fast speed [11, 12]. It has higher image resolution in both horizontal and vertical directions and will not affect overlap during the display of concealed fractures.

In order to improve the clinical detection rate of extremity bone and joint fractures, the hospital conveniently selected 80 cases of extremity bone and joint fracture patients treated from October 2019 to April 2020 as the research objects and compared with DR (DR). The diagnostic results of the postprocessing technology of slices and MSCT have achieved certain research results.

2. Methods and Materials

2.1. General Materials. 80 cases of extremity bone and joint fracture patients admitted to the hospital were selected as the research object. The patient's fracture was mainly caused by traffic accidents, collisions, falls, and other factors. The number of males and females was analyzed. There were 44 males and 36 females. The age ranged from 27 to 59 years, with an average of (44.41 ± 1.26) years old. Traffic accidents, collisions, and falls were 21 cases, 29 cases, and 30 cases. Fracture location: limb and pelvic trauma were 58 cases and 23 cases. The specific conditions of 80 patients are shown in Figure 1.

2.2. Apparatus and Methods. All patients with bone and joint fractures of the extremities undergo digital X-ray plain film examination first, and the X-ray camera is provided by Philips. Then, we use MSCT to scan 80 patients with extremity bone and joint fractures. We use relevant operating instruments to adjust the patient's posture and posture to establish the correct scanning method.

In the process of CT scanning, the scanning range is divided. Position the fracture image of the patient and set the scan parameters reasonably. The control parameter is 120 kV, the reconstruction interval is 0.9 mm, the layer thickness is 5.1 mm, the reconstruction layer thickness is 1.26 mm, the bone window is osteo, and the reconstruction function is B80 svery sharp. Process the scanned data and reconstruct the image. According to the displayed surface shadow reorganization multiplane and three-dimensional imaging reconstruction technology, understand and master the multidirectional lesions of patients with extremity bone and joint fractures. The process of MSCT scanning fracture is shown in Figure 2.

2.3. Observation Indicators. We observe the fracture images of patients with limb bone and joint fractures, analyze the data of the patient's fracture lesions, understand and grasp the patient's fracture situation, and determine the types of limb bone and joint fractures. Finally, we made statistics on the detection rate of occult fractures of limbs and joints.

2.4. Statistical Methods. The statistical software SPSS18.0 was used to analyze the data in this study, using $(x \pm s)$ to represent measurement data and using the t-test method for comparison; using the test, percentage (%) represents counting data; when $P < 0.05$, the difference is statistically significant.

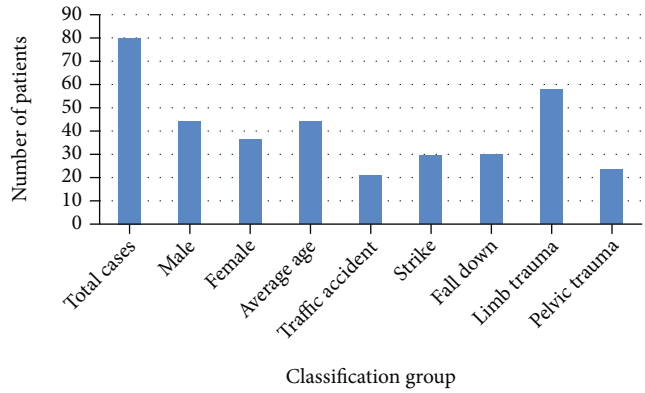

Figure 1: The specific situation of 80 patients.

3. Results

3.1. Orthopaedic Imaging. Among 80 patients, 100 fractures were found. 22 cases of shoulder fractures included surgical neck fractures of the humerus with avulsion of the greater tuberosity, acromion of the clavicle of the shoulder joint with avulsion fractures of the humeral head, and scapular fractures. 17 cases of elbow joint fractures included humeral epicondyle fractures and radial head fractures, 21 cases of wrist joint fractures included scaphoid fractures and distal radius fractures, 14 cases of metacarpal base fractures, and 26 cases of hip fractures included iliac and acetabulum. Fractures can be combined with posterior dislocation of the femoral head, femoral neck, and intertrochanteric fractures. Figure 3 shows DR plain film and MSCT images.

It can be seen from Figure 3 that the fractures shown on the DR film are all suspicious, while the MPR axis of the MSCT is conducive to the diagnosis of subtle fractures, and the image shows the separation of fracture fragments more clearly. Ilium, acetabulum, patella, ankle joint, posterior ankle, internal epicondyle of the humerus, and the base of the fourth and fifth metacarpal bones are easily misdiagnosed on DR digital radiographs due to overlapping images, small fracture lines, and no obvious misalignment. Using MSCT scan, which is then reconstructed by MPR, SSD, and VRT, the fracture image is clearly visible, especially the relationship between the fracture line, small fracture fragments, and adjacent tissue structures can be clearly displayed on multiple levels through MPR.

3.2. Comparative Results of Occult Fractures. We research and analyze the bone and joint fractures of the extremities, monitor the results of the X-ray detection data, analyze the abnormal detection of the X-ray, count the number of concealed fractures, and use the X-ray to detect the concealed fractures of the limbs and joints. There were 7 patients, and the detection ratio was 8.75%. Using MSCT postprocessing technology, 25 patients with occult fractures of limbs and joints were detected, with a detection rate of 31.25%. The difference of the detected data was compared,

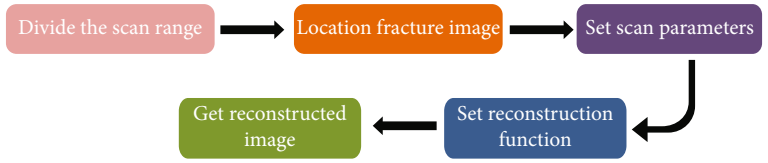

Figure 2: Flow chart of MSCT scanning fracture.

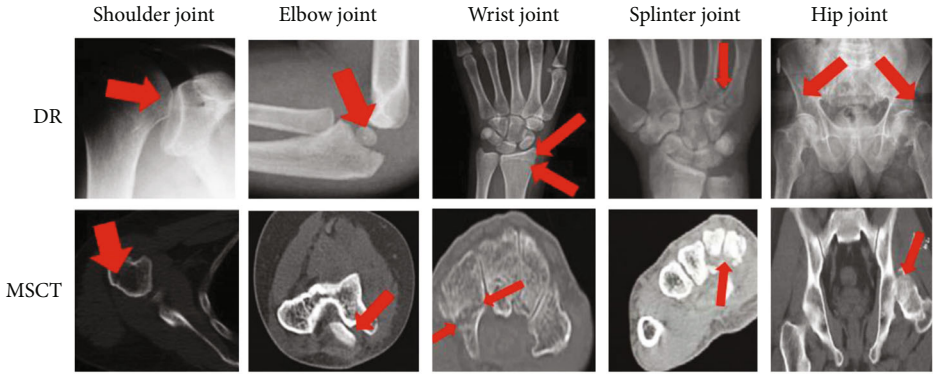

Figure 3: X-ray DR plain film and MSCT image.

and the difference was obvious ($\chi^2 = 12.1443$, $P < 0.05$), which was statistically significant, as shown in Table 1.

DR examination of the ilium, acetabulum, posterior ankle of ankle, internal epicondyle of the homers, and the base of the 4th to 5th metacarpal bone overlaps, the fracture line is small, the dislocation is usually not obvious, and the misdiagnosis is easy to occur. In this case, using MSCT scanning to examine patients with occult fractures and then display surface shadows and reconstruction planes and reconstruct three-dimensional imaging, one can clearly observe the fracture images of patients with occult fractures, especially the reconstruction planes, which can be displayed on multiple levels. The upper will clearly show the patient's fracture line, relatively small fracture fragments, and the relationship between adjacent tissue structures.

3.3. Postprocessing Results of MSCT. The study showed that a total of 100 fractures were found in the enrolled patients, of which 69 fractures were found by DR examination, with a detection rate of 69%. After MSCT postprocessing technology inspection, MPR, SSD, and VRT found 96 fractures, 98 fractures, and 99 fractures, and the detection rates were 96%, 98%, and 99%. The paired test of the two inspection methods found that the accuracy of MSCT postprocessing technology in diagnosing limbs and joint fractures was significantly higher than that of digital X-ray. There was a statistically significant difference between linear photography and plain film ($P < 0.05$). The results of different methods of diagnosing joint injury types are shown in Figure 4.

4. Discussion

The MSCT scan speed is fast, and the image has high horizontal and vertical resolution [12, 13]. It shows that the hidden suspicious fracture has no image overlap with the X-ray plain film, and the image is clear. In this group of 80 patients, MPR can display fracture lines and bone fragments from any direction in two-dimensional cross-sectional, sagittal, coronal, oblique, and curved images on the display screen according to the needs of diagnosis, so as to have a more comprehensive understanding of the scope of fractures.

The three-dimensional effects of SSD and VRT are obvious [14–17]. Because SSD adopts threshold imaging, it is suitable for the display of the surface morphology of the skeletal system. It has a strong spatial three-dimensional effect and a clear surface anatomy relationship, which is conducive to the positioning of the fracture and the extent of the fracture line. The performance is obviously affected by the segmentation threshold in image processing, so the internal structure of the object cannot be displayed, and the density information of the object cannot be provided.

VRT uses all the voxel data of spiral CT volume scanning [18]. According to the CT value of each voxel and its surface characteristics, all voxels in the imaging volume are given different colors and different transparency through image reorganization and simulated light source illumination, as to show the full picture of organ or tissue structure with stereoscopic visual effect. VRT image can not only show the surface morphology of the observed object but also can display the morphology of any level inside the observed object according to the needs of the observer, helping to determine the bone and joint damage the main feature of the image of the positional relationship with the surrounding important structures is high resolution [19, 20]. It displays the density information while displaying the spatial structure to make up for the lack of SSD, but it is not as good as MPR in displaying the fine structure and small changes inside the fractured bone. SSD and VRT are inferior to MPR (patella fracture) when showing small fracture lines

Table 1: Comparative results of occult fractures of the two methods.

Method	Number of cases	Number of occult fractures	Proportion (%)
DR	80	7	8.75
MSCT	80	25	31.25
χ^2		12.1443	
P		0.02	

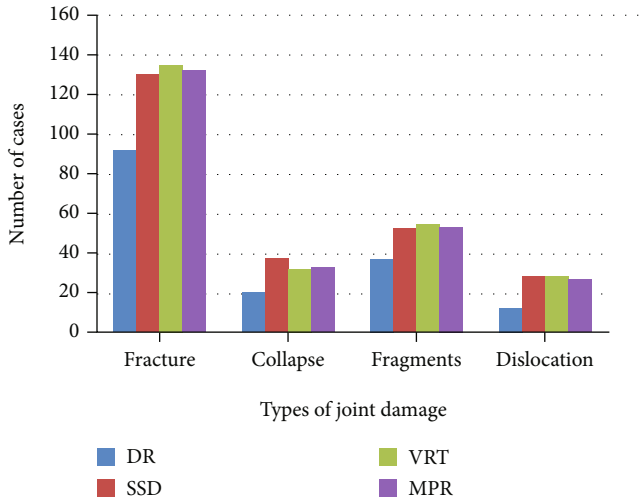

Figure 4: The results of different methods to diagnose the type of joint damage.

without obvious dislocation, and it is also inferior to MPR in terms of soft tissue damage and swelling [21]. MPR can better show the subtle and complex anatomical relationship between bone and joint damage and surrounding tissues and organs.

Due to the different fracture sites of the limbs and joints, the difficulty of detection is also greater, showing incremental and progressive changes. Among the bone and joint fractures of the extremities, occult fractures are difficult to diagnose. During the diagnosis process, many fracture problems are difficult to find as soon as possible, and omissions often occur, which are very detrimental to the rehabilitation of patients with bone and joint fractures [22]. This requires the determination of the principle of occult fractures and accurate determination and evaluation, so that the accuracy of clinical diagnosis can be effectively guaranteed. In diagnosing patients with bone and joint fractures of the extremities, although the use of X-ray films can be helpful, X-ray films have certain limitations in application. X-ray film limitation is very unfavorable for doctors to accurately judge the fracture status of limbs and joints in patients. The effective use of MSCT postprocessing technology is more advantageous than the application of X-ray film [23].

MSCT postprocessing technology not only has a fast-scanning speed but also has a very good scanning effect [24]. It can understand and master the vertical and horizontal changes of the scanned image and study and analyze the characteristics of the image. Suspicious fracture locations and hidden fracture locations are found and more in-depth assumptions and judgments of the symptoms of patients with limbs and joints. After the use of MSCT scanning, changes in the cross-section of the patient's limbs and joints will appear [25]. The cross-section, sagittal plane, coronal plane, and inclined plane are all planes. We distinguish the fracture line of the scanned image and understand the distribution of bone fragments in patients with limbs and joints. In this way, the range of fractures of limbs and joints in patients can be clearly defined. In the future, deep learning can be used for automatic diagnosis of patients and rehabilitation training through verification of external mechanical equipment [26–29]. After understanding the range of the patient's fracture range, research and analysis of the patient's soft tissue changes and accurately summarizes the data of the fracture of the limbs and joints. The mechanical information of such fractures are generally based on the material properties [30, 31].

5. Conclusion

Through the comparison of the detection results of occult fractures and the comparative analysis of the detection rate of fractures, it can be concluded that the postprocessing technology of MSCT is more advantageous than plain radiographs in judging the limbs and joints.

The use of MSCT postprocessing technology can detect the condition of the fractured parts of patients with extremity bone and joint fractures in a timely manner, effectively achieve clinical diagnosis, and have significant diagnostic results, so that the comprehensiveness and timeliness of treatment can be guaranteed. For patients with extremity bone and joint fractures, the staff can also give more accurate and comprehensive diagnosis results and use this as a basis to assist surgeons in formulating the corresponding fracture surgical treatment methods. At the same time, for patients with extremity bone and joint fractures, rehabilitation is also very helpful.

Data Availability

The image data used to support the findings of this study have been deposited in the Musculoskeletal Radiographs (MURA) dataset (https://stanfordmlgroup.github.io/competitions/mura/).

Conflicts of Interest

The authors declare that they have no conflicts of interest.

Acknowledgments

The authors would like to thank the staff and students of Hainan General Hospital and University for their help in processing the image scans obtained in this study.

References

[1] R. Watson-Jones, "Fractures and other bone and joint injuries," *American Journal of Physical Medicine & Rehabilitation*, vol. 10, no. 21, p. 1831, 1941.

[2] M. Laroche, G. Ricq, and A. Cantagrel, "Bone and joint involvement in adults with Werner's syndrome," *Revue du Rhumatisme*, vol. 64, no. 12, pp. 843–846, 1997.

[3] R. Vardasca, M. T. Restivo, and J. Mendes, "Skin temperature bilateral differences at upper limbs and joints in healthy subjects," in *European Congress on Computational Methods in Applied Sciences and Engineering*, pp. 1005–1010, Springer, Cham, 2017.

[4] D. Kotsianos, C. Rock, E. Euler et al., "3D imaging with a mobile surgical image enhancement equipment (ISO-C-3D). Initial examples of fracture diagnosis of peripheral joints in comparison with spiral CT and conventional radiography," *Der Unfallchirurg*, vol. 104, no. 9, pp. 834–838, 2001.

[5] Z. I. Urazgil'Deev and A. S. Roskidaĭlo, "Treatment of ununited fractures and pseudarthrosis of long bones of the lower limbs complicated by osteomyelitis," *Khirurgiia*, vol. 9, pp. 48–54, 1999.

[6] L. De-Xiang, "The application of anatomic locking compression plate in comminuted fractures of the limbs close to the joints about fracture patients," *Guide of China Medicine*, vol. 15, 2009.

[7] I. Coc, T. Banic, and V. Bilic, "Neurological recovery after early reposition, decompression and instrumented fusion of C-type L2 fracture: a case report," *Global Spine Journal*, vol. 6, 2017.

[8] A. Hollinger, A. Christe, M. J. Thali et al., "Incidence of auditory ossicle luxation and petrous bone fractures detected in post-mortem multislice computed tomography (MSCT)," *Forensic Science International*, vol. 183, no. 1-3, pp. 60–66, 2009.

[9] U. Wedegärtner, C. Gatzka, and J. M. Rueger, "Multislice CT (MSCT) in der Detektion und Klassifikation von Becken- und Azetabulumfrakturen," *RoeFo-Fortschritte auf dem Gebiete der Roentgenstrahlen und der Neuen Bildgebenden Verfahren*, vol. 175, no. 1, pp. 105–111, 2003.

[10] O. Ronneberger, D. Kainmueller, and E. Vorontsov, "The value of MSCT with three dimensional reconstruction in chest trauma fractures," *Journal of Medical Imaging*, vol. 86, no. 4, pp. 227–248, 2009.

[11] R. P. K. Poudel, S. Manish, and G. Montana, "The value of MSCT in the diagnosis of costae and costicartilage occult fractures," *Journal of Practical Medical Imaging*, vol. 45, no. 8, pp. 78–84, 2015.

[12] M. Huaguo, "The diagnosis value of X-ray and MSCT in dislocation of scaphoid-lunate joint," *Journal of Mathematical Medicine*, vol. 112, no. 17, pp. 227–240, 2011.

[13] B. M. Nigg, S. Y. Bae, and J. H. Lee, "X-ray and MSCT in the diagnosis of severe spinal injury," *Image Technology*, vol. 53, no. 8, pp. 66–70, 2012.

[14] M. W. Weinberg and N. P. Davidson, "Clinical evaluation and diagnosis of 3D reconstruction and MPR with MSCT in tibial plateau fractures," *Journal of Medical Imaging*, vol. 27, no. 5, pp. 168–175, 2005.

[15] A. Goyal and S. Sharma, "Traumatic carotid-cavernous fistula: excellent demonstration on 3D CT angiography," *BMJ Case Reports*, vol. 2013, no. oct16 1, article bcr2013201707, 2013.

[16] C. Gang-Wei, M. U. Wen-Bin, and J. Zheng-Yu, "Optic canal fracture evaluation using three-dimensional computed tomography reconstructions," *Medical Journal of Peking Union Medical College Hospital*, vol. 22, no. 5, pp. 76–80, 2013.

[17] W. Jin, Z. Xue-Lin, and L. I. Shu-Xiang, "Clinical application of spiral CT to acetabular fracture: surface shaded display (SSD) and volume rendering (VR) techniques study and compared with two-dimensional CT (2DCT), X-ray and MPR," *Journal of Practical Radiology*, vol. 19, no. 11, pp. 1006–1010, 2003.

[18] N. Liu-Jin, L. I. Guang-Yu, and P. Han-Hua, "Clinical significance of spiral CT with three-dimensional reconstruction imaging on palvic fracture," *Progress in Modern Biomedicine*, vol. 96, no. 3, pp. 234–246, 2013.

[19] W. J. Shin, G. R. Hastie, and D. A. Goodman, "Clinical applications of VRT 3D reconstruction with spiral CT," *Journal of Clinical Radiology*, vol. 28, no. 4, pp. 221–235, 2000.

[20] B. Jankharia and N. Sosi, "Radiology of acetabular fractures," *Indian Journal of Orthopaedics*, vol. 68, no. 7, pp. 342–356, 2002.

[21] M. W. Weinberg and N. P. Davidson, "Three-dimensional reconstructive imaging of electron beam CT: the clinical application and evaluation," *Bulletin of Medical Postgraduate*, vol. 48, no. 6, pp. 48–59, 2000.

[22] J. M. Wolterink, F. Pernu, and S. Pezold, "Application of three-dimensional reconstruction technique of 16 slice spiral CT for complicated fractures," *Journal of Rare and Uncommon Diseases*, vol. 167, no. 3, pp. 176–183, 2007.

[23] L. C. Gerstenfeld, Y. Alkhiary, and E. A. Krall, "Three-dimensional reconstruction of fracture callus morphogenesis," *Journal of Histochemistry & Cytochemistry Official Journal of the Histochemistry Society*, vol. 54, no. 11, 2006.

[24] R. Y. L. Liow, P. D. Birdsall, and B. Mucci, "Spiral computed tomography with two- and three-dimensional reconstruction in the management of tibial plateau fractures," *Orthopedics*, vol. 22, no. 10, pp. 929–932, 1999.

[25] T. Kuroda, K. Ikeuchi, and K. Nakade, "Three-dimensional reconstruction of cleavage fracture surface for duplex stainless steel," *Vacuum*, vol. 65, no. 3-4, pp. 541–546, 2002.

[26] L. Huang, L. Yin, B. Liu, and Y. Yang, "Design and error evaluation of planar 2DOF remote center of motion mechanisms with cable transmissions," *Journal of Mechanical Design*, vol. 143, no. 1, p. 013301-1-12, 2021.

[27] H. Bo, Z. Changjiang, W. Hongbing, and Y. Lairong, "Prediction and validation of dynamic characteristics of a valve train system with flexible components and gyroscopic effect," *Mechanism and Machine Theory*, vol. 157, article 104222, 2021.

[28] K. K. L. Wong, G. Fortino, and D. Abbott, "Deep learning-based cardiovascular image diagnosis: a promising challenge," *Future Generation Computer Systems*, vol. 110, pp. 802–811, 2020.

[29] Z. Tang, G. Zhao, and T. Ouyang, "Two-phase deep learning model for short-term wind direction forecasting," *Renewable Energy*, vol. 173, pp. 1005–1016, 2021.

[30] X. Xinli, C. Zhang, F. Musharavati, T. A. Sebaey, and A. Khan, "UFSW tool pin profile effects on properties of aluminium-steel joint," *Vacuum*, vol. 192, no. 8, article 110460, 2021.

[31] X. Xu, C. Zhang, H. A. Derazkola, M. Demiral, A. M. Zain, and A. Khan, "Dispersion of waves characteristics of laminated composite nanoplate," *Steel and Composite Structures*, vol. 40, no. 3, pp. 355–367, 2021.

Hindawi
Computational and Mathematical Methods in Medicine
Volume 2021, Article ID 1980408, 8 pages
https://doi.org/10.1155/2021/1980408

Research Article

Blood Pressure Model Based on Hybrid Feature Convolution Neural Network in Promoting Rehabilitation of Patients with Hypertensive Intracerebral Hemorrhage

Zhixia Zheng, Limei Bai, and Shaoquan Li

Department of Neurosurgery, Cangzhou Central Hospital, Hebei 061001, China

Correspondence should be addressed to Zhixia Zheng; 1320613750@qq.com

Received 9 August 2021; Revised 24 October 2021; Accepted 10 November 2021; Published 7 December 2021

Academic Editor: Kelvin Wong

Objective. Accurate prediction of the rise of blood pressure is essential for the hypertensive intracerebral hemorrhage. This study uses the hybrid feature convolution neural network to establish the blood pressure model instead of the traditional method of pulse waves. *Methods*. The pulse waves of 100 patients were collected, and the pulse wave was decomposed into three bell wave compound forms to obtain the accurate pulse wave propagation time. Then, the mixed feature convolution neural network model ABP-net was proposed, which combined the pulse wave propagation time characteristics with the pulse wave waveform characteristics automatically extracted by one-dimensional convolution to predict the arterial blood pressure. Finally, according to the prediction results, 20 patients were treated before the high blood pressure appeared (model group), and another 20 patients with a daily fixed treatment scheme were selected as the control group. *Results*. In 80 training sets, compared with linear regression and the random forest method, the hybrid feature convolution neural network has higher accuracy in predicting blood pressure. In 20 test sets, the blood pressure error was eliminated within 5 mmHg. The total effective rate in the model group and the control group was 95.0% and 85.0%, respectively ($P = 0.035$). After treatment, the scores of self-care ability of daily life and limb motor function in the model group were higher than those in the control group ($P < 0.05$). There were 8 cases (13.6%) in the model group and 17 cases (28.3%) in the control group due to the recurrence of cerebrovascular accident ($P = 0.043$). *Conclusion*. Drug treatment guided by a blood pressure model based on a hybrid feature convolution neural network for patients with hypertensive cerebral hemorrhage can significantly and smoothly reduce blood pressure, promote the health recovery, and reduce the occurrence of cerebrovascular accidents.

1. Introduction

Hypertensive intracerebral hemorrhage is a typical cerebrovascular emergency and critical disease in neurosurgery [1]. It is often seen in middle-aged and older people. Patients with high blood pressure have a one-third chance of developing cerebral hemorrhage, while about 95% of patients with cerebral hemorrhage suffer from hypertension [2]. The disease is acute, rapid, and dangerous and has high morbidity and mortality. According to the literature, the early mortality rate can be as high as 49.4%, and less than half of the survivors can live [3]. Surgical treatment has always been an important treatment for hypertensive intracerebral hemorrhage [4].

However, multiple causes may induce readmission in the postoperative recovery period. The disability and mortality rates are significantly higher than those of the first bleeding, and the prognosis is lacking [5]. Rebleeding is a common cause for readmission, and it is related to many risk factors, especially the control of blood pressure [6]. Blood pressure is affected by many factors and changes in real time, so continuous blood pressure monitoring is essential for doctors to diagnose and control patients' conditions.

In recent years, medical research has shown that cerebrovascular events' timing is closely related to the circadian rhythm of human blood pressure [7]. With the birth and development of time medicine and its penetration and

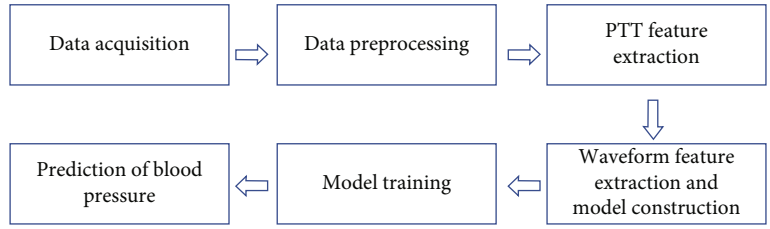

Figure 1: Algorithm flowchart of blood pressure modeling.

promotion of nursing discipline, today's nursing model has been derived, and time nursing has begun to attract scholars' attention [8–12]. So far, many kinds of regression models have been established for continuous measurement of blood pressure, among which pulse wave velocity (PWV) is the most common. PWV is the propagation velocity of the pressure wave in blood vessels. It is often estimated by the pulse transit time (PTT), which is the time when the heart beats around the body. There was a significant correlation between blood pressure and PTT. However, the accuracy of different PTT regression models for predicting blood pressure was low.

Machine learning has made great progress in the establishment of various prediction models [13, 14]. To solve the above problems, we first propose a pulse wave decomposition algorithm to locate the repetitive pulse wave location and obtain the accurate PTT. Then, a new blood pressure prediction model is proposed, which is a hybrid feature convolution neural network. Based on the traditional fully connected neural network constructed by PTT, the pulse wave features extracted automatically are added to predict blood pressure; then, the blood pressure model is established. Finally, we also use the model to guide the treatment of hypertensive intracerebral hemorrhage.

2. Materials and Methods

2.1. General Materials. A total of 120 patients with hypertensive intracerebral hemorrhage who were hospitalized in our hospital were selected. There were 74 males and 46 females, aged 56 ± 14 years old. The selection criteria were as follows: (1) patients had hypertensive cerebral hemorrhage diagnosed by computed tomography (CT) after admission and confirmed by operation; (2) patients were admitted to the hospital within 3 h after the onset of the disease, craniocerebral surgery was performed within 24 h after the onset of the disease, and the postoperative blood pressure of the patients was above 165/95 mmHg; (3) mental retardation was excluded; and (4) other chronic diseases were excluded.

The vital sign signals collected from the medical information system in 80 patients were used as the training sets. The remaining 40 patients were used as the testing sets and were randomly divided into two groups. The established model is verified in 20 patients, and they were treated before the high blood pressure appeared (model group), and another 20 patients with a daily fixed treatment scheme were selected as the control group. There was no significant difference in gender, education level, and course of disease between the two groups.

2.2. Blood Pressure Modeling Method Based on Hybrid Feature Convolution Neural Network. The algorithm flowchart of this study is shown in Figure 1.

2.2.1. Data Acquisition and Preprocessing. The signals used in this study include the electrocardiogram (ECG), photoplethysmograph (PPG), and arterial blood pressure (ABP). PPG is the finger volume pulse wave. The pretreatment includes the following stages:

(1) *Remove baseline drift*: wavelet decomposition is used to remove the low frequency ECG and PPG parts to achieve the purpose of removing the baseline

(2) *Division of cardiac cycle*: firstly, the R wave peak of the ECG is chosen as the starting point of the cardiac cycle; secondly, the cardiac cycle of PPG and ABP was divided. According to the time relationship, the first cardiac cycle of PPG and ABP was found from each R wave peak, and the ECG starting point and PPG and ABP segments belonging to the same cardiac cycle were combined; finally, the true systolic blood pressure (SBP) and diastolic blood pressure (DBP) were determined according to the ABP fragment

(3) *Noise sample removal*: rules are used to remove the cardiac cycle with obvious abnormal waveform shape, such as the long cardiac cycle caused by the wrong division of the starting point in PPG and ABP and the distortion of signal shape caused by equipment acquisition

2.2.2. PTT Feature Extraction. The pulse wave contains rich physiological information. The main characteristic points are pulse wave starting point A, main wave peak B, tide wave starting point C, tide wave ending point D, descending gorge E, and repetition wave peak F (Figure 2).

The main wave peak B is caused by ventricular contraction, blood from left ventricular to aorta, reflecting the ability of ventricular ejection and compliance of blood vessels, etc. The peak F of the heavy pulse wave is caused by the diastolic period of the heart; the closure of the aortic valve prevents blood from returning to the ventricle, reflecting the elasticity of the artery and the closing function of the active pulse valve. B and F are the two most important

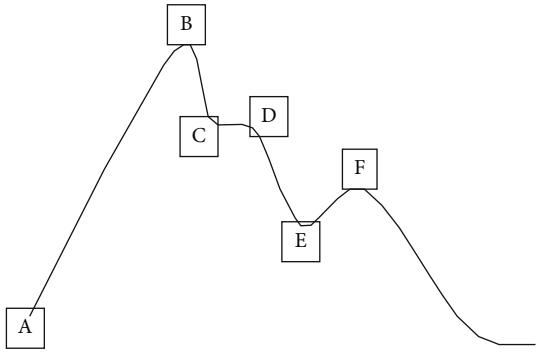

Figure 2: Single cardiac cycle pulse wave feature points.

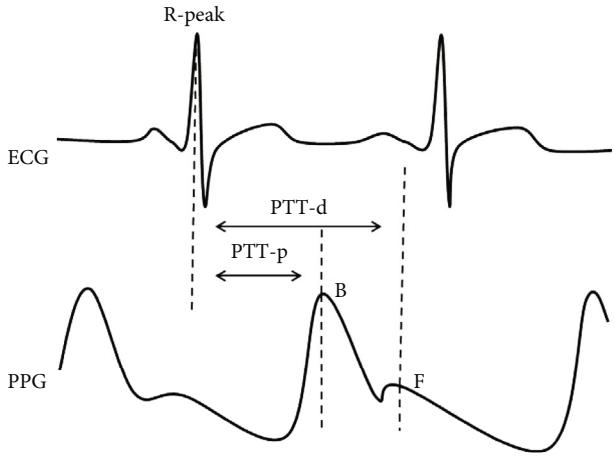

Figure 3: PTT feature extraction method.

characteristic points in a cardiac cycle. Therefore, B and F are selected as the termination points to calculate PTT and are recorded as PTT-p and PTT-d, respectively, as shown in Figure 3.

B is obtained by calculating the maximum position of PPG in a cardiac cycle, and F is obtained by continuous wavelet decomposition of PPG with gaus1 wavelet basis. The first zero crossing point after B is E, and the second zero crossing point is F.

2.2.3. Waveform Feature Extraction and Model Construction. This study proposes a new blood pressure prediction model ABP-net, which uses 1D-CNN to automatically extract the waveform features of PPG and predict blood pressure, and solves the problem of feature points being difficult to extract, as shown in Figure 4.

ABP-net is a convolutional neural network with mixed features, and the grey identification part is a model constructed with PTT features. In this study, PPG segments of the same cardiac cycle are also added to the network as input. One-dimensional convolution is used to extract the waveform features of the pulse wave, and the full connection layer is used to synthesize and select the extracted waveform features, and then, PTT features are used for blood pressure prediction. The model input contains two types of features: PTT is the traditional numerical feature and PPG is the formal feature (such as signal and image). ABP-net effectively integrates numerical features and formal features, which provides a new idea for using different types of features to model together, and improves the effectiveness and accuracy of the model by using the association between the two types of features and the output. ABP-net contains a variety of processing modules, and the dotted part is the residual structure.

The input-output feature maps in Conv-1D are all 1-dimensional; for a single sample, let $\mu_i(x)(i = 1, 2, \cdots, N)$ be the x-th node of the i-th feature map at input and N the number of input feature maps, $v_j(x)(j = 1, 2, \cdots, M)$ the x-th node of the j-th feature map at output and M the number of output feature maps, then Conv-1D is operated as follows:

$$v_j(x) = \sum_{i=1}^{N} \sum_{p=0}^{K-1} k_{i,j}(p) \bullet u_i(xS + p) + b_j, \tag{1}$$

where $k_{i,j}$ is the convolution kernel, connecting the two feature maps u_i and v_j, the length of the convolution kernel is K, S is the sliding step of the convolution kernel, and b_j is the bias.

BN solves the problem that the distribution of inputs at a certain layer in a deep network changes due to previous changes in network parameters. Let a batch be $B = \{x_1, x_2, \cdots, x_n\}$ and the algorithm be as follows:

$$u_B = \frac{1}{n} \sum_{i=1}^{n} x_i, \tag{2}$$

$$\sigma_B^2 = \frac{1}{n} \sum_{i=1}^{n} (x_i - \mu_B)^2, \tag{3}$$

$$\widehat{x}_i = \frac{x_i - \mu_B}{\sqrt{\sigma_B^2 + \varepsilon}}, \tag{4}$$

$$y_i = \gamma \widehat{x}_i + \beta, \tag{5}$$

where μ_B is the expectation of sample set B, σ_B^2 is the variance, y_i is the result normalized to batches of x_i, and γ and β are parameters to be learned, determined by training. When used in the 1-dimensional convolution section, set B is the set of values over all positions of that feature map for all samples of that match on the same feature map.

The activation function enables the model to obtain nonlinear modeling capability, and the ReLU function

$$\mathrm{f(x)} = \max\,(0, \mathrm{x}), \tag{6}$$

does not cause a gradient disappearance problem and is computationally simple, making the model forward computing faster.

Pooling can reduce feature dimensionality while acquiring the main information in a feature map and is divided into two types, maximum pooling and average pooling.

Pooling of maxima:

$$p_i(x) = \max\,\{u_i(p) \mid xS \ll p \ll xS + K - 1\}. \tag{7}$$

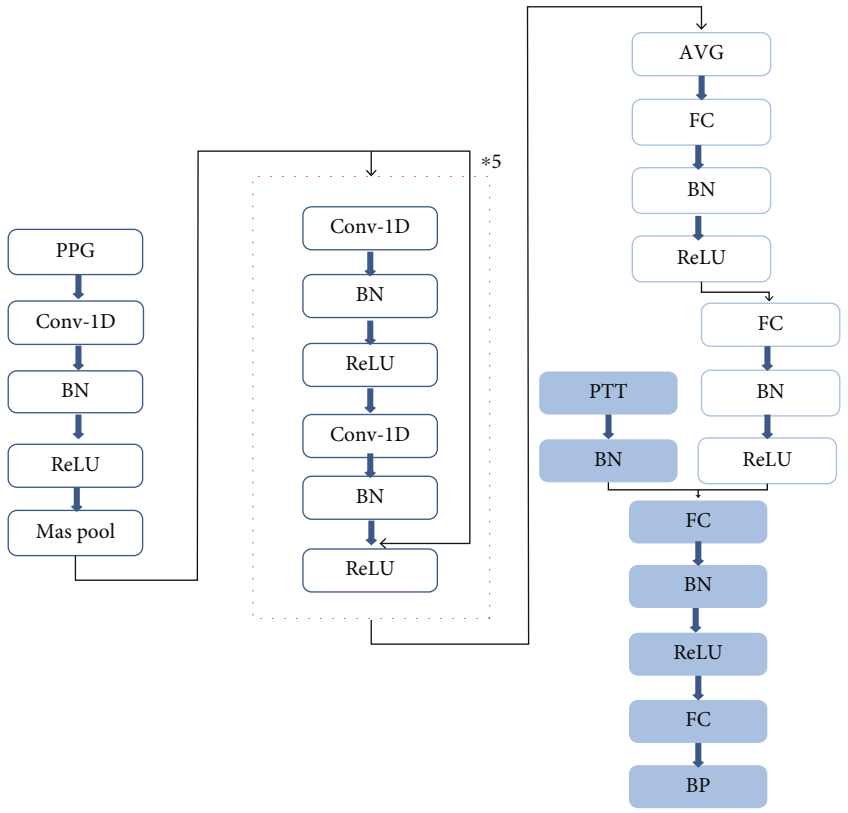

Figure 4: ABP-net network structure.

Pooling of means:

$$p_i(x) = \text{mean}\{u_i(p) \mid xS \ll p \ll xS + K - 1\}. \quad (8)$$

p_i is the result after pooling of eigenvectors u_i, K is the pooling window size, and S is the window sliding step.

The other modules are the traditional neural network modules, FC is the fully connected layer, and AVG is the input format that is needed to convert the output of the convolutional layer into a fully connected layer with the method of averaging.

2.2.4. Model Training. Model training is to update the network parameters iteratively to make the loss function converge to the global minimum in the training set. ABP-net is a regression model with blood pressure as the output. The loss function is defined as the mean square error (MSE). Let $y = (y_1, y_2, \cdots, y_n)$ be the real output of blood pressure and $\hat{y} = (\hat{y}_1, \hat{y}_2, \cdots, \hat{y}_n)$ be the model output of blood pressure

$$\text{MSE} = \frac{1}{n}\sum_{i=1}^{n}(y_i - y\wedge_i)^2, \quad (9)$$

where n is the size of a batch. In this study, batch gradient descent method is used to train the model and optimize the MSE.

2.3. Targeted Treatment. Patients in the control group received the routine blood pressure control measures: antihypertensive drugs three times a day and the rehabilitation did not control the time. The observation group used the model-predicted blood pressure increase pad to give targeted treatment. This seems to be a routine treatment after this.

According to the circadian rhythm fluctuation of blood pressure in patients with hypertensive intracerebral hemorrhage, the model group was given nursing intervention measures such as adjusting medication time and guiding patients' early limb function training according to the circadian rhythm fluctuation of blood pressure. The detailed biological clock control methods were as follows:

(1) *Medication control*: the patients adopted the best medication time according to the physiological rhythm: three times per day at 6:00, 15:00, and 22:00; two times per day at 6:00 and 22:00; and one time per day at 6:00

(2) *Early limb function training*: the training time of patients was based on the diurnal variation of blood pressure and avoided the peak time of blood pressure. Generally, they were selected from 6:00 to 7:00, 14:00 to 16:00, and 19:00 to 21:00. The blood pressure peak period was reduced, the activity was moderate, and the rest was increased to prevent the recurrence of cerebrovascular accident due to the further increase of blood pressure after the activity. The limb function training included passive limb

Table 1: Blood pressure model predicts SBP and DBP accuracy comparison.

Methods	SBP (mmHg)		DBP (mmHg)	
	PTT	PPG	PPT	PPG
ABP-net	3.32 ± 0.76	3.69 ± 0.92	1.77 ± 0.31	1.95 ± 0.39
Linear regression	6.52 ± 2.43	6.24 ± 1.85	3.44 ± 0.93	3.05 ± 0.69
Random forest	6.91 ± 2.31	4.51 ± 1.16	3.31 ± 0.87	2.22 ± 0.44

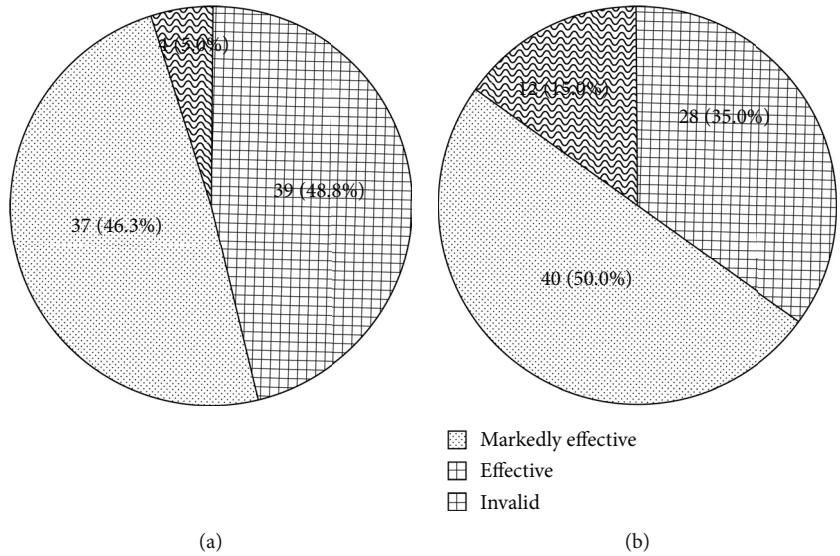

Figure 5: Antihypertensive effect in the model group (a) and control group (b).

movement exercise, active body movement, and daily life self-care activity training

(3) *Follow-up*: strengthen follow-up supervision after discharge. Taking the family as the center, the patients can understand the harmfulness of hypertensive cerebral hemorrhage and the importance of continuous medication and limb function training, improve the medication compliance of patients, teach the sense and family members to measure blood pressure, and enhance the self-care ability of patients

2.4. Observation Index. Via follow-up monitoring for 1 year, the antihypertensive effect and recurrence of the cerebrovascular accident in the two groups were monitored and compared. The Barthel score was used to evaluate the ability of daily living. The Fugl-Meyer score was used to evaluate limb motor function.

The blood pressure changes at 6:00, 4:00, 18:00, and 22:00 every day were compared to determine the measurement position, time, and sphygmomanometer, and the therapeutic effect was determined by a specially assigned person as follows: (1) *markedly effective*: the systolic and diastolic blood pressure decreased to the normal level or the diastolic blood pressure decreased by 10 mmHg and fell to the normal range; (2) *effective*: the effective blood pressure decreased significantly, but did not fall to the normal range, or the diastolic blood pressure decreased less than 10 mmHg but returned to normal or the diastolic blood pressure decreased by 10-19 mmHg or the systolic blood pressure decreased more than 40 mmHg; and (3) *invalid*: the blood pressure drop did not reach the effective index.

2.5. Statistical Treatment. The age, Barthel score, and Fugl-Meyer score of the two groups were compared by t test; the gender, education level, treatment effectiveness, and readmission rate of the two groups were compared by chi square test.

3. Results

3.1. The Validity of the Model. For each model, the prediction accuracy of DBP is higher, which indicates that DBP has higher correlation with PTT and PPG. For the traditional regression model, the model constructed by PPG is better than the model constructed by PTT, but the accuracy is lower than that of the ABP-net model, which shows that the ABP-net model is effective for the integration of PTT features and PPG features and has greater advantages than other models (Table 1).

3.2. Antihypertensive Rate. The antihypertensive effect of the two groups is shown in Figure 5. As the total effective rate was calculated by the sum of markedly effective rate and effective rate, the total effective rate in the model group and control group was 95.0% and 85.0%, respectively, and

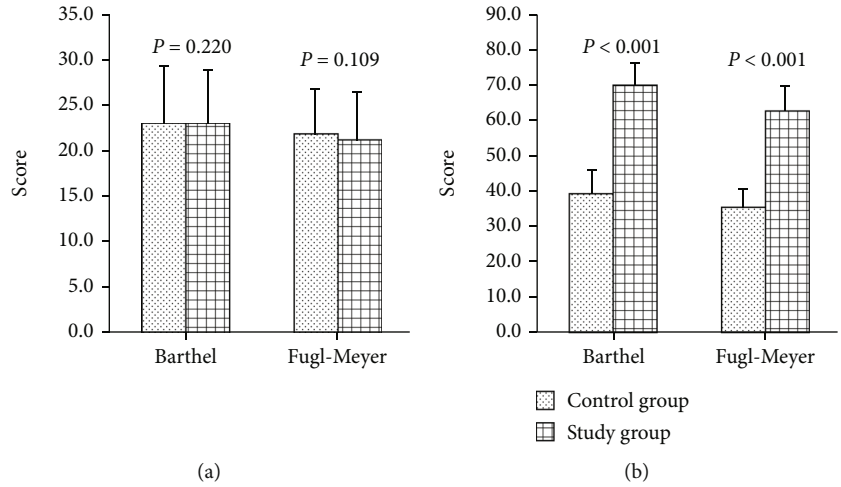

Figure 6: Comparison of daily life self-care ability and limb motor function in two groups: (a) before treatment; (b) after treatment.

the difference was statistically significant ($\chi^2 = 4.444$, $P = 0.035$).

3.3. Comparison of Daily Life Self-Care Ability and Limb Motor Function. Compared with the data before treatment, the daily life self-care ability and limb motor function after treatment in all the two groups were improved. After treatment, the score of the model group was higher than that of the control group ($P < 0.05$). The details are shown in Figure 6.

3.4. Readmission of Recurrent Cerebrovascular Accident. Eight (13.3%) patients in the model group and 17 (28.3%) patients in the control group were readmitted to the hospital because of recurrence of cerebrovascular accident. The recurrent rate between the two groups was statistically significant ($\chi^2 = 4.093$, $P = 0.043$).

4. Discussion

Hypertensive intracerebral hemorrhage is a common primary intracerebral hemorrhage, which is caused by the rupture of blood vessels when blood pressure rises abruptly on the basis of cerebral artery disease caused by hypertension. In recent years, the incidence rate has increased year by year, about $81/10^5$, and the mortality rate of cerebral hemorrhage patients is 38%~43% [15]. For patients with hypertensive intracerebral hemorrhage, we should not only grasp the best treatment time and take the best surgical treatment but also actively take effective nursing measures after operation, so as to ensure the effect of surgical treatment and reduce the incidence of complications and mortality [16]. In the recovery period of hypertensive intracerebral hemorrhage, many factors may induce rebleeding and other cerebrovascular accidents, and the risk may be reduced by active family, scientific, and effective nursing.

With the exploration of the physiological and pathological rhythm of hypertensive cerebral hemorrhage and the time rhythm of drug action, it has been recognized that the drug treatment effect of hypertensive cerebral hemorrhage is related not only to the pharmacological effect of antihypertensive drugs but also to the blood pressure fluctuation time rule, the medication time rule of patients itself [17]. With the birth and development of time medicine, time nursing has been gradually recognized by people. It refers to a new discipline wherein nurses use the intrinsic rhythm of the body itself to care for patients' psychological factors, medication time, physiology, and pathology [18]. In this study, according to the time rhythm of hypertensive intracerebral hemorrhage, we applied time nursing to comprehensive treatment and nursing intervention measures. The results showed that time nursing can effectively and steadily reduce blood pressure and reduce the occurrence of cerebrovascular accidents, so as to improve the quality of life of patients with hypertensive intracerebral hemorrhage.

The circadian rhythm curve of blood pressure in patients with hypertensive intracerebral hemorrhage is similar to that in normal people, but the overall blood pressure level is higher and the fluctuation range is larger. Even if the blood pressure has decreased after treatment, the rhythm can still exist. At 2:00-3:00 in the morning, it was at the lowest point and then showed an upward trend. After getting up in the morning, it rose rapidly, reaching the first peak at about 8:00-9:00 am and slightly higher at 5:00-6:00 p.m., which was the second peak, and then began to decline slowly. Therefore, the 24 h ambulatory blood pressure monitoring curve showed a double peak and a valley. In the traditional method of administration, the drug was administered by the method of average distribution, three time per day [19]. As the drug was not given according to the time rhythm, two adverse effects can occur. On the one hand, in some patients, the drug administration interval is too long and the blood drug concentration drops rapidly, which affects the curative effect; on the other hand, the drug accumulation is too much and causes poisoning of the drug's therapeutic effect in the human body [20].

In this study, we applied time nursing, according to the time law of circadian blood pressure changes; the patients with hypertensive intracerebral hemorrhage were given medicine three times per day at 6:00, 15:00, and 22:00; two

times per day at 6:00 and 22:00; and one time per day at 6:00. The blood pressure of hypertensive cerebral hemorrhage patients increased at 6:00, and the concentration of drugs in the blood was very low after overnight metabolism. At 6:00, the effective pharmacological actions in the body can be supplemented as soon as possible, so that the peak effect of antihypertensive drugs corresponds to the morning blood pressure peak, which is conducive to the control of morning peak blood pressure. At 15:00, the antihypertensive drug is given before the second peak of the blood pressure fluctuation, which can reduce blood pressure in time and reduce the damage to target organs after the blood pressure rises. The effective blood concentration can be maintained at night by administration at 22:00 and can reduce the incidence of complications.

And then, the drug treatment under the guidance of the hybrid feature convolution neural network was used, and the blood pressure prediction model of patients with hypertensive cerebral hemorrhage was established. Using the model to predict the blood pressure increase point of patients, targeted treatment for patients can significantly and smoothly reduce blood pressure, promote health recovery, and reduce the occurrence of cerebrovascular accidents.

Early limb function training can promote the reorganization of the central nervous function, significantly improve the body motor function, reduce the degree of damage and disability, promote the recovery of nerve function, improve the quality of life, and reduce the burden of society [21]. According to the diurnal and nocturnal changes, the blood pressure peak time is generally selected as 6:00-7:00, 14:00-16:00, and 19:00-21:00. During the peak blood pressure, moderate movement and increased rest should be adopted to prevent the recurrence of cerebrovascular accident.

5. Conclusions

In summary, mastering the drug treatment under the guidance of a hybrid feature convolution neural network and establishing the blood pressure prediction model of patients with hypertensive intracerebral hemorrhage can reduce the blood pressure of patients with hypertensive intracerebral hemorrhage, promote health recovery, and reduce the occurrence of cerebrovascular accidents. It has very important practical significance to improve the survival quality of patients with hypertensive intracerebral hemorrhage, which is worthy of further clinical investigation.

Data Availability

All data analyzed during this study are available from the corresponding author upon request.

Conflicts of Interest

The authors declare that there is no conflict of interest regarding the publication of this article.

Authors' Contributions

Z.Z. and S.L. performed the study and drafted the article. Z.Z. and L.B. conducted data acquisition and data analysis and interpretation. All authors discussed the results and agreed to be accountable for all aspects of the work. All authors read and approved the final manuscript.

References

[1] X. R. Che, Y. J. Wang, and H. Y. Zheng, "Prognostic value of intracranial pressure monitoring for the management of hypertensive intracerebral hemorrhage following minimally invasive surgery," *World Journal of Emergency Medicine*, vol. 11, no. 3, pp. 169–173, 2020.

[2] S. Andalib, S. Lattanzi, M. di Napoli et al., "Blood pressure variability: a new predicting factor for clinical outcomes of intracerebral hemorrhage," *Journal of Stroke and Cerebrovascular Diseases*, vol. 29, no. 12, 2020.

[3] J. Mao, W. Jiang, G. Liu, and B. Jiang, "Serum calcium levels at admission is associated with the outcomes in patients with hypertensive intracerebral hemorrhage," *British Journal of Neurosurgery*, vol. 33, no. 2, pp. 145–148, 2019.

[4] X. H. Zhao, S. Z. Zhang, J. Feng, Z. Z. Li, and Z. L. Ma, "Efficacy of neuroendoscopic surgery versus craniotomy for supratentorial hypertensive intracerebral hemorrhage: a meta-analysis of randomized controlled trials," *Brain and Behavior: A Cognitive Neuroscience Perspective*, vol. 9, no. 12, article e01471, 2019.

[5] S. Zhang, X. Zhang, Y. Ling, and A. Li, "Predicting recurrent hypertensive intracerebral hemorrhage: derivation and validation of a risk-scoring model based on clinical characteristics," *World Neurosurgery*, vol. 127, pp. e162–e171, 2019.

[6] A. A. Divani, X. Liu, A. Petersen et al., "The magnitude of blood pressure reduction predicts poor in-hospital outcome in acute intracerebral hemorrhage," *Neurocritical Care*, vol. 33, no. 2, pp. 389–398, 2020.

[7] Y. Lecarpentier, O. Schussler, J. L. Hébert, and A. Vallée, "Molecular mechanisms underlying the circadian rhythm of blood pressure in normotensive subjects," *Current Hypertension Reports*, vol. 22, no. 7, p. 50, 2020.

[8] A. Baumann, M. Hunsberger, M. Crea-Arsenio, N. Akhtar-Danesh, and M. Alameddine, "A government policy on full-time nursing employment in Ontario, Canada: an evaluation," *Health Policy*, vol. 122, no. 2, pp. 109–114, 2018.

[9] M. Beck, H. B. Bradley, L. L. Cook, J. B. Leasca, T. Lampley, and J. Gatti-Petito, "A paradigm shift from brick and mortar: full-time nursing faculty off campus," *Nursing Education Perspectives*, vol. 39, no. 2, pp. 107–109, 2018.

[10] E. P. H. Choi, M. Ho, and R. Smith, "What can we do for part-time nursing students during the COVID-19 pandemic?," *Medical Education*, vol. 54, no. 7, pp. 667-668, 2020.

[11] S. Luo, M. Ezrokhi, N. Cominos et al., "Experimental dopaminergic neuron lesion at the area of the biological clock pacemaker, suprachiasmatic nuclei (scn) induces metabolic syndrome in rats," *Diabetology and Metabolic Syndrome*, vol. 13, no. 1, p. 11, 2021.

[12] G. Mazzoccoli, S. De Cosmo, and T. Mazza, "The biological clock: a pivotal hub in non-alcoholic fatty liver disease pathogenesis," *Frontiers in Physiology*, vol. 9, 2018.

[13] Z. Tang, G. Zhao, and T. Ouyang, "Two-phase deep learning model for short-term wind direction forecasting," *Renewable Energy*, vol. 173, no. 72, pp. 1005–1016, 2021.

[14] K. Wong, G. Fortino, and D. Abbott, "Deep learning-based cardiovascular image diagnosis: a promising challenge," *Future Generation Computer Systems*, vol. 110, 2020.

[15] S. U. Lee, T. Kim, O. K. Kwon et al., "Trends in the incidence and treatment of cerebrovascular diseases in Korea: part i. Intracranial aneurysm, intracerebral hemorrhage, and arteriovenous malformation," *Journal of Korean Neurosurgical Association*, vol. 63, no. 1, pp. 56–68, 2020.

[16] M. M. Safaee, R. A. Morshed, J. Spatz, S. Sankaran, M. S. Berger, and M. K. Aghi, "Interfacility neurosurgical transfers: an analysis of nontraumatic inpatient and emergency department transfers with implications for improvements in care," *Journal of Neurosurgery*, vol. 131, no. 1, pp. 281–289, 2018.

[17] J. W. Guan, M. J. Chen, H. Li, Y. Y. Liu, C. You, and Z. R. Wang, "Characteristics of circadian rhythm in patients with intracerebral hemorrhage before death," *Neurosciences (Riyadh)*, vol. 16, no. 4, pp. 340–346, 2011.

[18] H. Shabbir, J. Stein, D. Tong, V. Bhalla, and A. Wang, "A real-time nursing intervention reduces dysglycemia and improves best practices in noncritically ill hospitalized patients," *Journal of Hospital Medicine*, vol. 5, no. 1, pp. E15–E20, 2010.

[19] S. Lattanzi, F. Brigo, and M. Silvestrini, "Managing blood pressure in acute intracerebral hemorrhage," *Journal of Clinical Hypertension (Greenwich, Conn.)*, vol. 21, no. 9, pp. 1332–1334, 2019.

[20] A. Mrochen, M. I. Sprügel, S. T. Gerner et al., "Blood pressure and anticoagulation reversal management during off-hours in oral anticoagulation-associated intracerebral hemorrhage," *Cerebrovascular Diseases*, vol. 49, no. 2, pp. 177–184, 2020.

[21] X. S. Dong, G. F. Song, C. J. Wu, C. Y. Zou, G. T. Sun, and Z. Y. Huang, "Effectiveness of rehabilitation training combined with acupuncture on aphasia after cerebral hemorrhage," *Medicine*, vol. 98, no. 24, article e16006, 2019.

Hindawi
Computational and Mathematical Methods in Medicine
Volume 2021, Article ID 9572363, 6 pages
https://doi.org/10.1155/2021/9572363

Research Article

Analysis of Sports Knee Fractures Based on X-Ray and Computed Tomography Imaging

Bo Cui,[1] Yan Liu,[2] and Shuxiang Chen[2]

[1]*Jiangmen Polytechnic, Jiangmen Guangdong 529000, China*
[2]*Department of Orthopaedic Surgery, Jiangmen TCM Affiliated Hospital of Jinan University, Jiangmen Guangdong 529000, China*

Correspondence should be addressed to Shuxiang Chen; cbtennis@126.com

Received 6 October 2021; Revised 5 November 2021; Accepted 19 November 2021; Published 1 December 2021

Academic Editor: Kelvin Wong

Objective. To analyse the X-ray and computed tomography (CT) findings of 128 patients with sports-related knee fractures and to improve the diagnosis rate based on the existing methods of diagnosis of sports knee fractures on X-ray and CT images. *Method*. In this study, we retrospectively analyse the medical records of 128 cases of sports-related fractures in the hospital, analyse the results of X-ray examination and CT imaging of patients with sports knee fractures, and compare the results obtained by the two examination methods, while referring to MRI images performed. *Results*. CT examination of knee fractures, tibial plateau fractures, and knee joint free body results were compared with X-ray results ($P < 0.05$), while CT examination of patella fractures and X-ray results were compared. The difference was not statistically significant ($P > 0.05$). *Conclusion*. For imaging examination of knee fractures, a single ordinary X-ray or CT scan should be selected according to the specific situation of the patient. For patients with suspected unstable fractures, when the patient's informed consent and the condition are not allowed, ordinary X-ray film combined with CT examination is used to improve the accuracy of diagnosis and avoid the existence of hidden fractures, resulting in medical accidents.

1. Introduction

With the continuous improvement of the quality of life, people are very easy to fall their knees in pursuit of extreme sports. At the same time, they are industrialized. When people produce labor sports, they are very easy to be injured by mechanical facilities [1]. Therefore, in recent years sports knees the share of fractures in bone and joint trauma continues to rise, and there are currently certain loopholes in the way of examination of sports knee joints, which leads to the patient's invisible fracture site not being treated in time, causing permanent injury to the patient's fracture site and actual inspection at the fracture site. In the middle and knee fractures, due to the very complicated anatomical structure, clinical diagnosis cannot be made in time, and it is easy to cause missed diagnosis, and there is a hidden danger of medical treatment accidents [2]. At present, there are two main diagnostic techniques for diagnosing sports knee fractures, which are X-ray examination and CT imaging examination.

X-ray examination and CT imaging examination as the main means of sports knee fracture are widely used in clinical practice. Upon application, these two examination techniques have certain advantages and disadvantages [3]. The advantages of X-ray examination are as follows: good diagnostic value for displaced fractures and opaque foreign body retention and finding that the patient is changing position fractures that can only be felt at the time. The disadvantages of X-ray examination are as follows: radiation is harmful to the human body, so it is not suitable for pregnant women and other special populations. X-ray examination still has unclear tissue imaging and poor contrast and cannot identify fine structures. The advantages of CT imaging examination are as follows: high-density tissue imaging is clear, and the accuracy of measuring the distance between bone structures is high [4].

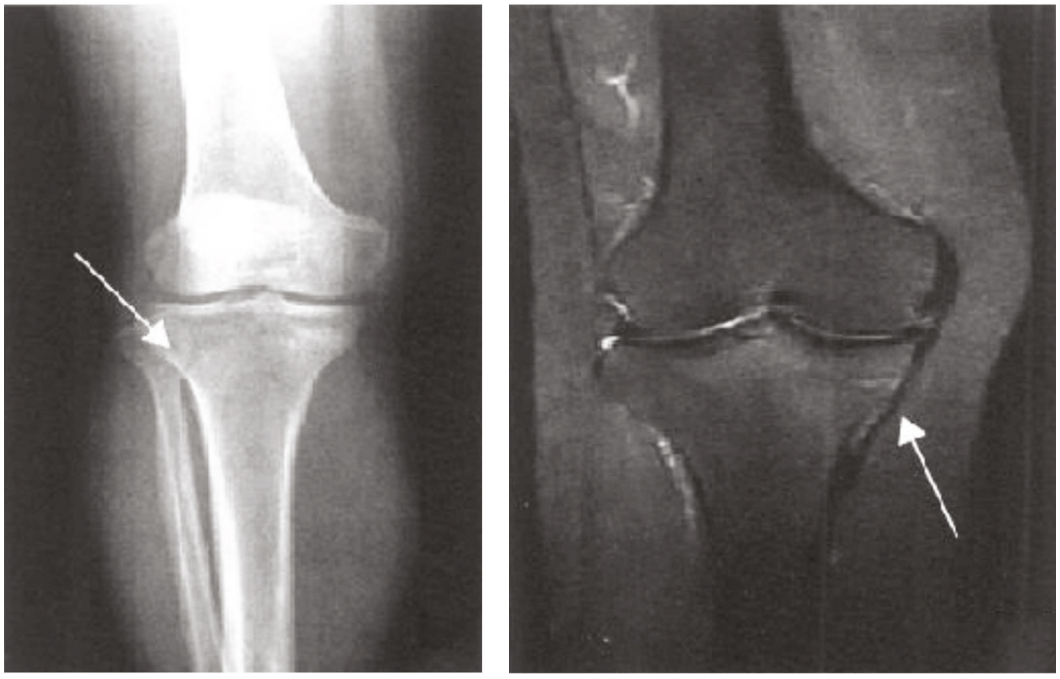

(a) (b)

Figure 1: Stress fracture associated with tibial condyle motion based on (a) DR-positive film and (b) MRI coronal radiograph.

Multirow spiral CT can carry out three-dimensional imaging, which is helpful to display tissue and organ lesions in three dimensions. The disadvantage of CT imaging examination is as follows: CT scanning is limited to the technical level of technical personnel. The interval limit of the scanning plane cannot correctly read the information of the examination site, resulting in a certain rate of missed diagnosis. CT has low definition and resolution of soft tissue imaging [5]. Due to radiation problems, pregnant women and special populations cannot use it. Because of these advantages and disadvantages, these two inspection techniques often have different detection results at different fracture sites, and there are certain inspection loopholes. The inspection results are inaccurate, which is likely to cause medical accidents during treatment and cause secondary injuries to patients.

Therefore, in order to reduce the loopholes in the examination of sports knee fractures in the future, this article retrospectively analysed the results of X-ray examination and CT examination of 128 sports knee fractures archived in the hospital medical record using χ^2 test and compared them [6]. The χ^2 test is mainly used to calculate the two attributes of two or more sets of data and the comparison between two or more phenomena. For example, to test the difference between the two sampling rates and the composition ratio, χ^2 is a kind of a simple and widely used difference significance test method, which can better compare the results of X-ray examination and CT examination of 128 cases of sports knee fractures and compare them. The following is our detailed experimental method. The implementation of multilayer spiral computed tomography (MSCT) scanning and three-dimensional reconstruction technology for patients with extremity bone and joint fractures can help to quickly and accurately diagnose the damage of extremities and joints [6–9] and provide more detailed imaging data for the clinical treatment of patients. The effective use of multislice spiral CT postprocessing technology can establish three-dimensional images and intuitively feedback the images of the patient's limbs and joint fractures.

2. Methods and Materials

2.1. General Materials. A total of 128 patients with sports knee fractures in the hospital were selected as the research object, including 76 males and 52 females, aged 14 to 69 years, with an average age of 38.64 ± 5.33 years. The time of consultation after injury was <24 h (56 cases) (43.75%), 24 h ~72 h (60 cases) (46.88%), and >72 h (12 cases) (9.38%); injured part: 48 cases (37.50%) of left knee joint injury, 50 cases of right knee joint injury cases (39.07%), and 30 cases of knee injury (23.44%); fracture causes: 69 cases of traffic injuries (53.91%), 22 cases of sports (17.09%), 20 cases of falls (15.63%), 17 cases of high-level fall injuries (13.28%); 21 cases (16.44%) with other site fractures, 13 cases (10.16%) of chest trauma, 9 cases (7.03%) of abdominal organ injuries, and 3 cases (2.34%) of craniocerebral injury; 128 patients: 54 cases (42.19%) with mid-knee pain, 24 cases (18.75%) with swelling, 19 cases (14.84%) with knee interlocking, and 11 cases (8.59%) with dysfunction; and 128 patients having positive lateral compression test: 43 cases (33.59%) and 23 cases positive for drawer test (17.97%).

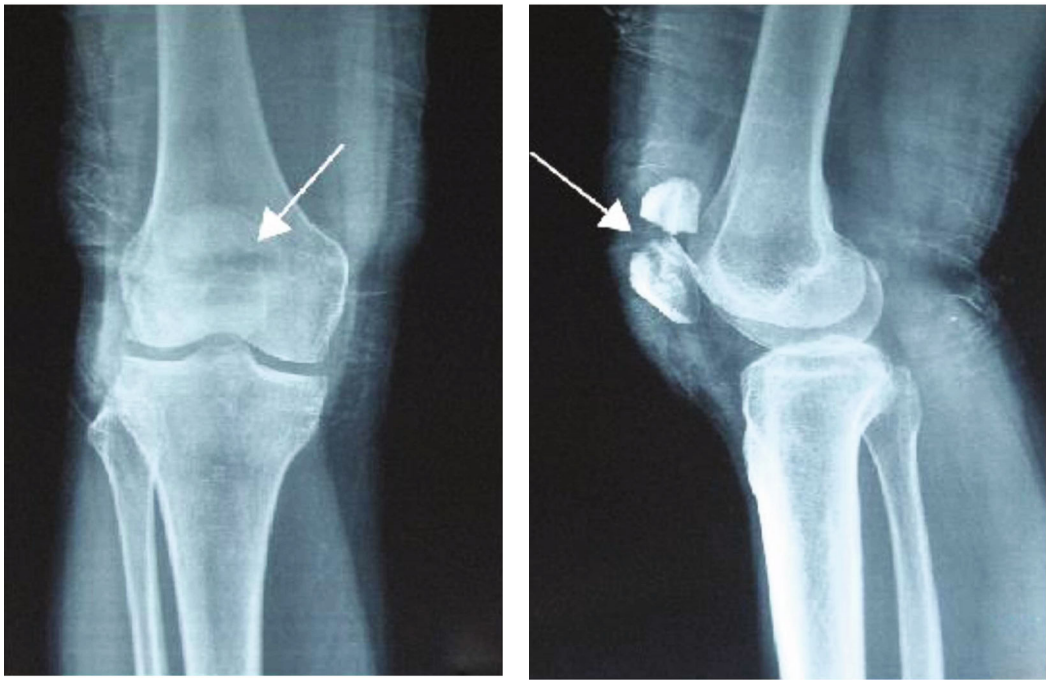

(a) (b)

Figure 2: Patient's upper tibial motion fracture based on (a) DR-positive film and (b) DR side slice.

2.2. Inspection Method. In all cases, routine and special X-ray plain film examinations are performed at the time of treatment after injury to observe the knee joint injury, whether there are suspicious fractures or hidden fractures. The CT examination was completed within 7 days after the injury, and all cases were examined using the Toshiba Activation 16TSX-031A multislice spiral CT machine [7]. The patient was lying on his back, with his feet advanced. The scanning range was determined by X-ray film. The scanning conditions were 120 kV, 200 mA, 3 mm layer thickness, 3 mm interval, and 512×512 array. When a meniscus fracture is suspected, a 1 mm continuous thin-layer scan is used. The scanning slice is as parallel as possible to the knee joint surface. The scanning range includes the proximal tibia and the distal femur [8]. Bone window was used to observe the fracture, and soft tissue window was used to observe the damage of soft tissue, ligament, and meniscus. Coronal and sagittal images were reconstructed and assisted with cutting techniques for the cases of tibial plateau collapse, tibial plateau fracture fragment displacement, meniscus injury, and dislocation of the knee joint, and each bone end making up the knee joint was observed separately [9].

Figure 3: Patient's metatarsal motion fracture.

2.3. Statistical Methods. The χ^2 test is a widely used, simple, and commonly used difference significance test method. It can be mainly used to count the two types of attributes of two or more groups of data and the comparison between two or more types of phenomena, such as testing the difference between two sample rates and composition ratios [10–13].

Basic principles and steps are as follows: the basic principle of the χ^2 test is to assume that each sample comes from the same attribute of the population; the difference between the actual data in each group is only due to sampling error; by calculating the discrete situation of the actual number and the theoretical number of each group, the total error is obtained χ^2 value, so as to determine the probability of the existence of the hypothesis, that is, the probability P. If the hypothesis is true, then, the χ^2 value will not be very large, but keep it within a certain range, the corresponding P value

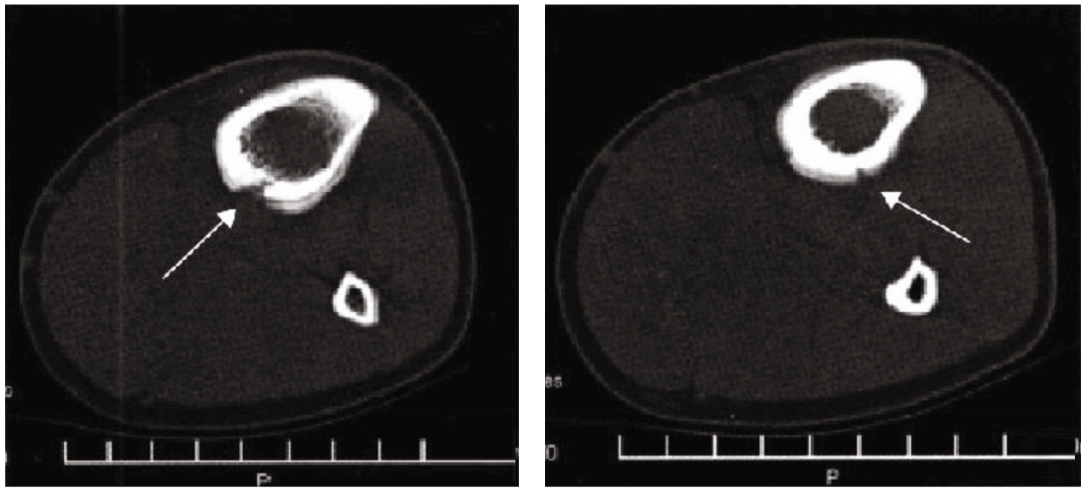

(a) (b)

Figure 4: The patient's middle and upper tibial motion fracture image diagnosis based on CT cross-section slice and (b) CT cross-section slice.

is greater than 5% ($P > 0.05$); that is, the probability of such a large difference between samples due to sampling errors alone is greater than 5%, indicating that there is no obvious difference between the samples in essence. They come from the population of the same attribute, and the assumption is affirmed. In other words, if the calculated χ^2 value is large and exceeds a certain range, the corresponding P value is less than 5% or 1%; that is, the probability of such a large difference between samples due to sampling errors is less than 5% or 1%; indicating that the difference between the groups is not due to sampling, there may be a difference between the two, they are not from the same attribute of the population, and the assumption is rejected [14].

3. Results

X-ray showed that the fracture was located on the posterior side of the medial condyle of the tibia. No abnormal findings were found on the DR examination film. Ten cases showed a localized compact line on the posterior side of the medial condyle of the tibia (Figure 1(a)). 21 cases of fractures located on the posterior side of the middle and upper tibia and the posterior side of the middle tibia had no abnormal findings on DR film; 19 cases showed bone injury reaction, 18 cases were laminar, 12 cases were mound-like, and 9 cases were marginal smooth. Five cases had uneven edges (Figure 2). If the fracture was located in the lower tibia, there were no abnormal findings in 2 cases of DR film, and 2 cases showed oblique dense lines. If the fracture is located on the outer posterior side of the lower femur, the DR film shows the reaction of the laminar bone injury on the outer posterior side, and the local bone density increases. The fractures were located in the middle and distal segment of the second metatarsal bone. In 4 cases, the bone injury reaction was seen, which was layered or mound-like, and the edges were smooth; 1 case had a thickened cortex and local hemispherical bulge, which was shaped like a button, and showed a "button sign" (Figure 3).

3.1. CT Manifestations. Among the CT-examined patients, 28 cases had no abnormal findings; 13 cases showed fracture lines, of which 8 cases were translucent lines and 5 cases were high-density lines; 15 cases showed periosteal reaction, of which 13 cases showed periosteal hyperplasia surrounding the cortical bone, a "double cortical sign"; 13 cases of local cortical thinning, blurred edges, showed a "gray cortical sign" as shown by (Figure 4(a)); 11 cases around the fracture line around the bone cortical periosteum reaction was partially interrupted, shaped like a navel, manifested as "umbilical concave sign," of which 7 cases showed double "umbilical concave sign" (Figure 4); 14 cases showed bone callus formation and increased bone marrow cavity density; 6 cases showed thickening of the cortical bone and smooth border; 9 examples show swelling of soft tissue.

Compared with the performance of reference MRI in fracture examination, patients with MRI examination all found positive findings, which were characterized by sharp line-like low-sign fracture lines on the edges of T1WI and T2WI and long T2 bone marrow enema signal; the border is unclear; STIR sequence showed a significant high signal (Figure 1(a)). 17 cases showed different degrees of soft tissue enema.

CT examination of floating knee fractures, tibial plateau fractures, and knee free body results were statistically significant compared with X-ray results ($P < 0.05$); while CT examination of patella fractures was compared with X-ray results, the difference was not statistically significant (academic significance: $P > 0.05$). The data can be depicted by Table 1.

4. Discussion

Current imaging methods for sports knee fractures include general X-ray, CT, MRI, and radiation computed tomography (ECT). In the clinical examination of sports knee fractures, X-ray positive photography is the preferred method of examination, but it can only show the structure of the knee joint from the front-back direction and the left-right direction and can only provide the general shape of the

Table 1: The results of X-ray and CT examination for the diagnosis of knee fracture.

Type of fracture	Number of cases	X-ray inspection results	CT examination results	χ^2	P
Floating knee fracture	50	42 (84.00)	49 (98.00)	5.98 < 0.05	
Type I bicondylar fracture	18	16 (88.89)	18 (100.00)		
Type II backbone fracture	20	17 (85.00)	20 (100.00)		
Type III is mixed	12	9 (75.00)	11 (91.67)		
Tibial plateau fracture	68	56 (82.35)	68 (100.00)	13.16 < 0.01	
Simple tibial lateral epicondyle split fracture	10	7 (70.00)	10 (100.00)		
Lateral epicondylar split fracture combined with platform Collapse fracture	8	4 (50.00)	8 (100.00)		
Simple platform central collapse fracture	7	4 (57.14)	7 (100.00)		
Medial platform fracture	12	10 (83.33)	12 (100.00)		
Fracture of medial and lateral epicondyle of tibia	13	13 (100.00)	13 (100.00)		
Tibial plateau fracture accompanied by tibia Fracture of metaphysis or diaphysis	18	18 (100.00)	18 (100.00)		
Patella fracture	7	5 (71.43)	7 (100.00)	1.86 > 0.05	
Patellar transverse fracture	2	2 (100.00)	2 (100.00)		
Comminuted patellar fracture	3	3 (100.00)	3 (100.00)		
Longitudinal patella fracture	1	0 (0.00)	1 (100.00)		
Avulsion fracture of small patella	1	0 (0.00)	1 (100.00)		
Knee free body	3	0 (0.00)	3 (100.00)	9.00 < 0.01	

bone. Online examinations are usually negative. Usually, it takes 2 to 3 weeks from the patient's symptoms to the positive signs of plain X-ray film [15].

Understanding the mechanical structures of the bones via medical imaging can allow us to comprehend the involved structural mechanics and help to understand fractures. For occult trabecular fractures and occult fractures, it can be seen that the local bone density exhibits uneven imaging characteristics. Because the front and back bones or left and right bones on the X-ray film overlap, it is impossible to clearly show the state of small fracture line tearing, traveling, or displaced bone fragments, and at the same time, it is impossible to show bone contusion, meniscus, and ligament damage. It is easy to miss the diagnosis.

Clinical diagnosis cannot provide accurate information. CT examination can obtain a clearer tomographic image, which is a more advanced examination method, which can accurately display the existence of avulsion fracture and its avulsion site, solve the problem of overlapping images, and display the fracture line more clearly [16]. There are changes in walking, location, type, degree of displacement, range, and surrounding soft tissue; however, its disadvantage is that it shows some concave lesions in the direction of the long axis, and it is impossible to analyse the changes of the fracture as a whole. The results showed that the detection rate of 128 cases of knee fractures by X-ray examination was 84.37%, which was 99.22% lower than the detection rate of CT examination, suggesting that CT examination has higher accuracy in diagnosis of sports knee fracture. CT three-dimensional reconstruction technology can better observe the internal condition of the patient's joints and avoid the limitations of plain X-ray diagnosis.

The results showed that patients with knee fractures could not be diagnosed only by X-ray examination, which could not fully reflect the actual situation of sports knee injury, and the examination results could only be used as a diagnostic reference. Therefore, after X-ray examination of patients in the clinic, CT and 3D reconstruction techniques should be used to improve the accuracy of diagnosis and avoid misdiagnosis and misdiagnosis of X-ray examination of patients. The three-dimensional effects of SSD and VRT are obvious [14–16]. Because SSD adopts threshold imaging, it is suitable for the display of the surface morphology of the skeletal system. It has a strong spatial three-dimensional effect and a clear surface anatomy relationship, which is conducive to the positioning of the fracture and the extent of the fracture line. The performance is obviously affected by the segmentation threshold in image processing, so the internal structure of the object cannot be displayed, and the density information of the object [17] cannot be provided. Orthopedic imaging can use deep learning for diagnosis [18].

5. Conclusion

In summary, in order to improve the diagnostic accuracy of sports knee fractures, when patients undergo X-ray or CT imaging tests, patients should be encouraged to undergo plain X-ray examinations, and CT examinations should be considered according to the patient's condition. For patients with suspected unstable fractures, if the patient's permission

is given and the patient's condition is informed, ordinary X-ray film combined with CT examination can be used to improve the accuracy of diagnosis, avoid hidden fractures, and cause harm to the patient's body, including psychology, which can ensure the accuracy of the test to the greatest extent and the effectiveness of the later treatment.

Data Availability

The image data used to support the findings of this study have been deposited in the I Do Imaging (IDI) dataset (https://idoimaging.com/home).

Conflicts of Interest

The authors declare that they have no conflicts of interest.

Authors' Contributions

Bo Cui and Yan Liu contributed equally to the work and should be considered co-first authors.

Acknowledgments

The authors thank the patient information provided by the Department of Orthopaedics, Affiliated to Jiangmen Traditional Chinese Medicine Hospital of Jinan University for its support.

References

[1] S. Xiao, S. Liu, M. Song, N. Ang, and H. Zhang, "Coupling rub-impact dynamics of double translational joints with subsidence for time-varying load in a planar mechanical system," *Multibody System Dynamics*, vol. 48, no. 4, pp. 451–486, 2020.

[2] S. Xiao, S. Liu, H. Wang, Y. Lin, M. Song, and H. Zhang, "Nonlinear dynamics of coupling rub-impact of double translational joints with subsidence considering the flexibility of piston rod," *Nonlinear Dynamics*, vol. 100, no. 2, pp. 1203–1229, 2020.

[3] L. Sharma, J. Song, D. T. Felson, S. Cahue, E. Shamiyeh, and D. D. Dunlop, "The role of knee alignment in disease progression and functional decline in knee osteoarthritis," *Journal of the American Medical Association*, vol. 286, no. 2, pp. 188–195, 2001.

[4] S. Mani, M. S. Kirkpatrick, A. Saranathan, L. G. Smith, A. J. Cosgarea, and J. J. Elias, "Tibial tuberosity osteotomy for patellofemoral realignment alters tibiofemoral kinematics," *American Journal of Sports Medicine*, vol. 39, no. 5, pp. 1024–1031, 2011.

[5] J. Laprade and E. Culham, "Radiographic measures in subjects who are asymptomatic and subjects with patellofemoral pain syndrome," *Clinical Orthopaedics and Related Research*, vol. 414, pp. 172–182, 2003.

[6] S. Scharf, "SPECT/CT imaging in general orthopedic practice," *Seminars in Nuclear Medicine*, vol. 39, no. 5, pp. 293–307, 2009.

[7] B. W. Lim, R. S. Hinman, T. V. Wrigley, L. Sharma, and K. L. Bennell, "Does knee malalignment mediate the effects of quadriceps strengthening on knee adduction moment, pain, and function in medial knee osteoarthritis? A randomized controlled trial," *Arthritis & Rheumatology*, vol. 59, no. 7, pp. 943–951, 2008.

[8] A. V. Specogna, T. B. Birmingham, M. A. Hunt et al., "Radiographic measures of knee alignment in patients with varus gonarthrosis," *American Journal of Sports Medicine*, vol. 35, no. 1, pp. 65–70, 2007.

[9] V. B. Kraus, G. McDaniel, T. W. Worrell et al., "Association of bone scintigraphic abnormalities with knee malalignment and pain," *Annals of the Rheumatic Diseases*, vol. 68, no. 11, pp. 1673–1679, 2009.

[10] T. Shiomi, T. Nishii, H. Tanaka et al., "Loading and knee alignment have significant influence on cartilage MRI T2 in porcine knee joints," *Osteoarthritis and Cartilage*, vol. 18, no. 7, pp. 902–908, 2010.

[11] L. Huang, L. Yin, B. Liu, and Y. Yang, "Design and error evaluation of planar 2DOF remote center of motion mechanisms with cable transmissions," *Journal of Mechanical Design*, vol. 143, no. 1, 2021.

[12] H. Bo, Z. Changjiang, W. Hongbing, and Y. Lairong, "Prediction and validation of dynamic characteristics of a valve train system with flexible components and gyroscopic effect," *Mechanism and Machine Theory*, vol. 157, article 104222, 2021.

[13] X. Xu, C. Zhang, F. Musharavati, T. A. Sebaey, and A. Khan, "Dispersion of waves characteristics of laminated composite nanoplate," *Steel and Composite Structures*, vol. 40, no. 3, pp. 355–367, 2021.

[14] S. Odenbring, A. M. Berggren, and L. Peil, "Roentgenographic assessment of the hip-knee-ankle axis in medial gonarthrosis," *Clinical Orthopaedics and Related Research*, no. 289, pp. 195-196, 1993.

[15] I. F. Petersson, T. Boegard, T. Saxne, A. J. Silman, and B. Svensson, "Radiographic osteoarthritis of the knee classified by the Ahlback and Kellgren & Lawrence systems for the tibiofemoral joint in people aged 35-54 years with chronic knee pain," *Annals of the Rheumatic Diseases*, vol. 56, no. 8, pp. 493–496, 1997.

[16] M. T. Hannan, D. T. Felson, and T. Pincus, "Analysis of the discordance between radiographic changes and knee pain in osteoarthritis of the knee," *The Journal of Rheumatology*, vol. 27, pp. 1513–1517, 2000.

[17] X. Xu, C. Zhang, H. A. Derazkola, M. Demiral, A. M. Zain, and A. Khan, "UFSW tool pin profile effects on properties of aluminium-steel joint," *Vacuum*, vol. 192, no. 8, article 110460, 2021.

[18] Z. Tang, G. Zhao, and T. Ouyang, "Two-phase deep learning model for short-term wind direction forecasting," *Renewable Energy*, vol. 173, pp. 1005–1016, 2021.

Hindawi
Computational and Mathematical Methods in Medicine
Volume 2021, Article ID 7748350, 9 pages
https://doi.org/10.1155/2021/7748350

Research Article

Effective Face Detector Based on YOLOv5 and Superresolution Reconstruction

Qingqing Xu, Zhiyu Zhu, Huilin Ge, Zheqing Zhang, and Xu Zang

School of Electronic Information, Jiangsu University of Science and Technology, Zhenjiang 212003, China

Correspondence should be addressed to Zhiyu Zhu; zzydzz@163.com

Received 3 September 2021; Revised 18 September 2021; Accepted 28 September 2021; Published 16 November 2021

Academic Editor: Kelvin Wong

The application of face detection and recognition technology in security monitoring systems has made a huge contribution to public security. Face detection is an essential first step in many face analysis systems. In complex scenes, the accuracy of face detection would be limited because of the missing and false detection of small faces, due to image quality, face scale, light, and other factors. In this paper, a two-level face detection model called SR-YOLOv5 is proposed to address some problems of dense small faces in actual scenarios. The research first optimized the backbone and loss function of YOLOv5, which is aimed at achieving better performance in terms of mean average precision (mAP) and speed. Then, to improve face detection in blurred scenes or low-resolution situations, we integrated image superresolution technology on the detection head. In addition, some representative deep-learning algorithm based on face detection is discussed by grouping them into a few major categories, and the popular face detection benchmarks are enumerated in detail. Finally, the wider face dataset is used to train and test the SR-YOLOv5 model. Compared with multitask convolutional neural network (MTCNN), Contextual Multi-Scale Region-based CNN (CMS-RCNN), Finding Tiny Faces (HR), Single Shot Scale-invariant Face Detector (S3FD), and TinaFace algorithms, it is verified that the proposed model has higher detection precision, which is 0.7%, 0.6%, and 2.9% higher than the top one. SR-YOLOv5 can effectively use face information to accurately detect hard-to-detect face targets in complex scenes.

1. Introduction

Face detection is indispensable for many visual tasks and has been widely used in various practical applications, such as intelligent surveillance for smart cities, face unlocking in smartphones, and beauty filters. However, face detection still has many challenges due to the interference of shooting angle, background noise, image quality, face scale, and other factors. In practical scenarios, the missing detection problem of small-scale faces results in poor performance of former face detectors. Thus, many scholars have launched researches on blurring small-size human faces.

Over the past decades, convolutional neural networks (CNNs) have been certified to be useful models for processing a wide range of visual tasks, and we have witnessed the rapid development of general object detectors. The commonly used target detection framework is divided into two branches [1], two-stage detectors and one-stage detectors. Typical algorithms of two-stage detectors include faster R-CNN [2], PANet [3], SPPNet [4], and Mask R-CNN [5]. The second is one-stage detectors, derived from SSD [6], YOLOv1 to YOLOv5 [7–11], and RetinaNet [12]. The former has higher detection accuracy, but its detection speed is slower, while the latter improves the detection speed and maintains performance. At the same time, the design of face detector gain has achieved the state-of-the-art (SOTA) architecture of general object detectors.

We consider face detector as a special task of general objector detection. General target detection is aimed at multiple categories, while face detection is a dichotomous problem that only detects the face category. In this paper, we design a face detector based on YOLOv5 [11] which has been verified for its superior performance in general target detection tasks. To resolve the challenge of multiscale, small faces, low-light, and dense scenes, we optimized the model with some practical tricks. We also use superresolution reconstruction technology [13] for processing false detection of fuzzy small-scale faces, contributing to richer

texture information and improves the authenticity of visual perception. The algorithm proposed in the paper is called SR-YOLOv5, which guarantees the detection speed while improving the detection accuracy of small targets.

2. Related Work

In this section, we introduce the related work from three following parts. First, we review recent progress on face detection in low-resolution conditions. Second, we give an overall description of the YOLO series. Third, we describe the principle of the SR network.

2.1. Face Detection. Face detection has received much attention due to its wide practical applications [14]. Before deep convolutional neural network (deep CNN) was widely used, hand-made features were a very important part of face detectors. Researchers proposed many robust hand-made features [15], such as HAAR [16], HOG [17], LBP [18], SIFT [19], DPM [20], and ACF [21]. However, the performance of these feature extractors has been far surpassed by deep CNN. In recent years, numerous models have emerged, and deep CNN has shown excellent performance in general target detection tasks. The target detection task is modeled as two problems of classification and regression of target candidate regions. There are many object detection networks including RCNN family [2, 5, 15, 22], SSD [6], YOLO series [7–11], FPN [23], MMDetection [24], EfficientDet [25], transformer (DETR) [26], and Centernet [22].

From the multiscale, small face, low light, dense scene, and other challenges encountered in face detection, face detection is the same as general target detection. Thus, face detection networks can learn from general object detection networks. There are also some specific problems containing scale, pose, occlusion, expression, and makeup. Many researchers developed methods to deal with the above problems, such as Cascade CNN, MTCNN, HR, and SSH. They also test their algorithm on public datasets [27].

2.2. SR. In the actual application scene, some images will be fuzzy and of low quality because of the limitation of environment and shooting technology. Such images have poor performance in the region of interest (RoI). Therefore, the researchers proposed the image superresolution reconstruction technology to enrich the detailed information of low-resolution images and improve the expression ability of images. Currently, superresolution reconstruction technology [13] based on deep learning is widely used. Among them, the superresolution image generated by the Generative Adversarial Networks (GAN) [12] has a better visual effect, which is called SRGAN. By training a generation function, SRGAN converts the input low-resolution image into the corresponding superresolution image [28]. Based on SRResNet, SRGAN uses perceptual loss and adversarial loss to make the generated images closer to the target images.

The SRGAN network is composed of a generator and a discriminator, and its network model is shown as in Figure 1 [13] below. The core of the generator network is multiple residual blocks, each residual block containing two 3×3 convolutional layers. After the convolutional layer is a batch normalization layer, PReLU is used as the activation function [29]. The discriminant network uses a network structure similar to VGG-19, but without maximum pooling. The discriminant network contains eight convolutional layers. As the number of network layers increases, the number of features increases, and the size of features decreases. Leaky ReLU acts as an activation function. Finally, the network uses two full convolution layers and a sigmoid activation function to capture the potentiality of the learned real sample, which is used to determine whether the image comes from the high-resolution image of the real sample or the superresolution image of the fake sample.

2.3. YOLO. In the past five years, the YOLO algorithm has been transformed into the fifth version with many innovative ideas from the object detection community. The first three versions including YOLOv1 [7], YOLOv2 [8], and YOLOv3 [9] were all proposed by the author of the original YOLO algorithm, and YOLOv3 [9] is recognized as a milestone with big improvements in performance and speed. We can find multiscale features (FPN) [23], a better backbone network (Darknet53), and replacing the soft-max loss with the binary cross-entropy loss in this algorithm.

YOLOv4 [10] was released by a different research team in early 2020. The team explored a lot of options in almost all aspects of the YOLOv3 [9] algorithm, including the backbone, and what they call bags of freebies and bags of specials. One month later, the YOLOv5 [11] was released by another different research team which significantly reduced size, increased in speed [10], and had a full implementation in Python (PyTorch). It is welcome by the object detection community until now.

YOLOv5 using CSPDarknet as a network of feature extraction, target information is extracted from the input image. The combination of CSP and Darknet formed the CSPDarknet. Figure 2 shows the structure of CSPDarknet. For the input tensor, CSP divides it into two parts in the channel, one part is convoluted once, the other part is convolution-residuals multiple times. The tensor is obtained by multiple convolution-residual operations, and the tensor obtained by one convolution of the previous part is spliced in channel dimensions. CSP makes the output graph retain more network gradient information and maintains the performance of the network while reducing the computational effort.

In the operation, the features of the previous stage can be used as the input of the next stage for up-sampling or down-sampling, and at the same time, the CONCAT with the feature map of the same size in the main part. This pyramid structure makes the high-level feature map integrate the accurate position information of the low level [30] and improves the accuracy of regression.

During detection, the input tensor is divided into $S \times S$ grids, and any one of the grids will be responsible for detecting the target if the center point of the target is located in it. For each grid, there will be B anchors. Specifically, for each anchor frame, $(5 + C)$ values are predicted, with the first 5 values used to regress anchor's center point position, the size of the anchor frame, then to determine whether there is a

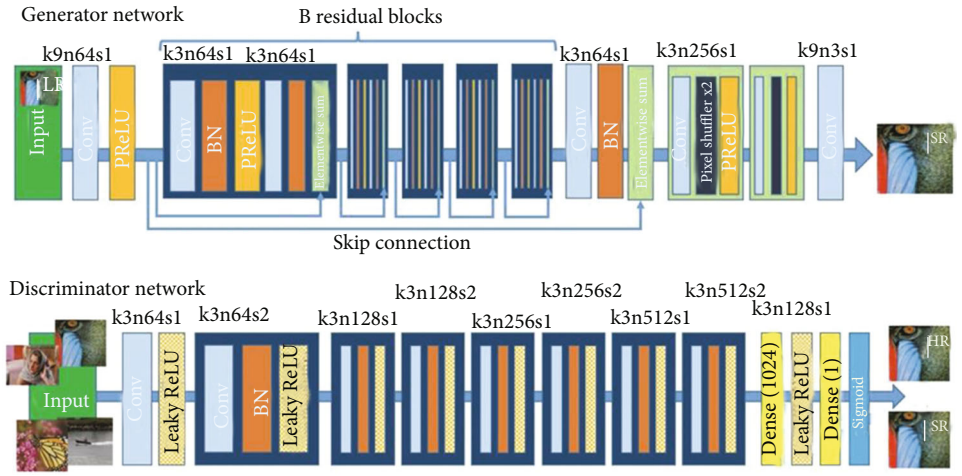

Figure 1: SRGAN network model.

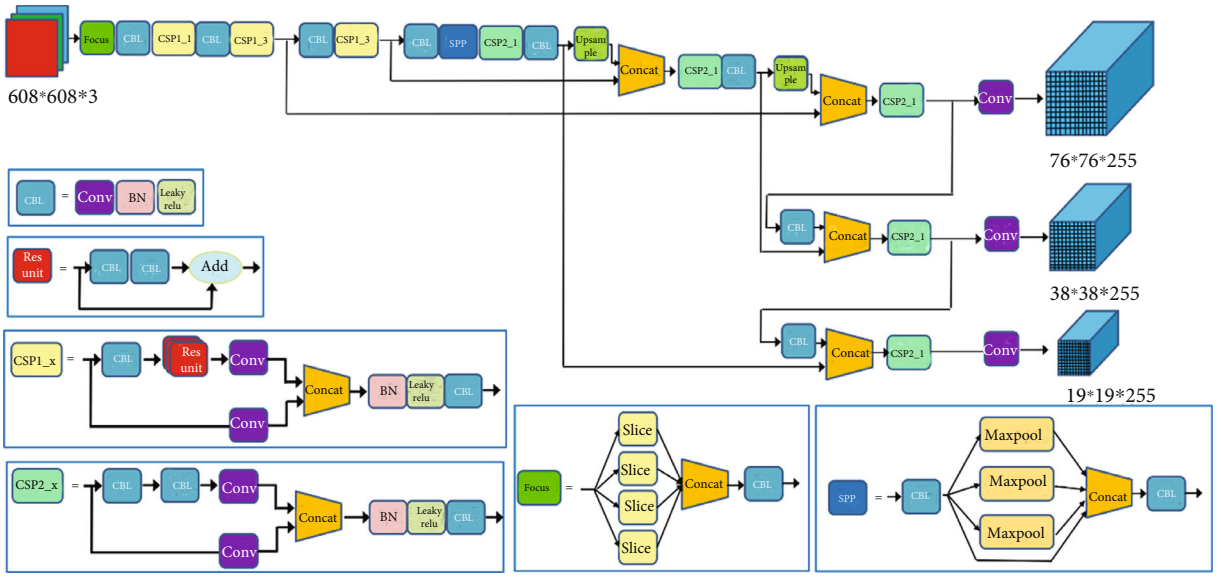

Figure 2: Structures of YOLOv5s.

target. C is the total number of target categories. If the center of the target is in this grid, then the target will be acquired and judge whether it is a human face. The position of the regression box of the target can be obtained by the following formula:

$$C_i^j = P_{i,j} * \mathrm{IOU}_{\mathrm{pred}}^{\mathrm{truth}}. \tag{1}$$

In the above parameters, i and j represent the jth regression box of the ith grid, C_i^j represents the confidence score of the jth bounding box of the ith grid. $P_{i,j}$ represents whether there is a target, if the target is in the jth box, the value of $P_{i,j} = 1$; otherwise, $P_{i,j} = 0$. The $\mathrm{IOU}_{\mathrm{pred}}^{\mathrm{truth}}$ is a widely used parameter that represents the intersection over union between the predicted box and ground truth box [31]. The higher the IOU score, the more accurate the position of the predicted box.

2.4. Loss Function of YOLOv5s. The loss function can be expressed as follows:

$$\mathrm{loss} = l_{\mathrm{box}} + l_{\mathrm{cls}} + l_{\mathrm{obj}}, \tag{2}$$

where l_{box}, l_{cls}, and l_{obj} are bounding box regression loss function, classification loss function, and confidence loss function, respectively.

The bounding box regression loss function is defined as

$$l_{\mathrm{box}} = \lambda_{\mathrm{coord}} \sum_{i=0}^{S^2} \sum_{j=0}^{B} I_{i,j}^{\mathrm{ojb}} bj(2 - w_i \times h_i) \left[\left(x_i - x\wedge_i^j\right)^2 + \left(y_i - y\wedge_i^j\right)^2 + \left(w_i - w\wedge_i^j\right)^2 + \left(h_i - h\wedge_i^j\right)^2 \right]. \tag{3}$$

The classification loss function is defined as

$$l_{\text{cls}} = \lambda_{\text{class}} \sum_{i=0}^{S^2} \sum_{j=0}^{B} I_{i,j}^{\text{obj}} \sum_{C \in \text{classes}} p_i(c) \log\left(\widehat{p}_l(c)\right). \tag{4}$$

The confidence loss function is defined as

$$l_{\text{obj}} = \lambda_{\text{noobj}} \sum_{i=0}^{S^2} \sum_{j=0}^{B} I_{i,j}^{\text{noobj}} (c_i - c\wedge_l)^2 + \lambda_{\text{obj}} \sum_{i=0}^{s^2} \sum_{j=0}^{B} I_{i,j}^{\text{obj}} (c_i - c\wedge_l)^2, \tag{5}$$

where λ_{coord} is the position loss coefficient, λ_{class} is the category loss coefficient, $\hat{x}$, $\hat{y}$is the true central coordinate of the target, and $\hat{w}$, $\hat{h}$ is the width and height of the target.

If the anchor box at (i, j) contains targets, then the value $I_{i,j}^{\text{obj}}$ is 1; otherwise, the value is 0. $p_i(c)$ represents the category probability of the target, and $\widehat{p}_l(c)$ is the true value of the category. The length of the two is equal to the total number of categories C.

3. Method

This paper focuses on improving the detection accuracy of small faces in surveillance images. Because of the comparison of the four versions of YOLOv5 including YOLOv5m, YOLOv5l, YOLOv5x, and YOLOv5s, the YOLOv5s model is smaller and easier to deploy quickly. Therefore, our research is based on the YOLOv5s model. We optimize the backbone, then integrate image superresolution technology on the head and improve the loss function to ensure efficient detection speed.

3.1. SR-YOLOv5

3.1.1. Adaptive Anchor. The calculation of adaptive anchor is added in YOLOv5s. Before each training, the K-means algorithm is used to cluster the ground truth of all samples in the training set and to find out the optimal group of anchor point frames in the high complexity and high recall rate. The results of anchor boxes clustered by the algorithm are shown in Table 1.

3.1.2. Network Architecture

(1) Backbone. The overall architecture of improved YOLOv5s is depicted in Figure 3 which consists of the backbone, detection neck, and detection head. Firstly, a newly designed backbone named CSPNet is used. We change it with a new block called CBS consists of Conv layer, BN layer, and a SILU [32]. Secondly, a stem block is used to replace the focus layer in YOLOv5s. Thirdly, a C3 block is used to replace the original CSP block with two halves. One is passed through a CBS block, some bottleneck blocks, and a Conv layer, while another consists of a Conv layer. After the two paths with a CONCAT and a CBS block followed, we also change the SPP block [4] to improve the face detection performance. In this block, the size of the three kernels is modified to smaller kernels.

Table 1: Results of anchor boxes of the training set.

Feature map	Size	Anchor
Predict one	13×13	(43, 59) (76, 89) (178, 234)
Predict two	26×26	(30, 36) (22, 26) (15, 18)
Predict three	52×52	(10, 12) (7, 9) (5, 6)

(2) Detection Neck. The structure of the detection neck is also shown in Figure 3 which consists of a normal feature pyramid network (FPN) [23] and path aggregation network (PAN) [3]. However, we modify the details of some modules, such as the CS block and the CBS block we proposed.

(3) Detection Head. Through feature pyramid structure and path aggregation [33] network, the front segment of the network realizes the full fusion of low-level features and high-level features to obtain rich feature maps, which can detect the most high-resolution face samples. However, for low-resolution images, feature fusion cannot enhance the original information of the image, and through layers of iteration, the prior information of small faces is still lacking. To enhance the detection rate of small faces in low-resolution images, SR is fused in the detection head part of the network. For the grid to be determined, the region information is input into SRGAN to carry out superresolution reconstruction and face detection again through its coordinate information. Finally, the output of the two-stage face detector is integrated and output.

3.2. Loss Function.

IOU is a frequently used index in target detection. In most anchor-based [34] methods, it is used not only to judge the positive and negative sample but also to assess the distance between the location of the predicted box and the ground truth. The paper proposes that a regression positioning loss [35] should be considered: overlapping area, center point distance, and aspect ratio, which have aroused wide concern. At present, more and more researchers propose better performance algorithms, such as IOU, GIOU, DIOU, and CIOU. In this paper, we propose to replace GIOU in YOLOv5s with CIOU and nonmaximal suppression (NMS).

Our bounding box regression loss function is defined as

$$l'_{\text{box}} = 1 - \text{IOU} + \frac{\rho^2\left(b, \widehat{b}\right)}{c^2} + \frac{16}{\pi^4} \frac{\left(\arctan\left(w\wedge/h\wedge\right) - \arctan\left(w/h\right)\right)^4}{1 - \text{IOU} + \left(4/\pi^2\right)\left(\arctan\left(w\wedge/h\wedge\right) - \arctan\left(w/h\right)\right)^2}, \tag{6}$$

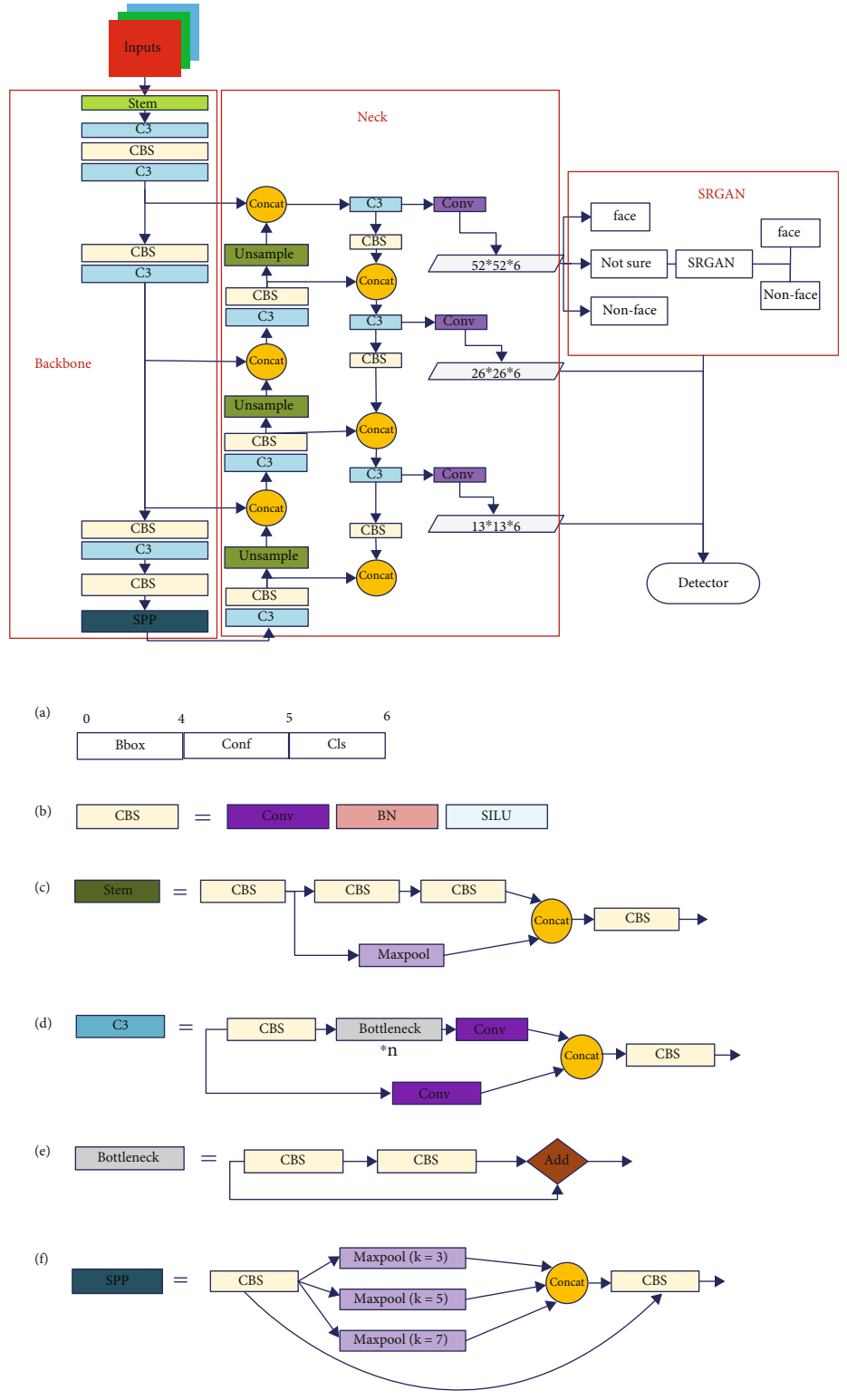

Figure 3: The architecture of improved SR-YOLOv5.

where b, b' represents the center point of the box, ρ represents the Euclidean distance, c represents the diagonal distance of the minimum enclosing rectangle, and $\widehat{w}$, $\widehat{h}$ is the width and height of the target.

In surveillance video images [36], face targets are not only numerous but also stacked, which leads to more than one target in each grid. However, judging by a single threshold often leads to a low recall rate [37]. Therefore, through

the combination of CIOU and NMS, the candidate box in the same grid can be judged and screened several times through the cyclic structure, which can effectively avoid the problem of missed detection.

4. Experiments

4.1. Dataset and Experimental Environment Configuration. This experiment uses a face detection benchmark called wider face [27], which is recognized as the largest one among public available datasets. The details of publicly available datasets are shown in Table 2. These faces in the wider face dataset have great changes in scale, posture, and occlusion with an average of 12.2 faces per image, and there are many dense small faces. The dataset contains three parts: training set, validation set, and test set, accounting for 40%, 10%, and 50% of the sample number, respectively. This paper focuses on the detection of small faces, which will be more difficult to detect. Therefore, the verification set and test set are divided into three difficulty levels: easy, medium, and hard. There are many small-scale faces in the hard subset, most of which are 10 pixels~50 pixels. Thus, this benchmark is suitable to verify the effectiveness and performance in realistic scenes. The experimental environment configuration is shown in Table 3.

Table 2: Available datasets.

Datasets	Pictures	Faces
Wider face	32203	393703
AFW	205	473
FDDB	2845	5171
Pascal face	851	1341
IJB-A	24327	49759
MALF	5250	11931

Table 3: Experimental environment configuration.

Experimental environment	Configuration
Operating system	Linux 64
GPU	TITAN Xp
CPU	Intel(R)Core i7-3770CPU@
Deep learning framework	PyTorch

4.2. Training and Testing of SR-YOLOv5 Models

4.2.1. Training Model. The YOLOv5s code [11] is used as our basic framework, and we implement all the modifications as described above in PyTorch. We set the initial learning rate at $1E$-2, and then we go down to $1E$-5 with the decay rate of $5E$-3. We set momentum at 0.8 in the first 20 epochs. After that, the momentum is 0.937. The precision-recall (PR) curves of our SR-YOLOv5 detector are shown in Figure 4.

4.2.2. Testing Model. The detection effect of our improved algorithm on the wider face dataset is shown in Figure 5. It can be seen that this method has good robustness and high accuracy for small faces in various complex scenes. (a) The figure can detect faces with slight occlusion. (b) The figure itself has a low resolution, but the detection result shows that the detection effect is still good. (c) The figure fully shows that numerous small faces can be well detected even in a high-density crowd.

4.3. Evaluation Index. In the evaluation of the effect of face detection, there are some relevant parameters: TP (true positives) means that the face is detected, and there are faces in the actual picture; TN (true negatives) means that no face is detected, and no face exists in the actual picture; FP (false positives) means that faces are detected when there is no face in the actual image. FN (false negatives) means that no face is detected, but there are faces in the actual image. The evaluation indexes of the model in this paper include recall rate R, accuracy rate P, and F_1 score. The recall rate is used to evaluate the proportion of faces detected to the total face price in the sample. The accuracy rate is used to evaluate the proportion of the correct face detected in the total face detected, When the two are close, refer to F_1 score, and the higher the score of F_1, the better the algorithm will be.

$$P = \frac{\mathrm{TP}}{\mathrm{TP} + \mathrm{FP}}, \tag{7}$$

$$R = \frac{\mathrm{TP}}{\mathrm{TP} + \mathrm{FN}}, \tag{8}$$

$$F_1 = \frac{2 \times P \times R}{P + R}. \tag{9}$$

The trained model is verified on the validation set, and the recall rate $R = 0.96$, accuracy rate $P = 0.975$, and $F_1 = 96.75$ were obtained from Equations (6), (8), and (9). From the point of view of the score, the proposed algorithm has better performance.

4.4. Model Performance Analysis. After the fusion of SRGAN in the YOLOv5 network, the rationality and effectiveness of the fused network should be verified first. We select 1000 pictures from the test set for network model test and comparison. As shown in Table 4, compared with YOLOv3, the speed of the network after the fusion of superpartition reconstruction technology is reduced, because the network depth is increased when the new network is integrated. Compared with the HR using Resnet101 as the backbone network, the average detection accuracy of the improved network has been significantly improved, which is 2.3% higher than HR.

4.5. Comparison of Accuracy of Relevant Algorithms. To demonstrate the effectiveness of the algorithm, some excellent face detection algorithms are selected to test on the wider face dataset, and the results are analyzed. As shown in Table 5, all existing methods achieve mAP in a range of 85.1-95.6% on the easy subset, 82.0-94.3% on the medium subset, and 62.9-85.3% on the hard subset. The mean average precision of the proposed algorithm on the easy, medium, and hard validation subsets are 96.3%, 94.9%,

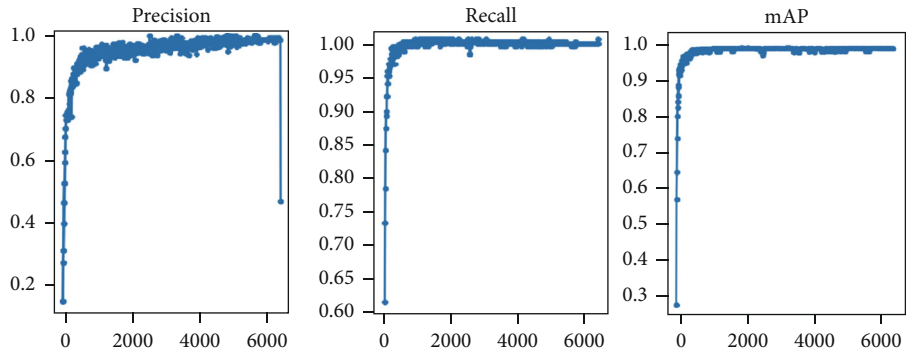

Figure 4: Precision-recall (PR) curves of our SR-YOLOv5 detector.

(a) Blocking faces

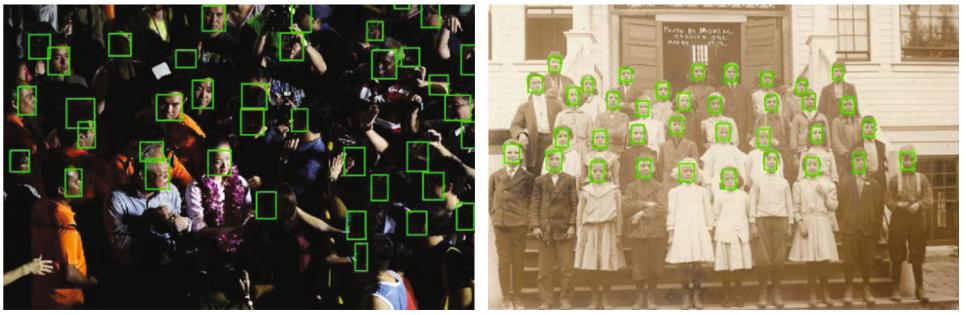

(b) Fuzzy scene

(c) Dense small faces

Figure 5: Part of the test results.

Table 4: Performance comparison using different models.

Model	Backbone	AP50	Time/ms
HR	Resnet101	57.5%	198
YOLOv3	Darknet53	57.9%	51
Ours	YOLOv5s-SRGAN	59.8%	75

and 88.2%, respectively, which is 0.7%, 0.6%, and 2.9% higher than the top one.

The SR-YOLOv5 proposed in this paper is improved on the YOLOv5s network, and the image superresolution reconstruction technology is introduced for the secondary detection of small-scale fuzzy faces, deepening the network to make facial features easier to be detected, capturing small target information, and making the network more accurate when processing complex face and nonface classification

Table 5: Comparison of mAP using different face detection algorithms.

Face detection algorithms	Easy	Medium	Hard
MTCNN	85.1%	82.0%	62.9%
CMS-RCNN	90.2%	87.4%	64.3%
HR	92.5%	91.0%	81.9%
S3FD	93.7%	92.5%	85.9%
TinaFace	95.6%	94.3%	85.3%
Ours	96.3%	94.9%	88.2%

and detection. Through the comparative experiment on the wider face dataset, it is verified that the method used in this paper has higher detection accuracy and better robustness, especially in the hard subset, it has more outstanding performance.

5. Conclusion

To improve the face detection rate of security surveillance scenes with diverse scales in dense face images, this paper proposes a small face detection algorithm suitable for complex scenes. We integrate the image superresolution reconstruction technology into the network structure of the target detection algorithm YOLOv5s. YOLOv5s has a fast detection speed, but its detection accuracy is reduced compared with other SOTA detection algorithms. SRGAN is used to improve the performance of the detection head and then improve the detection accuracy of small-scale fuzzy faces in complex scenes. In the same environment with other face detection algorithms, using the same dataset to carry out comparative experiments, the results confirm the feasibility and superiority of the proposed method.

Data Availability

The data (wider face dataset) used in this research is cited in the references.

Conflicts of Interest

We declare that there are no conflicts of interest to report regarding the present study.

Acknowledgments

This work was supported by the National Natural Science Foundation of China (No. 62006102).

References

[1] Z. Zou, Z. Shi, Y. Guo, and J. Ye, "Object detection in 20 years: a survey," 2019, https://arxiv.org/abs/1905.05055.

[2] S. Ren, K. He, R. Girshick, and J. Sun, "Faster r-cnn: towards real-time object detection with region proposal networks," *Advances in Neural Information Processing Systems*, vol. 28, pp. 91–99, 2015.

[3] S. Liu, L. Qi, H. Qin, J. Shi, and J. Jia, "Path aggregation network for instance segmentation," in *Proceedings of the IEEE conference on computer vision and pattern recognition*, pp. 8759–8768, Salt Lake City, UT, United States, 2018.

[4] K. He, X. Zhang, S. Ren, and J. Sun, "Spatial pyramid pooling in deep convolutional networks for visual recognition," *IEEE Transactions on Pattern Analysis and Machine Intelligence*, vol. 37, no. 9, pp. 1904–1916, 2015.

[5] K. He, G. Gkioxari, P. Dollár, and R. Girshick, "Mask r-cnn.," in *Proceedings of the IEEE international conference on computer vision*, pp. 2961–2969, Venice, Italy, 2017.

[6] W. Liu, D. Anguelov, D. Erhan et al., "Ssd: single shot multibox detector," in *Computer Vision – ECCV 2016*, Lecture Notes in Computer Science, Springer, 2016.

[7] J. Redmon, S. Divvala, R. Girshick, and A. Farhadi, "You only look once: unified, real-time object detection," in *Proceedings of the IEEE conference on computer vision and pattern recognition*, pp. 779–788, Las Vegas, NV, United States, 2016.

[8] J. Redmon and A. Farhadi, "YOLO9000: better, faster, stronger," in *Proceedings of the IEEE conference on computer vision and pattern recognition*, pp. 7263–7271, Honolulu, HI, United States, 2017.

[9] J. Redmon and A. Farhadi, "Yolov3: an incremental improvement," 2018, https://arxiv.org/abs/1804.02767.

[10] A. Bochkovskiy, C. Y. Wang, and H. Y. M. Liao, "Yolov4: optimal speed and accuracy of object detection," 2020, https://arxiv.org/abs/2004.10934.

[11] Ultralytics, "Yolov5," 2021, February 2021, https://github.com/ultralytics/yolov5.

[12] J. Deng, J. Guo, Y. Zhou, J. Yu, I. Kotsia, and S. Zafeiriou, "Retinaface: single-stage dense face localization in the wild," 2019, https://arxiv.org/abs/1905.00641.

[13] C. Ledig, L. Theis, F. Huszár et al., "Photo-realistic single image super-resolution using a generative adversarial network," in *Proceedings of the IEEE conference on computer vision and pattern recognition*, pp. 4681–4690, Honolulu, HI, United States, 2017.

[14] C. Xu, Z. Gao, H. Zhang, S. Li, and V. H. C. de Albuquerque, "Video salient object detection using dual-stream spatiotemporal attention," *Applied Soft Computing*, vol. 108, p. 107433, 2021.

[15] D. Qi, W. Tan, Q. Yao, and J. Liu, "YOLO5Face: why reinventing a face detector," 2021, https://arxiv.org/abs/2105.12931.

[16] R. Lienhart and J. Maydt, "An extended set of haar-like features for rapid object detection," in *Proceedings. Iinternational conference on image processing*, Rochester, NY, United States, 2002, September.

[17] N. Dalal and B. Triggs, "Histograms of oriented gradients for human detection," in *2005 IEEE computer society conference on computer vision and pattern recognition (CVPR'05)*, pp. 886–893, San Diego, CA, United States, 2005, June.

[18] T. Ahonen, A. Hadid, and M. Pietikainen, "Face description with local binary patterns: application to face recognition," *IEEE Transactions on Pattern Analysis and Machine Intelligence*, vol. 28, no. 12, pp. 2037–2041, 2006.

[19] J. Long, E. Shelhamer, and T. Darrell, "Fully convolutional networks for semantic segmentation," in *Proceedings of the IEEE conference on computer vision and pattern recognition*, pp. 3431–3440, Boston, MA, United States, 2015.

[20] L. Zheng, L. Shen, L. Tian, S. Wang, J. Wang, and Q. Tian, "Scalable person re-identification: a benchmark," in *Proceedings of the IEEE international conference on computer vision*, pp. 1116–1124, Santiago, Chile, 2015.

[21] S. Hwang, J. Park, N. Kim, Y. Choi, and I. So Kweon, "Multispectral pedestrian detection: benchmark dataset and baseline," in *Proceedings of the IEEE conference on computer vision and pattern recognition*, pp. 1037–1045, Boston, MA, United States, 2015.

[22] Z. Cai and N. Vasconcelos, "Cascade r-cnn: delving into high quality object detection," in *Proceedings of the IEEE conference on computer vision and pattern recognition*, pp. 6154–6162, Salt Lake City, UT, United States, 2018.

[23] T. Y. Lin, P. Dollár, R. Girshick, K. He, B. Hariharan, and S. Belongie, "Feature pyramid networks for object detection," in *Proceedings of the IEEE conference on computer vision and pattern recognition*, pp. 2117–2125, Honolulu, HI, United States, 2017.

[24] K. Chen, J. Wang, J. Pang et al., "MMDetection: open mmlab detection toolbox and benchmark.," 2019, https://arxiv.org/abs/1906.07155.

[25] M. Tan, R. Pang, and Q. V. Le, "Efficientdet: scalable and efficient object detection," in *Proceedings of the IEEE/CVF conference on computer vision and pattern recognition*, pp. 10781–10790, Virtual, Online, United States, 2020.

[26] N. Carion, F. Massa, G. Synnaeve, N. Usunier, A. Kirillov, and S. Zagoruyko, "End-to-end object detection with transformers," in *Computer Vision – ECCV 202*, Springer, 2020.

[27] S. Yang, P. Luo, C. C. Loy, and X. Tang, "Wider face: a face detection benchmark," in *Proceedings of the IEEE conference on computer vision and pattern recognition*, pp. 5525–5533, Las Vegas, NV, United States, 2016.

[28] C. Wang, S. Dong, X. Zhao, G. Papanastasiou, H. Zhang, and G. Yang, "SaliencyGAN: deep learning semi-supervised salient object detection in the fog of IoTC," *IEEE Transactions on Industrial Informatics*, vol. 16, no. 4, pp. 2667–2676, 2016.

[29] T. Jiang and J. Cheng, "Target recognition based on CNN with LeakyReLU and PReLU activation functions," in *2019 International Conference on Sensing, Diagnostics, Prognostics, and Control (SDPC)*, pp. 718–722, Beijing, China, 2019, August.

[30] S. Liu, K. Han, Z. Song, and M. Li, "Texture characteristic extraction of medical images based on pyramid structure wavelet transform," in *2010 International Conference on Computer Design and Applications*, pp. 342–345, Qinhuangdao, Hebei, China, 2010, June.

[31] C. Huang, Y. Zong, J. Chen, W. Liu, J. Lloret, and M. Mukherjee, "A deep segmentation network of stent Structs based on IoT for interventional cardiovascular diagnosis," *IEEE Wireless Communications*, vol. 28, no. 3, pp. 36–43, 2021.

[32] S. Elfwing, E. Uchibe, and K. Doya, "Sigmoid-weighted linear units for neural network function approximation in reinforcement learning," *Neural Networks*, vol. 107, pp. 3–11, 2018.

[33] H. Bai, J. Cheng, X. Huang, S. Liu, and C. Deng, "HCANet: a hierarchical context aggregation network for semantic segmentation of high-resolution remote sensing images," *IEEE Geoscience and Remote Sensing Letters.*, pp. 1–5, 2021.

[34] B. Yu and D. Tao, "Anchor cascade for efficient face detection," *IEEE Transactions on Image Processing*, vol. 28, no. 5, pp. 2490–2501, 2019.

[35] C. Chen, X. Yang, R. Huang et al., "Region proposal network with graph prior and IoU-balance loss for landmark detection in 3D ultrasound," in *2020 IEEE 17th International Symposium on Biomedical Imaging (ISBI)*, pp. 1–5, Iowa City, IA, USA, 2020, April.

[36] C. Ding and D. Tao, "Trunk-branch ensemble convolutional neural networks for video-based face recognition," *IEEE Transactions on Pattern Analysis and Machine Intelligence*, vol. 40, no. 4, pp. 1002–1014, 2018.

[37] Z. Tang, G. Zhao, and T. Ouyang, "Two-phase deep learning model for short-term wind direction forecasting," *Renewable Energy*, vol. 173, pp. 1005–1016, 2021.

Hindawi
Computational and Mathematical Methods in Medicine
Volume 2021, Article ID 3781028, 7 pages
https://doi.org/10.1155/2021/3781028

Research Article

Medical Image Diagnostic Value of Computed Tomography for Bladder Tumors

Lin Li,[1] Risu Na,[1] Tao Mi,[1] Hao Cheng,[1] Lili Ma,[2] and Guojun Chen[3]

[1]*Graduate School of the Affiliated Hospital of Qinghai University, Graduate School, Xining, Qinghai 810000, China*
[2]*Qinghai University, Xining, Qinghai 810000, China*
[3]*Department of Urology, Affiliated Hospital of Qinghai University, Xining, Qinghai 810000, China*

Correspondence should be addressed to Lili Ma; 625364113@qq.com and Guojun Chen; 19105109631@qhu.edu.cn

Received 21 July 2021; Revised 21 August 2021; Accepted 18 October 2021; Published 16 November 2021

Academic Editor: Kelvin Wong

Objective. To study computed tomography (CT) imaging characteristics of bladder tumors, to explore the value of CT in tumor diagnosis, and to identify the relevant factors of CT missed diagnosis so that medical staff can be more accurate in the diagnosis of bladder tumors. *Methods*. To retrospectively analyze the CT manifestations of 153 bladder tumor cases confirmed by paraffin pathology in our hospital and to study the difference between the benign and CT imaging features. CT indicators mainly include the number, location, morphology, calcification, bladder wall smoothness, CT value, degree of enhancement, and invasion of surrounding tissues and organs. Then, we retrospectively analyze 17 cases of CT missed diagnosis of bladder tumors, analyze related factors, and discuss the role of CT in the diagnosis of bladder tumors. *Results*. This study has shown that with the help of CT images, the diagnosis rate of bladder tumors has been greatly improved. Of the 153 patients studied, noninvasive urothelial carcinoma accounted for 18.95% of all benign and malignant bladder tumors, invasive urothelial carcinoma accounted for 67.93%, prostatic metastatic carcinoma and inflammatory myofibroblastoma accounted for 8.47%, pheochromocytoma accounted for 1.31%, inverted papilloma accounted for 1.31%, tubular choriocarcinoma accounted for 0.63%, and endocystitis accounted for 1.31%. In addition, the blood supply level, CT index bladder wall smoothness, and CT value are also statistically significant ($P < 0.05$). *Conclusions*. CT is of high value in the diagnosis of bladder tumors, and benign and malignant bladder tumors have CT and CT imaging features. The size of bladder tumors is related to the missed diagnosis rate of CT. The application of CT examination technology can improve the accuracy of diagnosis of bladder tumors.

1. Introduction

The bladder tumor is the most common tumor in the genitourinary system, generally more men than women [1, 2]. Bladder tumors mostly come from epithelial tissues, mainly including transitional epithelial cancer, adenocarcinoma, squamous cell carcinoma, and inverted papilloma. Nonepithelial bladder tumors mainly include inflammatory myofibroblastoma, pheochromocytoma sarcoma, hemangioma, and lymphoma. Bladder cancer is the most common bladder cancer [3–5].

Bladder tumors are the most common tumors in the urinary system, and bladder cancers are the most common lesions of bladder tumors. At present, the incidence of bladder cancer ranks 9th among common tumors worldwide, and the mortality rate ranks 13th. It accounts for about 4% of all malignant tumors in the whole body and is the 5th cause of death in men over 75 years old. The most common sites are the bladder triangle, the lateral wall, and the posterior wall, with multicentric lesions being the most common morphology. Academically, the lesions are mostly local cauliflower-like protrusions [6–9]. Therefore, early detection and early diagnosis are crucial to the treatment and prognosis of the disease.

The main causes of bladder cancer are as follows. (1) Studies have shown that long-term exposure to aromatic chemicals can cause an increase in the incidence of bladder cancer, so those chemical factory workers are a high-risk group for bladder cancer. (2) Long-term smokers are also a high-incidence group of bladder tumors, but the specific

pathogenic mechanism needs further study. (3) The bladder mucosa has been subjected to local long-term irritation, such as chronic infection and bladder stones. (4) Certain drugs and parasitic diseases have a high correlation with the occurrence of bladder cancer and have already attracted clinical attention. The most common clinical symptom of bladder cancer is painless gross hematuria throughout the process, and sometimes, it can also be manifested as microscopic hematuria. Diagnosing bladder cancer based on clinical symptoms alone has a large error because the hematuria is often not directly proportional to the tumor. Therefore, an auxiliary examination is needed to clarify the condition of the tumor. CT is a commonly used examination method [10, 11].

In the clinical diagnosis and treatment of bladder diseases, electronic computed tomography (CT) examination is an effective localization examination method. Compared with ultrasound, CT examination can better show the tissue structure around the bladder, whether there is an invasion of the surrounding tissue, the extent of invasion, and pelvic or retroperitoneal lymph node metastasis. Enhanced CT imaging can better reflect the blood supply of the lesion, and through the reconstruction of the target blood vessel image, the blood vessel structure is clearly displayed, which is of great significance to the diagnosis and treatment of the lesion. Past studies have shown that 64-slice CT examination has a sensitivity of about 85% and a specificity of about 85% for the diagnosis of bladder cancer. Thin-layer enhanced CT scanning can be used for preoperative diagnosis and staging of bladder cancer, which is of great value for the rational choice of clinical treatment and prognostic evaluation.

Nowadays, CT urography has developed rapidly and has been widely used in the clinical work of bladder tumor diagnosis and treatment. CT is a method of observing CT scan images before and after intravenous injection of the contrast agent. It is a fast, simple, noninvasive, and comprehensive urinary tract examination method. It can detect bladder lesions and describe their relationship with adjacent tissues and organs. The relationship between the discovery of lymph node metastasis outside the bladder and the distant metastasis of the tumor has now become an essential test in the diagnosis and treatment of bladder cancer.

With the development of CT instruments, the combination of some new technologies can improve the diagnosis rate of bladder tumors. Studies have shown that the low-emission CT virtual cystoscope has a sensitivity of 100% for bladder tumors larger than 0.5 cm, the bladder tumors at 0.5 cm can also achieve high sensitivity, and the average radiation absorption equivalent (6.9 mSv) is significantly less than that of conventional 16-row spiral CT. Spiral CT and its reconstruction technology can show the enhancement of the mass and the thickening of the bladder wall, which is of great value in the diagnosis of bladder cancer [12]. Studies have shown that multislice spiral enhanced CT dual-phase scanning combined with virtual endoscopic imaging is of great value for preoperative clinical staging of bladder cancer. The staging accuracy rate is 94.5%. When the tumor is limited to the bladder wall (≤T2b), the diagnosis accuracy rate is 91.2%; when the tumor invades the outer structure of the bladder wall (≥T3), the diagnosis accuracy rate is 100%. In recent years, cone-beam CT has been used to guide radiation therapy for bladder cancer, and it has opened up new fields for the application of imaging to bladder cancer.

Nowadays, CT examination has been more and more widely used in the clinic. As a commonly used imaging examination method, CT can not only observe the location, density, size, shape, and boundary of the lesion, the CT value, and the degree of enhancement when detecting bladder space-occupying lesions but also understand whether the lesion is cystic or bleeding, calcified, etc. At the same time, it can better show the structure of the surrounding bladder, whether there is an invasion of the surrounding tissue, the extent of invasion, and pelvic or retroperitoneal lymph node metastasis. It can also understand whether there are enlarged lymph nodes and abnormal changes around the bladder. By rebuilding the target blood vessel image, we can then display the vascular structure in the diagnosis of bladder cancer, tumor staging, and selection of treatment methods [13, 14].

2. Materials and Methods

2.1. Research Subjects. We select patients who underwent urinary bladder enhancement CT examination in our hospital from January 2016 to July 2020 before undergoing surgical treatment in the urology department of our hospital, and we exclude cases with no clear pathological results. Finally, 153 patients were included, including 127 males and 26 females, with a male to female ratio of 4.88 : 1. The age range is 19-92 years, with an average age of 62.44 ± 11.19 years and a median age of 63 years. All tumors were confirmed by paraffin pathology.

2.2. Research Methods

2.2.1. Equipment Selection. CT instrument: 16-layer and 64-layer LightSpeed CT scanners of GE company are used.

Contrast agent:the agent used is itopride (35% or 37%), the dose is 100 ml, the injection rate is 2-3 ml/s, and it is injected through the peripheral vein [15].

2.2.2. CT Inspection Method. The patient fasted for 3 to 5 hours before examination, the bladder was moderately filled, the supine position was taken, the scan range was from the diaphragm top to the pubic symphysis, and the breath was scanned after breathing in deeply. Scanning parameters are as follows: layer thickness 2.5~5.0 mm and layer distance 1.25~5.0 mm; CT scan was first, and then we injected iodine via the superficial elbow vein (iodine 350 mg/100 ml or iodine 370 mg/100 ml, 35% or 37%). The dose is 100 ml, and the injection rate is 2 to 3 ml/s. We took the enhanced early scan 20-40 s after injection and the enhanced late scan 40-60 s. All images are stored in this machine or uploaded to an image archiving and communication system for retrospective analysis.

In this study, we observed the number, location, shape, presence or absence of calcification, bladder wall smoothness at the junction of the lesion, and tumor invasion of

surrounding tissues and organs on CT images and recorded the CT value and degree of enhancement of the lesion.

The specific inspection categories are as follows:

(1) Number. According to the number of lesions, it is divided into single and multiple.

(2) Location. According to the growth position of the lesion in the bladder, it is divided into the anterior wall, posterior wall, and top, bottom, and side walls.

(3) Morphology. According to the shape of the lesion, it is divided into the bulge type and infiltration type.

*(4) CT Value.*We determine the maximum level of the lesion, measured with a $5\,mm^2$ circular area, using the Hounsfield unit (Hu).

(5) Bladder Wall Smoothness. According to the smoothness of the bladder wall at the junction of the lesion and the bladder, it is divided into smooth and nonsmooth.

(6) Judgment Method of Calcification. If the CT value of the plain scan exceeds 100 Hu, it is regarded as calcification.

(7) Degree of Enhancement. According to the results of the lesion enhancement scan compared with the surrounding normal bladder wall, it is divided into two categories: no significant enhancement and significant enhancement.

(8) Infiltration and Metastasis of Surrounding Tissues. According to the relationship between the bladder tumor and ureter and other adjacent tissues and lymph node metastasis, it is divided into no infiltration metastasis and infiltration metastasis.

2.2.3. Analysis Content. Two professionally trained doctors performed retrospective analysis of the images without knowing the pathological results. If there is any inconsistency between the qualitative data, the two will negotiate and record the data after reaching an agreement. According to the pathological results of paraffin, the cases of CT missed diagnosis were analyzed. In CT detection, the size, number, morphology, echo level, calcification, bladder wall continuity, and invasion of surrounding tissues and organs of the lesion were observed. We observed the size, number, morphology, presence or absence of calcification, bladder wall smoothness at the junction of the lesion, and tumor invasion of surrounding tissues and organs on CT images and recorded the CT value and degree of enhancement of the lesion.

2.3. Statistical Methods. The data in this study are statistically processed by software SPSS 20.0. Normal measurement data is expressed by $(x \pm s)$, the comparison of count data between groups is the X^2 test, and the count data is expressed by the number of cases (n (%)). The t-test was used for comparison between the two groups, with $P < 0.05$ indicating that the difference was statistically significant.

3. Results

3.1. Pathological Results and General Conditions. For the study of 153 patients, according to the paraffin pathological diagnosis, the pathological types were divided into the following: (1) 145 cases of malignant bladder tumors: 29 cases of noninvasive urothelial carcinoma, including 2 cases of carcinoma *in situ*, and noninvasive urothelial carcinoma with 1 case of focal squamous cell metaplasia and one case of noninvasive urothelial carcinoma with glandular differentiation, 104 cases of invasive urothelial carcinoma, including 1 case of invasive urothelial carcinoma with adenocarcinoma differentiation, and 12 cases of prostatic metastatic carcinoma; and (2) 8 cases of benign bladder lesions: 2 cases of pheochromocytoma, 2 cases of inverted papilloma, 1 case of tubular choriocarcinoma, 1 case of inflammatory myofibroblastoma, and 2 cases of endocystitis. The pathological results of 153 patients are summarized in Table 1.

Table 1: Pathological diagnosis results.

Pathological type	Number of cases	Percentage (%)
Noninvasive urothelial carcinoma	29	18.95
Invasive urothelial carcinoma	104	67.93
Prostatic metastatic carcinoma	12	7.84
Pheochromocytoma	2	1.31
Inverted papilloma	2	1.31
Tubular choriocarcinoma	1	0.63
Inflammatory myofibroblastoma	1	0.63
Endocystitis	2	1.31
Total	153	100

Table 2: Average age and sex distribution of patients with benign and malignant bladder lesions.

		Benign tumor ($n = 30$)	Malignant tumor ($n = 132$)	P value
Gender	Male	5	122	0.60
	Female	3	23	
Age		52.30 ± 14.56	66.14 ± 12.10	≤0.01

Among the 153 patients studied, there were 8 benign bladder tumors, with an average age of 52.30 ± 14.56 years, and 145 malignant bladder tumors, with an average age of 66.14 ± 12.10 years. The difference was statistically significant ($P < 0.01$), and the summary is shown in Table 2. The study found that the average age of patients with malignant bladder tumors is significantly greater than the average age of patients with benign bladder tumors. The gender distribution of benign and malignant tumors was not statistically significant.

3.2. CT Imaging Analysis. In order to more intuitively demonstrate the role of CT examination in the diagnosis of bladder tumors, this study selected CT examination images of multiple patients for analysis. The schematic diagram of CT examination of multiple patients and their corresponding pathological conditions are shown below. Through the four images in Figure 1, we can draw the CT image to determine the growth position of the bladder tumor and visually observe the performance of the tumor lesion.

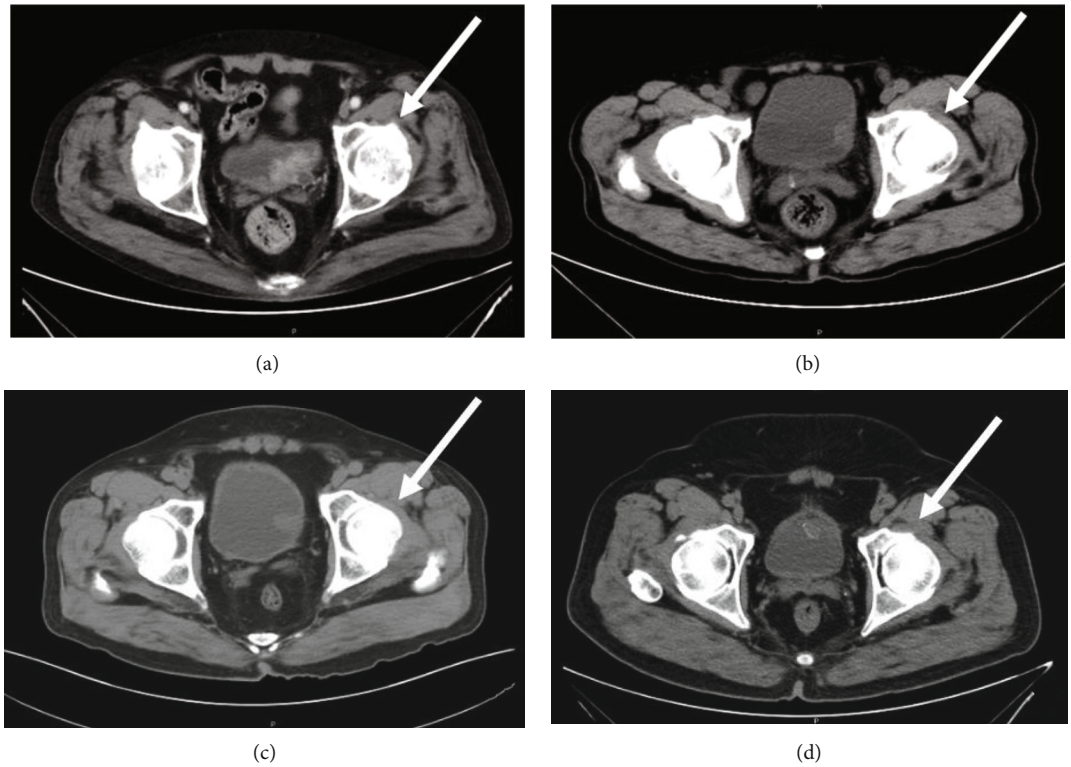

Figure 1: CT medical image of the patient depicting the following: multiple lesions in the bladder (a); round bulge-like lesions in the bladder (b); bladder wall unevenness at the junction of the lesions (c); plaque calcification in the lesions (d).

3.3. CT Diagnosis of Benign and Malignant Bladder Tumors. In this group of studies, there were 5 benign single lesions, 3 multiple lesions, 100 malignant single lesions, and 45 multiple lesions. There was no statistical difference between the two ($X^2 = 0.21$, $P > 0.05$). There is no obvious correlation between the benign and malignant tumors and their number (see Table 3).

According to the CT detection results, the location of the tumor was located. The results showed that the posterior walls of the bladder were the highest site of tumors, followed by the side of the bladder. See Table 4 for the distribution of the growth sites of good and bad lesions. Benign bladder tumors were located in the following: 1 at the anterior wall of the bladder, 3 at the posterior walls, 2 at the top, 1 at the bottom, and 1 at the lateral walls. Malignant bladder tumors were located in the following: 15 at the anterior walls, 75 at the posterior walls, 3 at the top, 2 at the bottom, and 50 at the lateral walls. The growth position of benign and malignant tumors is statistically different ($P < 0.05$). Malignant tumors occur most frequently on the posterior wall of the bladder, while benign tumors are relatively rare on the side wall of the bladder. The distribution of the growth positions of benign and malignant tumors is shown in Table 4, and the statistical diagram of tumor growth positions is shown in Figure 2.

The results showed that the average CT scan value of malignant tumors was 36.26 ± 7.97 Hu, range 17~58 Hu, and the average enhancement (arterial phase) CT value was 70.47 ± 17.57 Hu, range 29~131 Hu; for the average scan of benign tumors, the CT value was 41.11 ± 12.68 Hu, ranging from 24 to 77 Hu, and the average enhancement (arterial phase) CT value was 62.26 ± 27.36 Hu, ranging from 31 to 121 Hu. The average CT scan of benign and malignant tumors and the enhancement (arterial phase) CT value difference were statistically significant ($P = 0.02$ and $P = 0.01$). We analyzed the morphology of the lesion and the smoothness, calcification, and enhancement of the bladder wall at the junction of the lesion. After the statistical results, it was

Table 3: Single multiple cases of benign and malignant lesions.

		Benign	Malignant	Total	X^2	P value
Number	Single	5	100	105	0.21	0.65
	Multiple	3	45	48		

Table 4: Distribution of benign and malignant bladder tumor growth locations.

		Benign	Malignant	Total	X^2	P value
Position	Anterior wall	1	15	16	16.28	0.03
	Posterior wall	3	75	78		
	Top	2	3	5		
	Bottom	1	2	3		
	Side wall	1	50	51		

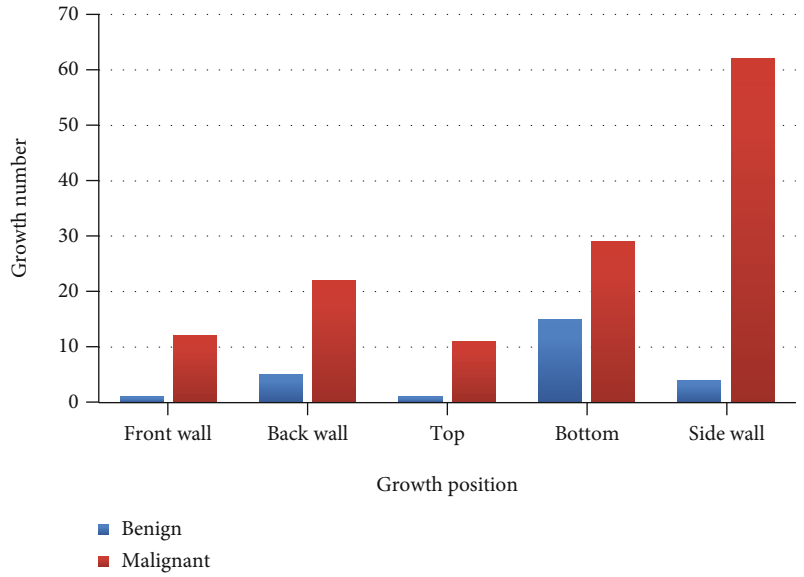

Figure 2: Statistics of the tumor growth number and position (the X axis is the growth position of the bladder tumor, and the Y axis is the growth number of the bladder tumor).

found that the smoothness of the connection between the tumor and the bladder wall and the degree of tumor enhancement between the benign and malignant groups were statistically significant ($P < 0.05$). It shows that the benign and malignant tumors are related to the above CT features. Malignant tumors are more likely to be roughened bladder walls. The enhanced CT showed that most of the malignant tumors were significantly strengthened, and the difference in the degree of enhancement of benign and malignant tumors was statistically significant. There was no statistically significant difference between the benign and malignant groups in the morphology of the tumor and the presence or absence of calcification ($P > 0.05$).

4. Discussion

CT examination can allow us to analyze the degree of enhancement of the lesion, understand whether the lesion is cystic or calcified, and make a certain diagnosis for bladder-occupying diseases. Moreover, CT has an important reference value for the selection of disease treatment methods by observing the surrounding tissue, pelvic or abdominal lymph node metastasis, and metastasis status [16].

CT is the use of an X-ray beam to scan a certain thickness of a certain part of the human body and then input it into the computer for processing to form a CT image. CT examination can observe the CT value and degree of enhancement of the lesion, understand whether the lesion is cystic or calcified, and make a certain diagnosis for bladder-occupying diseases. Moreover, CT has a high value for the diagnosis of bladder tumors by observing the surrounding tissue, pelvic or abdominal lymph node metastasis, and metastasis status [17–20].

However, CT examination also has certain deficiencies, and it is not easy to distinguish the lesions that do not cause bladder wall thickening, which may cause missed diagnosis. The accuracy of CT examination has a certain correlation with the size of bladder tumor lesions, and the detection accuracy decreases for tumor diameters less than 10 mm [12, 21, 22]. The results of this study show that CT has a missed diagnosis rate of 64.71% for bladder tumors smaller than 10 mm, which is consistent with previous literature reports [23–28]. However, the combination of some professional new technologies in clinical work now can improve the diagnosis rate of CT for microbladder tumors. Studies have shown that the low-radiation CT virtual cystoscope has a sensitivity of 100% for bladder tumors larger than 5 mm and can also achieve higher sensitivity for bladder tumors smaller than 5 mm. On the other hand, CT is most likely to miss a tumor in the top of the bladder, followed by the side wall and bottom. For tumors in the anterior wall of the bladder, the CT diagnosis rate in this study was 100% [29–31].

All cases in this study were confirmed by paraffin pathology, and the male to female ratio was 4.88 : 1, which was similar to previous reports in the literature [32, 33]. In the identification of benign and malignant bladder tumors, this study first found that the average age of patients with benign and malignant bladder tumors was statistically different. The average age of patients with malignant bladder tumors was higher than that of patients with benign bladder tumors. In addition, in this group of cases, the posterior wall of the bladder is the most frequent site of tumors, followed by the anterior and side walls of the bladder, and the bottom wall and top of the bladder have fewer tumors. The growth position of benign and malignant tumors does not also have a statistical difference ($P < 0.05$). Malignant tumors and benign tumors occur most on the posterior wall of the bladder, and both of them are relatively rare on the bottom wall of the bladder.

5. Conclusion

In summary, CT has a certain value in the differentiation of benign and malignant tumors of the bladder, but the specific imaging indicators are relatively few. The bladder tumors of different pathological types have certain self-imaging characteristics in CT imaging. So CT examination can further improve the accuracy of preoperative diagnosis of bladder tumors.

The missed diagnosis of CT examination has a certain correlation with the size of bladder tumor lesions and the gender difference, and there was no significant correlation between age, tumor number, and growth location. CT examination can play a certain role and improve the diagnosis of bladder tumors.

Data Availability

The image data used to support the findings of this study have been deposited in the International Cancer Genome Consortium (ICGC) (https://dcc.icgc.org/).

Conflicts of Interest

The authors declare no conflicts of interest.

Authors' Contributions

Lin Li and Risu Na contributed equally to the work and should be considered co-first authors. The corresponding authors Lili Ma and Guojun Chen have the same contribution to this work and should be regarded as the first communication together.

References

[1] W. Chen, R. Zheng, P. D. Baade et al., "Cancer statistics in China, 2015," *CA: A Cancer Journal for Clinicians*, vol. 66, no. 2, pp. 115–132, 2016.

[2] M. Babjuk, M. Burger, R. Zigeuner et al., "EAU guidelines on non-muscle-invasive urothelial carcinoma of the bladder: update 2013," *European Urology*, vol. 64, no. 4, pp. 639–653, 2013.

[3] L. A. McHugh and T. R. L. Griffiths, "T1G3 transitional cell carcinoma of the bladder: recurrence, progression and survival," *BJU International*, vol. 94, no. 1, p. 193, 2004.

[4] X. R. Zhang, C. Feng, W. D. Zhu et al., "Two micrometer continuous-wave thulium laser treating primary non-muscle-invasive bladder cancer: is it feasible? A randomized prospective study," *Photomedicine and Laser Surgery*, vol. 33, no. 10, pp. 517–523, 2015.

[5] K. Li, Y. Xu, M. Tan, S. Xia, Z. Xu, and D. Xu, "A retrospective comparison of thulium laser en bloc resection of bladder tumor and plasmakinetic transurethral resection of bladder tumor in primary non-muscle invasive bladder cancer," *Lasers in Medical Science*, vol. 34, no. 1, pp. 85–92, 2019.

[6] R. Migliari, A. Buffardi, and H. Ghabin, "Thulium laser endoscopic en bloc enucleation of nonmuscle-invasive bladder cancer," *Journal of Endourology*, vol. 29, no. 11, pp. 1258–1262, 2015.

[7] J. R. Gregg, B. McCormick, and L. Wang, "Short term complications from transurethral resection of bladder tumor," *The Canadian Journal of Urology*, vol. 5, pp. 46–50, 2016.

[8] M. van de Kamp, R. Meijer, F. Pos et al., "Intravesical recurrence after bladder sparing treatment of small cell carcinoma of the bladder: characteristics, treatment, and outcome," *Urologic Oncology: Seminars and Original Investigation*, vol. 36, no. 6, pp. 307.e1–307.e8, 2018.

[9] N. E. Power and J. Izawa, "Comparison of guidelines on non-muscle invasive bladder cancer (EAU, CUA, AUA, NCCN, NICE)," *Bladder Cancer*, vol. 1, pp. 78–82, 2016.

[10] M. W. Kramer, I. F. Abdelkawi, M. Wolters et al., "Current evidence for transurethral en bloc resection of non-muscle-invasive bladder cancer," *Minimally Invasive Therapy & Allied Technologies*, vol. 23, no. 4, pp. 206–213, 2014.

[11] S. Sureka, V. Agarwal, S. Agnihotri, R. Kapoor, A. Srivastava, and A. Mandhani, "Is en-bloc transurethral resection of bladder tumor for non-muscle invasive bladder carcinoma better than conventional technique in terms of recurrence and progression? A prospective study," *Indian Journal of Urology*, vol. 30, no. 2, pp. 144–149, 2014.

[12] E. Regnier-Rosencher, N. Bizet, and L. Méry, "Pyoderma gangrenosum associated with renal carcinoma," *Journal of the American Academy of Dermatology*, vol. 64, no. 6, pp. 1208–1211, 2011.

[13] H. Liu, J. Wu, S. Xue et al., "Comparison of the safety and efficacy of conventional monopolar and 2-micron laser transurethral resection in the management of multiple nonmuscle-invasive bladder cancer," *Journal of International Medical Research*, vol. 41, no. 4, pp. 984–992, 2013.

[14] M. Burger, J. W. F. Catto, G. Dalbagni et al., "Epidemiology and risk factors of urothelial bladder cancer," *European Urology*, vol. 63, no. 2, pp. 234–241, 2013.

[15] H. Engilbertsson, K. E. Aaltonen, S. Björnsson et al., "Transurethral bladder tumor resection can cause seeding of cancer cells into the bloodstream," *The Journal of Urology*, vol. 193, no. 1, pp. 53–57, 2015.

[16] D. Moher, A. Liberati, J. Tetzlaff, D. G. Altman, and The PRISMA Group, "Preferred reporting items for systematic reviews and meta-analyses: the PRISMA statement," *BMJ: British Medical Journal*, vol. 6, no. 7, pp. 40–50, 2009.

[17] M. Lodde, L. Lusuardi, S. Palermo et al., "En bloc transurethral resection of bladder tumors: use and limits," *Urology*, vol. 62, no. 6, pp. 1089–1091, 2003.

[18] L. A. Torre, F. Bray, R. L. Siegel, J. Ferlay, J. Lortet-Tieulent, and A. Jemal, "Global cancer statistics, 2012," *CA: A Cancer Journal for Clinicians*, vol. 65, no. 2, pp. 87–108, 2015.

[19] R. L. Siegel, K. D. Miller, and A. Jemal, "Cancer statistics, 2015," *CA: A Cancer Journal for Clinicians*, vol. 65, no. 1, pp. 5–29, 2015.

[20] M. Hayakawa, T. Hatano, A. Tsuji, F. Nakajima, and Y. Ogawa, "Patients with renal cysts associated with renal cell carcinoma and the clinical implications of cyst puncture: a study of 223 cases," *Urology*, vol. 47, no. 5, pp. 643–646, 1996.

[21] A. Leiba, J. D. Kark, A. Afek et al., "Adolescent obesity and paternal country of origin predict renal cell carcinoma: a cohort study of 1.1 million 16 to 19-year-old males," *The Journal of Urology*, vol. 189, no. 1, pp. 25–29, 2013.

[22] J. H. Mydlo, J. Kaplan, W. Thelmo, and R. J. Macchia, "Spontaneous renal hemorrhage associated with renal tumors," *Clinical Imaging*, vol. 21, no. 4, pp. 287–289, 1997.

[23] C. Cattrini and F. Boccardo, "Atezolizumab and bladder cancer: facing a complex disease," *The Lancet*, vol. 391, no. 10118, pp. 305-306, 2018.

[24] L. Huang, L. Yin, B. Liu, and Y. Yang, "Design and error evaluation of planar 2-DOF remote center of motion mechanisms with cable transmissions," *ASME Journal of Mechanical Design*, vol. 143, no. 1, article 013301, 2021.

[25] H. Bo, Z. Changjiang, W. Hongbing, and Y. Lairong, "Prediction and validation of dynamic characteristics of a valve train system with flexible components and gyroscopic effect," *Mechanism and Machine Theory*, vol. 157, p. 104222, 2021.

[26] A. Pan, H. Zhang, Y. Li et al., "Disulfide-crosslinked nanomicelles confer cancer-specific drug delivery and improve efficacy of paclitaxel in bladder cancer," *Nanotechnology*, vol. 27, no. 42, pp. 425103–425130, 2016.

[27] S. Sideris, F. Aoun, M. Zanaty et al., "Efficacy of weekly paclitaxel treatment as a single agent chemotherapy following first-line cisplatin treatment in urothelial bladder cancer," *Molecular and Clinical Oncology*, vol. 4, no. 6, pp. 1063–1067, 2016.

[28] Z. Tang, G. Zhao, and T. Ouyang, "Two-phase deep learning model for short-term wind direction forecasting," *Renewable Energy*, vol. 173, pp. 1005–1016, 2021.

[29] C. Sukapiriya and C. Bandidwattanawong, "Case of renal cell carcinoma associated with synchronous contralateral renal pelvic cancer and bladder cancer," *Urology Case Reports*, vol. 32, article 101267, 2020.

[30] F. Chen, N. Patel, J. Legout, and M. Caserta, "Development of complex renal cysts: a complication associated with crizotinib therapy," *Clinical Imaging*, vol. 27, pp. 289–293, 2009.

[31] S.-J. Li, S.-T. Xu, H.-P. Chen et al., "Clinical and morphologic spectrum of renal involvement in patients with HBV-associated cryoglobulinaemia," *Nephrology*, vol. 22, no. 6, pp. 449–455, 2017.

[32] E. Akintoye, I. Obaitan, A. Muthusamy, O. Akanbi, M. Olusunmade, and D. Levine, "Endoscopic submucosal dissection of gastric tumors: a systematic review and meta-analysis," *World Journal of Gastrointestinal Endoscopy*, vol. 8, no. 15, pp. 517–564, 2016.

[33] K. Tsuji, N. Yoshida, H. Nakanishi, K. Takemura, S. Yamada, and H. Doyama, "Recent traction methods for endoscopic submucosal dissection," *World Journal of Gastroenterology*, vol. 22, no. 26, pp. 5917–5922, 2016.

Hindawi
Computational and Mathematical Methods in Medicine
Volume 2021, Article ID 8437260, 7 pages
https://doi.org/10.1155/2021/8437260

Research Article

Diagnosis of Schizophrenia Based on Deep Learning Using fMRI

JinChi Zheng,[1] **XiaoLan Wei**,[2] **JinYi Wang**,[1] **HuaSong Lin**,[3] **HongRun Pan**,[4] **and YuQing Shi**[4]

[1]*Quanzhou Third Hospital, Quanzhou 362000, China*
[2]*Quanzhou First Hospital Affiliated to Fujian Medical University Neurology Department, Fujian, China*
[3]*The Second Affiliated Hospital of Fujian Medical University Neurology Department, Fujian, China*
[4]*Jinjiang Third Hospital, Quanzhou 362000, China*

Correspondence should be addressed to JinChi Zheng; 445310297@qq.com and HuaSong Lin; huasonglin980@163.com

Received 7 August 2021; Revised 12 September 2021; Accepted 4 October 2021; Published 9 November 2021

Academic Editor: Kelvin Wong

Schizophrenia is a brain disease that frequently occurs in young people. Early diagnosis and treatment can reduce family burdens and reduce social costs. There is no objective evaluation index for schizophrenia. In order to improve the classification effect of traditional classification methods on magnetic resonance data, a method of classification of functional magnetic resonance imaging data is proposed in conjunction with the convolutional neural network algorithm. We take functional magnetic resonance imaging (fMRI) data for schizophrenia as an example, to extract effective time series from preprocessed fMRI data, and perform correlation analysis on regions of interest, using transfer learning and VGG16 net, and the functional connection between schizophrenia and healthy controls is classified. Experimental results show that the classification accuracy of fMRI based on VGG16 is up to 84.3%. On the one hand, it can improve the early diagnosis of schizophrenia, and on the other hand, it can solve the classification problem of small samples and high-dimensional data and effectively improve the generalization ability of deep learning models.

1. Introduction

Schizophrenia is a serious and disabling mental illness. It is manifested as obstacles such as thinking, emotion, and behavior, the condition shows a slow and progressive development, and there are various degrees of social function defects. Symptoms include false beliefs, unclear or confused thinking, hearing voices that others cannot hear, reduced social participation and emotional expression, and lack of motivation. It not only brings great pain to the patient, but also a heavy burden to the family and society. It is about 1% of the diseased population worldwide [1]. Early diagnosis and effective intervention and treatment of schizophrenia can improve the disease. The cure rate is to prevent the prolonged course of the disease. However, the etiology and pathogenesis of schizophrenia are still unclear, and objective laboratory diagnostic indicators, as well as diagnostic criteria for equipment, are lacking. The clinical diagnosis is mainly based on medical history, combined with psychiatric symptoms and the law of progression of the disease and scales. Due to the complexity of the pathological mechanism, the early diagnosis of schizophrenia is still a challenging problem. Schizophrenia has a serious negative impact on human perception, thinking, emotion, and behavior, and it mostly occurs in people aged 15 to 34. This disease has the characteristics of early controllable, late recurrent attacks, and severely impaired cognitive function [2].

At present, the diagnosis of schizophrenia is mainly based on the patient's behavior, such as the commonly used positive and negative symptom scales for quantitative evaluation [3]. The clinical diagnosis of patients is mainly based on the doctor's experience and related scale evaluations, and there is a lack of objective diagnostic criteria. Some studies have even found that after effective treatment, the level of inflammatory factors in patients with schizophrenia will decrease significantly. IL-6 may be the most important

cytokine involved in the inflammatory response. IL-8 is a member of the chemokine family. Previous studies have found that both are positively correlated with negative symptoms of schizophrenia [4]. Other scholars have found that IL-1β gene expression level is positively correlated with PANSS general psychopathological symptoms, and serum IL-1β of patients with schizophrenia is significantly positively correlated with PANSS total score. As a multifunctional proinflammatory factor, TNF-α has been found to be negatively correlated with the total score of PANSS and the score of general psychopathological symptoms in patients with chronic schizophrenia. It is suggested that the level of the abovementioned proinflammatory factors may be related to the symptoms of schizophrenia patients. However, it may be affected by confounding factors such as small sample size and failure to control substance use. Due to the complexity of the correlation between schizophrenia and inflammatory factors and the subjectivity of the doctor's diagnosis, missed and misdiagnosed situations may occur. Therefore, there is an urgent need to develop an effective computer-aided diagnosis system to assist doctors in achieving accurate diagnosis of schizophrenia.

With the rapid development of science and technology, with the implementation of deep learning [5], computer-aided diagnosis has been widely used in brain structure functional magnetic resonance image, fMRI research, such as brain tumor segmentation [6–8], Alzheimer's disease classification [9–11], and ADHD diagnosis [12–14]; it also provides an effective method for the classification of schizophrenia.

Between 2014 and 2018, more than 55% of neuroimaging studies of brain diseases used support vector machine (SVM) [15]. Lu et al. [16] proposed schizophrenia as MRI study calculated the gray matter and white matter volumes of each brain region of interest (ROI) and took the significant difference between the two as input features and used SVM classification. Liu et al. [17] constructed a hierarchical brain network by measuring the cortical thickness of each ROI of the brain, extracting the node and edge features of the network, and inputting it into the SVM to realize the auxiliary diagnosis of schizophrenia. Huang et al. use the mathematical tool Pearson's correlation coefficient to calculate the correlation coefficient between fMRI brain regions, and the features after dimensionality reduction by principal component analysis are used for SVM learning. Yang et al. used three methods to analyze fMRI images to obtain three fMRI features, and the three features were used to train three capsule neural networks. Finally, the classification result is obtained through the method of ensemble learning. Yang et al. input the functional connection coefficients after PCA dimensionality reduction as features into the neural network to obtain a classification model.

At present, some reviews have summarized and analyzed the application of deep learning [18–21] in the field of medical imaging [22]. However, there is no literature to systematically sort out and summarize the deep learning methods based on magnetic resonance imaging used in the diagnosis of schizophrenia. In view of this, this article will start from the perspective of deep learning and use VGG16 to extract effective information from fMRI data to diagnose patients with schizophrenia.

2. Methodology

2.1. VGG16. The convolutional neural network (CNN) [22] is shown in Figure 1, which includes a convolutional layer, a downsampling layer, and a fully connected layer. Each layer has multiple feature maps, and each feature map has multiple neurons, and the input features are extracted through the convolution filter [23]. The parameter sharing mechanism of the convolutional layer greatly reduces the number of parameters [24].

The research is based on the VGG16 network to optimize and improve the network. The main structure of VGG16 [16] consists of 5 convolution modules, 3 fully connected layers, and an input layer and output layer. Each convolution layer module is downsampled through max pool.

The expression of the convolutional layer is as follows:

$$x_j^l = f\left(\sum_{i \in M_j} x_i^{l-1} * k_{ij}^l + b_j^l\right). \tag{1}$$

In Equation (1), assuming that $l-1$ is the input layer or the pooling layer, and the l layer is the convolutional layer, then x_i^l is the j-th feature map of the l convolutional layer; the right side of Equation (1) represents the feature map of the $l-1$ layer. Perform convolution operation with the j-th convolution kernel k_{ij}^l of the l layer and sum; b represents the bias; $f(\cdot)$ is the activation function ReLU.

The pooling layer closely follows the convolutional layer and plays the role of scaling dimensionality. The calculation equation is as follows:

$$x_i^l = f\left(\beta_j^l \text{down}\left(x_i^{l-1}\right) + b_j^l\right). \tag{2}$$

In Equation (2), down$(\cdot)$ is the pooling function, which seeks the maximum value for a region of the feature map; β_j^l and b_j^l, respectively, represent the weight and bias of pooling.

The input layer size of VGG16 is $224 \times 224 \times 3$, and the convolution module is composed of a stack of convolution layers and pooling layers. The convolution kernel is usually 3×3 with a step size of 1, and the pooling layer is a 2×2 max pool. Using the convolutional layer and the pooling layer to cooperate, on the one hand, the image size is reduced and the amount of model calculation is controlled. On the other hand, the convolution data of the large receptive field is obtained indirectly, and the high-dimensional feature map is obtained. The convolution module is followed by three fully connected layers to obtain the classification information of the feature map, and finally, the softmax layer is used to output the classification results. The structure diagram of the VGG16 network is shown in Figure 2.

The increase in the depth of the convolutional neural network in the VGG16 network and the use of small convolution kernels have a great impact on the final classification

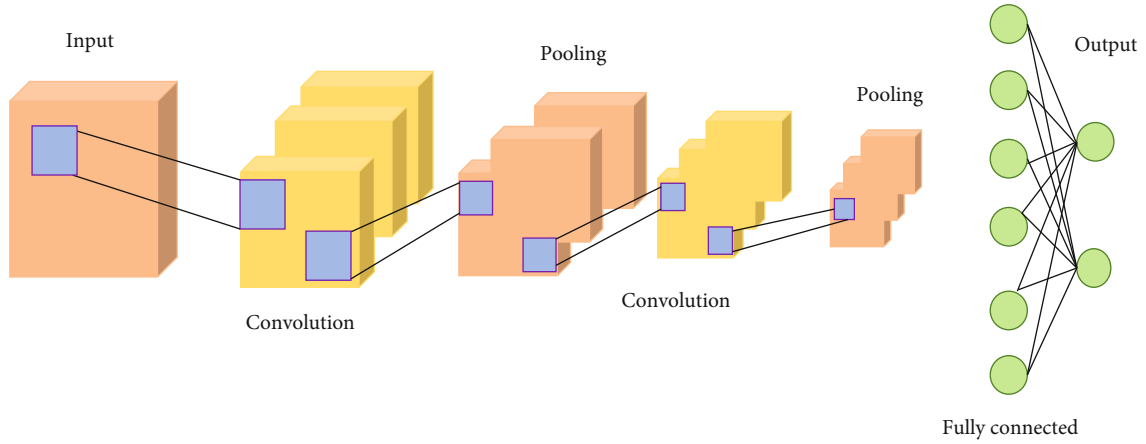

Figure 1: Convolutional neural network structure.

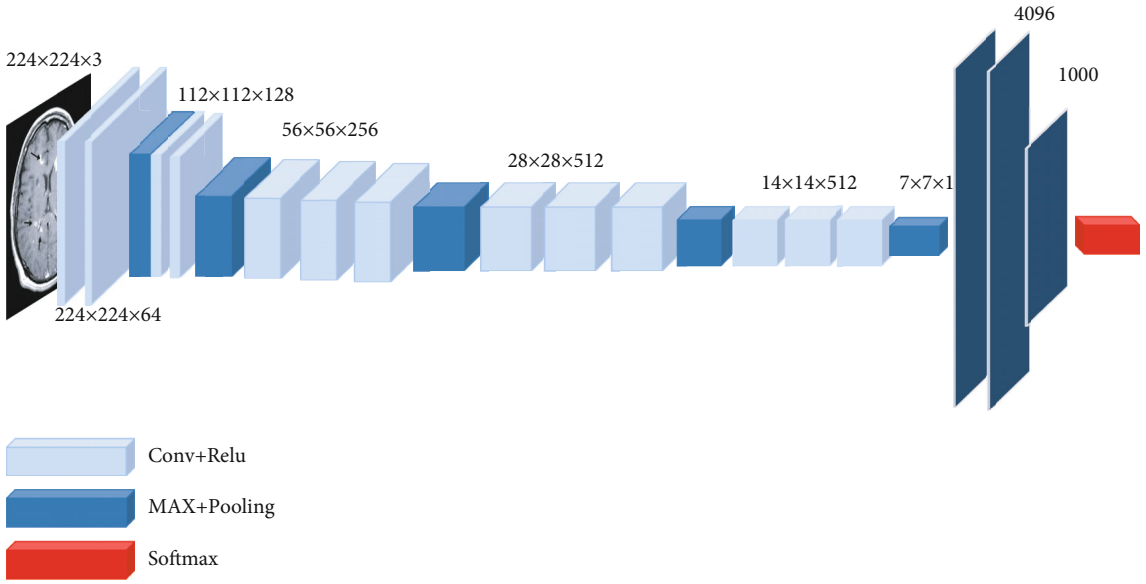

Figure 2: VGG16 structure.

and recognition effect of the network. The convolutional layers all use the same 3-size convolution kernel parameters, and the pooling layers all use the same pooling kernel parameters. The combination of multiple 3×3 convolutional layers not only has a small amount of calculation, but also obtains the same receptive field of the large convolution kernel at the same time. The deep network structure verifies the conjecture that network performance can be improved by continuously deepening the network structure. But for some data, a too deep network only greatly increases the training time, but does not improve the accuracy. The convolution kernel of VGG16 increases from 64 to 512 sequentially, and the number of image channels is first reduced to 64 and then increased to 512. However, due to the large amount of image data, this change in the number of channels will cause the data to lose a lot of information. Increasing the time cost of training and the network structure of VGG16 for this research task, while increasing the depth of the network, cannot improve the accuracy of the network.

2.2. Improved VGG16 Model. Convolutional neural networks are mainly composed of convolutional layers, nonlinear units, pooling layers, and fully connected layers. In the classification problem, the convolutional layer, the nonlinear unit, and the pooling layer are used as the feature extraction layer to extract features, and the fully connected layer is used as the classification layer for classification. The convolutional layer is the core of the convolutional neural network, and the convolution equation is shown in Equation (3).

$$y(t) = \int_{-\infty}^{\infty} x(p)h(t-p)dp = x(t) \times h(t). \tag{3}$$

The nonlinear unit is the ReLU activation function, and its expression is shown in Equation (4).

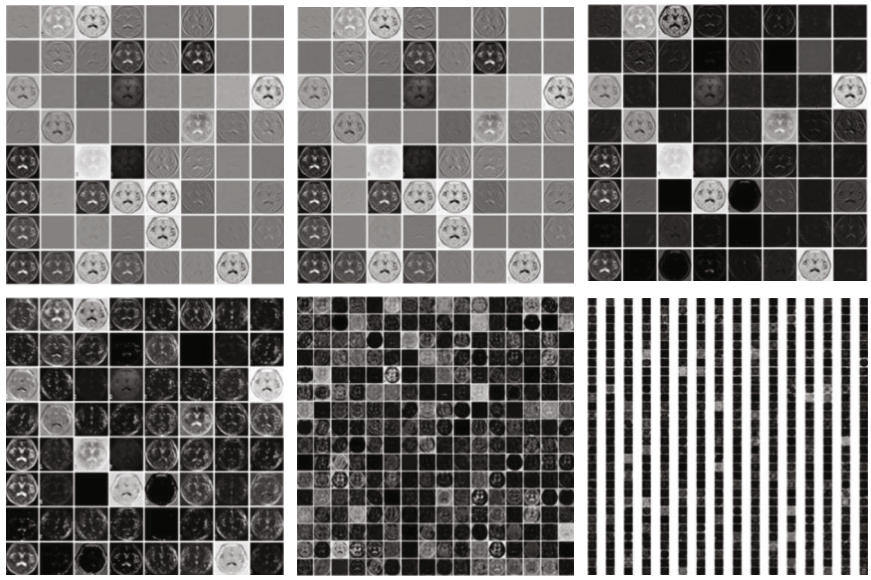

Figure 3: Feature visualization.

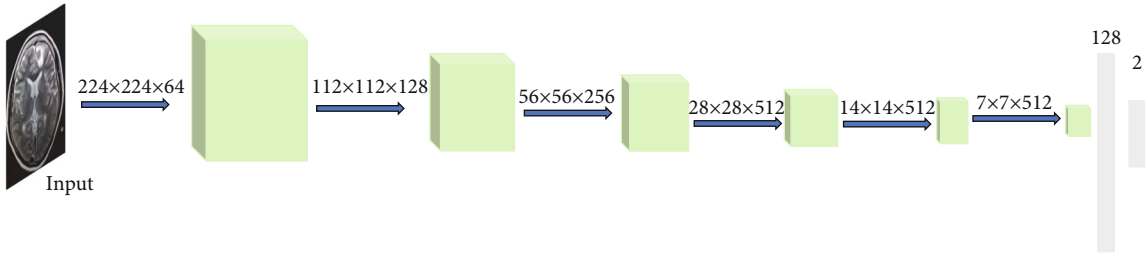

Figure 4: The improved VGG16 schizophrenia classification model.

$$y = \max(0, x). \tag{4}$$

The pooling layer is a downsampling operation to reduce the dimensionality of the extracted features while retaining important information of the features.

The VGG16 network is trained on a large data set ImageNet. The ImageNet data set is a 1000 classification problem data set, so the classification layer parameters of the VGG16 network are huge. The diagnosis of schizophrenia is a two-class classification problem and does not require a complex classification layer. Therefore, the feature extraction layer of the VGG16 network is retained, the classification layer is redesigned, and the original 3-layer fully connected layer is improved to a 2-layer fully connected layer. We take the features of 3 convolutional layers and 3 pooling layers as an example, and the process of part of the extracted features is shown in Figure 3. Use the ReLU activation function, and add a dropout layer to prevent overfitting, and change the final output classification to two categories. The data can be divided into schizophrenia and nonschizophrenia, and the amount of parameters is reduced, so that the network converges faster, and the recognition speed of the data is improved. Figure 4 shows the improved VGG16 schizophrenia classification model.

2.3. Transfer Learning. Transfer learning solves the shortcomings of deep learning that requires a large number of sample training models. By training a pretrained model on a large data set, it is possible to use a small number of data sets to train the model. Fine-tune is a training method that retains the model feature extraction layer and retrains the model classification layer. The pretraining model used is the VGG16 network pretrained on the ImageNet data set, and the feature extraction layer of the pretraining model is fixed. Retrain the improved classification layer of VGG16 to complete the training of the schizophrenia classification model. Figure 5 shows the transfer learning training process.

3. Results

3.1. Data Set. This experimental data set comes from the public data set of the Center for Biomedical Research Excellence (COBRE). The address of the COBRE data set is http://fcon_1000.Projects.nitrc.org/indi/retro/cobre.html. The data set in this paper contains 200 samples between the ages of 18 and 65. The information is shown in Table 1. In this paper, the original data is preprocessed by binarization, standardization, and smoothing. The specific process is shown in Figure 6.

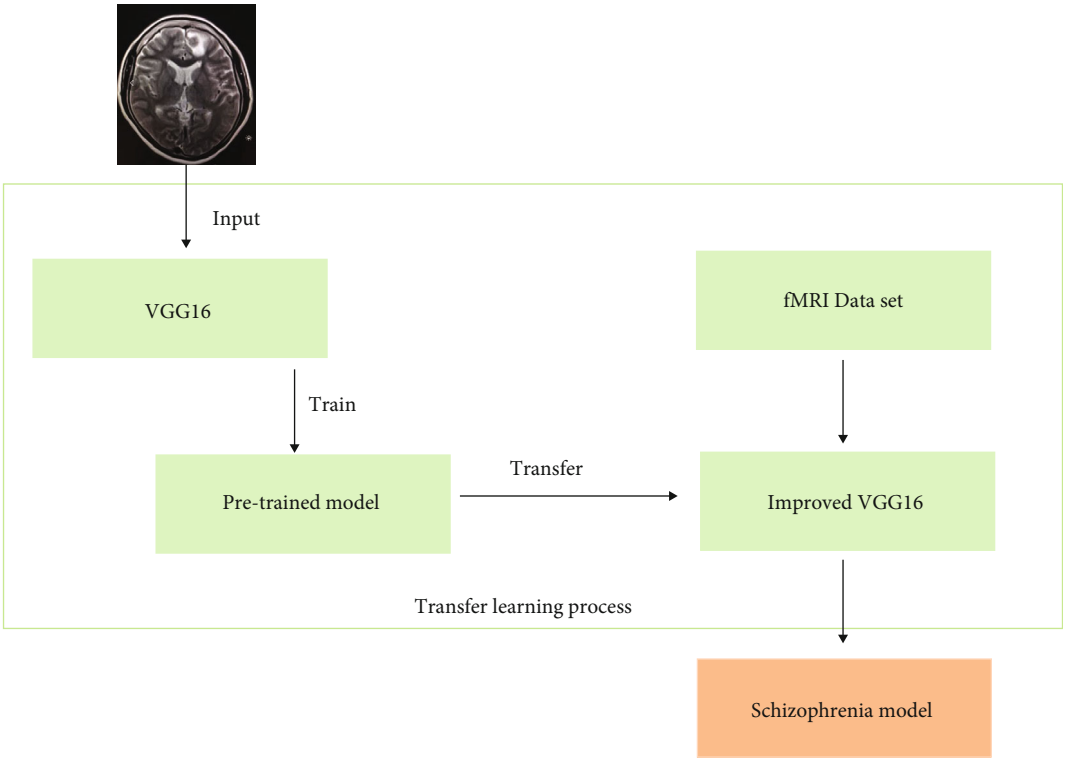

Figure 5: Transfer learning training process.

Table 1: Participant information.

Category	Healthy	Sick	*P* value
Number of people	102	98	
Average age (standard deviation)	36.85 (11.86)	37.46 (12.99)	0.55
Gender (male/female)	55/47	59/39	

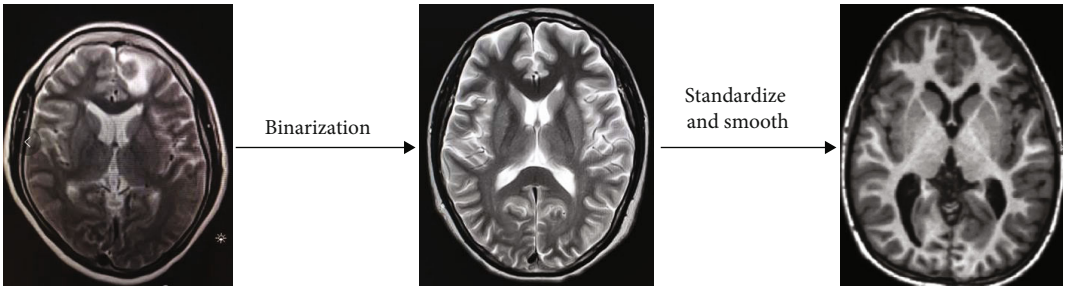

Figure 6: Data preprocessing process.

3.2. Evaluation Index. We use evaluation indicators commonly used in classification tasks: precision, recall, accuracy, and AUC. Table 2 illustrates the classification task through the confusion matrix. True positive (TP) indicates that the positive class is predicted as a positive class, and the number of sample positive classes was actually predicted by the model. False negative indicates (FN) that the positive class is predicted as a negative class, and the number of negative classes in the sample was actually predicted by the model. False positive (FP) indicates that the negative class is predicted as a positive class, and the number of positive classes of samples was actually predicted by the model. True negative (TN) indicates that the negative class is predicted as a negative class, and the number of sample negative classes was actually predicted by the model.

The definition of recall rate: it is the proportion of the true correct accounted for all actual positive. The calculation equation is as follows.

$$\text{Recall} = \frac{\text{TP}}{\text{TP} + \text{FN}}. \tag{5}$$

Table 2: Confusion matrix.

Data type	Predicted positive class	Predicted negative class
Actual positive class	TP	FN
Actual negative class	FP	TN

Table 3: Comparison of effects of different models.

Different models	Accuracy	Precision	Recall	AUC
AlexNet	78.36%	81.29%	75.66%	0.76
VGG16	85.27%	86.33%	87.48%	0.83
ResNet	83.09%	86.59%	79.98%	0.81
Our model	87.58%	87.11%	89.63%	0.85

The definition of accuracy: it is the proportion of all predictions that are truly correct. The calculation equation is as follows.

$$\text{Precision} = \frac{\text{TP}}{\text{TP} + \text{FP}}. \tag{6}$$

3.3. Model Comparison. The algorithm under study is implemented on the deep learning framework TensorFlow and PyTorch platform and is programmed in Python language. The experiment did a detailed study on the schizophrenia recognition rate, accuracy rate, recall rate, and area under curve (AUC). The framework proposed by the research uses the COBRE data set. In order to further verify the effectiveness and superiority of the model proposed in this research, the test set is compared with the existing mainstream framework models. Table 3 gives the results of the evaluation indicators of different models. It can be seen that the framework proposed in this study has the highest classification accuracy rate (87.85%) and the highest accuracy rate (87.11%) compared with the current several popular methods. And the highest recall rate is 89.63%. The diagnostic accuracy rates of AlexNet, VGG16, and ResNet50 models are 78.36%, 85.27%, and 83.09%, respectively. It shows that the proposed schizophrenia diagnosis network is better than other comparison models in accuracy, precision, and recall and can effectively complete the classification task. The receiver operating characteristic (ROC) curves of the four models are shown in Figure 7. Unlike other network models, the accuracy and recall rates of our proposed network model are relatively balanced. At the same time, the AUC index of our proposed model is also higher than that of other models, which proves our model that can learn the essential feature of the data. The generalization ability of the model is better.

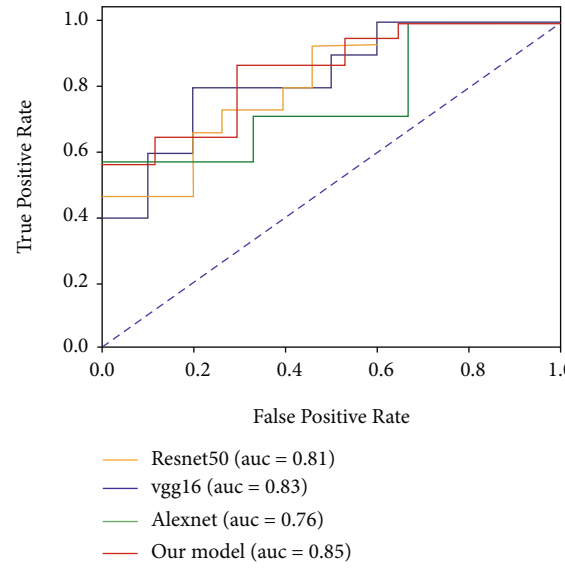

Figure 7: The ROC curves of the four models.

4. Discussion

In this study, the diagnosis model of schizophrenia patients and normal people is based on the deep learning algorithm of fMRI data. Schizophrenia is a very serious mental disorder. At present, it is diagnosed clinically based on the corresponding diagnostic scale and doctor's experience, mainly based on the progress of the disease. This study uses objective EEG data and uses deep learning algorithms to establish a mathematical model for differential diagnosis of the disease, and good results have been achieved.

It can provide a reference for clinical diagnosis and improve the diagnosis ability of clinicians for schizophrenia so as to find the condition in time and give timely treatment.

In order to solve the problems of low accuracy in pathological recognition and complex feature engineering construction in traditional artificial recognition, a schizophrenia diagnosis model based on convolutional neural network algorithm was constructed through deep learning. The network first uses VGG16 for migration learning, then extracts the features of fMRI by designing the convolution structure of the neural network, and finally uses the fully connected layer for training and continuous optimization to obtain the optimal weight parameters.

Finally, the recognition of schizophrenia diagnosis can be achieved. The proposed model has a strong characterization ability for data features and achieved an accuracy of 87.85% in COBRE, which is 2.31 percentage points higher than the existing VGG16 algorithm. Further improvements are needed to meet actual application requirements. It has good application prospects. The application of deep learning in the diagnosis of schizophrenia based on magnetic resonance imaging is a research direction with both challenges and opportunities. In order to promote the transformation of deep learning models from the research stage to practical applications, researchers still need to conduct more systematic and in-depth exploration.

Data Availability

The image data used to support the findings of this study have been deposited in the Center for Biomedical Research Excellence (COBRE) data set (http://fcon_1000.Projects.nitrc.org/indi/retro/cobre.html).

Conflicts of Interest

The authors declare no conflicts of interest.

Authors' Contributions

JinChi Zheng and XiaoLan Wei contributed equally to this paper.

Acknowledgments

This research is funded by the Science Foundation of Quanzhou (No. 2020N046s).

References

[1] R. Freedman, "Schizophrenia," *The New England Journal of Medicine*, vol. 349, no. 18, pp. 1738–1749, 2003.

[2] J. Klosterkotter, F. Schultze-Lutter, A. Bechdolf, and S. Ruhrmann, "Prediction and prevention of schizophrenia: what has been achieved and where to go next?," *World Psychiatry*, vol. 10, no. 3, pp. 165–174, 2011.

[3] S. Key, "The positive and negative syndrome (PANSS) for schizophrenia," *Biological Psychiatry*, vol. 20, 1987.

[4] M. H. Lv, Y. L. Tan, S. X. Yan et al., "Decreased serum TNF-alpha levels in chronic schizophrenia patients on long-term antipsychotics: correlation with psychopathology and cognition," *Psychopharmacology*, vol. 232, no. 1, pp. 165–172, 2015.

[5] Z. Tang, G. Zhao, and T. Ouyang, "Two-phase deep learning model for short-term wind direction forecasting," *Renewable Energy*, vol. 173, no. 72, pp. 1005–1016, 2021.

[6] N. Tajbakhsh, J. Y. Shin, S. R. Gurudu et al., "Convolutional neural networks for medical image analysis: full training or fine tuning?," *IEEE Transactions on Medical Imaging*, vol. 35, no. 5, pp. 1299–1312, 2016.

[7] X. Zhao, Y. Wu, G. Song, Z. Li, Y. Zhang, and Y. Fan, "A deep learning model integrating FCNNs and CRFs for brain tumor segmentation," *Medical Image Analysis*, vol. 43, pp. 98–111, 2018.

[8] Z. Xiao, R. Huang, Y. Ding et al., "A deep learning-based segmentation method for brain tumor in MR images," in *2016 IEEE 6th International Conference on Computational Advances in Bio and Medical Sciences (ICCABS)*, pp. 1–6, Atlanta, GA, USA, 2016.

[9] S. Sarraf, G. Tofighi, and for the Alzheimer's Disease Neuroimaging Initiative, "DeepAD: Alzheimer's disease classification via deep convolutional neural networks using MRI and fMRI," 2016, https://www.biorxiv.org/content/10.1101/070441v1.

[10] S. Sarraf and G. Tofighi, "Classification of Alzheimer's disease using fMRI data and deep learning convolutional neural networks," 2016, https://arxiv.org/abs/1603.08631.

[11] F. Li, L. Tran, K. H. Thung, S. Ji, D. Shen, and J. Li, *Robust Deep Learning for Improved Classification of AD/MCI Patients 5th International Workshop, MLMI*, vol. 8679, Springer International Publishing, 2014.

[12] C. W. Chang, C. C. Ho, and J. H. Chen, "ADHD classification by a texture analysis of anatomical brain MRI data," *Frontiers in Systems Neuroscience*, vol. 6, p. 66, 2012.

[13] D. Kuang and L. He, "Classification on ADHD with deep learning," in *2014 International Conference on Cloud Computing and Big Data*, pp. 27–32, Wuhan, China, 2014.

[14] A. Vahid, A. Bluschke, V. Roessner, S. Stober, and C. Beste, "Deep learning based on event-related EEG differentiates children with ADHD from healthy controls," *Journal of Clinical Medicine*, vol. 8, no. 7, p. 1055, 2019.

[15] K. Sakai and K. Yamada, "Machine learning studies on major brain diseases: 5-year trends of 2014–2018," *Japanese journal of radiology*, vol. 37, no. 1, pp. 34–72, 2019.

[16] X. Lu, Y. Yang, F. Wu et al., "Discriminative analysis of schizophrenia using support vector machine and recursive feature elimination on structural MRI images," *Medicine*, vol. 95, no. 30, article e3973, 2016.

[17] J. Liu, M. Li, Y. Pan, F. X. Wu, X. Chen, and J. Wang, "Classification of schizophrenia based on individual hierarchical brain networks constructed from structural MRI images," *IEEE Transactions on Nanobioscience*, vol. 16, no. 7, pp. 600–608, 2017.

[18] A. Krizhevsky, I. Sutskever, and G. E. Hinton, "ImageNet classification with deep convolutional neural networks," *Advances in Neural Information Processing Systems*, vol. 60, no. 6, pp. 84–90, 2017.

[19] D. Tschumperlé and R. Deriche, "Proceedings of the IEEE Computer Society Conference on Computer Vision and Pattern Recognition," *IEEE Computer Society*, vol. 1, 2016.

[20] K. Simonyan and A. Zisserman, "Very deep convolutional networks for large-scale image recognition," 2014, https://arxiv.org/abs/1409.1556.

[21] K. He, X. Zhang, S. Ren, and J. Sun, "Deep residual learning for image recognition," in *2016 IEEE Conference on Computer Vision and Pattern Recognition (CVPR)*, pp. 770–778, Las Vegas, NV, USA, 2016.

[22] Z. Yan, H. Zhang, R. Piramuthu et al., "HD-CNN: hierarchical deep convolutional neural networks for large scale visual recognition," in *IEEE International Conference on Computer Vision (ICCV 2015)*, pp. 2740–2748, Santiago, Chile, 2015.

[23] R. T. Schirrmeister, J. T. Springenberg, L. D. J. Fiederer et al., "Deep learning with convolutional neural networks for EEG decoding and visualization," *Human Brain Mapping*, vol. 38, no. 11, pp. 5391–5420, 2017.

[24] H. C. Shin, H. R. Roth, M. Gao et al., "Deep convolutional neural networks for computer-aided detection: CNN architectures, dataset characteristics and transfer learning," *IEEE Transactions on Medical Imaging*, vol. 35, no. 5, pp. 1285–1298, 2016.

Hindawi
Computational and Mathematical Methods in Medicine
Volume 2021, Article ID 2144472, 6 pages
https://doi.org/10.1155/2021/2144472

Research Article

Single Shot Multibox Detector Automatic Polyp Detection Network Based on Gastrointestinal Endoscopic Images

Xiaoling Chen,[1] **Kuiling Zhang**,[1] **Shuying Lin**,[2] **Kai Feng Dai**,[3] **and Yang Yun**[4]

[1]*Department of Gastroenterology, Quanzhou First Hospital Affiliated to Fujian Medical University, Quanzhou, Fujian 362000, China*
[2]*Department of Endoscope Room, Quanzhou First Hospital Affiliated to Fujian Medical University, Quanzhou, Fujian 362000, China*
[3]*Imaging Department, Quanzhou First Hospital Affiliated to Fujian Medical University, Quanzhou, Fujian 362000, China*
[4]*Department of Health Medicine, Joint Service Support Force 910 Hospital, Quanzhou, Fujian 362000, China*

Correspondence should be addressed to Xiaoling Chen; 156314270@qq.com

Received 1 September 2021; Revised 11 October 2021; Accepted 15 October 2021; Published 5 November 2021

Academic Editor: Kelvin Wong

Purpose. In order to resolve the situation of high missed diagnosis rate and high misdiagnosis rate of the pathological analysis of the gastrointestinal endoscopic images by experts, we propose an automatic polyp detection algorithm based on Single Shot Multibox Detector (SSD). *Method*. In the paper, SSD is based on VGG-16, the fully connected layer is changed to a convolutional layer, and four convolutional layers with successively decreasing scales are added as a new network structure. In order to verify the practicability, it is not only compared with manual polyp detection but also with Mask R-CNN. *Results*. Multiple experimental results show that the mean Average Precision (mAP) of the SSD network is 95.74%, which is 12.4% higher than the manual detection and 5.7% higher than the Mask R-CNN. When detecting a single frame of image, the detection speed of SSD is 8.41 times that of manual detection. *Conclusion*. Based on the traditional pattern recognition algorithm and the target detection algorithm using deep learning, we select a variety of algorithms to identify and classify polyps to achieve efficient detection results. Our research demonstrates that deep learning has a lot of room for development in the field of gastrointestinal image recognition.

1. Introduction

Endoscope technology is widely used in the diagnosis of gastrointestinal diseases [1–3]. However, a large number of medical images will be generated during the detection process. It is a very time-consuming and laborious task to only rely on the doctor's naked eyes to identify the lesion-containing part from the large number of gastrointestinal endoscopic images [4–7], and the diagnosis process mainly relies on the doctor's experience and pathology. The diversity of features and the complexity of the gastrointestinal environment and the rate of misdetection and missed detection of lesions are still high, so it is particularly important to develop efficient and accurate endoscopic image lesion detection methods.

The rapid development of medical equipment has promoted the improvement of medical standards to a certain extent and provided guarantee for the timely treatment of the majority of patients. However, each endoscopy will produce a large number of images, and most of them do not contain lesion information. Therefore, before making a diagnosis, clinicians need to spend a lot of energy and time to find images containing lesions from a huge image data set, which increases the workload of doctors. Therefore, it is very necessary to help doctors quickly find and diagnose early lesions, improve doctors' work efficiency, and solve patients' problems in a timely manner. Accurate detection of lesions in medical images provides a guarantee of diagnostic information for clinical applications. This topic is useful for assisting doctors in screening. Diagnosing lesions has important theoretical significance and application value.

In recent years, with the rise of machine learning and artificial intelligence, computer vision has also been further

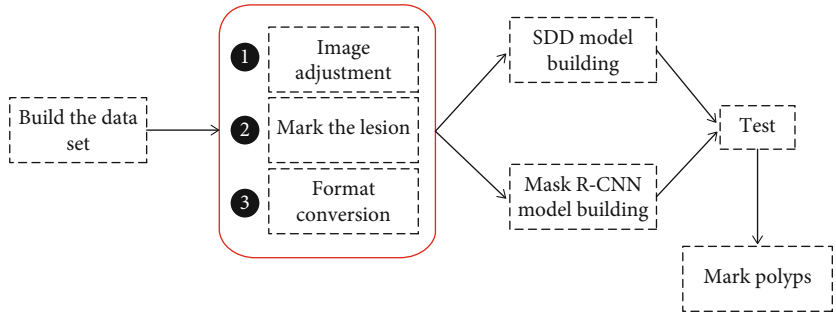

Figure 1: Polyp detection flowchart of deep learning algorithm.

developed. Computer vision mainly uses a computer to simulate people to perform related processing on images and obtain valuable information in pictures. Computer vision has been widely used in many fields such as medical image processing, industrial robots, image monitoring, and unmanned driving, and the effect is also very significant. Target detection is a basic field in computer vision applications. Target detection mainly combines target segmentation and target recognition. Its recognition accuracy, recognition efficiency, and positioning accuracy are the main performance indicators of the entire system. In recent years, with the annual PASCAL VOC challenge [8], more and more teams have participated. Each year, the participating teams propose some advanced algorithms or propose improvements on existing algorithms. It is precisely because of their efforts that target detection has developed rapidly.

With the rise of machine learning, artificial intelligence, and deep learning, many institutions and many colleges and universities have carried out a lot of exploratory work. In 2014, Girshick et al. proposed a deep learning target detection algorithm RCNN [9] based on a region of interest [10] combined with a convolutional neural network (CNN) [11–13], which made a breakthrough in target detection. It has also inspired a large number of outstanding talents to study the target detection algorithm based on deep learning.

The current target detection algorithms based on deep learning are roughly divided into deep learning target detection algorithms based on regions of interest and deep learning target detection algorithms based on regression. Among them, deep learning target detection algorithms based on regions of interest include RCNN [14, 15], SPP-net [16, 17], Fast RCNN [18, 19], Faster RCNN [20, 21], Mask R-CNN [22–25], and YOLO [26, 27].

Gastric polyps have many effects on the stomach. For example, if gastric polyps grow in the cardia, it may cause difficulty in swallowing, because the position of gastric polyps affects normal swallowing ability. If polyps grow in the antrum of the stomach, which is commonly referred to as the pylorus, problems such as pyloric obstruction will easily occur, which will affect the postmeal state. Patients may experience bloating after meals, and in more severe cases, symptoms such as nausea and vomiting may occur. Some patients do not deal with it in time when gastric polyps appear, and eventually they may become cancerous and become gastric cancer.

In order to break the situation of high missed diagnosis rate and high misdiagnosis rate of the pathological part of the gastrointestinal endoscopy image recognized by experts with naked eyes, we propose an algorithm for automatic polyp detection based on SSD [28]. Our purpose is to help doctors quickly find and diagnose early lesions, improve doctors' work efficiency, and solve patients' problems in a timely manner.

2. Mythology

2.1. Deep Learning

2.1.1. Detection Framework. The polyp detection process based on deep learning algorithm is shown in Figure 1. In the first step, in order to select a clearer lesion-containing image from the endoscopy and construct a data set, preprocessing is required. The preprocessing mainly includes random adjustment of the original image, lesion marking, and data format conversion. The second is to build two deep learning algorithm network models. Model building is an important part of the entire process. The choice of algorithm will directly affect the results of lesion detection. Next, train the sample set and export the training model. Finally, the obtained model is applied to the test set for detection, and the performance of the algorithm model is compared by evaluating the accuracy and detection speed.

2.1.2. SDD Network Structure. Single Shot MultiBox Detector (SDD) is a 2016 ICCV paper. It is the main target detection algorithm so far. SSD is based on a forward propagation CNN network, which generates a series of fixed-size bounding boxes, and the possibility of object instances contained in each box, namely, score. After that, perform a nonmaximum suppression to get the final predictions. The SSD network structure can be seen from the figure divided into two parts: basic network + pyramid network. The basic network is the first 4 layers of VGG-16. The pyramid network is a simple convolutional network that gradually becomes smaller in feature maps and consists of 5 parts. The network structure of SSD is shown as in Figure 2.

2.1.3. Mask R-CNN. The Mask R-CNN network structure is designed on the basis of Faster R-CNN to achieve target detection. The feature extraction backbone network of VGG16 is replaced with Res Net-FPN; the pixel of the feature map and the candidate area cannot be aligned due to

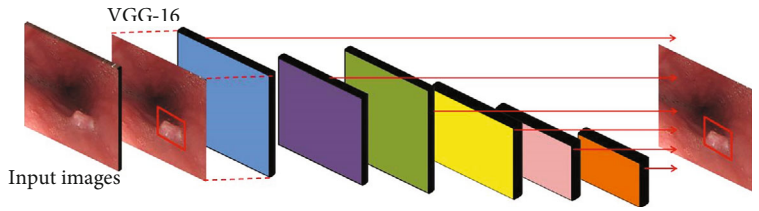

Figure 2: SSD network structure.

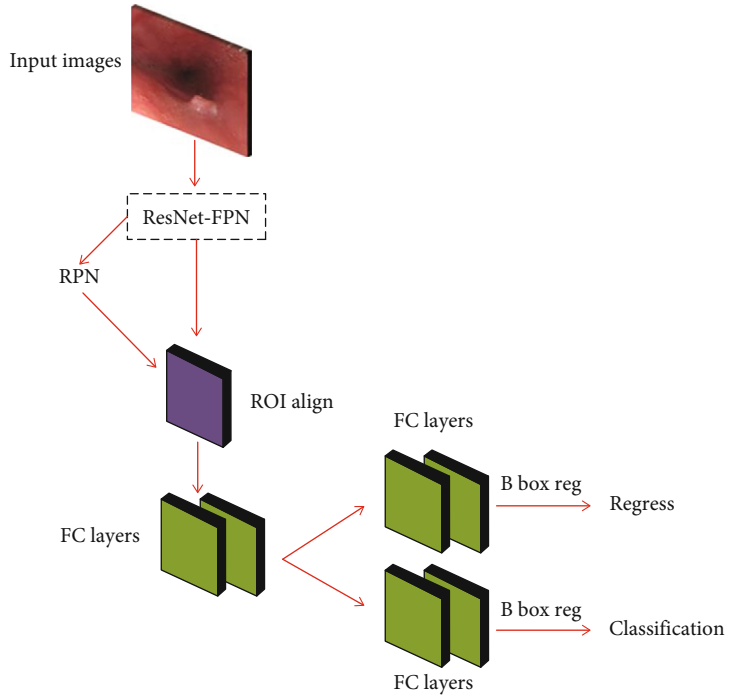

Figure 3: Mask R-CNN algorithm architecture diagram.

Table 1: Gastrointestinal endoscopy image data set.

Style	Train	Eval	Test
Polyp	1200	800	850
Bleeding	800	700	650
Total	2000	1500	1400

the rounding operation. The ROI Pooling layer is replaced by the ROI Align layer; adding an FCN branch to achieve semantic segmentation at the same time has shown excellent results in many large public data sets. The structure of the Mask R-CNN algorithm is shown in Figure 3.

2.2. Experimental Treatment

2.2.1. Build a Data Set. In this paper, a total of 4900 gastrointestinal endoscopy images are used for experiments. Two types of lesion images are constructed at the same ratio. The total training set is 2000, and the total verification set is 1500. The test set is divided into images with lesions and normal images without lesions, a total of 1400 open. The specific data division is shown in Table 1.

2.2.2. Image Preprocessing. Image preprocessing is an indispensable link before model training and learning. The purpose is to remove the interference information that is not conducive to model training in the original gastrointestinal endoscopy image, highlight the characteristic information of the included lesions, and improve the efficiency of training and learning. The preprocessing process of this article mainly includes three parts, random adjustment of the original image, lesion marking, and data format conversion.

2.3. Evaluation Index. Mean Average Precision (mAP) is a performance metric for this type of algorithm that predicts the target location and category. mAP is very useful for evaluating target localization models, target detection models, and instance segmentation models.

3. Results

3.1. Data Set Experimental Results

3.1.1. The Impact of Data Set Categories. We, respectively, performed 6000 iterations of Train, Eval, and Test in the esophageal cancer image data set and the mAP (%) of the

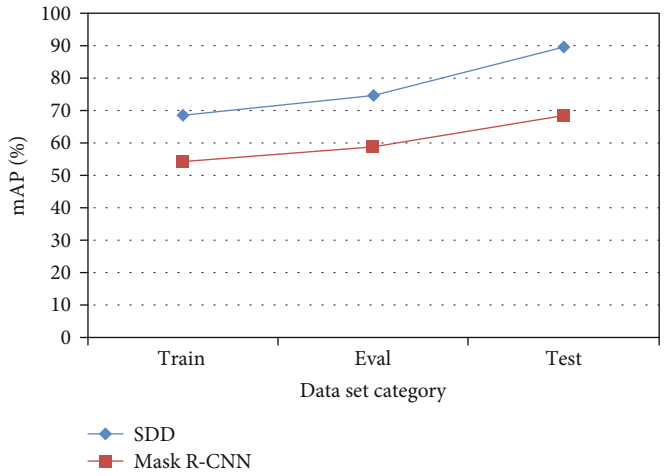

Figure 4: mAP of each data set in 6000 iterations.

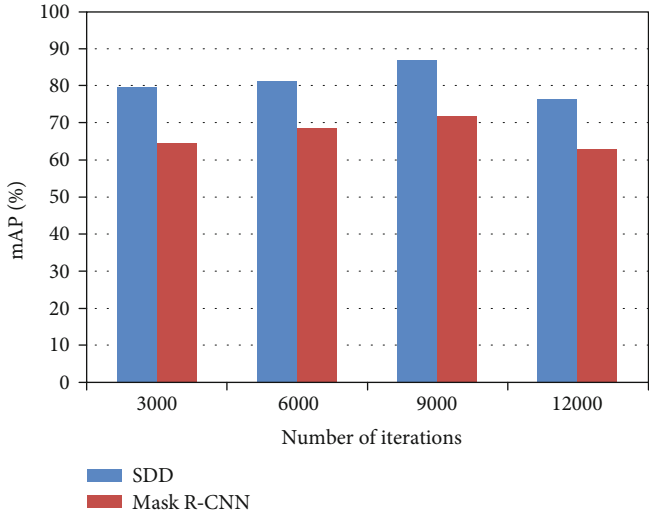

Figure 5: Iterate the mAP of two models of 3000, 6000, 9000, and 12000.

SDD algorithm and Mask R-CNN algorithm on the image test set. The detection results are shown in Figure 4.

It can be seen from Figure 4 that comparing the SDD algorithm and the Mask R-CNN algorithm, the mAP of the training verification sample set Test on the esophageal cancer image test set is higher than the training sample set Train and Eval.

3.1.2. The Influence of the Number of Iterations. When we iterate 3000, 6000, 9000, and 12000 times on the image training verification sample set Test, the mAP (%) of the SDD algorithm, and Mask R-CNN algorithm on the gastrointestinal endoscopy image test sample set, the test results are shown in Figure 5.

It can be seen from the experimental results that comparing the SDD algorithm and the Mask R-CNN algorithm, it is found that as the number of training iterations increases for each algorithm, the average accuracy of the detection on the esophageal cancer image test set is also improving but not increase infinitely. That is, for any one of the above three algorithms, the average accuracy mean mAP has an upper limit. Comparing the experimental results of the two algorithms on the esophageal cancer image test sample set at the same number of iterations, the mAP of the SDD algorithm on the esophageal cancer test sample set is better than the mAP of the Mask R-CNN algorithm on the esophageal cancer test sample set.

3.2. The Effect of Gastrointestinal Endoscopy Image Verification. As shown in Figure 6, the contrast images of SDD, Mask R-CNN, and manual segmentation of gastrointestinal endoscopy images. Red represents SDD, green represents Mask R-CNN, and yellow represents the effect of manual segmentation. It can be seen from Figure 6 that the red recognition is the most accurate, the manual recognition is the second, and the worst is Mask R-CNN.

4. Discussion

Gastrointestinal endoscopic images are the basis for the judgment of gastrointestinal diseases. Due to the complexity

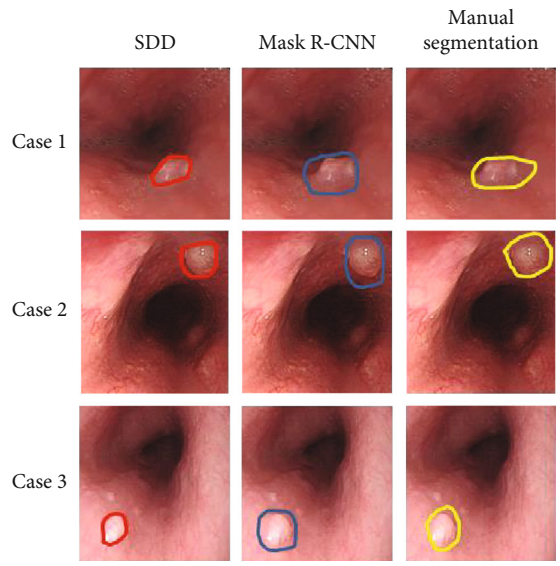

Figure 6: Comparison of the effects of three ways to identify polyps.

of the internal environment, the concealment of pathological features, the blurring of lens shooting, and the complexity of image processing, the occurrence of missed and misdiagnosed phenomena occurs. How to effectively improve the lesion, the real-time performance and accuracy of the detection algorithm is still a more difficult problem. This paper fully understands the current status and challenges of gastrointestinal image lesion detection technology, deeply researches traditional pattern recognition algorithms and deep learning-based target detection algorithms, selects effective algorithms to identify and classify multiple lesions, and achieves efficient detection results.

Lesion detection still faces great challenges, and there are some problems to be solved.

Due to the variable shape and complex texture of gastrointestinal lesions, the number of existing endoscopic pictures is lacking. There are tens of thousands of pictures in a gastrointestinal endoscopy, and few can be used for actual labeling. After screening, an average of 30 can be used for image labeling. The data sets of the three types of lesions constructed in this paper need to be greatly expanded, and the collection of a large number of endoscopic images is a necessary work for further research.

The algorithm in this paper is mainly for single image detection, which cannot meet the real-time detection of video images in practical applications. It is necessary to build a lesion detection system for gastrointestinal endoscopy images and establish a relational database between patients and medical staff.

mAP needs to be improved. Due to the limitations of many factors, the experimental results of this article still have a lot of room for improvement in detection accuracy. The algorithm and network framework need to be further improved, and the weight settings between each network layer are measured to achieve the best detection effect.. The use of convolutional neural networks to extract lesion features requires higher equipment requirements, and the complex network structure will result in slower algorithm processing speed. Therefore, how to improve the processing speed of the algorithm while making full use of the features of the convolutional neural network will be the focus of future research.

This paper makes a preliminary exploration of the deep learning target detection algorithm based on the region of interest on the esophageal cancer image, and further research is needed. At the same time, it is still necessary to study the experimental effects of other deep learning target detection algorithms on esophageal cancer images.

5. Conclusion

The mean Average Precision (mAP) of our proposed SSD network is 95.74%, 12.4% higher than manual detection, and 5.7% higher than Mask R-CNN. When detecting a single frame of image, the detection speed of SSD is 8.41 times that of manual detection. We select a variety of algorithms to identify and classify polyps to achieve efficient detection results. It shows that deep learning has a lot of room for development in the field of gastrointestinal image recognition.

Data Availability

The image data used to support the findings of this study have been deposited in the Kvasir-SEG data set (https://munin.uit.no/handle/10037/18342).

Conflicts of Interest

The authors declare that they have no conflicts of interest.

References

[1] Q. Y. Zhao, Y. P. Wang, and Y. N. Zhou, "Research of the diagnosis of early gastric by combined endoscope technology," *Journal of Lanzhou University (Medical Sciences)*, vol. 1, no. 2, pp. 42–62, 2014.

[2] Y. Yong, Y. Chen, and X. Long, "The application of OMOM capsule endoscope in the treatment and diagnosis of gastrointestinal diseases," *Journal of Military Surgeon in Southwest China*, vol. 56, no. 8, p. 45, 2011.

[3] T. Shibuya and S. Watanabe, "Diagnosis of small-intestinal disease with capsule endoscopy," *Juntendo Medical Journal*, vol. 60, no. 2, pp. 94–99, 2014.

[4] K. V. Asari, S. Kumar, and D. Radhakrishnan, "A new approach for nonlinear distortion correction in endoscopic images based on least squares estimation," *IEEE Transactions on Medical Imaging*, vol. 18, no. 4, pp. 345–354, 1999.

[5] D. Burschka, M. Li, M. Ishii, R. H. Taylor, and G. D. Hager, "Scale-invariant registration of monocular endoscopic images to CT-scans for sinus surgery," *Medical Image Analysis*, vol. 9, no. 5, pp. 413–426, 2005.

[6] P. Wang, S. M. Krishnan, C. Kugean, and M. P. Tjoa, "Classification of endoscopic images based on texture and neural network," in *2001 Conference Proceedings of the 23rd Annual International Conference of the IEEE Engineering in Medicine and Biology Society*, Istanbul, Turkey, 2001IEEE.

[7] S. Ono, M. Kato, Y. Ono et al., "Characteristics of magnified endoscopic images of gastric extranodal marginal zone B-cell

lymphoma of the mucosa-associated lymphoid tissue, including changes after treatment," *Gastrointestinal Endoscopy*, vol. 68, no. 4, pp. 624–631, 2008.

[8] M. Everingham, S. M. A. Eslami, L. Van Gool, C. K. I. Williams, J. Winn, and A. Zisserman, "The Pascal visual object classes challenge: a retrospective," *International Journal of Computer Vision*, vol. 111, no. 1, pp. 98–136, 2015.

[9] R. Girshick, J. Donahue, T. Darrell, and J. Malik, "Rich feature hierarchies for accurate object detection and semantic segmentation," *IEEE Computer Society*, vol. 88, no. 5, pp. 132–140, 2013.

[10] S. S. Bangalore, K. M. R. Prasad, D. M. Montrose, D. D. Goradia, V. A. Diwadkar, and M. S. Keshavan, "Cannabis use and brain structural alterations in first episode schizophrenia – a region of interest, voxel based morphometric study," *Schizophrenia Research*, vol. 99, no. 1-3, pp. 1–6, 2008.

[11] D. E. Diamantis, A. E. Zacharia, D. K. Iakovidis, and A. Koulaouzidis, "Towards the substitution of real with artificially generated endoscopic images for CNN training," in *2019 IEEE 19th International Conference on Bioinformatics and Bioengineering (BIBE)*IEEE.

[12] T. Okamoto, M. Odagawa, T. Koide et al., "Feature extraction of colorectal endoscopic images for computer-aided diagnosis with CNN," in *2019 2nd International Symposium on Devices, Circuits and Systems (ISDCS)*, Higashi-Hiroshima, Japan, 2019IEEE.

[13] W. Zheng, X. Zhang, J. J. Kim et al., "High accuracy of convolutional neural network for evaluation of Helicobacter pylori infection based on endoscopic images: preliminary experience," *Clinical and Translational Gastroenterology*, vol. 10, no. 12, pp. 157–160, 2019.

[14] D. Zhang, J. Zhan, L. Tan, Y. Gao, and R. Župan, "Comparison of two deep learning methods for ship target recognition with optical remotely sensed data," *Neural Computing and Applications*, vol. 1, pp. 128–134, 2021.

[15] Q. Hu and L. Zhai, "RGB-D image multi-target detection method based on 3D DSF R-CNN," *International Journal of Pattern Recognition and Artificial Intelligence*, vol. 33, no. 8, pp. 1954026–1954250, 2019.

[16] S. Ren, K. He, R. Girshick, and J. Sun, "Faster R-CNN: towards real-time object detection with region proposal networks," *IEEE Transactions on Pattern Analysis and Machine Intelligence*, vol. 39, no. 6, pp. 1137–1149, 2017.

[17] D. Chagas-Paula, T. Oliveira, T. Zhang, R. A. Edrada-Ebel, and F. D. Costa, "Prediction of anti-inflammatory plants and discovery of their biomarkers by machine learning algorithms and metabolomic studies," *Planta Medica*, vol. 81, no. 6, pp. 450–458, 2015.

[18] Y. Liu, "An improved Faster R-CNN for object detection," in *2018 11th International Symposium on Computational Intelligence and Design (ISCID)*, Hangzhou, China, 2018.

[19] D. Wang, J. L. Tang, W. Zhu, H. Li, J. Xin, and D. He, "Dairy goat detection based on Faster R-CNN from surveillance video," *Computers and Electronics in Agriculture*, vol. 154, pp. 443–449, 2018.

[20] J. Zheng, W. Li, M. Xia, R. Dong, H. Fu, and S. Yuan, "Large-scale oil palm tree detection from high-resolution remote sensing images using Faster-RCNN," in *IGARSS-2019 IEEE International Geoscience and Remote Sensing Symposium*, Yokohama, Japan, 2019IEEE.

[21] R. A. Bindu, A. A. Neloy, S. Alam, and S. Siddique, "3-survivor: a rough terrain negotiable teleoperated mobile rescue robot with passive control mechanism," in *Computer Science, Engineering*, vol. 25, no. 8pp. 42–46, ArXiv, 2020.

[22] H. Jin, M. Yan, J. Lu, L. Zhu, K. Wang, and S. Bai, "Performance comparison of moving target recognition between Faster R-CNN and SSD," in *2019 International Joint Conference on Information, Media and Engineering (IJCIME)*, 2019.

[23] B. Xu, W. Wang, G. Falzon et al., "Automated cattle counting using Mask R-CNN in quadcopter vision system," *Computers and Electronics in Agriculture*, vol. 171, p. 105300, 2020.

[24] Z. Tang, G. Zhao, and T. Ouyang, "Two-phase deep learning model for short-term wind direction forecasting," *Renewable Energy*, vol. 173, pp. 1005–1016, 2021.

[25] J. Shi, Y. Zhou, and Q. Zhang, "Service robot item recognition system based on improved Mask RCNN and Kinect," *Chinese Journal of Scientific Instrument*, vol. 11, no. 9, pp. 40–52, 2019.

[26] A. Reghukumar, L. J. Anbarasi, J. Prassanna, R. Manikandan, and F. Al-Turjman, "Vision based segmentation and classification of cracks using deep neural networks," *International Journal of Uncertainty, Fuzziness and Knowledge-Based Systems*, vol. 25, no. 1, pp. 68–70, 2021.

[27] S. Srivastava, A. V. Divekar, C. Anilkumar, I. Naik, V. Kulkarni, and V. Pattabiraman, "Comparative analysis of deep learning image detection algorithms," *Journal of Big Data*, vol. 8, no. 1, pp. 76–83, 2021.

[28] Y. Wang, W. Cui, and H. Yang, "A small target recognition algorithm based on improved SSD," in *2019 International Conference on Artificial Intelligence and Advanced Manufacturing (AIAM)*, Dublin, Ireland, 2019IEEE.

Hindawi
Computational and Mathematical Methods in Medicine
Volume 2021, Article ID 9548312, 8 pages
https://doi.org/10.1155/2021/9548312

Research Article

Image Enhancement Model Based on Deep Learning Applied to the Ureteroscopic Diagnosis of Ureteral Stones during Pregnancy

Xiao-Yan Miao,[1] **Xiao-Nan Miao**,[2] **Li-Yin Ye**,[3] **and Hong Cheng**[4]

[1]*Department of Radiation Oncology, The First People's Hospital of Fuyang (Fuyang First Affiliated Hospital of Zhejiang Chinese Medical University Ben Giang College), Hangzhou, China 311400*
[2]*Department of Endocrinology, The First People's Hospital of Fuyang (Fuyang First Affiliated Hospital of Zhejiang Chinese Medical University Ben Giang College), Hangzhou, China 311400*
[3]*Department of Urology, The First People's Hospital of Fuyang (Fuyang First Affiliated Hospital of Zhejiang Chinese Medical University Ben Giang College), Hangzhou, China 311400*
[4]*Department of Ultrasound, The First People's Hospital of Fuyang (Fuyang First Affiliated Hospital of Zhejiang Chinese Medical University Ben Giang College), Hangzhou, China 311400*

Correspondence should be addressed to Xiao-Yan Miao; fyyyflk@163.com

Received 24 August 2021; Revised 20 September 2021; Accepted 28 September 2021; Published 29 October 2021

Academic Editor: Kelvin Wong

Objective. To explore the image enhancement model based on deep learning on the effect of ureteroscopy with double J tube placement and drainage on ureteral stones during pregnancy. We compare the clinical effect of ureteroscopy with double J tube placement on pregnancy complicated with ureteral stones and use medical imaging to diagnose the patient's condition and design a treatment plan. *Methods*. The image enhancement model is constructed using deep learning and implemented for quality improvement in terms of image clarity. In the way, the relationship of the media transmittance and the image with blurring artifacts was established, and the model can estimate the ureteral stone predicted map of each region. Firstly, we proposed the evolution-based detail enhancement method. Then, the feature extraction network is used to capture blurring artifact-related features. Finally, the regression subnetwork is used to predict the media transmittance in the local area. Eighty pregnant patients with ureteral calculi treated in our hospital were selected as the research object and were divided into a test group and a control group according to the random number table method, 40 cases in each group. The test group underwent ureteroscopy double J tube placement, and the control group underwent ureteroscopy lithotripsy. Combined with the ultrasound scan results of the patients before and after the operation, the operation time, time to get out of bed, and hospitalization time of the two groups of patients were compared. The operation success rate and the incidence of complications within 1 month after surgery were counted in the two groups of patients. *Results*. We are able to improve the quality of the images prior to medical diagnosis. The total effective rate of the observation group was 100.0%, which is higher than that of the control group (90.0%). The difference between the two groups was statistically significant ($P < 0.05$). The adverse reaction rate in the observation group was 5.0%, which was lower than 17.5% in the control group. The difference between the two groups was statistically significant ($P < 0.05$). The comparison results are then prepared. *Conclusions*. The image enhancement model based on deep learning is able to improve medical diagnosis which can assist radiologists to better locate the ureteral stones. Based on our method, double J tube placement under ureteroscopy has a significant effect on the treatment of ureteral stones during pregnancy, and it has good safety and is worthy of widespread application.

1. Introduction

To study the problem of medical image enhancement, it is necessary to have a comprehensive and accurate understanding of its related models, related theories, and current research status, so as to complete the modeling of image enhancement. In this paper, we mainly focus on the research of medical image deblur enhancement technology and

underwater medical image enhancement technology. This paper is mainly divided into two parts. As for medical image deblur enhancement technology, we mainly introduce medical deep learning based on a convolutional neural network model. The deep learning model is the main model of medical image deblur enhancement technology, and the color theory and color balance are applied in the medical image enhancement method proposed by us. This paper uses this method to study the application of deep learning in ureteral calculi during pregnancy.

Ureteral stones are one of the most common diseases in urology, and it is not uncommon in clinical work for ureteral stones to progress to urosepsis. Such patients have a rapid onset, rapid progress, and a dangerous condition. Some patients even have systemic inflammatory response syndrome even before the hospital admission. The vital signs have been unstable. If they are not treated promptly and correctly, the condition will quickly get out of control and deteriorate. The case fatality rate is as high as 22%-76%. Pregnant women often develop urinary calculi due to changes in endocrine status in the body, but considering the safety of mothers and infants, conservative medical treatment is often used; for pregnant women who do not respond to medical treatment, appropriate surgical procedures for gravel are very important to ensure the safety of mothers and infants [1].

The incidence of ureteral stones during pregnancy is about 0.026% to 0.0531%. The incidence of menopausal women is higher than that of primiparous women, with an average age of 27 years [2–4]. The incidence during pregnancy is almost the same as that during nonpregnancy, with a ratio of 1 : 1500 to 1 : 200 [5]. 80% to 90% of patients have stone-related clinical manifestations in the second trimester (13 to 27 weeks of gestation) and the third trimester (28 to 40 weeks of gestation) [6–9], and stone-related clinical manifestations in the first trimester (1 to 12 weeks of pregnancy) are rare. Changes in special physiological anatomy during pregnancy lead to a higher incidence of stones on the right than on the left, and calcium phosphate stones are more common [10]. Although the incidence of ureteral stones during pregnancy is relatively low, renal colic caused by ureteral stones is the main reason for nonobstetric hospital admission during pregnancy [11]. The diagnosis and treatment of ureteral stones during pregnancy are special and complicated and often require joint diagnosis and treatment of multiple departments. In the diagnosis and treatment of patients with ureteral stones during pregnancy, the safety of pregnant women and fetuses must be considered. Because radiation (CT) has a clear detrimental effect on fetal development, it is not recommended as a routine diagnosis and treatment technique for urinary stones during pregnancy. Ultrasound examination has no damage to fetal development, so it can be used as a first-line method for diagnosing ureteral stones. Most patients with symptomatic ureteral stones during pregnancy can be relieved by conservative treatments such as spasmolysis, analgesia, and anti-infection. However, for patients with unsatisfactory results of conservative treatment, surgical intervention should be actively given to minimize the potential harm of surgery on pregnant women and fetuses and surgical stimulation-induced threatened abortion.

Ultrasound is a sound wave with a frequency higher than 20000 Hz. It has good directivity and strong reflection ability, and it obtains more concentrated acoustic energy easily. The propagation distance in water is farther than that in air. It can be used for distance measurement, speed measurement, cleaning, sterilization, etc. There are many applications in medicine. Ultrasound is named because its lower frequency limit exceeds the upper limit of human hearing. The working principle of medical ultrasound examination is similar to that of sonar; that is, the ultrasound is emitted into the human body. When it meets the interface in the body, it will reflect and refract, and it may be absorbed and attenuated in human tissue. Because the shape and structure of various tissues of the human body are different, the degree of reflection and refraction and absorption of ultrasonic waves are also different. Doctors are distinguishing by the characteristics of the wave mode, curve, or image reflected by the instrument.

In recent years, the number of patients with ureteral calculus obstruction has also increased in recent years. Ureteral calculi obstruction disease itself will not have a great impact on pregnancy, but complications such as urinary tract infections caused by stones may cause premature delivery or even miscarriage.

For patients with ureteral calculi obstruction in late pregnancy, minimally invasive surgery should be taken in time. In the diagnosis and treatment of patients with ureteral calculi during pregnancy, the safety of pregnant women and fetuses must be considered. Because radiation (CT) has a clear detrimental effect on fetal development, it is not recommended as a routine diagnosis and treatment technique for urinary stones during pregnancy. Ultrasound examination has no damage to fetal development, so it can be used as a first-line method for diagnosing ureteral stones. Most patients with symptomatic ureteral stones during pregnancy can be relieved by conservative treatments such as spasmolysis, analgesia, and anti-infection. However, for patients who are not satisfied with conservative treatment, surgical intervention should be actively given to minimize the potential harm of surgery on pregnant women and fetuses and surgical stimulation-induced threatened abortion.

2. Materials and Methods

2.1. Image Enhancement Based on the Regional Neural Network

2.1.1. Overview of Image Deblur and Enhancement Methods. In order to improve the effect and stability of the blurring artifact removal and enhancement work, to obtain blurring artifact-free images with complete details and saturation and contrast restored, and to improve the efficiency of the work, we introduce the convolutional neural network model into the blurring artifact removal and enhancement work. By establishing the relationship between the media transmittance and the image with blurring artifacts, the model can estimate the media transmittance map of each region in

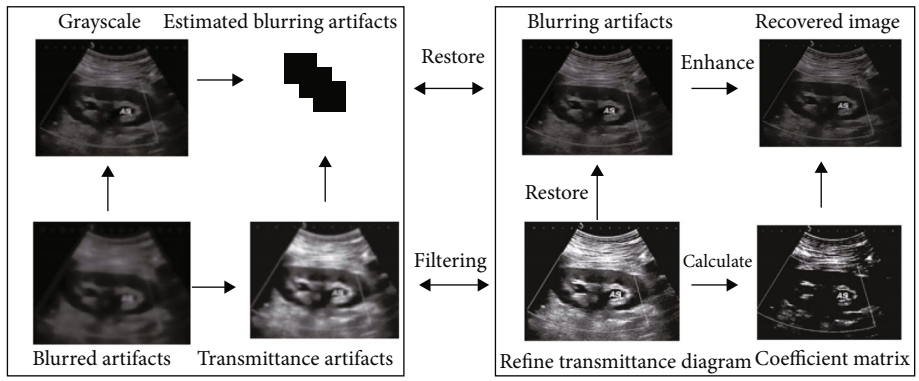

Figure 1: The deblur and image enhancement method.

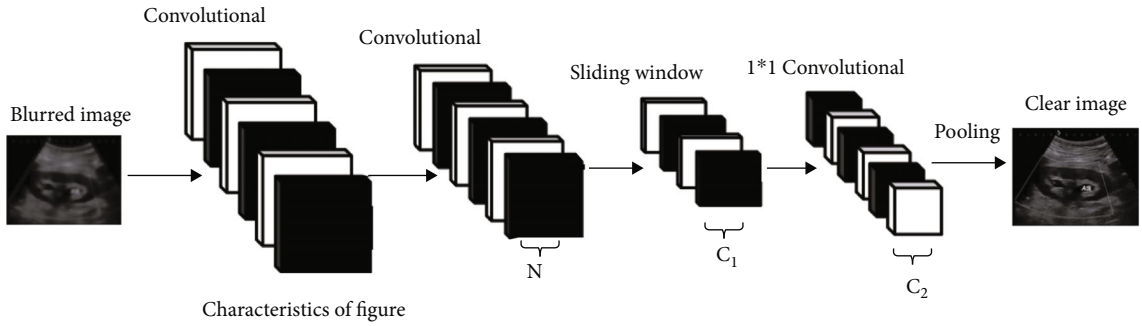

Figure 2: Region-based neural network model processing flow.

the image with blurring artifacts. In order to preserve the integrity of the restored blurring artifact-free image in detail, we also added the detail enhancement operation. In order to enable the operation to complete the autonomous parameter adjustment, we combined this method with the evolutionary algorithm and proposed the evolution-based detail enhancement method. The deblur artifact enhancement method proposed is shown in Figure 1, where the left box is the neural network deblur artifact model, which is used to estimate the media transmittance of the input image with blurring artifacts and the right box is the blurring artifact removal and enhancement image. The left box part is the detail enhancement part, which carries out the detail enhancement operation on the image after the blurring artifact removal enhancement.

2.1.2. Deblurring and Identification of Ureteral Stones in Images Using Region-Based Neural Networks. The region-based neural network model of blurring artifact removal takes the blur images as input and outputs the media transmissivities of blurring artifacts, in which each point corresponds to a local region in the input image. In our design, the neural network model is a full convolution structure, as shown in Figure 2.

The network structure consists of a feature extraction network and a regression subnetwork. The feature extraction network is used to capture blurring artifact-related features in the input image, while the regression subnetwork is used to predict the media transmittance in the local area. In order to connect the two network structures, each position on the N-channel feature map output by the feature extraction network will be transmitted to the sliding windows of the c1 group, and the size of each sliding window is 3×3. For each sliding window, the output is a feature vector in dimension c1, and each feature vector corresponds to a local region in the input image with blurring artifacts. Then, all the eigenvectors are mapped to a set of features in c2 dimension by a set of 1×1 convolution. Obtain the final prediction of the ureteral stone predicted map. The connection between the sliding window and the local region of the blurring artifact image is called the anchor connection. The corresponding local region in the input image can be regarded as the anchor point, and the media transmittance in an anchor point can be approximately a constant. The process is described as follows:

$$\tilde{t}(p) = F(I(i)), iIw_r(P), \tag{1}$$

where F is the deblur artifact neural network model, which takes blurring artifact image I as its input. $t\tilde{}(p)$ is the value of transmittance in the $R * R$ region centered on P.

3. Feature Extraction through the Convolutional Neural Network

In this stage, the network structure is mainly composed of two basic network units, which are used to extract relevant features from input images.

(1) We designed and integrated multiple levels of features. The input x is passed through two separate branches, and the outputs of these branches are then recombined. The specific operation can be expressed as follows:

$$y_a = f(x) + g(x), \tag{2}$$

$$f(x) = W_{|x|} * \theta(W_{3*3} * \theta(x)), \tag{3}$$

$$g(x) = W_{|x|} * \theta\left(W_{|x|} * x\right), \tag{4}$$

where $W_{1\times1}$ and $W_{3\times3}$ represent 1×1 and 3×3 convolution kernels, respectively.

Specifically, $f(x)$ is a convolutional neural network structure based on heterogeneous convolutional kernels, which are composed of 3×3 and 1×1 convolutional layers. Among them, 1×1 convolution operation can capture more details of blurring artifacts, while 3×3 convolution operation can better extract the overall distribution features of blurring artifacts.

(2) A module has a residual structure. Networks with residual modules are easier to optimize and can achieve better performance as the number of layers of the network model increases as defined as follows:

$$y_b = f(x) + x, \tag{5}$$

where y_b represents the underlying mapping and $f(x)$ is a residual mapping constructed by stacking nonlinear layers.

3.1. Patient Information. Eighty pregnant patients with ureteral stones treated in the urology department of our hospital from December 2018 to October 2019 were selected as the research subjects, and all patients met the diagnostic criteria of pregnancy with ureteral stones [12–14]. Exclusion criteria were as follows: suffering from pregnancy combined with hypertension, diabetes, etc.; combined with severe organic and mental diseases such as heart, liver, kidney, and other organs; and combined with other surgical contraindications. Patients and their families signed an informed consent form.

The study was approved by the hospital ethics committee and was filed by the medical department. All patients were divided into the test group and control group according to random number table method, 40 cases in each group. The age of the test group was 24 years to 39 years, the average age was 29.31 ± 3.65 years, the gestational week was 5 weeks to 35 weeks, and the average was 28.63 ± 5.64 weeks. Among them, there were 12 cases in the early pregnancy, 17 cases in the middle period, and 11 cases in the late period; in the control group, the age was 25-40 years, the average age was 29.41 ± 3.55 years, the gestational week was 5 weeks to 36 weeks, and the average was 28.71 ± 5.58 weeks, including 11 cases in early pregnancy, 19 cases in the midterm, and 10 cases in the late period. There was no statistically significant difference in the basic conditions such as age and gestational age between the two groups ($P > 0.05$), and they were comparable.

3.2. Treatment Method. All patients were given symptomatic treatment such as antispasmodic and analgesic after admission. Patients with lower urinary tract infection were treated with conventional anti-infective treatment. Before the operation, routine care was performed [15–17]. Progesterone was injected intramuscularly 20 minutes before the operation. The experimental group underwent cystoscopy double J tube placement: the patient took the bladder lithotomy position for local anesthesia of the urethral mucosa, and we placed the cystoscope through the urethral opening, looked for stones under the endoscope, and guided the guidewire to guide the ureteral opening into the 6F double J tube, and observed the urine drainage situation and routine postoperative B-ultrasound to confirm the placement of the double J tube. The images were then further improved in terms of better resolution and quality by our proposed image enhancement and deblur technique. The control group underwent ureteroscopy lithotripsy: the patient took the bladder lithotomy position and received epidural anesthesia after routine disinfection. A ureteroscope was placed through the urethral orifice, under the guidance of the guidewire into the affected ureter, and a lithotripsy probe was inserted. Continuous pulses are used to crush stones, and the size of the stones does not exceed 3 mm. Large stones can be removed by foreign body forceps, and double J catheters are routinely placed. All patients had double J catheters removed through ureteroscopy 4 weeks after surgery and were given routine anti-infective and symptomatic treatment after surgery.

3.3. Observation Index. Comparing the operation time, time to get out of bed, and hospitalization time of the 2 groups of patients, the operation success rate of the 2 groups of patients and the incidence of complications within 1 month after surgery were counted. Reexamination of B-ultrasound 1 month after the operation revealed that the diameter of the remaining stones was <3 mm, and the patient's symptoms such as nausea, vomiting, and hematuria disappeared, indicating successful operation.

3.4. Statistical Method. SPSS19.0 statistical software was used to process the data. The measurement data was expressed as $x \pm s$, the t-test was used, the count data was expressed as a percentage, and the X^2 test was used. $P < 0.05$ means that the difference was statistically significant.

4. Results

4.1. Comparative Analysis. As shown in Figure 3, the original images (Figure 3(a)) are improved by our proposed image enhancement and deblur technique, which results in images (Figure 3(b)) with better resolution and quality.

4.2. Comparative Analysis of Medical Images. In order to make the treatment of ureteral stones during pregnancy with double J tube placement under ureteroscopy better and more

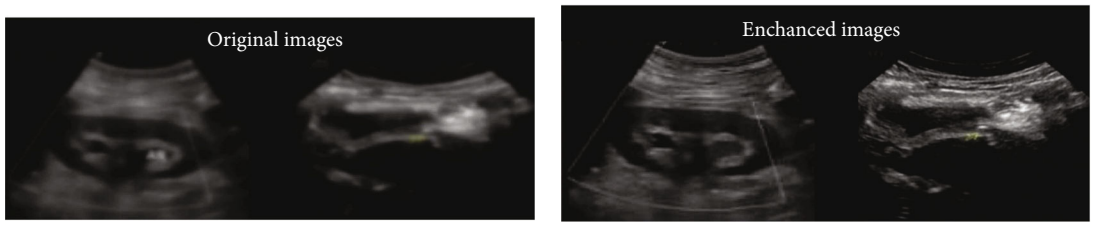

(a) (b)

Figure 3: Comparison of (a) original and (b) improved images.

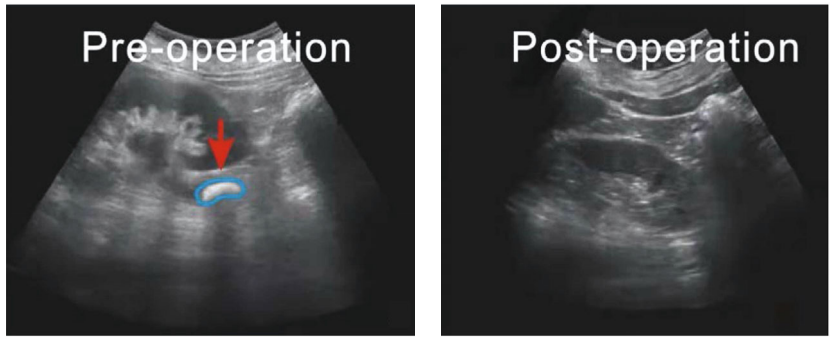

(a) (b)

Figure 4: Ultrasound scan image of ureteral stones in subject 1 ((a) original scan image and (b) postoperative scan image). The arrow points to the location of the ureteral stones. Note that the stones were located much easier by the radiologists after image quality enhancement. This demonstrates that the medical image deblur and denoising algorithms are useful and have strong clinical applicability in accurate medical image diagnosis.

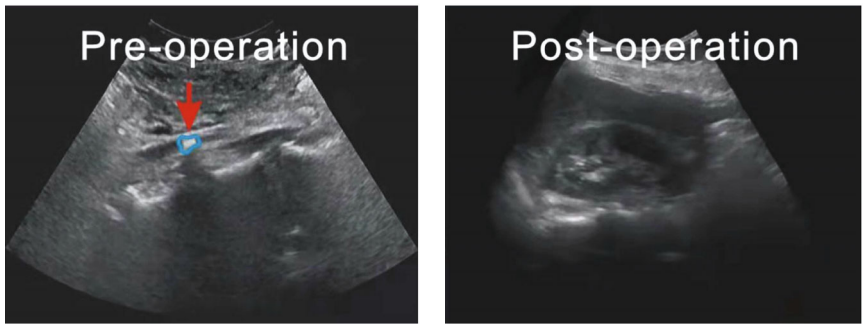

(a) (b)

Figure 5: Ultrasound scan image of ureteral stones in subject 2 ((a) original scan image and (b) postoperative scan image). The arrows in the medical images point to the ureteral stones, which show up clearly after image enhancement.

obvious, this study selected two sample patients for in-depth study and demonstration, which we denote as subject 1 and subject 2. Figure 4 is an ultrasound scan image of subject 1, and Figure 5 is an ultrasound scan image of subject 2. Note that this image comparison is performed after performing denoising and deblur.

4.3. Comparison of Treatment Effect. The total effective rate of the observation group was 100.0%, which is higher than that of the control group (90.0%). The difference between the two groups was statistically significant ($P < 0.05$). The treatment situation is shown in Table 1. The statistical graph of treatment effect is shown in Figure 6.

Table 1: Treatment effect statistics ($n = 40$).

Group	Marked effect	Effective	Invalid	Total efficiency
Observation group	32	8	0	40 (100.0%)
Control group	27	9	4	36 (90.0%)
X^2	10.384	0.323	11.982	11.982
P value	0.001	0.426	0.001	0.001

4.4. Comparison of Adverse Reactions. The adverse reaction rate in the observation group was 5.0%, which was lower than 17.5% in the control group. The difference between

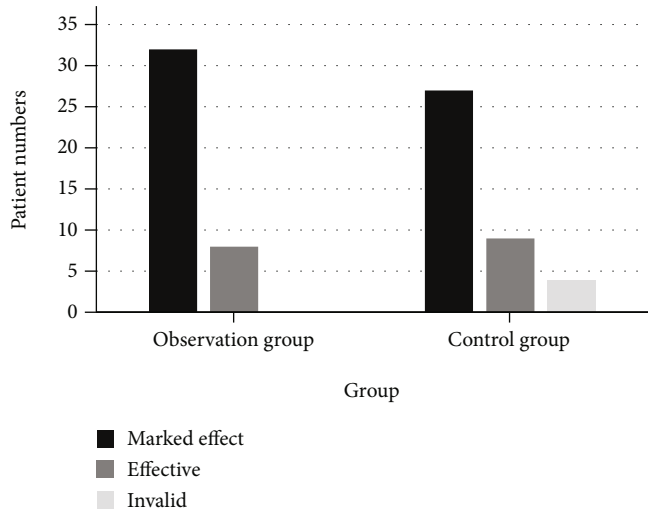

Figure 6: Statistics of the treatment effect.

Table 2: Statistics of the occurrence of adverse reactions ($n = 40$).

Group	Bleeding in the vagina	Mild urinary system infection	Abortion	Premature delivery	Total adverse reaction rate
Observation group	1 (2.5%)	1 (2.5%)	0	0	2 (5.0%)
Control group	3 (7.5%)	2 (5.0%)	1 (2.5%)	1 (2.5%)	7 (17.5%)
X^2	1.094	0.358	1.024	2.093	4.601
P value	0.294	0.540	0.311	0.149	0.032

the two groups was statistically significant ($P < 0.05$). The comparison results are shown in Table 2.

5. Discussion

Ureteral calculi and renal colic during pregnancy are two of the common emergencies for nonobstetric causes of pregnant women. The incidence of ureteral stones in pregnant women is reported to be from 0.04% to 0.5% [18]. Decreased estrogen levels during pregnancy will lead to increased blood calcium, while increased progesterone levels will cause ureteral smooth muscle tension to decrease, thicken the wall, and reduce peristalsis, which will increase the probability of stones staying in the ureter. In addition, the enlarged uterus during pregnancy and the right-handed uterus will also compress the ureter, resulting in obstruction of urinary flow and dilation of the ureter. It is also an important factor that induces the formation of stones and affects the discharge of stones [19, 20]. However, renal colic, urinary tract obstruction, and urinary tract infections caused by ureteral stones during pregnancy may cause miscarriage and premature delivery of pregnant women, and timely and effective treatment is urgently needed. For patients with ureteral calculi during pregnancy with small stone diameters and mild symptoms, conservative treatment can be tried first, including anti-infection, antispasmodic analgesia, and hydration. Some ureteral stones can be discharged by themselves.

Due to changes in hormone levels and physiological structure in pregnant women, ureteral stones are a common disease of pregnant women. In addition to the current dietary changes, the incidence of ureteral stones has also increased year by year. Pregnancy combined with ureteral stones has often multiple stones, which is easy to cause urinary tract obstruction and severe pain. If it is not diagnosed in time and no appropriate treatment is taken, it will cause patients with hydronephrosis [21–23]. Clinical treatment of pregnancy combined with ureteral calculi often adopts conservative medical methods. For patients who do not respond to medical treatment, two surgical methods cystoscopy double J tube placement and ureteroscopy lithotripsy are commonly used [24, 25]. The purpose of this study is to compare the clinical effects of these two surgical methods in the treatment of pregnancy with ureteral stones and to provide a reference for clinical treatment.

In recent years, the incidence of ureteral calculi obstruction has increased in the second and third trimesters of pregnancy. Patients have symptoms such as dysuria, pain, and even hematuria [26, 27]. Mainly due to the increase in kidney circulation during pregnancy, it leads to an increase in water-soluble vitamins in patients' urine, which leads to urinary tract infection [28]. It has also been suggested in the study that an excessively large uterus may also cause compression of the ureter, making it difficult for stones to be expelled. And in recent years, it has been clinically proposed that the incidence of ureteral calculi obstruction in the second and third trimesters of pregnancy is also affected by factors such as physiological changes in pregnant women during pregnancy. For patients with ureteral stone obstruction in the second and third trimesters of pregnancy, early treatment can improve the patient's prognosis and reduce

the incidence of adverse pregnancy outcomes. Clinically, ureteroscopy double J tube placement, ballistic lithotripsy, etc. are commonly used in the treatment of late pregnancy with ureteral calculi obstruction, but the effect after ballistic lithotripsy is not satisfactory, and the stone removal rate is low, so the residual stones are more common. And there are many postoperative complications, which are easy to cause urinary tract infection and affect the prognosis [29].

This paper shows that the operation time of the experimental group with double J tube placement under cystoscopy was significantly shorter than that of the control group, but the hospitalization time was significantly longer than that of the control group; there was no difference in the average time to get out of bed and the success rate of surgery between the two groups.

And there were no postoperative complications. The purpose of surgical treatment of ureteral stones is to relieve urethral obstruction, thereby alleviating the symptoms. The improved ultrasound scans in terms of image quality can assist the radiologists to better locate the ureteral stones. Ureteroscopic lithotripsy is the first surgical method for clinical treatment of ureteral calculi because of its simple operation, accurate treatment effect, and few postoperative complications. It is widely used in clinic, and the surgical method is relatively mature [30]. It can manually adjust the ultrasonic amplitude to ensure the safety of the mother and baby, the treatment time is short, and the hospitalization cost can be reduced. Cystoscopy double J tube placement is a new surgical method that has emerged with the rapid development of material technology in recent years. Some studies have shown that its treatment of pregnancy with ureteral calculi has a significant effect and not only can relieve urinary tract obstruction but also can effectively reduce the renal pelvis. Internal pressure can also drain urine, thereby reducing the risk of infection. Double J tube placement surgery can avoid ultrasonic lithotripsy, maximize the safety of pregnant women and fetuses, and ensure continued pregnancy. The material of the double J tube is stable, and it is not easy to produce stimulation and rejection reaction to the human body and can be left in the body for a long time. Cystoscopy double J tube placement and ureteroscopy lithotripsy have significant effects and safety in the treatment of pregnancy with ureteral calculi [31]. We also realize that it is important that deep learning-based frameworks [32–34] be implemented to deblur or even segment the regions of interest in the medical images for a better analysis. In summary, cystoscopy double J-tube placement and ureteroscopy lithotripsy have significant effects on pregnancy and ureteral calculi, and they have good safety. The clinical method can be selected according to the patient's wishes and specific circumstances.

6. Conclusion

The ureteroscope has the advantages of less trauma and less infection, and if residual gravel is found in the actual lithotripsy treatment or the ureter is twisted, it can be reinserted into the soft ureteroscope to clean it again, which can significantly improve the rate of stone removal and prevent the recurrence of stones. At the same time, the double J tube is placed in the lithotripsy, the lens body and the optical fiber are always unified, and the advantage of treating ureteral stone obstruction is more obvious.

The results of the study show that after ureteroscopy double J tube implantation, the patient's stone removal and drainage are significantly better than those of patients with sinus lithotripsy, suggesting that the treatment effect of ureteroscopy double J tube implantation is more ideal. The results of this study are consistent with this. And in this study, the observation group had a higher success rate of lithotripsy than the control group, and the total adverse reaction rate was lower than that of the control group, suggesting that ureteroscopy double J tube placement surgery has higher safety and successful operation.

According to the influence of medical image quality, we propose the deblur enhancement method and medical image enhancement method, respectively. In medical image enhancement methods to the blurring modeling based on a deep learning problem by a deep neural network model to estimate the blurring image transmission rate of media and through the inverse operation of deep learning, restore clear medical images and put forward a detail enhancement algorithm based on evolutionary finish to restore clear details of medical image enhancement operation. Finally, we apply the simplified deblur model to low computing power.

In summary, combined with medical image deblur techniques and ultrasound scanning, the effect of ureteroscopy double J tube implantation in the treatment of midlate pregnancy with ureteral stone obstruction is ideal, which greatly improves clinical symptoms, promotes recovery, and reduces the incidence of adverse reactions.

Data Availability

The image data used to support the findings of this study have been deposited in the renal and ureteral stone dataset (https://www.payititi.com/nlpdataset/show-1437.html).

Conflicts of Interest

The authors declare that there is no conflict of interest in this paper.

Acknowledgments

The authors are thankful for the relevant information of patients provided by the urology department of their hospital.

References

[1] S. T. Tan, X. N. Chen, M. Sun, and B. Wu, "Reply to letter to the editor entitled "replay to the comparation of effects and security of double-J stent retention and ureteroscopy lithotripsy in the treatment of symptomatic ureteral calculi during pregnancy"," *European Journal of Obstetrics & Gynecology*, vol. 229, p. 199, 2018.

[2] P. Soma-Pillay, C. Nelson-Piercy, H. Tolppanen, and A. Mebazaa, "Physiological changes in pregnancy," *Cardiovascular Journal of Africa*, vol. 27, no. 2, pp. 89–94, 2016.

[3] G. Masselli, M. Derme, M. G. Bernieri et al., "Stone disease in pregnancy: imaging-guided therapy," *Insights into Imaging*, vol. 5, no. 6, pp. 691–696, 2014.

[4] M. E. Rivera, K. L. McAlvany, T. S. Brinton, M. T. Gettman, and A. E. Krambeck, "Anesthetic exposure in the treatment of symptomatic urinary calculi in pregnant women," *Urology*, vol. 84, no. 6, pp. 1275–1278, 2014.

[5] B. Matlaga and M. Semins, "Management of urolithiasis in pregnancy," *International Journal of Women's Health*, vol. 4, pp. 77–79, 2013.

[6] Y. Bozkurt, M. Atar, N. Penbegul, H. Soylemez, and A. A. Sancaktutar, "The efficacy and safety of ureteroscopy for ureteral calculi in pregnancy: our experience in 32 patients," *Urological Research*, vol. 6, pp. 66–70, 2012.

[7] E. B. Johnson, A. E. Krambeck, W. M. White et al., "Obstetric complications of ureteroscopy during pregnancy," *The Journal of Urology*, vol. 188, pp. 89–92, 2012.

[8] H. J. Evans and T. A. Wollin, "The management of urinary calculi in pregnancy," *Current Opinion in Urology*, vol. 11, no. 4, pp. 379–384, 2001.

[9] A. A. Shokeir, M. R. Mahran, and M. Abdulmaaboud, "Renal colic in pregnant women: role of renal resistive index," *Urology*, vol. 55, no. 3, pp. 344–347, 2000.

[10] M. J. Semins and B. R. Matlaga, "Management of stone disease in pregnancy," *Current Opinion in Urology*, vol. 20, no. 2, pp. 174–177, 2010.

[11] A. E. Ross, H. Shelly, and B. R. Matlaga, "Kidney stones during pregnancy: an investigation into stone composition," *Urological Research*, vol. 3, pp. 22–29, 2008.

[12] R. H. Wachsberg, "Unilateral absence of ureteral jets in the third trimester of pregnancy: pitfall in color Doppler US diagnosis of urinary obstruction," *Radiology*, vol. 209, no. 1, pp. 279–281, 1998.

[13] M. Mitterberger, G. M. Pinggera, E. Maier et al., "Value of 3-dimensional transrectal/transvaginal sonography in diagnosis of distal ureteral calculi," *Journal of Ultrasound in Medicine*, vol. 26, no. 1, pp. 19–27, 2007.

[14] B. S. Hertzberg, B. A. Carroll, J. D. Bowie, S. S. Paine, and M. A. Kliewer, "Doppler US assessment of maternal kidneys: analysis of intrarenal resistivity indexes in normal pregnancy and physiologic pelvicaliectasis," *Radiology*, vol. 4, pp. 34–40, 1993.

[15] A. A. Thomas, A. Z. Thomas, S. C. Campbell, and J. S. Palmer, "Urologic emergencies in pregnancy," *Urology*, vol. 76, no. 2, pp. 453–460, 2010.

[16] S. Goldberg-Stein, B. Liu, and F. Peter, "Body CT during pregnancy: utilization trends, examination indications, and fetal radiation doses," *American Journal of Roentgenology*, vol. 2, pp. 30–40, 2011.

[17] N. Tirada, D. Dreizin, and N. J. Khati, "Imaging pregnant and lactating patients," *Radiographics*, vol. 4, pp. 78–82, 2015.

[18] S. A. Goldberg-Stein, B. Liu, and P. F. Hahn, "Radiation dose management: part 2, estimating fetal radiation risk from CT during pregnancy," *American Journal of Roentgenology*, vol. 11, pp. 92–97, 2008.

[19] F. M. Smaill and J. C. Vazquez, "Antibiotics for asymptomatic bacteriuria in pregnancy," *Cochrane Database of Systematic Reviews*, vol. 1, pp. 34–40, 2019.

[20] K. L. Burgess, M. T. Gettman, L. J. Rangel, and A. Krambeck, "Diagnosis of urolithiasis and rate of spontaneous passage during pregnancy," *The Journal of Urology*, vol. 186, no. 6, pp. 2280–2284, 2011.

[21] B. K. Somani, A. Dellis, E. Liatsikos, and A. Skolarikos, "Review on diagnosis and management of urolithiasis in pregnancy: an ESUT practical guide for urologists," *World Journal of Urology*, vol. 35, no. 11, pp. 1637–1649, 2017.

[22] P. B. Bookstaver, C. M. Bland, B. Griffin, K. R. Stover, L. S. Eiland, and M. McLaughlin, "A review of antibiotic use in pregnancy," *Pharmacotherapy*, vol. 35, no. 11, pp. 1052–1062, 2015.

[23] M. E. Rivera, K. L. McAlvany, T. S. Brinton, M. T. Gettman, and A. Krambeck, "Anesthetic exposure in the treatment of symptomatic urinary calculi in pregnant women," *Urology*, vol. 84, no. 6, pp. 1275–1278, 2014.

[24] G. Masselli, M. Derme, F. Laghi, E. Polettini, R. Brunelli, and M. L. Framarino, "Imaging of stone disease in pregnancy," *Abdominal Imaging*, vol. 38, no. 6, pp. 1409–1414, 2013.

[25] Z. F. Wang, L. Xu, Z. X. Su, C. Yao, and Z. Chen, "Invasive management of proximal ureteral calculi during pregnancy," *Urology*, vol. 7, pp. 23–28, 2013.

[26] Y. Song, X. Fei, and Y. S. Song, "Diagnosis and operative intervention for problematic ureteral calculi during pregnancy," *International Journal of Gynecology & Obstetrics*, vol. 1, pp. 33–36, 2013.

[27] M. J. Semins and B. R. Matlaga, "Kidney stones and pregnancy," *Advances in Chronic Kidney Disease*, vol. 20, no. 3, pp. 260–264, 2013.

[28] C. Roger, "Definitions for sepsis and organ failure," *Critical Care Medicine*, vol. 20, no. 6, pp. 724–726, 1992.

[29] C. L. Xu, H. Tang, X. F. Gao, X. Gao, B. Yang, and Y. B. Sun, "Management of forgotten ureteral stents with holmium laser," *Lasers in Medical Science*, vol. 2, pp. 89–92, 2009.

[30] B. H. Chew, B. E. Knudsen, and J. D. Denstedt, "The use of stents in contemporary urology," *Current Opinion in Urology*, vol. 14, no. 2, pp. 111–115, 2004.

[31] O. Fainaru, B. Almog, R. Gamzu, J. B. Lessing, and M. Kupferminc, "The management of symptomatic hydronephrosis in pregnancy," *BJOG: An International Journal of Obstetrics and Gynaecology*, vol. 109, no. 12, pp. 1385–1387, 2002.

[32] H. Z. Tang, G. Zhao, and T. Ouyang, "Two-phase deep learning model for short-term wind direction forecasting," *Renewable Energy*, vol. 173, pp. 1005–1016, 2021.

[33] J. S. Shi, Y. G. Ye, D. X. Zhu, L. T. Su, Y. F. Huang, and J. L. Huang, "Automatic segmentation of cardiac magnetic resonance images based on multi-input fusion network," *Computer Methods and Programs in Biomedicine*, vol. 209, article 106323, 2021.

[34] J. S. Shi, Y. G. Ye, D. X. Zhu, L. T. Su, Y. F. Huang, and J. L. Huang, "Comparative analysis of pulmonary nodules segmentation using multiscale residual U-Net and fuzzy C-means clustering," *Computer Methods and Programs in Biomedicine*, vol. 209, article 106332, 2021.

Hindawi
Computational and Mathematical Methods in Medicine
Volume 2021, Article ID 1972662, 13 pages
https://doi.org/10.1155/2021/1972662

Research Article

A Deep Learning-Based Classification Method for Different Frequency EEG Data

Tingxi Wen,[1,2] Yu Du,[1] Ting Pan,[1] Chuanbo Huang,[1] and Zhongnan Zhang[3]

[1]*College of Engineering, Huaqiao University, Quanzhou 362021, China*
[2]*Postdoctoral Workstation of Linewell Software Company Limited, Quanzhou 362000, China*
[3]*School of Informatics, Xiamen University, Xiamen, China*

Correspondence should be addressed to Chuanbo Huang; huangchuanbo@hqu.edu.cn
and Zhongnan Zhang; zhongnan_zhang@xmu.edu.cn

Received 30 May 2021; Revised 26 July 2021; Accepted 13 September 2021; Published 21 October 2021

Academic Editor: Kelvin Wong

In recent years, the research on electroencephalography (EEG) has focused on the feature extraction of EEG signals. The development of convenient and simple EEG acquisition devices has produced a variety of EEG signal sources and the diversity of the EEG data. Thus, the adaptability of EEG classification methods has become significant. This study proposed a deep network model for autonomous learning and classification of EEG signals, which could self-adaptively classify EEG signals with different sampling frequencies and lengths. The artificial design feature extraction methods could not obtain stable classification results when analyzing EEG data with different sampling frequencies. However, the proposed depth network model showed considerably better universality and classification accuracy, particularly for EEG signals with short length, which was validated by two datasets.

1. Introduction

Epilepsy is characterized by recurrent seizures caused by the abnormal discharge of brain neurons, which often bring physical and psychological harm to patients. Approximately 50 million epilepsy patients have been documented globally, and epilepsy has become one of the most common nervous system diseases endangering human health worldwide. Brain wave is a synaptic postsynaptic potential generated by numerous neurons when the brain is active. It can record brain wave changes during brain activity and reflect the electrophysiological activities of the cerebral cortex or scalp surface of brain neurons [1]. Accordingly, brain wave analysis has become an effective and important method for the study of epilepsy.

Since the 1980s, scholars have been conducting research on epilepsy based on electroencephalography (EEG), among which the identification of epilepsy by analyzing EEG data is one of the important research contents [2]. With the development of computer science and technology, numerous studies have focused on the classification of features extracted from EEG signals by using a computer classification model [3, 4]. Such a research often follows the following steps: EEG data acquisition and prepossessing, feature extraction, classification model training, and data prediction. Feature extraction from EEG data is one of the most important steps. Numerous methods are used to extract EEG features, including time-domain, frequency-domain, and time-frequency analyses and chaotic features [5–7]. Moreover, some studies have combined or redesigned these methods to obtain new features, thereby eventually achieving good classification results [8–10].

With the development of science and technology, the accuracy of medical EEG acquisition equipment has been improved. In addition, some portable EEG acquisition equipment has been developed. For example, emotive has been widely used in brain-computer interface [11–13] because it is lightweight and inexpensive and has similar performance to medical equipment. However, although a variety of medical devices or portable EEG acquisition

devices produce numerous EEG data that can be used for epilepsy research, the different data sources result in a lack of uniform data formats, such as different sampling frequencies, different signal lengths, and different sampling channels. The inconsistency of data specifications often affects the features obtained by traditional feature extraction methods. This situation raises a question on how to improve the ability of classification methods to adapt to new data. Hence, the universality of classification methods should be improved, while ensuring the enhanced detection and recognition of EEG data.

At present, in-depth learning technology is a popular research area. Given this technology's autonomous learning characteristics from data, it can directly skip the manual design features and extraction process in the traditional methods, avoid the difficulties of manual design features in traditional methods, and manually adjust numerous parameters. In-depth learning technology can accomplish numerous tasks that are difficult to complete in the traditional methods [14]. Some researchers have studied EEG via a deep network [15]. Tabar and Halici [16] converted one-dimensional (1D) brain waves into two-dimensional (2D) image data through short-time Fourier transform and accessed the deep network for classification. Bashivan et al. [17] converted the frequency bands extracted from brain waves into topographical maps (2D images) through spectral power and classified the images into depth networks. Hosseini et al. [18] used an in-depth learning method based on a cloud platform to propose a solution for epilepsy prevention and control. Xun et al. [19] and Masci et al. [20] proposed a coding method for epileptic EEG signals based on the deep network. However, the majority of these studies have focused on regular data, such as the same frequency and same length of the sample data. In the feature design aspect, these studies have converted 1D EEG data into 2D image data in advance and classified the features via the deep network. The current study constructed a classification model based on the deep convolution network to automatically learn the characteristics of EEG and adapt to the EEG data of different sampling frequencies and lengths. Our method (including network model and training method) can considerably identify different forms of EEG data.

The remainder of this paper is organized as follows. Section 2 first simulates the EEG data with different frequencies. Thereafter, we classify the data with existing manual feature design classification methods and indicate their disadvantages compared with our model. Section 3 provides details of our proposed network model, training methods, and data processing methods. Section 4 compares our model with existing methods and discusses the advantages of our model. Section 5 presents the summary.

2. Experimental Result

This section first describes two open datasets and classifies and compares the EEG data at different sampling frequencies using an artificial design feature method and deep network autonomous feature learning method.

2.1. Data Description and Data Synthesis

2.1.1. Dataset 1. The first dataset comes from the dataset published by Andrzejak et al. [21]. This dataset consists of five subsets (represented as A to E). Each subset contains 100 EEG signals of 23.6 sec in length, and the sampling frequency is 173.6 Hz. The data include records of healthy and epileptic patients. Among them, there were two subsets of EEG recorded during epileptic seizures, which had 200 samples, and one set of EEG records in the seizure period had 100 samples. Figure 1 shows two types of signals in epilepsy patients during nonepilepsy and epilepsy. They are classified as F and S, respectively. Among them, 200 samples are classified as F and 100 samples are classified as S. Class F is labeled as a nonepileptic seizure EEG signal, while class S is a seizure signal.

2.1.2. Dataset 2. The second dataset was collected by Boston Children's Hospital [22]. EEG signals are obtained by measuring electrical activity in the brain by connecting multiple electrodes to a patient's scalp. Data length is approximately from half an hour to one hour, including epileptic seizure and nonepileptic data. The sampling frequency of each data sample is 256 Hz, which contains 23–25 channels, and the sample length is approximately 921600. The dataset has 24 subjects. The first 10 subjects are selected for experiment. Each channel in the sample has a name; for example, the first channel was named FP1-F7 (see Figure 2). We selected one of the 23 channels for our study. When epilepsy occurs, the EEG signal will fluctuate substantially, resulting in an increase in the signal variance. We make channel selection based on variance [23]. The method is as follows. We calculate the variance of each channel in each sample, with each sample having a channel with the largest variance, and derive the statistics on these channels thereafter with the largest variance in the sample. The "FT9-FT10" channel has the highest number of occurrences, thereby leading us to choose this channel. A total of 200 EEG samples of epileptic seizures and 200 nonepileptic seizures were randomly intercepted on the FT9-FT10 channel. The length of each signal sample was 4096 (or 16 sec). Class F remains to be labeled as a nonepileptic seizure EEG signal in dataset 2, while class S is a seizure signal.

The signal is a cortical signal, the signal on the left side of the black line is no epilepsy, and the signal on the right side of the black line is epilepsy, as shown in Figure 2.

The two datasets are the most widely used in the current research on epilepsy data classification and detection. Given that the sampling frequency of signals in the two datasets is fixed, we use the signal processing library in SciPy [24] to obtain additional EEG data with different sampling frequencies, particularly to resample the existing data and obtain a new sampling frequency dataset thereafter. For example, the sampling frequency of the original dataset 1 is 173.61 Hz, and the original dataset is resampled at 163.61, 153.61, 143.61, 133.61, 123.61, 113.61, and 103.61 Hz (decreasing at 10 Hz). In this example, 1-0 represents the original 173.61 Hz data and 1-1 represents the 163.61 Hz data. By analogy, the resampled new dataset is shown in

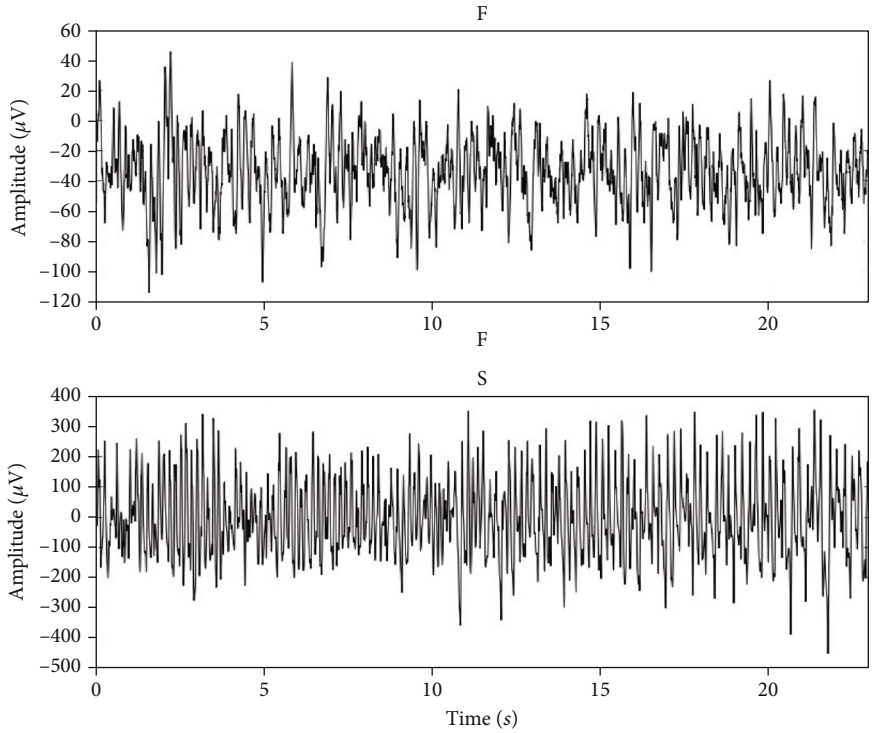

Figure 1: Signal samples of categories F and S in dataset 1.

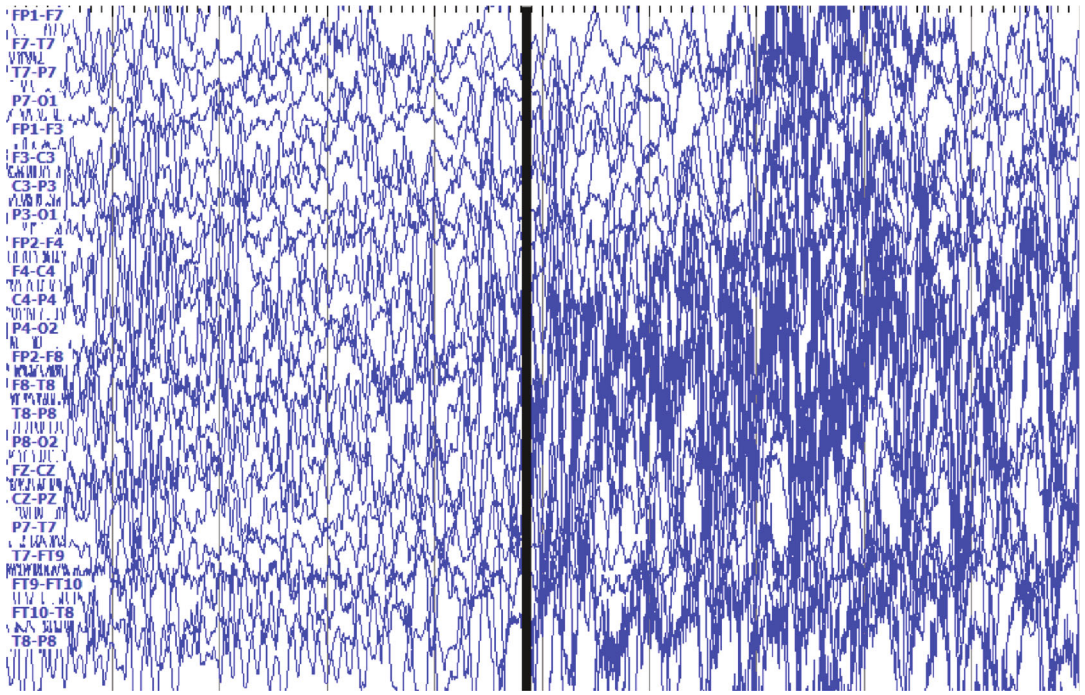

Figure 2: Signal samples of dataset 2.

Table 1. Table 2 shows that for the resampling of data 2, the sampling frequency of the original dataset 2 is 256 Hz. In this example, the original dataset 2 is resampled at 236, 216, 196, 176, 156, 136, and 116 Hz (decreasing at 20 Hz). Hence, new datasets can be obtained, in which 2-0 still represents data of the original dataset 2.

2.2. Classification Results Based on the Artificial Design Feature Extraction Method. Features or design new features should be selected for classification based on the artificial design feature extraction method. The current study selects the feature extraction methods [25–27], which have a good classification effect in the existing research, including

Table 1: List of datasets obtained after resampling for dataset 1.

Dataset name	Sample frequency (Hz)	Sample length	Time length (s)
1-0	173.61	4096	23.6
1-1	163.61	3861	23.6
1-2	153.61	3625	23.6
1-3	143.61	3153	23.6
1-4	133.61	3389	23.6
1-5	123.61	2917	23.6
1-6	113.61	2681	23.6
1-7	103.61	2445	23.6

Table 2: List of datasets after resampling for dataset 2.

Dataset name	Sample frequency (Hz)	Sample length	Time length (s)
2-0	256	4096	16
2-1	236	3776	16
2-2	216	3616	16
2-3	196	3136	16
2-4	176	2816	16
2-5	156	2496	16
2-6	136	2176	16
2-7	116	1856	16

Table 3: Classification accuracy of various classifiers on 1-0 using the artificial design feature method.

k-fold	*k*-NN	LDA	SVM	DT	MLP	GNB	AVG
3	0.9066	0.8703	0.9265	0.8264	0.7894	0.6966	0.836
5	0.92	0.9067	0.9533	0.83	0.8133	0.7367	0.86
10	0.9333	0.91	0.9633	0.8333	0.8567	0.7467	0.8739

Table 4: Classification accuracy of various classifiers on raw data 2 using the artificial design feature method.

k-fold	*k*-NN	LDA	SVM	DT	MLP	GNB	AVG
3	0.975	0.9776	0.98	0.95	0.9726	0.9377	0.9655
5	0. 9725	0.9775	0. 9775	0. 9475	0. 98	0.96	0.9692
10	0.975	0.9775	0.975	0.955	0.98	0.955	0.9696

Table 5: Classification accuracy of the 5-fold classifier for datasets 1-0 to 1-7.

Dataset	*k*-NN	LAD	SVM	DT	MLP	GNB	AVG
1-0	0.92	0. 9067	0.9533	0.83	0.8133	0.7367	0.8600
1-1	0.93	0.9300	0.95	0.8067	0.84	0.7367	0.8656
1-2	0.9367	0.94	0.9567	0.8233	0.8167	0.72	0.8656
1-3	0.9233	0.91	0.9367	0.78	0.81	0.6833	0.8406
1-4	0.91	0.9033	0.9567	0.81	0.7667	0.68	0.8378
1-5	0.8833	0.8733	0.91	0.8033	0.77	0.6833	0.8206
1-6	0.8667	0.8767	0.89	0.77	0.8033	0.6767	0.8139
1-7	0.8833	0.9233	0.9267	0.8	0.78	0.6867	0.8333

Table 6: Classification accuracy of the 5-fold classifier for datasets 2-0 to 2-7.

Dataset	*k*-NN	LAD	SVM	DT	MLP	GNB	AVG
2-0	0.9725	0.9775	0.9775	0.9475	0.98	0.96	0.9692
2-1	0.9275	0.965	0.975	0.8825	0.9575	0.845	0.9254
2-2	0.9425	0.9675	0.975	0.9025	0.97	0.88	0.9396
2-3	0.9325	0.955	0.955	0.86	0.9475	0.8175	0.9112
2-4	0.9225	0.955	0.95	0.88	0.94	0.8175	0.9108
2-5	0.91	0.9575	0.95	0.7975	0.9225	0.75	0.8812
2-6	0.93	0.9575	0.965	0.7975	0.9425	0.8425	0.9058
2-7	0.925	0.9275	0.96	0.8625	0.92	0.855	0.9083

integral absolute value, root mean square, waveform length, sample entropy, Lee's index, Hurst index, DFA index, and multifractal feature. After feature extraction, several common classifiers are selected from the scikit-learn library [28], including *k*-nearest neighbor (*k*-NN), linear classifier (LDA), support vector machine (SVM), decision tree (DT), multilayer perceptron (MLP), and Gaussian naive Bayes (GNB). These classification algorithms adopt self-contained parameters in the library. Tables 3 and 4 use the aforementioned features and classifiers to classify datasets 1-0 and 2-0, respectively. The table shows the results of the 3-, 5-, and 10-fold cross-validations. The last column of AVG is the average classification accuracy of each classifier. SVM, which is the commonly used classifier, achieves good classification accuracy and validates the effectiveness of the feature extraction methods.

Tables 5 and 6 show the accuracy of the 5-fold classification of datasets by various classifiers.

Table 5 shows that under different sampling frequencies, traditional classification methods based on artificial design feature have different classification results in different classifiers. For example, the classification results of SVM should be optimized to GNB. When sampling frequency decreases, classification accuracy fluctuates. For example, the classification accuracy of *k*-NN decreases, and those of LDA and SVM change substantially. Table 6 shows that the average accuracy of the last column is higher than that of Table 5. This result indicates that the classification method based on artificial design features can achieve superior classification results in datasets 2-0 to 2-7. However, the classification accuracy of data with different sampling frequencies continues to fluctuate significantly. Figure 3 shows the average classification accuracy of two datasets based on artificial design features at different sampling frequencies. The classification results of datasets 1-0 to 1-7 are not ideal, while datasets 2-0 to 2-7 have better classification results. These synthesizations show that the method based on artificial design features depends on the selection of classifiers. Moreover, this method's characteristics are sensitive to the data of different sampling frequencies, which substantially reduces the applicability of the method.

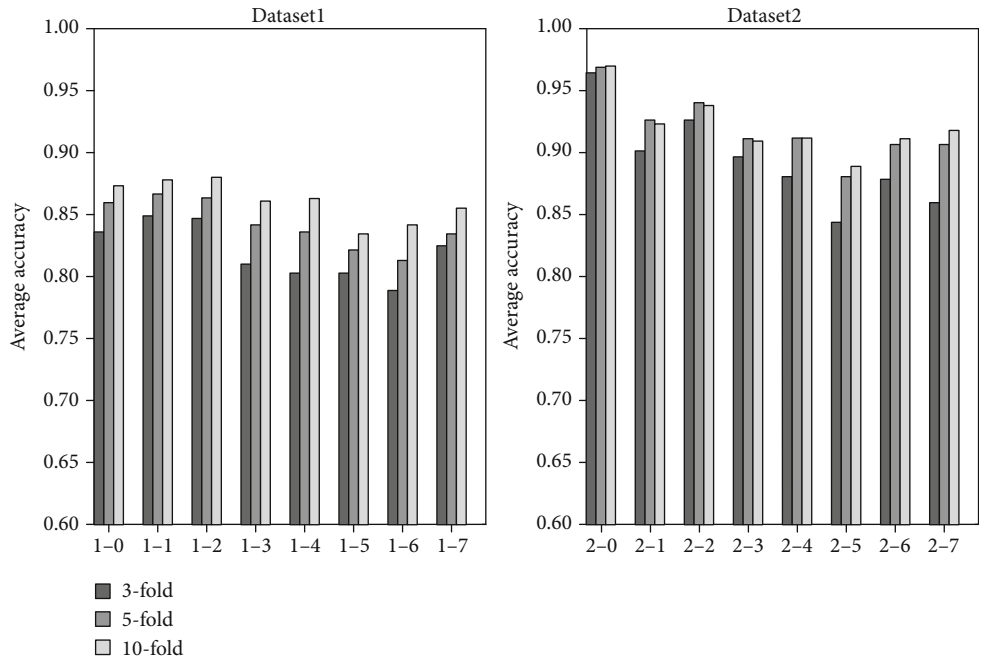

Figure 3: Generation of new datasets for the two original datasets and the average classification results of 3-, 5-, and 10-fold.

Table 7: Model categorization datasets generated by dataset 1.

k-fold	1-0	1-1	1-2	1-3	1-4	1-5	1-6	1-7
3	0.9832	0.9663	0.9630	0.9764	0.9697	0.9697	0.9596	0.9562
5	0.9800	0.9667	0.9667	0.9500	0.9733	0.9700	0.9700	0.9833
10	0.9700	0.9833	0.9800	0.9633	0.9867	0.9800	0.9700	0.9800

Table 8: Model categorization datasets generated by dataset 2.

k-fold	2-0	2-1	2-2	2-3	2-4	2-5	2-6	2-7
3	0.9318	0.9192	0.9040	0.9091	0.8813	0.8990	0.9015	0.9192
5	0.9325	0.9475	0.9200	0.9150	0.9275	0.9400	0.9300	0.9375
10	0.9350	0.9450	0.9100	0.9275	0.9325	0.9325	0.9250	0.9525

2.3. Classification Results Based on the Convolutional Neural Network. This section presents the classification results of the self-learning feature method based on the convolutional neural network (CNN) for the preceding datasets. Tables 7 and 8 categorize the two datasets at different sampling frequencies. A comparison of Tables 5 and 6 indicates that our model has more stable classification results and better classification accuracy.

The results of training and testing for the same sampling frequency data are listed in Tables 1 to 6. Whether or not these methods are effective in the case of mixing various frequency data needs further analysis. Moreover, whether or not a classification model can train the datasets of existing sampling frequencies and effectively predict the data of new sampling frequencies should be further discussed. For example, the model is trained with the 173.61 Hz and 163.61 Hz data to predict the type of the 153.61 Hz data. Given these problems, the third part of this paper explains the solutions and further discusses and analyzes these problems in the fourth part.

3. Methodology

This section first describes the model structure based on CNN and the training methods for different length sample data.

3.1. Classification Model Based on CNN. Numerous methods of feature extraction are based on artificial design. However, when the data changes, the classification effect based on the general feature extraction method is not stable. In this study, the classification model based on CNN can independently learn and classify data features, including the two steps of feature extraction and classification (see Figure 4). It attempts to obtain good and stable classification results

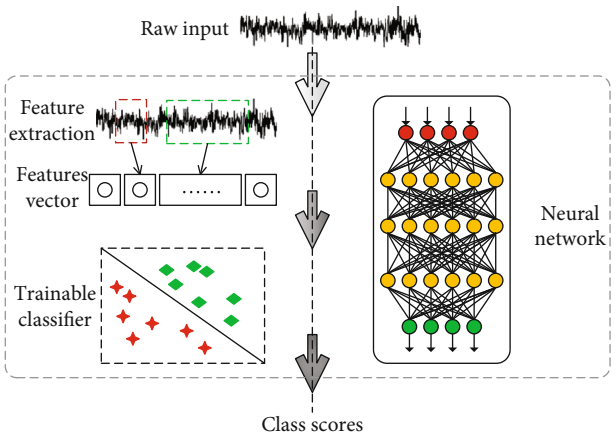

FIGURE 4: Process diagram of the artificial design features and network learning model.

when facing different sampling frequencies or different lengths of the sample data.

The left side is a classification process based on artificial design features, which requires two steps. The right side is to input data into the network model and output the classification results directly, as shown in Figure 4.

CNN is a feedforward neural network that improves the classification ability of patterns by posterior probability. The network mainly includes convolutional, pooling, fully connected, and softmax layers. The convolution layer convolutes the input signal data through different convolution kernels to obtain the feature map (i.e., number of convolution kernels equals the number of feature maps). The pooling layer is the process of downsampling the feature map obtained from the convolution operation of the upper layer. The network often increases the network depth by iterating the convolutional and pooling layers. Meanwhile, the fully connected layer connects all feature maps from the upper layer to the hidden layer of a common neural network and eventually outputs the classification results through the softmax layer. This study proposes a multilayer network with cubic iterative convolutional and pooling layers, fully connected layer, and softmax layer to classify EEG data (hereinafter referred to as CNN-E). The model classifies the one-dimensional EEG data of a single channel and makes the input sample data X. The convolutional layer is equivalent to the feature extractor. This layer uses multiple convolution kernels to convolute x and obtains several feature maps that can keep the main components of the input signal. The convolution calculation formula is as follows:

$$f_n^k = g_k\left(\sum_{\forall m}\left(f_m^{k-1} * w_{m,n}^k\right) + b_n^k\right), \tag{1}$$

where f_n^k represents the feature map of layer k, f_m^{k-1} is the feature map of the upper layer, $w_{m,n}^k$ represents the convolution kernels of the mth feature map of layer $k-1$ to the nth feature map of layer k, b_n^k is the neuron bias, and $g_k(\cdot)$ is the activation function. When $k=1$, that is, the first convolution operation on sample data, $f_m^{k-1} = x$ and $M=1$, because only one feature map in the upper layer is x and N is the number of convolution kernels. Given that the input data X is one-dimensional, the feature map f_n^k output by convolution operation is also one-dimensional. In this model, the pooling operation divides f_n^k with length l into J regions of equal length without overlap, and each region has i/j elements and extracts the maximum value from each region. Hence, the size of the feature map can be reduced to a downsampling. In this way, the strongest features in each region can be selected, and the ability to distinguish the overall features of the model can be enhanced. After the pooling operation, f_n^k changes from the original length l to j, where the maximum pooling operation is $p_k(f_n^{k-1}, i)$, and $i = l/j$ is the reduction ratio of the feature map. Thereafter, the pooling operation is as follows:

$$s_n^k = p_k\left(f_n^{k-1}, i\right). \tag{2}$$

Each neuron in the fully connected layer connects to all neurons in the upper layer f_n^{k-1}. The output of all neurons in the upper layer f_n^{k-1} is mapped to a dimension array V by reshape operation, and V is input to the fully connected layer. Thereafter, the fully connected layer can be expressed as follows:

$$c = g_c(v * w_c + b_c), \tag{3}$$

where w_c and b_c are the weights and biases, respectively, of the fully connected layer and c is the output of the fully connected layer. Lastly, the final result is output via softmax, and the operation is as follows:

$$y = \text{softmax}(c). \tag{4}$$

The classification result y is obtained.

Assuming that there are N training samples, $x^{(i)}$ represents a sample labeled $l^{(i)}$. Sample $x^{(i)}$ is calculated by the model to obtain $y^{(i)}$. Thereafter, cross-entropy is used as the loss function of the model. The formula is as follows:

$$\text{Loss}(x) = -\sum_i l^{(i)} \log\left(y^{(i)}\right). \tag{5}$$

The loss function of the network model is optimized by the SGD [26] optimizer.

3.2. Model Training. Section 3.1 explained the basic structure and principle of the CNN-E model. This section further introduces the parameter setting and model training of the model.

Figure 5 shows the CNN-E frame diagram of the neural network model used in this research. Given that a sample signal is stored in an array, each small rectangle in the graph represents the elements of the signal, and numerous small rectangles constitute a sample signal. The length of the input sample signal is 4096. After the calculation of three

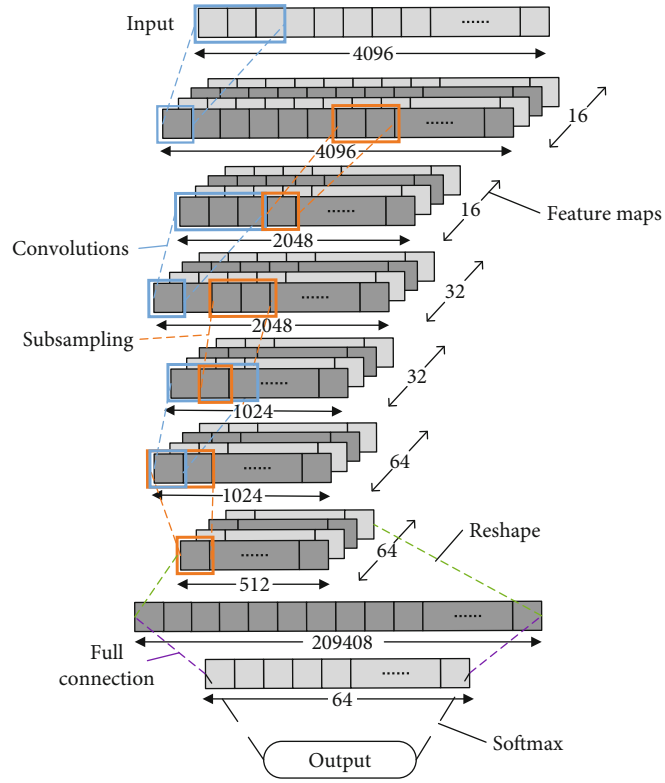

Figure 5: CNN-E framework diagram of the neural network model.

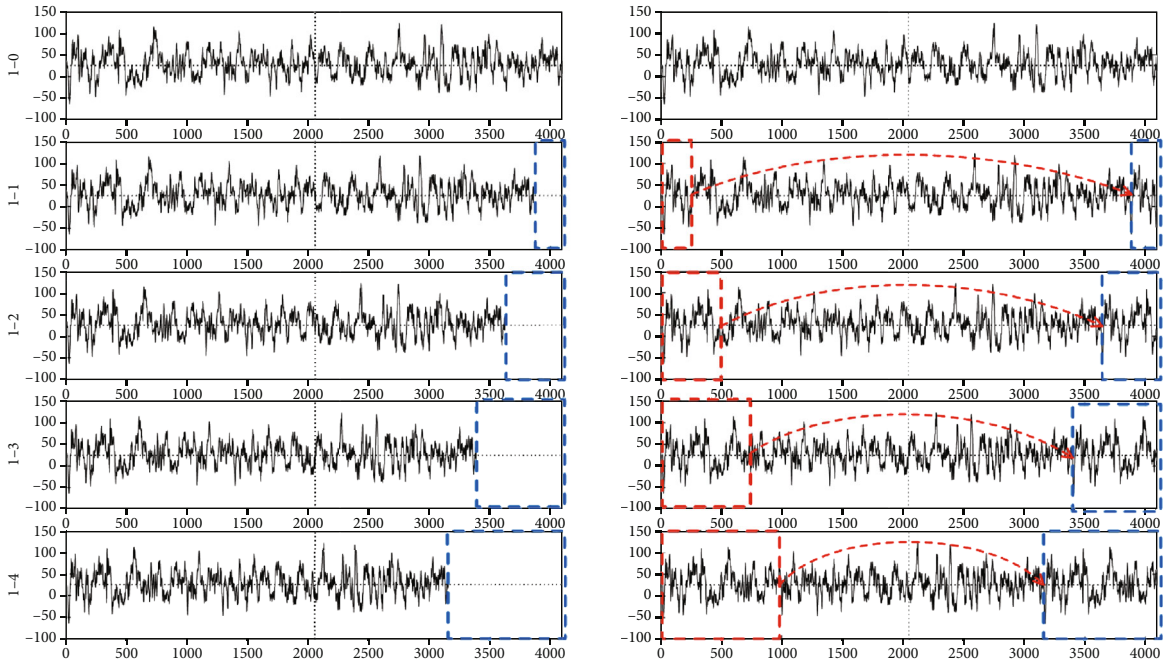

Figure 6: Completion of sample data at different sampling frequencies.

convolution layers, the number of convolution kernels in the first, second, and third convolution calculations are 16, 32, and 64, respectively. After each downsampling, the signal length changed to half of the original length, and the number of neurons in the fully connected layer was 64. In the first convolution operation, the sigmoid function is used as the activation function, while the ReLU function is used as the other activation functions.

After determining the model, we input training samples to train the model. We know that the length of each sample

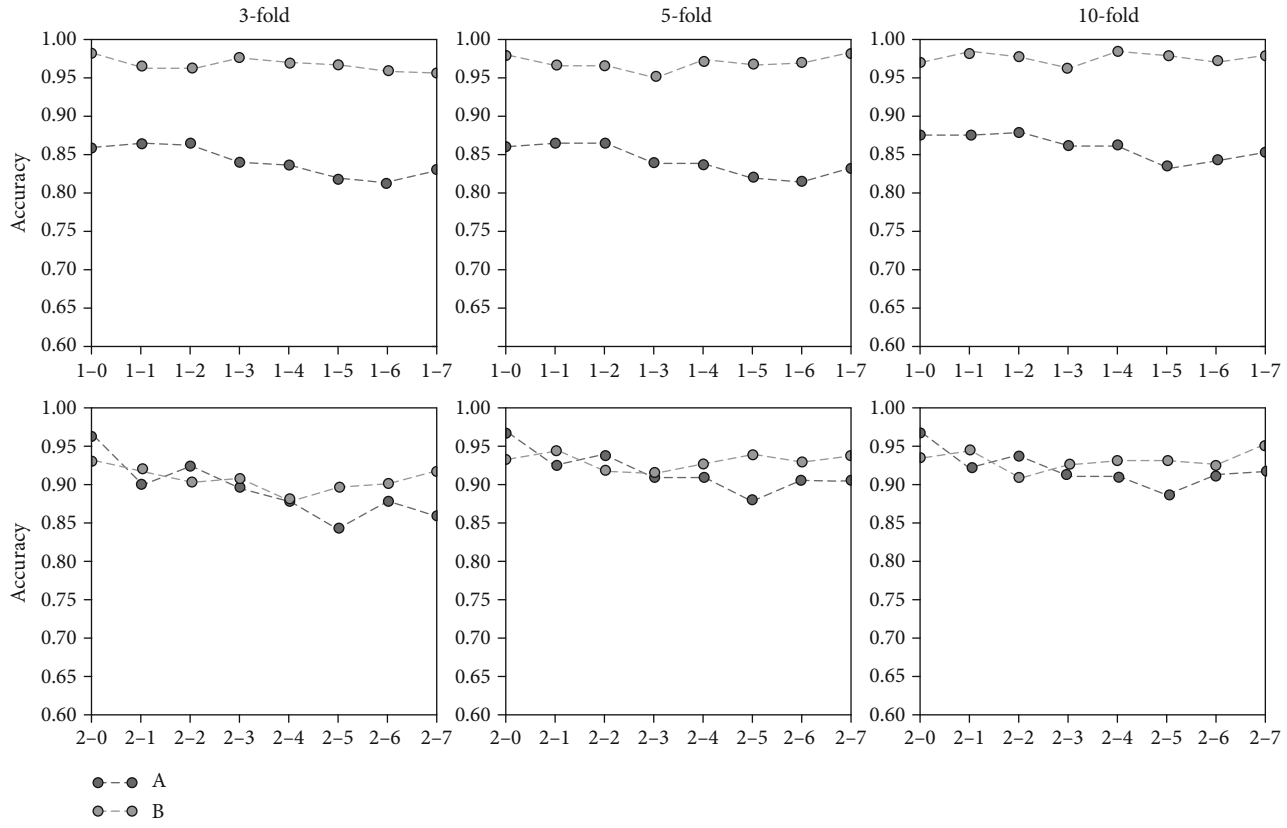

Figure 7: Comparing the classification readiness of the two methods at the same sampling frequency.

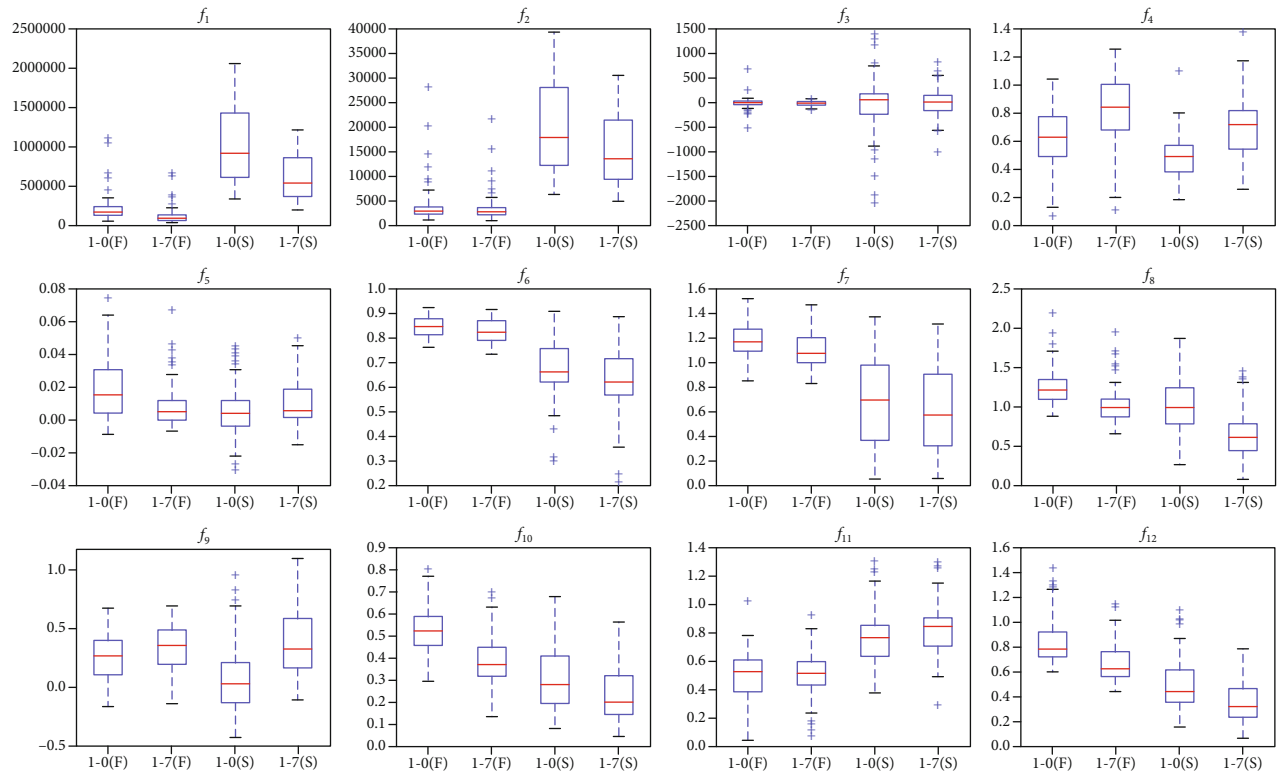

Figure 8: Classification of the F and S features in dataset 1 in 1-0 and 1-7.

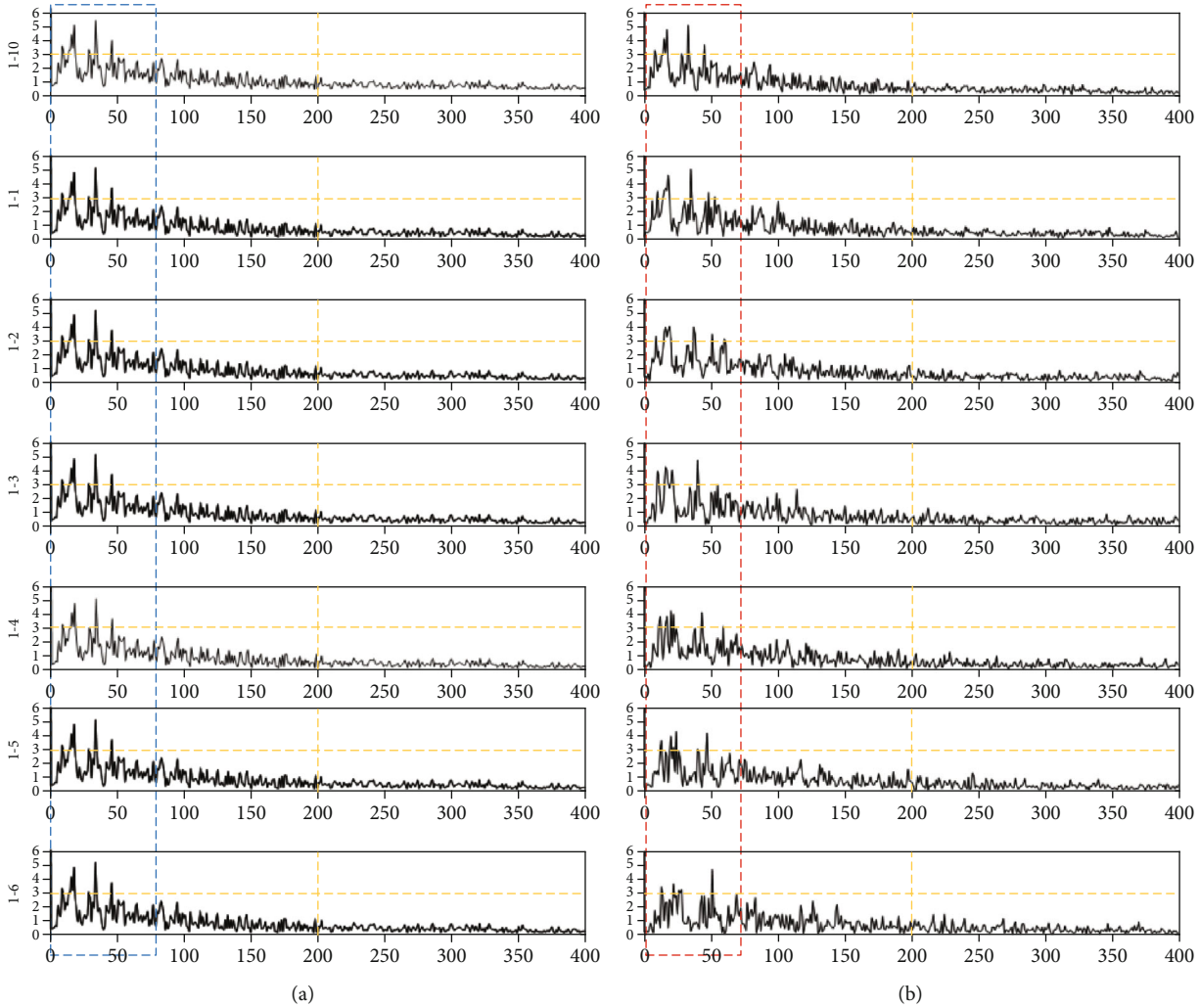

Figure 9: Spectrum of samples at different sampling frequencies.

in datasets 1-0 and 2-0 is 4096, and the length of the new frequency data obtained by resampling changes. The resampling method is operated using the Fourier resampling method in the signal processing toolkit of SciPy. In Figure 6(a), one sample in dataset 1-0 and four new samples (i.e., 1-1, 1-2, 1-3, and 1-4) generated by the sample at different sampling frequencies are presented. With the decrease in sampling frequency, the sample length becomes considerably short. However, the length of input data acceptable to the model is fixed. This study used the complementation method to cut a certain length of data from the head of the sample and supplement it to the tail. Thus, the length of the sample data reaches 4096. Figure 6(b) shows that the data in the red rectangle is replicated and supplemented to the blue rectangle. In this way, the model can be adapted to different length data. If the sample data is above 4096, then the 4096-length data is input into the model.

To enhance the universality of the model, there is no data preprocessing operation in data training. For example, the majority of the data in dataset 1 range from −500 to 500, and a small part of the data may be extended to −2000 to 2000 owing to abnormal or noise fluctuations. Thereafter, the sigmoid function used in the first convolution can reduce the impact of these abnormal data on model training.

Figure 6(a) is the new data generated by using different sampling frequencies for the original data, and Figure 6(b) is the sample data after completing the data in Figure 6(a).

4. Discussion

This section compares the classification results of the artificial design feature method and CNN-E model and different sampling frequencies.

4.1. Comparative and Characteristic Analyses of the Classification Results with the Same Frequency. Data were trained and classified at the same sampling frequency. Figure 7 shows the classification accuracy of the two methods for two datasets. Among them, A represents the average classification result of the classification method based on artificial design features. B is the classification result of the current CNN-E model. In datasets 1-0 to 1-7, we find that the classification accuracy of the CNN-E model

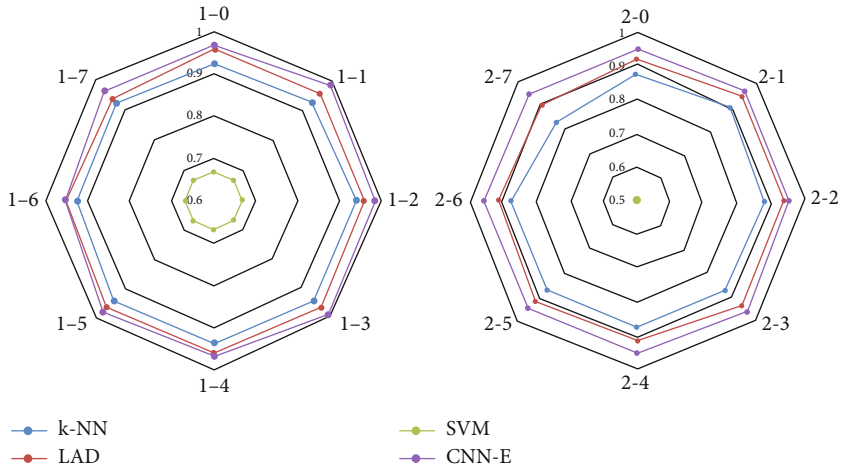

Figure 10: Tests of the classification accuracy of the current frequency data using other sampling frequency trainings.

is above 0.95, which has a good classification effect. In datasets 2-0 to 2-7, the classification accuracy of only 2-0 and 2-2 is lower than that of the classification method based on artificial design features. The majority of the others are higher than those of the classification method based on artificial design features. Moreover, we find that for the two datasets, the classification accuracy tends to decline with a decreasing frequency of adoption. CNN-E continues to maintain relatively stable classification accuracy.

A is a classification method based on artificial design features, and B is a classification method based on CNN-E, as shown in Figure 7.

Figure 8 shows the distribution of the F and S data features in datasets 1-0 and 1-7. Under different sampling frequencies, the calculated distribution of features is relatively different. For example, the two types of features are easy to distinguish in f_1, the two types of features in f_6 and f_{11} are nearly unchanged, and the feature f_5 becomes difficult to distinguish. These aspects reflect that the artificial design feature method is considerably dependent on the actual data signal. When the sampling frequency changes, the feature distribution also changes. This situation is also the reason why the classification accuracy decreases with a decrease in sampling frequency in the preceding experiments. From the classification results of datasets 2-0 to 2-7 in Figure 3, the artificial design feature method remains effective. First, the majority of the features (12) are used. Second, Figure 7 shows that these features change regularly at different sampling frequencies. Lastly, these features are selected from the existing features with good experimental results. However, the performance of these features in datasets 1-0 to 1-7 is poor, which also shows that the classification methods based on artificial design feature extraction have considerable differences in the performance of different datasets. However, the features obtained by CNN-E have profound meanings and local features. Although these deep features are difficult to visualize, they have good adaptability, as shown in Figure 7.

In the previous section, the classification method based on artificial design feature design and the classification results of CNN-E at the same sampling frequency are analyzed. This section uses the classification results of different sampling frequency data to show the universality of the CNN-E model. Figure 9 shows that some characteristic distributions of the sample data will change at different sampling frequencies. Given that the data resampling method is based on the Fourier resampling method, the characteristic changes in the frequency domain are relatively small. Figure 9 shows the spectrum of samples at different sampling frequencies. Figure 9(a) lists the spectrum obtained by applying different sampling frequencies to the same sample. This series of spectrum is nearly identical in the blue rectangular frame. To ensure that the model can be adapted to data of different lengths, the length of input samples is supplemented by the complementary method (see Figure 6). The spectrum also changes after completing the sample data of different sampling frequencies. For example, Figure 9(b) shows that with the change of sampling frequency, the spectrum of the new sample is increasingly different from that of the original sample.

Figure 9(a) is listed as the spectrum of samples at different sampling frequencies, and Figure 9(b) is listed as the spectrum of samples after the complementation method.

Table 9: Changes of dataset 1-0 divided by different lengths of 1 to 5 seconds.

Dataset name	Length of time (s)	Sample length	Sample size
1-0	1	174	6900
1-0	2	348	3300
1-0	3	521	2100
1-0	4	695	1500
1-0	5	868	1200
1-1	1	163	6900
1-1	2	328	3300
1-1	3	491	2100
1-1	4	655	1500
1-1	5	818	1200

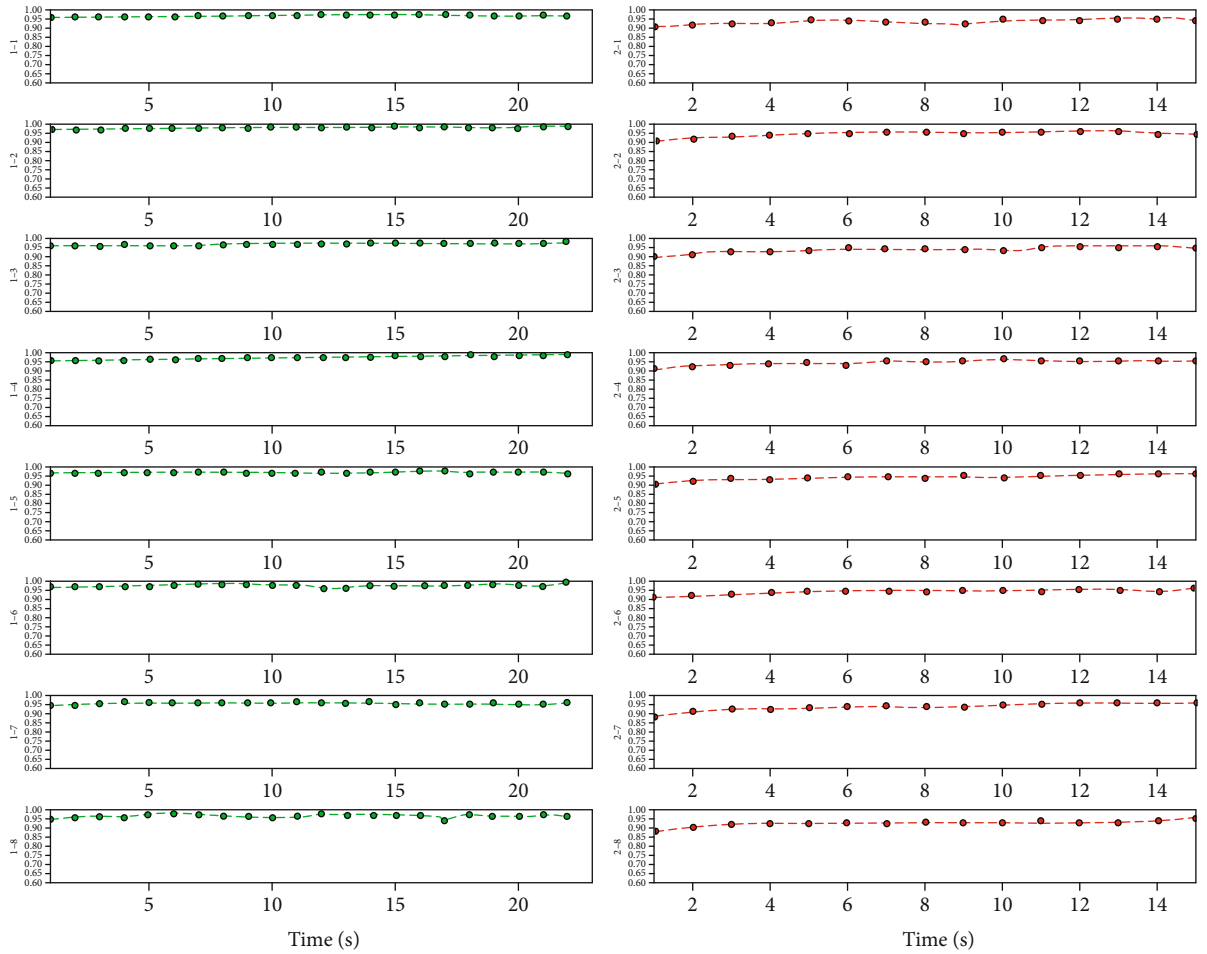

Figure 11: Secondary classification accuracy of samples based on the CNN classification model.

Figure 10 shows that the classification results of the CNN-E model for different frequency sampled data are better than those of the traditional classification methods based on artificial design features (e.g., *k*-NN, LAD, and SVM). Although there are considerable differences in the spectral characteristics of samples when the input sample signal is supplemented, the CNN-E model can extract deep features and reduce the feature dimension of the samples. Hence, the model achieves a good classification effect.

4.2. Nonequal Length Sample Testing. In practical application, the EEG classification model faces different sampling frequency data and can also process different lengths of signal data. However, numerous artificial design features have constraints on data length when extracting features. For example, when data length is only one second or the sampling frequency is not high, meaningful time-domain, frequency-domain, or nondynamic features cannot be extracted. Previous classification studies are mostly based on time windows. All samples are divided into new sample sets according to a certain length of time windows, and training and test sets are divided thereafter for training and testing, respectively, the model. Given that the proposed model can be adapted to different lengths of the sample data, we use the experiments in the previous section as bases in utilizing different lengths of time windows to segment the sample data without overlap. The window length is 1 sec, 2 seconds to the signal length. If the sample length of dataset 1-0 is 23.6 sec, then its maximum window length is 23 sec. The sample length of dataset 2 is 16 sec, and its maximum window length is 16 sec. Table 9 shows that datasets 1-0 and 1-1 are divided into different time lengths of 1 to 5 sec, respectively, and the changes of the sample length and sample number are obtained.

Figure 11 shows the classification accuracy of different datasets divided by different time lengths based on the CNN-E classification model. From the graph, the model proposed in this research achieves a good classification effect (i.e., amount of data in 1 sec can obtain a high classification accuracy) and has high timeliness on the premise of ensuring high accuracy.

5. Conclusion

In real life, there are diverse types of EEG signals. The current research on EEG classification has focused on classification accuracy, but the universality of the methods has seldom been discussed. To solve the problem, this study constructed a CNN-E classification model based on CNN. The model could be applied to classify EEG signals with different

sampling frequencies and could be adapted to signals of different lengths. This study also analyzed the possible problems in the classification of EEG signals with different sampling frequencies by the traditional feature extraction-based classification method. Our results showed that the traditional method has relied heavily on the design of the feature extraction method, and there were difficulties in feature design and selection. Moreover, the classification accuracy fluctuated substantially for EEG data with different sampling frequencies. These feature extraction methods had length constraints when processing samples with short data length. However, the CNN-E model could independently learn the characteristics of the sample data and could be adapted to all types of data length because of the use of effective data completion methods. Our results showed that the CNN-E model performed well in the classification of EEG data at the same sampling frequency, at different sampling frequencies, and at different lengths.

Although we only used two different datasets to test the robustness of the CNN-E model, we would use additional datasets to validate the reliability of this model in the future. Moreover, the performance of the CNN-E model, particularly the visual expression of the features learned by the CNN network, needs further improvement.

Data Availability

The first dataset comes from the dataset published by Andrzejak et al. The second dataset was collected by Boston Children's Hospital.

Conflicts of Interest

The authors declare that they have no conflicts of interest.

Acknowledgments

This work was supported by the Science and Technology Program of Quanzhou (Nos. 2019C094R and 2019C108), supported by the Natural Science Foundation of Fujian Province (No. 2020J01086), and supported in part by the NSF of China under Grant No. 61972156, the Program for Innovative Research Team in Science and Technology in Fujian Province University, and the Education and Scientific Research Project for Young and Middle-aged Teachers of Fujian Province (No. JAT190511).

References

[1] N. Sheehy, *Electroencephalography: Basic Principles, Clinical Applications and Related Fields*, Williams & Williams, 1982.

[2] J. Gotman, "Automatic recognition of epileptic seizures in the EEG," *Electroencephalography & Clinical Neurophysiology*, vol. 54, no. 5, pp. 530–540, 1982.

[3] L. Boubchir, B. Daachi, and V. Pangracious, "A review of feature extraction for EEG epileptic seizure detection and classification," in *2017 40th International Conference on Telecommunications and Signal Processing (TSP)*, pp. 456–460, 2017.

[4] R. Jenke, A. Peer, and M. Buss, "Feature extraction and selection for emotion recognition from EEG," *IEEE Transactions on Affective Computing*, vol. 5, no. 3, pp. 327–339, 2017.

[5] A. S. Zandi, M. Javidan, G. A. Dumont, and R. Tafreshi, "Automated real-time epileptic seizure detection in scalp EEG recordings using an algorithm based on wavelet packet transform," *IEEE transactions on bio-medical engineering*, vol. 57, no. 7, pp. 1639–1651, 2010.

[6] K. Polat and S. Güneş, "Classification of epileptiform EEG using a hybrid system based on decision tree classifier and fast Fourier transform," *Applied Mathematics & Computation*, vol. 187, no. 2, pp. 1017–1026, 2007.

[7] U. R. Acharya, H. Fujita, V. K. Sudarshan, S. Bhat, and J. E. W. Koh, "Application of entropies for automated diagnosis of epilepsy using EEG signals: a review," *Knowledge-Based Systems*, vol. 88, pp. 85–96, 2015.

[8] T. Wen and Z. Zhang, "Effective and extensible feature extraction method using genetic algorithm-based frequency-domain feature search for epileptic EEG multiclassification," *Medicine*, vol. 96, no. 19, article e6879, 2017.

[9] T. Wen, Z. Zhang, M. Qiu, M. Zeng, and W. Luo, "A two-dimensional matrix image based feature extraction method for classification of sEMG: a comparative analysis based on SVM, KNN and RBF-NN," *Journal of X-ray science and technology*, vol. 25, no. 2, pp. 287–300, 2017.

[10] R. Sharma and R. B. Pachori, "Classification of epileptic seizures in EEG signals based on phase space representation of intrinsic mode functions," *Expert Systems with Applications*, vol. 42, no. 3, pp. 1106–1117, 2015.

[11] K. Stytsenko, E. Jablonskis, and C. Prahm, "Evaluation of consumer EEG device Emotiv EPOC," Stytsenko, 2011.

[12] H. H. Kha, V. A. Kha, and D. Q. Hung, "Brainwave-controlled applications with the Emotiv EPOC using support vector machine," in *International Conference on Information Technology, Computer, and Electrical Engineering*, pp. 106–111, Semarang, Indonesia, 2017.

[13] M. Duvinage, T. Castermans, T. Dutoit et al., "A P300-based quantitative comparison between the Emotiv EPOC headset and a medical EEG device," in *Biomedical Engineering / 765: Telehealth / 766: Assistive Technologies*, Canada, 2012.

[14] R. Vargas, A. Mosavi, and L. Ruiz, "Deep learning: a review," in *Advances in Intelligent Systems and Computing*, pp. 232–244, Springer, 2017.

[15] Z. Tang, G. Zhao, and T. Ouyang, "Two-phase deep learning model for short-term wind direction forecasting," *Renewable Energy*, vol. 173, pp. 1005–1016, 2021.

[16] Y. R. Tabar and U. Halici, "A novel deep learning approach for classification of EEG motor imagery signals," *Journal of Neural Engineering*, vol. 14, no. 1, article 016003, 2016.

[17] P. Bashivan, I. Rish, M. Yeasin, and N. Codella, "Learning representations from EEG with deep recurrent-convolutional neural networks," *Computer Science*, 2015, http://arxiv.org/abs/1511.06448.

[18] M.-P. Hosseini, H. Soltanian-Zadeh, K. Elisevich, and D. Pompili, "Cloud-based deep learning of big EEG data for epileptic seizure prediction," in *2016 IEEE Global Conference on Signal and Information Processing (GlobalSIP)*, Washington, DC, USA, 2016.

[19] G. Xun, X. Jia, and A. Zhang, "Detecting epileptic seizures with electroencephalogram via a context-learning model," *BMC Medical Informatics and Decision Making*, vol. 16, no. S2, 2016.

[20] J. Masci, U. Meier, C. Dan, C. Dan, and J. Schmidhuber, "Stacked convolutional auto-encoders for hierarchical feature extraction," in *International Conference on Artificial Neural Networks*, pp. 52–59, Springer, Verlag, 2011.

[21] R. G. Andrzejak, K. Lehnertz, F. Mormann, C. Rieke, P. David, and C. E. Elger, "Indications of nonlinear deterministic and finite-dimensional structures in time series of brain electrical activity: dependence on recording region and brain state," *Physical Review E Statistical Nonlinear & Soft Matter Physics*, vol. 64, no. 6, article 061907, 2001.

[22] A. H. Shoeb, "Application of machine learning to epileptic seizure onset detection and treatment," Massachusetts Institute of Technology, 2009.

[23] T. Alotaiby, F. E. A. el-Samie, S. A. Alshebeili, and I. Ahmad, "A review of channel selection algorithms for EEG signal processing," *Eurasip Journal on Advances in Signal Processing*, vol. 2015, no. 1, 2015.

[24] E. Jones, T. Oliphant, and P. Peterson, "SciPy: open source scientific tools for python," 2014, Available at http://scipy.org.

[25] A. S. Murugavel and S. Ramakrishnan, "Hierarchical multiclass SVM with ELM kernel for epileptic EEG signal classification," *Medical & Biological Engineering & Computing*, vol. 54, no. 1, pp. 149–161, 2016.

[26] Z. Zhang, T. Wen, W. Huang, M. Wang, and C. Li, "Automatic epileptic seizure detection in EEGs using MF-DFA, SVM based on cloud computing," *Journal of X-ray science and technology*, vol. 25, no. 2, pp. 261–272, 2017.

[27] L. Guo, D. Rivero, J. Dorado, J. R. Rabuñal, and A. Pazos, "Automatic epileptic seizure detection in EEGs based on line length feature and artificial neural networks," *Journal of Neuroscience Methods*, vol. 191, no. 1, pp. 101–109, 2010.

[28] F. Pedregosa, G. Varoquaux, A. Gramfort et al., "Scikit-learn: machine learning in python," *Journal of Machine Learning Research*, vol. 12, no. 10, pp. 2825–2830, 2012.

Hindawi
Computational and Mathematical Methods in Medicine
Volume 2021, Article ID 2638495, 10 pages
https://doi.org/10.1155/2021/2638495

Research Article

Application of Medical Imaging Based on Deep Learning in the Treatment of Lumbar Degenerative Diseases and Osteoporosis with Bone Cement Screws

Shengkai Mu, Jingxu Wang, and Shuyi Gong

Shenyang Orthopedic Hospital, Shenyang, Liaoning 110044, China

Correspondence should be addressed to Shengkai Mu; msk2022@126.com

Received 21 July 2021; Revised 21 August 2021; Accepted 17 September 2021; Published 11 October 2021

Academic Editor: Kelvin Wong

Objective. To explore the application value of magnetic resonance spectroscopy (MRS) and GSI-energy spectrum electronic computed tomography (CT) medical imaging based on the deep convolutional neural network (CNN) in the treatment of lumbar degenerative disease and osteoporosis. *Methods*. There were 56 cases of suspected lumbar degenerative disease and osteoporosis. A group of 56 subjects were examined using 1.5 TMR spectrum (MRS) and dual-energy X-ray absorptiometry (DXA) to collect the lumbar L3 vertebral body fat ratio (FF) and L1~4 vertebral bone mineral density (BMD) value. We divided the subjects into 2 groups with T value -2.5 as the critical point. Set T value > -2.5 as the negative group and T value ≤ -2.5 as the positive group. Pearson's method is used for FF-MRS and BMD correlation analyses. A group of all patients underwent GSI-energy spectrum CT scan, and X-ray bone mineral density (DXA) test results (bone density per unit area) were used as the gold standard to analyze the diagnosis of osteoporosis by the GSI-energy spectrum CT scan method value. *Results*. The differences in FF and BMD between the negative group and the positive group were statistically significant ($P < 0.01$), and there was a highly negative correlation between the average value of FF and BMD. 30 cases were diagnosed as osteoporosis by DXA. The accuracy of GSI-energy spectrum CT medical imaging in diagnosing osteoporosis is 89.30%. The GSI-energy spectrum CT diagnosis of osteoporosis and DXA examination results have good consistency. *Conclusion*. Based on the deep convolutional neural network (CNN) MRS technology, GSI-energy spectrum CT medical imaging is used in the clinical diagnosis and treatment of lumbar degenerative lesions and osteoporosis. It has a good advantage in assessing bone quality and has good consistency with DXA examination and has better application value high.

1. Introduction

Lumbar degenerative disease can cause spondylolisthesis, intervertebral disc herniation, lumbar spinal stenosis, etc. If it is combined with osteoporosis, it will undoubtedly accelerate the development of the disease. If some prognosis is not timely, segmental instability, small joint hyperplasia, and vertebral disc regression change, etc., is currently recognized as a problem that endangers global public health. At present, bone cement screws are often used for treatment, which can exert the advantages of high safety, easy operation, and less trauma, which is beneficial to the recovery and stabilization of limb function, and the prognosis effect is good [1]. Medical images can provide doctors with patient information to the maximum and have gradually become an important basis for doctors' diagnosis. Sometimes, they play a decisive role in doctors' diagnosis of diseases and the choice of treatment methods and methods.

In the past, the diagnosis of osteoporosis used DXA examination, energy spectrum CT, and magnetic resonance spectroscopy (MRS). The deep convolutional neural network (CNN) has excellent image classification capabilities and is applied to medical images. With the development of precision medical technology, medical image segmentation technology has become one of the researches focuses in the field of medical image processing. Based on this, this study

explores the application value of diagnostic medical imaging based on deep learning in lumbar degenerative disease and osteoporosis.

2. Related Work

2.1. Inspection Technology

2.1.1. DXA Inspection. According to recent research results, bone strength mainly depends on two aspects: BMD and bone quality. BMD refers to the combination of peak bone mass and bone loss, which can only reflect about 60% of the bone strength state; bone mass refers to bone metabolism, bone microstructure damage (including trabecular bone), and bone mineralization. The general term for bone biomechanics. DXA has been widely used to evaluate BMD due to its economy, simplicity, and low radiation, and WHO also recommends it as the "gold standard" for the diagnosis of OP [2]. However, DXA reflects the area density within the region and cannot effectively distinguish between cancellous bone and cortical bone, and the accuracy and sensitivity are poor.

2.1.2. Magnetic Resonance Spectroscopy. Magnetic resonance spectroscopy (MRS) fat measurement technology uses chemical shifts to detect bone marrow water and adipose tissue and can measure its concentration. It can measure its concentration, analyze its biochemical composition and metabolic changes in vivo, and recognize the pathological changes from the molecular level. It is a new examination method for the diagnosis and prevention of osteoporosis.

The basis for the evaluation of osteoporosis by MRS technology: In the human body, bone marrow accounts for a relatively small proportion, but its main components, water and fat, are of great significance in the quantitative application of MRS bone marrow. Red bone marrow contains approximately 60% hematopoietic tissue (including water) and 40% adipose tissue; and yellow bone marrow contains more than 90% adipose tissue. When a person is born, there is almost red bone marrow in the bone marrow cavity. With age, the hematopoietic tissue and water in the bone marrow cavity gradually decrease, the trabecular bone becomes thinner and the gap expands, and the fat tissue continues to increase and fill it. The nature of the bone marrow is an important factor affecting bone quality. Bone marrow stem cell studies have confirmed that bone marrow adipocytes increase, compete, and inhibit the growth of osteoblasts to reduce them, which is an important mechanism leading to osteoporosis and fragility fractures. MRS can detect the water and fat components in the bone marrow and can quantitatively measure the fat fraction, thereby indirectly assessing the bone quality and opening up a new way for the early diagnosis and prevention of osteoporosis [3].

1H-MRS is the most commonly used technology in OP clinical and research. Earlier, Layer et al. confirmed the feasibility of 1H-MRS technology through in vivo bone marrow fat quantitative research. Recent domestic studies have also confirmed the accuracy and effectiveness of the application of 1H-MRS fat quantification technology. One of the most important indicators used by FF MRS fat quantification technology is also a hot research topic. FF stands for fat content. There are two commonly used definitions: one is the definition of signal intensity, that is, the ratio of fat signal intensity to the total signal intensity of water-fat; the other is to use the area under the peak definition, that is, the ratio of the area under the fat signal peak to the sum of the area under the water-fat peak, both of which are expressed as a percentage. Both definitions are used in the literature, but the definition of signal intensity is the most common [4]. It may be that the fat component is too complicated and the peak signal intensity is more representative. This study also adopted this definition.

2.1.3. Energy Spectrum CT Scan. Energy spectrum CT can provide more accurate absolute CT values and can qualitatively separate and quantitatively determine and analyze substances. Its principle is mainly to calculate the spatial image by detecting the attenuation of X-rays and obtain the X-ray attenuation curve of the substance. The attenuation of each substance can be expressed by two "base substances." The more common base substance pairs are iodine/water, hydroxyapatite (HAP)/water, and calcium/-water, of which water and iodine are the two most commonly used base substances. Energy spectrum CT can quantitatively determine the content of calcium, HAP, and other minerals and fat in the vertebral body. Vertebral osteoporosis is mainly due to the decrease of bone mineral content in the vertebral body and the increase of bone marrow fat content. The representative of bone mineral is HAP, so the quantitative determination of HAP becomes the key to the diagnosis of osteoporosis. By measuring the quantitative parameters of energy spectrum CT, Dong Qiang and others found that the use of HAP/water as a base material is more accurate for the measured bone density, has a higher correlation with bone biomechanics, and can most accurately quantitatively evaluate bone strength.

In recent years, with the continuous development of spiral CT technology, GSI-energy spectrum CT medical imaging has been continuously used in the clinical diagnosis of osteoporosis because it can obtain images of water-based and calcium-based materials and has a certain value. Compared with conventional CT, GSI-energy spectrum CT can not only realize the diagnosis of density value and cell morphology but also analyze the imaging modes of multiple parameters. Its multiparameter imaging advantages greatly enrich the image information. Based on the temporal and spatial resolution of conventional CT, GSI-energy spectrum CT realizes imaging with energy resolution [5]. GSI-energy spectrum CT realizes the analysis of the chemical composition of the substance and the evaluation of the nature and function of the tissue through single-energy imaging, material separation technology, and the drawing of the energy spectrum curve, providing more information and reference [6].

2.2. Deep Convolutional Neural Network Image Segmentation Processing Technology. The convolutional neural network (CNN) is a type of feedforward neural network

that contains convolutional calculations and has a deep structure. It is one of the representative algorithms of deep learning and the basis of many deep learning networks. Convolutional neural networks usually include an input layer, a convolutional layer, a pooling layer, and a fully connected layer, as shown in Figure 1.

Based on CNN, Long et al. proposed a fully connected network FCN, which solves the problem of input image quality degradation and low-resolution output caused by continuous convolution operations and pooling layers [7]. Inspired by FCN, Ronneberger et al. proposed the U-Net architecture, which is widely used in the field of medical imaging and later extended to a three-dimensional version to directly process three-dimensional images such as CT, as shown in Figure 2.

In the image classification task, CNN mainly performs a series of convolutional pooling operations on the image and then converts the image data into category probabilities through several fully connected layers for classification. In CNN, convolution is used to extract features, pooling is used to narrow the feature map to expand the convolution receptive field, and the fully connected layer reorganizes the features through the weight matrix. The results obtained through these operations are not easily affected by the feature and the position of the pixel itself in the image, so it has a good effect in the classification task. Medical image segmentation is of great significance in clinical diagnosis and treatment. For example, medical image segmentation can be used for 3D reconstruction of medical images, which is convenient for doctors to formulate surgical procedures, perform simulated operations, and quantify lesions [8].

Medical image segmentation, which is a computer-aided diagnosis technology applied in the medical field, can well help doctors complete the observation and analysis of medical images including magnetic resonance imaging, positron emission tomography, and computer tomography. Image segmentation is the area segmentation of the original image. The purpose of medical image segmentation is to obtain the anatomical structure of specific organs and tissues or to find regions of interest (ROI/VOI) by identifying contours and internal regions, such as lumbar degenerative lesions. Recently, deep learning technology has proven to be effective in segmenting tasks, and it is one of the common research topics in the field of deep learning applied medical imaging. The application methods of the deep convolutional neural network in medical image segmentation include transfer learning, hole convolution, and multiscale.

2.2.1. Transfer Learning. CNN requires a large amount of labeled data for learning and modeling. However, in the medical field, especially medical image segmentation, it is very difficult to obtain a large number of labeled images, because it takes a lot of time for professionals to label, and the cost of labeling is very high. Therefore, transfer learning is suitable for the medical field. Migration learning uses neural networks pretrained with other data sets (the shallow network learns simple features, and the deep network learns complex features) and fine-tune the parameters of the network on the data set that needs to be segmented, thereby reducing the need for labeling data. Experiments show that using networks trained on similar data sets for migration learning has better data processing effects [9]. At the same time, the number of fine-tuning layers in migration learning should also be determined according to the similarity between the migration data set and the labeled data and the number of labeled data.

2.2.2. Hole Convolution. In CNN, the pooling operation is usually used to reduce the size of the feature map and expand the receptive field, so that the network can learn more complex features, but each pooling operation will greatly reduce the image resolution, which is not good for pixel-level segmentation tasks. Therefore, the concept of hole convolution is introduced to replace the pooling operation to expand the receptive field, as shown in Figure 3 (the size of the convolution kernel is 3, the input stride is 2, and the output stride is 1) and Figure 2 (red in the figure). The point is the value in the original $3 * 3$ convolution kernel, and the remaining values are 0 [10–12]. Ordinary convolution takes an area with the same size as the convolution kernel each time, multiplies it pixel by pixel, and accumulates it as the convolution output of the center pixel of the area. The difference of hole convolution is that it adds the concept of rate of expansion (rate) to represent the distance between every 2 points in the convolution kernel. For example, when the expansion rate is 1, it is normal convolution, and when it is 2, it means that the two points in the convolution kernel are 1 pixel apart. The original $3 * 3$ convolution kernel will be equivalently expanded to $5 * 5$, which is the convolution kernel parameter shown in the red dot in Figure 2 (the nonred dots in the $5 * 5$ square are filled with 0). Equivalent to that in Figure 3, the input stride is 2 and the output stride is 1 convolution operation. This is equivalent to increasing the convolution kernel, that is, expanding the receptive field. This method is widely used in segmentation tasks.

2.2.3. Multiscale. A number of studies have shown that the introduction of multiscale elements in the segmentation task can effectively improve the segmentation effect. Common methods are as follows.

(1) Encoder-Decoder Model. The encoding-decoding model is relatively common in the field of natural language processing and is also used in the field of image processing. The classic network U-Net in medical image segmentation uses the encoding-decoding model. U-Net first downsamples the image through a series of convolution pooling operations and then restores the image size through deconvolution to form a U-shaped structure, as shown in Figure 4. The convolution kernel of convolution and deconvolution requires parameter learning, and the original image of the same layer of convolution will be spliced as information supplement during each deconvolution.

(2) Spatial Pyramid Pooling Method. The established network structure often requires the input of fixed-size data, so that when processing pictures of different sizes, and the pictures must be cropped or scaled to a fixed size, causing

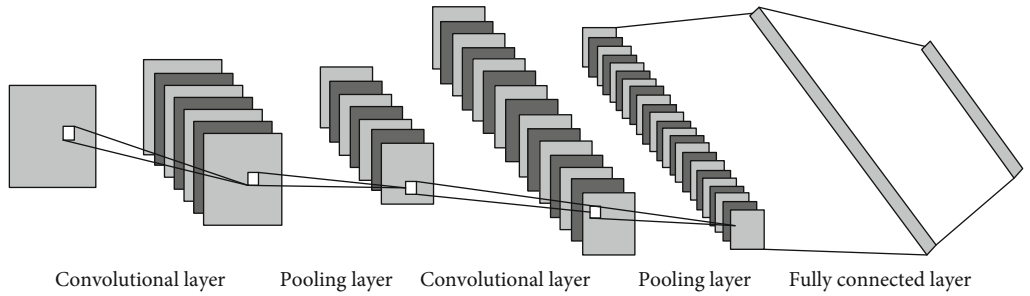

Figure 1: The structure of the convolutional neural network.

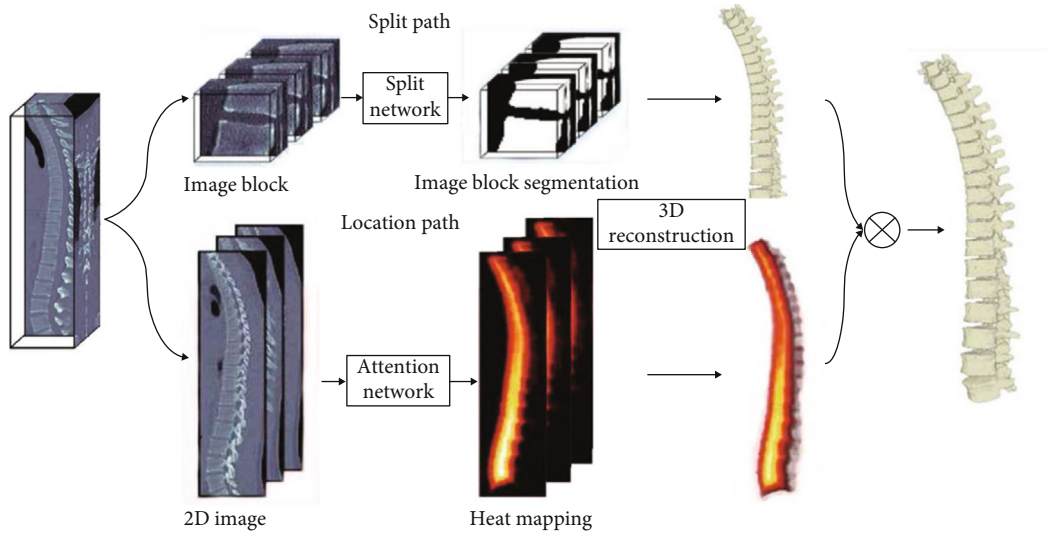

Figure 2: Spine segmentation network structure for positioning+segmentation.

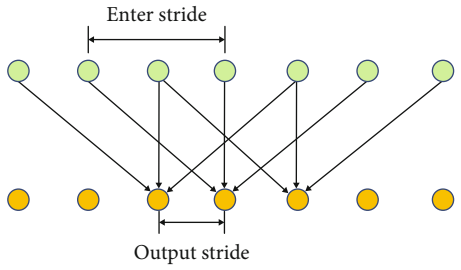

Figure 3: Hole convolution in one-dimensional state.

some information to be lost. The spatial pyramid pooling method (spatial pyramid pooling (SPP)) can make the network adapt to any size of image input and, at the same time, use the classic feature extraction method of spatial pyramid to extract image features of different scales from the same image, so that the segmentation task can be further optimized [13]. SPP can also be combined with void convolution to form a new atrous spatial pyramid pooling (ASPP) method, which also has a good effect on segmentation tasks, as shown in Figure 5.

Another way to introduce multiscale elements is to downsample the input image from the beginning and then input the multiscale downsampling pictures into the network separately and combine to obtain the final segmentation result. This method is also used in medical image segmentation and has achieved better segmentation results than U-Net [14]. Taking a picture of $256 * 256$ pixels as the initial input data, 8x, 4x, and 2x downsampling was performed, respectively, and then the downsampling output results were input together with the original image into 4 segmentation networks; at the same time, the coarse-grained segmentation result is used as the input data and then input into the fine-grained segmentation network through supersampling. For example, perform 2x oversampling on the output result of 8 times downsampling and input the 4 times downsampling image together with the original image to obtain the 4 times downsampling segmentation result. In this way, the segmentation result of the original image is obtained by continuous refinement [15]. The 4 networks are also cyclically trained from coarse-grained to fine-grained one by one, as shown in Figure 6.

3. Materials and Methods

In order to improve the efficiency of diagnosis and reduce the amount of calculation, the diagnosis of lumbar degenerative disease and osteoporosis needs to detect the region of

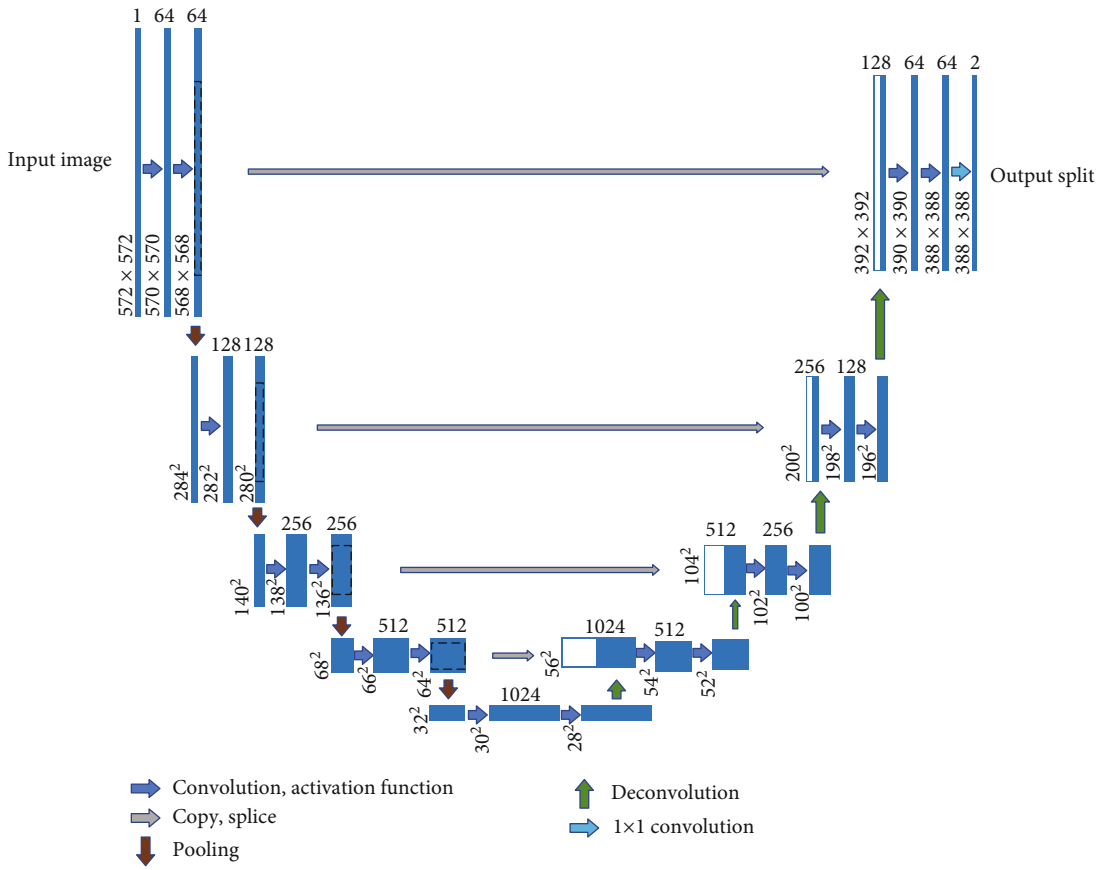

Figure 4: Classic U-Net structure.

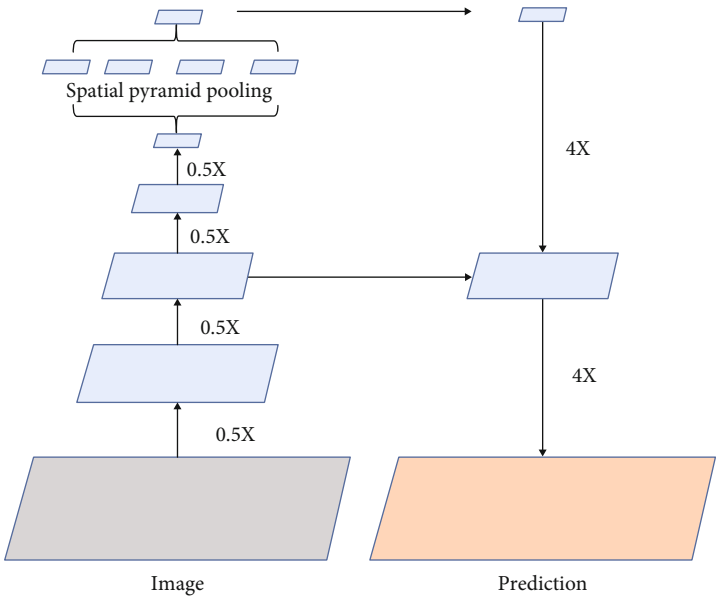

Figure 5: ASSP method diagram.

interest (ROI), that is, the lumbar region. The higher the detection accuracy, the maximum the removal of surrounding tissues and the preservation of the target area. The deep learning CNN algorithm is used to realize the detection function of the spine contour and the independent vertebra contour ROI area, and finally, the lumbar degenerative disease area is segmented through the contour overlap.

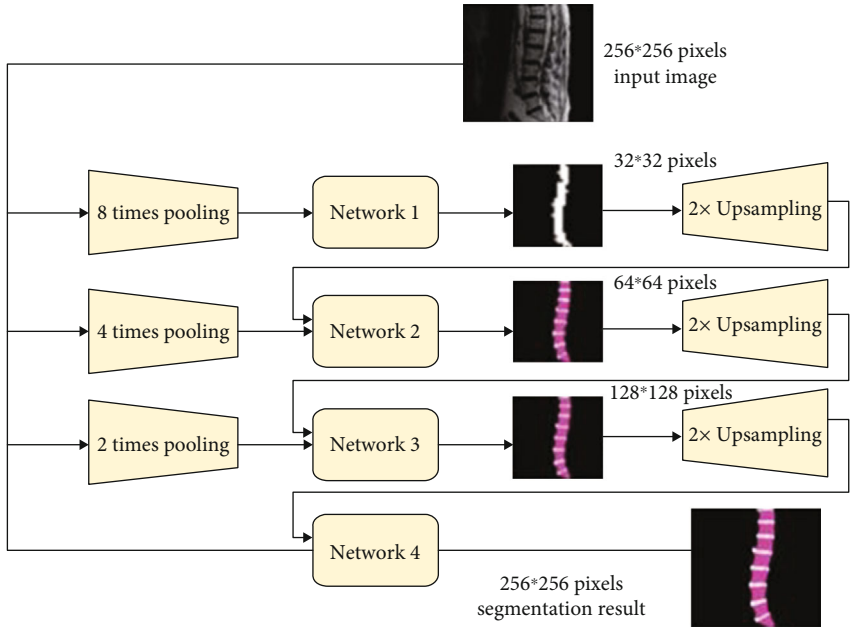

Figure 6: Schematic diagram of cascade structure.

3.1. DXA Inspection and MRS Inspection. From April 2019 to September 2020, 56 cases (35 males and 21 females, age 40-80 years old) examined by dual-energy X-ray bone mineral density (DXA) were collected in our hospital. And the 1H-MRS examination was completed within 1 day to exclude endocrine, gastrointestinal, and kidney diseases that affect bone metabolism and absorption, various congenital and acquired abnormal bone metabolism diseases, multiple myeloma, and lumbar fractures. All subjects gave informed consent, and this study was approved by the ethics committee of our hospital.

The Lunar-Prodigy dual-energy X-ray bone densitometer from the American GE company was used to measure the patient's lumbar vertebrae 1 ~4 vertebral body and the femoral neck, intertrochanter, greater trochanter, and Ward's area of one hip [16]. Scanning conditions are as follows: tube voltage 140/100 kV and tube current 2.5 mA. Before the examination, instrument performance and quality control tests were performed, input of patient-related information was completed, and the patient was correctly positioned. The BMD value and T value of the abovementioned vertebral body were recorded. According to the recommended standards of the World Health Organization (WHO), T value = -2.5 is divided into 2 groups: >-2.5 is the negative group (normal or decreased bone mass) and ≤-2.5 is the positive group (OP).

We used the Philips Achieva1.5 T superconducting MR scanner (gradient field strength 27 mT/ms, effective switching rate 75 $mT \cdot m^{-1} \cdot ms^{-1}$) spine phased array surface coil. L3 vertebral body 1H-MRS scan was performed to exclude MR contraindications such as cardiac coronary stent implantation and claustrophobia. 1H-MRS scanning parameters are as follows: using single-point analysis spectrum (PRESS) for sagittal and transverse scanning, TR 3000 ms, TE 30 ms, reversal angle 90°, excitation times (NEX) 8 times, voxel (Voxel)20 mm × 20 mm × 15 mm, select the cancellous center of the vertebral body as the area of interest, and avoid the endplate cartilage and cortical bone. First, a saturation zone and parallel shimming around the area of interest were added, using unpressurized water MRS scanning [17]. Measure the water peak of the L3 cone at around 4.70 ppm and the lipid peak between 1.30 and 0.90 ppm. The research index fat ratio (FF) was collected, that is, the percentage of the relative signal intensity amplitude of fat to the total signal intensity amplitude (water and fat). The mathematical expression is

$$FF = \left[\frac{\text{Amapfat}}{\text{Ampfat} + \text{Anpwater}}\right] \times 100\%. \quad (1)$$

The collected data is analyzed using the software that comes with the MR device.

The MRS scan was performed by an experienced technician, and the MRS images were read by two senior diagnostic imaging doctors [18]. If there is a difference in the results of the reading, an agreement is reached through consultation.

Using SPSS 19.0 statistical software, the FF value and BMD value measured by the MRS and DXA of the two groups were described by $x \pm s$ statistical parallel normality test, and the two groups conformed to the normal distribution. The t-test was used to analyze the correlation between the FF value and the BMD value by Pearson's method. The difference was statistically significant with $P < 0.05$.

3.2. DXA Inspection and Energy Spectrum CT Inspection. 56 patients with suspected osteoporosis who were treated in our hospital from June 2017 to February 2019 were selected, including 22 males and 24 females; age 45-69 years, average (58.55 ± 5.05) years old, body weight 66~82 kg, and average

body weight (76.00 ± 4.55) kg. This study was approved by the medical ethics committee of our hospital.

All patients undergo GSI-energy spectrum CT scan first and choose the German Siemens FLASH Hyun-speed two-photon CT machine. During the examination, keep the supine position and enter the bed with the foot first, and let the patient take a deep breath until the end of the scan to scan the patient's lumbar painful part. A tube voltage 80 kV, effective power supply 250 mAs, B tube 140 KV, effective current 125 mAs, open real-time dynamic exposure dose adjustment CARE Dose4D, collimator64 × 0.6 mm, pitch 0.7, speed 39.37 mm/cycle, rotation time 0.8 s/r, and at the same time, inject 300 mL of iohexol contrast agent (1.5 mL/kg) through the cubital vein at a rate of 3.0 ~ 3.5 mL/s, with a maximum of 100 mL of contrast agent. To scan to the lung nodules, the tube voltage and tube current should be adjusted to a low-dose 120 KV, 29 mAs. After the scan, the scanned image is transmitted to the VIA222266 workstation, the image data is processed by giveaway, and the calcium-water-based material image is obtained. The water-calcium density value of the three ROIs is measured at the vertebral cancellous level. Taking the average value, the determined ROI should include all the cancellous bone to the largest extent. The edge of the talar cortex is about 5 mm away from the bone island and venous plexus. The ROI is within 300 mm^2 [19].

After the GSI-energy spectrum CT inspection is completed, DXA inspection is performed. For DXA inspection, GE Lunar Prodigy or iDXA model DXA scanner is selected, and the bone density of L1-4, femoral neck, and total hip is measured. Routine DXA scans of the lumbar spine and hips were performed. Bone density ROI includes L1-4, femoral neck, and total hip. The phantom scan was calibrated horizontally, using the European spine phantom (ESP-No. 145), and the patient's lesion was scanned approximately 10 times on the DXA machine. After each center completes the export of DXA data, it is uploaded to the data center, and the data is cleaned, checked, and corrected in a unified manner [20]. Divided by 5 years of age group, the average bone density of the patients at each site of the lesion in the sample was obtained, and the highest average bone density of the age group was selected as the peak bone density and the standard deviation, T = (bone density measurement − bone density peak value)/standard deviation, refer to the diagnostic criteria recommended by the World Health Organization in 1994, but each site $T \leq -2.5$ is diagnosed as osteoporosis in this site of the patient.

Without knowing the DXA results at all, two radiologists with extensive experience will use a double-blind method to read the film together, and the diagnosis will be confirmed after discussion.

(1) Diagnostic value: take the DXA test result as the "gold standard" for diagnosis, analyze the diagnostic value of GSI-energy spectrum CT medical imaging in the diagnosis of osteoporosis, with a for true positive, d for true negative, c for false positive, and b for False negative

Table 1: Comparison of FF-MRS and BMD between the negative and positive groups.

Group	Number of cases	FF-MRS (%)	BMD (g/cm^2)
Negative group	24	43.3 ± 0.3	1.22 ± 0.21
Positive group	32	73.2 ± 0.4	0.58 ± 0.45

$$\begin{aligned} \text{accuracy} &= \frac{a+d}{a+b+c+d} \times 100\%, \\ \text{sensitivity} &= \frac{a}{a+c} \times 100\%, \\ \text{specificity} &= \frac{d}{b+d} \times 100\% \\ \text{positive predictive value} &= \frac{a}{a+b} \times 100\% \\ \text{negative predictive value} &= \frac{d}{c+d} \times 100\% \end{aligned} \tag{2}$$

(2) Consistency test: use Kappa to test consistency, and analyze the consistency of GSI-energy spectrum CT medical imaging to diagnose osteoporosis and DXA

We use SPSS 20.0 statistical software to analyze data and use Kappa to perform consistency test. When Kappa < 0.4, it indicates poor consistency; when 0.4 ≤ Kappa < 0.75, it indicates general consistency; when Kappa ≥ 0.75, it indicates good consistency, and $P < 0.05$ indicates that the difference is statistically significant.

4. Result Analysis

4.1. DXA Inspection and MRS Inspection Result Analysis. The FF-MRS and DXA bone mineral density test results of 56 subjects (24 cases in the negative group and 32 cases in the positive group) were collected for statistical analysis. After the t-test, the differences in FF and BMD between the negative group and the positive group were statistically analyzed. For academic significance ($P < 0.01$), see Table 1. The special cases are shown in Figures 7 and 8.

4.2. DXA Inspection and Energy Spectrum CT Inspection Result Analysis. For DXA results, among the selected 56 patients with suspected osteoporosis, 30 were diagnosed as osteoporosis by DXA.

In the comparison of the results of GSI-energy spectrum CT and MRI examination, the accuracy of GSI-energy spectrum CT scanning for osteoporosis is 89.30%, sensitivity is 86.67%, specificity is 92.31%, positive predictive value is 92.86%, and negative predictive value is 85.71%, see Table 2 for details.

In the consistency test, according to the Kappa consistency measurement, the GSI-energy spectrum CT diagnosis of osteoporosis and DXA test results are more consistent than the above. It is used in the clinical diagnosis of osteoporosis.

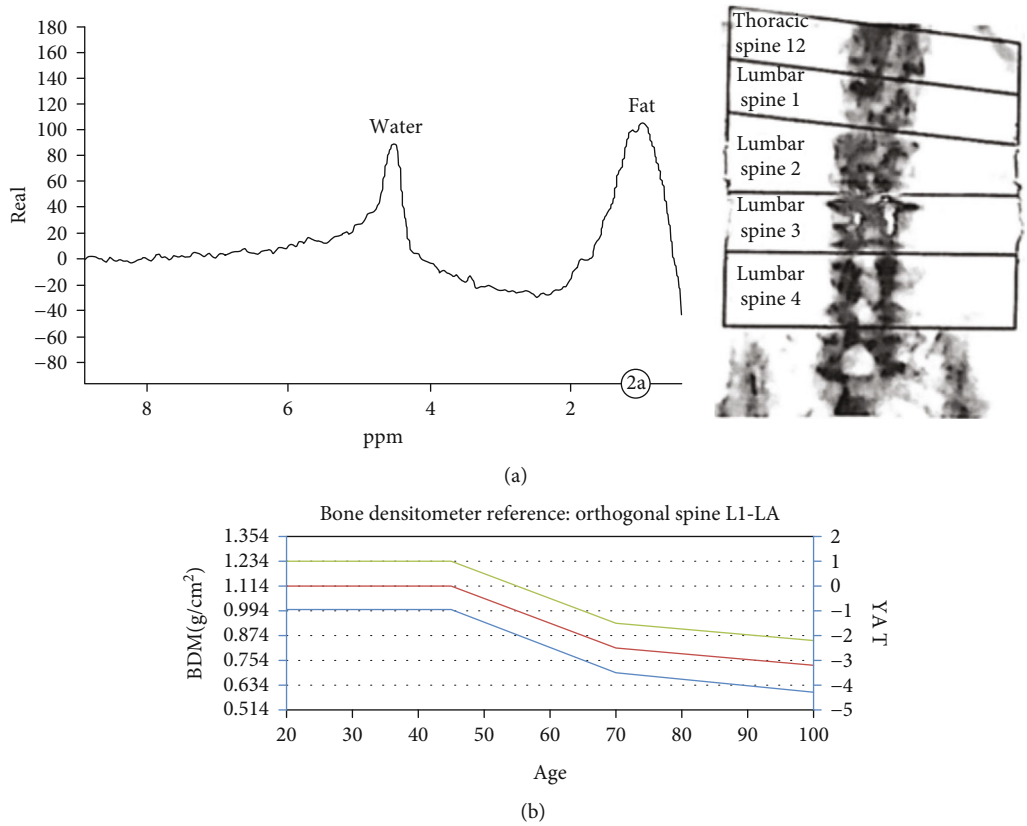

Figure 7: A 55-year-old male, osteoporotic MRS location map ((a) T2WI sagittal L3 vertebral body interest area and (b) T2WI transverse position L3 vertebral body interest area).

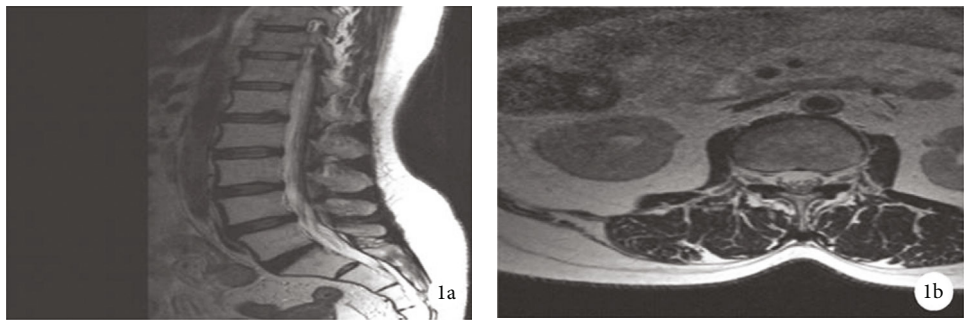

Figure 8: Male, 73 years old, osteoporosis ((a) MRS shows that the lipid peak at 1.30~0.90 ppm is significantly higher than the water peak at 4.70 ppm, FF = 59.3% and (b) BMD value measured by DXA = 0.758 g/cm^2 and T value = -2.8).

The accuracy, specificity, positive predictive value, sensitivity, and negative predictive value of GSI-energy spectrum CT medical imaging are not low, and the consistency with DXA examination is good, and the application value is high (Kappa = 0.786, $P \leq 0.001$).

4.3. Bone Cement Screw Treatment. The patient was diagnosed with degenerative lumbar spine disease by X-ray and CT examination. The treatment method of bone cement screw are as follows: combined spinal-epidural anesthesia, prone position, posterior median surgery, and conventional tissue exposure, fix herringbone crest and joint For the face joints, lamina, and spinous process, and insert the needle at the apex of the lumbar herringbone ridge. After the guide needle is inserted, the direction and position of the positioning needle are appropriately adjusted under the guidance of the fluoroscopy machine. We further expand the nail channel (using a 5.5 mm opener), adjust the bone cement, pour it in at the early stage of the dough, and inject 1.5 mL bone cement into each nail channel. During the infusion, we pay attention to injecting and exiting. Bone cement push rod to ensure that the entire pedicle screw channel is completely filled, and then, all pedicle screws are inserted. Under the observation of the guiding machine, we check the dispersion in the vertebral body and prepare a disposable bone cement and place them separately; the 8 pedicle screws were

Table 2: Comparison of GSI-energy spectrum CT scan results and DXA inspection results.

GSI-energy spectrum CT scan	DXA inspection results		Total
	Positive	Negative	
Positive	26	2	28
Negative	4	24	28
Total	30	26	56

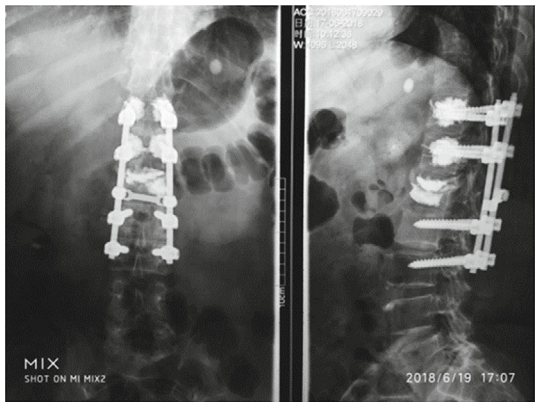

Figure 9: After treatment with bone cement screws.

adjusted to cement again. We pay attention to relieve the nerve compression, perform segmental decompression, remove the endplate cartilage and intervertebral disc nucleus pulposus, process the bone graft bed, and finally observe the position of the intervertebral fusion cage under guidance. If there is no abnormality, we suture the incision layer by layer, place a drainage tube, flush the wound, and cover with a sterile dressing. In postoperative treatment: the drainage tube can be removed within 48 hours after the operation, anti-infective drugs are used for three consecutive days, and bed rest is maintained for 14 days. The brace is protected for 1 to 2 months. Under the protection of the lumbar brace, the patient gets out of bed. After the operation, symptomatic treatments such as calcitonin or bisphosphonates, vitamin D, and calcium are needed.

After treatment, the Cobb angle of the fixed segment, the height of the adjacent upper intervertebral space, and the angle of the inferior endplate of the vertebral body were better than before treatment ($P < 0.05$), as shown in Figure 9.

5. Conclusion

DXA examination and energy spectrum CT examination result analysis showed that FF was closely related to BMD ($r = -0.86$, $P < 0.01$). According to research, bone density reduction is always accompanied by excessive accumulation of bone marrow adipose tissue. The bone marrow fat content of osteoporotic patients is significantly higher than that of healthy people of the same age. Li et al. also confirmed through experimental studies that increased bone marrow fat content is always accompanied by damage to the trabecular bone microstructure; Yeung et al. also made the same result and further pointed out that the unsaturated fatty acid index was significantly reduced during osteoporosis [21]. The index is obviously negatively correlated with fat content. Bone marrow fat accumulation and the imbalance between osteoblasts and fat cells are an important mechanism leading to osteoporosis. The diagnostic threshold of FF for osteoporosis is currently inconclusive. According to foreign reports, the range is about 58.2%-67.8%, which is basically in line with the results of this study 58.8%. Bone marrow fat is composed of multiple components, and it has been reported that there are no less than 20 types, but the specific relationship between each fat component and BMD is still unclear, and further research is still needed; secondly, the fat composition in the bone marrow may be different from the fat composition in other parts of the body. It shows that BMD is significantly negatively correlated with age and bone marrow FF but has no obvious correlation with gender, height, body weight, BMI, waist circumference, hip circumference, abdominal subcutaneous fat, and visceral fat. MRS technology has good advantages in assessing bone quality and can provide an effective auxiliary method for the assessment of primary osteoporosis.

The results of DXA examination and energy spectrum CT examination showed that the accuracy of GSI-energy spectrum CT scan for osteoporosis was 89.30%, the sensitivity was 86.67%, the specificity was 92.31%, the positive predictive value was 92.86%, and the negative predictive value was 85.71%; according to the Kappa consistency measurement, the GSI-energy spectrum CT diagnosis of osteoporosis and the DXA examination result have good consistency [20]. It shows that the sensitivity, accuracy, positive predictive value, specificity, and negative predictive value of GSI-energy spectrum CT medical imaging used in the clinical diagnosis of osteoporosis are at a high level, and the consistency with DXA examination is good. The application value is high. Scanning using GSI-energy spectrum CT medical imaging showed that long bones mainly showed thinning of the cortical bone, disordered or sparse bone trabeculae, stratification of bone, widening of joint space, surrounding bone degeneration, blurred trabecular structure, and other phenomena. The spine is deformed, the vertebral body is biconcave, the gap is widened, the bone trabecula is disordered, and the cartilage collapses, showing a fusiform or fishtail shape. In addition, the GSI-energy spectrum CT medical imaging uses single-tube dual energy to switch GSI in a short time. Due to its own material separation and material density quantitative measurement technology, it can obtain the GSI calcium-water density value of the cancellous bone of the vertebral body. Any object has a different X-ray energy absorption spectrum. When different base materials are combined, the X-ray attenuation will also change due to different X-ray absorption ratios. This process is called material separation [22]. When the matched base substance is the main component present in the tissue, measuring the value of the base substance can reflect the relative content of the substance in the tissue. In summary, in the clinical diagnosis of osteoporosis, the accuracy, specificity, positive predictive value, sensitivity, and negative predictive value of the GSI-energy spectrum CT medical imaging used

in the clinical diagnosis of osteoporosis are not low and has better consistency with DXA inspection and higher application value.

Medical imaging is an important reference for doctors to make a diagnosis. Image segmentation helps doctors identify lesions and improve diagnosis efficiency. The deep learning method in medical image segmentation can reduce the influence of doctors' subjective factors and dig out hidden information from a large number of images. Deep learning does not require manual setting of parameters and automatic feature extraction without prior knowledge, which is convenient for doctors to use [23]. This can not only assist doctors in clinical diagnosis but also has important significance for medical big data research in the era of big data. In the future, in the context of further combining specific medical application scenarios with segmentation tasks, deep neural networks may become a major medical image segmentation method.

Data Availability

The image data used to support the findings of this study have been deposited in the VerSe 2019 data set (https://osf.io/nqjyw/).

Conflicts of Interest

The authors declare no conflicts of interest.

References

[1] R. Ren, Q. F. Guo, Z. W. Li, Z. Q. Li, and B. M. Tang, "A self-controlled clinical trial of modified posterior interbody fusion combined with bone cement for the treatment of degenerative lumbar spondylolisthesis in elderly patients," *China Tissue Engineering Research*, vol. 22, no. 15, pp. 2350–2354, 2018.

[2] Y. P. Wang and W. B. Niu, *Application of GSI-Energy Spectrum CT Scan in Osteoporosis*, Harbin Pharmaceutical Group, 2021.

[3] B. Weisenthal, S. Chotai, A. Sivaganesan, J. Hills, and C. J. Devin, "Healthcare burden of osteoporosis," *Seminars in Spine Surgery*, vol. 30, no. 1, pp. 2–7, 2018.

[4] Y. Liu, S. Wu, R. Cui et al., "Proton Magnetic Resonance Spectroscopy–Detected Changes of Marrow Fat Content in a Rabbit Model of Osteoporosis Treated With Epigallocatechin-3-Gallate," *Journal of computer assisted tomography*, vol. 41, no. 2, pp. 231–235, 2017.

[5] C. C. Liu, D. J. Theodorou, S. J. Theodorou et al., "Quantitative computed tomography in the evaluation of spinal osteoporosis following spinal cord injury," *Osteoporosis international*, vol. 11, no. 10, pp. 889–896, 2000.

[6] M. Chen, Y. Zhang, and H. S. Yuan, "Correlation and consistency of rapid kV switched energy spectrum CT and QCT for determination of bone mineral density in sheep vertebral body," *Chinese Journal of Osteoporosis*, vol. 25, no. 3, pp. 326–329, 2019.

[7] Z. Tang, G. Zhao, and T. Ouyang, "Two-phase deep learning model for short-term wind direction forecasting," *Renewable Energy*, vol. 173, pp. 1005–1016, 2021.

[8] E. D. Bigler, "Neuroimaging as a biomarker in symptom validity and performance validity testing," *Brain Imaging and Behavior*, vol. 9, no. 3, pp. 421–444, 2015.

[9] H. B. Zhang, *Deep learning based image segmentation research and applications*, Electronic Science And Technology Student, Chengdu, 2018.

[10] Z. Y. Jin, "Application of artificial intelligence in medical imaging: reality and challenges," *Radiology Practice*, vol. 33, pp. 989–991, 2018.

[11] L. Huang, L. Yin, B. Liu, and Y. Yang, "Design and error evaluation of planar 2-DOF remote center of motion mechanisms with cable transmissions," *ASME Journal of Mechanical Design*, vol. 143, no. 1, article 013301, 2021.

[12] H. Bo, Z. Changjiang, W. Hongbing, and Y. Lairong, "Prediction and validation of dynamic characteristics of a valve train system with flexible components and gyroscopic effect," *Mechanism and Machine Theory*, vol. 157, article 104222, 2021.

[13] Y. Zhu, D. Hou, M. Lan, X. Sun, and X. Ma, "A comparison of ultra-high-resolution CT target scan versus conventional CT target reconstruction in the evaluation of ground-glass-nodule-like lung adenocarcinoma," *Quantitative imaging in medicine and surgery*, vol. 9, no. 6, pp. 1087–1094, 2019.

[14] Y. Gao, Z. Liu, P. L. Qin, and L. F. Wang, "Medical image super-resolution algorithm based on deep residual generation adversarial network," *Journal of Computer Applications*, vol. 38, no. 9, pp. 2689–2695, 2018.

[15] Z. Wang, J. Chen, and S. C. Hoi, "Deep learning for image super-resolution: a survey," *IEEE Transactions on Pattern Analysis and Machine Intelligence*, vol. 43, no. 10, pp. 3365–3387, 2021.

[16] L. Liu, "Bone mineral densitometry and DXA imaging in the diagnosis of primary osteoporosis," *Imaging Research and Medical Applications*, vol. 3, no. 17, pp. 50-51, 2019.

[17] Y. Noguchi, T. Murakami, T. Kim et al., "Detection of hypervascular hepatocellular carcinoma by dynamic magnetic resonance imaging with double-echo chemical shift in-phase and opposed-phase gradient echo technique: comparison with dynamic helical computed tomography imaging with double arterial phase," *Journal of computer assisted tomography*, vol. 26, no. 6, pp. 981–987, 2002.

[18] S. H. Zhang, S. Shi, and X. R. Yang, "Challenges facing healthcare big data applications and strategy discussion," *Chinese Journal of P Health Information Science*, vol. 15, no. 6, pp. 629–632, 2018.

[19] X. B. Liu and S. X. Sun, "Quantitative CT and dual echo MR imaging to evaluate osteoporosis," *Imaging Research and Medical Applications*, vol. 3, no. 12, pp. 90-91, 2019.

[20] C. J. Tyrrell, G. M. Blake, P. Iversen, A. V. Kaisary, and I. Melezinek, "The non-steroidal antiandrogen, bicalutamide ('Casodex'), may preserve bone mineral density as compared with castration: results of a preliminary study," *World journal of urology*, vol. 21, no. 1, pp. 37–42, 2003.

[21] C. G. Ball, S. M. Hameed, D. Evans, J. B. Kortbeek, A. W. Kirkpatrick, and T. C. T. T. Collaborative, "Occult pneumothorax in the mechanically ventilated trauma patient," *Canadian journal of surgery*, vol. 46, no. 5, pp. 373–379, 2003.

[22] S. F. Gao, "Application and result classification of low dose spiral CT in lung cancer screening," *Imaging Research and Medical Application*, vol. 4, no. 15, pp. 94-95, 2020.

[23] K. Wu and X. Z. Yang, "Deep learning of artificial intelligence," *Shihezi family Technology*, vol. 6, pp. 44-45, 2020.

Hindawi
Computational and Mathematical Methods in Medicine
Volume 2021, Article ID 8129044, 10 pages
https://doi.org/10.1155/2021/8129044

Research Article

Segmentation of Prefrontal Lobe Based on Improved Clustering Algorithm in Patients with Diabetes

Na Zhao,[1] **Qingzhen Zhao**,[1] **Liang Wang**,[1] **Xiuqing Wu**,[1] **Rui Zhang**,[1] **and Haijun Feng**[2]

[1]*Department of Anesthesiology, The Affiliated Hospital of Medical School of Ningbo University, Ningbo 315020, China*
[2]*Department of Anesthesiology, Affiliated Suzhou Science & Technology Town Hospital of Nanjing Medical University, Suzhou 215153, China*

Correspondence should be addressed to Haijun Feng; fenghaijun@njmu.edu.cn

Received 2 August 2021; Revised 12 September 2021; Accepted 14 September 2021; Published 7 October 2021

Academic Editor: Kelvin Wong

Diabetics are prone to postoperative cognitive dysfunction (POCD). The occurrence may be related to the damage of the prefrontal lobe. In this study, the prefrontal lobe was segmented based on an improved clustering algorithm in patients with diabetes, in order to evaluate the relationship between prefrontal lobe volume and COPD. In this study, a total of 48 diabetics who underwent selective noncardiac surgery were selected. Preoperative magnetic resonance imaging (MRI) images of the patients were segmented based on the improved clustering algorithm, and their prefrontal volume was measured. The correlation between the volume of the prefrontal lobe and Z-score or blood glucose was analyzed. Qualitative analysis shows that the gray matter, white matter, and cerebrospinal fluid based on the improved clustering algorithm were easy to distinguish. Quantitative evaluation results show that the proposed segmentation algorithm can obtain the optimal Jaccard coefficient and the least average segmentation time. There was a negative correlation between the volume of the prefrontal lobe and the Z-score. The cut-off value of prefrontal lobe volume for predicting POCD was <179.8, with the high specificity. There was a negative correlation between blood glucose and volume of the prefrontal lobe. From the results, we concluded that the segmentation of the prefrontal lobe based on an improved clustering algorithm before operation may predict the occurrence of POCD in diabetics.

1. Introduction

More and more evidence shows that the type 2 diabetes mellitus (T2DM) can cause damage to the function and integrity of brain tissue [1–4]. Cognitive damage is one of the manifestations of brain damage, and the damage of cognitive function is accompanied by the change of brain tissue structure [5, 6]. With the development of the course of disease, the cognitive impairment of T2DM can be manifested in various aspects, such as the decline of memory, attention, and learning ability, and gradually aggravate until dementia [7, 8].

Postoperative cognitive dysfunction (POCD) is a common complication of anesthesia operation [9], which often occurs in the elderly [10]. The incidence of POCD is higher because of the possible brain damage in diabetic patients [11]. POCD not only affects the patients' quality of life after operation but also leads to an increased incidence of postoperative pulmonary infection and death [12]. At present, there is no effective index to predict the occurrence of POCD [13].

The prefrontal cortex is located in front of the motor center of the body, which is the combined cortex of the frontal lobe. Research shows that the prefrontal lobe is closely related to cognitive function [14–17]. The results of neuroimaging show that the degree of prefrontal cortex atrophy can predict the change of cognitive function [18–20]. The improved clustering segmentation algorithm can effectively avoid the blindness of the initial cluster center selection and make the segmentation results faster and more accurate. Thus, the purpose of this study was to evaluate the accuracy

of preoperative volume of the prefrontal lobe in magnetic resonance imaging (MRI) on predicting the occurrence of POCD in diabetics, in order to provide a reference for clinical practice.

2. Materials and Methods

2.1. General Information. In this study, 48 patients with T2DM who were 60-85 years old were enrolled in our hospital from January 2017 to December 2019. This study has been approved by the ethics committee of our hospital.

The inclusion criteria are as follows: (1) T2DM was diagnosed according to the diabetes diagnosis standard recommended by the WHO; (2) elective noncardiac surgery; (3) age from 60 to 85; (4) American Society of Anesthesiologists (ASA) levels I-III; and (5) informed consent by the patients.

The exclusion criteria are as follows: (1) preoperative depression or cognitive impairment; (2) drug abuse, alcohol abuse, or long-term use of benzodiazepines, antidepressants; (3) hearing or visual impairment; (4) cardiovascular and cerebrovascular accidents within 6 months or with neurological sequelae; (5) previous cardiac or central nervous system surgery; (6) emergency surgery or craniocerebral surgery; (7) illiteracy; and (8) have participated in other clinical studies.

2.2. Anesthesia Program. Before anesthesia, Atropine 0.5 mg and Phenobarbital 100 mg were intramuscularly injected. The invasive BP, HR, SpO_2, and $P_{et}CO_2$ were monitored through catheterization of the radial artery, and the CVP was monitored catheterization of the right internal jugular vein. Auditory evoked potential index (AAI) was monitored by an A-line MLAFP ARX index monitor.

Anesthesia was induced by intravenous injection of midazolam 0.05-0.10 mg/kg, fentanyl 3-5 μg/kg, vecuronium 0.1 mg/kg, and propofol 1.0-1.5 mg/kg. Mechanical ventilation was performed after tracheal intubation to maintain p-stare at $P_{et}CO_2$ 23-40 mmHg.

Anesthesia maintenance: inhalation of 1%~3% sevoflurane, intermittent intravenous infusion of fentanyl 2.5~5.0 μg/kg·h, and intravenous vecuronium 0.025~0.050 mg/kg. When necessary, remifentanil 0.05~0.20 mg/kg·min and propofol 3~9 mg/kg·min were infused intravenously. When the MAP was less than 30% of basic value, intravenous ephedrine 5~10 mg/time was used. When the HR was less than 50 times/min, Atropine 0.2 mg/time was injected intravenously. The fluctuation of SP was kept within 30% of basic value, HR 50~100 times/min, AAI 15~25. After the operation, the patient will be sent back to the ward or intensive care unit according to the condition.

2.3. Cognitive Evaluation. Neuropsychological tests were conducted before and 4 days after the operation, including Wechsler adult memory, sensitive items in intelligence scale, connecting line, and nail board tests. The detailed test items were as follows:

(1) Cumulative test: adding the same number (e.g., 3 or 4) to 49 continuously from 1, recording the time needed to complete and the number of errors and omissions, calculating rough scores according to the formula, this test content can reflect attention and calculation ability

(2) Visual regeneration: allows the subjects to see 3 designed figures (a, b, and c) 10 s, and let them draw the figure and grade it according to the accuracy of the copied figure. This test content can reflect the ability of visual memory and the ability of visual-spatial analysis

(3) Associative learning: designs a group of 10 pairs of words, reads them to the subjects in a specific order, writes them on 10 cards, and presents them to the subjects at the same time. The first word was read out by the tester, and the subject was asked to say another word according to his memory. The test was carried out three times in total, and the score was made according to the accuracy of the answer. This test content can reflect the language memory ability and visual memory ability

(4) Digital breadth: this test includes two tests, consequent and reverse. Give the subject a group of numbers, and then, ask them to repeat the numbers with consequent and reverse direction. Score with the highest number of correct retelling. This test item can reflect the degree of concentration

(5) Number sign: arranges a group of symbols and numbers, and then, the subjects match the numbers and symbols within 90 s and record the correct number. The correct number is the score. This test content can reflect the mental movement speed

(6) Connecting line: allows the subjects to connect the numbers (including the numbers in upper and lower case) in order as soon as possible and record the required time. This test content can reflect the attention and mental movement speed

(7) Nail board: insert a short stick on a special board by dominant hand and nondominant hand, respectively, and record the required time. This test content can reflect the fine movement speed

According to the occurrence of POCD, the patients were divided into the POCD group and the non-POCD group. The specific steps are as follows: (1) calculate the standard deviation(s) according to the first test result of the single test for the healthy elderly; (2) calculate the difference between the single preoperative test result and the postoperative test result of each patient (X_i); (3) $Z_i = X_i/s$, total Z-score $= Z_1 + Z_2 + +Z_9$; and (4) POCD occurs when total Z-score ≥ 1.96.

2.4. Blood Glucose Test. All patients fasted after 8:00 p.m. for 3 consecutive days before operation; peripheral blood glucose was measured 7 times a day, i.e., before and after three meals and before sleep. Take the average blood glucose before three meals and bedtime as the average fasting blood glucose

(FBI), and the average of blood glucose after three meals as the average 2 hours postprandial blood glucose (PBI).

2.5. Brain MR Image Segmentation Process. This paper presents an automatic segmentation algorithm for brain MR images. Firstly, color coding is applied to the source image to enhance the regions of interest in the image and make it easier to identify different tissues. Then, the initial clustering centers of white matter, gray matter, and cerebrospinal fluid regions are determined according to the anatomical prior knowledge and probability gray histogram; finally, the iterative operation is carried out according to the clustering segmentation algorithm, and the convergence is achieved when the set threshold is reached to complete the automatic image segmentation.

2.5.1. Image Color Coding. Gray image is only represented by intensity values of 0-255, while color image can be represented by RGB color space. CIE LAB space is established on the basis of the international standard of color measurement formulated by the International Commission on lighting. It uses digital methods to describe human visual perception and can be converted into RGB color space. CIE LAB uses b, a, and L coordinate axes to define CIE color space, where image brightness L, the value range is [0,100], which means from pure black to pure white; chroma a means red-green axis, chroma b means blue-yellow axis, and the value range of them is [0, 10]. The image brightness is calculated by the YIQ color system formula and given by formula (1). The chromaticity value is obtained from the color spectrum of the source image.

$$L = B \times 0.114 + G \times 0.587 + R \times 0.299. \quad (1)$$

The steps of image color coding are as follows: I, I_C, and I_T are input gray image, source color spectrum image, and target image, respectively, and they have the same scale size; the corresponding image pixels are represented as P, P_c, and P_T.

(1) The intensity L of gray image pixel P is obtained

(2) The color spectral image pixel PC of the source image is obtained and converted into intensity L_c by formula (1)

(3) The Euclidean distance formula is used to compare the intensities L and L_c. Given by formula (2), gp and cp represent the number of pixels of the image, respectively

$$\mathbf{D} = \left|\mathbf{L_i} - \mathbf{L_{Cj}}\right|, \quad \mathbf{i = 1, 2, 3 \cdots gp, j = 1, 2, 3 \cdots cp} \quad (2)$$

(4) When $0 \le D \le 4$, skip step (3); otherwise, convert P and P_c to CIE LAB color space

2.5.2. Clustering Segmentation Algorithm. A clustering algorithm is an unsupervised model learning method [12], which can efficiently cluster large data and is widely used in image segmentation, pattern recognition, data mining, and other fields. The basic idea is as follows: select K objects as the initial clustering center; then, according to the clustering function, classify the sample points to the nearest cluster center, and update the new cluster center after adjustment; when the change range of two adjacent cluster centers is less than the set critical value, the clustering operation stops. The clustering objective function proposed in this paper is shown in formula (3). At this time, the image segmentation process is transformed into using the objective function to divide the voxels in the image into their categories.

$$\mathbf{R_{(z,k)}} = \sum_{\mathbf{x=0}}^{\mathbf{m-1}} \sum_{\mathbf{y=0}}^{\mathbf{n-1}} \sum_{\mathbf{tc=0}}^{\mathbf{k-1}} \sum_{\mathbf{tp=0}}^{\mathbf{z-1}} \left|\mathbf{V_{(x,y,tp)}} - \mathbf{C_{(z,tc)}}\right|. \quad (3)$$

When $z > 1$, 3D images can be processed, and when $z = 1$, they are applied to 2D images; $\mathbf{R_{(z,k)}}$ represents the number of initial clustering centers, that is, the number of segmented regions; $\mathbf{V_{(x,y,tp)}}$ represents the voxel value at the $(\mathbf{x}, \mathbf{y}, \mathbf{tp})$ position in the image, $\mathbf{C_{(z,tc)}}$ represents the tc initial clustering centers on the z plane, and $\mathbf{V_{(x,y,tp)}} - \mathbf{C_{(z,tc)}}$ represents the distance measure from the voxel $\mathbf{V_{(x,y,tp)}}$ to the clustering center $\mathbf{C_{(z,tc)}}$; m, n represents the size of each plane image.

2.5.3. Initial Clustering Center Based on Gray Histogram. The selection of the initial cluster center has a great influence on the clustering results. If it is not selected properly, the global optimal classification results are hard to be obtained. In this paper, the image gray histogram is used to determine the initial clustering center. The gray histogram is given by

$$\mathbf{H_z} = \sum_{\mathbf{p=0}}^{\mathbf{z-1}} \sum_{\mathbf{x=0}}^{\mathbf{n-1}} \sum_{\mathbf{y=0}}^{\mathbf{m-1}} \mathbf{g(z, x, y)}. \quad (4)$$

The process of determining the initial cluster center can be explained by Figure 1. Firstly, the histogram of the source image is calculated, and then, the triangle is drawn to analyze the overlapping area, and the histogram curve is obtained. Finally, the initial clustering center point is obtained according to the intersection of the histogram curve. The specific steps are as follows:

(1) Use formula (4) to traverse the histogram and detect all peak points

$$\mathbf{HO_{(z)}} = \left\{\mathbf{H_{(z,i)}} \mid \mathbf{H_{(z,i)}} > \mathbf{H_{(z,i-1)}}, \mathbf{H_{(z,i)}} > \mathbf{H_{(z,i+1)}}, \mathbf{1 \ll i \ll 255}\right\} \quad (5)$$

(2) All peak points are screened by formula (6), and the peak points less than 5% of the maximum peak point are removed to get the peak point set PZ

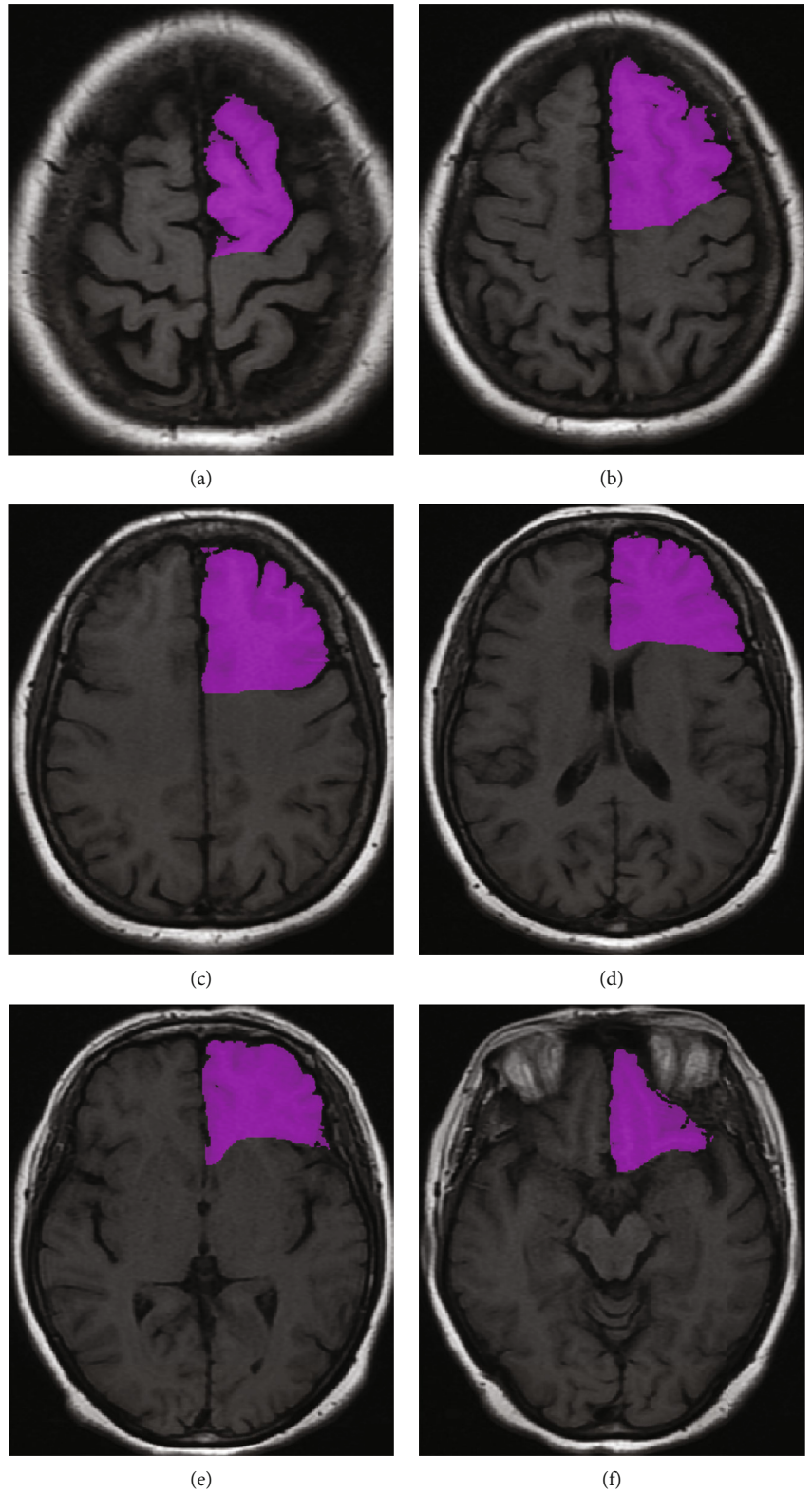

Figure 1: Segmentation of the prefrontal lobe on the transverse plane. (a–c) Three typical transverse plane between the upper end of the frontal lobe to the lateral ventricle. Find the anterior central sulcus, along the deepest part of the sulcus, draw a straight line perpendicular to the longitudinal fissure of the brain. (d) Typical plane through the lateral ventricle. Draw along the anterior central sulcus to the front point of the lateral ventricle; then, draw a straight line to connect with the deepest point of the longitudinal fissure. (e) Typical plane through the lateral sulcus. Draw a line along the front of the lateral sulcus to the front point of the lateral ventricle. (f) Typical plane with the disappeared lateral ventricle. The lateral fissure was the posterior boundary of the prefrontal lobe and delineated along the boundary of the frontal lobe.

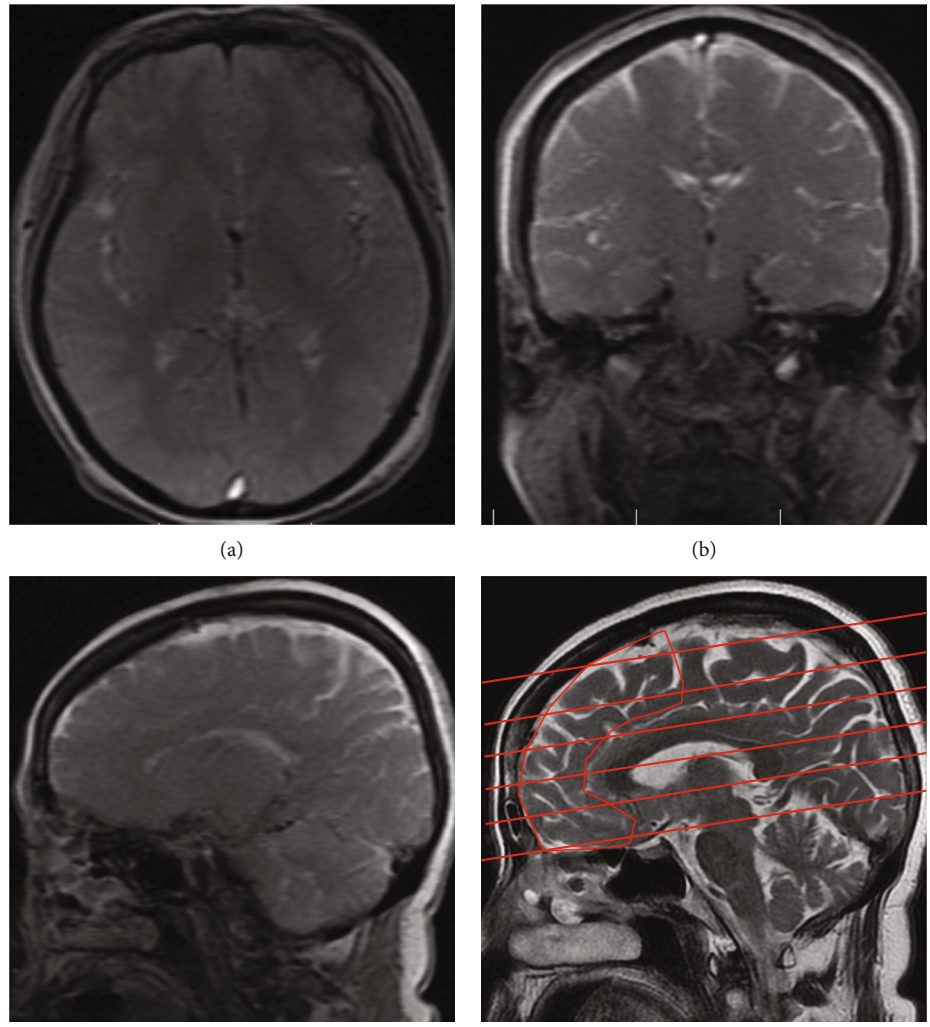

Figure 2: Localization of the prefrontal lobe: (a) transverse plane; (b) coronal plan; (c) sagittal plan; (d) median sagittal plane. The irregular shape area is the prefrontal lobe. The lines were the position of the typical transverse plane in the median sagittal plane.

$$P_z = \left\{ (i) \mid \frac{\mathrm{HO}_{(z,i)}}{\mathrm{HO}_{(z,\max)}} > \frac{\left(\mathrm{HO}_{(z,\max)} \times 5\right)}{100}, 0 \ll i \ll 255 \right\} \quad (6)$$

(3) A new set of peak points is calculated by formula (7) to generate significant peak points in each region

$$\mathbf{Pl_z} = \left\{ \mathbf{P_{(z,i)}} \mid \mathbf{P_{(z,i+1)}} - \mathbf{P_{(z,i)}} > 10, 0 \ll \mathbf{i} \ll \mathbf{255} \right\} \quad (7)$$

(4) Formula (8) is used to calculate the initial clustering center $\mathbf{C_{(z,k)}}$ of each region, in which $\mathbf{Range_{min\ (z,k)}}$ and $\mathbf{Range_{max\ (z,k)}}$ represent the smaller and larger range of each image plane z, respectively

$$\mathbf{C_{(z,k)}} = \left\{ \mathbf{PI_{(z,i)}} \mid \mathbf{Range_{min\ (z,k)}} < \mathbf{PI_{(z,k)}} \ll \mathbf{Range_{max\ (z,k)}} \right\} \quad (8)$$

2.6. Evaluation of MRI. The 1.5T MRI machine (Siemens, Germany) was used to evaluate the volume of the prefrontal lobe. After the transverse, sagittal, and coronal stereoscopic localization was carried out, the frontal lobe area was scanned parallel to the line from anterior commissure to posterior commissure in the median sagittal plane (Figure 2).

In the transverse plane, adjust the appropriate window width and position, and use the mouse to draw the region of interest (ROI) of the prefrontal lobe boundary layer by layer. Because the frontal gyri were surrounded by cerebrospinal fluid, they can be semiautomatic identified by computer software. Thus, the key to delineate the frontal ROI was to determine the posterior boundary, which needs manual recognition. In order to unify the delineation of the posterior prefrontal boundary, the criteria for the

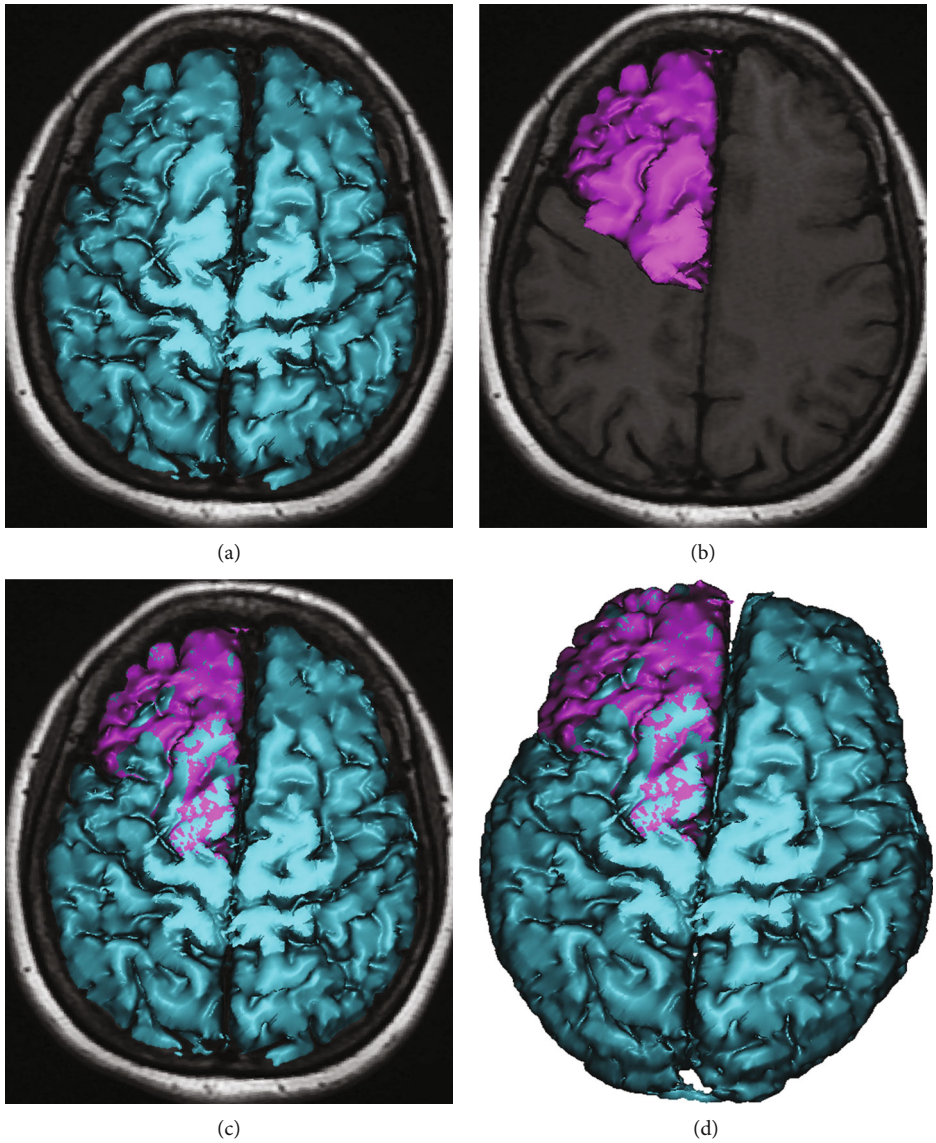

Figure 3: Three-dimensional reconstruction of the prefrontal lobe and whole brain: (a) whole brain alone; (b) prefrontal lobe alone; (c, d) both the brain and the prefrontal lobe were shown.

demarcation of ROI in the frontal lobe were formulated with reference to the standard neuroanatomical atlas and under the guidance of neuroimaging and anatomists, the detail is shown in Figure 1.

In the three-dimensional (3D) reconstruction software, the prefrontal lobe and the whole brain's 3D image were reconstructed through the transverse plane, and the volume of the prefrontal lobe and brain is viewed and recorded through the property function (Figure 3). Then, the standardized volume of the prefrontal lobe = (measured volume of prefrontal lobe/volume of whole brain) × 1000.

2.7. Statistical Analysis. The SPSS 23.0 statistical software was used for the analysis of our biodata. The quantitative data were analyzed by the normality test. As the results were consistent with normal distribution, these data were expressed by $\boldsymbol{x} \pm s$. The data before and after operation were compared by the paired t-test, while the data in the POCD group and non-POCD were compared by Student's t-test. The qualitative data in various groups were compared by the chi-square test. The relationship between the volume of the prefrontal lobe and the Z-score or blood glucose was carried out by the Pearson correlation analysis. The receiver operator characteristic (ROC) curve was selected to calculate the cut-off value of prefrontal lobe volume, area under the curve (AUC), sensitivity, and specificity of volume of the prefrontal lobe for predicting POCD.

3. Results

3.1. Segmentation Results Based on Improved Clustering Algorithm. Qualitative analysis shows that the gray matter, white matter, and cerebrospinal fluid based on the improved clustering algorithm were easy to distinguish. Quantitative evaluation results show that the proposed segmentation

Table 1: Average time-consuming results of different segmentation algorithms.

Item	Categories	Iterations	Jaccard coefficient	Average time
Multithreshold algorithm	4	1	0.347	1.709
Level set algorithm	0	1	0.546	2.894
K-means clustering	4	31	0.504	27.852
Improved clustering algorithm	4	1	0.886	0.142

Table 2: The general information and intraoperative index in two groups.

Item	POCD ($n = 12$)	Non-POCD ($n = 36$)	t or χ^2	P
Age (year)	72.4 ± 6.8	71.6 ± 5.9	0.392	0.697
Sex (male/female)	8/4	19/17	0.705	0.401
BMI (kg/m^2)	22.3 ± 2.1	21.4 ± 2.5	1.120	0.268
Education level (year)	6.7 ± 1.2	7.1 ± 1.4	0.886	0.380
ASA (II/III)	9/3	24/12	0.291	0.589
Operation time (min)	184.6 ± 45.2	192.5 ± 62.3	0.404	0.688
Anesthesia time (min)	214.3 ± 48.9	221.9 ± 51.2	0.450	0.655
Propofol dosage (mg)	289.4 ± 87.6	297.2 ± 92.8	0.256	0.799
Sevoflurane dosage (ml)	16.4 ± 5.2	17.3 ± 4.9	0.543	0.590
Vasoactive drugs (yes/no)	7/5	19/17	0.112	0.738

algorithm can obtain the optimal Jaccard coefficient and the least average segmentation time (Table 1).

3.2. General Information and Intraoperative Index. In all the 48 diabetics, the POCD was found in 12 cases, and the incidence was 25%. The general information, including age, sex, body mass index (BMI), education level, and the intraoperative index, including ASA, operative time, anesthesia time, propofol dosage, sevoflurane dosage, and the use of vasoactive drugs, is shown in Table 2. There was no significant difference between the POCD and non-POCD groups (all $P > 0.05$), which indicated that the preoperative state of patients and the effect of anesthesia on the two groups were basically the same.

3.3. Neuropsychological Test. The detailed neuropsychological test results are shown in Table 3. The total Z-scores in the POCD and non-POCD groups were 3.0 ± 0.7 and 1.1 ± 0.5; the difference is statistically significant ($P < 0.001$). Compared with preoperative data, the postoperative cumulative test, visual regeneration, associative learning, and digital breadth (reverse) test were lower in the POCD group (all $P < 0.05$). In the non-POCD groups, only the cumulative test before and after operation has the statistical differences ($P < 0.05$).

3.4. Volume of the Frontal Lobe. The volume of the prefrontal lobe in the POCD group was 167.1 ± 16.6 cm^3, while the volume of the prefrontal lobe in the non-POCD group was 196.0 ± 19.8 cm^3. The volume of the prefrontal lobe in the POCD group was significantly smaller than the volume in the non-POCD group ($t = 5.107$, $P < 0.001$). There was a negative correlation between the volume of the prefrontal lobe and the Z-score ($r = -0.324$, $P = 0.003$). In the ROC curve, the cut-off value of the volume of the prefrontal lobe for predicting POCD was <179.8 (AUC = 0.859, $P < 0.001$), with the sensitivity, specificity, and Youden's index of 77.4%, 82.4%, and 0.598, respectively (Figure 4).

3.5. Blood Glucose. The FBI and PBI in POCD and non-POCD are shown in Figure 5. Compared with the non-POCD group, the FBI and PBI in the POCD group were relatively higher. There was a negative correlation between the volume of the prefrontal lobe and FBI ($r = -0.418$, $P = 0.007$) or PBI ($r = 0.464$, $P = 0.012$).

4. Discussion

In this study, there was no difference between the two groups in general and intraoperative conditions, which made the groups comparable. In this study, the AAI was maintained 15~25 during the operation, and the vital signs were stable. Thus, the effects of anesthesia depth and hemodynamic fluctuation on the test results were excluded [21].

The neuropsychological test used in this study shows that POCD has high specificity and sensitivity. The visual speech learning test and concept conversion task in the neuropsychological test methods (including 6 items) were recommended by the international organization for the study of postoperative cognitive impairment. The test and alphanumeric symbol test are basically similar to the associative learning test, online test, and digital symbol test [22]. The neuropsychological test used in this study can objectively reflect the cognitive function of the human brain.

Table 3: The neuropsychological test in two groups (score).

Item	POCD ($n = 12$)	Non-POCD ($n = 36$)	t	P
Cumulative test				
Before operation	62.4 ± 21.2	73.1 ± 22.8	1.431	0.159
After operation	28.9 ± 13.7	61.4 ± 18.3	5.632	<0.001
t/P	4.598/<0.001	2.401/0.019		
Visual regeneration				
Before operation	10.4 ± 1.8	10.2 ± 2.1	0.295	0.769
After operation	8.1 ± 2.1	9.4 ± 1.8	2.079	0.043
t/P	2.881/0.009	1.735/0.087		
Associative learning				
Before operation	13.4 ± 2.3	13.6 ± 2.4	0.252	0.802
After operation	9.8 ± 2.6	12.5 ± 3.1	2.711	0.009
t/P	3.593/0.002	1.683/0.097		
Digital breadth (consequent)				
Before operation	5.7 ± 1.6	5.8 ± 1.4	0.207	0.837
After operation	5.5 ± 1.5	5.7 ± 1.1	0.497	0.622
t/P	0.316/0.755	0.337/0.737		
Digital breadth (reverse)				
Before operation	3.4 ± 0.9	3.3 ± 0.8	0.364	0.718
After operation	2.6 ± 0.8	3.1 ± 0.7	2.068	0.044
t/P	2.909/0.006	1.129/0.263		
Number sign				
Before operation	18.2 ± 3.7	17.4 ± 4.1	0.599	0.552
After operation	16.5 ± 2.8	16.2 ± 2.7	0.330	0.743
t/P	1.269/0.278	1.467/0.147		
Connecting line				
Before operation	62.8 ± 13.9	64.5 ± 15.4	0.339	0.736
After operation	64.2 ± 11.4	65.1 ± 16.8	0.172	0.864
t/P	0.270/0.790	0.158/0.875		
Nail board (dominant hand)				
Before operation	64.2 ± 11.8	62.3 ± 12.7	0.457	0.650
After operation	64.7 ± 12.1	62.1 ± 13.1	0.606	0.547
t/P	0.102/0.919	0.066/0.948		
Nail board (nondominant hand)				
Before operation	74.5 ± 15.9	73.2 ± 15.1	0.255	0.800
After operation	76.1 ± 11.6	75.8 ± 17.4	0.056	0.956
t/P	0.282/0.781	0.677/0.501		
Total Z	3.0 ± 0.7	1.1 ± 0.5	10.281	<0.001

In this study, parallel version is used to reduce the learning effect in the process of testing; each test is conducted by the same tester in the same environment and in the same time period to overcome the variability. It has been reported by foreign scholars that increasing the items of the neuropsychological test can not only improve the sensitivity of the test method but also significantly improve the false-positive rate [23]. The false-positive rate can affect the results of POCD-related studies, so that the results of similar studies are not comparable.

MRI has a good contrast resolution for soft tissue and multidirectional imaging characteristics [24]. It can clearly show the true anatomy section images of various layers of brain structure, because the volume of the prefrontal lobe can be affected by the volume of cranial content, which leads to the lack of comparability of data. In this study, the volume

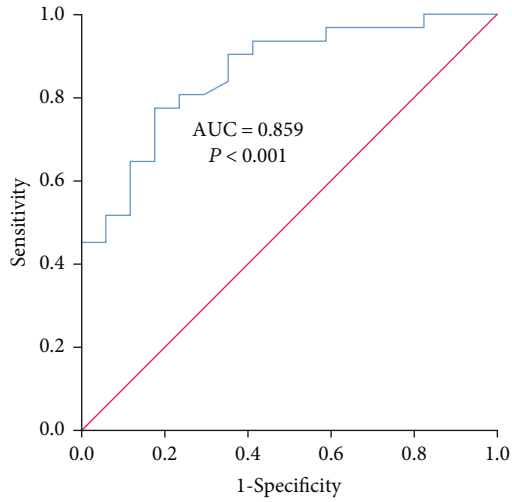

Figure 4: The ROC curve of prefrontal lobe volume for predicting POCD.

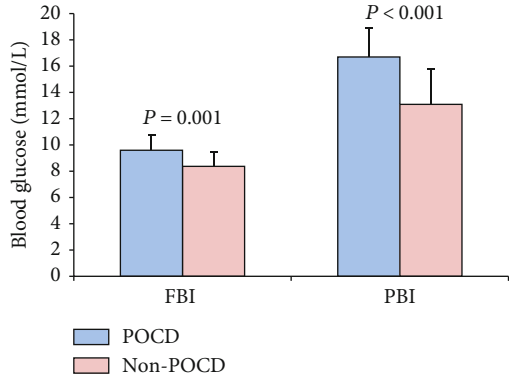

Figure 5: The blood glucose in POCD and non-POCD groups.

of the prefrontal lobe was standardized to eliminate the influence of the whole brain.

The results showed that the volume of the prefrontal lobe in the POCD group was smaller than that in the non-POCD group, and there was a negative correlation between the volume of the prefrontal lobe and the Z-score. The sensitivity, specificity, and Youden's index of predicting the occurrence of POCD were 77.4%, 82.4%, and 0.598, indicating that the preoperative volume of the prefrontal lobe measured in MRI can predict the occurrence of POCD. The cut-off value of frontal volume between patients with POCD and those without POCD was 179.8.

We further analyzed the relationship between blood glucose, volume of prefrontal, and POCD. The results showed that the FBI and PBI in POCD were significantly higher than the data in non-POCD, indicating that the high blood glucose is more likely to cause POCD. In addition, there was a negative correlation between the volume of the prefrontal lobe and FBI or PBI. Long-time hyperglycemia has damaged brain tissue, which is the morphological basis of POCD.

From our study, we implemented prefrontal image segmentation based on an improved clustering algorithm and used them in the prevention of POCD. However, we do not know the specific advantages of this method and other artificial intelligence algorithms [25, 26]. Reports also showed that different types of intracerebral hemorrhage can lead to changes in brain texture. So, whether POCD will cause brain texture changes is one of the directions we will consider in the future [27].

5. Conclusions

In conclusion, the segmentation of the prefrontal lobe based on an improved clustering algorithm before operation may predict the occurrence of POCD in diabetics. There was a negative correlation between blood glucose and volume of the prefrontal lobe. The reduction of the prefrontal lobe is related to the increase of blood glucose.

Data Availability

The data used to support the findings of this study are available from the corresponding author upon request.

Conflicts of Interest

All authors declare no conflicts of interest in this paper.

References

[1] L. Zhao, L. Mao, Q. Liu, X. Chen, X. Tang, and D. An, "Cognitive impairment in type 2 diabetes patients with and without diabetic peripheral neuropathy: a mismatch negativity study," *Neuroreport*, vol. 32, no. 14, pp. 1223–1228, 2021.

[2] L. A. Zilliox, K. Chadrasekaran, J. Y. Kwan, and J. W. Russell, "Diabetes and cognitive impairment," *Current Diabetes Reports*, vol. 16, no. 9, p. 87, 2016.

[3] X. Y. Yuan and X. G. Wang, "Mild cognitive impairment in type 2 diabetes mellitus and related risk factors: a review," *Reviews in the Neurosciences*, vol. 28, no. 7, pp. 715–723, 2017.

[4] S. Albahli, "Type 2 machine learning: an effective hybrid prediction model for early type 2 diabetes detection," *Journal of Medical Imaging and Health Informatics*, vol. 10, no. 5, pp. 1069–1075, 2020.

[5] R. Simó, A. Ciudin, O. Simó-Servat, and C. Hernández, "Cognitive impairment and dementia: a new emerging complication of type 2 diabetes-the diabetologist's perspective," *Acta Diabetologica*, vol. 54, no. 5, pp. 417–424, 2017.

[6] M. Xue, W. Xu, Y. N. Ou et al., "Diabetes mellitus and risks of cognitive impairment and dementia: a systematic review and meta-analysis of 144 prospective studies," *Ageing Research Reviews*, vol. 55, article 100944, 2019.

[7] G. J. Biessels and F. Despa, "Cognitive decline and dementia in diabetes mellitus: mechanisms and clinical implications," *Nature Reviews. Endocrinology*, vol. 14, no. 10, pp. 591–604, 2018.

[8] M. Callisaya and K. Nosaka, "Effects of exercise on type 2 diabetes mellitus-related cognitive impairment and dementia," *Journal of Alzheimer's Disease*, vol. 59, no. 2, pp. 503–513, 2017.

[9] C. D. Spies, C. Knaak, M. Mertens et al., "Physostigmine for prevention of postoperative delirium and long-term cognitive dysfunction in liver surgery: a double-blinded randomised

controlled trial," *European Journal of Anaesthesiology*, vol. 38, no. 9, pp. 943–956, 2021.

[10] R. Alalawi and N. Yasmeen, "Postoperative cognitive dysfunction in the elderly: a review comparing the effects of desflurane and sevflurane," *Journal of Perianesthesia Nursing*, vol. 33, no. 5, pp. 732–740, 2018.

[11] G. Lachmann, I. Feinkohl, F. Borchers et al., "Diabetes, but not hypertension and obesity, is associated with postoperative cognitive dysfunction," *Dementia and Geriatric Cognitive Disorders*, vol. 46, no. 3-4, pp. 193–206, 2018.

[12] M. J. Needham, C. E. Webb, and D. C. Bryden, "Postoperative cognitive dysfunction and dementia: what we need to know and do," *British Journal of Anaesthesia*, vol. 119, suppl_1, pp. i115–i125, 2017.

[13] N. Kotekar, A. Shenkar, and R. Nagaraj, "Postoperative cognitive dysfunction - current preventive strategies," *Clinical Interventions in Aging*, vol. Volume 13, pp. 2267–2273, 2018.

[14] A. Henri-Bhargava, D. T. Stuss, and M. Freedman, "Clinical assessment of prefrontal lobe functions," *CONTINUUM: Lifelong Learning in Neurology*, vol. 24, no. 3, pp. 704–726, 2018.

[15] P. W. Burgess and D. T. Stuss, "Fifty years of prefrontal cortex research: impact on assessment," *Journal of the International Neuropsychological Society*, vol. 23, no. 9-10, pp. 755–767, 2017.

[16] H. Chang, K. Kim, Y. J. Jung, and M. Kato, "Effects of acute high-intensity resistance exercise on cognitive function and oxygenation in prefrontal cortex," *Journal of Exercise Nutrition & Biochemistry*, vol. 21, no. 2, pp. 1–8, 2017.

[17] J. W. Paylor, E. Wendlandt, T. S. Freeman et al., "Impaired cognitive function after perineuronal net degradation in the medial prefrontal cortex," *Eneuro*, vol. 5, no. 6, 2018.

[18] B. Chen, S. Wang, W. Sun et al., "Functional and structural changes in gray matter of Parkinson's disease patients with mild cognitive impairment," *European Journal of Radiology*, vol. 93, pp. 16–23, 2017.

[19] K. Matsuoka, F. Yasuno, A. Hashimoto et al., "Left dorsolateral prefrontal cortex atrophy is associated with frontal lobe function in Alzheimer's disease and contributes to caregiver burden," *International Journal of Geriatric Psychiatry*, vol. 33, no. 5, pp. 703–709, 2018.

[20] R. Paul, S. M. Grieve, B. Chaudary et al., "Relative contributions of the cerebellar vermis and prefrontal lobe volumes on cognitive function across the adult lifespan," *Neurobiology of Aging*, vol. 30, no. 3, pp. 457–465, 2009.

[21] I. Rundshagen, "Postoperative cognitive dysfunction," *Deutsches Ärzteblatt International*, vol. 111, no. 8, pp. 119–125, 2014.

[22] H. E. Feenstra, I. E. Vermeulen, J. M. Murre, and S. B. Schagen, "Online cognition: factors facilitating reliable online neuropsychological test results," *The Clinical Neuropsychologist*, vol. 31, no. 1, pp. 59–84, 2017.

[23] M. S. Lewis, P. Maruff, B. S. Silbert, L. A. Evered, and D. A. Scott, "Detection of postoperative cognitive decline after coronary artery bypass graft surgery is affected by the number of neuropsychological tests in the assessment battery," *The Annals of Thoracic Surgery*, vol. 81, no. 6, pp. 2097–2104, 2006.

[24] C. Korponay, M. Pujara, P. Deming et al., "Impulsive-antisocial psychopathic traits linked to increased volume and functional connectivity within prefrontal cortex," *Social Cognitive and Affective Neuroscience*, vol. 12, no. 7, pp. 1169–1178, 2017.

[25] J. Shi, Y. Ye, D. Zhu, L. Su, Y. Huang, and J. Huang, "Automatic segmentation of cardiac magnetic resonance images based on multi- input fusion network," *Computer Methods and Programs in Biomedicine*, vol. 209, article 106323, 2021.

[26] Z. Tang, G. Zhao, and T. Ouyang, "Two-phase deep learning model for short-term wind direction forecasting," *Renewable Energy*, vol. 173, pp. 1005–1016, 2021.

[27] Y. Liu, Q. Fang, A. Jiang, Q. Meng, G. Pang, and X. Deng, "Texture analysis based on u-net neural network for intracranial hemorrhage identification predicts early enlargement," *Computer Methods and Programs in Biomedicine*, vol. 206, article 106140, 2021.

Hindawi
Computational and Mathematical Methods in Medicine
Volume 2021, Article ID 2827556, 7 pages
https://doi.org/10.1155/2021/2827556

Research Article

Computed Tomographic Image Processing and Reconstruction in the Diagnosis of Rare Osteochondroma

Ting Zhao[1,2] **and Hongyan Zhao**[1,3]

[1]*Department of Nursing, Shengjing Hospital of China Medical University, Shenyang, Liaoning 110004, China*
[2]*Department of General Surgery, Shengjing Hospital of China Medical University, Shenyang, Liaoning 110004, China*
[3]*Department of Orthopedics, Shengjing Hospital of China Medical University, Shenyang, Liaoning 110004, China*

Correspondence should be addressed to Hongyan Zhao; zhaohy1970@163.com

Received 20 June 2021; Revised 23 July 2021; Accepted 2 August 2021; Published 16 August 2021

Academic Editor: Kelvin Wong

Objective. We applied computed tomography (CT) to explore the imaging manifestations of rare parts of osteochondroma. Based on the medical images, deblurring using a convolutional neural network (CNN), and three-dimensional (3D) reconstruction of the images is performed in order to improve the image diagnosis. *Methods*. Twelve cases of osteochondroma in rare locations confirmed by surgical pathology or clinical long-term dynamic observation were retrospectively analyzed using medical imaging and image reconstruction. There are 7 males and 5 females, with an average age of 43 years. CT examinations were performed in all cases. Image deblurring via the GAN model is performed followed by the 3D reconstruction of the higher quality images is implemented. A retrospective study was performed on the imaging manifestations of the above cases; the imaging characteristics were summarized. *Results*. The imaging features are the following lesions, including 4 cases of the proximal radius, 4 cases of the scapula, 2 cases of the pelvis, and 2 cases of the proximal ribs. The cartilage caps, cortex, and sternum were typical structures of the bone surface of the studied cases. In the continuous imaging features, calcification was visible in some cases, and no significant enhancement was seen in enhanced scans; there was no obvious direction of lesion growth. The image processing techniques that we performed are useful in enhancing the quality of the medical diagnosis. *Conclusions*. Rare site osteochondroma has certain imaging features. In most cases, we can accurately diagnose rare site osteochondroma through these features via the image processing methods that are proposed in this paper.

1. Introduction

At present, the research in the field of image deblurring in the medical field mainly includes the medical image processing of data sets following the implementation of deblurring algorithms. In the field of medical deep learning, the status of image map data sets is self-evident, and the quality of the data set directly affects the quality of the experimental results. Compared with other image degradation and restoration problems, it is more difficult to obtain a data set for medical image deblurring, because it is difficult to capture a pair of clear images with exactly the same factors in a real lesion map, even if two consecutive images are taken. These two images will not correspond exactly due to changes in some factors, so it is almost impossible to obtain a pair of clear and blurred images with exactly the same content.

Osteochondroma is a common benign bone tumor in childhood. It is usually located on the cortex of one side of the metaphysis and grows to the surface of the bone. It is also called exoskeleton wart. Osteochondroma can be divided into single and multiple; the latter has a genetic predisposition and affects the development of epiphyseal or limb deformities, known as multiple hereditary osteochondroma disease, or continuation of the backbone. Lesions are located in the metaphysis, most commonly, the distal femur, the proximal tibia, and the proximal humerus. Clinically, osteochondroma has no pain or tenderness and produces corresponding symptoms when the nerve is compressed.

Osteochondroma is a common benign tumor in clinical work, accounting for 10-15% of all bone tumors and 20-50% of benign bone tumors. The ratio of male to female is 1.6 : 1 [1, 2], and the most common sites are the distal femur and the proximal tibia, followed by the proximal humerus, the distal radius, and the ends of the fibula, and can also occur in flat bones and other places [3]. This article focuses on the analysis of osteochondroma that occurs in flat bones, irregular bones, and proximal radiuses. Occurrence of osteochondroma in rare parts, due to its special location, generally does not attract the attention of clinicians; diagnostic experience is limited; in actual work, there are still diagnostic errors. This article summarizes the performance of 12 cases of osteochondroma in rare parts, and strives to improve the imaging diagnosis of osteochondroma in rare parts.

2. Materials and Methods

2.1. Convolutional Neural Network. Convolutional neural network is a classic deep learning network that promotes the rapid development of artificial intelligence. Convolutional neural network is composed of input layer, convolutional layer, activation function, pooling layer, and fully connected layer. Among them, the input layer is used to load the image with the input pixel size of $H \times W \times D$ into the network; the convolution layer is used to extract image features; the input image and the convolution kernel should be multiplied by position elements and then summed, and finally, the convolution of the feature map after the product. In convolution operations, weight sharing is usually used to reduce the amount of calculation. Shared weights are different images or the same image sharing a convolution kernel. Using weight sharing can reduce the number of convolution kernels and speed up the training of the network. In order to better connect local information, convolution kernels generally use partial overlap sliding in the feature map to perform convolution operations. Overlap sliding means that there is an overlap between two adjacent convolution kernels. This sliding method makes the convolution calculation of the local receptive fields reduce the amount of calculation and at the same time ensures that there is a certain connection between the information extracted by the two local receptive fields. The neural network convolution operation is shown in Figure 1.

2.2. Patients Information. A retrospective study was performed to collect 12 cases of osteochondroma diagnosed in rare locations confirmed by surgical pathology or clinical follow-up observation. There were 7 males and 5 females, with an average age of 43 years. Ten patients were diagnosed with local palpitation, and two cases had lesions found during normal physical examination. All patients underwent CT examinations.

2.3. Indications for Surgery. Surgical treatment is performed for cases with obvious clinical symptoms, which include pain, limited joint movement, neurovascular compression, bursitis, or severely affected appearance. For patients with single-pedicled osteochondroma that occurs in the long tubular bones of the extremities, there are only regular follow-up observations if there are no clinical symptoms [4–6]. Consider surgical resection of osteochondroma with (1) clinical symptoms such as pain or discomfort; (2) fracture of the diseased pedicle; (3) local bursitis; (4) affecting joint activity; (5) compression of nerve blood vessels; (6) the lesions may increase in a short time or the symptoms may be aggravated; malignant changes may be suspected; (7) patients who affect the appearance strongly demand surgery. As for multiple osteochondroma, due to multiple lesions throughout the body, patients should be selected to perform surgery on the areas that affect them the most. Most of these areas seriously affect the appearance or joint activity and even cause joint deformities or they should be vigilant in the short term. Here, the malignant areas are seen to be existent.

Comparative analysis of the image characteristics includes the incidence of the case studied, the number of lesions, the shape of the cartilage cap, the density of the lesion, and the change in the density of the lesion after enhanced scanning, the condition of the adjacent bone cortex and bone structure, the direction of lesion growth, and the surrounding soft tissue. We summarize its imaging characteristics and improve the accuracy of diagnosis.

2.4. Surgical Resection Range. Longitudinal incision, separated to the surface of the mass, cut the bursa, cut the periosteum in a ring along 0.5~1 cm outside the base of the mass, cut the normal bone cortex of the host bone with a scalpel along this line, and then loosen along the bottom of the mass. Plasmas make sure to remove the fibrous membrane, cartilage cap, and bone warts outside the cartilage of the tumor together with the surrounding normal periosteum and cortical bone.

3. Results

3.1. Distribution of Lesions. In order to verify the effectiveness of the model, this paper explores the performance of the image motion blur removal model proposed in this paper from three aspects: visual effect, peak signal-to-noise ratio, and training time. The model in this article converges after being trained 200,000 times on the above training set, and the effect of the model is tested on the test set.

The effect of removing the blurred part of the image from the image in the data set is shown in Figure 2. On the left is the original blurred image in the data set, and on the right is the clear image generated after the model in this article. It can be seen from the experimental visual effects that the model proposed in this paper achieves a clear resolution of the visual effect of removing the blur of medical image images, and the calculation time of each step during training is increased by 0.04 seconds, and the test time is also reduced by 0.04 seconds.

This paper uses peak signal-to-noise ratio (PSNR) to measure the effect of image processing. The PSNR is an engineering term that represents the ratio of the maximum possible power of a signal to the destructive noise power that affects its representation accuracy. Since many signals have a very wide dynamic range, they are often expressed in

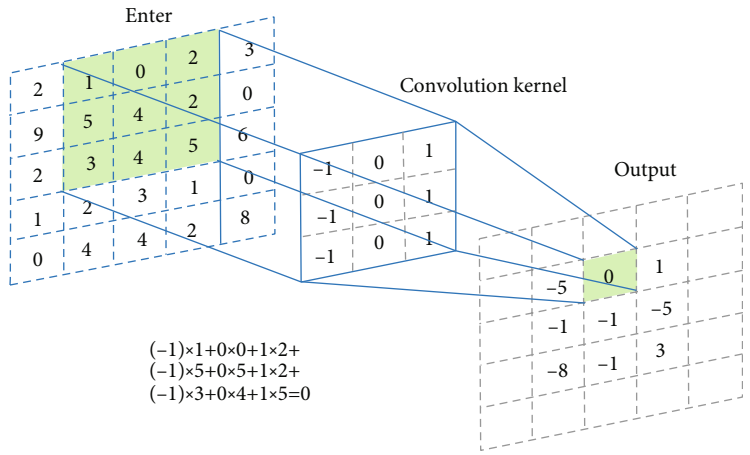

Figure 1: Convolution neural network operation.

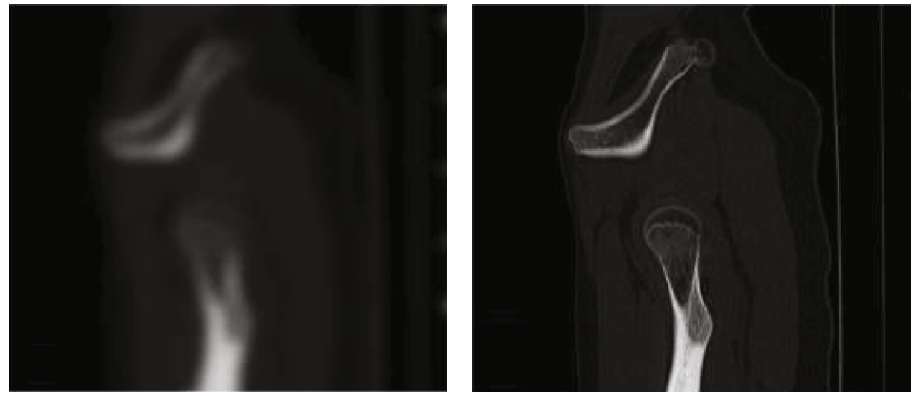

(a) (b)

Figure 2: (a) changed to (b) is to remove the image blur state test effect diagram.

logarithmic decibel units. The higher the peak signal-to-noise ratio, the higher the similarity between the restored image and the original image. This paper compares this metric with CNN-15, the deblurring method based on l0 norm, and our previous work SRN method. The experimental results are shown in Table 1.

The convergence of model training over time is shown in Figure 3.

Red represents the model in this paper, and blue represents the image blurring model based on the generative adversarial network in work. It can be seen that the model in this paper converges faster than the model in work.

There were 4 cases of proximal radius, 4 cases of scapula, 2 cases of pelvis, and 2 cases of proximal ribs (as shown in Table 2). There were 2 cases of the proximal radius (Figure 4), 4 cases of the scapula body, all located above the dorsal scapula (Figure 5), 2 cases of the pelvis (Figure 6), and 2 cases of the proximal rib (Figure 7). CT examinations were performed in all the studied cases to exclude possible osteochondroma lesions in other prevalent sites, and it was judged that the patients studied were single cases.

The middle part 4 of the proximal radius of the limb is shown, for example, in Figure 4 based on CT using medical images and 3D analysis based on the image reconstruction. There were 4 cases of scapula and 2 cases of pelvis in front of the scapula. The left mandibular angle is shown in Figure 5. The left mandibular coronoid process is shown in Figure 6. The proximal rib 2 is shown in Figure 7.

3.2. Cartilage Cap Morphology. The top of osteochondroma is covered with cartilage, called a cartilage cap, which varies in thickness. The thin ones are only linear translucent areas, which are not easy to see. The tumor surface of 7 patients who underwent the CT examination showed typical cartilage signals. Combined with CT and the 3D image reconstruction, 3 cases of spotted and strip-like calcifications were found inside the cartilage cap. The patients in this group are mainly sessile, the lesions are dish-shaped or hemispherical, and the apex is uneven, showing nodular and cauliflower-like changes. Lesion cartilage caps are small and well-defined, suggesting benign growth.

3.3. Changes in Lesions and Enhanced Scans. Of the 12 patients, 3 had punctate and strip-like calcifications inside the lesion, and the rest of the lesion had cartilage and changes in bone density or signal. There was no obvious abnormal enhancement in all lesions on the enhanced scan, indicating that the blood flow of the lesion was not abundant.

Table 1: Comparison of experimental results of peak signal-to-noise ratio.

Method	PSNR
CNN-15	28.63
Based on l_0 norm	28.32
DEBLURGAN	29.96
SRN	29.57
Algorithm	30.04

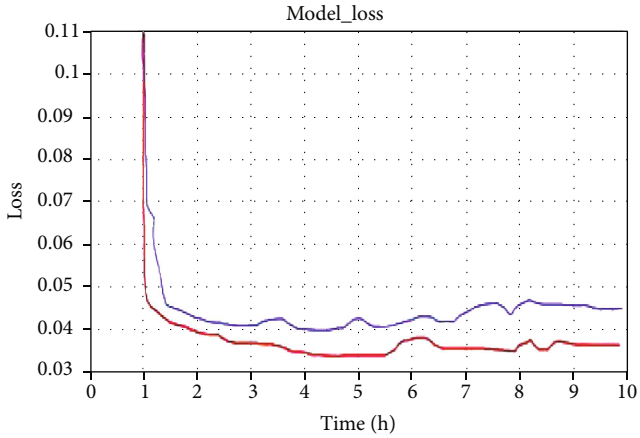

Figure 3: Convergence of model training over time.

Table 2: Situation of the case studied.

Occurrence site	Proximal radius	Shoulder blade	Pelvis	Rib cage
Number of cases	4	4	2	2

3.4. Near the Cortex and Bone Structure. All lesions showed signs of continuous connection with the adjacent normal bone (female bone) cortex. No obvious bone destruction and periosteal reaction were found in the adjacent bones.

3.5. Direction of Lesion Growth. Occurrence of osteochondroma in the proximal radius is a local bulge without obvious directionality. Osteochondroma of the scapula body showed a local bony hump in the posterior part of the scapula without obvious directionality. Pelvic chondroma grows outward. Two cases of rib osteochondroma occurred near the ribs and grew along the long axis of the ribs.

3.6. Surrounding Soft Tissue. In the studied case, the bone cortex was intact, there was no obvious swelling of the local soft tissue, and there was no abnormal density change inside. No abnormal enhancement was seen on the enhanced scan.

4. Discussion

4.1. The Etiology and Pathological Basis of Osteochondroma. Some studies conclude that osteochondroma is a real tumor, and some scholars suggest that it is caused by the lack of growth of the developmental epiphysis [7–9]. Virchow et al. proposed that a single osteochondroma is a tumor formed when the epiphyseal cartilage plate is separated and grows laterally outside the bone during development. Lihtenstein et al. believe that the periosteum develops abnormally, and the displaced cartilage nest continues to grow [10–13]. Osteochondroma is a three-layer typical structure: (1) the surface layer is collagen connective tissue with scarce blood vessels, which is connected with the surrounding periosteum and is closely attached to the underlying tissue; (2) the middle layer is gray-blue transparent cartilage, that is, "cartilage cap," which is similar to normal cartilage and often calcified; (3) the base layer is the main body of the tumor, and the bone marrow containing yellow bone marrow is connected to the affected bone. In theory, osteochondroma can occur in any bone with cartilage internalized bone, an ossified form [12].

4.2. Advantages of General Radiography, CT, MRI, and Other Imaging Methods for Diagnosis. X-ray diagnosis is simple and easy. It is a basic examination method. It can initially determine the growth direction of osteochondroma lesions, internal calcification, and whether the cortex is connected. It has obvious advantages in the diagnosis of osteochondroma in the middle limbs. For areas with many overlapping areas, such as the pelvis, ribs, and scapula, further CT scans are needed to confirm. CT examination and three-dimensional reconstruction can clearly show the relationship between the tumor and the affected bone, showing that the lesion is continuous with the surrounding bone cortex, calcification of the cartilage cap of the lesion, and the condition of the surrounding soft tissue [13, 14]. Combined with the enhanced scan to judge the blood flow of the lesion, the diagnosis can be basically confirmed. It is the preferred method for the diagnosis of osteochondroma in rare sites; it is also helpful for the differential diagnosis of osteochondroma and periosteal chondrosarcoma.

MRI can also independently diagnose osteochondroma [15]. It can show the connection between the tumor and the affected bone from multiple angles. It can directly display the cartilage signal of the cartilage cap. MRI can also show changes in the bursa around the lesion. The basal periphery of the tumor on the MRI is a linear cortical bone connected to the normal female bone, with low signal on T1WI and T2WI; cancellous bone with fatty pulp in it, high signal on T1WI and moderate signal on T2WI; noncalcified cartilage. The appearance of the cap is leaf-shaped, containing uniform and consistent cartilage. T1WI is low signal, and T2WI is high signal. The calcified cartilage caps T1WI and T2WI are both banded or cauliflower-shaped low signal regions. The surface fibrous membrane is linear low signal [16, 17].

4.3. Differential Diagnosis. (1) Chondrosarcoma: It usually occurs in the long bones of the extremities. Most are thought to be related to embryonic tissue or ectopic, most of which are endogenous, exogeneous, or paracortical, tumors are lobulated and have fibrous envelopes, and the main component is hyaline cartilage. Homogeneous high-signal hyaline cartilage is separated by low-signal fibrous compartments and changes in leaf shape or uneven signal; the degree of

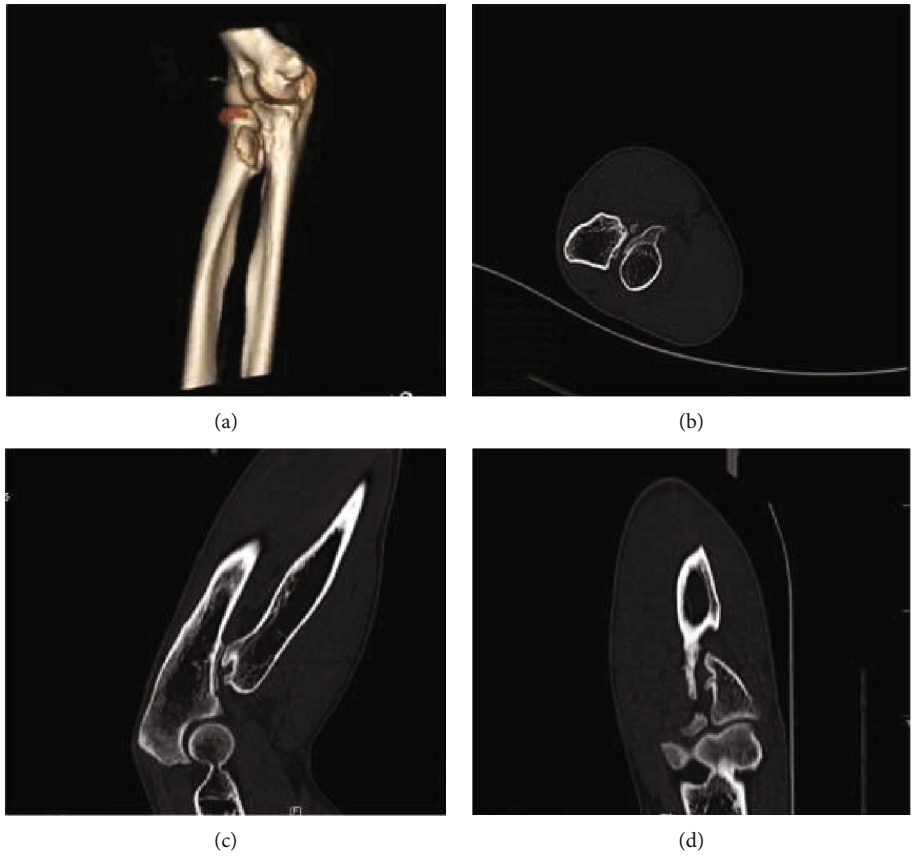

(a) (b) (c) (d)

Figure 4: Based on the 3D image reconstruction, the right radial bone is locally irregularly raised, the internal density is unevenly reduced, the CT lesion is continuous with the surrounding cortex, and the interior is cartilage density or signal.

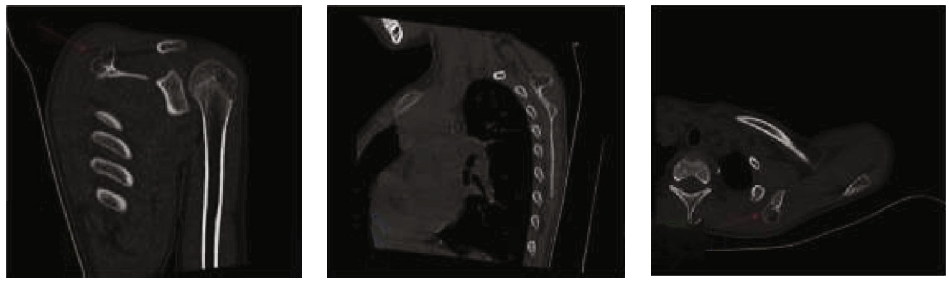

(a) (b) (c)

Figure 5: Osteochondroma protruding from the left scapula posterolaterally after image deblurring.

malignancy is higher. In patients with multiple hereditary exostosis, the risk of malignant transformation into chondrosarcoma is greater. Chondrosarcoma is more likely if the thickness of the cartilage cap is greater than 2 cm [18].

(2) Malignant changes of osteochondroma: The main manifestations are as follows: (1) tumors grow rapidly; (2) the thickness of cartilage caps is greater than 1.0 cm or a large number of irregular calcifications; (3) the density of calcification of cartilage caps suddenly fades; translucent areas appear newly; soft tissue masses appear around the tumor, distant metastases from the tumor.

(3) Bone islands: It shows uniform density shadows in any part of the bone, mostly uniform high density shadows, that is, dense bone islands, and there are uniform low density shadow changes, such as osteoporotic bone islands. It is a common developmental mutation that is a benign change; however, it rarely rises from the growth of the cortical bone, and its uniform internal density is its characteristic.

4.4. Medical Image Processing Techniques Used in Medical Diagnosis. In recent years, with the popularization of imaging equipment and the large-scale use of digital images, the application value of image deblurring continues to increase, and many algorithms blindly improve the effect of removing image blur, but ignore the running time of the algorithm. In order to further improve the effectiveness and

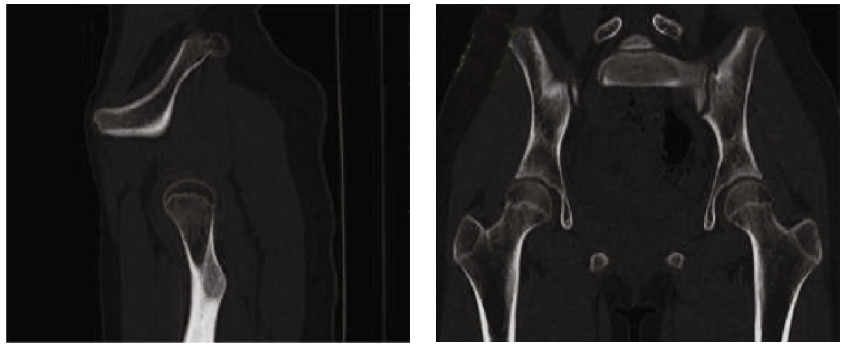

(a) (b)

Figure 6: Osteochondroma protruding from the right pelvis (sacrum) posterolaterally.

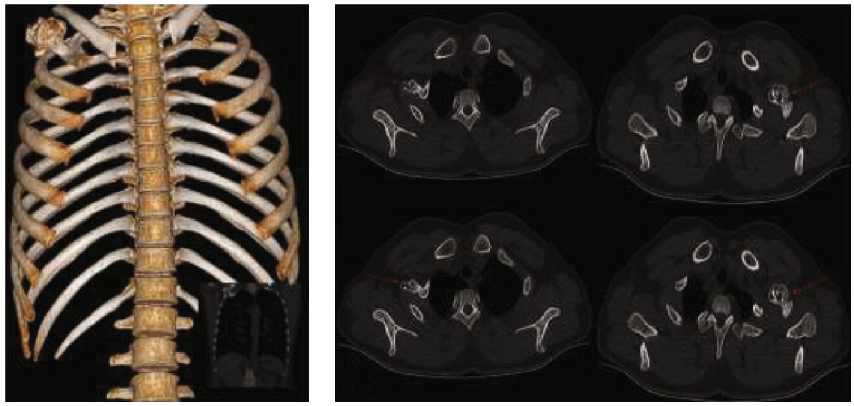

(a) (b)

Figure 7: Osteochondroma of the right rib is continuously displayed around the outer cortex based on 3D reconstruction of the structure.

practicability of the algorithm, this paper combines a large amount of related work and proposes a model based on the generation of countermeasure network to remove image motion blur, which greatly improves the practicability of the model; on this basis, a further method based on convolutional neural network can be used to remove the image blurring.

In addition to the rare osteochondroma described in this paper, osteochondromas of the spine and clavicle have also been reported in the literature [19]. Among them, spinal osteochondroma is more common in spinal appendages, especially spinous processes.

In short, in addition to the common features of some common osteochondromas, the rare parts of osteochondroma combine with this group of cases and related literature [20].

5. Conclusion

This paper utilized 3D medical image reconstruction based on CT and summarizes the following characteristics: osteochondromas may appear in the scapula, proximal radius, and pelvis, rare parts such as ribs; the lesions are solitary; the broad bottom is connected to the female bone, the cortex continues from the female bone to the tumor, the outer edge is cortical bone connected to normal bone, and the inner is cancellous bone, which communicates with the mother's medullary cavity; the top is the structure of the cartilage cap. CT can show the presence of the cartilage cap; malignant changes are rare; there is no obvious direction of growth. Because there are few cases in this group, osteochondroma of all rare parts is not included, so the imaging study of rare parts of osteochondromas needs to be further studied and expanded. Furthermore, the 3D medical image diagnosis can be applied after superresolution image reconstruction is implemented so as to achieve a better quality image.

Data Availability

The image data used to support the findings of this study are available from the corresponding author upon request.

Ethical Approval

There is no ethics approval required for this paper.

Conflicts of Interest

The authors declare that they have no conflicts of interest.

Acknowledgments

The authors appreciate the Shengjing Hospital for assisting in processing of the medical images and the medical engineer for assisting them in the medical image reconstruction and diagnosis.

References

[1] S. Baer-Henney, M. Tatagiba, and M. Samii, "Osteochondroma of the servical spine causing occipital nerve neuralgia. Case report," *Neurological Research*, vol. 23, no. 7, pp. 777–779, 2001.

[2] K. G. Buchan, V. Zamvar, K. M. Mandana, E. Nihal, and P. Kulatilake, "Juxtacardiac costal osteochondroma presenting as recurrent haemothorax," *European Journal of Cardio-Thoracic Surgery*, vol. 20, no. 1, pp. 208–210, 2001.

[3] Y. Xing, B. Xu, X. Sheng et al., "Transformation from persistent atrial fibrillation to paroxysmal type after initial ablation predicts success of repeated ablation," *International Journal of Cardiology*, vol. 268, pp. 120–124, 2018.

[4] B. Liu, G. Xu, Y. Sun et al., "Association between maternal prepregnancy obesity and preterm birth according to maternal age and race or ethnicity: a population-based study," *The Lancet Diabetes & Endocrinology*, vol. 7, no. 9, pp. 707–714, 2019.

[5] Q. Zhang, H. Hu, H. Liu et al., "RNA sequencing enables systematic identification of platelet transcriptomic alterations in NSCLC patients," *Pharmacotherapy*, vol. 105, pp. 204–214, 2018.

[6] J. Ouyang, X. Chen, Z. Huangfu, C. Lu, D. Huang, and Y. Li, "Application of distributed temperature sensing for cracking control of mass concrete," *Construction and Building Materials*, vol. 197, pp. 778–791, 2019.

[7] Z. Lin, Y. Nie, X. Cai et al., "Benchmarking of ^{232}Th evaluation by a 14.8 MeV neutron leakage spectra experiment with slab samples," *Annals of Nuclear Energy*, vol. 96, pp. 181–186, 2016.

[8] S. Xiao, S. Liu, H. Wang, Y. Lin, M. Song, and H. Zhang, "Nonlinear dynamics of coupling rub-impact of double translational joints with subsidence considering the flexibility of piston rod," *Nonlinear Dynamics*, vol. 100, no. 2, pp. 1203–1229, 2020.

[9] S. Xiao, S. Liu, M. Song, N. Ang, and H. Zhang, "Coupling rub-impact dynamics of double translational joints with subsidence for time-varying load in a planar mechanical system," *Multibody System Dynamics*, vol. 48, no. 4, pp. 451–486, 2020.

[10] B. Liu, H.-J. Lehmler, Y. Sun et al., "Bisphenol A substitutes and obesity in US adults: analysis of a population- based, cross-sectional study," *The Lancet Planetary Health*, vol. 1, no. 3, pp. e114–e122, 2017.

[11] L. Huang, L. Yin, B. Liu, and Y. Yang, "Design and error evaluation of planar 2-DOF remote center of motion mechanisms with cable transmissions," *Journal of Mechanical Design*, vol. 143, no. 1, article 013301, 2021.

[12] B. Hu, C. Zhou, H. Wang, and L. Yin, "Prediction and validation of dynamic characteristics of a valve train system with flexible components and gyroscopic effect," *Mechanism and Machine Theory*, vol. 157, article 104222, 2021.

[13] Y. Fan, X. Zhao, X. Hu, M. Miao, A. Warren, and W. Song, "Taxonomy and molecular phylogeny of two novel ciliates, with establishment of a new genus, _Pseudogastrostyla_ n. g. (Ciliophora, Hypotrichia, Oxytrichidae)," *European Journal of Protistology*, vol. 51, no. 5, pp. 374–385, 2015.

[14] E. G. Gentry, B. W. Henderson, M. Gearing, Y. Feng, and J. H. Herskowitz, "O2-12-04: Rho kinase ii (ROCK2) inhibition reduces tau levels via autophagy in neurons," *Alzheimer's & Dementia*, vol. 11, no. 7S_Part_4, p. 203, 2015.

[15] T. Li, Y. Chen, X. Hu, Y. Li, and L. Wang, "Exploiting negative Poisson's ratio to design 3D-printed composites with enhanced mechanical properties," *Materials & Design*, vol. 142, pp. 247–258, 2018.

[16] W. Wu, H. Ueda, K. Löbmann, T. Rades, and H. Grohganz, "Organic acids as co-formers for co-amorphous systems - influence of variation in molar ratio on the physicochemical properties of the co-amorphous systems," *European Journal of Pharmaceutics and Biopharmaceutics*, vol. 131, pp. 25–32, 2018.

[17] E. T. Mombeshora, P. G. Ndungu, and V. O. Nyamori, "Effect of graphite/sodium nitrate ratio and reaction time on the physicochemical properties of graphene oxide," *Carbon*, vol. 124, p. 724, 2017.

[18] J. Leymarie, P. Disseix, M. Rezki, C. Monier, A. Vasson, and A.-M. Vasson, "Conduction band offset ratio of the (In,Ga)As/GaAs system and (In,Ga)As alloy properties," *Materials Science and Engineering: B*, vol. 44, no. 1-3, pp. 147–150, 1997.

[19] H. Moriceau, B. Ferrand, J. Daval, and D. Challeton, "Influence of the CaCO3GeO2 ratio on Y Sm Lu Ca Fe Ge garnet films properties," *Materials Research Bulletin*, vol. 15, no. 1, pp. 107–111, 1980.

[20] G. K. Kristiansen, "Further properties of Kuhn's ratio," *Archiv der Mathematik*, vol. 49, no. 6, pp. 513–520, 1987.

Hindawi
Computational and Mathematical Methods in Medicine
Volume 2021, Article ID 8214304, 8 pages
https://doi.org/10.1155/2021/8214304

Research Article

Cardiac Magnetic Resonance Images Superresolution via Multichannel Residual Attention Networks

Defu Qiu,[1,2] **Yuhu Cheng**,[1,2] **and Xuesong Wang**[1,2]

[1]*Engineering Research Center of Intelligent Control for Underground Space, Ministry of Education, China University of Mining and Technology, Xuzhou 221116, China*
[2]*School of Information and Control Engineering, China University of Mining and Technology, Xuzhou 221116, China*

Correspondence should be addressed to Xuesong Wang; wangxuesong@cumt.edu.cn

Received 10 June 2021; Revised 9 July 2021; Accepted 28 July 2021; Published 13 August 2021

Academic Editor: Kelvin Wong

The deep neural network has achieved good results in medical image superresolution. However, due to the medical equipment limitations and the complexity of the human body structure, it is difficult to reconstruct clear cardiac magnetic resonance (CMR) superresolution images. To reconstruct clearer CMR images, we propose a CMR image superresolution (SR) algorithm based on multichannel residual attention networks (MCRN), which uses the idea of residual learning to alleviate the difficulty of training and fully explore the feature information of the image and uses the back-projection learning mechanism to learn the interdependence between high-resolution images and low-resolution images. Furthermore, the MCRN model introduces an attention mechanism to dynamically allocate each feature map with different attention resources to discover more high-frequency information and learn the dependency between each channel of the feature map. Extensive benchmark evaluation shows that compared with state-of-the-art image SR methods, our MCRN algorithm not only improves the objective index significantly but also provides richer texture information for the reconstructed CMR images, and our MCRN algorithm is better than the Bicubic algorithm in evaluating the information entropy and average gradient of the reconstructed image quality.

1. Introduction

The heart is the core organ that ensures the continuation of human life and metabolism. Its main function is to provide power for blood flow in the body through the contraction pressure of the heart muscle. Cardiac magnetic resonance (CMR) imaging [1] is an important technique for the functional analysis of the heart. It is suitable for the accurate assessment and analysis of the local and global function of cardiac tissue structures, and it plays an important role in assisting physicians in diagnosis and treatment and improving diagnostic accuracy. The CMR imaging can perform multiphase imaging in the time domain to form a dynamic image sequence of the cardiac cycle. Based on the imaging results, cardiac function evaluation indicators, such as ejection fraction, myocardial mass, and myocardial thickness, can be obtained, which is convenient for medical experts to analyze the systolic function of the heart and diagnose diseases [2–4]. However, the CMR images are very different from conventional images. Due to the performance limitations of medical equipment and the complexity of human body structure, the CMR images often have very low resolution and have a lot of noise, which directly affects expert judgment of heart disease [5]. Therefore, there are an urgent need and practical significance for the study of image SR reconstruction algorithms for CMR images.

With the deepening of research on SR tasks, many SR algorithms have emerged. These algorithms can be roughly divided into three categories: interpolation-based methods [6], reconstruction-based methods [7], and learning-based methods [8]. Since deep learning has achieved outstanding performance in various fields of computer vision in recent years, learning-based SR methods have also become a hot spot in superresolution technology research, whose purpose to recover high-resolution (HR) images from low-resolution (LR) images. Dong et al. [9] proposed the SR convolutional neural network (SRCNN) and achieved excellent performance. On this basis, Dong et al. [10] improved the

SRCNN algorithm and proposed the fast SR convolutional neural networks (FSRCNN) to accelerate the training speed of the network. Kim et al. [11] proposed the superresolution using very deep convolutional network (VDSR), which uses the idea of residual error to alleviate the problem of gradient disappearance or gradient explosion. Since only the high frequency of the image is learned information, the convergence speed is significantly improved; at the same time, a larger receptive field is used in VDSR to improve the effect and multiscale issues considered in the single model.

After that, Kim et al. [12] considered the problem of parameter scale and proposed the deep recursive convolutional network (DRCN), which uses a recursive network structure to share parameters between network structures, which effectively reduces the difficulty of training; in addition, the authors also use skip connection and integration strategies to further improve performance. Subsequently, Shi et al. [13] proposed the efficient subpixel convolutional neural network (ESPCN), which uses LR images as input and uses subpixel convolutional layers at the back end of the network structure to implicitly map LR images to HR images, effectively reducing computational complexity and improving reconstruction efficiency. Lai et al. [14] proposed the Laplacian pyramid networks (LapSRN), the idea of Laplace pyramid is introduced into deep learning, and the experimental results prove the superiority of step-by-step sampling operation. In addition, the residual results predicted at each level are monitored during the training process, which further improves the performance. Lim et al. [15] proposed the enhanced deep residual networks for single image superresolution (EDSR) by removing the redundant modules in the literature [16] and using the L1 norm as the loss function. Zhang et al. [17] proposed the residual channel attention network (RCAN), by using the channel attention mechanism, a feature channel with rich information can be selected. The above network structures are mostly feed-forward structures, ignoring the interdependence of HR images and LR images and the error when upsampling LR images. In addition, Haris et al. [18] proposed the deep back-projection networks (DBPN), which uses the upsampling interconnection strategy and error feedback mechanism to learn the mutual mapping relationship between HR and LR and uses the deep cascade structure to cascade different stages of HR and LR features to reconstruct HR images. However, it is neglected that when the HR image is reconstructed, the contribution of the HR features generated at different stages may be different, and the reconstructed HR is too smooth due to the increase of the network depth, and some high-frequency information is lost.

In order to reconstruct a clearer SR image of CMR images, we propose the multichannel residual attention network (MCRN); our contributions are three-fold:

(1) We propose the multichannel residual dilated convolution structure by combining the idea of dilated convolution and residual learning, which can efficiently extract the multichannel contextual information of CMR image

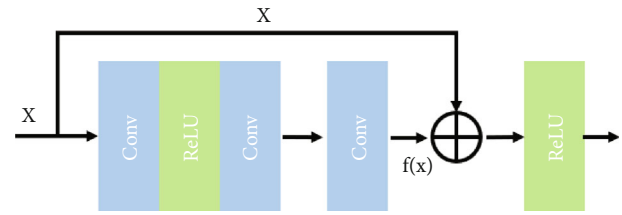

Figure 1: Structure of residual learning.

(2) We design the residual framework of long and short skip connections to improve the accuracy of image feature information acquisition

(3) We introduce the attention mechanism to automatically allocate attention resources to the feature maps generated at each stage of the residual back-projection block and each channel of the feature map

2. Related Work

2.1. Residual Learning. When training a very deep network structure, since the initialization parameters are very close to zero, it is easy to cause gradient dispersion when the network reversely broadcasts the update parameters. This makes deepening the network structure not only unable to improve network performance but also even worse. In response to this problem, He et al. [19] proposed the residual net (ResNet), using the idea of residual learning to alleviate the problem of gradient dispersion. The main idea is to add a direct connection channel to the network, allowing a certain percentage of the previous network output to be retained. However, there are certain difficulties in learning identity mapping. To avoid learning the parameters of identity mapping, the ResNet uses the network structure shown in Figure 1, namely, $H(x) = F(x) + x$. It can be converted to $F(x) = H(x) - x$, where $F(x)$ is the residual term. When the residual term is $F(x) = 0$, the identity mapping $H(x) = x$ can be easily constructed. Compared to learning the identity mapping $H(x) = x$, learning $F(x) = 0$ is easier.

2.2. Deep Back-Projection Network. Haris et al. [18] proposed the deep back-projection networks (DBPN), which use an iterative back-projection method to learn the mapping relationship between LR and HR images and use an error feedback mechanism to correct the reconstruction between LR and HR images error. According to Figure 2, the DBPN algorithm contains several serial upsampling layers, and the spatial detail information in the picture is extracted through continuous degradation and SR reconstruction of the picture. For the input LR image, first perform initial feature extraction to obtain shallow features, and then use several iterative up-block and down-block to learn the reconstruction error between HR and LR features, and finally the HR feature maps generated in the previous stages are cascaded and the predicted image is reconstructed. In addition, each back-projection includes up-block and down-block operations, where up-block and down-block are implemented using a deconvolution layer and a convolution layer, respectively.

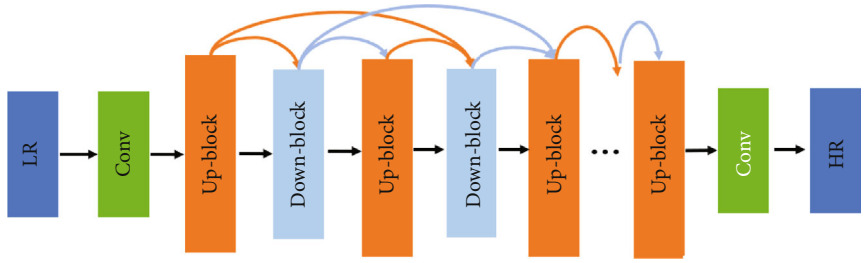

Figure 2: The architect of deep back-projection network.

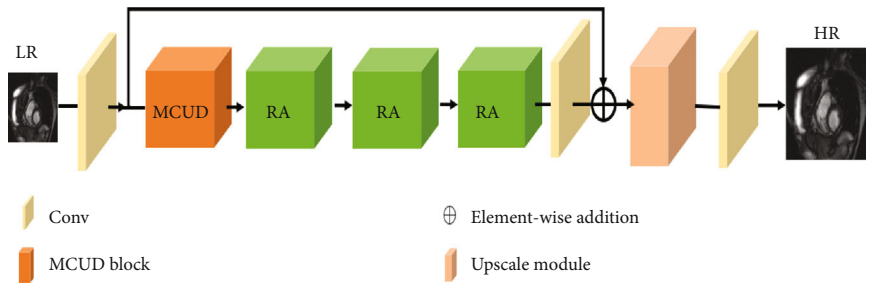

Figure 3: The architect of multichannel residual attention network.

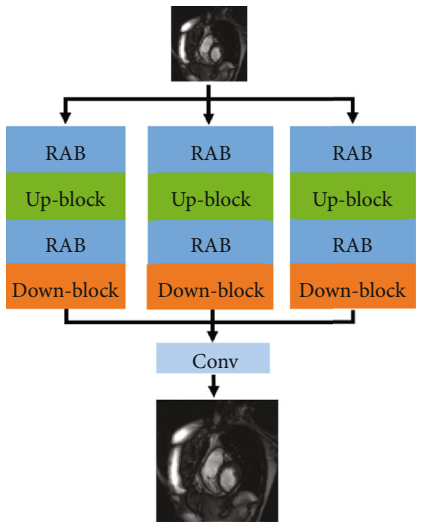

Figure 4: The architect of multichannel up-block and down-block residual modules.

3. Methodology

Aiming at the problem of loss of feature information and gradient dispersion in the learning process caused by the deeper network structure, as can be seen from Figure 3, we propose the multichannel residual attention network structure, which mainly includes initial layer, multichannel up-block and down-block residual attention module (MCUD), residual attention module (RA), and reconstruction layer.

3.1. Multichannel Up-Block and Down-Block Residual Attention Modules. To solve the problem of high-frequency information loss the longitudinal deepening network, a multichannel residual cavity convolutional network was proposed, as shown in Figure 4. Combining the idea of dilated convolution and residual error, it can obtain the multichannel background information of CMR images more effectively. Furthermore, to increase the receptive field without pooling loss information, so that each convolution output contains a larger range of information, we have introduced dilated convolution in the multichannel up-block and down-block residual modules, the difference is that the dilated convolution uses expansion rates of 1, 3, and 5 to add different receptive fields, and the parameters are shown in Table 1.

Regarding the up-block module, the input of the up-block is the output of the down-block in the previous projection unit cascaded with this projection unit, that is, the input of n up-blocks is $[L^1,\cdots,L^{n-1}]$, and then the input of the projection block is cascaded together using the cascade layer. At the same time, to reduce the amount of calculation, a convolutional layer with a convolution kernel size of $1 * 1$ is used to reduce the dimensionality of the feature map to obtain feature L^{n-1}, and then perform upsampling and downsampling operations on L^{n-1} to obtain H_0^n and L_0^n, respectively, and calculate L^{n-1} and L_0^n, and use e_n^1 to correct the mapping relationship between HR features and LR features.

The up-block module is defined as follows:

$$\text{Scale up}: H_0^n = \left(L^{n-1} * p_n\right)\uparrow^s, \tag{1}$$

$$\text{Scale down}: L_0^{\mathrm{n}} = \left(H_0^n * g_n\right)\downarrow_s, \tag{2}$$

$$\text{Residual}: e_n^l = L_0^n - L^{n-1}, \tag{3}$$

$$\text{Scake residual up}: H_1^n = \left(e_n^1 * q_n\right)\uparrow^s, \tag{4}$$

$$\text{Output feature map}: H^n = H_0^n + H_1^n. \tag{5}$$

Regarding the down-block module, the input of the down-block is also the result of cascading the residual learning of the previous projection blocks of this projection unit,

Table 1: The feature size of the MCRN for CMR images SR.

Network components	Kernel size	Stride	Padding	Input size	Output size
Initial layer	3∗3	1	1	H∗W∗1	H∗W∗64
RAB					
Conv 1	3∗3	1	1	H∗W∗64	H∗W∗64
Conv 2	1∗1	1	0	H∗W∗64	H∗W∗4
Conv 3	1∗1	1	0	H∗W∗4	H∗W∗64
Up-block					
DeConv	4∗4	2	1	H∗W∗64	H∗W∗128
Conv	4∗4	2	1	H∗W∗128	H∗W∗64
DeConv	4∗4	2	1	H∗W∗64	H∗W∗128
Down-block					
Conv	4∗4	2	1	H∗W∗128	H∗W∗64
DeConv	4∗4	2	1	H∗W∗64	H∗W∗128
Conv	4∗4	2	1	H∗W∗128	H∗W∗64
Middle layer	3∗3	1	1	H∗W∗64	H∗W∗64
Upsample	3∗3	1	1	H∗W∗64	2H∗2 W∗64
Reconstruction layer	3∗3	1	1	2H∗2 W∗64	2H∗2 W∗1

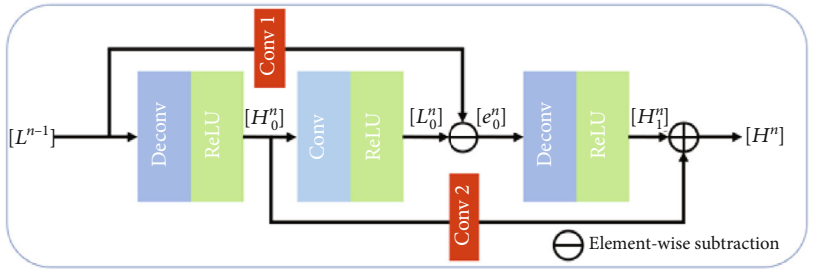

(a) Up-block module

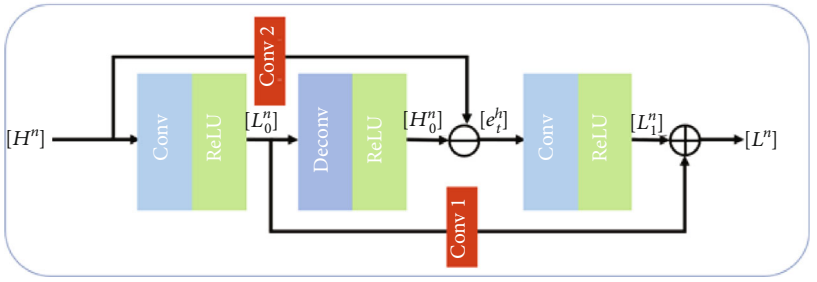

(b) Down-block module

Figure 5: Structure of up- and down-block modules.

and the input feature information is sequentially cascaded and linearly mapped to obtain the feature map H^n. Subsequently, the down- and upsampling operations are sequentially performed, and the reconstruction error e_h^n is calculated, and the secondary reconstruction error is used to guide the reconstruction of the LR feature map.

The down-block module is defined as follows:

$$\text{Scale down}: L_1^n = (H_2^n * g_n)\downarrow_s, \tag{6}$$

$$\text{Scale up}: H_3^n = (L_1^n * p_n)\uparrow^s, \tag{7}$$

$$\text{Residual}: e_h^n = H_3^n - (H_2^n * k_n), \tag{8}$$

$$\text{Scale residual up}: L_2^n = (e_h^n * g_n)\downarrow_s, \tag{9}$$

$$\text{Output feature map}: L^n = L_0^n + L_1^n, \tag{10}$$

where $*$ is the convolution operator, $\uparrow^s$ and $\downarrow_s$ are the upsampling and downsampling operations with scale factor s, respectively, p_n is the upsampling deconvolutional layer of

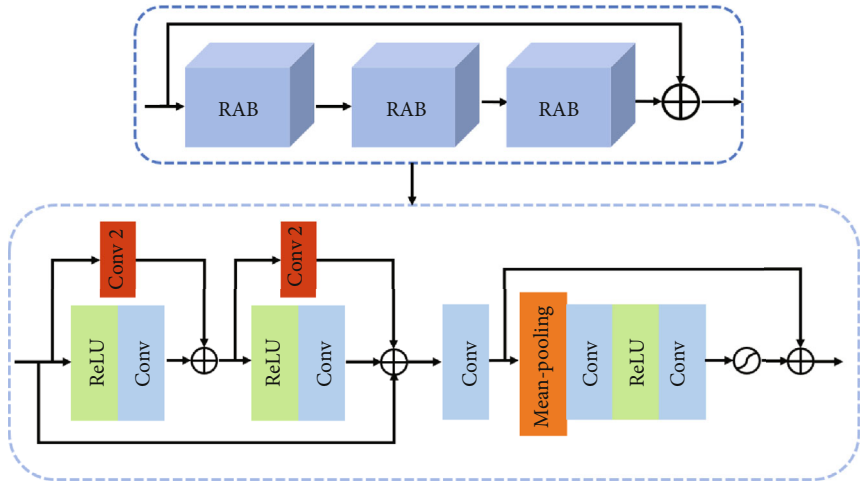

Figure 6: Structure of residual attention module.

the n-th up-block and down-block (UD), g_n is the downsampling convolutional layer of the n-th UD, q_n is 128-dimensional feature fusion layer of the n-th UD, and k_n denotes the n-th UD of 64-dimensional feature fusion layer [20] as shown in Figure 5.

3.2. Residual Attention Module. To better extract the feature information of the CMR image, the MCRN model deepens the number of network layers. Further, the residual attention module (RA) contains 3 residual attention block modules (RAB), and the network structure is shown in Figure 6. As the number of network layers deepens, the residual structure is introduced. There are two reasons for introducing the residual structure here: one is that the network deepening has network degradation problems, and learning residuals can reduce the impact of such problems in deep network training. Furthermore, since there are a lot of similar low-frequency information between HR images, using the residual structure can reduce repeated learning of similar low-frequency information, speed up the network convergence speed, and save computing time. Secondly, the attention mechanism is introduced to allocate different attention resources to the feature maps in different stages of interconnection and different channels of different feature maps, to learn deeper feature information.

3.3. Reconstruction Layer. In the high-power reconstruction part, first use $3 * 3$ convolution to sort and filter redundant information to reconstruct the optimal sparse network structure, and then use subpixel convolution to upsample T to the target multiple γ. Finally, the mapping from I^{LR} to I^{SR} is completed through a layer of $3 * 3$ convolution to generate a clear SR image; the specific formula is as follows:

$$I^{\mathrm{SR}} = \sigma\,\omega^{l}_{3\times 3} \times \mathrm{SF}\,\sigma\,\omega^{l-2}_{3\times 3} \times T + b^{l-2} + b^{l}, \tag{11}$$

where I^{SR} represents the predicted HR image, the symbol $\times$ represents the convolution operator, the symbol + represents the pixel-by-pixel addition operator, SF x represents the subpixel convolution operation of rearranging the combined

Table 2: Average PSNR/SSIM of various SSIR methods; the best and second-best results are in bold and italics.

Algorithm	Scale	Set 5		Set 14		Urban 100	
		PSNR	SSIM	PSNR	SSIM	PSNR	SSIM
Bicubic [6]	2×	33.69	0.931	30.25	0.870	26.88	0.841
A+ [27]	2×	36.60	0.955	32.32	0.906	29.25	0.895
SCN [28]	2×	36.58	0.954	32.35	0.905	29.52	0.897
SRCNN [9]	2×	36.72	0.955	32.51	0.908	29.53	0.896
FSRCNN [10]	2×	37.05	0.956	32.66	0.909	29.88	0.902
VDSR [11]	2×	37.53	*0.959*	33.05	0.913	30.77	*0.914*
DRCN [12]	2×	37.63	*0.959*	33.06	0.912	30.76	*0.914*
LapSRN [14]	2×	37.52	*0.959*	33.08	0.913	30.41	0.910
DRRN [29]	2×	*37.74*	*0.959*	*33.23*	*0.914*	*31.23*	**0.919**
MCRN (ours)	2×	**37.88**	**0.961**	**33.63**	**0.919**	**31.27**	**0.919**
Bicubic [6]	3×	30.41	0.869	27.79	0.775	24.46	0.735
A+ [27]	3×	32.62	0.909	29.15	0.820	26.05	0.799
SCN [28]	3×	32.62	0.908	29.16	0.818	26.21	0.801
SRCNN [9]	3×	32.78	0.909	29.32	0.823	26.25	0.801
FSRCNN [10]	3×	33.18	0.914	29.37	0.824	26.43	0.808
VDSR [11]	3×	33.67	0.921	29.78	0.832	27.14	0.829
DRCN [12]	3×	33.83	0.922	29.77	0.832	27.15	*0.828*
LapSRN [14]	3×	33.82	0.922	29.87	0.832	27.07	*0.828*
DRRN [29]	3×	**34.03**	*0.924*	*29.96*	*0.835*	**27.53**	0.764
MCRN (ours)	3×	*33.99*	**0.925**	**30.28**	**0.844**	*27.27*	**0.830**
Bicubic [6]	4×	28.43	0.811	26.22	0.715	23.14	0.658
A+ [27]	4×	30.32	0.860	27.34	0.751	24.34	0.721
SCN [28]	4×	30.41	0.863	27.39	0.751	24.52	0.726
SRCNN [9]	4×	30.50	0.863	27.52	0.753	24.53	0.725
FSRCNN [10]	4×	30.72	0.866	27.61	0.755	24.62	0.728
VDSR [11]	4×	31.35	0.883	28.02	0.768	25.18	0.754
DRCN [12]	4×	31.54	0.884	28.03	0.768	25.14	0.752
LapSRN [14]	4×	31.54	0.885	28.19	*0.772*	25.21	0.756
DRRN [29]	4×	**31.68**	**0.888**	*28.21*	*0.772*	**25.44**	**0.764**
MCRN(ours)	4×	*31.67*	*0.887*	**28.45**	**0.783**	*25.25*	*0.759*

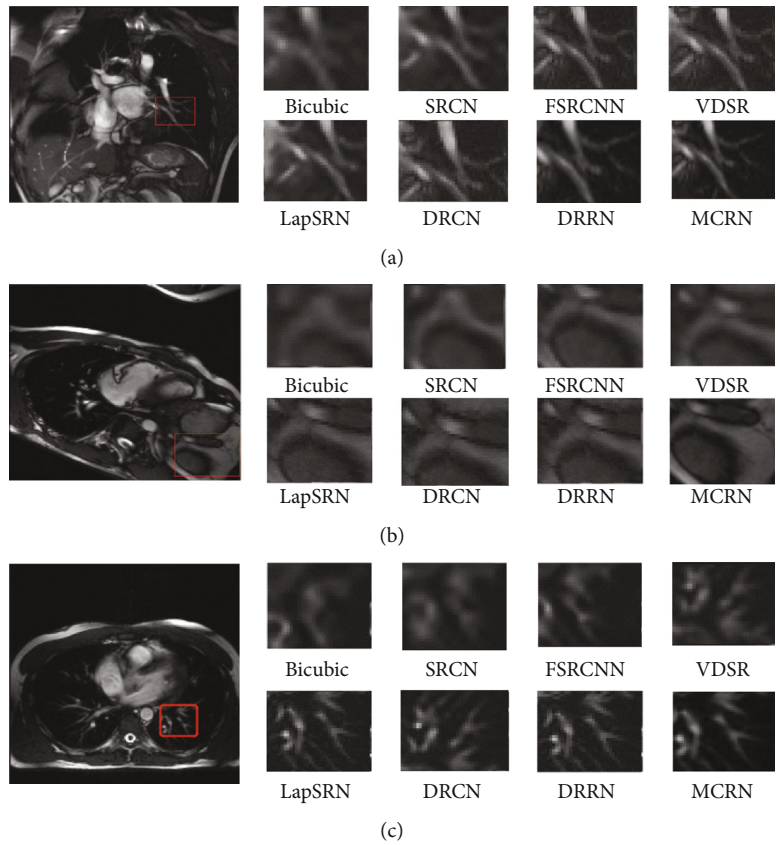

Figure 7: Comparison of rendering of images with superresolution magnification of 4 under our MCRN and other state-of-art methods. (a) Aorta in short axis orientation ($3 \times 11 \times 25$, coronal), (b) aorta in short axis orientation ($3 \times 11 \times 25$, axial), and (c) heart imaged in 3 orthogonal orientations (axial).

pixels, and the l in the variable superscript is the last one in the network convolutional layer and $l-2$ is the first convolutional layer of the reconstruction part.

4. Experiment and Analysis

4.1. Dataset and Training Details. Owing to the relatively deep network, the algorithm needs to use a larger training set to train better results. T91 [21] dataset and Berkeley Segmentation Dataset 500 (BSD500) are selected, respectively, with a total of 591 images [5]. In order to make full use of the depth image, the dataset image is rotated by 90°, 180°, and 270° and scaled according to the coefficients of 0.9, 0.8, and 0.7 and then saved the picture; a total of 9456 images are generated; and the test dataset uses Set5 [20], Set14 [22], and Urban100 [23] datasets.

To build a CMR diagnosis model based on deep learning, we tested it on the public CMR datasets. We used the cardiac MRI dataset [24], which is the medical imaging data of atrium in patients with heart disease, including cardiac MR images of 33 subjects, with a total of 7980 images (Cardiac MRI dataset: http://www.cse.yorku.ca/~mridataset/).

Furthermore, our algorithm was trained on Ubuntu 16.04, CUDA Toolkit 10.0, PyTorch 1.20, python 3.7, and GPU NVIDIA GeForce RTX 1080Ti. In addition, the initial learning rate is set to 10^{-4}, the Adam optimizer was set with $\beta_1 = 0.9, \beta_2 = 0.999$, $\varepsilon = 10^{-8}$, and L_1-normalization was used as the loss function. To evaluate the performance of the proposed MCRN, we use the peak signal-to-noise ratio (PSNR) [25] and structural similarity index (SSIM) [26] as the evaluating metrics. The specific operations of PSNR and SSIM are shown in Equations (12) and (13).

$$\mathrm{PSNR} = 10 \lg \frac{MN}{\|I_H - I_S\|^2}, \tag{12}$$

where M and N represent the sizes of the HR image and the SR image.

$$\mathrm{SSIM} = \frac{(2\mu_H\mu_S + C_1)(\sigma_{HS} + C_2)}{(\mu_H{}^2 + \mu_S{}^2 + C_1)(\sigma_H{}^2 + \sigma_S{}^2 + C_2)}, \tag{13}$$

where μ_H and μ_S represent the average grey values of the HR image and the SR image, σ_H and σ_S represent the variances of the HR image and the SR image, and σ_{HS} denotes the covariance of the HR image and the SR image.

4.2. Comparison with Other State-Of-The-Art Algorithms. We compare our method with 9 state-of-the-art SR algorithms: Bicubic [6], A+ [27], SCN [28], SRCNN [9], FSRCNN [10], VDSR [11], DRCN [12], LapSRN [14], and DRRN [29].

Table 2 shows the comparison of experimental results with an amplification factor of 2, 3, and 4. It can be found from Table 2 that when the scaling factors are 2, 3, and 4, the algorithm proposed in this paper achieves the best performance in PSNR and SSIM on each dataset. When the scaling factor is 2, the algorithm in this paper achieves the optimal reconstruction effect for each index on each dataset. Among them, when the scaling factor is 2 on the Set14 dataset, the PSNR improvement of this algorithm is the most obvious compared with other algorithms. It reaches 33.72 dB, which is 0.40 dB higher than the PSNR of the suboptimal DRRN algorithm.

As can be seen from the Figure 7, the image reconstructed by Bicubic [3] appears severely blurred, and the details of CMR cannot be observed. The image reconstructed by SRCNN [9], FSRCNN [10], and LapSRN [15] appears severely distorted, and the details of the information are not enough. Moreover, the result of the reconstruction of VDSR [18], DRCN [13], and DRRN [19] algorithms obtains a better visual experience, and there is still a lack of detailed information. In fact, compared with state-of-the-art methods, our MCRN algorithm restores the details of the original image and improves the clarity of the CMR image, indicating that our model shows obvious superiority in both objective indicators and visual effects.

5. Conclusion

In this paper, we propose a CMR image superresolution algorithm based on multichannel residual attention network (MCRN), which mainly uses the back-projection method and combines residual learning and attention mechanisms to alleviate the problems of insufficient feature information and loss of high-frequency information in the learning process. At the same time, the difference between feature maps is fully utilized, so that more useful high-frequency information can be discovered when reconstructing the predicted image. The experimental results prove the superiority of the algorithm in the PSNR and SSIM indicators, and the detailed information of the predicted CMR image is more abundant, which effectively improves the clarity of the CMR image and can effectively assist the CMR diagnosis and quantitative evaluation. For future implementation, we will consider improving the image reconstruction part so that the reconstruction part can make full use of the characteristics of network learning and achieve the excellent image reconstruction effects.

Data Availability

The image data used to support the findings of this study have been deposited in the Cardiac MRI Dataset repository (http://www.cse.yorku.ca/~mridataset/) and AMRG Cardiac Atlas repository (http://www.cardiacatlas.org/studies/amrg-cardiac-atlas/).

Conflicts of Interest

The authors declare that they have no conflicts of interest.

Acknowledgments

This work was supported by the National Natural Science Foundation of China (Grant Nos. 61772532 and 61976215).

References

[1] N. Rashedi, L. Landeras, V. Mor-Avi et al., "Validation of non-contrast multiple overlapping thin-slab 4D-flow cardiac magnetic resonance imaging," *Magnetic Resonance Imaging*, vol. 74, pp. 223–231, 2020.

[2] M. A. Fagiry, I. A. Hassan, and Z. Mustafa, "Two-dimensional echocardiography in the diagnosis of ischemic heart disease," *Journal of Radiation Research and Applied Sciences*, vol. 12, pp. 177–185, 2020.

[3] N. Iannino, K. Fischer, M. Friedrich, T. Hafyane, F. P. Mongeon, and M. White, "Myocardial vascular function assessed by dynamic oxygenation-sensitive cardiac magnetic resonance imaging long-term following cardiac transplantation," *Transplantation*, vol. 105, no. 6, pp. 1347–1355, 2021.

[4] E. Martín-González, T. Sevilla, A. Revilla-Orodea, P. Casaseca-de-la-Higuera, and C. Alberola-López, "Groupwise non-rigid registration with deep learning: an affordable solution applied to 2D cardiac cine MRI reconstruction," *Entropy*, vol. 22, no. 6, p. 687, 2020.

[5] D. Qiu, L. Zheng, J. Zhu, and D. Huang, "Multiple improved residual networks for medical image super-resolution," *Future Generation Computer Systems*, vol. 116, pp. 200–208, 2021.

[6] R. G. Keys, "Cubic convolution interpolation for digital image processing," *IEEE Transactions on Acoustics, Speech, and Signal Processing*, vol. 29, no. 6, pp. 1153–1160, 1981.

[7] D. Y. Ge, X. F. Yao, and Z. T. Lian, "Binocular vision calibration and 3D reconstruction with an orthogonal learning neural network," *Multimedia Tools and Applications*, vol. 75, no. 23, pp. 15635–15650, 2016.

[8] Y. Zhang, L. Sun, C. Yan, X. Ji, and Q. Dai, "Adaptive residual networks for high-quality image restoration," *IEEE Transactions on Image Processing*, vol. 27, no. 7, pp. 3150–3163, 2018.

[9] C. Dong, C. C. Loy, K. He, and X. Tang, "Image super-resolution using deep convolutional networks," *IEEE Transactions on Pattern Analysis and Machine Intelligence*, vol. 38, no. 2, pp. 295–307, 2016.

[10] C. Dong, C. C. Loy, and X. Tang, "Accelerating the super-resolution convolutional neural network," in *European Conference on Computer Vision*, pp. 391–407, Amsterdam: Springer, 2016.

[11] J. Kim, J. Kwon Lee, and L. K. Mu, "Accurate image super resolution using very deep convolutional networks," in *2016 IEEE Conference on Computer Vision and Pattern Recognition (CVPR)*, pp. 1646–1654, Las Vegas, NV, USA, 2016.

[12] J. Kim, J. Kwon Lee, and K. Mu Lee, "Deeply-recursive convolutional network for image super-resolution," in *Proceedings of the IEEE Conference on Computer Vision and Pattern Recognition*, pp. 1637–1645, Las Vegas, NV, USA, 2016.

[13] W. Shi, J. Caballero, F. Huszar et al., "Real-time single image and video super-resolution using an efficient sub-pixel convolutional neural network," in *IEEE Conference on Computer Vision and Pattern Recognition*, pp. 1874–1883, Las Vegas, 2016.

[14] W.-S. Lai, J.-B. Huang, N. Ahuja, and M.-H. Yang, "Deep Laplacian pyramid networks for fast and accurate super

resolution," in *IEEE Conference on Computer Vision and Pattern Recognition*, pp. 5835–5843, Las Vegas, 2017.

[15] B. Lim, S. Son, H. Kim, S. Nah, and K. M. Lee, "Enhanced deep residual networks for single image super-resolution," in *IEEE Conference on Computer Vision and Pattern Recognition Workshops (CVPRW)*, pp. 136–144, Honolulu, HI, USA, 2017.

[16] C. Ledig, L. Theis, F. Huszar et al., "Photo-realistic single image super-resolution using a generative adversarial network," in *2017 IEEE Conference on Computer Vision and Pattern Recognition (CVPR)*, pp. 105–114, Honolulu, HI, USA, 2017.

[17] Y. Zhang, K. Li, K. Li, L. Wang, B. Zhong, and Y. Fu, "Image super-resolution using very deep residual channel attention networks," in *Computer Vision – ECCV 2018*, vol. 11211, no. 7-pp. 294–310, Springer, 2018.

[18] M. Haris, G. Shakhnarovich, and N. Ukita, "Deep back-projection networks for super-resolution," in *2018 IEEE/CVF Conference on Computer Vision and Pattern Recognition*, pp. 1664–1673, Salt Lake City, UT, USA, 2018.

[19] K. He, X. Zhang, S. Ren, and J. Sun, "Deep residual learning for image recognition," in *IEEE Conference on Computer Vision and Pattern Recognition*, pp. 770–778, Las Vegas, 2016.

[20] M. Bevilacqua, A. Roumy, C. Guillemot, and M.-l. A. Morel, "Low-complexity single-image super-resolution based on non-negative neighbor embedding," in *British Machine Vision Conference*, pp. 1–10, Guildford, 2012.

[21] J. Kim, J. K. Lee, and K. M. Lee, "Accurate image super-resolution using very deep convolutional networks," in *Computer Vision and Pattern Recognition*, pp. 1646–1654, Las Vegas, NV, USA, 2016.

[22] R. Zeyde, M. Elad, and M. Protter, "On single image scale-up using sparse-representations," in *International Conference on Curves & Surfaces*, pp. 711–730, Springer, Avignon, 2010.

[23] J. B. Huang, A. Singh, and N. Ahuja, "Single image super-resolution from transformed self-exemplars," in *IEEE Conference on Computer Vision and Pattern Recognition*, pp. 5197–5206, Boston, 2015.

[24] Z. Wang, A. C. Bovik, H. R. Sheikh, and E. P. Simoncelli, "Image quality assessment: from error visibility to structural similarity," *IEEE Transactions on Image Processing*, vol. 13, no. 4, pp. 600–612, 2004.

[25] K. Zhang, W. Zuo, and L. Zhang, "Learning a single convolutional super-resolution network for multiple degradations," in *2018 IEEE/CVF conference on computer vision and pattern recognition*, pp. 3262–3271, Salt Lake City, UT, USA, 2018.

[26] D. Qiu, S. Zhang, Y. Liu, J. Zhu, and L. Zheng, "Super-resolution reconstruction of knee magnetic resonance imaging based on deep learning," *Computer Methods and Programs in Biomedicine*, vol. 187, article 105059, 2020.

[27] R. Timofte, V. De Smet, and L. Van Gool, "A+: adjusted anchored neighborhood regression for fast super-resolution," in *Asian Conference on Computer Vision*, pp. 111–126, Springer, Cham, 2014.

[28] Z. Wang, D. Liu, J. Yang, W. Han, and T. Huang, "Deep networks for image super-resolution with sparse prior," in *2015 IEEE International Conference on Computer Vision (ICCV)*, pp. 1–15, Santiago, Chile, 2015.

[29] Y. Tai, J. Yang, and X. Liu, "Image super-resolution via deep recursive residual network," in *2017 IEEE Conference on Computer Vision and Pattern Recognition (CVPR)*, pp. 2790–2798, Honolulu, HI, USA, 2017.